UNIVERSITY OF SOUTHAMPTON

FACULTY OF PHYSICAL SCIENCES AND ENGINEERING]

Optoelectronics Research Centre

Cryogenically-Cooled Neodymium-Doped Solid-State Lasers

by

Sung Jin Yoon

Thesis for the degree of Doctor of Philosophy

December 2016

UNIVERSITY OF SOUTHAMPTON

ABSTRACT

FACULTY OF PHYSICAL SCIENCES AND ENGINEERING

Optoelectronics Research Centre

Thesis for the degree of Doctor of Philosophy

Cryogenically-Cooled Neodymium-Doped Solid-State Lasers

by Sung Jin Yoon

The central idea of this thesis is to study cryogenically-cooled neodymium (Nd^{3+}) doped lasers operating on the $^4F_{3/2} \rightarrow {}^4I_{9/2}$ transition around 0.95 microns, known as a quasi-four-level (QFL) transition. The QFL transition has unavoidable reabsorption loss at room temperature that introduces additional saturable losses into the laser cavity and must be overcome to achieve efficient operation. In general, this particular transition has lower gain than the dominant four-level $^4F_{3/2} \rightarrow {}^4I_{11/2}$ transition, around 1 micron. While the advantages of cryogenically cooled gain media have been recognised since the birth of the laser, in more recent times there has been a trend in exploiting these advantages for power-scaling QFL lasers, such as Yb-doped gain media.

The first part of the thesis explores the extensive characterization of the spectroscopic properties of Nd^{3+} doped crystals. The present work tracks the spectroscopic changes over the temperature range from 77K to 450K. A number of crystals (YAG, GSAG, YVO4, GdVO4, KGW, YLF) hosting Nd^{3+} ions have been studied. The absorption cross section spectra for 800nm and 870nm bands were determined with 0.1nm resolution. The absorbance was measured exploiting the Beer-Lambert law and a bespoke set-up using two separate broadband light sources. The fluorescence spectrum was collected and characterized for the transitions to $^4I_{9/2}$, $^4I_{11/2}$, and $^4I_{13/2}$ energy-levels from the metastable level, $^4F_{3/2}$, from which we calculated the stimulated emission cross section of the various crystals and over the temperature range by applying the Füchtbauer-Ladenburg equation, with the measured fluorescence lifetime. Furthermore, in this report we determine the energy transfer upconversion parameters, for the same set of crystals, using the Z-scan technique. The technique measures the change in transmittance of a probe beam tuned to an absorption peak of crystal sample. The measured transmitted power changes as the intensity incident on the crystal is varied via scanning the beam size and correlated to the saturation intensity through a spatially-dependent rate equation model, we found excellent fit between experiment and simulation.

The second part of this thesis reports the development of cryogenic lasers. The design strategies are described by end-pumped and side-pumped systems, with two different crystal geometries reported. Conventional radially-cooled rods are first reported with an end-pumping arrangement, then with a slab (Brewster angled, and afterwards AR coated), and finally a side-pumped Zigzag slab configuration. A rod geometry is tested using a Nd:YAG and a Nd:GSAG crystal for generation of QFL laser emission. The first end-pumped Nd:YAG rod have demonstrated 3.8W at 946nm for 12.8W of pump being absorbed and slope efficiency of 47%. Similar experiment was duplicated with Nd:GSAG rod demonstrating 3.5W at 942nm for 10.5W of pump absorbed. Both suffered significant modal instability during laser oscillation, which afterwards for the Nd:GSAG crystal was found to be due to AR-coating damage. A Nd:YAG slab crystal was tested for the both pumping configurations, using a wavelength-locked 869nm diode bar as a pump source. For this in-band pump-source, the quantum defect is only 8%, in the case of the main QFL transition. A top/bottom-face cooled slab presented effective mitigation of the previously observed modal stability, assumed to be associated with reducing birefringence losses. Despite the coating damage/contamination, which was repeatedly encountered, 946nm emission for both configurations was demonstrated. An end-pumping configuration has demonstrated 5.5W for 13.6W of absorbed pump with 47% slope efficiency. While the side-pumping the zigzag slab produced 6.3W for 30W of absorbed pump with 30% slope efficiency. It is expected that with improvements in the cleanliness within the vacuum chamber used for the cryogenic setup, better results in terms of slope efficiency, output power and beam quality will be realised in the near future.

Table of Contents

List of Tables

List of Figures

DECLARATION OF AUTHORSHIP

I, Sung Jin Yoon declare that this thesis and the work presented in it are my own and has been generated by me as the result of my own original research. Cryogenically-cooled Neodymium-doped Solid-state Lasers

I confirm that:

1. This work was done wholly or mainly while in candidature for a research degree at this University;
2. Where any part of this thesis has previously been submitted for a degree or any other qualification at this University or any other institution, this has been clearly stated;
3. Where I have consulted the published work of others, this is always clearly attributed;
4. Where I have quoted from the work of others, the source is always given. With the exception of such quotations, this thesis is entirely my own work;
5. I have acknowledged all main sources of help;
6. Where the thesis is based on work done by myself jointly with others, I have made clear exactly what was done by others and what I have contributed myself;
7. Parts of this work have been published: see List of Publications on page 287

Signed: .....

Date: .....

Nomenclature

AR	Anti-reflection
ASE	Amplified spontaneous emission
BS	Beam splitter
BPP	Beam parameter product
CPFS	Coplanar pumped folded slab
CPW	Cold pressure welded
CR	Cross relaxation
CW	Continuous wave
DFB	Distributed Bragg reflector
DFB	Distributed feedback
DPSS	Diode pumped solid-state
DUV	Deep ultra violet
ESA	Excited state absorption
ETU	Energy transfer upconversion
FAC	Fast axis collimator
FL	Füchterbauer-Landenburg
FWHM	Full width half maximum
GSA	Ground state absorption
HR	High reflective
LED	Light emitting diode
LIDT	Laser induced damage threshold
LN	Liquid nitrogen
LNT	Liquid nitrogen temperature
NA	Numerical aperture
OC	Output coupler
OD	Optical density
OSA	Optical spectrum analyser
PD	Photodiode

PER	Polarization extinction ratio
QCW	Quasi-CW
QD	Quantum defect
Q-F-L	Quasi-four-level
RE	Rare Earth
RM	Reciprocity method
RT	Room temperature
ROC	Radius of curvature
SAC	Slow axis collimator
STD	Standard deviation
TEC	Thermo electric cooler
TIR	Total internal reflection
UHP	Ultra high pressure
UV	Ultraviolet
VBG	Volume Bragg grating
W_{CR}	CR coefficient
W_{ETU}	ETU coefficient
ZPL	Zero photon line
ZZ	Zigzag

Acknowledgements

First and foremost, I would like to express my gratitude to my supervisor, Dr Jacob Mackenzie for his invaluable support and discussion throughout the PhD course. This thesis would not be possible without his guidance and encouragement. I would like to acknowledge Prof Andy Clarkson and Prof David Shepherd for numerous useful technical discussion and constructive feedback.

I would like to acknowledge Dr Stephen Beecher for his precious advice and for insightful technical discussions. I thank Dr Wendell Bailey for his advice on vacuum technology and cryogenic crystal mount. I would like to thank group members of the PWSL and ASSS: Dr. Peter Shardlow, Dr Jae Daniel, Dr Alex Butler, Dr Jaclyn Chan, Dr Masaki Tokurakawa, Dr Matthew Eckold, Dr Jakub Szela, Dr Renpeng Yan, Dr Nikita Simakov, Mr Stan Vassilev, Dr Di Lin, Mr Henry Stenhouse, Dr Stefano Valle, Mr Antonin Bilaud, Mr Callum Smith, and Mr Robin Uren. Also, I would like to thank all the past office mates of Portakavin and B46/3026.

I am also grateful to acknowledge collaborators in physics workshop and ORC workshop. I would also like to acknowledge Mr Mark Scully for his generous support at mechanical workshop.

I would like to gratefully acknowledge the support of Charm Engineering and former company president Mr Han In-Soo for sponsoring the first half of my PhD course. I would like to thank PSK Inc. and vice chairman, Mr Park Kyoung-Soo for sponsoring the second half of my PhD study in ORC. I would like to thank Dr Kevin Lee for his inspiring encouragement towards my thesis work.

Special thanks to the past and present members of Southampton Korean Church for support and prayers. I would like to thank and proudly acknowledge my parents Yoon Jum-Bok, Lee Ju-Ok for their support and encouragement. My little daughter Jiah and UK-born son Jisoo are also deserve a big thank for filling a chapter of family time in Southampton. Special mention goes to Jiho, a new member of family on board. Finally I acknowledge my wife, Kang Hyun-Ha who dedicated her time and career to make companion in UK. I dedicate this thesis to her with great pleasure.

Chapter 1:

Introduction

1.1 Topic overview

The word LASER is the acronym of, Light Amplification by Stimulated Emission of Radiation, and it is the coherence provided by the stimulated emission of a laser, which distinguishes it from other natural light sources. In 1917, Albert Einstein established a theoretical approach on the quantum theory of radiation [1], where he described the effect of electro-magnetic radiation upon the electronic structure of atoms, defining the coefficients for absorption, spontaneous emission and stimulated emission. Stimulated emission is realized if population inversion, where majority of atoms elevated to higher energy state, could be achieved then the light could be amplified coherently. Population inversion is the event where a majority of atoms in a collective have been excited. The excited electrons are elevated to a higher stable energy state. The de-excitation by stimulated emission is caused by the replication of a passing photon of the right energy between the electronic energy states. Einstein proposed that light could be amplified with avalanching gain with the population inversion. First demonstration of laser was presented by Maiman using ruby as a gain media, pumped via a flash lamp in 1960 [2]. Since then researchers have developed many gain media consisting of a solid host material. One of most common solid state host is a YAG (yttrium aluminium garnet) which permits good thermal and optical properties [3]. Modern development of diode laser has dramatically improved the optical brightness. Diode laser has high electrical input to optical output efficiency of more than 50% [4], and have many attractive features for solid-state lasers such as narrow spectra below 3nm, better beam quality and longer lifetime than lamps, 10,000 hours [4]. The diode pumped system increases efficiency and beam quality by using selective pump spectra, that enables to match the narrow diode laser spectra at peak absorption line of gain media. The diode laser pump light is easily altered to allow spatial matching to laser signal. Thus diode laser enables to design various geometry of gain and allowed a major breakthrough for solid-state lasers. Pumping schemes classified by end pumping and side pumping geometry. Both methods have advantages and disadvantages, End-pumping enables matching the pump radiation with the resonating laser mode efficiently but requires quality coatings to reflect resonating wavelength and transmit the pump spectra. Side-pump provide pump light perpendicular to laser resonator, it usually has poor overlap however good overlap is

available upon operation system design. These two pumping geometries enable diverse geometry of gain medium, offering variety of spectral ranges and output powers.

Diode pumped solid state lasers (DPSS) performance has improved dramatically since their first demonstration in 1964 [5]. The DPSS has a number of advantages of establishing highly reliable, high power and adapting the efficient use of diode lasers as a pump source. Despite the potential efficiency of DPSS lasers, power scaling has is hindered by the thermal problems within the laser medium. The heat deposited in the crystal via high power diode laser becomes a major drawback affects beam quality and efficiency. Heat deposited in conventional rod or slab limits the output power due to the lack of thermal dissipation. Internal thermal gradient inside gain material is dependent on the thermal properties such as thermal conductivity (k) and temperature coefficient of refractive index (dn/dT). The thermo-optical aberrations add the unwanted lens in resonating cavity, also the thermal stress exceeds the physical strength of gain media causes a physical fracture, a catastrophic damage within the crystal. The thermal management is one of the key issues over the last decades motivating researchers to demonstrate various geometries and different crystals to design high power laser systems. Among the geometries that have been reported, two geometries are considered as good approaches for power scaling. One is thin disk lasers, designed to flow heat in one direction over a thin layer of gain [6] and waveguide laser. Fibre has a well demonstrated geometry of waveguide which raises output power by an order of magnitude every decade in between 1μm and 2μm using Ytterbium [7, 8], Erbium [9, 10] and Thulium [11, 12] as a doping material. Both fibre and thin disk uses its geometric advantages to reduce the pump-volume-to-cooling-surface ratio. The thermal load is spread over a long fibre which removes heat efficiently and hence temperature gradient in the core is much smaller than rod. Thin disk laser uses very thin active layer which has ~200μm mounted onto a heat sink. This scheme applies high pump density without temperature gradient changes within, thus reduce thermal distortion over laser signal round-trip. Cryogenic cooling of laser gain medium is an attractive approach to improve the laser performance. This is due to gain has significantly improves both thermo-optical properties and spectroscopic properties under cryogenic temperature [13].

Nd^{3+} doped laser output power is limited by thermal deposition on to crystal. It is due to the large amount of heat is accumulated near pump region. The stress induced from thermal distribution over crystal field that induces mechanical tension to the centre of pump field and outer regions. Quantum defect (QD) is regarded the main heating mechanism within non-radiative transitions between pump and lasing energy levels. Pump absorption and dopant concentration is linearly correlated. High absorption of pump result in larger heat deposition which induces greater

thermal stress and stepper gradient within the crystal. This is due to number of non-radiative decay process, which generate heat, involved in laser operation. These contributions are highly correlated to the population in metastable energy level, i.e. high pump power or high absorption coefficient. These mechanisms are upconversion, cross relaxation and excited state absorption (ESA). These mechanisms use excited electrons for other non-lasing transitions which adds additional heat load. The other source of heat generation is quantum efficiency, as some of 'dead Nd^{3+} ions' only absorb the pump light but not contributing gain [14].

Nd^{3+} has 4 energy states under metastable energy level ($^4F_{3/2}$) that can make energy transition to emit 900 nm to 1800 nm.946 nm transition of Nd:YAG was studied, this transition is comparable to Yb^{3+} system in terms of low QD ~9.5 % in-band pump. However, the transition from Nd^{3+} has shorter wavelength due to higher energy level. The transition at this wavelength is of interest for generating blue emission by frequency doubling the fundamental wavelength [15]. Further novel investigation include UV generation via harmonic generation, 237 nm (quadruple harmonic generation 946 nm) or even 220 nm (quadruple harmonic generation 880 nm, R1→Z3) that can replace Excimer lasers via further power scaling of the cryogenic laser. This thesis explores the spectroscopy measure of Nd^{3+} in various crystals that take advantage of cryogenic temperature. Little is known about the change of spectroscopic properties at different temperatures. Part of this thesis will discuss the methods of measuring spectroscopic properties of various Nd^{3+} ion-doped crystals. We also report the preliminary report on cryogenic quasi-four-level 946 nm of Nd:YAG laser operating at cryogenic temperature.

1.2 Background: Quasi-four-level Nd-doped solid state lasers

This section reviews the basic information required in the thesis. It starts with describing the principle of the solid-state laser. The gain medium of active element classifies the laser system as, Gas lasers, Dye lasers, Solid-state lasers. Solid-state lasers are then classified by the geometry of gain media, rod, thin disk, slab and fibre. This thesis uses rare earth (RE) doped optical crystal, pumped by diode lasers. The spectroscopy of RE ions is explained in following subsection. This subsection gives a general description of neodymium (Nd^{3+}) ion. Next two subsections contain details of quasi-four level transition. First discuss laser energy levels where energy transition made in between, then to discuss the limits of sub-main transitions. The description of the progress has leads to cryogenic quasi-four level lasers.

1.2.1 Principle of solid-state laser

Figure 1-1 shows the typical configuration of solid state laser with three main components: Gain medium, pump source and Mirrors forming a cavity. Gain mediums in solid state lasers are crystals, ceramic or glasses doped with rare earth ions or metal ions. The gain medium builds up energy received from pump then adds the energy to optical amplified light. Solid state gain media requires optical pump to excite the ions. The phonon emission is stimulated in this case, where phonon emission interacts with an excited atomic electron. The dominant stimulated emission over spontaneous emission allows the beam of light to be coherent laser beam, which has the same phase, direction and energy. The optical pumping is to supply energy to the gain medium that to achieve population inversion within the gain medium hence the phonon within the cavity gets amplified. Population inversion is only available with input of energy from external energy source, leave more electrons in metastable than in lower level [3].

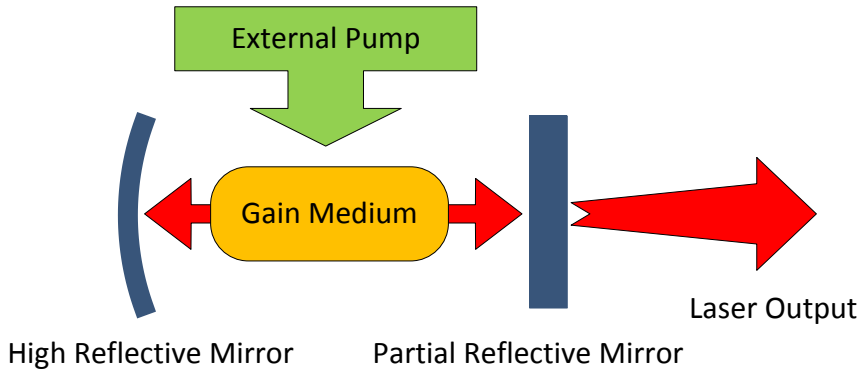

Figure 1-1 Schematic of simple side pumped laser

The overall single pass gain is very small and most of excited atoms emit spontaneously. The highly excited gain media requires having a positive feedback, forming a resonator. Simple resonator forms with two mirrors. The reflecting mirrors are coated to give near total reflection. One of the mirrors allows portion of the energy to leave the optical resonator. The resonator provides feedback to excited gain where energy is built up and amplified, via stimulated atom.

A laser is operative only if the gain is higher than the resonator losses. Resonator losses are consisting of light scatter loss and also unwanted absorption or transmission in optical component. Above laser threshold, where gain is equal to resonator losses then cavity power remains constant. The light emitted in laser are all coherent in one direction as its emissions are stimulated.

1.2.2 Spectroscopy of rare earth ions

The core components of gain media are RE ions that have been admixed. It determines the optical gain and pumping absorption. The work reported in this thesis is based on Nd^{3+} doped crystals. Detailed studies on Nd spectroscopy follow in *Part 1 Spectroscopy of Nd doped crystals* and *Chapter 2.3 Spectroscopy modelling theory*. In this section we briefly describe RE ions with energy level diagram showing the laser transitions in between manifolds.

Common RE ions used as doping material in gain media are lanthanides. Lanthanides, which consist of f block elements correspond to the filling of the 4f shell, are the collection of seventeen chemical atomic number 57(Lanthanum) to 71(Lutetium). Likewise, scandium and yttrium are considered as RE since they have similar chemical properties. Electronic transitions between levels of 4f shell, which is well shielded by outer 5s and 5p and hence retain the atomic character, determines the fluorescence spectra that the electronic structure of each ion and energy level depends on the crystal field strength. This is comparable to Ti^{3+} characteristics, which has 3d shell where laser transition is made, but also exposed without shield shell. Therefore strong interaction of electron to host lattice vibration coupled, leads to broad emission spectra, allowing wide tuning range of 670-1100 nm for Ti:sapphire [16, 17]. Bismuth doped glass has been interest to researchers recently, that can generate broad 1100-1550 nm luminescence range [18].

Nd^{3+} is well-studied dopant and being most successful active RE for solid-state lasers. Electronic structure of Nd atom is [Xe] $6s^2$ $4f^4$. The Nd^{3+} ion is triply ionised, as it losses 2 electrons from 6s orbit and one f-electron. The ground configuration of Nd^{3+} is 4I, which has total orbital angular quantum number L = 6 and the total spin quantum number S=3/2. This gives total angular momentum quantum number J = 15/2, 13/2, 11/2, 9/2. Using the notation $^{2S+1}L_J$, ground state levels are $^4I_{9/2}$, $^4I_{11/2}$, $^4I_{13/2}$, $^4I_{15/2}$ and excited state level is $^4F_{3/2}$, $^4F_{5/2}$, $^4F_{7/2}$ and $^4F_{9/2}$. The crystal field splits into number of sublevels, so called Stark level. The $^4I_{9/2}$ state splits by 5 crystal field and $^4F_{3/2}$, the metastable state into 2 components, respectively.

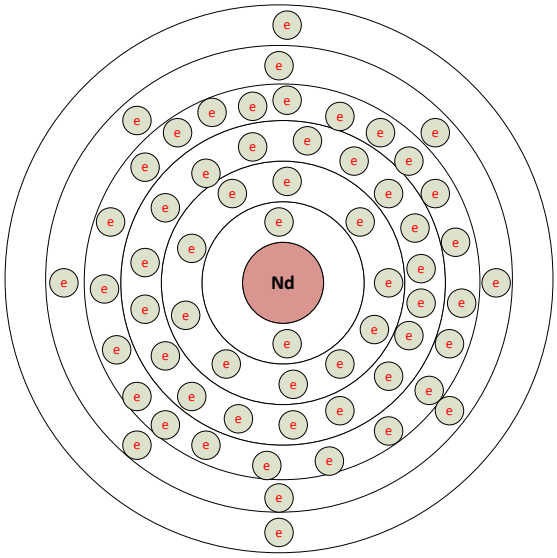

Figure 1-2 Schematic of electron shell 1s2 2s2 2p6 3s2 3p6 3d10 4s2 4p6 4d10 5s2 5p6 [Xe] 4f4 6s2 shell,6s2 and one 4f lost in Nd^{3+} ion

Many high power lasers have been developed using Nd doped gain media. Most well-known solid-state laser transition is at dominant 1 μm, $^4F_{3/2} \rightarrow {}^4I_{11/2}$. 3 other transitions have opportunity to lase at $^4I_{15/2}$, $^4I_{13/2}$ and $^4I_{9/2}$, respectively. The pump absorption is made from the ground energy level, $^4I_{9/2}$ manifold to upper excited state, $^5F_{3/2}+{}^2H_{9/2}$ (S), using the nomenclature of [19]. These higher lying levels depopulate non-radiatively and instead, populate $^4F_{3/2}$ metastable energy level. In case of in-band pump using 870-880nm, absorbing manifold is $^4F_{3/2}$ as shown in Fig 1-3.

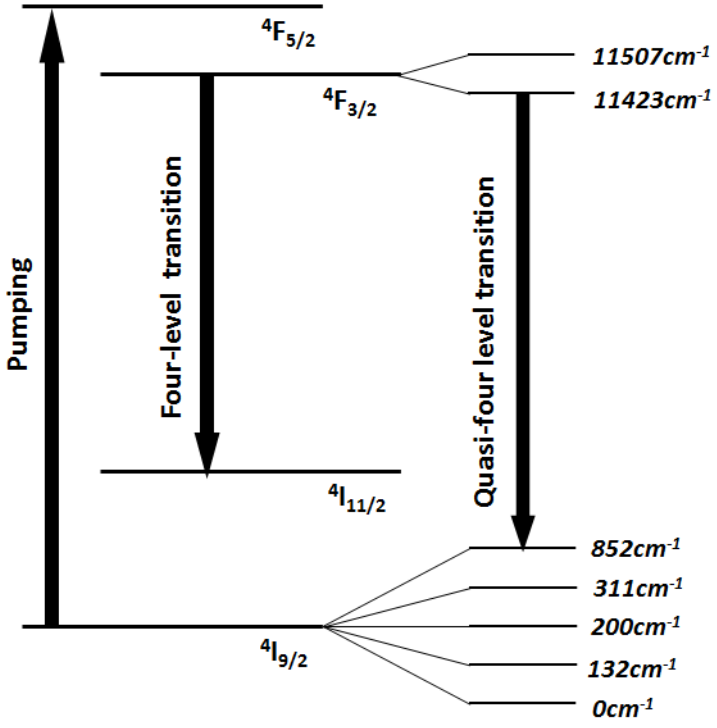

Figure 1-3 Energy level diagram for Nd:YAG

1.2.3 Quasi-four-level lasers

The typical four-level laser system is shown in Fig 1-3. A transition between $^4F_{3/2} \rightarrow {}^4I_{11/2}$ in case of Nd^{3+}, 1.1 μm transition has been well-studied solid-state laser wavelength despite relatively high quantum defect, $\eta_q=\lambda_p/\lambda_l$ (~25 % for using 808 nm diode source as pumping wavelength, λ_p and lasing wavelength, λ_l at 1064 nm). The quasi-four level transition of Nd:YAG at 946 nm could potentially be more efficient due to the lower quantum defect. Furthermore with in-band pump directly to metastable energy level, $^4F_{3/2}$ could improve quantum defect even lower (8.2 % for 869 nm pumping and lasing at 946 nm) however this laser is severely affected by detrimental thermal effects due to reabsorption of laser wavelength which also add losses in cavity. $^4F_{3/2} \rightarrow {}^4I_{9/2}$ transition has 7 times smaller gain compare to the dominant 1064 nm four-level transition. The termination on the highest Stark level of ground state manifold, 852 cm^{-1} and has population of 0.7 % in room temperature (RT). The solution to this problem requires a careful design of the gain medium geometry, considering the thermal management issues, and a high pump irradiance. Tightly focussed end pumping creates significant thermal loads, resulting in a high level of thermal lensing. ETU is also a deleterious factor degrading the laser efficiency [20, 21], involving two excited ions in the upper laser level, one relaxes to a lower energy level and transfers energy to a nearby ion, which is excited to a higher energy level and then relaxes back to the upper laser energy level; hence the population of available ions in upper laser level decreases by one for every ETU event. The energy given to the excited ion mostly results in the heating of the gain medium [22].

The term quasi-four level, was neatly defined by Walsh [23], focusing on the laser gain analysis. Starting with small signal gain $g_\circ$, as given by Barnes *et al* [24].

$$g_\circ = \sigma_e \left[\gamma N_2 - (\gamma - 1) N_a\right] \qquad 1\text{-}1$$

where σ_e is the effective stimulated emission cross section, and N_2 is the population density in the upper laser manifold, N_a is the density of all of the active ions in gain medium. The term γ is the 'inversion reduction factor' of the upper and lower levels, which is equivalent to the thermal Boltzmann factors in lower and upper level. The thermal population of terminal Stark level of ground manifold is given by Boltzmann distribution

$$N_i(T) = \frac{g_l N_o}{Z(T)} e^{\left(\frac{-E_i}{\kappa_B T}\right)} \qquad 1\text{-}2$$

where N_i is the Stark level population g_l is the degeneracy of the Stark level, N_o is the total manifold population, $Z(T)$ is the partition function, E_i is the energy of the Stark level, κ_B is the Boltzmann's constant, an T is the temperature. the energy of the Stark level is shown by,

$$E_i = hcv_i \qquad 1\text{-}3$$

where c is the speed of light, and h is a Planck's constant.

The partition function, $Z(T)$ is shown,

$$Z(T) = \sum_l g_i e^{\left(\frac{-E_l}{\kappa_B T}\right)} \qquad 1\text{-}4$$

Where g_i is the degeneracy of the Stark levels for the lower manifold.

The term $\gamma = 1 + (f_u / f_l)$, where f_l and f_u are the fractional Boltzmann factor of the respective energy levels. Ruby (Cr:Al_2O_3) is an example of a three level laser system where the population of N_2 needs to be more than half of N_a to achieve signal gain. The lower manifold of Nd:YAG for the 1um transition is ~2000 cm^{-1} above ground level, approaching zero population in steady state. The term γ = 1 and γ = 2 describes the difference between a four level and three level laser. The terminology presented by Walsh is that quasi-four and quasi-three levels are set by the value of γ. For γ smaller than 1.5, it is quasi four level and γ greater than 1.5 would be a quasi-three level system. Figure 1-4 shows 3 RE dopants (Nd^{3+}, Yb^{3+}, and Tm^{3+}) in YAG. These well-known transitions terminate to one of Stark level in ground state. The population fraction of the upper and lower energy level, γ are close to 1 for these crystals

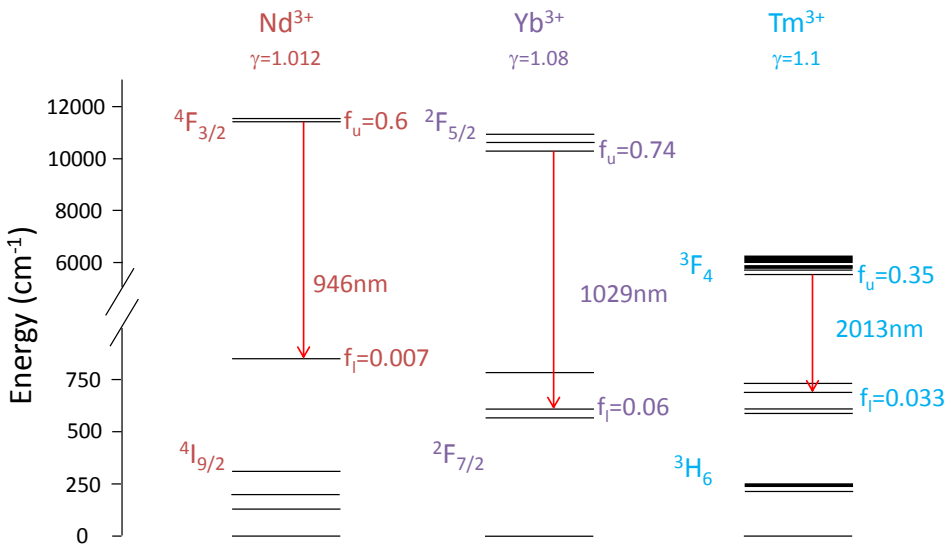

Figure 1-4 Schematic of energy level for Nd^{3+}, Yb^{3+} and Tm^{3+} ions

In recent years the output power and efficiency of the Nd:YAG laser operating at 946 nm has improved significantly. Zhou et al reported 15.2W end pumped using composite end capped NdYAG rod [25]. Delen et al used single crystal fibre to emit 946 nm reporting 34 W output power [26]. Cho et al reported cryogenic 946 nm with 24 W, 75 % slope efficiency using a monolithic crystal [27]. The highest output power was reported by Ng *et al* in [28] show 100 W for using planar waveguide structure. This also implies 34 W diffraction limited with external cavity.

1.2.4 Cryogenically cooled operation

Cryogenic cooling of the gain medium was one of the factors improving the laser performance from the beginning of laser development. Soon after first demonstration of laser, ruby ($Cr:Al_2O_3$) operating at room temperature reported by Maiman in 1960 [2], the second reported laser, uranium doped CaF2 was reported by P.P. Sorokin and M.J. Stevenson [29]. Sorokin et al cooled the crystal to liquid helium temperature with the purpose of achieving lower threshold by reducing the lower laser level population, hence less population inversion was needed. Early cryogenic lasers focused on the benefits of improvement in spectroscopic and lasing properties. Some particular metal-ion increased fluorescence lifetime at lower temperature which reduced laser threshold [30, 31].

In 1974, U-CaF2 crystal became the first demonstrated diode laser pumped laser, reported by Keyes and Quists [5]. The first demonstration of LN cooled Yb:YAG laser was demonstrated using a InGaAs diode operating in room temperature (RT) by Lacovara *et al* in 1991 [32]. In recent researches focus on physical properties include mechanical, thermal, thermo-optical properties under cryogenic temperature [33–35]. The essential changes of crystal property under cryogenic temperature are as follows: increase in thermal conductivity, reduced temperature dependent refractive index (*dn/dT*) and thermal expansion. This thermal contribution enables providing higher power and improved beam quality. Yb^{3+} ion is well demonstrated for using at cryogenic temperatures which enables four-level operation by depopulating the lower state manifold. Recent research on Yb^{3+} doped YAG, conducted by Brown *et al*, achieved 940 W near diffraction limited beam driven by 500W pumped oscillator followed by 2 kW pumped amplifier [36].

In Nd:YAG the population of the Z5 energy level, the highest stark level of the ground state manifold $^4I_{9/2}$, becomes nearly zero at liquid nitrogen temperature (LNT). Commonly used rare-earth ions, i.e. Nd^{3+} or Er^{3+} have number of ground state Stark levels that are few hundred wavenumbers above the zero level. Laser transitions to these levels are quasi-four level at room temperature, and as the population of these levels decrease with temperature, the reabsorption

losses also diminish, resulting in lower laser threshold and the transitions becoming essentially four-level. The γ, which discussed in Eq.1-1 reaches almost 1 below 120 K as shown in Fig 1-5.

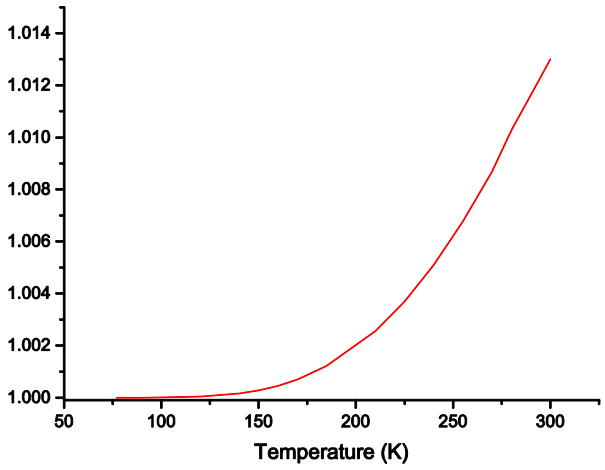

Figure 1-5 γ of Nd:YAG for temperature range of 70K to 300K

1.3 Layout of report (synopsis)

In this thesis author concentrates on two detailed studies. The two main themes have been divided into two sections: *PART I. Spectroscopy of Nd Doped Crystals*, discusses spectroscopic measurements of various Nd^{3+} doped crystals at various temperatures. *PART II. Cryogenic Lasers,* discusses a detail of the end-pump and side pump laser.

Chapter 1 and 2 introduces the background of this thesis. Chapter 1 introduces the overview of the cryogenic laser and motivation of using cryogen into laser system. We discuss the background information on cryogenic lasers. It begins with discussion of the principle of solid-state laser and brief introduction of spectroscopy of rare earth ions. The challenges and limits in further power scaling of quasi-four levels and particular emphasis on introducing cryogenically cooled laser is explained.

Chapter 2 introduces the details of the theory and background information on spectroscopic studies and thermo-optical properties over solid-state laser gain media. The review consists of spectroscopy measurement, absorption and emission of the investigated crystals. The chapter followed by an introduction to rate equation modelling for predicting laser performance. The first part of which introduces the approach to derive the rate equations based upon spatially distributed temperature in the gain medium with additional accounts for energy transfer upconversion of the laser crystal.

The experimental section of the work is divided into two parts, 4 chapters.

Part 1 focuses on the measure of spectroscopy measure of Nd^{3+} doped crystals. Chapter 3 examines the change of spectroscopic of Nd:YAG crystal over the temperature range of 77 K to 450 K. The discussion in Chapter 3 identifies broadband ground state absorption (GSA) measurements carried out within 800 nm and 870 nm spectral ranges. The following section includes measurement of emission spectra and fluorescence lifetime from metastable energy level. Experimental results of spectroscopic data for Nd^{3+} doped YVO4, GdVO4, YLF, KGW, GSAG are also reported.

Chapter 4 presents ETU data determined via Z-scan technique, for different Nd^{3+} concentrations. The chapter starts with brief description of Z-scan technique of its experimental setups and modelling which was used to determine upconversion parameter. The following section discusses how the effect of ETU correspond to laser performance.

Part 2 reports the laser experiments conducted for end-pumping and side-pumping cryogenic lasers. Chapter 5 describes the design, development of the cryogenic end-pumped Nd:YAG and Nd:GSAG laser that emitted quasi-four level transition. The preliminary results implicate the high intensity pumping have in cryogenic conditions. Then Chapter 6 reports the result of side pumping zigzag (ZZ) slab configuration. The crystal was tested to correspond different pump geometries. Results are discussed to verify the zigzag design.

Chapter 7 summarises the results in this thesis and discuss future aspects.

We report the measure of absorption and emission cross sections of Nd^{3+} doped crystals at a wide range of temperature, recorded at high resolution. These results provide important information for laser characterization. The measured data are included in Appendix A.

References

1. A. Einstein, "On the quantum theory of radiaion," Phys. Z 18, 8 (1917).
2. T. H. Maiman, "Stimulated optical radiation in ruby," Nature 187, 493 (1960).
3. W.Koechner, *Solid-state laser engineering*, 6th edition (Springer, 2005).
4. DILAS, http://www.dilas.com/products2016.
5. R. J. Keyes, and T. M. Quist, "Injection luminescent pumping of CaF2:U3+ with GaAs diode lasers," Applied Physics Letters 4, 50-52 (1964).
6. A. Giesen, H. Hugel, A. Voss, K. Wittig, U. Brauch, and H. Opower, "Scalable Concept for Diode-Pumped High-Power Solid-State Lasers," Applied Physics B: Lasers and Optics 58, 365-372 (1994).
7. Nufern, (2016), http://www.nufern.com.
8. IPG, (2016), http://www.ipgphotonics.com.
9. Q. Wang, and Q. Yu, "Continuously tunable S and C+L bands ultra wideband erbium-doped fiber ring laser," Laser Physics Letters. 610, 607-610 (2009).
10. M. A. Jebali, J. N. Maran, S. LaRochelle, S. Chatigny, M. A. Lapointe, and E. Gagnon, "A 103W High efficiency in-band cladding-pumped 1593nm all-fiber erbium doped fiber laser," in Lasers Electro-optics(JTh1I.3, 2012).
11. S. D. Jackson, "Cross relaxation and energy transfer upconversion processes relevant to the functioning of 2mm Tm3+-doped silica fibre lasers," Optical communications 230, 197-203 (2004).
12. G.D. Goodno, L. D. Book, and J. E. Rothenberg, "Low-phase-noise, single-frequency, single-mode 608W thulium fiber amplifier," Optics Letters 34, 1204-1206 (2009).
13. R. L. Aggarwal, D. J. Ripin, J. R. Ochoa, and T. Y. Fan, "Measurement of thermo-optic properties of Y3Al5O12, Lu3Al5O12, YAlO(3), LiYF4, LiLuF4, BaY2F8, KGd(WO4)(2), and KY(WO4)(2) laser crystals in the 80-300 K temperature range," Journal of Applied Physics 98 (2005).
14. D. S. Sumida, and T. Y. Fan, "Effect of Radiation Trapping on Fluorescence Lifetime and Emission Cross-section measurements in Solid-State Laser Media," Optics Letters 19, 1343-1345 (1994).
15. R. K. V. Pruneri, P. G. Kazansky, W. A. Clarkson, P. St. J. Russell, and D. C. Hanna, "49mW of cw blue light generated by first-order quasi-phase-matched frequency doubling of a diode-pumped 946nm Nd:YAG laser," Optics Letters 20, 2375-2377 (1995).
16. P. Schwendimann, E. Sigmund, and K. Zeile, "Modal for laser action in vibronic systems," Physic Review A 37, 3018 (1988).

17. P. F. Moulton, "Spectroscopic and laser characteristics of Ti:Al2O3," Journal of Optical Society of America B 3, 125-133 (1986).

18. E M Dianov, S V Firstov, S V Alyshev, K E Riumkin, A V Shubin, V F Khopin, A N Gur'yanov, O I Medvedkov, and M. A. Mel'kumov, "A new bismuth-doped fibre laser, emitting in the range 1625 – 1775 nm," Quantum Electronics 44 (2014).

19. E. H. Calrson, and G. H. Dieke, "The State of the Nd3+ Ion as Derived from the Absorption and Fluorescence Spectra of NdCl3 and Their Zeeman Effects " Journal of Chemical Physics 34, 9 (1961).

20. S. Bjurshagen, and R. Koch, "Modeling of energy-transfer upconversion and thermal effects in end-pumped quasi-three-level lasers," Applied Optics 43, 4753-4767 (2004).

21. Y. Guyot, H. Manaa, J. Y. Rivoire, R. Moncorge, N. Garnier, E. Descroix, M. Bon, and P. Laporte, "Excited-State-Absorption and Up-conversion Studies of Nd3+-Doped-Single Crystals Y3Al5O12, YLiF4, and LaMgAl11O19," Physical Review B 51, 784-799 (1995).

22. M. Pollnau, P. J. Hardman, W. A. Clarkson, and D. C. Hanna, "Upconversion, lifetime quenching, and ground-state bleaching in Nd3+: LiYF4," Optical Communications 147, 203-211 (1998).

23. B. M. Walsh, "Review of Tm and Ho materials; spectroscopy and lasers," Laser Physics 19, 855-866 (2009).

24. N. P. Barnes, B. M. Walsh, R. L. Hutcheson, and R. W. Equall, "Pulsed F-4(3/2) to I-4(9/2) operation of Nd lasers," Journal of the Optical Society of America B: Optical Physics 16, 2169-2177 (1999).

25. R. Zhou, E. Li, H. Li, P. Wang, and J. Yao, "Continuous-wave, 15.2 W diode-end-pumped Nd : YAG laser operating at 946 nm," Optics Letters 31, 1869-1871 (2006).

26. X. Delen, I. Martial, J. Didierjean, N. Aubry, D. Sangla, F. Balembois, and P. Georges, "34 W continuous wave Nd:YAG single crystal fiber laser emitting at 946 nm," Applied Physics B: Lasers and Optics 104, 1-4 (2011).

27. C. Y. Cho, C. Y. Lee, C. C. Chang, P. H. Tuan, K. F. Huang, and Y. F. Chen, "24-W cryogenically cooled Nd:YAG monolithic 946-nm laser with a slope efficiency > 70%," Optics Express 23, 10126-10131 (2015).

28. S. P. Ng, and J. I. Mackenzie, "Power and radiance scaling of a 946 nm Nd:YAG planar waveguide laser," Laser Physics 22, 494-498 (2012).

29. P.P. Sorokin, and M.J. Stevenson, "Stimulated infrared emission from trivalent uranium," Physical review letters 5, 557 (1960).

30. L. H. Johnson, H. J. Guggenheim, and R. A. Thomas, "Photon-terminated optical masers," Physical Review 149, 179-185 (1966).

31. J. J. Adams, C. Bibeau, R. H. Page, D. M. Krol, L. H. Furu, and S. A. Payne, "4.0 4.5-mm lasing of FeZnSe below 180K, a new mid-infrared laser material," Optics Letters 24, 1720-1722 (1999).

32. P. Lacovara, H. K. Choi, C. A. Wang, R. L. Aggarwal, and T. Y. Fan, "Room-temperature diode-pumped Yb:YAG laser," Optics Letters 16, 1089-1091 (1991).

33. T. Y. Fan, D. J. Ripin, R. L. Aggarwal, J. R. Ochoa, B. Chann, M. Tilleman, and J. Spitzberg, "Cryogenic Yb3+-doped solid-state lasers," IEEE Journal of Selected Topics in Quantum Electronics 13, 448-459 (2007).

34. D. C. Brown, S. Tornegard, J. Kolis, C. McMillen, C. Moore, L. Sanjeewa, and C. Hancock, "The Application of Cryogenic Laser Physics to the Development of High Average Power Ultra-Short Pulse Lasers," Applied Science-Basel 6 (2016).

35. D. C. Brown, "The promise of cryogenic solid-state lasers," IEEE Journal of Selected Topics in Quantum Electronics 11, 587-599 (2005).

36. D. C. Brown, J. M. Singley, K. Kowalewski, J. Guelzow, and V. Vitali, "High sustained average power cw and ultrafast Yb:YAG near-diffraction-limited cryogenic solid-state laser," Optics Express 18, 24770-24792 (2010).

Chapter 2:

Theoretical background

2.1 Introduction

This chapter introduces the background theory for the following experimental work presented in this thesis. In section 2.2, we first discuss the thermo-optical effects within a laser crystal associated with the waste heat created during the pumping cycle. The effect of heat flow is presented for an end-pump laser, with the model presented including temperature dependence of various crystal properties, including the thermal conductivity. The techniques required to determine the spectroscopic properties of Nd^{3+} ions in a host material are presented in section 2.3. Numerical models for predicting laser performance for which there are reabsorption losses at the lasing wavelength are presented in section 2.4. Finally a simple approach for measuring the beam quality (M^2) without moving parts is explained in section 2.5.

The information discussed in this chapter, is required for later chapters, describing key physical phenomena that determine the performance of cryogenic cooling of the active gain medium. As the focus of this report is cryogenic cooling such media, we will discuss the benefits of cryogenic cooling in each section.

2.2 Thermo-optic effects

The non-radiative decay achieved by phonon emission is generating heat in the gain medium. There are a number of non-radiative decay paths via different energy transfer processes. The main contribution to the thermal load comes from the quantum defect, which is given by:

$$\eta_q = 1 - \frac{\lambda_p}{\lambda_l} \qquad 2\text{-}1$$

where λ_p is the pump wavelength, and λ_l is the laser wavelength. There is extra heat load generated in the pumped region of the gain medium due to energy transfer up-conversion and subsequent non-radiative transitions of the highly excited Nd^{3+} ions back to the metastable state, as will be discussed in Section 2.3.3. The heat deposited into the crystal is then conducted to the edge of the gain material where there is a sink and where it can be dissipated. Therefore, there is

a non-uniform temperature distribution over the pumped area of a gain medium, which is strongly dependent upon the material properties, its geometry, and the thermal interface.

As scaling diffraction-limited output power of solid-state lasers is generally limited by the induced thermal lens and associated aberrations created by the temperature gradient across the pumped region, it is paramount for engineers trying to improve laser performance to mitigate the effects of the waste heat deposited within the gain medium [1]. For near ambient-temperature conditions, three laser geometries have been reported that have enabled scaling of near-diffraction-limited powers into the kW regime from a single oscillator, thin-slabs [2], the thin-disk [3], and optical fibres [4]. Two other promising techniques capitalise on different time constants for the heat flux, either by rotating the gain media [5] or the cavity [6], or exploiting cryogenically cooling of the gain media to enhance the thermal diffusivity [7, 8], albeit with more complex engineering for the thermal management. In the following, with consideration of the last approach, we first review the critical thermo-optical parameters as a function of temperature, then introduce a numerical approach to model the heat distribution within a cryogenically-cooled crystal.

There are three main contributions to the thermo-optical effects in solid-state lasers, namely, thermal expansion coefficient, stress-optic effect, and the thermo-optic coefficient (*dn/dT*) [9]. These key parameters are dependent on the host material properties, and primarily the induced thermal gradient, which is dominated by the thermal conductivity. Hence, the nature of thermally induced aberrations can be minimised by using suitable crystals with high conductivity but small coefficients for the other parameters. YAG has superior thermal conductivity, k_c, compared to other host materials [3,5], increasing from 10~11$Wm^{-1}K^{-1}$ at room temperature by nearly an order of magnitude to ~90$Wm^{-1}K^{-1}$ [12] at the liquid nitrogen boiling temperature.

The heat equation under steady-state conditions, where $\partial T / \partial t = 0$, is:

$$\nabla \cdot k_c(\nabla T(r,z)) + Q(r,z) = 0 \qquad \text{2-2}$$

The deposited heat by the pumping process and subsequent dissipation to the boundary, which is defined by the thermal conductivity, determines the temperature gradient inside the crystal. We will discuss the boundary condition shortly, as it can severely affect the absolute temperature rise. For a longitudinally Gaussian-pumped cylindrical-rod, if the heat flow is radial and the crystal isotropic over crystal volume, the heat flow equation yields [15]

$$2\pi r\Delta zh(r,z)=\int_{z}^{z+\Delta z}\int_{0}^{r}\alpha\eta_q I_p(r',z')2\pi r'\,dr'\,dz' \qquad 2\text{-}3$$

Where α is the absorption coefficient and $I_p(r',z')$ is the intensity of the incident pump when r is the variable transverse radial coordinate and z is the coordinate along the axis.

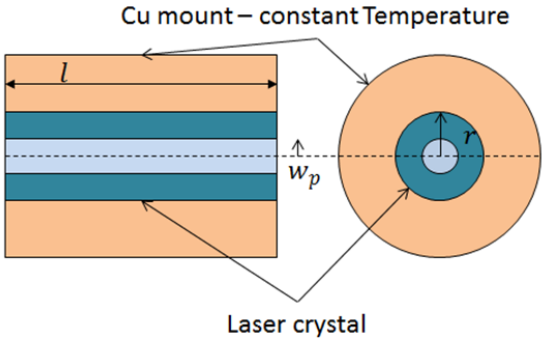

Figure 2-1 Side and End-view of laser rod and Cu mount, given that rod radius *r* and length *l* and the pump beam radius w_p

We assumed a Gaussian pump profile and power, P_p, then the intensity is given by

$$I_p(r,z)=\frac{2P_p}{\pi w_p^{\,2}}\exp\left(\frac{-2r^2}{w_p^{\,2}}\right)\exp(-\alpha z) \qquad 2\text{-}4$$

Substitute Eq.2-12 into Eq.2-11 then performing the integration gives,

$$h(r,z)=\frac{\alpha P_{ph}}{2\pi}\exp(-\alpha z)\left(\frac{1-\exp(-2r^2/w_p^{\,2})}{r}\right) \qquad 2\text{-}5$$

Where $P_{ph}=\eta_q P_p$ is the heating power generated from the absorbed pump not converted to radiation. Now we can derive the radial temperature change from the edge of rod at any position z along the crystal axis.

It is assumed that the pump beam is diffraction limited, and the temperature change calculated with respect to the generated heat in the longitudinal slice Δz by substituting Eq.2-13 into Eq.2-10, then integrating to the crystal boundary, r_b, giving [15],

$$\Delta T(r,z)=\frac{\alpha P_{ph}\exp(-\alpha z)}{4\pi k}\left[\ln\left(\frac{r_b^{\,2}}{r^2}\right)+E_i\left(\frac{2r_b^{\,2}}{w_p^{\,2}}\right)-E_i\left(\frac{2r^2}{w_p^{\,2}}\right)\right]. \qquad 2\text{-}6$$

Where $\Delta T(r,z)=T(r,z)-T(r_b,z)$, and assuming the absorption coefficient is unsaturated. E_i is the exponential integral function,

$$E_i(x) = \int_x^{\infty} e^{-t} / t \, dt \qquad 2\text{-}7$$

Assuming the crystal rod has an ideal contact with the heat dissipating material. Copper is a common intermediate material, due to its high thermal conductivity ~400Wm^{-1}K^{-1}. In our case, we assume the temperature of the copper heat sink is uniform and temperature matched to the active coolant, T_c, e.g. cooling water. However, the temperature of the copper and crystal is not always equal and a heat transfer coefficient, H, can be used to express the surface conductance at the boundary.

$$-k\left(\frac{\partial T}{\partial r}\right) = H(T(r_b) - T_c) \qquad 2\text{-}8$$

Chenais *et al* [16] expressed the temperature at the boundary of crystal.

$$T_{rb} = \frac{k}{H} \frac{2(T(0) - T_{rb})}{r_b(1 + 2\ln(r_b / w_p))} \qquad 2\text{-}9$$

The heat transfer coefficient, which describes the surface heat conductance at the boundary, is found to have a wide range of possible values, that are in range of 1-10 Wcm^{-2}K^{-1}. Carslaw and Jaeger [17] reported that a thin oxygen layer between a rod and the mount can cause a large thermal resistance. Eq.2-9 explains the effect of thermal contact for crystal cooling.

Figure 2-2 shows the simulated temperature distribution for a 1 at.% doped Nd:YAG rod, when applying Eq.2-8 and Eq.2-9. Using a rod radius, r_b = 1.5 mm and length of l_c = 7 mm, a pumping spot radius of w_p = 0.3 mm, with an absorbed pump power of P_p = 40W, the value for k, determined with Eq.2-8, is 11 Wm^{-1}K^{-1}, and using a value for α that we measured at room temperature, being 2.39 cm^{-1}. In this model we assumed a constant exponential pump decay along the crystal, i.e. without saturation.

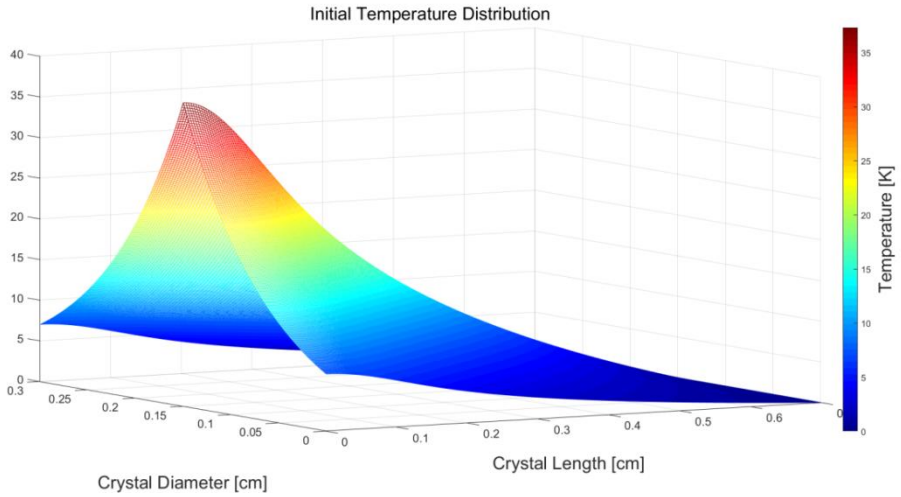

Figure 2-2 Simulated temperature profile of 1 at.% doped Nd:YAG rod image

The heat deposited into the crystal raises the temperature at the centre to 37.3 K higher than the boundary temperature. We have set constant values for the absorption coefficient and thermal conductivity. However, as we will show in the following chapter, there is a temperature dependence for many of the key crystal properties, both spectroscopic and physical in nature. As we will also show in Chapter 3, the peak absorption spectroscopic properties, can be fitted by a Taylor's expansion, accounting for the fact that the absorption coefficient depends not only on absorption cross section spectrum, but also the spectral characteristics of the pump source. Here we can state temperature dependence as follow:

$$\alpha_T(r,z) = \alpha(\Delta T(r,z) + T_o) \qquad 2\text{-}10$$

where $\alpha_T(r,z)$ is temperature dependent absorption coefficient over pump medium, T_o is an initial temperature and $\Delta T(r,z)$ is the temperature at each point throughout the crystal volume. A similar analogy can be made for the thermal conductivity, $k_T(r,z)$ defined as a function of the local temperature, $k(T)$ using the analytical fit reported by Brown [14] for thermal modelling of YAG gain media:

$$k(T) = \frac{a}{(\ln(bT))^c} - \frac{d}{T} \qquad 2\text{-}11$$

Where a, b, c, and d are constant and given a=1.9x10^6($Wcm^{-1}K^{-1}$), b=5.33(K^{-1}), c=7.14, and d=331 (Wcm^{-1}). The fit function operates for 30 K to 500 K with given thermal conductivity unit ($Wcm^{-1}K^{-1}$) was found to be a good match to actual parameters. These two functions calculated according to the temperature distribution shown is shown in Fig 2-3. The thermal conductivity is reduced in the hotter areas, Fig 2-3(a), instead the absorption coefficient increases, Fig 2-3(b).

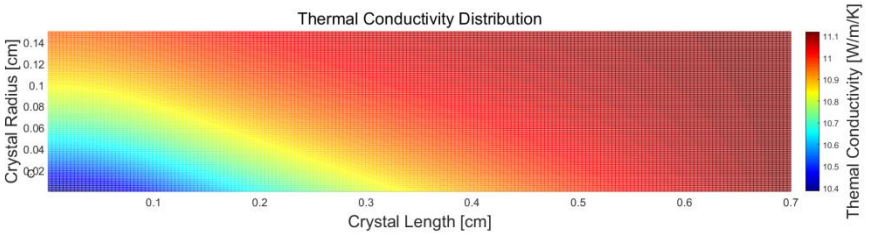

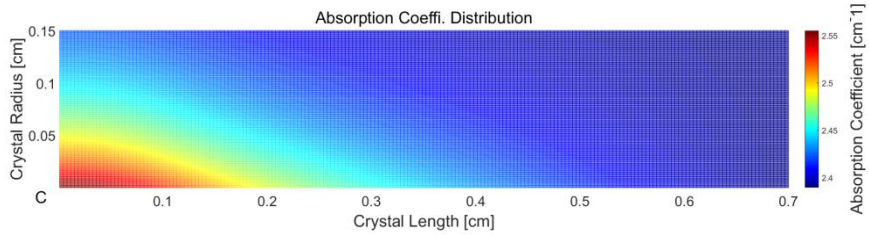

(b)

Figure 2-3 Simulation of temperature dependent thermal conductivity (a) and effective absorption coefficient (b)along the centre of rod

In the assumption that the changes in thermal conductivity and absorption coefficient are small over the crystal temperatures reached, as calculated via Eq.2-6, to a first approximation we can modified the expression to include the spatially-dependent absorption coefficient and thermal conductivity, i.e.,

$$\Delta T(r,z) = \frac{\alpha_T(r,z) P_{ph} \exp(-\alpha_T(r,z) z)}{4\pi k_T(r,z)} \left[\ln\left(\frac{r_b^2}{r^2}\right) + E_i\left(\frac{2r_b^2}{w_p^2}\right) - E_i\left(\frac{2r^2}{w_p^2}\right) \right] \qquad 2\text{-}12$$

By iterating the calculation of this equation multiple times, using the new temperature distribution as the seed for the next iteration, we find that the temperature rise at the centre of rod converges to a maximal increase of 44.4 K as shown in Fig 2-4, which is 7.1K higher than the peak found using constant values. The temperature distribution for the two cases shows a very similar distribution, despite the different peak temperature at the rod centre.

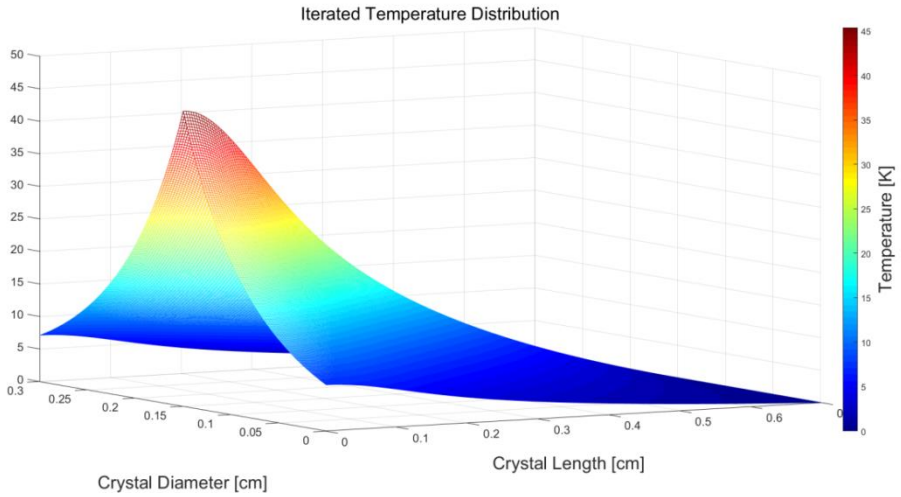

Figure 2-4 Simulation of 5 times iterated temperature profile of 1 at.% doped Nd:YAG rod image

2.3 Spectroscopy

Study of the spectroscopic properties of a given gain medium provides key information about the strength of the absorption and emission cross sections, required to quantify the potential laser performance. It was essential to undertake a comprehensive study of both the absorption and emission properties for the crystals of potential interest for cryogenic operation, to determine how the laser performance would benefit. After describing the theory underpinning the absorption measurements, we will review two theories for the determination of the emission cross section spectra, i.e. a) Füchtbauer-Ladenburg (FL) theory, and, b) the McCumber or reciprocity method (RM).

2.3.1 Absorption cross section

The study of ground state absorption (GSA) measurements correspond key parameters for laser design. The line-broadening mechanism in real gain media has introduced transition cross sections along energy levels. GSA determines the pump absorption rate, defining the total population inversion created by the pump field's intensity. The information can be used to infer the saturation intensity of a given gain media and the pump source with knowledge of lifetime. Important design criteria for laser or amplifiers are gain geometry, thermal management, and dopant concentration.

Here we introduce a brief description for determining the absorbance of a material using the Beer-Lambert law. The law relates to the absorption of light as it passes through the body of the medium.

$$A = -\log \frac{I_t}{I_o} \qquad 2\text{-}13$$

where I_t is unabsorbed intensity, I_o is the incident optical intensity on the crystal. A is the absorbance of the light passing through the sample, giving:

$$\frac{I_t}{I_o} = \exp(-\sigma_{abs} N_t l_c) \qquad 2\text{-}14$$

where σ_{abs} is absorption cross section, N_t is ion density of crystal, l_c is gain material path length. Substituting Eq.2-13 into Eq.2-14, gives the simple expression

$$\sigma_{abs} = \frac{2.303 * A}{N_t l_c} \qquad 2\text{-}15$$

Note, for all sample surfaces either AR coated or uncoated, it is necessary to correct the measured transmission for each surface. The transmission over the spectrum of the probe light. For AR coated surfaces, this is best done by measuring the transmission for "out of band wavelengths", e.g. for absorption into the Nd^{3+} S-levels (following the notation of Calrson *et al* [18]) around the wavelengths of 770 nm and 840 nm. The spectral loss can then be used to set the background for the entire spectrum, i.e. $I_t = I_o L e^{-\alpha l}$, where L is the fraction of light lost, such as AR coating loss (for coated), Fresnel loss (for uncoated) and scattering losses. For the experiments to be discussed in the next Chapter, the coating loss was on the order of ~2-3 % around 800 nm for the AR coatings optimized for a lasing wavelength of 1 μm, or for uncoated surfaces the Fresnel reflection, ranged from ~4 % for the fluoride crystals to nearly 10 % for the high index oxides, like vanadate or tungstate.

For anisotropic crystals, which have natural birefringence, the probe light was polarised and aligned to one of the crystal's principal axes, where the respective absorption spectra were measured. For the monoclinic crystals, such as potassium gadolinium tungstate (KGW), different crystal cuts were employed when determining the polarized absorption spectra for each axis.

2.3.2 Emission cross section

A material's emission cross section is used for calculating laser threshold and determining the potential gain achievable, it can be determined using a few methods. In the following section, we

describe two models namely, the Füchtbauer-Landenburg (F-L) method [19-21], and McCumber or reciprocity method [21, 22].

Füchtbauer-Landenburg equation

The F-L analysis exploits the fluorescence to determine the emission cross section of a particular active ion in a host medium. Starting with a degenerate two-level systems, as described by Einstein's transition coefficients, the transition probability for a finite spectral linewidth can be calculated [23]. A summary of the F-L formula derivation is presented in the following, where we will discuss the main assumptions made.

The rate equation for the change in the number of photons of an incident light beam, which denotes the number photons added to (or taken away from) the light beam per unit volume per unit time, is given by,

$$\frac{dN_2}{dt} = B_{21} g_{em}(\nu_p) \rho N_2 - B_{12} g_{abs}(\nu_p) \rho N_1 \qquad 2\text{-}16$$

where ν_p is the frequency of the pump light, N_2 and N_1 are the population densities of the upper and lower energy levels of the active element, B_{21} and B_{12} are the Einstein coefficients, $g_{abs}(\nu_p)$ and $g_{em}(\nu_p)$ are absorption and emission lineshape functions, and ρ is the spectral energy density, which can be expressed in terms intensity, $\rho = I/(c/n)$, where I is light intensity, c the speed of light in a material of refractive index, n. Here we neglect photons spontaneously emitted from the upper level, as they are not contributing coherently to the amplification/absorption process. Using the relationship between the two degenerate levels, g_1 and g_2, and the assumption that the two levels are equally populated, or, have the same rate of induced transition, Einstein's first relation is

$$B_{21} g_2 = B_{12} g_1 \qquad 2\text{-}17$$

According to the Beer-Lambert Law, light is absorbed as propagates in the gain medium, according to:

$$\frac{dI(z)}{dz} = -\alpha(\nu) I(z) \qquad 2\text{-}18$$

Where $\alpha(\nu)$ is the absorption coefficient and $I(z)$ is the intensity of the pump light after a distance z from the front surface of the medium. Given that $d\rho/dt = dN/dt \; h\nu/(c/n)$, the absorption

coefficient can be expressed in terms of Einstein's B coefficient and the population of two levels such that:

$$\alpha(\nu) = (B_{12}N_1 g_{abs}(\nu_p) - B_{21}N_2 g_{em}(\nu_p))\frac{h\nu}{c/n} \quad \text{2-19}$$

Substituting in Eq.2-17, and integrating over all frequencies for the absorption line. Eq.2-19 becomes

$$\int \alpha(\nu)d\nu = \int\left(\frac{g_2}{g_1}N_1 g_{abs}(\nu_p) - N_2 g_{em}(\nu_p)\right)\frac{B_{21}h\nu}{c/n} \quad \text{2-20}$$

The number of absorbing and emitting atoms per frequency range is expressed as $dN_{1\nu}/d\nu = g_{abs}(\nu_p)N_1$ and $dN_{2\nu}/d\nu = g_{em}(\nu_p)N_2$. By inserting these expressions into Eq.2-20, then the integrated absorption coefficient can be expressed, assuming a narrow spectral linewidth where the frequency bandwidth is replaced by a peak frequency, ν_o

$$\int \alpha(\nu)d\nu = \left(\frac{g_2}{g_1}N_1 - N_2\right)\frac{B_{21}h\nu_o}{c/n} \quad \text{2-21}$$

Optical gain can be achieved when a population inversion is reached,

$$\alpha(\nu) = \sigma_{21}(\nu)N_2 - \sigma_{12}(\nu)N_1. \quad \text{2-22}$$

Where the emission cross section, σ_{21}, and absorption cross section, σ_{12}, are defined through the integrated FL relations,

$$\int \nu^2\sigma_{21}(\nu)d\nu = \frac{A_{21}c^2}{8\pi n^2} \quad \text{2-23}$$

$$\int \nu^2\sigma_{12}(\nu)d\nu = \frac{g_2}{g_1}\frac{A_{21}c^2}{8\pi n^2} \quad \text{2-24}$$

A_{21} is Einstein A coefficient, which is the rate of radiative emission, often expressed as the reciprocal value τ_{21}, that is the radiative lifetime. The second of Einstein's relations is given by

$$A_{21} = \frac{8\pi h\nu^3}{c^3}B_{21} \quad \text{2-25}$$

Equation 2-23 and 2-24 is called the F-L relation of emission and absorption. The two cross sections can be written in their general form as:

$$g_2 \int \nu^2 \sigma_{21}(\nu) d\nu = g_1 \int \nu^2 \sigma_{12}(\nu) d\nu \,. \qquad 2\text{-}26$$

Determination of the magnitude of the transition cross section can be achieved using the F-L relations, the measured fluorescence or absorption spectrum and radiative lifetime. Aull *et al* [21] reported the derived expression, which calculates the emission cross section by measuring the entire fluorescence spectrum along with the upper level lifetime,

$$\sigma_{em}(i-j,\lambda) = \frac{1}{8\pi} \frac{\lambda^5 \eta \beta_{ij}}{n^2 c \tau_f} \frac{I(\lambda)}{\int_{i-j} I(\lambda) \lambda d\lambda} \,. \qquad 2\text{-}27$$

Where $I(\lambda)$ is the entire fluorescence emission spectrum, β_{ij} is the branching ratio for the respective transitions from i to j manifolds, λ is the transition wavelength, η is the quantum efficiency of the upper level. *n*, the refractive index can be determined via the Sellmeier dispersion formula [24]. β_{ij} is calculated via:

$$\beta_{ij} = \frac{\int \lambda I_{ij}(\lambda) d\lambda}{\sum_{i'j'} \int \lambda I_{i'j'}(\lambda) d\lambda} \,. \qquad 2\text{-}28$$

In anisotropic media, the F-L equation for the respective principal optical axes is defined for light polarized along each, i.e. a,b,c, as given by Payne *et al* [25]:

$$\sigma_{em}(i-j,\lambda) = \frac{1}{8\pi} \frac{\lambda^5 \eta \beta_{ij}}{n_x{}^2 c \tau_f} \frac{I_x(\lambda)}{\sum_{x=principleaxes} \int_{i-j} I_x(\lambda) \lambda d\lambda} \,. \qquad 2\text{-}29$$

Where n_x is the refractive index for the x – the polarization, and I_x for the intensity of each polarization axes.

Reciprocity Method

The reciprocity method (RM), on the other hand, allows for the calculation of either the emission (or absorption) cross section from an accurate measurement of the other and knowing the energy levels of the transition for the active material in question. RM capitalises upon the coupled relationship of two level, unlike the F-L equation, which requires the measurement of the entire fluorescence spectrum to determine the proper scaling factors for each of the available transitions. Nonetheless, the RM is based upon a few general assumptions, with the derivation summarised in following.

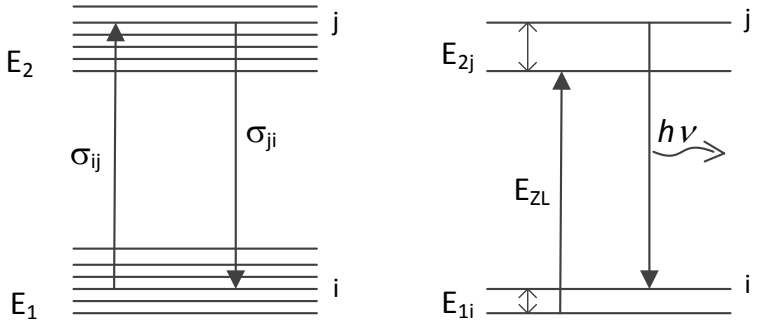

Figure 2-5 Diagram of two stark manifolds with degeneracies split. (a) shows the transition cross section between i and j and (b) shows the photon energy for the transition between i and j

Figure 2-5 illustrates two electron-orbital energy levels with their associated Stark splitting. The energy levels, depicted as E_1 and E_2 are the lower and upper transition states for the emission (absorption) of a photon and have individual sublevels d_i and d_j [21]. In this case, the two-level transition cross section is related to the ratio of degeneracy of the two levels,

$$d_i\sigma_{ij} = d_j\sigma_{ji} \qquad 2\text{-}30$$

This is the reciprocity theory, which is only valid for a normalised population distribution. The photon energy of any transition can be derived considering the two energy levels,

$$\Delta E_{dj} - \Delta E_{di} = h\nu - E_{ZL}\,. \qquad 2\text{-}31$$

Where E_{ZL} is the zero-line energy, which is the energy difference between the two lowest sub-levels of each manifold, ΔE_{0i0j}.

The Stark-level population each energy manifold is described by the Boltzmann distribution, which is considered to be in thermal equilibrium. The overall emission and absorption cross sections are then given by [26],

$$\sigma_{21}(\nu) = \sum_{d_i,d_j} \frac{\exp(-\Delta E_{dj}/k_bT)}{Z_2}\sigma_{djdi}(\nu)\,. \qquad 2\text{-}32$$

Where k_b is the Boltzmann constant, and Z_2 is partition function given by [26]

$$Z_2 = \sum_{d_j} \exp(-\Delta E_{dj}/k_bT) \qquad 2\text{-}33$$

Also for the reciprocal absorption cross section, $\sigma_{12}(\nu)$, with a partition function Z_1, that is:

$$\sigma_{12}(\nu) = \sum_{d_i, d_j} \frac{\exp(-\Delta E_{di} / k_b T)}{Z_1} \sigma_{didj}(\nu) \qquad 2\text{-}34$$

$$Z_1 = \sum_{d_i} \exp(-\Delta E_{di} / k_b T) \, . \qquad 2\text{-}35$$

σ_{didj} is the spectroscopic cross section for transitions between two individual Stark sub-levels. Dividing Eq.2-32 and 2-34 and using Eq.2-33 and 2-35 leads to,

$$\frac{\sigma_{21}(\nu)}{\sigma_{12}(\nu)} = \frac{Z_1}{Z_2} \frac{\sum_{d_i, d_j} \exp(-\Delta E_{dj} / k_b T) \sigma_{djdi}(\nu)}{\sum_{d_i, d_j} \exp(-\Delta E_{di} / k_b T) \sigma_{didj}(\nu)}$$

$$= \frac{Z_1}{Z_2} \exp\left({(E_{ZR} - h\nu)} \middle/ {k_b T} \right) \, . \qquad 2\text{-}36$$

Which can be reordered to give,

$$\sigma_{21}(\nu) = \sigma_{12}(\nu) \frac{Z_1}{Z_2} \exp\left({(E_{ZR} - h\nu)} \middle/ {k_b T} \right). \qquad 2\text{-}37$$

This is the equation reported by McCumber, describing the reciprocity relationship for the emission and absorption cross sections.

Ground-state reabsorption of fluorescence

A portion of the radiative fluorescence of Nd^{3+} ions corresponds to a transition to the ground-state. Whereupon, by reciprocity, there is a chance for neighbouring Nd^{3+} ions in their ground-states to absorb the passing photons. Consequently, depending upon the distance travelled through the media, the measured spectral power density of the fluorescence can be distorted by reabsorption, which can affect the accuracy in determining the emission cross section via the F-L equation. Typically therefore, the RM is used to determine the emission cross section to the ground state, and compared with the F-L equation results. Alternatively, the pumping beam can be brought close to the edge of the sample crystal to minimize the chance of reabsorption. It was particularly important to determine the exact emission cross section around the zero-phonon line, to be able to have a good estimate of the effective absorption cross section for the in-band pumping scheme.

2.3.3 Energy transfer upconversion

A radiative transition is the process of the emission of a photon, with an energy equivalent to the difference between the energy levels involved, as discussed in the prior section (section 2.3.2). Non-radiative transitions, instead, dissipate the excess energy through generation of phonon vibrations in the host lattice. Typically the emission of a photon is phonon-assisted, where the portion of the energy difference between the photon energy and that between the upper level and the ground state, is coupled to phonons. As a consequence, these phonons induce heating of the lattice, with an energy difference equal to the quantum defect.

In this report, two other important energy transfer interactions are discussed. These are ion-ion energy exchange processes, the first, cross relaxation (CR), and the second, energy transfer upconversion (ETU).

Cross-relaxation interactions are energy exchange processes between neighbouring excited and ground state ions, resulting in two excited ions in a mid-level energy state. Pollnau *et al* [27] and Palatella [28] reported 3 CR process for the Nd^{3+} ion.

$$\begin{aligned} CR_1 \quad & {}^4F_{3/2} \rightarrow {}^4I_{15/2} \quad {}^4I_{9/2} \rightarrow {}^4I_{15/2} \\ CR_2 \quad & {}^4F_{3/2} \rightarrow {}^4I_{15/2} \quad {}^4I_{9/2} \rightarrow {}^4I_{13/2} \\ CR_3 \quad & {}^4F_{3/2} \rightarrow {}^4I_{13/2} \quad {}^4I_{9/2} \rightarrow {}^4I_{15/2} \end{aligned} \qquad \text{2-38}$$

Only the CR_1 transitions have near equivalent energy differences and as such undergo a direct interionic exchange, the other two, CR_2 and CR_3 each have relatively large energy mismatch, making the process less likely occur [29]. However, cross relaxation is analysed from a macroscopic viewpoint, and as such, can be described with a single parameter, W_{CR}. Due to the large energy gap between ${}^4F_{3/2}$ and ${}^4I_{15/2}$, being at least six times larger than the maximum phonon energy of the YAG crystal host, for example, the probability of multi-phonon non-radiative relaxation can be neglected. On the other hand, as the upper pump levels (${}^4F_{5/2}$, ${}^2H_{9/2}$) are only ~800 cm^{-1} above the meta-stable level, these excited ions rapidly (~ns timescale) relax into the energy state of interest ${}^4F_{3/2}$.

The second potentially significant parameter that adds to the non-radiative de-excitation of the meta-stable energy level during excitation of the doped crystal is energy transfer upconversion. The ETU process involves two Nd^{3+} ions in their excited meta-stable state, ${}^4F_{3/2}$, one of which receives the stored energy of the other, and, is subsequently excited to a higher energy state (${}^4G_{5/2}$, ${}^4G_{7/2}$, or ${}^2G_{9/2}$), while the other one is returned to a lower state (${}^4I_{15/2}$, ${}^4I_{13/2}$, or ${}^4I_{11/2}$) respectively [30]. Depending upon the strength of the ETU processes, this can have a detrimental

effect on laser performance, firstly as an additional source of heat, which ultimately leads to increasing cavity losses with higher pump powers, and secondly, by reducing the population inversion thus lowering the achievable gain. This is potentially catastrophic for the already relatively low-gain 946 nm transition.

For crystals with low dopant concentrations and where the multiphonon decay rate is negligible, the radiative lifetime, τ_R, approaches the intrinsic meta-stable level lifetime, τ_o. However, with increasing dopant concentration there is stronger ion-ion energy coupling, thus the lifetime is reduced. Deviation from the ideal exponential decay of the meta-stable level can be determined via measuring the fluorescence lifetime, τ_f, which is influenced by these non –linear energy transfer mechanisms, i.e. W_{NR}, which are obtained through the relationship:

$$\frac{1}{\tau_f} = \frac{1}{\tau_o} + W_{NR} . \qquad 2\text{-}39$$

Here $W_{NR} = W_{CR} + W_{ETU}$, W_{ETU} is near zero for weak excitation, hence value of W_{CR} is obtained.

Z-scan techniques for quantifying the upconversion parameter

Using the Z-scan technique, provides accurate control of the irradiance of an incident probe, simply by scanning a “slowly” converging/diverging laser beam through the sample under test [31]. If the probe laser is tuned to an absorption transition of the sample in question, this technique therefore allows the study of the saturation of the absorption, which is related to the saturation intensity of the material at that pump wavelength. However, to fully appreciate the change in transmission of the probe laser, it is necessary to know the small-signal transmission derived from the doping concentration and absorption cross section of the material at the wavelength of interest, which was discussed in the previous section 2.3.1. To determine the ETU coefficient the incident irradiance must range from values much lower than the saturation irradiance (intensity), to one that is comparable, if not higher than it. At the higher irradiance levels, depletion of the number of ions in their ground state increases the pump transmission, however, ETU counteracts this by effectively depopulating the upper level, equivalent to effectively increasing the saturation irradiance condition. A suitably configured Z-scan measurement provides an incident irradiance that can be scaled over several orders of magnitude, without requiring this degree of sensitivity or linearity from the detectors and associated digitization equipment. Consequently, this method can provide a very sensitive measure of the magnitude of the ETU coefficient.

For Nd:YAG we can treat the problem as a two-level system between the ground state ($^4I_{9/2}$ – N_1) and the metastable level ($^4F_{3/2}$ – N_2), for which the rate equations under steady state pumping conditions, are expressed as:

$$\frac{\partial N_1(r,z)}{\partial t} = -\frac{I_P(r,z)}{h\upsilon_P}\sigma_{abs}N_1(r,z) + \frac{N_2(r,z)}{\tau_0} + W_{ETU}N_2(r,z)^2 + W_{CR}N_1(r,z)N_2(r,z) \qquad 2\text{-}40$$

$$\frac{\partial N_2(r,z)}{\partial t} = \frac{I_P(r,z)}{h\upsilon_P}\sigma_{abs}N_1(r,z) - \frac{N_2(r,z)}{\tau_0} - W_{ETU}N_2(r,z)^2 - W_{CR}N_1(r,z)N_2(r,z) \qquad 2\text{-}41$$

where τ_0 is the intrinsic radiative lifetime for Nd:YAG, σ_{abs} is the effective absorption cross section for the ground state level, $h\upsilon_P$ is the pump photon energy, W_{ETU} is the ETU coefficient, W_{CR} is the CR coefficient, and $I_P(r,z)$ is the pump irradiance distribution along the sample's length, governed by:

$$\frac{dI_P(r,z)}{dz} = I_P(r,z)(-\sigma_{abs}N_1(r,z)) \qquad 2\text{-}42$$

By solving Eq.2-40 - 2-42 numerically, for a fixed pump power and a range of beam radii $\omega(z)$, the power transmitted through the crystal can be calculated, equivalent to the experimental conditions of scanning the sample along the Z-direction of the pump laser beam. Figure 2-6 shows the expected transmission of a Nd:YAG crystal, of the same length as our sample, at a wavelength tuned to the peak absorption around 808 nm and in function of the incident pump irradiance, with and without ETU effects, at room temperature and with no coating losses. A value of W_{CR} = 3.0 × 10^{-18}cm^3/s is used in our model, obtained from the measured fluorescence lifetime of our sample, 235±5 μs, together with the assumption that the intrinsic lifetime of Nd^{3+} in YAG is 260 μs [32], and for very low pump excitation CR is the only decay mechanism other than spontaneous emission. Three graphs drawn in Fig 2-6 show the expected transmission of 3.2 mm long Nd:YAG crystal with a doping concentration of 1.33 ×10^{20} ions/cm^3, versus the incident pump irradiance, at room temperature, with and without ETU effects. Comparing the case without ETU to the lowest reported value 5 x 10^{-17} cm^3/s [33], the pump transmission would increase by almost a factor of two when the peak on-axis incident pump irradiance reached 50 kW/cm^2, nearly four times higher than the saturation irradiance of the material. ETU acts to reduce the change in transmission as a function of the incident irradiance so can be used as a fitting parameter between the modelled and experimentally measured transmitted power.

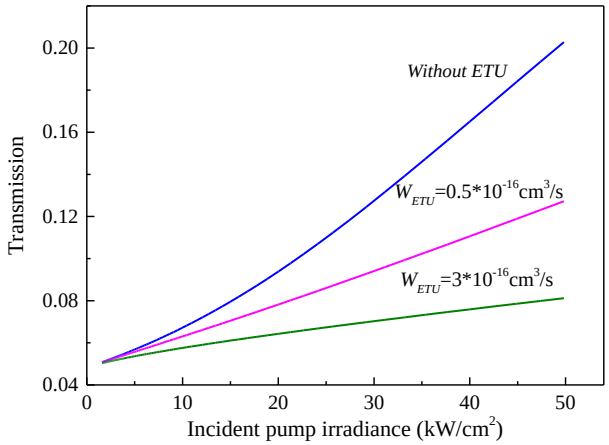

Figure 2-6 The transmission of Nd:YAG crystal versus incident pump irradiance

2.4 Review of laser performance modelling

This section presents the modelling approaches to predict the performance of end-pumped lasers. There are several previous studies of rate equations for longitudinally pumped lasers, which describe the spatially distributed population inversion density, and cavity photon number, including reabsorption losses and energy transfer upconversion (ETU) [30, 34]. Since this thesis reports on the quasi-four-level transition of Nd extensively, the effect of reabsorption and ETU is presented. It is well known that a gain material with reabsorption loss at the laser wavelength generally requires a tightly focused pump to create sufficient population inversion to overcome this loss and that of the cavity. ETU, as discussed previously reduces the population of a metastable energy level, which in effect reduces the effective lifetime of the upper laser level, and often will degrade the performance of the laser.

2.4.1 Rate equation

There are many approaches to model the Nd^{3+} ion doped laser system, with Risk [35] producing some general scaling curves that included the effect of mode overlap between the pump and signal photon distributions in the crystal. Bjurshagen *et al* [30] extended the analysis, including the influence of mode overlap, reabsorption loss, upconversion effects, and thermal induced aberrations on the laser performance.

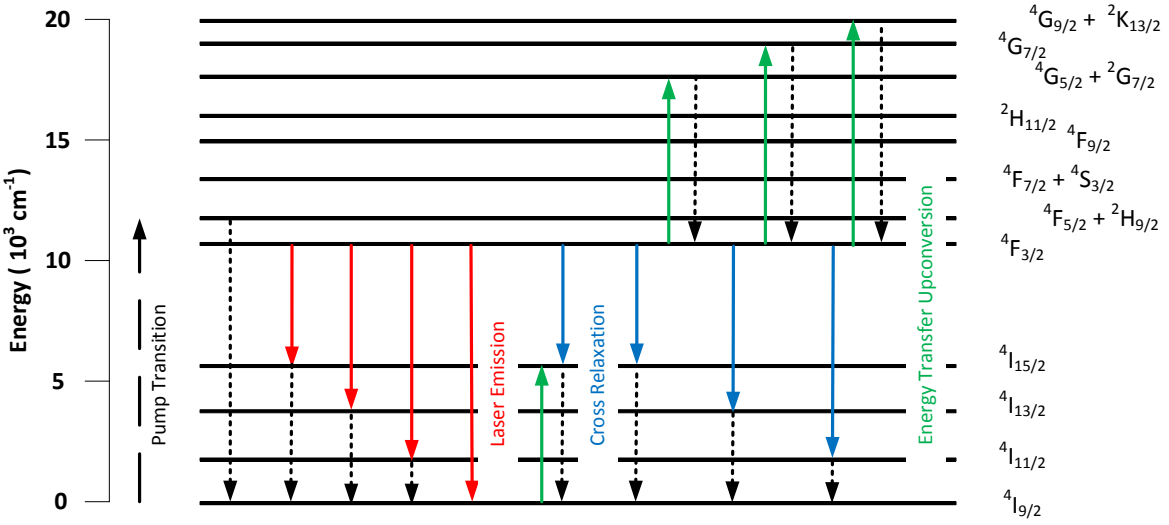

Figure 2-7 Energy level diagram of trivalent Nd^{3+} ion and transitions from metastable level, $^4F_{3/2}$ [36]

Figure 2-7 extended from simple energy diagram of Nd:YAG presented in Chapter 1. The figure includes four fluorescent transitions and multiphoton relaxations to ground level and three upconversion processes towards a higher state in $^4G_{5/2}$, $^4G_{7/2}$ and $^2G_{9/2}$ levels. The modelling describes a quasi-four-level energy transition in between lower crystal field (R1) of the upper laser level, $^4F_{3/2}$ and the top crystal field of (Z5) of Ground state ($^4I_{9/2}$). Under steady-state conditions, the population of all crystal fields in both manifolds obeys a Boltzmann distribution, thus the population density of two energy levels that are involved in the laser transition are denoted as a fraction of the total population density in each manifold.

$N_b = f_b N_2$ the population of the upper laser level

$N_a = f_a N_0$ the population of the lower laser level

The model accounts in the cross-relaxation as we used concentration dependent fluorescence lifetime, τ the term in the equation. Cross-relaxation can be dominant for some RE dopants, e.g. erbium ion doped lasers or at high doping concentration that is not valid for our case.

The steady-state rate equations for upper energy state is written as,

$$\frac{dN_2(r,z)}{dt} = Rr_p(r,z) - \frac{N_2(r,z)}{\tau} - \sigma_{SE}(r,z)\frac{c}{n}\Delta N(r,z)\Phi\phi(r,z) - W_{ETU}N_2(r,z)^2 = 0 \qquad 2\text{-}43$$

Where $\Delta N(r,z) = N_2(r,z) - N_1(r,z)$ is the population inversion density, the rate equation for the population inversion density is,

$$\frac{d\Delta N(r,z)}{dt} = fRr_p(r,z) - \frac{\Delta N(r,z) - \Delta N^0}{\tau} - f\sigma_{SE}\frac{c}{n}\Delta N(r,z)\Phi\phi(r,z) - \frac{W_{ETU}}{f}\left[\Delta N(r,z) - \Delta N^0\right]^2 = 0 \quad 2\text{-}44$$

Where f is the sum of the occupational fraction of the population at each manifold, ΔN^0 is the thermal equilibrium population inversion density. The pump rate R is given by $R = P_p \eta_a / h\nu_p$, where P_p is the incident pump power, η_a is the pump absorption efficiency that can be expressed as $\eta_a = 1 - \exp(-\alpha_p l)$ where gain length and absorption efficiency is α_p. Total number of laser photons in cavity Φ is given by $\Phi = 2nl_c P_l / ch\nu_l$, where P_l is the cavity laser power, l_c is the optical path length of the cavity with gain media, $h\nu_p$ and $h\nu_l$ are pump photon energy and laser photon laser energy, respectively. $r_p(r,z)$ and $\phi(r,z)$ are the normalized spatial distribution of pump energy and laser photon distribution, respectively and are normalized over the crystal and cavity

$$\int_{crystal} r_p(r,z)dV = 1 \qquad \text{2-45}$$

$$\int_{cavity} \phi(r,z)dV = 1. \qquad \text{2-46}$$

The corresponding rate equation for the cavity photon number is,

$$\frac{d\Phi}{dt} = \frac{c}{n}\sigma_{SE}\int_{crystal} \Delta N(r,z)\Phi\phi(r,z)dV - \frac{\Phi}{\tau_c}. \qquad \text{2-47}$$

Where cavity photon lifetime, τ_c is given by $2l_c/c\delta$, $\delta = L + \ln\left[1/\left(1-T_{OC}\right)\right]$ is the round trip-loss, and L is the intrinsic cavity loss where T_{OC} is output coupler transmittance. This definition of δ assumes the value of T_{OC} is small.

Under thermal equilibrium condition, we can assume the population at the ground manifold is dominant which allows ΔN^0 to be written as $-N_0{}^0$, which is unpumped population density of the ground manifold. Therefore, we can derive the population density below threshold by substituting in $\Phi = 0$ into Eq.2-44

$$\Delta N_{th} = \frac{2\tau f R_{th} r_p}{1 + (1 + 4W\tau^2 R_{th} r_p)^{1/2}} - N_0{}^0 \qquad \text{2-48}$$

And the steady state population inversion density is calculated to be,

$$\Delta N = \frac{2\tau f R r_p + 2\frac{c\sigma_{SE}\tau}{n} f N_o{}^o \Phi\phi}{1 + \frac{c\sigma_{SE}\tau}{n} f\Phi\phi(r,z) + \left[\left(1 + \frac{c\sigma_{SE}\tau}{n} f\Phi\phi\right)^2 + 4W\tau^2 R r_p + 4W\tau^2 \frac{c\sigma_{SE}}{n} N_0{}^0 \Phi\phi\right]^{1/2}} - N_0{}^0 \qquad \text{2-49}$$

Here the equation expresses that the total inversion is dependent upon upconversion and reabsorption, which is the additional term increases the complexity in modelling quasi-four-level lasers compared with a true-four-level transition.

The equation 2-48 can be substituted into Eq.2-43 where the pump rate yields the total laser cavity photon number.

$$\frac{2\sigma_{SE} l_c}{n} \int_{crystal} \Delta N(r,z)\phi(r,z)dV = \delta \qquad 2\text{-}50$$

$$\frac{2\sigma_{SE} l_c}{n} \int_{crystal} \frac{2\tau\, fRr_p\phi + 2\frac{c\sigma_{SE}\tau}{n} fN_o{}^{o}\Phi\phi^2}{1+\frac{c\sigma_{SE}\tau}{n} f\Phi\phi + \left[\left(1+\frac{c\sigma_{SE}\tau}{n} f\Phi\phi\right)^2 + 4W\tau^2 Rr_p + 4W\tau^2 \frac{c\sigma_{SE}}{n} N_0{}^{0}\Phi\phi\right]^{1/2}} dV = \delta + \delta_l \qquad 2\text{-}51$$

Where $\delta_l = 2N_o{}^{o}\sigma_{SE}\frac{l_c}{n}\int_{crystal}\phi dV$ is the reabsorption loss added to lower laser level, Eq.2-50 indicates the term cavity loss, which includes cavity loss and output transmission, is equal to the total gain over the laser crystal including reabsorption and upconversion losses above threshold. We can substitute Eq.2-48 into Eq.2-47, the pump rate at threshold can be derived to be,

$$R_{th} = \frac{\delta+\delta_l}{2\sigma_{SE}\tau\, fl_c}\left[\int_{crystal}\frac{2r_p\phi}{1+(1+4W\tau^2 R_{th}r_p)^{1/2}}dV\right]^{-1} \qquad 2\text{-}52$$

where $R_{th}(T,r,z)$ is the pump rate at laser threshold.

2.4.2 Laser threshold and slope efficiency

We now evaluate laser threshold and slope efficiency in an end-pumped configuration. First considering a Gaussian distribution for both pump and laser beam, assuming that beam size for both the pump beam and cavity-mode are unchanged over the length of the gain media. The normalized pump and laser photon distributions in Eq.2-45 and 2-46 are then given by,

$$r_p(r,z) = \frac{2\alpha}{\eta_a \pi w_p{}^2}\exp\left(\frac{-2r^2}{w_p{}^2}\right)\exp(-\alpha z) \qquad 2\text{-}53$$

and

$$\phi(r,z) = \frac{2\alpha}{\pi w_l{}^2 l_c}\exp\left(\frac{-2r^2}{w_l{}^2}\right). \qquad 2\text{-}54$$

With w_p and w_l, the Gaussian beam radii for the pump and laser-beam, respectively.

We use the terms defined by Risk [35] and Bjurshagen [30] to solve Eq.2-51,

$$a = \frac{w_p}{w_l}, \tag{2-55}$$

$$x = \frac{2r^2}{w_p{}^2} \tag{2-56}$$

$$F = \frac{4\tau\sigma_{SE}R}{\pi w_l{}^2\delta} \tag{2-57}$$

$$S = \frac{2c\sigma_{SE}\tau\Phi}{\pi w_l{}^2 l_c} \tag{2-58}$$

$$B = \frac{2N_0{}^0\sigma_{SE}l}{\delta} \tag{2-59}$$

$$U = \frac{2W\tau\delta}{f\sigma_{SE}l} \tag{2-60}$$

Where a is the ratio of the pump and laser beam waists, F is a normalized parameter proportional to the pump power, S is a normalized parameter proportional to the internal laser power, B is the ratio of reabsorption loss to the cavity loss, and U is a normalized parameter proportional to upconversion loss. Substituting Eq.2-55 to Eq.2-60 into Eq.2-51 we obtain,

$$F = \frac{1+B-\frac{2Ba^2}{l}\int_0^\infty\int_0^l \frac{fS\exp(-2a^2x)}{1+fS\exp(-a^2x)+\left[\left(1+fS\exp(-a^2x)\right)^2+\left(\alpha l/\eta_a a^2\right)fUF\exp(-x)\exp(-\alpha z)+fUBS(\exp(-a^2x)\right]^{1/2}}dzdr}{2f\frac{\alpha}{\eta_a}\int_0^\infty\int_0^l \frac{\exp\left[-\left(a^2+1\right)x\right]\exp(-\alpha z)}{1+fS\exp(-a^2x)+\left[\left(1+fS\exp(-a^2x)\right)^2+\left(\alpha l/\eta_a a^2\right)fUF\exp(-x)\exp(-\alpha z)+fUBS\exp(-a^2x)\right]^{1/2}}dzdr} \tag{2-61}$$

At threshold, the output power is zero, substitute S=0 in Eq.2-61 we obtain F_{th}

$$F_{th} = \frac{1+B}{2f\frac{\alpha}{\eta_a}\int_0^\infty\int_0^l \frac{\exp\left(-\left(a^2+1\right)x\right)\exp(-\alpha z)}{1+\left[1+\alpha l/\eta_a a^2 XfUF_{th}\exp(-x)\exp(-\alpha z)\right]^{1/2}}dzdr} \tag{2-62}$$

Kim *et al* [37] made an analytical expression for threshold power for using a top-hat pump distribution, assuming the most of pump light is being absorbed.

$$P_{th} \approx \frac{h\nu p\pi(w_p^{\,2} + w_l^{\,2})}{4f\sigma\tau\eta_q}(\delta + 2f_1\sigma(1-\exp(-2a^2))N_0^{\,0}l)\left[1 + \frac{W\tau\alpha}{4f\sigma(1-\exp(-2a^2))}(\delta + 2f_1\sigma(1-\exp(-2a^2))N_0^{\,0}l)\right] \quad \text{2-63}$$

Note, this expression is simply related to an equivalent system with top-hat pumping beam, as given by Taira *et al* [38].

$$\frac{P_{th}(top-hat)}{P_{th}(Gaussian)} = \frac{2a^2}{(1+a^2)\left[1-\exp(2a^2)\right]} \quad \text{2-64}$$

The slope efficiency as given by Risk [35] is,

$$\frac{dP_l}{dP_p} = \frac{T}{L+T}\frac{\nu_l}{\nu_p}\eta_a(T,r,z)\frac{dS}{dF}, \quad \text{2-65}$$

which depends on four factors, quantum defect, the fraction of laser photons that escape the cavity, the absorption efficiency of the pump photons, and the photon conversion efficiency, dS/dF. The photon conversion efficiency quantifies the pump and laser mode overlap, the effects of saturation, through S, and the number of times over threshold, F, which as shown in Eq.2-61, which depends upon reabsorption, and upconversion [38].

The term W and $2f_1\sigma(1-\exp(-2a^2))$ in Eq.2-63 show the additions of quadratic dependence in quasi-four-level transitions and upconversion gives more impact compare to four-level transition cases. Cryogenic laser operation turns the R1 → Z5 transition to four-level transition where reabsorption is negligible, but further information of upconversion changes at low temperature is still required in order to estimate additional heat generation. In Chapter 4 we determined laser threshold based on measured upconversion parameter.

2.5 Beam quality: real time measure

Thermal loading from the waste power pump light is generally more important for low-gain laser systems. Furthermore, the Q-F-L transition of Nd:YAG needs high pump irradiance to reach threshold, which implies a high-thermal-density that introduces strong aberrations in the gain medium. It is essential to maintain or build a laser system that can provide near-diffraction-limited beam. A real-time beam diagnostic system that can characterize the beam parameter product (BPP) and laser output power would ensure quick optimization compared to other scanning methods to measure the beam quality [39]. The real-time technique described by Ng *et al* [40] simultaneously takes the image of the near field, along with the far field (the beam profile in the Fourier-plane of a lens), which defines the M^2 in real time without moving optical parts.

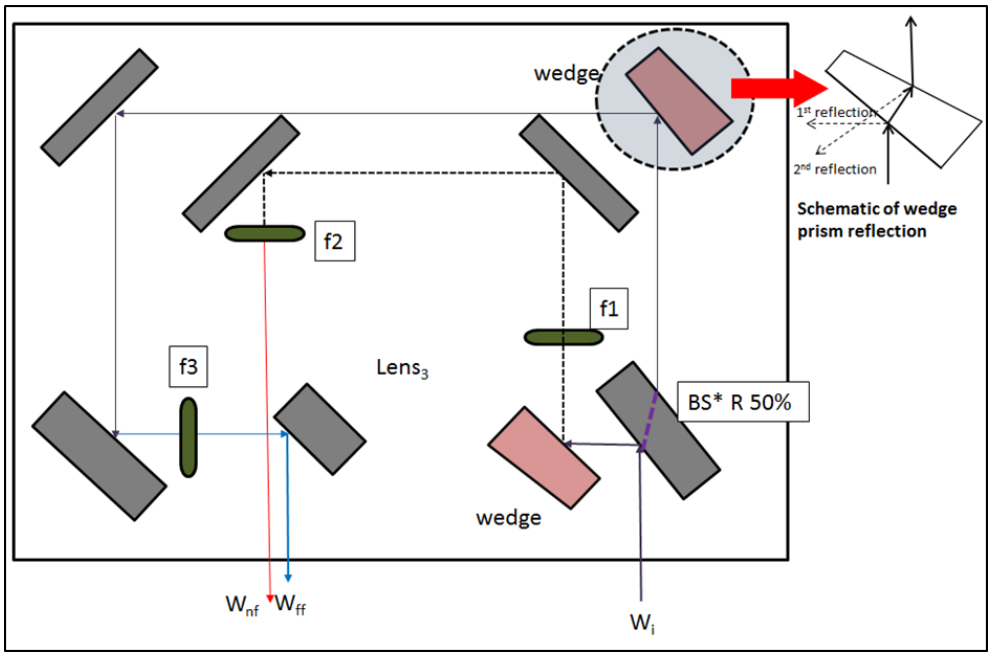

Figure 2-8 Schematic of the real-time M^2 measurement set-up

w_{nf} , a near field image is product of a simple imaging telescope defined by the ratio of two lens, f_1 and f_2 . The measured image w_{nf} is then define the original beam waist, w_o .

$$w_{nf} = \frac{f_2}{f_1} w_o \qquad 2\text{-}66$$

While the Fourier transform of the incident laser beam is measured at the focal plane of lens, f_3 . The beam waist, w_{ff} is related to the incident beam's divergence, θ_o .

$$w_{ff} = \theta_o f_3 \qquad 2\text{-}67$$

The beam divergence as defined in Gaussian beam propagation theory, is proportional to the wavelength, λ and the beam quality, and inversely proportional to the beam waist, w_o .

$$\theta_o = \frac{M^2 \lambda}{\pi w_o} \qquad 2\text{-}68$$

Combining the Eq.2-67 and 2-68 allows the expression for the beam quality factor which can be defined from measurable quantities.

$$M^2 = \frac{\pi}{\lambda} \frac{f_1}{f_2 f_3} w_{nf} w_{ff} \qquad 2\text{-}69$$

Figure 2-8 is a schematic diagram of an experimental set-up that was built to accommodate lasers in the near infrared region. The 1st beam splitter (BS) was coated to reflect 50% for incoming light

for 900-1100 nm range. The two lenses for the near field system, f_1 = 75 mm and f_2 = 150 mm are a relay imaging afocal telescope. Therefore, the beam waist at w_{nf} is a two times magnified image of the input plane. An achromatic lens, f_3, was adjusted to ensure that the Fourier plane is at the detection plane, where w_{nf} was positioned. The Fourier plane of f_3 was found initially by passing two parallel beams through the lens then setting its position to make the point of convergence at the CCD camera. A Spiricon CCD was used for the experiment and measured both beam profiles w_{nf} and w_{ff}. All lenses were AR coated (B-coating, Thorlabs [41]). Reflections were made with mirrors HR (EO3, 750-110 nm >99 %, Thorlabs [41]) or uncoated wedge prisms. Uncoated wedges were selected to reflect 4 % of incident light, thus helping to attenuate the laser intensity. Furthermore, a shallow-angle wedge prism is particularly useful as a beam splitter as well, with the 2nd reflection from the back surface also used. The beam quality parameter can be calculated quickly based on Eq.2-69.

References

1. W. A. Clarkson, "Thermal effects and their mitigation in end-pumped solid-state lasers," Journal of Physics D: applied Physics **34**, 2381-2395 (2001).

2. K.M. Du, N.L. Wu, J.D. Xu, J. Giesekus, P. Loosen, and P. R, "Partially end-pumped Nd:YAG slab laser with a hybrid resonator," Optics Letters **23**, 370-372 (1998).

3. A. Giesen, H. Hugel, A. Voss, K. Wittig, U. Brauch, and H. Opower, "Scalable Concept for Diode-Pumped High-Power Solid-State Lasers," Applied Physics B: Lasers and Optics **58**, 365-372 (1994).

4. V. Khitrov, J.D. Minelly, R. Tumminelli, V. Petit, and E. S. Pooler, "3kW single-mode direct diode-pumped fiber laser," in *Proc. SPIE 8961, Fiber lasers XI: Technology, Systems, and Applications, 89610V (March 12, 2014)*(2014).

5. A.P. Ongstad, M. Guy, and J. R. Chavez, "High power Nd:YAG spinning disk laser," Optics Express **24**, 108-113 (2016).

6. W. Clarkson, M. Eckold., and J. I. Mackenzie, "New approach for power scaling solid-state lasers with intracavity motion," Optics Letters **42,** 775-778(2017).

7. T. Y. Fan, D. J. Ripin, R. L. Aggarwal, J. R. Ochoa, B. Chann, M. Tilleman, and J. Spitzberg, "Cryogenic Yb3+-doped solid-state lasers," IEEE Journal of Selected Topics in Quantum Electronics **13**, 448-459 (2007).

8. D. C. Brown, S. Tornegard, J. Kolis, C. McMillen, C. Moore, L. Sanjeewa, and C. Hancock, "The Application of Cryogenic Laser Physics to the Development of High Average Power Ultra-Short Pulse Lasers," Applied Science-Basel **6** (2016).

9. W.Koechner, *Solid-state laser engineering, 6th edition* (Springer, 2005).

10. William Jones, and N. H. March, *TheoreticalSolid State Physics - Non-Equilibrium and Disorder* (Courier Dover Publications, 1985).

11. C. Kittel, *Introduction to Solid State Physics, 8th Edition* (Wiley, 2005).

12. R. L. Aggarwal, D. J. Ripin, J. R. Ochoa, and T. Y. Fan, "Measurement of thermo-optic properties of Y3Al5O12, Lu3Al5O12, YAlO(3), LiYF4, LiLuF4, BaY2F8, KGd(WO4)(2), and KY(WO4)(2) laser crystals in the 80-300 K temperature range," Journal of Applied Physics **98** (2005).

13. W. J. Parker, R. J. Jenkins, C. P. Butler, and G. L. Abbott, "Flash Method of Determining Thermal Diffusivity, Heat Capacity, and Thermal Conductivity," Journal of Applied Physics **32**, 1679-1684 (1961).

14. D. C. Brown, "Ultrahigh-average-power diode-pumped Nd:YAG and Yb:YAG lasers," IEEE Journal of Quantum Electronics **33**, 861-873 (1997).

15. M. E. Innocenzi, H. T. Yura, C. L. Fincher, and R. A. Fields, "Thermal Modeling of Continous-Wave End-Pumped Solid-State Lasers," Applied Physics Letters **56**, 1831-1833 (1990).

16. S. Chenais, F. Druon, S. Forget, F. Balembois, and P. Georges, "On thermal effects in solid-state lasers: The case of ytterbium-doped materials," Progress in Quantum Electronics **30**, 89-153 (2006).

17. H. S. Carslaw, and J. C. Jaeger, *Conduction of Heat in Solids* (Oxford University Press, 1986).

18. E. H. Calrson, and G. H. Dieke, "The State of the Nd3+ Ion as Derived from the Absorption and Fluorescence Spectra of NdCl3 and Their Zeeman Effects " Journal of Chemical Physics **34**, 9 (1961).

19. W. F. Krupke, "Induced-emission cross-sections in neodymium laser glasses," IEEE Journal of Quantum Electronics **10**, 450 (1974).

20. W. B. Fowler, and D. L. Dexter, "Relation between Absorption and Emission Probabilities in Luminescent Centers in Ionic Solids," Physical Review Letters **128**, 2154 (1962).

21. B. F. Aull, and H. P. Jenssen, "Vibronic Interactions in Nd-YAG Resulting in Nonreciprocity of Absorption and Stimulated-Emission Cross-Sections," IEEE Journal of Quantum Electronics **18**, 925-930 (1982).

22. D. E. McCumber, "Einstein Relations Connecting Broadband Emission and Absroption Spectra," Physical Review Letters **136**, A954 (1964).

23. A. Einstein, "The quantum theory of radiation," Physikalische Zeitschrift **18**, 8 (1917).

24. Optical Socierty of America, *Handbook of Optics* (Mcgraw-hill, 2000).

25. S. A. Payne, J. A. Caird, L. L. Chase, L. K. Smith, N. D. Nielsen, and W. F. Krupke, "Spectroscopy and Gain Measurements of Nd3+ in SRF2 and Other Fluorite-Structure Hosts," Journal of the Optical Society of America B-Optical Physics **8**, 726-740 (1991).

26. S. A. Payne, L. L. Chase, L. K. Smith, W. L. Kway, and W. F. Krupke, "Infrared Cross-Section Measurements for Crystals Doped with Er3+, Tm3+, and Ho3+," IEEE Journal of Quantum Electronics **28**, 2619-2630 (1992).

27. M. Pollnau, P. J. Hardman, M. A. Kern, W. A. Clarkson, and D. C. Hanna, "Upconversion-induced heat generation and thermal lensing in Nd : YLF and Nd : YAG," Physical Reviews B **58**, 16076-16092 (1998).

28. L. Palatella, F. Cornacchia, A. Toncelli, and M. Tonelli, "Microscopic treatment of upconversion in Nd3+-doped samples," Journal of the Optical Society of America B-Optical Physics **20**, 1708-1714 (2003).

29. M. Pollnau, P. J. Hardman, W. A. Clarkson, and D. C. Hanna, "Upconversion, lifetime quenching, and ground-state bleaching in Nd3+:LiYF4," Optical Communications **147**, 203-211 (1998).

30. S. Bjurshagen, and R. Koch, "Modeling of energy-transfer upconversion and thermal effects in end-pumped quasi-three-level lasers," Applied Optics **43**, 4753-4767 (2004).

31. J. O. White, and C. E. Mungan, "Measurement of upconversion in Er:YAG via z-scan," Journal of the Optical Society of America B-Optical Physics **28**, 2358-2361 (2011).

32. V. Lupei, and A. Lupei, "Emission dynamics of the F-4(3/2) level of Nd3+ in YAG at low pump intensities," Physical Reviews B **61**, 8087-8098 (2000).

33. S. Guy, C. L. Bonner, D. P. Shepherd, D. C. Hanna, and A. C. Tropper, "High-inversion densities in Nd : YAG: Upconversion and bleaching," IEEE Journal of Quantum Electronics **34**, 900-909 (1998).

34. Y. Guyot, H. Manaa, J. Y. Rivoire, R. Moncorge, N. Garnier, E. Descroix, M. Bon, and P. Laporte, "Excited-State-Absorption and Up-conversion Studies of Nd3+-Doped-Single Crystals Y3Al5O12, YLiF4, and LaMgAl11O19," Physical Reviews B **51**, 784-799 (1995).

35. W. P. Risk, "Modeling of Longitudinally Pumped Solid-State Lasers Exhibiting Reabsorption Losses," Journal of the Optical Society of America B-Optical Physics **5**, 1412-1423 (1988).

36. A. A. Kaminskii, *Crystalline lasers: physical processes and operating schemes* (CRC Press, 1996).

37. J. W. Kim, J. I. Mackenzie, and W. A. Clarkson, "Influence of energy-transfer-upconversion on threshold pump power in quasi-three-level solid-state lasers," Optics Express **17**, 11935-11943 (2009).

38. T. Taira, W. M. Tulloch, and R. L. Byer, "Modeling of quasi-three-level lasers and operation of cw Yb:YAG lasers," Applied Optics **36**, 1867-1874 (1997).

39. B. Neuenschwander, R. Weber, and H. P. Weber, "Determination of the Thermal Lens in Solid-State Lasers with Stable Cavity," IEEE Journal of Quantum Electronics **31**, 1082-1087 (1995).

40. S. P. Ng, and J. I. Mackenzie, "Planar Waveguide Laser Optimization and Characterization Employing Real-Time Beam Quality Measurement," IEEE Journal of Quantum Electronics **49**, 146-153 (2013).

41. Thorlabs, www.thorlabs.com2016.

Part I

Spectroscopy of Nd Doped Crystals

Chapter 3:

Neodymium spectroscopic measurements

This chapter reports the high-resolution measurements of the emission and absorption cross section of Nd^{3+} ions doped into various host crystals, which are widely used in many commercial lasers. As such the investigated crystals are readily available and therefore well known, with the majority of their properties of interest already reported in the literature. However, the data described herein details the temperature dependence of these key parameters, which are generally not to be found in the public domain. In particular, we describe the measurement of the temperature dependence of the key spectroscopic properties of garnet, fluoride, vanadate, and tungstate crystals. For the anisotropic crystals, all measurements were undertaken with polarization taken into consideration, therefore we obtain a comparison of the independent spectroscopic properties according to the orientation of the host crystal. Measurements were performed at range of temperatures ranging from 77 K to 450 K, to provide comparison with reported data (for a couple of the crystals) at elevated temperatures, as well as, new data for the colder conditions. The importance of this study is that it provides useful information about the respective crystals that could be utilised in lasers operating at atypical temperatures, such as under cryogenic conditions.

In the following sections, we first introduce the respective host crystals and their properties that make them attractive for lasers, then present the methodology for the experimental procedures to determine the spectroscopic properties, followed by a discussion of the key results and a chapter summary. Each of the measured spectral curves for the crystals investigated, at the respective temperatures, are reported in Appendix A for reference. A summary of the measured data is provided in section 3.4, with polynomial fits to cover the change in peak cross section values over the range of measured temperatures investigated. Finally, a study of fluorescence lifetime, for different doping concentrations, in several of the crystal types was performed, as the measured lifetime is important for determining the potential efficiency of the respective laser crystals.

3.1 Host media (YAG, YVO4, KGW, YLF, GSAG, GdVO4)

To enable a RE ion of interest to be optically active it needs a physical environment in which to sit, such as a crystal lattice, moreover the lattice must have special symmetrical properties to ensure that the electrons in the 4f shell of the RE ion, suitably shielded by the filled 5d electron shell, are able to interact with the nucleus, through spin-orbit coupling, and the surrounding crystal field. There are a range of possible symmetry groups that enable optical activity of many of the RE ions, and a few of the most popular crystals are introduced below. Figure 3-1 shows the energy level splitting diagram for 6 crystal hosts, YAG, GSAG, YVO4, GdVO4, KGW and YLF at RT, Table 3-1 presents some key parameters of them [1-8].

Table 3-1 crystal properties of Nd doped crystal hosts [2-8]

	Nd:YAG	Nd:GSAG	Nd:YVO4	Nd:GdVO4	Nd:KGW	Nd:YLF
Lattice symmetry	Cubic	Cubic	Tetragonal	Tetragonal	Monoclinic	Tetragonal
Lattice constant (Å)	12	12.39	a=7.12 c=6.289	a=7.123 c=6.291	Ng=8.1 Np=10.43 Nm=7.6	a=5.18 c=10.74
Nd lattice site (1 at.% doped, $10^{20}cm^{-3}$)	1.39	1.2	1.255	1.25	0.633	1.39
Refractive index @1μm	1.822	1.89	No=1.958 Ne=1.216	No=1.97 Ne=1.22	Ng=2.033 Np=1.937 Nm=1.986	No=1.454 Ne=1.477
Thermal conductivity ($Wm^{-1}K^{-1}$ @300K)	11	10.5	9(a) 12(c)	8.6(a) 10.4(c)	2.6 (Ng) 3.8(Np) 3.4(Nm)	7.2(a) 5.8(c)
Thermal expansion coefficient ($10^{-6}K^{-1}$ @300K)	7.5	7.7	1.69(a) 8.19(c)	1.14(a) 7.89(c)	4(Ng) 3.5(Np) 8.5(Nm)	13.3(a) 8.3(c)
dn/dT @1μm ($10^{-6}K^{-1}$ @300K)	7.3	8.9	7.9(c)	13.8(a) 10.1(c)	0.4	-2(a) -4.3(c)

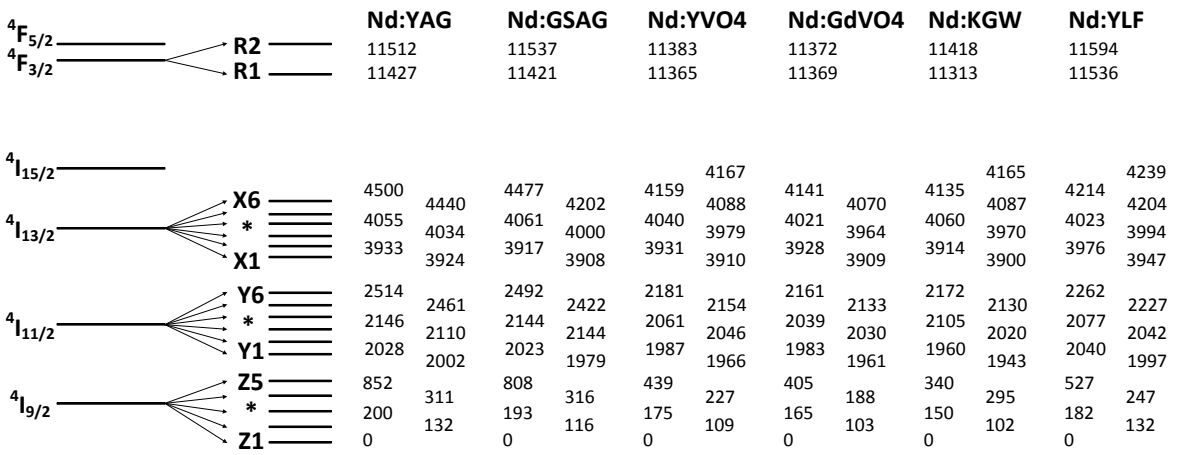

Figure 3-1 RT energy level scheme for Nd doped crystal hosts [1]

Garnets (YAG and GSAG)

Synthetic garnet crystals have long been exploited as laser gain media with rare-earth doping, with yttrium aluminium garnet (YAG - $Y_3Al_5O_{12}$) the most prominent material for crystalline solid-state lasers [8], due to its superior optical and physical properties. It has a wide transmission window (300 nm - 4 μm), and can be grown to quite large boule-sizes (~100 mm diameter) via the Czochralski method, with very high optical quality. An isotropic material with relatively high thermal conductivity, combined with its hardness and moderate thermal expansion coefficient, this crystal has one of the best thermal shock parameters of commonly used gain media, which permits high-power laser operation. Due to the relatively large ionic radii of the yttrium ion, it is well suited to impurity substitution with many of the RE ions, e.g. Nd^{3+}, Tm^{3+}, Er^{3+}, Ho^{3+}, and Yb^{3+} [4, 9-11]. For Nd^{3+} the RE of interest in this thesis, doped into YAG, the relatively large crystal field strength introduces strong Stark splitting of the ion's energy levels. In particular, at room temperature, the $^4I_{9/2}$ ground state of Nd:YAG is split into 5 Stark levels with the highest at 857 cm^{-1} above the unperturbed ion ground state, which provides a virtually empty lower laser level (~0.7 % of all of the dopant population). This is the terminal laser level for the 946 nm transition, starting from the lowest Stark level of the upper metastable energy level, $^4F_{3/2}$.

Gadolinium Scandium Aluminium Garnet (GSAG – $GdSc_2Al_5O_{12}$) is an isomorph of YAG, where the three yttrium atoms of the fundamental YAG unit cell are replaced with gadolinium and scandium. This substitution of atoms was investigated as a way to tune the potential laser wavelengths accessible from a particular RE ion, due to the change in the relative crystal field strengths around the respective ion in the lattice, and subsequent shifts in it's Stark levels. Compositional tuning was exploited by researchers [2, 12] to realise lasers at specific wavelengths for applications, such as Diferrential Absorption LIDAR (DIAL), targeting water vapour lines in the vicinity of 942 nm [13, 14]. With slightly weaker crystal fields in comparison to its cousin (YAG), Nd:GSAG

cooled to cryogenic temperatures could be a strong candidate for a higher energy 942 nm laser source for long range DIAL applications.

Vanadates (YVO4 and GdVO4)

YVO4 (Yttrium orthovanadate) is one of most efficient crystal for hosting Nd^{3+} ions, enables end-pumping configuration. It is an optically uniaxial crystal belonging to the crystal group family of tetragonal compounds [15]. The cross section spectrum for both absorption and emission is significantly stronger for light polarized with the electric field aligned with the c-axis (π - pol) then for the perpendicular orientation (σ - pol) and the relatively wide absorption band around 809 nm allows for a reasonably large tolerance in the temperature of operation for pump diode lasers. Despite the fact that thermal conductivity and expansion coefficient are anisotropic [5], leading to asymmetric thermal lensing during high-power pumping, YVO4 has attractive features for diode-laser pump-sources in end-pumped systems. GdVO4, another vanadate crystal where yttirium is replaced with gadolinium, has comparable thermal properties as YVO4, but also exhibits very favourable spectroscopic properties, such as 7 times higher absorption at 808 nm and 3-times higher emission cross section at 1.06 μm than in comparison with Nd:YAG. Recently, Sato and Taira presented very accurate measure of thermal expansion coefficient and *dn/dT* (temperature coefficients of refractive index) for Nd:YAG, Nd:YVO4 and Nd:GdVO4, respectively. The result shows advantage of GdVO4 over YVO4 for using c-axis and GdVO4 usually have better conversion efficiency [5, 6].

Tungstate (KGW)

Tungstate crystal families were an early focal point in solid-state-laser history, with one of the first lasers demonstrated using Nd:CaWO4 [16]. Recently researchers have focused on the potential of monoclic double-tungstates (e.g. AB[WO4]2) that are well suited to doping with RE ions. This is because the monoclinic crystal structure, group C2/m, provides one of the largest spacing between the RE-ions impurities, for equivalent doping concentrations. Moreover, some isomorphs (e.g. KGW) can be quite highly doped before detrimental processes affect the RE-ion spectroscopic properties. These unique properties imply minimal fluorescence quenching, with up to 20 at.%. Yb^{3+} doped crystals readily available commercially, of interest for their broad gain-bandwidths and a small quantum defect [8] that provide a route to ultra-short pulses and high average powers [17]. Finally, despite the poorer thermal conductivity values and a negative dependence of the refractive index on temperature, compared with the harder crystals like the garnets or vanadates, it has been shown that there are crystal orientations that access high-gain

polarizations and a positive thermal lens [18, 19]. Nonetheless thermal lens anisotropy can be a limiting factor in scaling the output power of lasers based around these materials.

Potassium gadolinium tungstate (KGd[WO4]2) is a well studied monoclinic double tungstate, which offers intense and broad absorption and emission bands [3]. KGW is the best host for Nd^{3+} ion doping due to the similarity of the ionic radii, of eight-fold oxygen-coordinated Gd^{3+} (1.053 Å) and Nd^{3+} (1.109 Å) [1], allowing up to 10 at.% doping (even though this corresponds to nominally half the ion density for equivalent doping levels in garnet and fluorides). With its strong anisotropy, depolarization loss and thermal birefringence can be negligible effects, although the thermal lens often is not (as mentioned above). Another spectroscopic feature is energy transfer upconversion (ETU) of this crystal, which will be discussed in greater detail in Chapter 4. The ETU parameter of this crystal appears to be relatively low in comparison to the other hosts. The spectroscopic features enable low threshold, and highly efficient laser systems [20]. The broad emission band is comparable to glass but the thermal conductivity is three times higher as the host has potential for microchip lasers or thin disk geometry. These geometries with having Nd^{3+} ion doped system provides chance for higher gain/cm than vanadate hosts, leading to achieve low threshold and high optical-to-optical laser efficiency.

Fluoride (YLF)

LiYF4 (often called YLF) is one of the most widely used laser crystal, along with YAG and YVO4. The crystal has a beneficial thermo-optical property for the weaker (at room temperature) of it's two main transition lines in the 1 micron region. Due to opposing thermal lensing parameters, associated with the change of refractive index as a function of temperature, *dN/dT*, being negative, while the thermal expansion coefficient and thus end face bulging is positive, the result is the induced-lens created inside crystal for end-pump geometries is relatively weak. With its longer fluorescence lifetime, 500 μs compared to 90 μs of Nd:YVO4 and 230 μs of Nd:YAG [8], Nd:YLF offers greater energy storage, which is beneficial in obtaining higher pulse-energy. Nonetheless, the peak power can be limited by strong upconversion processes that reduce the energy storage lifetime significantly, as will be discussed in Chapter 4. The birefringent crystal naturally generates polarized laser emission, similar to the vanadates and tungstates. The transition to ground level delivers 903 nm for π polarization and 908 nm for σ polarization, the ground laser manifold lies only 529 cm^{-1} above the unperturbed ion ground state, which populates 3.4 % of all the dopant population.

3.2 Methodology and experiment set-up

Fluorescence and absorption measurements, for different neodymium-doped crystals, were performed with a novel experimental arrangement, Fig 3-2, which could be tailored to determine the cross section values over a wide range of temperatures, i.e. above and below room temperature. This data was not readily available in the public domain, yet is extremely important for engineering neodymium-lasers away from ambient conditions. The setup could also easily accommodate anisotropic crystals with the addition of a polarizer. As such, accurate spectroscopic characterization of various samples of interest was achieved in the two main pump-absorption and emission wavelength bands.

3.2.1 Absorption cross section measurement

To cover a very wide potential operating-temperature range, different configurations for controlling the crystal temperature were employed. For sub-ambient (<~300 K) conditions, each crystal was mounted on the cold-head of a vacuum-sealed liquid nitrogen (LN) cryostat, with the temperature monitored in the crystal mount and regulated by the LN boil-off rate and the thermal mass of the system. Whereas for elevated temperatures (>~300 K), the crystal was mounted onto a fixture attached to a resistive load, capable of being heated upto 450 K in air, with some minor shielding to reduce convective cooling. Fig 3-2 represents the general experimental set-up for measuring the absorption spectrum of the respective crystal samples.

For the sub-ambient conditions, the crystal and copper (Cu) mount, thermally isolated from the external environment via a vacuum of $<10^{-6}$ Bar. Two 6 mm-thick windows, anti-reflection (AR) coated for wavelengths between 0.65-1.05 μm, allowed for optical access to the crystals from both ends and acted as sealing plates for the vacuum chamber. To study supra-ambient conditions, the crystal "heating stage" (Fig 3-2) was used in place of the cryostat. Therefore simply exchanging the crystal mounting scheme, the absorption measurement configuration was able to cover a crystal temperature range from 77 K to 450 K. With this set up we investigated the temperature dependence of the absorption cross section from the $^4I_{9/2}$ (Z) ground state to the $^4F_{3/2}$ (R), and $^4F_{5/2}$ and $^2H_{9/2}$ (S) Nd^{3+} excited states [21].

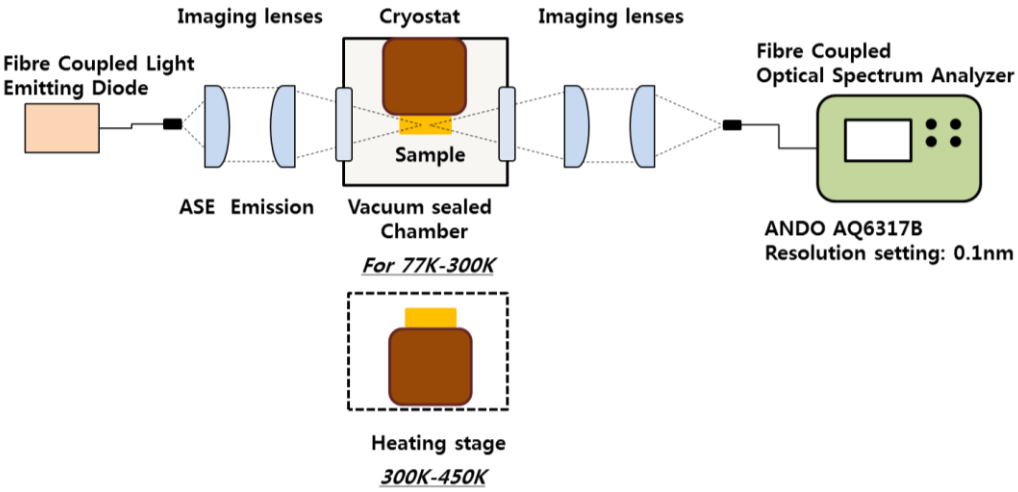

Figure 3-2 Schematic of the experimental setup for the absorption spectra measurement

Two separate optical sources were employed to study the S-band [21] and R-band [22] absorption spectral ranges. Firstly, utilizing the broadband amplified spontaneous emission (ASE) of a fibre-coupled diode laser (LIMO60-F200-DL808) operating just below it's threshold current (<6.7 A), we had an optical source that covered a wavelength range with a FWHM of ~40 nm about the S-band, i.e. 780 nm to 820 nm, as shown in Fig 3-3. With this setup we obtained 10 mW of optical power exiting the Ø200 μm, NA 0.22 fibre core. A second broadband light source was needed for the R-band absorption measurement, for which we employed a high-power LED (Roithner, Lasertechnik JET-870-05). The broader emission covered the range of 820 nm to 900 nm, but with significantly lower optical power than the sub-threshold diode-laser above, therefore it was necessary to operate this source in QCW mode with at 10 % duty cycle and 10 μsec pulses, and 1.0 A peak currents corresponded with 150 mW peak powers from the LED. However, due to the highly divergent nature of this light source, only a small portion was collected by the same Ø200 μm, NA0.22 fibre detailed above. Therefore although providing the exact same setup shown in Fig 3-2, the peak optical power obtained was about 1 mW at the exit face of the collecting fibre.

A 3 X afocal telescope re-imaged the facet of the source-fibre, to produce a 600 μm diameter focal spot in the crystal sample. Light passing through the sample was then re-imaged into a fibre patch cord (Ø300 um, NA 0.22) and coupled to an optical spectrum analyzer (OSA) (ANDO AQ6317B). The ASE spectrum was measured with and without the crystal with a resolution of 0.1 nm and the absorption spectrum derived from the difference. In the calculations to determine the absorption cross section, the measured transmission data were corrected for the transmission of the optical coatings and set-up, exploiting out of band transmission values and background measurements. The subtraction of the base line was determined very carefully before recording the absorption spectrum for each sample. Each baseline (a background) was determined in every

case of changing sample crystal then subtracted with special attention. Baseline of measured cross section was estimated for every sample temperature and optical axis of sample. Fresnel losses associated with uncoated samples were calculated using the known refractive index, while anisotropic crystals needed to account for the different refractive index associated with each principal optical axis. Baseline fitting points were chosen close to the edge of the absorption spectral band, but not too close as to be affected by the tail of an absorption peak. The absorption cross section measurement was determined after baseline subtraction, through the calculation of the absorption coefficient via the Beers law (Eq.2-13 in section 2.3) and crystal length, with the best fit determined through comparison of many samples that provided a consistent data set for the expected doping concentration.

To obtain an optimum signal to noise ratio (SNR) we used samples with a maximum absorption of <99 %, particularly for the weaker optical source, where the dynamic range was limited. For crystals that had an optical density (OD) >2, we used a Lorentzian fitting function to predict the major absorption peaks, this was especially true for some crystals when cooled, as was previously done by Glur *et al* [23]. Therefore, where strong absorption peaks were already reaching the limit of the dynamic range of our set up at room temperature, for some crystals it was only possible to measure the elevated temperature spectra. Furthermore, longer crystals were required for the weaker $^4F_{3/2}$ absorption measurements, to compensate for the lower SNR associated with the lower irradiance of LED (light emitting diode) source. To ensure the crystals were indeed at the expected cryogenic temperatures, measurements were performed with each sample wrapped in indium foil and affixed to a temperature-controlled mount with a spring loaded clamp.

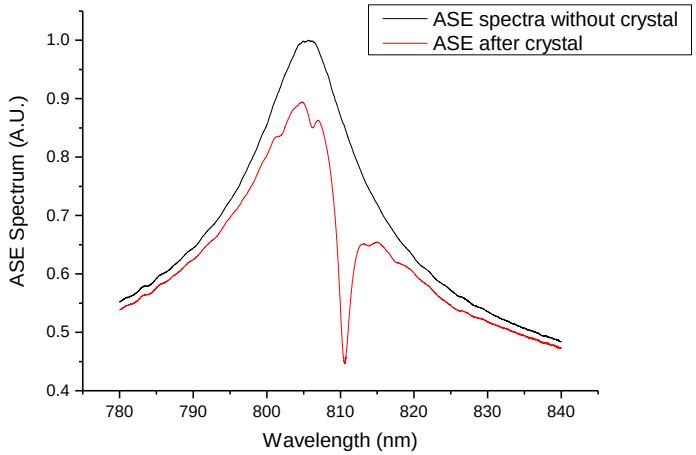

Figure 3-3 Measured ASE spectra before and after a crystal (Nd:KGW E//Nm axis)

For the anisotropic crystals, a broadband cube polarizer (Newport, 10FC16PB.5) was used to select the respective principal polarization axes of interest. Figure 3-4 illustrates the modified setup. Additionally, for the biaxial crystal Nd:KGW, we investigated two 1 mm thick crystals with

different crystal cuts, providing access to the three principal optical axes, e.g. Ng, Np, and Nm. The Ng-cut crystal provided access to the two other principal polarization states, namely E//Nm and E//Np. A second crystal, which was Nm-cut, provided access to E//Ng and E//Np polarization axes.

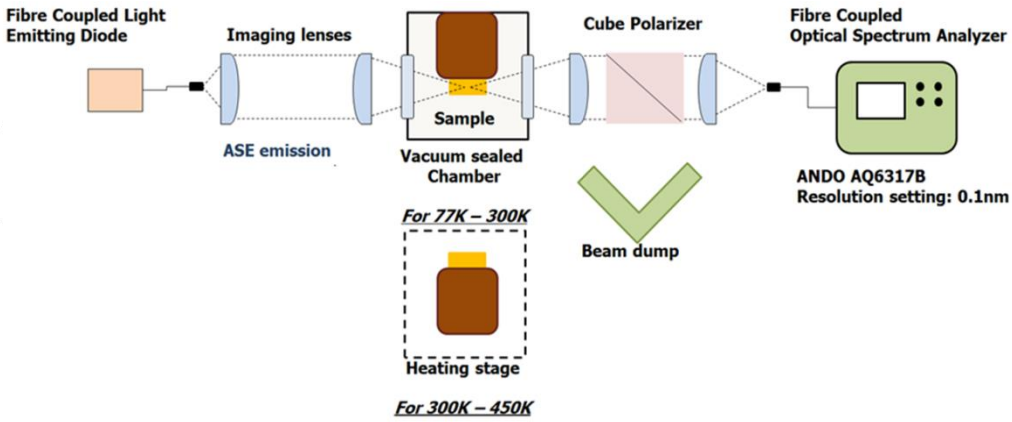

Figure 3-4 Schematic of the experimental setup for the absorption spectral measurement for anisotropic crystals.

3.2.2 Emission cross section measurement

A slight variation from the absorption measurement setup was used to measure the emission spectrum of the respective crystal samples, as shown in Fig 3-5 and Fig 3-6. Again two different configurations were used in consideration of the temperature control of the crystals, as described in the previous section.

For the fluorescence measurements, we used a non-collinear pumping configuration, with a high-brightness fibre-coupled diode-laser excitation source (i.e. a Lumics 795 nm DL coupled to a 100 μm diameter, 0.115 NA fibre, Model: LU0793T040). The pump light emitting less than 1 W was focused at one edge of the crystal sample with arrangement of 4X telescope, and bouncing of the side face, using a pumping irradiance of <1.5 $kWcm^{-2}$ (weak compared to a pump saturation irradiance of ~70 $kWcm^{-2}$ for YAG and 7.4 $kWcm^{-2}$ for KGW, E//Nm), to minimise amplified spontaneous emission and bleaching of the ground state compromising the measured emission spectrum. Fluorescence were collected via an f = 120 mm and f = 50 mm lens combination re-imaging the excited side face of the crystal into a fibre patch cable (Ø 300 μm, NA 0.22). The fluorescence spectrum from 850 nm – 1450 nm was measured using an OSA in three separate spectral ranges, using a 0.1 nm resolution. The neodymium emission from YAG does not depend on polarization, so just one measured fluorescence spectrum from these crystals was needed for the emission cross section calculation via the F-L formula. To determine the fluorescence spectral distribution, the spectral power density associated with each of the transitions to the lower $^4I_{13/2}$, $^4I_{11/2}$, and $^4I_{9/2}$ levels, was obtained by integrating over three main spectral regions, 850 nm-

950 nm, 1050 nm–1130 nm, and 1300 nm-1450 nm for Nd:YAG crystal. The typically much weaker emission channel to the $^4I_{15/2}$ energy level at a wavelength around 1.8 μm was omitted, as it was not within the spectral measurement range of the OSA and generally has a <1 % contribution to the total emission [24]. The recorded spectral response was corrected for background and the spectral transmission of the optical system prior to applying the F-L formula. Anisotropic crystals required the measurement of the luminescence for each of the polarization states, corresponding to the electric field aligned to each of crystal's principal axes. Thus multiple fluorescence measurements were required for these crystals, to enable normalisation of the total emission of the Nd^{3+} ions. We presented in detail the FL equation for measuring anisotropic crystals in Chapter 2, Eq.2-29.

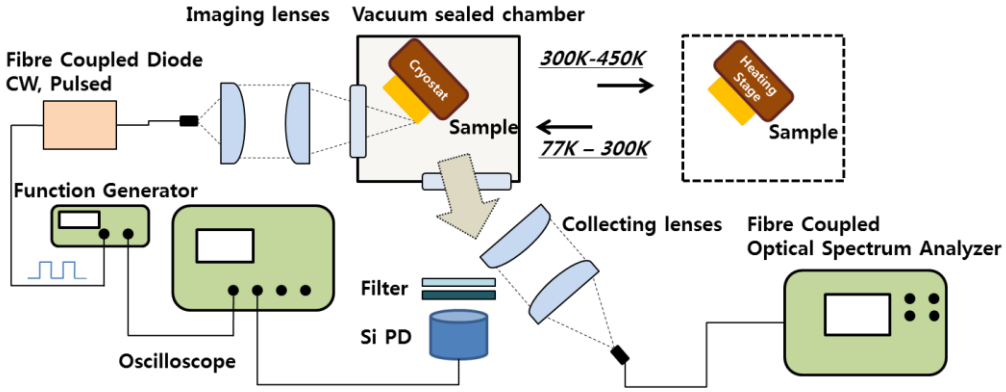

Figure 3-5 Schematic of the experimental setup for the emission spectra measurement and fluorescence lifetime

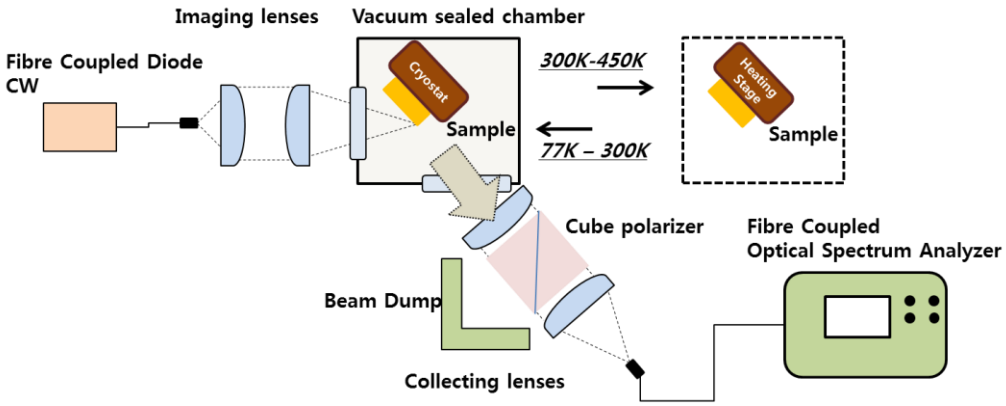

Figure 3-6 Schematic of the experimental setup for the anisotropic emission spectra measurement

Lastly, to utilise the F-L formula, the fluorescence lifetime of the RE ion is needed. In this case the same setup as above was employed, however a large-area un-biased Si photodiode was used to detect the fluorescence. The DL was driven with a pulsed current source, to provide a fast rise/fall time (<15 μs) excitation pulse, after which the emission would slowly decay according to the

exponential time constant, the lifetime. we used various collecting optics to couple the fluorescence to the photo diode, dependent on the fluorescence intensity and space availability for the respective set-ups. Two sets of longpass filters (FGL850 and an 800 nm cut-off filter [48]) were installed in series to filter any residue pump beam that may increase fluorescence lifetime.

In addition, we used the McCumber or Reciprocity method, which is described in more detail in section 2.3, using the absorption cross section data to determine the emission cross section for transitions terminating in the ground-state manifold. This was especially important for crystals with strong absorption features around the zero-phonon line, due to the strong reabsorption of the fluorescence in this region, which can significantly bias the F-L calculated emission cross section spectra toward longer wavelengths.

3.3 Results

In the following section, the absorption and emission cross section for a range of crystals is reported. The crystals investigate and their physical properties are list in Table 3.2

Table 3-2 Physical properties of investigated crystals

Crystal	Atomic doping concentration	Dimensions (mm) (w x h x l) / (Ø x l)	Crystal orientaion	Facets coatings
Nd:YAG	1.1%	3x3x1	Cubic	X
	1.0%	Ø3 x 3.2	Cubic	O
	0.6%	3x3x1	Cubic	X
	0.3%	3x3x1	Cubic	X
Nd:GSAG	1.0%	Ø3 x 7.0	Cubic	O
Nd:YVO4	0.5%	3x3x1	a-axis	X
Nd:GdVO4	0.5%	3x3x1	a-axis	X
Nd:KGW	3%	3x3x1	Ng Cut	X
	4%	3x3x1	Nm Cut	X
Nd:YLF	0.5%	3x3x1	a-axis	X

3.3.1 Absorption cross section measurement results

Garnets (YAG and GSAG)

Figure 3-7 and Figure 3-8 shows the derived effective absorption cross section ($\sigma_\alpha$eff) spectra for 1 at.% Nd:YAG at various temperatures between 450 K and LNT. The neodymium concentration in the crystal was confirmed by comparing several crystals of different lengths with a comparable specified doping-level. At RT a maximum value for $\sigma_\alpha$eff = 6.9 ± 0.1 pm^2 was determined at 808.7 ± 0.1 nm. As expected from previous work [25], a decreasing temperature typically increases the peak amplitudes (for transitions starting from the lowest Stark levels), whilst reducing the bandwidth in equal measure, as shown in Fig 3-7. However, a small deviation from this is observed at the lower temperatures, as the peak at 808nm increased to a maximum of $\sigma_\alpha$eff = 18 ± 0.2 pm^2 around 120 K, then reduced to 16.9 ± 0.2 pm^2 at 77 K. This is attributed to the fact that this peak in fact consists of two lines, Z1 → S1 and Z3 → S4, and the fractional population in Z3 starts to diminish quickly below 170 K, while Z1 is gaining over the same temperature range, nearly a 2-fold increase at LNT with respect to RT. The same trend was observed when heating the crystal above ambient conditions, i.e. lower temperatures invoked higher peak cross section values. The highest peak value at 450 K for $\sigma_\alpha$eff at 808.7 nm reduced to 3.8 ± 0.3 pm^2 and broadened in bandwidth, so that it was not feasible to define a FWHM value. At this temperature, it is found through calculating the Boltzmann's distribution of the ground state, that the population in the Z1 Stark level decreased to 80 % of the RT value, while Z3 increased by ~15%. For the main 808 nm absorption peak, the combined FWHM bandwidth decreased from ~1 nm at RT to 0.3 nm with the crystal cooled to LNT. The peak central wavelength blue-shifted by 0.5 nm going from 450 K down to 77 K, as shown in Fig 3-9, in line with most of the other transitions as reported by Kushida [22].

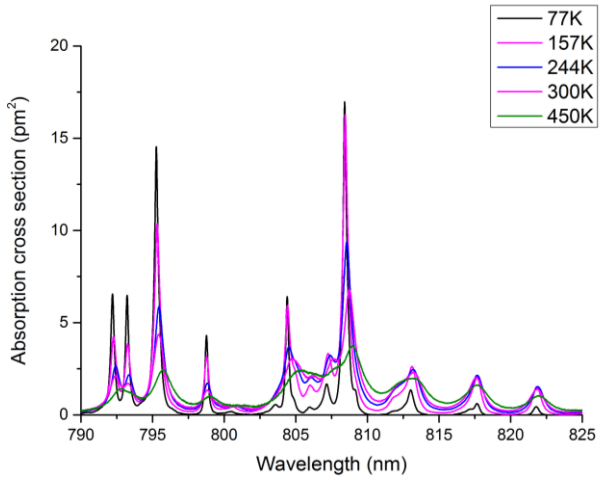

Figure 3-7 $^4I_{9/2}$ → $^4F_{5/2}$, $^2H_{9/2}$ absorption cross section for Nd:YAG at several temperatures between 77 K and 450 K.

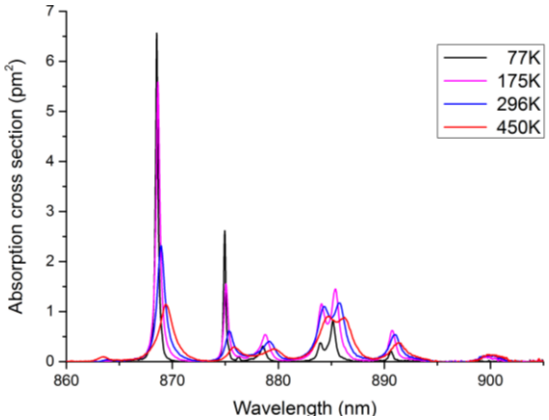

Figure 3-8 $^4I_{9/2} \rightarrow {}^4F_{3/2}$ absorption cross section for Nd:YAG at several temperatures between 77 K and 450 K.

The measurement of the absorption to the $^4F_{3/2}$ upper laser level, hence applicable to in-band pumping, is shown in Fig 3-8. At RT the strongest Nd:YAG absorption peak, was observed to be at 869 nm (Z1 → R2), more than 2 times higher than any other peak in this pump band. The temperature dependence absorption cross section spectra for the Z1 to R2 and R1 levels was observed to be similar to that found for the Z1 → S transitions. Measurement of the thermally boosted absorption transition Z5 to R1 and R2 [26], was not possible with the current setup, due the limited irradiance from the light source in this spectral band.

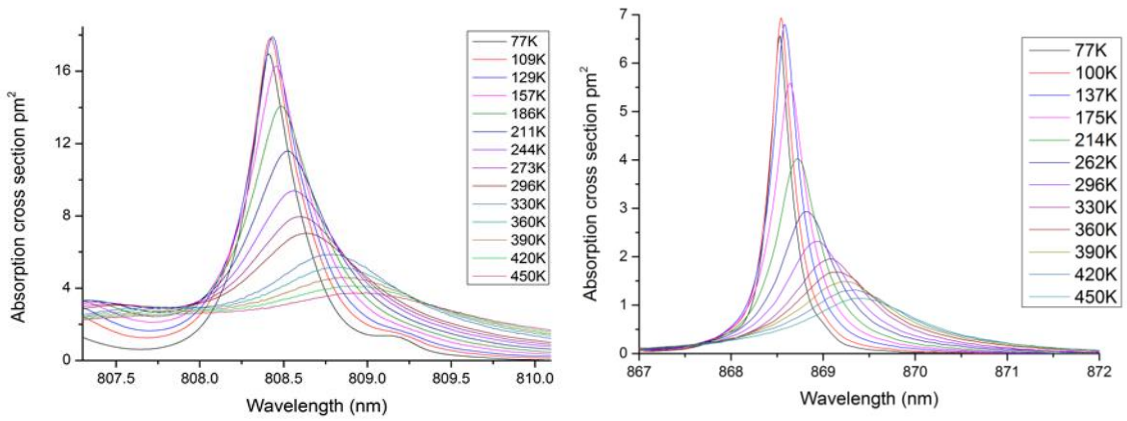

(a) (b)

Figure 3-9 Enlarged Nd:YAG absorption cross section for the main absorption peaks at (a) 808 nm and (b) 869 nm and temperature between of 77 K to 450 K.

The $\sigma_\alpha$eff peak amplitude at 869 nm increased from 1.1 ± 0.05 pm^2 to 6.5 ± 0.1 pm^2 over the temperature range of 77 K to 450 K. As such at 77 K the absorption peak is comparable with 808nm absorption at RT. High-power 869 nm diode lasers are commercially available, however due to the narrow bandwidth of this peak at LNT, i.e. 0.68 nm FWHM, spectral narrowing of these diode laser arrays needs to be employed. Volume Bragg Gratings (VBGs) are an effective means to

narrow the spectral bandwidth of such pump sources and were exploited in our studies in later chapters.

The temperature dependence of the absorption cross section of Nd:GSAG over the range of LNT to RT, is shown in Fig 3-10. Absorption maxima are positioned at a similar location to that of Nd:YAG, for example at RT temperature the peak absorption cross section is at 808.5 nm with a magnitude of 4.2 pm^2 and a bandwidth of ~1 nm FWHM. However, the Nd concentration density in GSAG crystal is 1.2 X 10^{20} $ions/cm^3$, nominally ~85 % of Nd:YAG [27], which implies lower absorption coefficients. Similar behaviour is also observed for the changing absorption spectra as to that of Nd:YAG when cooling to cryogenic temperatures, the peak absorption increases 2.5-fold while the bandwidth is halved at LNT compared with RT. The peak wavelength also blue shifted, but only by 0.2 nm over the full temperature range investigated.

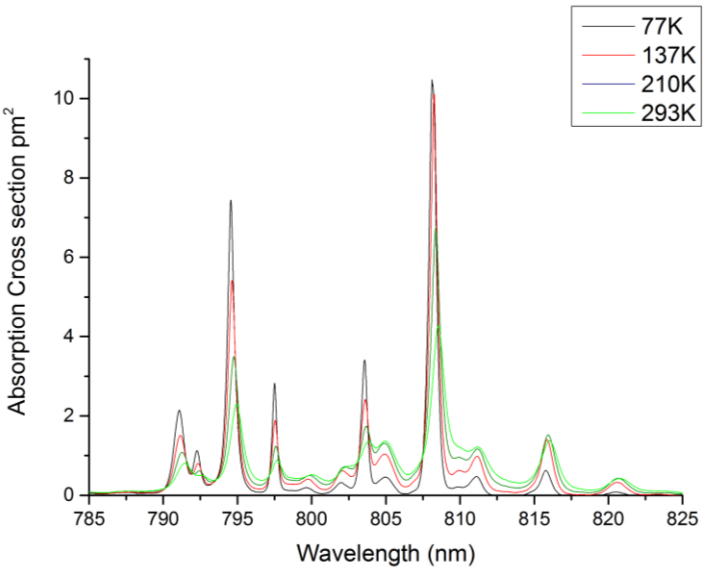

Figure 3-10 $^4I_{9/2}$ → $^4F_{5/2}$, $^2H_{9/2}$ absorption cross section for Nd:GSAG over the temperature range of 77 K to 293 K.

Vanadates (YVO4 and GdVO4)

Measurements of the absorption spectra for Nd:YVO4 and Nd:GdVO4 crystals were only collected for the transitions corresponding to the $^4I_{9/2}$ → $^4F_{5/2}$ energy levels, shown in Fig 3-11, for the respective polarization states. The data matches well published data for these anisotropic crystals [28] were the largest absorption cross section peak is observed for π polarized light. For Nd:YVO4 and π–polarization, the main absorption band for the $^4I_{9/2}$ → $^4F_{5/2}$ has a peak value of σ_α eff(π) = 60 ± 0.7 pm^2 at 808.5 nm and a FWHM of 1.6 nm. Similarly, for Nd:GdVO4, the main absorption peak had a amplitude σ_α eff(π) = 55 ± 0.6 pm^2 at 807.8 nm and a FWHM of 1.5 nm. As is well known and exploited in lasers using grazing incidence in the cavity [29], both vanadates

exhibits very short absorption lengths in comparison to Nd:YAG crystal. Further measurements for these vanadates of the temperature dependence or for the other main in-band pumping transition to the $^4F_{3/2}$ energy level, were not conducted as this material was not the focus of the main aims to investigate cryogenically-cooled operation. Nonetheless it was important to obtain a good understanding of the absorption characteristics in this wavelength band for us to make comparative energy transfer upconversion measurements as described in Chapter 4.

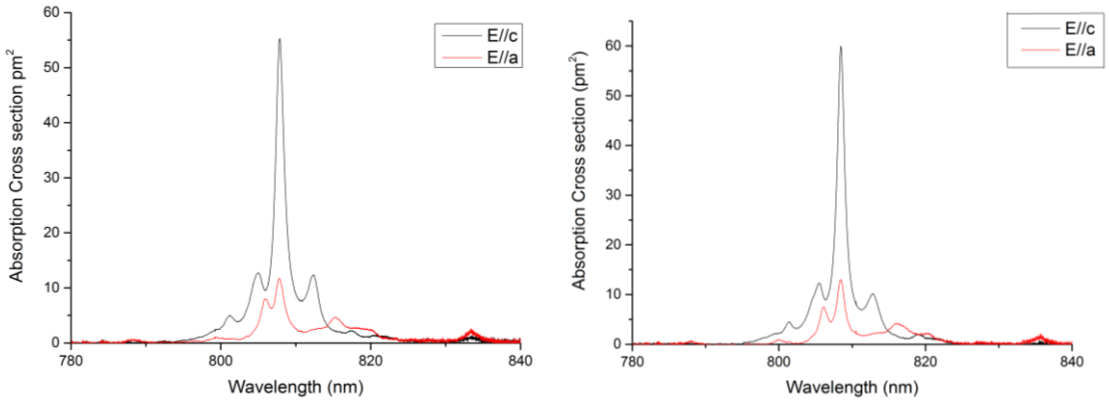

(a) (b)

Figure 3-11 $^4I_{9/2} \rightarrow {}^4F_{5/2}, {}^2H_{9/2}$ absorption cross section for (a) Nd:GdVO4 and (b) Nd:YVO4 at 300K

Tungstate (KGW)

The absorption cross section spectrum for a N_g-cut Nd:KGW crystal for the transitions $^4I_{9/2} \rightarrow {}^4F_{5/2}$ and $^4I_{9/2} \rightarrow {}^4F_{3/2}$ are shown in Fig 3-12, for the two orthogonal polarization states, E // Nm and E // Np. For both transitions, a significant anisotropy is confirmed with the larger absorption cross-sections ($\sigma_\alpha$eff) corresponding to E // Nm [19]. For the $^4I_{9/2} \rightarrow {}^4F_{5/2}$ transition and light polarization E // Nm, the absorption band contains an intense peak with a maximum $\sigma_\alpha$eff (E//Nm) = 29 ± 0.3 pm^2 at 810.5 nm with a FWHM of 1.7 nm. For E // Np, this band contains two peaks of similar intensity centered at 806.2 and 810.5 nm with their maxima $\sigma_\alpha$eff (E//Np) 6 ± 0.1 pm^2. For in-band pumping, the $^4I_{9/2} \rightarrow {}^4F_{3/2}$ transition, both polarizations have two intense peaks centered at 875.7 nm (FWHM = 2.3 nm) and 883.8 nm (FWHM =1.6 nm). The two peaks are the zero-phonon line, a transition between lowest-lying energy level in both absorption manifold and ground manifold. The second peak dominates and the corresponding values for the maximum absorption cross-sections are $\sigma_\alpha$eff (E//Nm) = 8.8 ± 0.1 and $\sigma_\alpha$eff (E//Np) = 4.8 ± 0.5 pm^2.

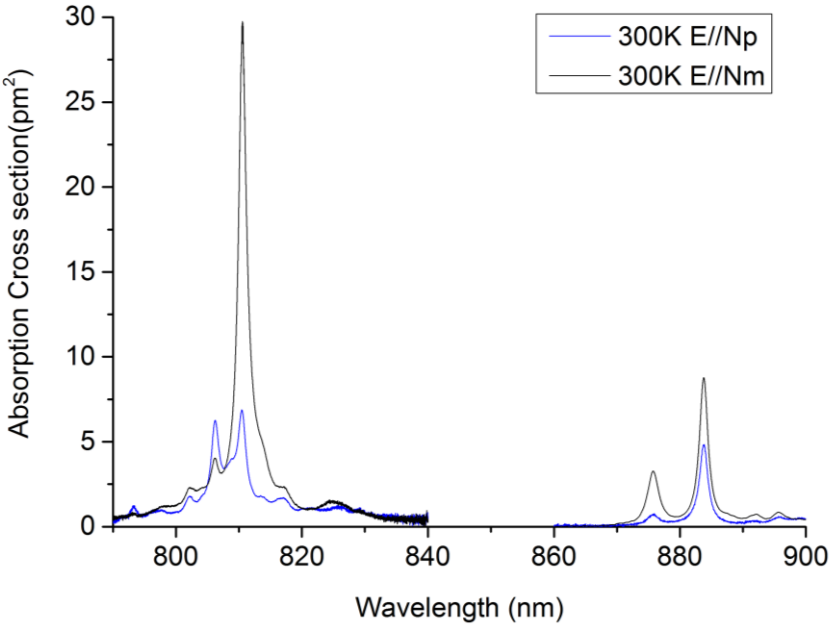

Figure 3-12 $^4I_{9/2} \rightarrow {}^4F_{5/2}$, $^2H_{9/2}$ and $^4I_{9/2} \rightarrow {}^4F_{3/2}$ absorption cross sections for E//Nm and E//Np of Nd:KGW at 300K

As the strongest absorption in Nd:KGW corresponds to the polarization state E//Nm, we have performed temperature-dependent measurements for the Ng-cut crystal only. Unfortunately, for the $^4I_{9/2} \rightarrow {}^4F_{5/2}$ transition at low temperatures, even for the lowest concentration available (3 at.%) the measurements were limited by the very strong absorbance of the 1 mm-thick crystal. As such the measurements for this transition were only conducted for the 300 - 450 K range, Fig 3-13. For E//Nm, at the maximum elevated temperature tested (450K), the $\sigma_\alpha$eff (E//Nm) peak decreased by a factor of 1.8 with respect to its room-temperature value, while the FWHM bandwidth increased to 2.7 nm. For the in-band-pumping $^4I_{9/2} \rightarrow {}^4F_{3/2}$ transition however, the limitation of strong absorption could be mitigated by fitting the base of the saturated peaks with individual Lorentzian functions corresponding to each of the Stark-Stark level transitions for low temperature, as can be expected for Raman broadened transitions [30]. The fit was applied to the data taken at low temperature (<120 K) where the absorbance got saturated, where the $\sigma_\alpha$eff is above 15 pm^2 in our cases, where the dynamic range of the measurement system reached its limit for this crystal. Both polarization states, E//Nm and E//Np, were characterized in this way. The neighbouring absorption peak next to the main peak, where the crystal's absorbance at 885nm was strongest, is at least 8 nm away, therefore a good Lorentzian fit could be made without disturbance by adjacent transitions. However small deviation of change was influenced significantly by detection limit value, 15 pm^2 in this case. The fitted peak was carefully chosen but the level of confidence was higher for determining the peak value. We scaled the level of confidence to 10 % for the crystal. This allowed us to estimate the absorption spectra for this

band over the whole 77 – 450 K range investigated, as shown in Fig 3-14. The spectrum is dominated by the peak centred at 883.8 nm, with the LNT σ_{α}eff (E//Nm) estimated to be 62 ± 6.2 pm^2 (FWHM = 0.3 nm), while at 450 K, σ_{α}eff (E//Nm) is reduced to 4.7 ± 0.07 pm^2 (FWHM = 3.2 nm) for E//Nm. E//Np at 77 K was measured at 883nm peak and estimated to be 20 ± 2 pm^2.

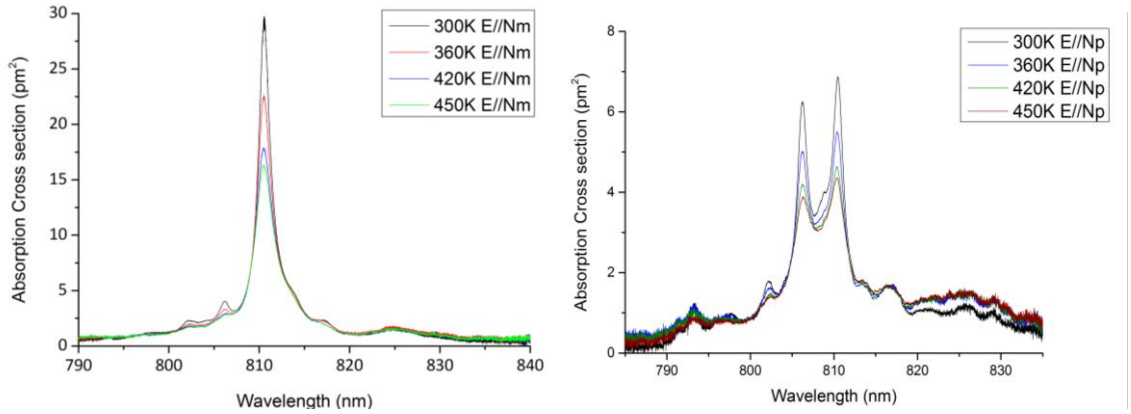

(a) (b)

Figure 3-13 $^4I_{9/2} \rightarrow {}^4F_{5/2}, {}^2H_{9/2}$ absorption cross section for Nd:KGW, with (a) E//Nm and (b) E//Np, over the temperature range of 300K to 450K

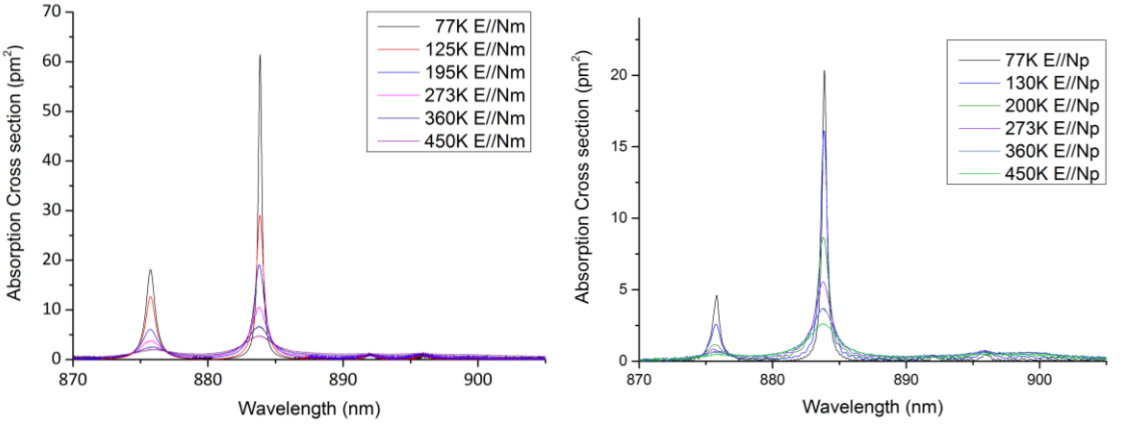

(a) (b)

Figure 3-14 $^4I_{9/2} \rightarrow {}^4F_{3/2}$ absorption cross section for Nd:KGW, with (a) E//Nm and (b) E//Np of Nd:KGW, over the temperature range of 77 K to 450K.

Fluoride (YLF)

The absorption cross section of Nd:YLF changes quite dramatically going from RT to LNT as shown in Fig 3-15. As previously reported with the uniaxial crystals, both σ-pol and π-pol, transitions from the ground to $^4F_{5/2}$ and $^4F_{3/2}$ were measured. At RT, the strongest absorption peak is

11.8 ± 0.15 pm^2 at 791.9 nm for π-pol light, with a bandwidth of 1.4 nm FWHM. Conversely, for σ-pol light, the strongest peak is only 2.4 pm^2 centred at 797nm and with a FWHM bandwidth of 1.8 nm. At LNT the 792 nm peak amplitude increases by a factor of 5.8, with an associated decrease in bandwidth to 0.3 nm. In Fig 3-15(b), the strongest peak is at 862.5nm for π-pol with the maximum of 5.0 ± 0. 1 pm^2. In contrast, the σ-pol spectrum contains two weak (~0.6 pm^2) peaks, at 862.5 nm and 866.6 nm, associated with absorption from the lowest ground-state Stark level to the two Stark levels of $^4F_{3/2}$. Cooling to LNT the strongest π-pol absorption peak is blue shifted by 0.6 nm and increased in magnitude 8-fold, while for the main σ-pol peak there was a 13-fold increase in magnitude, while the bandwidth appears to only have reduced by a factor of 2.

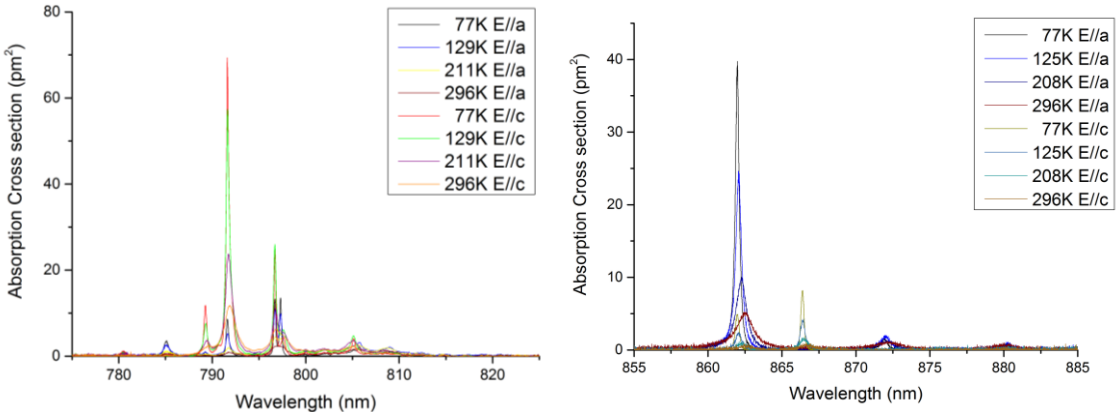

(a) (b)

Figure 3-15 Absorption cross section for Nd:YLF and the polarization states E//a and E//c and the transitions (a) $^4I_{9/2} \rightarrow {}^4F_{5/2}$, $^2H_{9/2}$, and (b) $^4I_{9/2} \rightarrow {}^4F_{3/2}$, over the temperature range of 77 K to 296K.

3.3.2 Emission cross section measurement results

Firstly, to calculate the emission cross section for the crystals of interest, the fluorescence lifetime, refractive index, and branching ratios to each of the potential energy levels below the metastable state, needed to be determined. With these values the effective emission cross section could be determined using the Füchtbauer-Ladenburg method described in Chapter 2.

Garnet (Nd:YAG and Nd:GSAG)

Nd:YAG

Fluorescence lifetime/ Refractive index/ Branch ratio

The fluorescence lifetime was determined by monitoring the temporal response for the emission fluorescence, originating from R1 and R2 Stark levels of the $^4F_{3/2}$ manifold and terminating in the lower manifold, during and after a ~2 ms long excitation pulse. The dependence of the fluorescence lifetime as a function of temperature was also measured for the temperature range of LNT - RT. To within error margins it was confirmed that the lifetime for the samples investigated was independent of their temperature. As such further measurements during the supra-ambient experiments were not made. As can be seen from Table 3-3, for the respective samples there was a distinct change in lifetime due to the concentration density of neodymium. The following emission data were made on 1 at% doped sample, running two identical test to ensure the detection error. The obtained value for 1st run was given a mean value of 242 μs with 1.6 respective standard deviation (STD) then a mean value of 234.6 μs with 1.9 STD for 2nd run. Two data set shows no noticeable trend via temperature changes. Hence we used 240 μs in the F-L calculations, a value near average of those obtained (238.5 μs) given that within the STD, 4.4 μs.

Table 3-3 Measured τ_f of 1at.% doped Nd:YAG over temperature 77K - 300K

Temperature (K)	Measured τ_f (μs)	
	1st Run	2nd Run
300	239.7	234.3
235	243.8	236.5
170	244	236.7
130	242.5	233
77	242.6	232.7

There are several reports for the refractive index for YAG, therefore the Sellmeier dispersion formula reported in [31] was used across the wavelength band studied. The equation typically written as,

$$n^2(\lambda) = A + \frac{B\lambda^2}{\lambda^2 - C} + \frac{D\lambda^2}{\lambda^2 - E} \qquad 3\text{-}1$$

With the coefficients given for A, B, C, D, E, where *n* is the refractive index and λ is the wavelength. The Sellmeier's coefficients for a YAG crystal are shown below table:

Table 3-4 Sellmeier's coefficient for YAG crystal [32]

Coefficient	Value
A	1
B	2.282
C	0.01185
D	3.27644
E	282.734

To determine the branching ratios in function of temperature, the full fluorescence spectra were recorded at several discrete temperatures between RT and LNT, and the relative spectral densities for each intra-manifold transition were normalised by the sum of them all, with the results given in Table 3-5. As the emission was collected from the side-facet of the crystal instead of longitudinal configuration, the mean-path-length for the fluorescence before escaping the crystal was very short, on the order of a few hundred microns, as such reabsorption of light emitted from a transition to the ground state could be considered to be negligible. This method is expected to provide a more accurate determination of the branching ratios and improve the assessment of all the emission cross section values. The respective manifold branching ratios for elevated temperatures from 300 K to 450 K were also considered but fell within an error range of ± 3% with respect to the RT values and with no noticeable trends. Again a transition to $^4I_{15/2}$ has been neglected here as its branch ratio is smaller than 1 %

Table 3-5 Nd:YAG branching ratios for temperature between 77K and 300K

$^4F_{3/2}$	300K	273K	235K	200K	170K	130K	100K	77K
$^4I_{9/2}$	31.1	29.7	27.8	31.1	30.6	32.1	29.8	33.9
$^4I_{11/2}$	56.5	57.7	59.7	57.5	58.7	58.2	58.5	54.7
$^4I_{13/2}$	12.4	12.6	12.5	11.4	10.7	9.7	11.7	11.4

F-L calculations

After the collection of the fluorescence spectra, the effective emission cross section, σ_{SE} was calculated for the three main emission bands from the $^4F_{3/2}$ manifold. The main transition of interest was R1 → Z5 at a wavelength of 946 nm, due to reasons outlined in Chapter 1. As illustrated in Fig 3-16(a) the magnitude of the 946 nm emission peak was observed to increase from 2.9 ± 0.04 pm^2 at 450 K to 8.4 ± 0.1 pm^2 at 77 K, a significant increase in the potential gain at this wavelength. It is noteworthy that this is approximately a two-fold reduction in the saturation fluence for this transition going to LNT from RT, which is an important factor for considering energy scaling. Moreover, due to the relatively large ground state splitting for Nd:YAG, the thermal population of the Z5 Stark level (852 cm^{-1}), which is 0.7 % of the available Nd-ions at room temperature, reduces by several orders of magnitude at LNT, thus eliminating reabsorption loss for this transition. There are two other noticeable emission peaks below 900 nm, Fig 3-16(a), the first at 885 nm (R1 → Z2) and second, 891 nm (R1 → Z3), which both showed a significant increase in emission cross section at LNT, i.e. 9.5 ± 0.11 pm^2 and 8.6 ± 0.11 pm^2, respectively. These lines could be of significant interest for low quantum defect operation with pumping at 869nm, despite the modest thermal population of 7.9 % and 2.1 %, respectively. The quantum defect is 1.8 % and 2.5 %, respectively, and significantly smaller than the 5.8 % of Yb:YAG when pumping its zero phonon line at 969 nm [33].

For the dominant transition in the 1 μm band from $^4F_{3/2}$ to $^4I_{11/2}$, the key point to note in Fig 3-16(b) is that the 1061 nm emission cross section becomes the strongest line at cryogenic temperatures, in fact below a temperature of 230 K [34], increasing by 3.5 times (21 ± 0.25 pm^2 → 78 ± 0.9 pm^2) going from RT to LNT. Cho *et al* exploit this fact and reported dual wavelength operation of Nd:YAG at cryogenic temperatures [34]. Such a strong potential-gain will be a major driver in the design for cryogenically-cooled Nd:YAG lasers in terms of mitigation of parasitic ASE or laser action. Note that the measured emission cross section at 450 K for 1061 nm is 12 ± 0.14 pm^2, which is half of that at 1064 nm at 24.5 ± 0.28 pm^2. As is well known [8], the main RT Nd:YAG emission wavelength of 1064 nm is actually composed of two overlapping lines, R2 → Y3 and R1 → Y2. Accurate determination of these two spectra lines required making a Lorentzian fit for each of the transitions. Given that the RT FWHM of the overlapped 1064 nm spectral feature is 5cm^{-1}, other lines had to be exploited to determine the energy of the respective Stark levels. To do this the energy level of R1 and R2 in $^4F_{3/2}$ were determined via the position of the emission at 869 nm (Z1 → R2) and 875 nm (Z1 → R1), while the energy levels Y2 and Y3 were determined measuring the line centres of the emission at 1054 nm (R2 → Y2) and 1074 nm (R1 → Y3). From these we derived the peak of the two overlapping Stark-level transitions at 1064 nm to be 9397.7 cm^{-1} (R2 -

Y3) and 9394.6 cm-1 (R1 – Y2), for which the energy difference is ~3 cm^{-1}. The amplitudes of the fitted σ_{SE} peaks at 1064.1 nm (R2 → Y3) was 26.8 ± 0.3 pm^2, and at 1064.4 nm (R1 → Y2) was 11.3 ± 0.14 pm^2. Krupke *et al* [35] reported the R2 → Y3 emission cross section at RT to be 28 pm^2, in good agreement to what was obtained here. A consequence of the dual-line nature of the 1064 nm transition is that they separate at lower temperatures, in addition the stronger of the two lines starts from the upper Stark level of the $^4F_{3/2}$ manifold and its Boltzmann occupation factor reduces with decreasing temperature, whereas the 1061 nm transition is derived from emission between the R1 → Y1 Stark levels and thus has an increasing population. It's also notable that for temperatures below ~160 K, the Boltzmann population ratio of R1 and R2 is < 0.5.

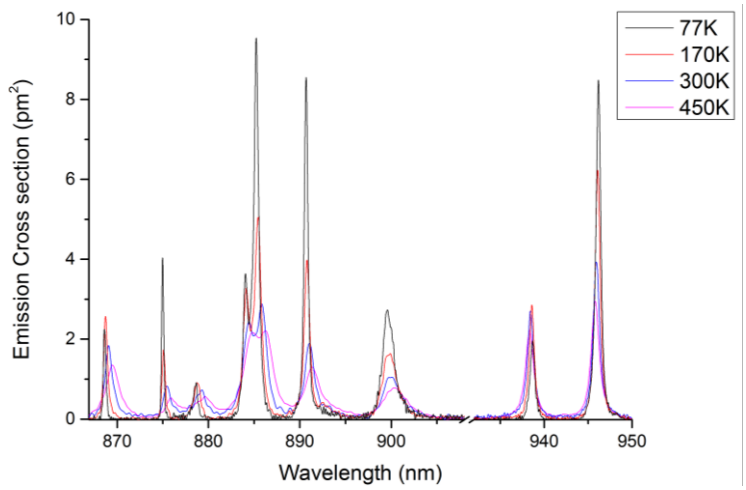

(a)

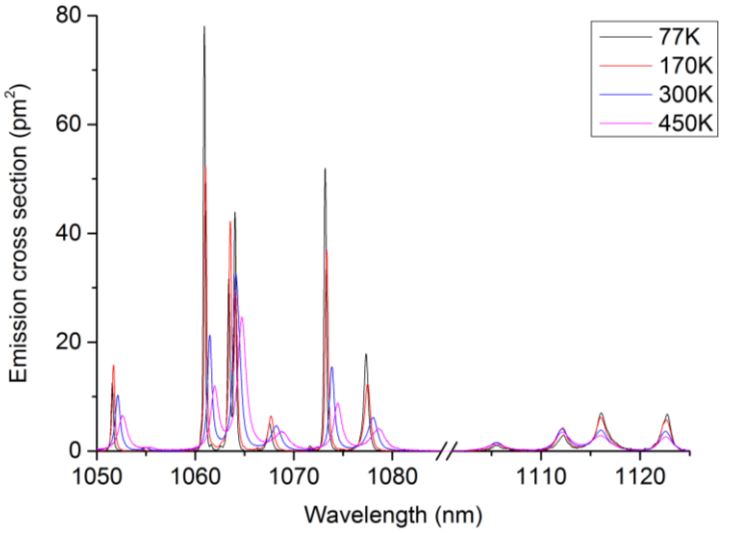

(b)

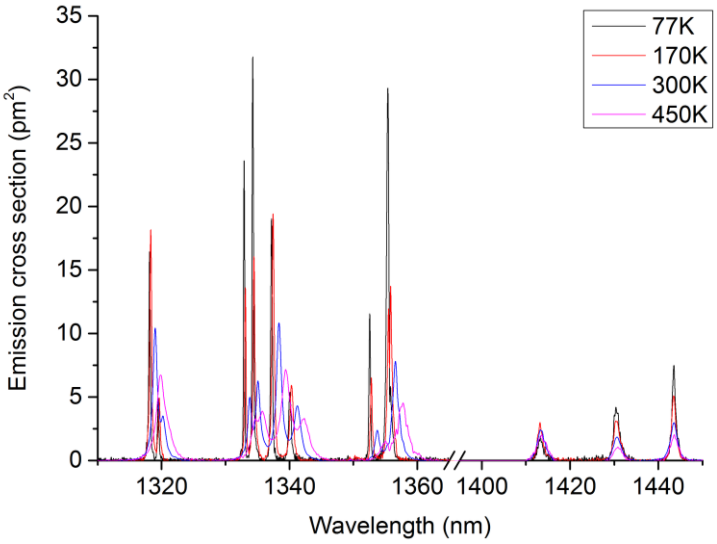

(c)

Figure 3-16 Emission cross section for Nd:YAG and transitions from $^4F_{3/2}$ to (a) $^4I_{9/2}$, (b) $^4I_{11/2}$, and (c) $^4I_{13/2}$, over the temperature range of 77 K to 450 K.

Nd:GSAG

Fluorescence Lifetime/ Refractive index/ Branch ratio

The fluorescence lifetime (τ_f) was only measured at RT for this crystal. The lifetime of the metastable state ($^4F_{3/2}$) was measured 220 μs. The measured τ_f was within reported value, 222 μs [36]. The following F-L equation was made on this fixed value. We also applied fixed value of refractive index as Sellmeier's coefficient for the crystal was not reported at best of knowledge.

The branching ratio of Nd:GSAG was determined in function of temperature. The recorded spectra are presented in Table 3-6. The emission was collected from the side-facet of the crystal to neglect any reabsorption as described in Nd:YAG section. The respective manifold branching fell within an error range of ± 3% with respect to the RT values. 130 K was measured beyond the error margin, ~7 % more fluorescence was measured for the transitions to $^4I_{9/2}$ and less to $^4I_{11/2}$ transition. However since there was no noticeable trend the data at 130 K is an experimental defect. Again a transition to $^4I_{15/2}$ has been neglected here as its branch ratio is smaller than 1 %

Table 3-6 Nd:GSAG branch ratio measured for temperature range 77 K to 300 K

$^4F_{3/2}$	300K	273K	235K	200K	160K	130K	100K	77K
$^4I_{9/2}$	28.5	27.8	28.3	27.5	30.2	36.6	28.5	31.5
$^4I_{11/2}$	58.7	60.4	60.2	61.3	59.5	53.5	61.4	57.2
$^4I_{13/2}$	12.8	11.8	11.5	11.2	10.3	9.9	10.1	11.3

F-L Calculations

A quaternary garnet, neodymium-doped GSAG displays similar spectroscopic properties to its ternary cousin Nd:YAG. However, the effective emission cross section for the longest wavelength of the $^4F_{3/2} \rightarrow {}^4I_{9/2}$ transition for Nd:GSAG at 942 nm is significantly weaker, ranging in magnitude from 2.5 ± 0.05 pm^2 to 5.1 ± 0.1 pm^2 over the temperature range of 300 K to 77 K.

Another key difference is that the transitions between the manifolds $^4F_{3/2} \rightarrow {}^4I_{13/2}$ become the dominant cross section values when the crystal temperature is lower than 105 K. The maximum peak is at 1380 nm with a magnitude σ_{SE} = 32 ± 0.4 pm^2, when the crystal is at 77 K. The 1380 nm emission cross section increased 3.5 times over the measured temperature RT to LNT.

The strongest 1-micronmeter emission peak at 1065 nm had σ_{SE} = 22.5 ± 0.3 pm^2, at LNT. Whereas the 1067 nm line is comparable to the 1064 nm line of Nd:YAG, comprising two transitions R2 → Y3 and R1 → Y2, which overlap at 300 K but separated at lower temperatures.

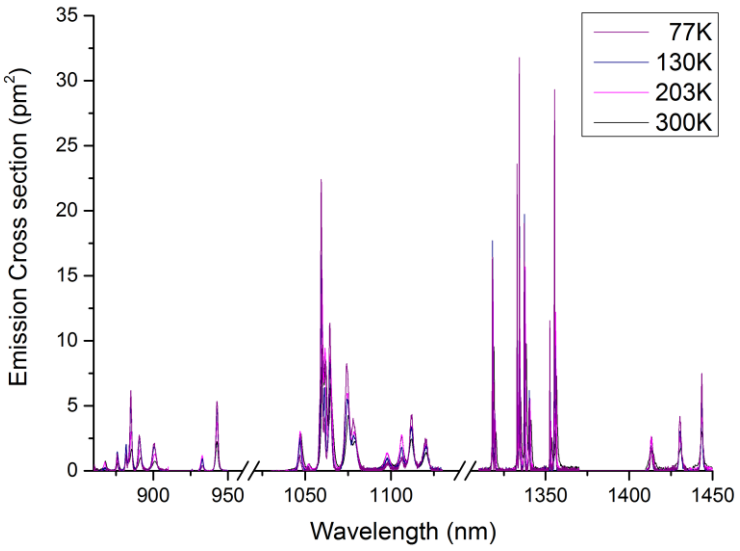

Figure 3-17 Emission cross section for Nd:GSAG and transitions from $^4F_{3/2}$ to $^4I_{9/2}$, $^4I_{11/2}$, and $^4I_{13/2}$, over the temperature range of 77 K to 300 K.

Tungstate (Nd:KGW)

Fluorescence lifetime/ Refractive index/ Branch ratio

A similar family to the vandates, the tungstates have strong cross section values, but are more complex crystals due to their biaxial nature. Nd^{3+} fluorescence lifetimes were measured from the $^4F_{3/2}$ manifold in the KGW host, with a value of 115 ± 5 µs. As previously observed with Nd:YAG

the lifetime of this state, was nearly independent of the temperature in the 77-450 K range. Furthermore, this value agrees with the one reported in [37] at room temperature, 117 μs, even though the intrinsic radiative lifetime for the $^4F_{3/2}$ manifold is reported as being 111 μs [37]. We conclude that there is a strong likelihood of radiation trapping that is lengthening the observed lifetime [38], nonetheless it appears the fluorescence quantum efficiency for this manifold is close to unity.

The refractive index of this crystal was determined by three axes as given by Pujol *et al* [39] Pujol described the refractive index variation by applying infrared-corrected Sellmeier's equation;

$$n(\lambda) = A + \frac{B}{1-\left(\frac{C}{\lambda}\right)^2} + D\lambda^2 \qquad 3\text{-}2$$

Table 3-7 lists the Sellmeier's coefficient fits for 350 nm to 1600 nm, the fit matches well which was given by Graf [3] at 1.06 μm.

Table 3-7 Sellmeier's coefficient for KGW crystal [39]

	A	B	C/nm	D/nm^{-2}
Ng	1.3867	0.6573	170.02	0.2931 X 10^{-9}
Nm	1.5437	0.4541	188.91	2.1567 X 10^{-9}
Np	1.5344	0.4360	186.18	2.0999 X 10^{-9}

The branch ratio of each principle axes were determined in function of temperature as discussed prior Nd:YAG section. The full fluorescence spectra were collected at few discrete temperatures between RT and LNT, then were analysed via each manifold transition as given in Table 3-8. The respective manifold branching ratios shows no noticeable trends and fell within an error range of ± 4% with respect to mean value. However the tolerance is larger than that we obtained from Nd:YAG, which implies the sensitiveness of crystal geometry against temperature changes, decreasing the level of confidence compare to isotropic crystal hence we increased the error margin of σ_{SE} to 2 %. Again the transition to $^4I_{15/2}$ has been neglected.

Table 3-8 Nd:KGW branching ratios for temperature between 77 K and 300 K with respect to principle axes

$^4F_{3/2}$		77K	95K	123K	162K	195K	235K	270K	300K
$^4I_{9/2}$	Ng	-	-	-	-	-	-	-	39.3
	Np	37.7	30.8	34.7	37.5	36.9	35.4	34.8	36.1
	Nm	34	41	38	36	35	42	41	39
$^4I_{11/2}$	Ng	-	-	-	-	-	-	-	51.3
	Np	53.8	56.9	55.6	55.6	55.9	55.8	55.5	54.6
	Nm	54	50	48	55	54	46	47	50
$^4I_{13/2}$	Ng	-	-	-	-	-	-	-	9.4
	Np	8.5	12.3	9.7	6.9	7.2	8.8	9.7	9.3
	Nm	12	8	14	9	11	12	12	11

F-L Calculation

σ_{SE}, cross-section spectra for Nd:KGW corresponding to the $^4F_{3/2} \rightarrow {}^4I_{13/2}$, $^4I_{11/2}$ and $^4I_{9/2}$ transitions, measured at 300 K, are shown in Fig 3-18 for polarizations E // Np, Nm, and Ng. The highest σ_{SE} values are observed for E//Nm as previously reported [37], with the maximum peak at 1067.3 nm with σ_{SE}(E//Nm) = 21.4 ± 0.4 pm^2. For E//Np at 1069.0 nm the peak is half the value, σ_{SE}(E//Np) = 9.5 ± 0.2 pm^2. Additionally, for E//Np, a second intense peak is observed at 1056.0 nm, which could be favourable for dual-wavelength laser operation.

Studies of the temperature-dependence of the emission cross-section spectra were made for the $^4F_{3/2} \rightarrow {}^4I_{9/2}$, $^4I_{11/2}$ and $^4I_{13/2}$ transitions, and for the polarizations, E // Nm and E//Np, which is of interest for various laser applications. These measurements were undertaken using the 3 at.% Ng-cut crystal and the branching ratios $\beta_i(JJ')$ as given in Table 3-8 and emission intensity scaling factors of Eq.2-29 were assumed constant across this temperature range. The results are presented in Fig 3-19 and Fig 3-20 and Appendix A. When the temperature is raised from 77 K to 450 K, the maximum σ_{SE} (pm^2) decreases from 61 to 16.8 pm^2 at 1067.3 nm. The width of the most intense emission peak corresponding to the $^4F_{3/2} \rightarrow {}^4I_{11/2}$ transition does not change significantly with increasing temperature, whilst at low temperatures it is split into two components centred at 1067.3 and 1069.2 nm corresponding to transitions to the two lowest $^4I_{11/2}$ Stark levels.

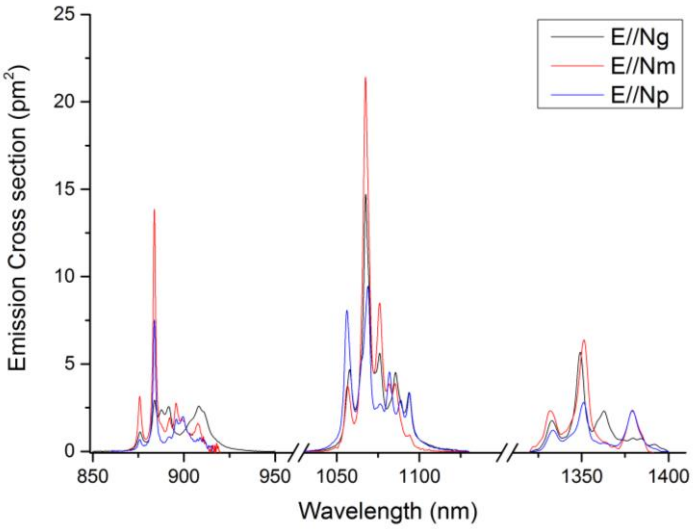

Figure 3-18 Emission cross section for Nd:KGW and transitions from $^4F_{3/2}$ to $^4I_{9/2}$, $^4I_{11/2}$, and $^4I_{13/2}$, at 300 K.

For the $^4F_{3/2} \rightarrow {}^4I_{9/2}$ transition, strong absorption around the zero-phonon line alters the shape of the measured fluorescence spectrum, which directly impacts the determination of the σ_{SE} cross section spectra through F-L equation. To obtain a clearer picture of the $^4F_{3/2} \rightarrow {}^4I_{9/2}$ σ_{SE} spectrum, the RM method was utilized with the excellent absorption spectra shown in Fig 3-14. Following this approach, we obtain maxima at 883.8 nm of σ_{SE}(E//Nm) = 13.8 ± 0.3 pm^2, σ_{SE}(E//Np) = 7.5 ± 0.15 pm^2, and σ_{SE}(E//Ng) = 3.0 pm^2. When the crystal was cooled to LNT, the zero emission line, 873.5 nm, reaches 66 ± 1.5 pm^2 this is higher than the main $^4F_{3/2} \rightarrow {}^4I_{11/2}$ transition, 1067.3 nm.

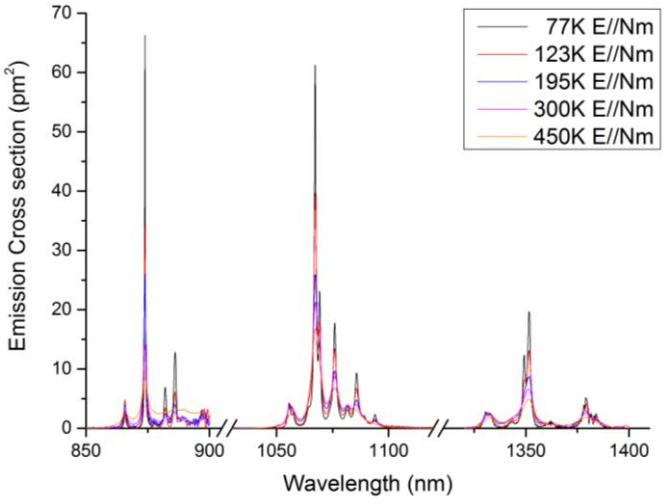

Figure 3-19 E//N_m emission cross section for Nd:KGW and transitions from $^4F_{3/2}$ to $^4I_{9/2}$, $^4I_{11/2}$, and $^4I_{13/2}$, over the temperature range of 77 K to 450 K.

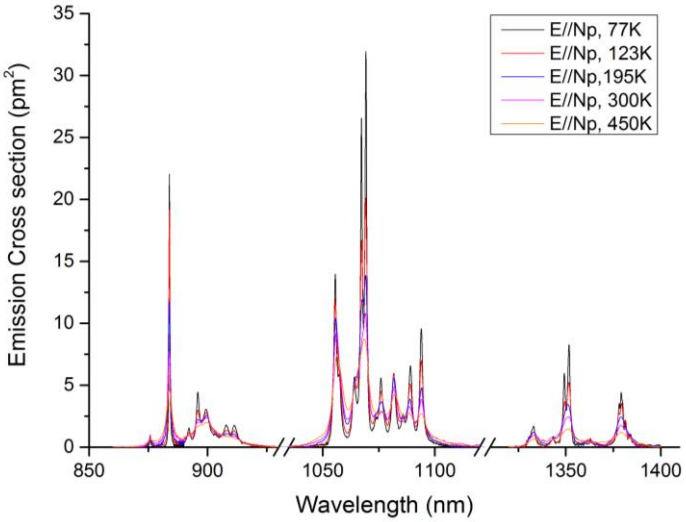

Figure 3-20 E//N_p emission cross section for Nd:KGW and transitions from $^4F_{3/2}$ to $^4I_{9/2}$, $^4I_{11/2}$, and $^4I_{13/2}$, over the temperature range of 77 K to 450 K.

For the $^4F_{3/2} \rightarrow {}^4I_{13/2}$ transition, the σ_{SE} cross-sections for the polarizations E//Nm and E//Ng are quite similar, 6.4 ± 0.15 pm^2 and 5.7 ± 0.15 pm^2 at 1351.3 nm, respectively. The values of σ_{SE} determined in the present study at room temperature are consistent with the emission spectra presented by Moncorge *et al* [40]. σ_{SE} for E//Nm measured at LNT at this transition increased 3-fold at 1351.6 nm, reaching 19.6 ± 0.3 pm^2.

Fluoride (Nd:YLF)

Fluorescence lifetime/ Refractive index/ Branch ratio

The fluorescence decay time for 0.5 at.% Nd^{3+} doped YLF from the $^4F_{3/2}$ state was measured to be 485 ± 5 μs at RT. The lifetime was measured at 502 ± 5 μs at 77 K. Fig 3-21 shows the fluorescence lifetime as a function of temperature. The lifetime measured at RT is well matched to the reported data [41, 42]. Unlike other Garnet or tungstate crystals, Nd:YLF clearly showed a change of τ_f over temperature.

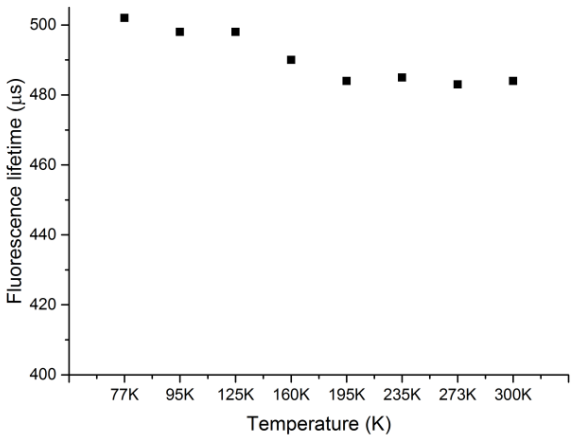

Figure 3-21 The measured τ_f of Nd:YLF for temperature range of 77 K to 300 K

The reported Sellmeier's coefficient was used to access the refractive index of both crystal axes [43]. The equation 3-1 was applied across the wavelength band and coefficients are given in Table 3-9

Table 3-9 Sellmeier's coefficient for Nd:YLF [43]

Coefficient	c-axis value (π-pol)	a-axis value (σ-pol)
A	1.31021	1.38757
B	0.84903	0.70757
C	0.0876	0.00931
D	0.53607	0.18849
E	134.9566	50.99741

The branch ratio of each principle axes were determined in function of temperature as discussed prior Nd:YAG and Nd:KGW section. The full fluorescence spectra were collected then analysed via each manifold transition as given in Table 3-10. The respective manifold branching ratios shows no noticeable trends and fell within an error range of ± 3 % with respect to mean value. Again the transition to $^4I_{15/2}$ has been neglected.

Table 3-10 Nd:YLF branching ratio for temperature range LNT to RT

$^4F_{3/2}$		300K	273K	230K	197K	160K	120K	100K	77K
$^4I_{9/2}$	σ-pol	30.7	30.3	30.1	29.7	35.9	34.5	30.7	31
	π-pol	36.2	36.6	35.8	36.8	37.2	35.1	32.5	34
$^4I_{11/2}$	σ-pol	58.7	58.9	60	59.8	53.7	54.1	59.1	59
	π-pol	54.3	53.5	55.3	53.5	52.1	54.7	55.7	53.5
$^4I_{13/2}$	σ-pol	10.6	10.8	9.9	10.5	10.4	11.4	10.2	10
	π-pol	9.5	9.9	8.9	9.7	10.7	10.2	11.8	12.5

F-L Calculations

σ_{SE} were calculated for the three main emission bands from metastable state, $^4F_{3/2}$ as illustrated in Fig 3-22(a, b, c) for temperature range of 77 K to 300 K with respect to crystal axis. The

measurement were undertaken using the 0.5 at.% dopant and the branching ratio and τ_f as given. The magnitude of dominant transition was observed to increase to 65 ± 1 pm^2(π-pol) and 121 ± 2 pm^2 (σ-pol), respectively. It is noticeable in the figure that the peak is switched from 1047 nm (π-pol) to 1053 nm (σ-pol) when crystal has cooled below 130 K. Cho *et al* exploit this fact and reported cryogenic cooled Nd:YLF operation [44]. The peak for σ-pol (1053 nm) is blue shifted ~0.25 nm and π-pol (1047 nm) is also blue shifted by ~0.7 nm when the crystal has reached LNT.

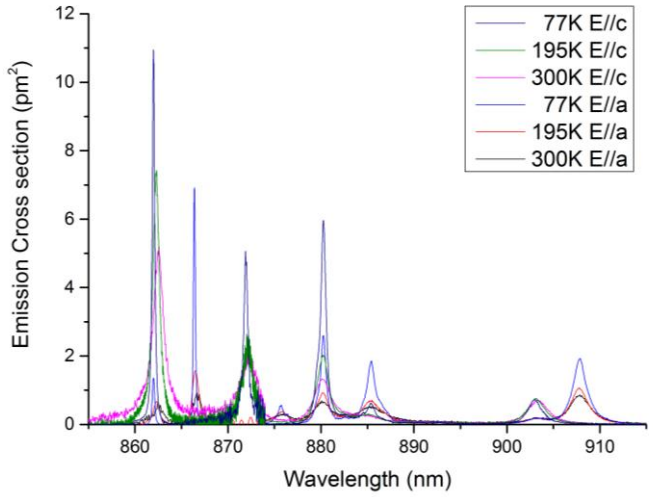

(a)

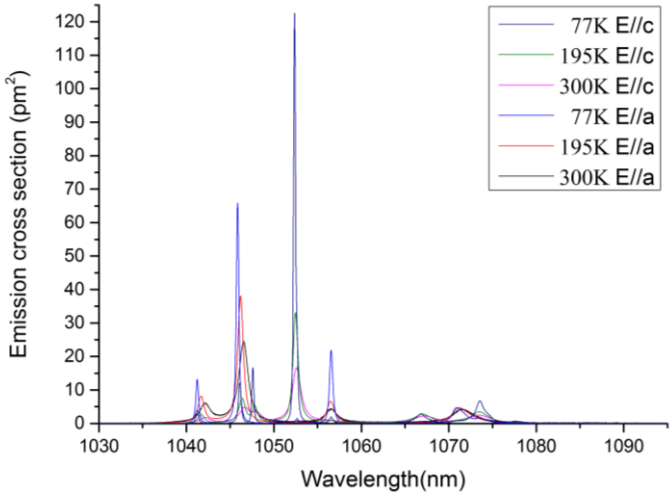

(b)

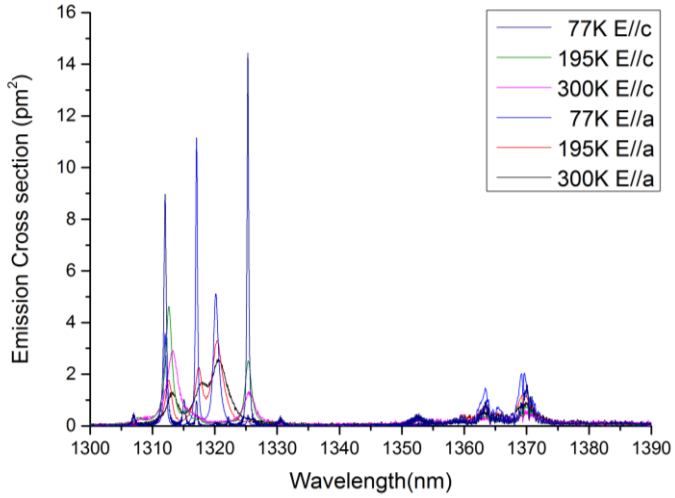

(c)

Figure 3-22 Emission cross section for transitions (a) $^4I_{9/2}$, (b) $^4I_{11/2}$ and (c) $^4I_{13/2}$, for Nd:YLF over the temperature range of 77 K – 300 K.

In determining the emission cross section for the $^4F_{3/2} \rightarrow {}^4I_{9/2}$ transition, it was necessary to utilize the RM method due to strong absorption around the zero-phonon-line. With the RM approach we obtain a maximum σ_{SE} at 867 nm (σ-pol) of 0.9 pm^2, and 862 nm (π-pol) of 5.1 ± 0.1 pm^2 in RT. When the crystal was cooled to LNT, the zero emission line reaches ~7 pm^2 (σ-pol) but the highest σ_{SE} at LNT is 11 ± 0.2 pm^2 at 862 nm (π-pol). Fluorescence at those two cross sections were strongly reabsorbed, leaving no fluorescence collectable at those two peaks. For the $^4F_{3/2} \rightarrow {}^4I_{13/2}$ transition, both polarization states have narrowing bands and increasing peak value, by a factor of 12-times at 1325 nm (14.4 ± 0.2 pm^2, σ-pol) and 7-times at 1318 nm (11.1 ± 0.2 pm^2, π-pol) when it reaches LNT.

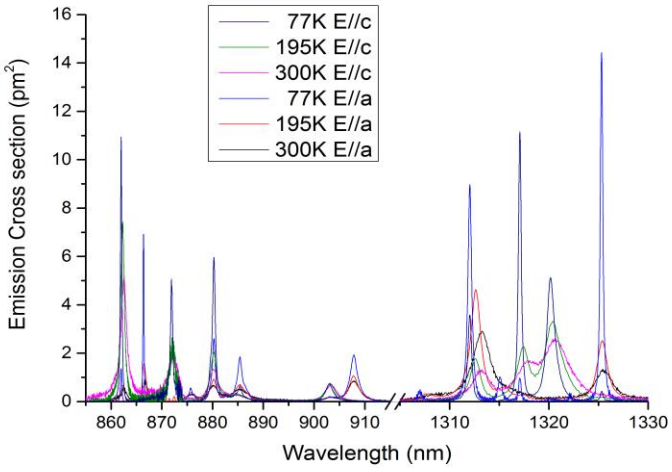

Figure 3-23 Enlarged plot for the emission cross section at 880nm, 908nm and 1325nm, over the temperature range of 77 K – 300 K.

Nd:YLF is a good candidate building a cryogenic cooled orthogonally polarized wavelength of dominant gain at 1053 nm. The maximum σ_{SE} peak of >120 pm^2, which obtained at LNT, is the highest among Nd^{3+} ions doped crystals, having good potential of building a high power laser system [45].

3.4 Discussion

Figure 3-9 shows the derived $\sigma_\alpha$eff spectra for Nd:YAG at various temperatures between RT and LNT, it illustrates that for many transitions the amplitude increases as the crystal gets colder whilst reducing the peaks' bandwidths in equal measure. Therefore, in considering cryogenic laser engineering with conventional diode lasers, the absorption rate is likely to decrease due to the typical few-nm bandwidths of these sources. However, one small deviation from this is observed at the lower temperatures, for the peak at 808 nm increased to a maximum of $\sigma_\alpha$eff = 18 ± 0.2 pm^2 around 120 K, then reduced to 16.9 ± 0.2 pm^2 at 77 K. This is attributed to the fact that this peak consists of two lines too, Z1 → S1 and Z3 → S4, and the fractional population in Z3 starts to diminish quickly below 170 K, while Z1 is gaining over the same temperature range. The combined affect is a nearly a 2-fold increase in the relative absorption coefficient for a narrowband (<~0.2 nm) pump at LNT with respect to RT (Fig 3-24). This traditional pump transition bandwidth (FWHM) decreases from ~1 nm at RT to 0.3 nm at LNT, and the peak wavelength is blue-shifted by 0.2 nm over this range in line with most other transitions as reported by Kushida [22]. The effective absorption coefficients for 808nm and 869nm absorption band (α) were determined with respect to conventional diodes (JOLD-30-CPXF-1L and JOLD-80-CPNN-1L) and a narrowband pump spectrum (~0.2 nm) e.g. Ti:Sapphire laser or VBG-locked laser diode. The FWHM was determined from actual spectral band of diode that has been measured.

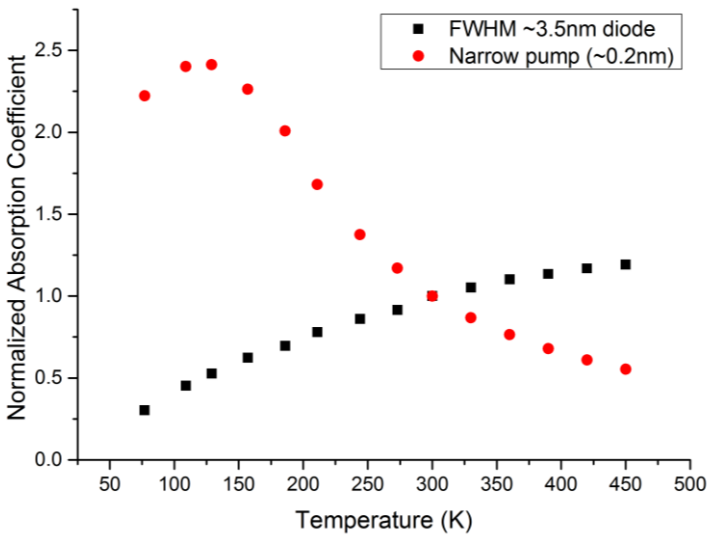

(a)

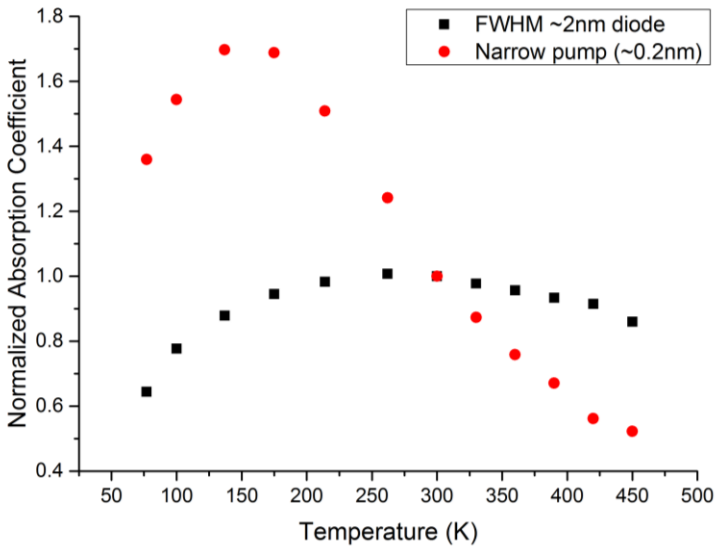

(b)

Figure 3-24 The relative change in absorption coefficient vs crystal temperature; for a conventional diode laser and a narrowband source, (a) 808 nm absorption band and (b) 869 nm absorption band. (Calculations made assuming negligible ground state bleaching)

The narrow and relatively high peak absorption at 869 nm is also attractive for cryogenic operation, where the longer in-band pump wavelength provides an advantage in terms of a lower quantum defect than obtained with 808 nm pumping. An important factor is the reduction of the thermal load in the crystal and thermo-optical distortions that are caused by the waste heat deposited into the crystal. Exploiting the properties of Volume Bragg Gratings to narrow the bandwidth of pump diode-laser, narrowband operation of these pump sources can be achieved whilst also locking the central wavelength to the absorption peak, which is discussed in greater detail in Chapter 5. Figure 3-24(b) shows the change in the effective absorption coefficient over temperature with respect to two pump sources centred at the 869 nm peak. As might be expected the narrowband pump absorption coefficient follows the trend in the transition strength, whereas for the broader bandwidth pump, absorption effectiveness for 808 nm pumping can increase at higher temperatures with respect to RT, but not for in-band pumping at 869 nm.

Exploiting the polynomial equation Eq.3-3, the temperature dependent cross section for either emission or absorption, can be described by:

$$\sigma_{e,a}(T) = \sigma_{e,a}(T_o)(e_o + e_1 T + e_2 T^2 ....) \qquad 3\text{-}3$$

Where e_0, e_1 and e_2 are the Taylor expansion coefficients, T_0 is the reference temperature, and for $\sigma_{e,a}(T_0)$ is the cross section peak value at the reference temperature. Second order polynomials

were used to represent the experimental data covering most of the useful temperature range for laser operation.

The polynomial expansion, Eq.3-3, was used to derive following Table 3-11. Figure 3-25 plotted both fitted curve and experimental data. The approximated data fits very well, and can be used for spatially distributed derivation using notation $\alpha(T)$, effective temperature dependent absorption coefficient. However, it requires pre-measured spectral data for the pump diode laser and absorption cross section for the temperature range of interest.

Table 3-11 Polynomial fit for Nd:YAG and Nd:GSAG absorption at 808nm

Wavelength	Crystal	$\alpha(T_o)$ (cm^{-1})	e_0	e_1	e_2	Applicable range (K)
808nm	Nd:GSAG	0.803	0.08578	0.01357	-2.162E-5	77 – 300
808nm	Nd:YAG	0.728	-0.05953	0.01562	-1.494E-5	77 – 450

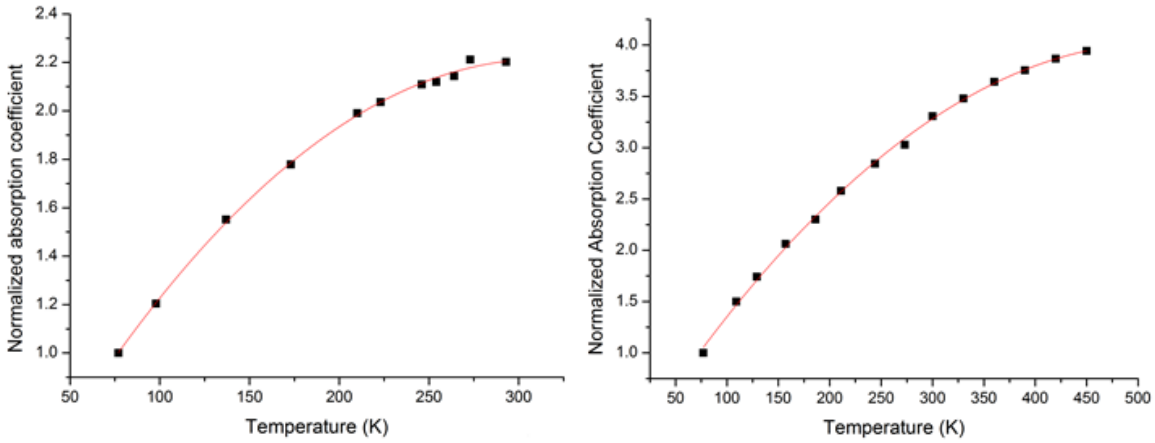

(a) (b)

Figure 3-25 Numerical fit of normalzed absorption of conventional 808nm diode laser change over Temperature (a) Nd:GSAG, (b) Nd:YAG

As stated in section 3.3.2 the emission cross section spectra around 1.06 μm is comprised of several Stark-Stark level transitions, this was modelled in more detail to gain a better understanding of the dynamics of the 1064 nm line in function of temperature. The analysis was performed by multiple peak fitting with the software Origin (Original Lab Inc. [44]). The position of individual lines was pre-determined by starting with reported the energy levels of each manifold at RT [1]. First, to comply the ZPL absorption peak from Z1 to R1 and R2. the energy transition from the ground energy level, 0 cm^{-1}, to R1 and R2 enables to track the actual energy level. The energy level changes over temperature was defined by tracking the peak absorption changes from Z1 to R1 and R2. We than tracked the single peak changes for energy transitions to Y1 - Y6 of $^4I_{11/2}$

from R1 and R2 of $^4F_{3/2}$. Each emission peak was defined experimentally, with pre-defined energy state of R1 and R2, the energy state of Y1-Y6 were found as the λ_{peak} is the actual transitions between two energy states. Figure 3-26 shows the deconvolution of the emission spectrum for 1064 nm at RT. Out of 12 transitions between $^4F_{3/2}$ to $^4I_{11/2}$, which consist of 2 energy levels from $^4F_{3/2}$ to 6 energy levels from $^4I_{11/2}$ manifolds, two emission peaks overlapped together. The two peaks (R1 → Y2 and R2 → Y3) were fitted according to the λ_{PEAK}.

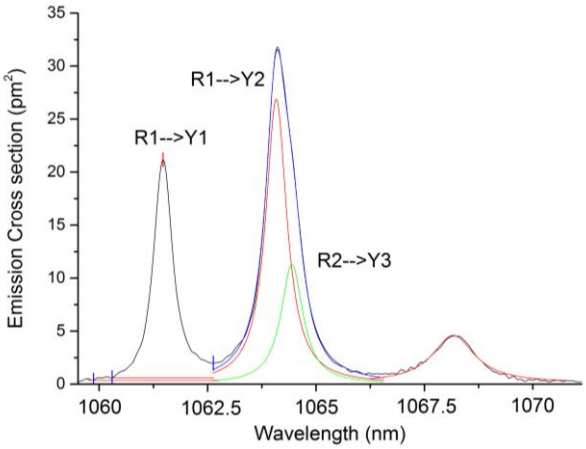

Figure 3-26 Example of the combined lines at 1064 nm for RT, Nd:YAG.

In Appendix A, Table A-1 & A-2 we provide table of the change of λ_{peak}, λ_{FWHM} and σ_{SE} with respect to each transition over LNT to RT. Figure 3-27 illustrates the temperature dependence for the peak of several key transitions, i.e. λ_{peak} for 938, 946, 1061, 1064.2, 1064.4 nm, in addition to the magnitude of the stimulated emission cross section, $\sigma_{peak,}$ and the bandwidth of these respective lines $\Delta\lambda_{FWHM}$. The thermal shifts in the peak positions agree with those reported by Kushida [22].

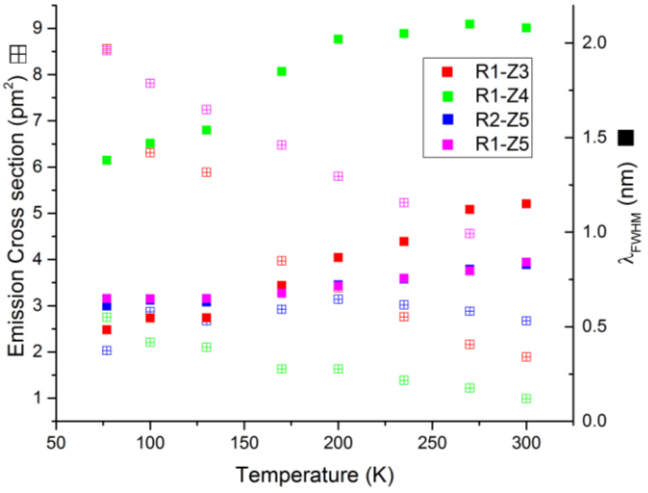

(a)

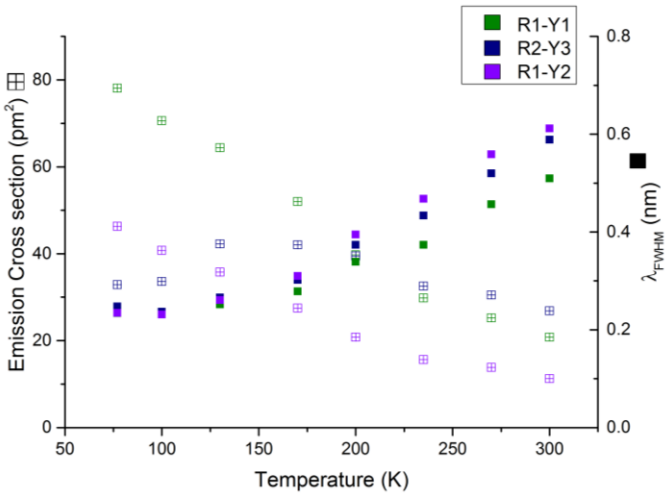

(b)

Figure 3-27 Emission cross section and transition bandwidth for several lines between manifolds (a) $^4F_{3/2}$ to $^4I_{9/2}$ and (b) $^4F_{3/2}$ to $^4I_{11/2}$, over the temperature range of 77 K to 300 K

The peak amplitude of the σ_{SE} is a key parameter for laser designs, for example, defining the potential gain and threshold condition. As such if a simple function can be used to describe the evolution of the peak σ_{α}eff as a function of temperature, it will improve the accuracy of modelling of the laser system. The change of λ_{peak} temperature dependence for the peak of several key transitions, i.e. for 938, 946, 1061, 1064.2, 1064.4 nm is plotted as a function of temperature in Fig 3-28.

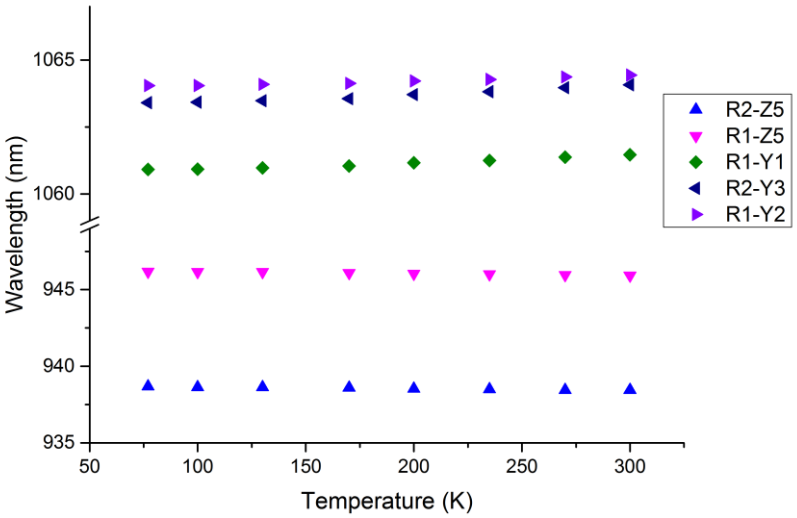

Figure 3-28 Change of Chosen R – Y λ_{Peak} for temperature change of 77 K to 300 K

Figure 3-29 shows the ratio of the strongest R → Z cross section line over the strongest R → Y line from temperature LNT to RT. Despite the 2-fold increase of σ_{SE} of 946 nm transition, the ratio actually increased as temperature reaches LNT.

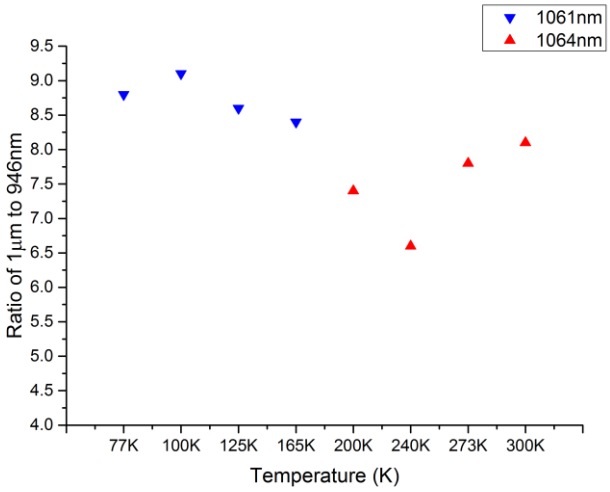

Figure 3-29 Ratio of the strongest R→ Z over the strongest R→Y line for temperature range 77 K – 300 K

Figure 3-30 duplicated the energy level for Nd:YAG at RT, where it has been drawn in Chapter 2, then compared its energy level changes when it reached LNT. The peak shift for line of interest, particularly Z5, and R1, R2 shows the relative rate of change in the Stark level position.

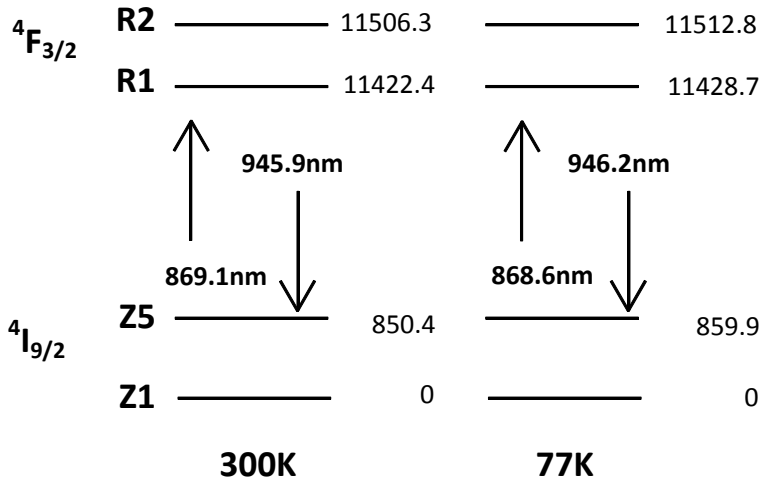

Figure 3-30 Measure of energy level (cm^{-1}) change of R1,2 and Z5 and shift of spectra peak for 300 K and 77 K

Taking the measured values of the peak σ_{α}eff, for the main transitions, covering a temperature range of 77 K to 450 K for 946 nm and 1061 nm, and 300 K to 450 K for 1064 nm (being the combination of the overlapping lines R2 - Y3 and R1 - Y2, which start to separate below ~270 K). Polynomial fit was made for emission cross section. T_0 for 946 nm and 1061 nm is set to 77 K, and

300 K for 1064 nm. Table 3-12 summarizes the fitting parameters within the respective measurement range. Figure 3-31 indicates the approximated fits and the measured σ_{SE} peaks with error bars, which are found to be within an error range (± 5 %). The measured σ_{SE} peaks were normalized at RT. Origin modelled the residual plot to assess the quality of statistical assumptions [46]. We have not found any trend in the residual curve and were within ± 4 % dependency.

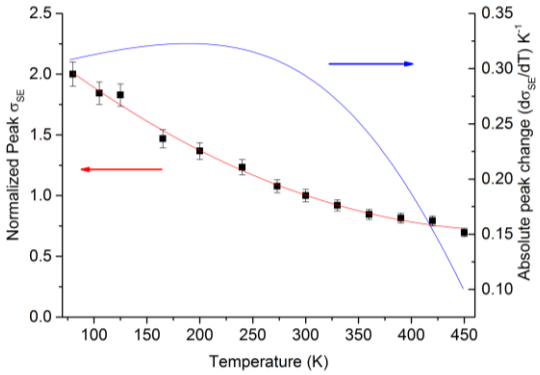

(a)

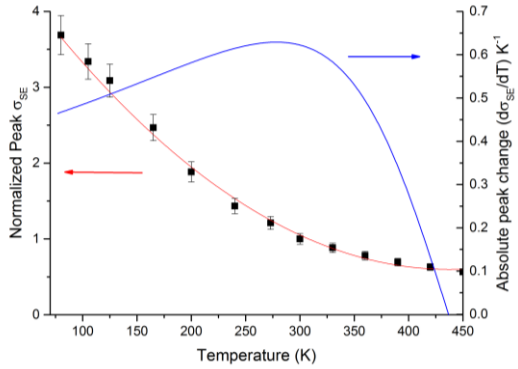

(b)

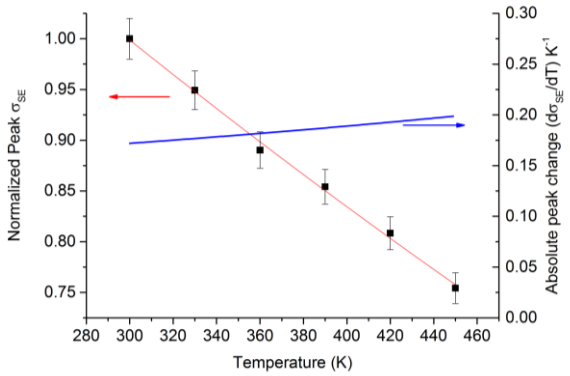

(c)

Figure 3-31 Numerical fit for intensity change over temperature 77 K to 450 K.
(a) 946 nm fit, (b) 1061 nm fit, (c) 1064 nm fit

Table 3-12 Polynomial fit for 946nm, 1061nm and 1064nm of Nd:YAG

Wavelength	Transitions	$\sigma_{SE}(T_o)$	e_0	e_1	e_2	Applicable range (K)
946 nm	R1 – Z5	8.48	2.55623	-0.0074	7.41774e-6	77 – 450
1061 nm	R1 - Y1	78.08	5.18215	-0.02096	2.39524e-5	77 - 450
1064 nm	R2 - Y3 & R1 - Y2	32.5	1.57634	-0.00214	7.06326e-7	300 - 450

The rate of peak changes, of which were drawn in blue solid curve, clearly shows the high temperature dependency of peaks at low temperature. However once crystal reaches or near room temperature the 1064 nm peak changes are very stable and drifts linearly at low rate, proves Nd:YAG as robust crystal. From Fig 3-31(a) it is determined that the rate of change in the peak value for σ_{SE} at 946 nm is ~0.3 % K^{-1}, within the range of 77 K to 300 K, then the rate of change starts to decrease gradually until reaching ~0.1 % K^{-1} by 450 K. For 1061 nm the rate increase from 0.45 % K^{-1} to 0.63 % K^{-1} at room temperature then decrease significantly to 0 % K^{-1} at 450 K. The rate of changed of the emission cross section at low temperatures is stronger for emission lines from R1. However, for 1064 nm, the rate change is relatively constant from 300 K to 450 K, at near 0.2 % K^{-1}. Sato and Taira [5] reported a similar numerical fit, showing a very stable rate of change 0.26 % K^{-1} for the temperature range of 288 K to 523 K.

3.5 Summary

In conclusion, we have investigated the spectroscopic properties of various Nd-doped crystals. A detailed study of the ground state absorption for the two main absorption bands of interest, around 808 nm and 870 nm, for near-IR lasers based upon $^4F_{3/2}$ emission, was realised by probing the samples absorbance with LED sources whilst changing the temperature of crystals. The data taken over a range of temperatures, from 77 K to 450 K, helped map out the dependence of the absorption coefficient of several Nd-doped crystals, which could be applied to narrow or "broadband" pump sources. At LNT the peak absorption of Nd:YAG at both 808 nm and 869 nm increased with respect to that observed at RT. Similarly, other Nd-doped crystals also showed

improved absorption coefficients at lower temperatures, albeit limited to using a narrow band pump source.

The emission cross section for the 946nm transition of Nd:YAG also increased by just over a factor of two, from RT to LNT, and second order polynomial functions has been derived to approximate the temperature dependent cross sections of this and other transitions of interest for NdYAG crystal. Using this polynomial expression, the temperature dependent gain could be modelled with greater accuracy and potentially improved numerical simulations of the performance of these systems, not only for different operating temperatures, but also to include the graded effective gain associated with the inherent thermal gradients within the laser crystals.

The study of the changes in the absorption coefficients with respect to temperature is vital for understanding and mapping out the potential laser efficiency under cryogenically-cooled operation, or under any arbitrary temperature within the measurement ranges. It is clearly evident that for cryogenic operation of a Nd:YAG laser, the pump source must have a bandwidth of <0.3 nm for efficient matching to the peak widths, and be tuned to the appropriate peak wavelength at the temperature of interest, as discussed by Cho *et al* [47]. As conventional diode lasers have a 2~4 nm bandwidth, special measures are required to improve the spectral brightness of these sources, locked to the appropriate wavelength for efficient absorption as crystal gets cold. A key technology that enables this are VBG's and their use will be discussed in Chapter 5, showing improved absorption characteristics over the bare diode laser array.

References

1. A. A. Kaminskii, Laser Crystals (Springer-Verlag, Berlin, Germany, 1990).

2. F. Kallmeyer, M. Dziedzina, X. Wang, H. J. Eichler, C. Czeranowsky, B. Ileri, K. Petermann, and G. Huber, "Nd : GSAG-pulsed laser operation at 943 nm and crystal growth," Applied Physics B: Lasers and Optics 89, 305-310 (2007).

3. T. Graf, and J. E. E. D. C. B. Balmer, "Lasing Properties of Diode Laser-Pumped Nd:KGW," Optical Engineering. 34, 2349-2352 (1995).

4. J. E. Geusic, H. M. Marcos, and L. G. V. Uitert, "Laser oscillations in Nd-doped yttrium aluminum, yttrium gallium and gadolinium garnets," Applied Physical Letters 4, 182 (1964).

5. Y. Sato, and T. Taira, "Temperature dependencies of stimulated emission cross section for Nd-doped solid-state laser materials," Optical Material Express 2, 1076-1087 (2012).

6. C. Q. Wang, Y. T. Chow, L. Reekie, W. A. Gambling, H. J. Zhang, L. Zhu, and X. L. Meng, "A comparative study of the laser performance of diode-laser-pumped Nd:GdVO4 and Nd:YVO4 crystals," Applied physics B 70, 769-772 (2000).

7. C. Czeranowsky, "Resonatorinterne frequenzverdopplung von diodengepupten neodym-lasern mit hohen ausgangsleistungen im blauen spektralbereich," PhD Thesis, University of Hamburg, Hamburg (2002).

8. W. Koechner, Solid-sate laser engineering, 6th edition (Springer, New York, 2006).

9. J. W. Kim, D. Y. Shen, J. K. Sahu, and W. A. Clarkson, "Fiber-laser -pumped Er:YAG lasers," IEEE Journal of Selected Topics in Quantum Electronics 15, 361-371 (2009).

10. T. Y. Fan, T. Crow, and B. Hoden, "Cooled Yb : YAG for high-power solid state lasers," in Airborne Laser Advanced Technology, T. D. Steiner, and P. H. Merritt, eds. (SPIE-International Society of Optical Engineering, Bellingham, 1998), pp. 200-205.

11. Z. J. Kiss, and R. J. Pressley, "Crystalline solid lasers," Proceedings of the IEEE 54, 1236-1248 (2005).

12. S. G. P. Strohmaier, H. J. Eichler, C. Czeranowsky, B. Ileri, K. Petermann, and G. Huber, "Diode pumped Nd : GSAG and Nd : YGG laser at 942 and 935 nm," Optics Communications 275, 170-172 (2007).

13. E. Browell, S. Ismail, and W. Grant, "Differentail absorption lidar (DIAL) measurements from air and space," Applied Physics B 67, 399-410 (1998).

14. V. Wulfmeyer, and J. Bosenberg, "Ground-based differential absorption lidar for water-vapor profiling: assessment of accuracy, resolution, and meteorological applications," Applied Optics 37, 3825 (1998).

15. A. A. Kaminskii, G. A. Bogomolava, and L. Li, "Absorption, luminescence, induced radiation and crystal splitting of the levels of ions of Nd3+ in the crystal YVO4," Bull. Acad. Sci 5, 613-690 (2003).

16. L. F. Johnson, G. D. Boyd, K. Nassau, and R. R. Soden, "Continuous operations of the CaWO4-Nd3+ optical maser," Proc. IRE 50 213 (1962).

17. O. Novák, T. Miura, M. Smrž, M. Chyla, S. Nagisetty, J. Mužík, J. Linnemann, H. Turčičová, V. Jambunathan, O. Slezák, M. Sawicka-Chyla, J. Pilař, S. Bonora, M. Divoký, J. Měsíček, A. Pranovich, P. Sikocinski, J. Huynh, P. Severová, P. Navrátil, D. Vojna, L. Horáčková, K. Mann, A. Lucianetti, A. Endo, D. Rostohar, and T. Mocek, "Status of the High Average Power Diode-Pumped Solid State Laser Development at HiLASE," Applied Sciences 5, 637 (2015).

18. M. S. Gaponenko, P. A. Loiko, N. V. Gusakova, K. V. Yumashev, N. V. Kuleshov, and A. A. Pavlyuk, "Thermal lensing and microchip laser performance of Ng-cut Tm3+:KY(WO4)2 crystal," Applied physics B 108, 603-607 (2012).

19. P. A. Loiko, V. E. Kisel, N. V. Kondratuk, K. V. Yumashev, N. V. Kuleshov, and A. A. Pavlyuk, "14W high-efficiency diode-pumped cw Yb:KGd(WO4)2 laser with low thermo-optics aberrations," Optical Materials 35, 582-585 (2013).

20. T. Y. Fan, D. J. Ripin, R. L. Aggarwal, J. R. Ochoa, B. Chann, M. Tilleman, and J. Spitzberg, "Cryogenic Yb3+-doped solid-state lasers," IEEE Journal of Selected Topics in Quantum Electronics 13, 448-459 (2007).

21. E. H. Calrson, and G. H. Dieke, "The State of the Nd3+ Ion as Derived from the Absorption and Fluorescence Spectra of NdCl3 and Their Zeeman Effects," Journal of Chemical Physics 34, 9 (1961).

22. T. Kushida, "Linewidths and thermal shifts of spectral lines in neodymium-doped yttrium aluminum garnet and calcium fluorophosphate," Physical Review 185, 9 (1969).

23. H. Glur, R. Lavi, and T. Graf, "Reduction of thermally induced lenses in Nd : YAG with low temperatures," IEEE Journal of Quantum Electronics 40, 499-504 (2004).

24. H. G. Danielmeyer, "progress in Nd:YAG lasers," in Lasers 4, A.K. Levine and A.J. DeMaria, eds. 1-71 (1976).

25. T. Kushida, H. M. Marcos, and J. E. Geusic, "Laser Transition Cross Section and Fluorescence Branching Ratio for Nd3+ in Yttrium Aluminum Garnet," Physical Review 167, 289-291 (1968).

26. S. Goldring, and R. Lavi, "Nd:YAG laser pumped at 946 nm," Optics Letters 33, 669-671 (2008).

27. X. Wang, F. Kallmeyer, S. Wang, A. Ding, and H. J. Eichler, "Frequency doubling of focused laser beams for high pulse energy at 471nm," in Laser Resonators and Beam Control Xi, A. V. Kudryashov, A. H. Paxton, V. S. Ilchenko, and L. Aschke, eds. (SPIE-International Society of Optical Engineering, Bellingham, 2009).

28. Y. Sato, T. Taira, N. Pavel, and V. Lupei, "Laser operation with near quantum-defect slope efficiency in Nd : YVO4 under direct pumping into the emitting level," Applied Physical Letters 82, 844-846 (2003).

29. M. J. Damzen, M. Trew, E. Rosas, and G. J. Crofts, "Continuous-wave Nd : YVO4 grazing-incidence laser with 22.5 W output power and 64% conversion efficiency," Optics Communications 196, 237-241 (2001).

30. M. Eichhorn, "Quasi-three-level solid-state lasers in the near and mid infrared based on trivalent rare earth ions," Applied physics B 93, 269 (2008).

31. Optical Society of America, Handbook of Optics (Mcgraw-hill, 2000).

32. D. E. Zelmon, D. L. Small, and R. Page, "Refractive-index measurements of undoped yttrium aluminum garnet from 0.4 to 5.0 μm," Applied Optics 37, 4933-4935 (1998).

33. T. Y. Fan, "Heat-Generation in Nd-YAG and Yb-YAG," IEEE Journal of Quantum Electronics 29, 1457-1459 (1993).

34. C. Y. Cho, P. H. Tuan, Y. T. Yu, K. F. Huang, and Y. F. Chen, "A cryogenically cooled Nd:YAG monolithic laser for efficient dual-wavelength operation at 1061 and 1064 nm," Laser Physical Letters 10, 45806-45806 (2013).

35. W. F. Krupke, "Radiative Transition Probabilities Within 4F3 Ground Configuration of ND-YAG," IEEE Journal of Quantum Electronics 7, 153-& (1971).

36. J. Su, B. Liu, L. H. Xu, Q. L. Zhang, and S. T. Yin, "Effective segregation during Czochralski growth and spectral properties of Nd3+ in GSAG crystal," Journal of Alloys and Compounds 512, 230-234 (2012).

37. Y. J. Chen, Y. F. Lin, X. H. Gong, Q. G. Tan, J. Zhuang, Z. D. Luo, and Y. D. Huang, "Polarized spectroscopic properties of Nd3+-doped KGd(WO4)(2) single crystal," Journal of Luminescence 126, 653-660 (2007).

38. H. Kühn, K. Petermann, and G. Huber, "Correction of reabsorption artifacts in fluorescence spectra by the pinhole method," Optics Letters 35, 1524-1526 (2010).

39. M. C. Pujol, M. Rico, C. Zaldo, R. Solé, V. Nikolov, X. Solans, M. Aguiló, and F. Díaz, "Crystalline structure and optical spectroscopy of Er3+-doped KGd(WO4)2 single crystals," Applied Physics B 68, 187-197 (1999).

40. R. Moncorge, B. Chambon, J. Y. Rivoire, N. Garnier, E. Descroix, P. Laporte, H. Guillet, S. Roy, J. Mareschal, D. Pelenc, J. Doury, and P. Farge, "Nd doped crystals for medical laser applications," Optical Materials 8, 109-119 (1997).

41. A. L. Harmer, A. Linz, and D. R. Gabbe, "Fluorescence of Nd 3+ in lithium yttrium fluoride," Journal of Physics and Chemistry of Solids 30, 1483-1491 (1969).

42. R. Reisfeld, M. Eyal, and C. K. Jorgensen, "Comparison of Laser Properties of Rare-Earths in Oxide and Fluoride Glasses," Journal of the Less Common Metals 126, 187-194 (1986).

43. N. P. Barnes, and D. J. Gettemy, "Temperature variation of the refractive indices of yttrium lithium fluoride," Journal of Optical Society of America 70, 1244-1247 (1980).

44. C. Y. Cho, T. L. Huang, S. M. Wen, Y. J. Huang, K. F. Huang, and Y. F. Chen, "Nd:YLF laser at cryogenic temperature with orthogonally polarized simultaneous emission at 1047nm and 1053nm," Optics Express 22, 25318-25323 (2014).

45. D. Rand, J. Hybl, and T. Y. Fan, "18 - Cryogenic lasers," in Handbook of Solid-State Lasers, B. Denker, and E. Shklovsky, eds. (Woodhand Publishing, 2013), pp. 525-550.

46. OriginLab, www.originlab.com/doc/Origin-Help/Residual-Plot-Analysis2016.

47. C. Y. Cho, T. L. Huang, H. P. Cheng, K. F. Huang, and Y. F. Chen, "Analysis of the optimal temperature for the cryogenic monolithic Nd:YAG laser at 946-nm," Optics Express 24, 1-8 (2016).

48. Thorlabs, www.thorlabs.com2016.

Chapter 4:

Energy transfer upconversion measurements for Nd doped gain materials

4.1 Introduction

Energy transfer is the phenomenon of transferring excited energy among laser active ions. The interaction of dipole-dipole resonant is closely related to the spacing between two ions, and vanishes with increasing distance in between. One ion which receives the stored energy of the other and is subsequently excited to a higher energy state ($^4G_{5/2}$, $^4G_{7/2}$, or $^2G_{9/2}$), while the other one is returned to a lower state ($^4I_{15/2}$, $^4I_{13/2}$, or $^4I_{11/2}$) respectively [1]. The strength of ETU processes can have a detrimental effect on laser performance as an additional source of heat, increased cavity losses, and by reducing the population inversion thus weaker laser gain. The reduction of population of metastable level at $^4F_{3/2}$ of Nd:YAG causes an increase in the laser threshold since population density is clamped by ETU loss [2]. The non-radiative transfer between energy level transition is inefficient increasing the thermal load in the gain medium, contributing to the thermal effect. The influence of ETU can be quite significant for the design and optimization of a laser system, especially for low gain lasers that typically require relatively high population inversion to overcome cavity loss. The effect of ETU is governed by several factors that include active-ion doping concentration, crystal structure and intra-ion spacing, and the spectroscopic properties of the medium, which can be neatly described by a macro-scopic parameter, the upconversion coefficient (W_{ETU}). In the previous chapter, we presented the temperature dependence of the Nd^{3+} spectroscopic properties in various host materials, especially for YAG, which has been the main material of choice when it comes to the following cryogenically cooled laser experiments. The temperature dependency of absorption and emission spectroscopy, especially absorption cross section of Nd:YAG at 808 nm changes 4-folds for 77 K to 450 K, which may suggests W_{ETU} is also a temperature dependent spectroscopic parameter. The temperature dependency of other RE doped crystal was also reported [3, 4].

The process of ETU, discussed in section 2.3.3, is known to contribute to additional heating of the gain material and increasing the threshold power. The determination of the ETU parameter is

considered quite challenging, due to its quadratic dependence upon the population in the upper laser level, thus sensitivity to the pump excitation distribution in the gain medium. In following chapter, we investigated the ETU coefficient measurement with a sensitive Z-scan technique. The Z-scan compares measured transmission as a function of incident pump irradiance. The data is compared with simulation based upon a two level spatially and temporally dependent rate equation, which has been discussed in Chapter 2.

Whilst there are many papers studying the influence of ETU on the quasi-four-level laser performance [1, 5], both experimental and in simulation, the magnitude of the ETU coefficient for Nd:YAG has been reported significant range of values from 5×10^{-17} to 3×10^{-16} cm^3/s [6, 8], as such its actual impact on performance can be difficult to ascertain with certainty. In this chapter, the methodology for Z-scan setup and ETU measurement is described. Following the temperature dependence from RT up to 450 K of metastable energy level and also the concentration dependence of the ETU coefficient in Nd:YAG is investigated. The data is compared with simulation based upon a two-level rate equation. Different types of Nd^{3+} doped crystals were also investigated using the Z-scan method. The report discusses the effect on laser performance both for CW oscillators and for high inversion systems such as Q-switched oscillators.

4.2 Methodology: ETU measurement via the Z-scan method

A schematic diagram of the Z-scan experimental setup is shown in Fig 4-1. The output beam of a continuous wave Ti:Sapphire laser was expanded 4 times with a telescope system (L_1, f = 75 and L_2, f = 300) and modulated by a mechanical chopper. The pulse duration of ~2.5 ms is sufficient to reach steady state without inducing a significant temperature rise during the pulse, while the duty cycle of 10 % is small enough to ensure the heat generated, considering our few hundred mW average power, diffuses away from the region of interest before the next pulse arrives. A focusing lens (L_3) of f = 200 mm was mounted to an electronically-controlled translation stage to change the beam size in the laser crystal, which provides precise control of the irradiance in the sample. The transmitted beam was collected and collimated by a second lens (L_4), mounted on the same translation stage, then split with an uncoated glass wedge, with ~92 % passing directly to a power meter and one surface reflection (~4 %) directed to a silicon photodiode (PD_1). Spontaneous emission was collected with a concave mirror (L_6, ROC = -100) and a focusing lens (L_5, f = 75), was monitored by an InGaAs photodiode (PD_2). A digital oscilloscope was used to record the amplitude of transmitted signal and measure the fluorescence lifetime. We can also neglect the scattering loss because of the excellent optical quality.

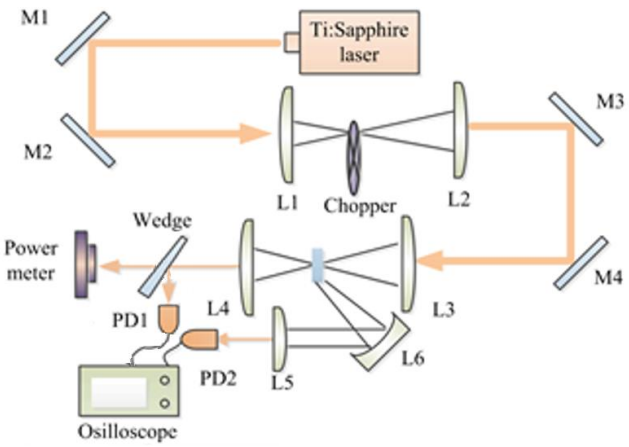

Figure 4-1 Experimental set-up for the Z-scan measurements

Using a beam profiler placed at the position of the sample, the laser beam size at many positions along the Z-axis relative to the beam waist was measured by scanning the focusing lens position as was done with the actual sample. The beam quality of the pump laser beam was calculated to be M^2 ~ 1.17 in both directions, and had waist radii of w_x = 20.7 ± 0.2 µm and w_y = 19.7 ± 0.2 µm after the focusing lens, L_3. The Rayleigh range for the beam was comparable to the crystal sample length and provided near constant beam size through the sample. Therefore the confocal parameter for this beam was slightly longer than the crystal length, which is close to the limit when considering the change in beam size throughout the sample and may introduce a slight asymmetry in the transmission response depending upon whether the pump beam is converging or diverging through the crystal. The pump irradiance incident on the crystal is defined by a Gaussian distribution and the model assumes an effective beam area (A_{eff}) obtained from the average beam radius over the crystal length calculated using Gaussian beam propagation theory, i.e.

$$A_{eff} = \frac{\pi}{l_c}\int_0^{l_c} \omega(z)^2 \, \mathrm{d}z \qquad 4\text{-}1$$

Two insets in Fig 4-2, illustrate the actual beam radii versus the calculated effective beam radius derived from Eq 4-1 using Gaussian beam propagation theory. At focus the “on axis” available pump irradiance reached 50 $kWcm^{-2}$, nearly four times higher than the saturation irradiance, when the wavelength was tuned to the absorption peak of Nd:YAG around 808.7 nm.

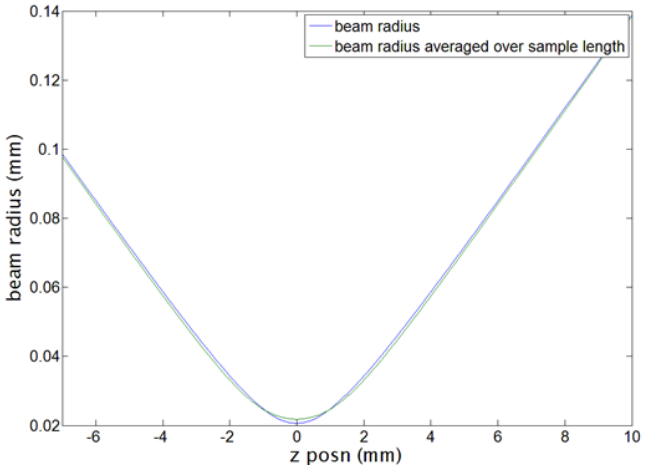

Figure 4-2 Beam radius as a function of position (blue curve) and beam radius averaged over sample length (green curve)

4.3 Results

As we use Z-scan technique to determine the upconversion parameter, as the technique requires an accurate measure of pump irradiance and an accurate spectroscopy data was measured prior performing the measurement. Pump rate which has been derived in Eq. 2.40–2.42 in detail, requires accurate absorption coefficient of sample crystal and physical properties of sample crystal, such as ion concentration, sample dimensions, Fresnel reflection etc. The following reported W_{ETU} value has measured its parameters prior performing Z-scan experiment.

4.3.1 Nd:YAG Test result

The Nd:YAG crystal transmission at 808nm at RT with respect to the focus position is presented in Fig 4-3. The figure shows the peak where the incident pump irradiance is highest. The figure also shows the simulated maximum crystal transmission without considering ETU, that is $W_{ETU} = 0$. The simulation (red dash curve) that doesn't count in the ETU coefficient, overestimated the transmission by ~50 % as pump irradiance reaches its maximum value. Considering three decay channels (fluorescence, ETU, cross relaxation) as described in section 2.3.3, at the highest pump irradiance the modelled peak transmission in match with the measured for ETU coefficient of $5.1 \pm 1 \times 10^{-17}$ cm^3/s, for our 0.95 at% Nd:YAG at room temperature. This is in good agreement with the value reported by Guy *et al* [7] and significantly lower than that reported by others [6, 8]. In simulation we found the maximum transmission is quite sensitive to the ETU coefficient value, however the simulation and the experimentally measured value show excellent agreement over the whole Z-scan range, which provides a high level of confidence in the accuracy of the measurement.

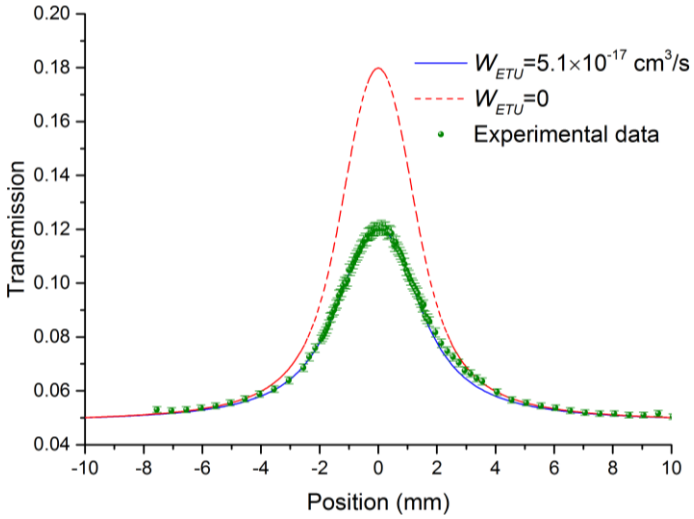

Figure 4-3 Transmission of 0.95 at% Nd:YAG crystal at RT, when varying the Z-position of the focusing lens system, about the focal point at zero

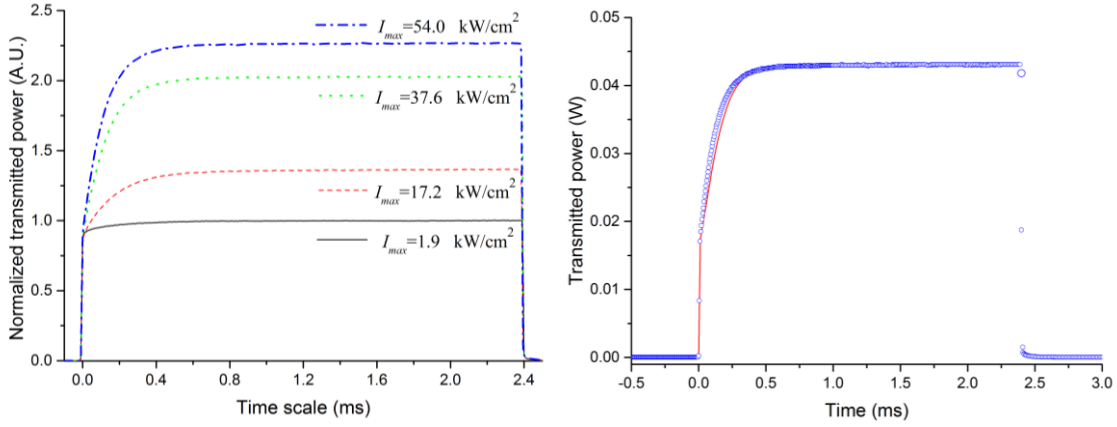

(a) (b)

Figure 4-4 Transmitted power temporal waveforms of (a) different incident pump irradiance and (b) measured temporal transmission of Nd:YAG at maximum pump irradiance

Temporal waveforms of the transmitted pump pulse were also recorded to compliment this analysis with and without the crystal. We could determine the temporal dependence by comparing two pulses, the bleaching effect for different pump irradiance level at different locations. Figure 4-4(a) presents several different pump irradiance conditions, corresponding to different Z-positions along the scan. The modelled waveform matches very well in steady-state which supports the observation in Fig 4-3. However, for the highest pump irradiance has slight difference between observation and simulation in the leading edge of waveform where Fig 4-4(b) shows the rate of bleaching in experiment is faster than the simulated curve at the beginning of the incident pump pulse. Later experiment was carried with shorter crystals (~1 mm) that matched better than longer crystal (3.25, 5 mm). The rate of bleaching is slower for longer crystals,

primarily driven by the larger effective beam area and thus lower “maximum” irradiance level due to their longer length. Nonetheless, the data fits very well in steady-state for both cases.

4.3.2 ETU dependency on temperature in Nd:YAG

The experiment from section 4.3.1 was the extended to determine the ETU coefficient dependence on temperature from room temperature upto 450 K. This information could help to improve spatially-dependent modelling of Nd:YAG lasers, where the heat deposited during the pump cycle giving rise to a temperature gradient within the gain medium, will have an additional contribution due to ETU dependent upon the local temperature. This effect could be quite significant for the performance of the weaker lasing transitions, and an additional component to thermal aberrations and induced losses within the gain medium.

Utilising the high resolution measurements of the 808 nm absorption cross section presented in the previous chapter, the saturation irradiance was determined as a function temperature. Thus the measured Z-scan transmission data could be compared at different temperatures to extract the temperature dependence of the ETU coefficient.

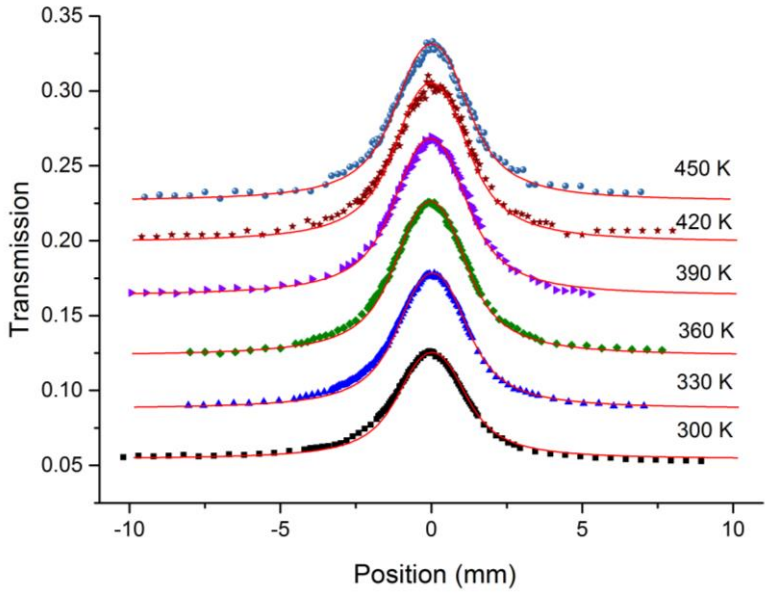

Figure 4-5 Nd:YAG crystal transmission at 808 nm vs Z-scan position relative to the focus at different temperature, 300 K – 450 K

The crystal was heated in a resistive oven to higher temperatures. The heater was made of Cu block and a high power resistor which was under control of an automated power supply, the temperature was read via thermocouple installed inside the block and tuned. Figure 4-5 shows the both experimental pump-power transmission observed and simulated results at several different temperatures from 300 K to 450 K. The absorption coefficient reduces at higher

temperatures as discussed in the previous chapter, which increases the small-signal pump transmission as the crystal temperature rises. Some instability in transmission at high temperature was most probably due to air turbulence and localized cooling of crystal. The simulation results are in good agreement with experimental data when varying the only free parameter ETU coefficient. Table 4-1 shows the estimated ETU coefficient over temperature include error range.

Table 4-1 W_{ETU} coefficient of 0.95 at.% Nd:YAG at different temperatures

Temperature (K)	**300**	**330**	**360**	**390**	**420**	**450**
W_{ETU} ($10^{-17}cm^3/s$)	5.1±1.0	4.0±0.8	3.5±0.7	3.2±0.6	2.5±0.5	2±0.4

4.3.3 ETU dependency of Nd concentration in Nd:YAG

It is well known that the magnitude of the ETU coefficient is dependent on the concentration of the rare earth ion, but the actualy dependence for Nd:YAG is not well covered in the literature yet. In this work, we investigate the concentration dependence of ETU coefficient in Nd:YAG. The measured transmission via Z-scan technique is compared with simulation data.

Four Nd:YAG samples with different neodymium concentrations were tested, their parameters shown in Table 4-2. The fluorescence lifetime of the 0.95 at.% Nd:YAG crystal was measured, in the small-signal regime with the measuring its dominant 1μm fluorescence, found to be 235 ± 5 μs as is typical for this concentration [9, 10]. At higher pump irradiance values this fluorescence lifetime reduced, down to 220 ± 5 μs at the maximum irradiance available (~50 $kWcm^{-2}$), which proves the trend of a reducing lifetime of the meta-stable state with an increasing population level. This trend was observed for all the samples, consistent with an irradiance dependent de-excitation process, such as ETU.

We determined the respective W_{CR} coefficient for each sample from their fluorescence lifetime, measured under weak excitation, as per Eq.2-39 in section 2.3.3, assuming that the intrinsic lifetime of Nd^{3+} in YAG is 260 μs [11] and that CR is the only decay mechanism apart from spontaneous emission under these conditions. The resulting values are given in Table 4-2.

Table 4-2 The parameters of Nd:YAG samples investigated.

Sample	1	2	3	4
Doping Concentration (at.%)	1.07	0.95	0.56	0.31
ion density ($x10^{20}$ions/cm^3)	1.477	1.311	0.773	0.428
Length (mm)	1.14	3.25[x]	1.09	5.1[x]
Fluorescence lifetime with weak excitation (μs)	232±5	235±5	250±5	252±5
W_{CR} ($x10^{-18}cm^3/s$)	3.06±0.60	2.96±0.65	1.85±1.00	2.94±1.90
W_{ETU} ($x10^{-17}cm^3/s$)	7.5±1.0	5.5±1.0	3.5±0.7	2.7±0.7

[x]. *These crystals had anti-reflection (AR) dielectric coatings on the input and output facets*

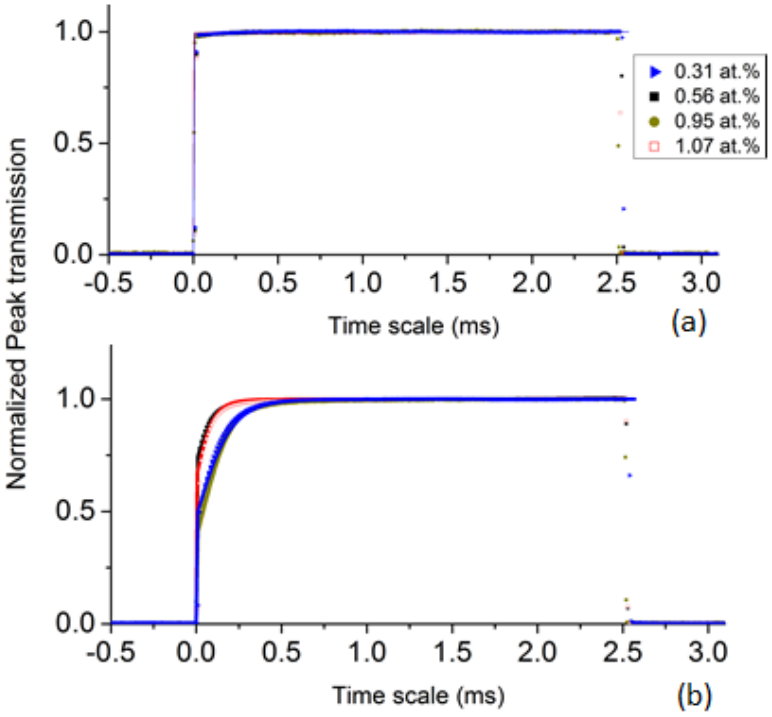

Figure 4-6 Measured (symbol) and simulated (solid line) temporal waveform of the transmitted power at (a) low pump irradiance, and (b) the maximum pump irradiance for different doping concentration of Nd:YAG

Figure 4-6 shows two of the temporal waveforms for Z-scan experimental data at (low and high irradiance values) and the corresponding simulation results, for the different doping concentrations tested. The doping concentration of each sample was determined by comparing the small signal absorption and calibrating with our previously determined absorption cross

section. As discussed in the previous section 4.3.1, the rate of bleaching is well-matched for the shorter crystals (~1 mm), as opposed to the longer crystals. This implies a lower effective irradiance due to larger effective beam area in the longer sample lengths. The Z-scan pump beam transmission through each of the samples is shown in Fig 4-7. The good fit between simulation and experimental data across the whole range of irradiance levels generated through the Z-scan gives confidence in the ETU coefficient values obtained. By fitting the model to the experimental data, with the ETU coefficient taken as the only free variable, we found that the magnitude of the ETU coefficient increased from $2.7 \pm 0.7 \times 10^{-17}$ cm^3/s for 0.31 at.% doped Nd:YAG to $7.5 \pm 1.0 \times 10^{-17}$ cm^3/s for a 1.07 at.% dopant concentration. For the 1.07 at.% doped crystal, a longer crystal was also tested to compare it with a shorter crystal to ensure that there were no crystal length dependencies in the measurement, for both lengths of crystal we obtained the same ETU coefficient within our error range. These error margins are dominated by the sensitivity of the experimental setup.

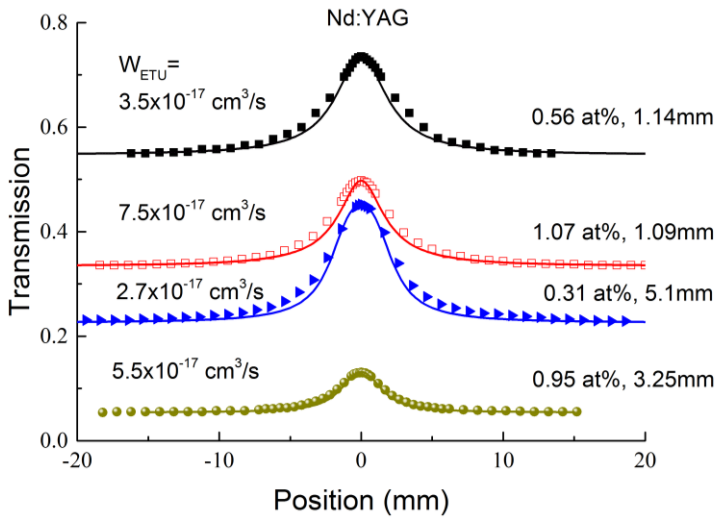

Figure 4-7 Nd:YAG crystal transmittance at 808 nm vs sample position relative to the focus for the samples with different dopant concentrations

For some of the samples we observed a 5 % variation in the pump transmission for transverse movements of the crystal at the beam waist position. The tightest focused beam size, which was defined ~40 μm at the highest irradiance, was clearly moved along X and Y axis during the Z-scan and not occupying the single area at the peak irradiance scan. The variation of scan area was lead to be cause a variation of transmission at its peak irradiance. It is not clear what caused the variation of the transmission along the X or Y axes variation but suggest either of crystal surface quality, including AR coatings or by a non-uniform distribution of Nd^{3+} ions in crystal. This will have an adverse effect on our measurement accuracy since the model relies on the assumption that there is homogeneous distribution of active ions or superior surface quality. The reported ETU coefficient in section 4.3.1 and 4.3.2 was measured for a 3.25 mm long 0.95 at.% doped

Nd:YAG crystal, which is the same sample that has been reported in this section. As is evident, the value reported in first temperature dependency experiments does not match from the following concentration dependency experiments; however, both values are within our error range, so the respective values are valid.

4.3.4 ETU coefficient measurements for other Nd^{3+} doped crystals

This section reports further investigations on measuring the ETU in various Nd^{3+} doped crystals. 4 different crystal families, consist of garnet, fluoride, tungstate and vanadate was investigated using various dopant concentration and crystal thickness upon availability. Absorption peak spectra and its cross section was defined prior experiment (Chapter 3). The ETU coefficients were all measured using the setup described in section 4.2 but the wavelength peak was adjusted to match the absorption peak of each crystal. Table 4-3 presents the key spectroscopic properties for the investigated crystals. Nd3+ doped crystal except Nd:YAG assumed the measured fluorescence lifetime as the intrinsic lifetime, neglecting cross relaxation since further investigation is beyond the scope for the report.

Table 4-3 Key spectroscopic properties of the investigated laser crystals

Host for Nd^{3+} ions and Axes	Dopant concentration (at.%)	Ion density ($x10^{20}/cm^3$)	Length (mm)	Fluorescence Lifetime (μs)	Absorption Peak λ (nm)	$\sigma_\alpha$eff (pm^2)
YAG	0.31	0.428	5	232±5	808.7	6.8
	0.56	0.773	1	235±5		
	0.95	1.311	3.25	250±5		
	1.07	1.477	1	252±5		
YLF (E//a)	0.5	0.66	1	520±10	797	12
YVO4 (E//a)	0.5	0.625	1	98±2	808.5	13.1
	1.0	1.25	1	90±2		
GdVO4 (E//a)	0.5	0.605	1	107±2	808.5	11.75
	1.0	1.21	1	98±2		
KGW (E//Np)	3	1.89	1	112±2		6.7
(E//Ng	3	1.89	1	112±2	810	3.5
(E//Np)	4	2.52	1	119±2		6.7

Nd:YLF

Nd:YLF has been one of most widely used laser medium for laser applications. The main 1 μm transition of crystal has advanced properties for its large stimulated emission cross section, a longer lifetime compare to other Nd^{3+} doped crystals and its natural birefringence. However the crystal was reported the reduced storage lifetime and decreased laser efficiency for its operation under high excitation density [12-14].

The fit for Nd:YLF is not as good as that obtained for Nd:YAG in this result, nonetheless the value is in agreement with the trend seen by comparing Jacinto's and Pollnau's measurements [15, 16]. It is possible that some processes are occurring that our simple model is not capable of capturing, such as depletion quenching rate from the metastable, $^4F_{3/2}$ level or significant energy migration within the localized substantial overlap of cross sections. There is no doubt however, that the peak transmission of the pump beam through the sample when the crystal is at focus is significantly lower than would be expected if no nonlinear lifetime quenching of the $^4F_{3/2}$ level or excited state absorption were occurring. The determined W_{ETU} coefficient value is nominally 3 times higher than that of Nd:YAG with a comparable doping concentration.

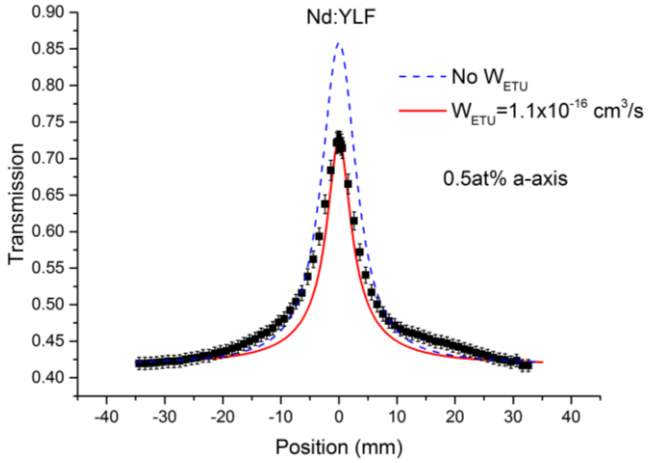

Figure 4-8 Transmission of a 1.1 mm thick 0.5 at% Nd:YLF crystal vs sample position relative to the focus. Measured for the pump-polarisation aligned with the crystal's a-axis.

Nd:YVO4

Nd:YVO4 crystal has the most efficient absorption at 808nm which achieves high pump absorption efficiency from the pumping diode laser. The crystal, which has a natural birefringent, is usually chosen for end-pumped system adapting smaller crystals as a gain medium. Two crystals each have 0.5 at.% and 1.0 at.% doped crystal were scanned on both two polarization axes. The

simulated fit for Nd:YVO4 is not well matched with the model, 0.5 at% a-axis curve fits better than 1 at.% a-axis however the 0.5 at.% curve also shows similar trend as seen with YLF result. The presented result consisted a-axis only since the high absorption at c-axis is highly saturated. The high absorption at strong c-axis adds unwanted thermal deposition and stimulated fluorescence which doesn't allow the simple two level rate equation valid. This also applies to other crystals that have very strong absorption features, however, the model has a reasonable match to experiment for a lower absorption cross section feature, such as using the weaker peaks of the s-polarisation in this case, which meant that the W_{ETU} coefficient could be retrieved. Consistent with the strong spectroscopy cross section values, the W_{ETU} coefficient of Nd:YVO4 is very large, almost two orders of magnitude higher than for Nd:YAG for comparable ion densities.

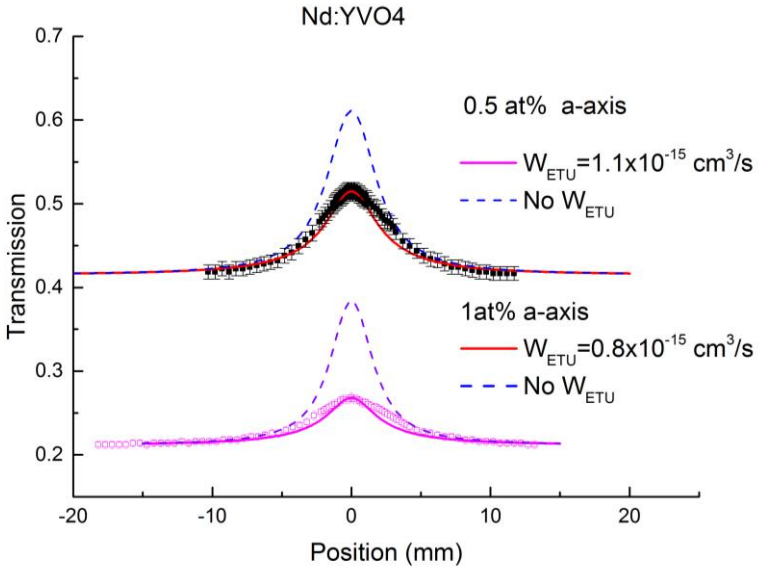

Figure 4-9 Transmission of 0.5 at% and 1.0 at% Nd:YVO4 crystals vs sample position relative to the focus. Measured for the pump-polarisation aligned with the crystal's a-axis.

Nd:GdVO4

Nd:GdVO4 is another vanadate family and one of most efficient crystal for diode pumped configurations. Its spectroscopic properties are similar to Nd:YVO4 but has superior thermos-mechanical properties. Again two crystals have different doping concentration was measured using Z-scan set-up for both polarization axes. The fit for 0.5 at.% a-axis is well matched to simulated curve within error range but not really well fitted for a-axis 1 at.% doped crystal. Again, c-axis was highly saturated due to high absorption in crystal and not presented. Vanadate families (YVO4 and GdVO4) show almost two orders of magnitude larger than Nd:YAG.

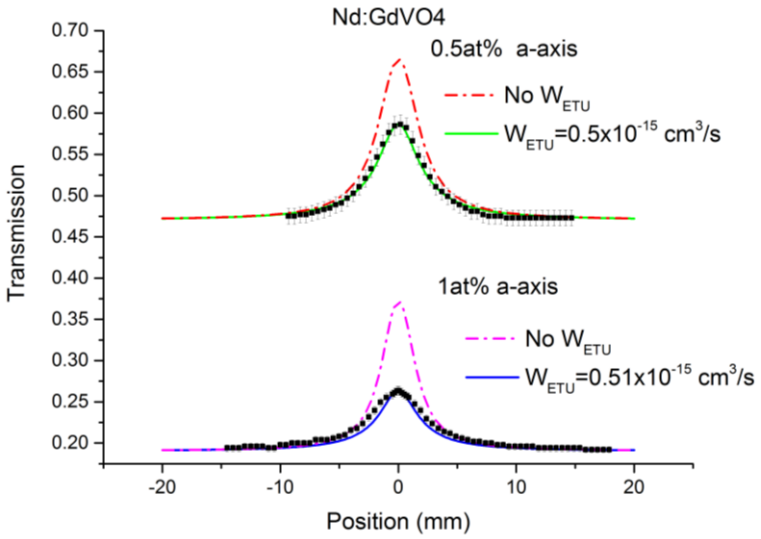

Figure 4-10 Transmission of 0.5 at.% and 1 at.% Nd:GdVO4 crystals vs sample position relative to the focus at RT, Measured for a-axis

Nd:KGW

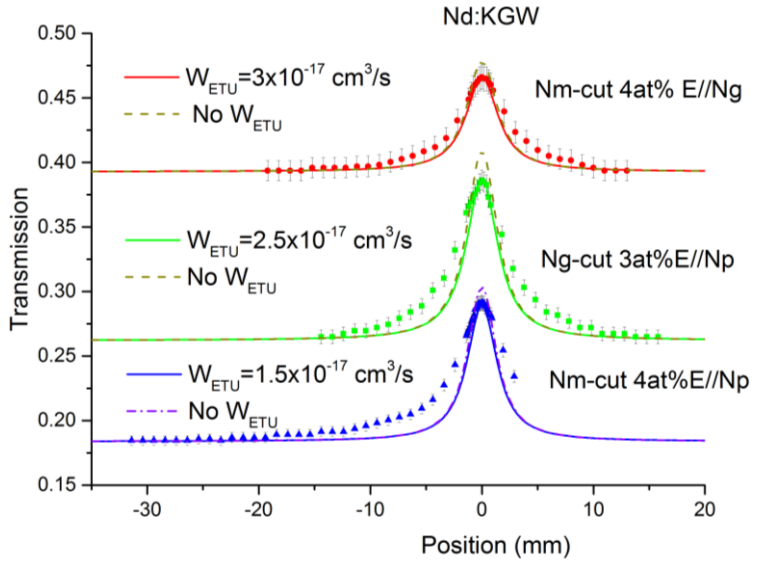

Figure 4-11 Transmission of 3 at% (Ng cut) and 4 at.%(Ng cut) Nd:KGW crystals vs sample position relative to the focus. Measure for pump-polarisations corresponding to E//Np and E//Ng principal axes.

Double tungstate crystal has exceptionally intense and broad spectroscopy band with strong polarization anisotropy. Gd matches very well with number of RE ions which allows very high doping concentration without significant luminescence quenching. Doping up to 10% is possible with Nd^{3+} ion since the size matches, comparing the ionic radii for 1.053 Å of Gd^{3+} to 1.109 Å of Nd^{3+}, particularly well. The crystal is under re-evaluation since its orientation was determined by cutting along one of principal axes (Ng-cut). For the measurement, two different crystals having a

dopant concentration of 3 at.% (E//Ng cut) and 4 at.% (E//Nm cut) were tested, with two polarization axes, E//Np and E//Ng were measured. Again high absorption axis, E//Nm was excluded as we observed a non-saturating dependence of pump pulse. The predicted ETU for E//Np at 3 at.% and 4 at.% is 2.52 x 10^{-17} cm^3/s and 1.89 x 10^{-17} cm^3/s, respectively. 4 at.% crystal is E//Nm cut crystal thus assess E//Ng measure, which yields 3.0 x 10^{-17} cm^3/s. The confidence of measured data is ± 50 % as the response was not fitting the simulation curve precisely. This discrepancy is attributed to additional energy decay pathways such as excited state absorption and possible energy migration associated with absorption and emission spectra overlap at its metastable energy level, which contribute to more complicated energy dynamics then our simple model caters for.

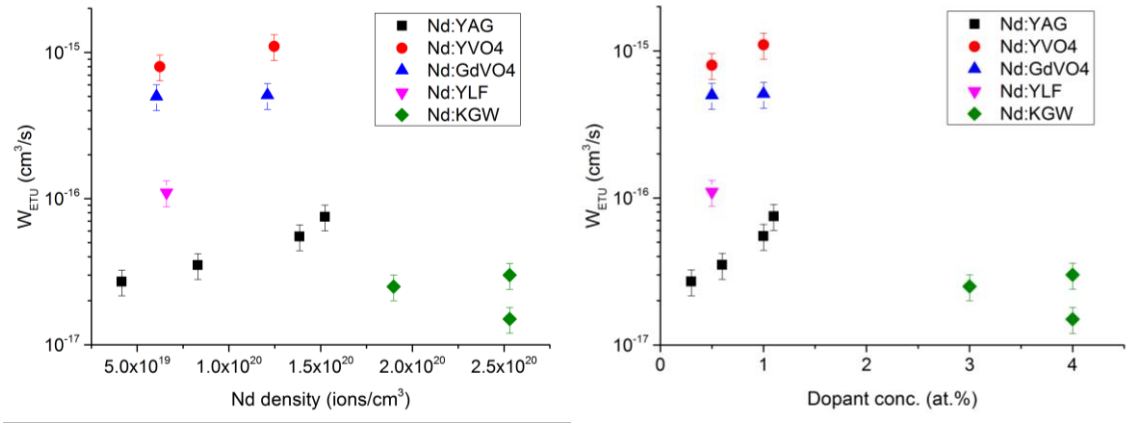

(a) (b)

Figure 4-12 W_{ETU} coefficient as a function of (a) Nd^{3+} ion density for crystal and (b) atomic dopant concentration

Figure 4-12 presents a summary of the ETU coefficient for different crystals. The graphs denote the doping concentration in atomic weight and in ions density (ions/cm^3). Ion density allows for a better comparison of relative ETU coefficients for the respective host materials and therefore the possibility to compare the relative transfer rates for each under realistic operating conditions.

4.4 Discussion

Elevated temperature and concentration dependency of ETU for Nd:YAG

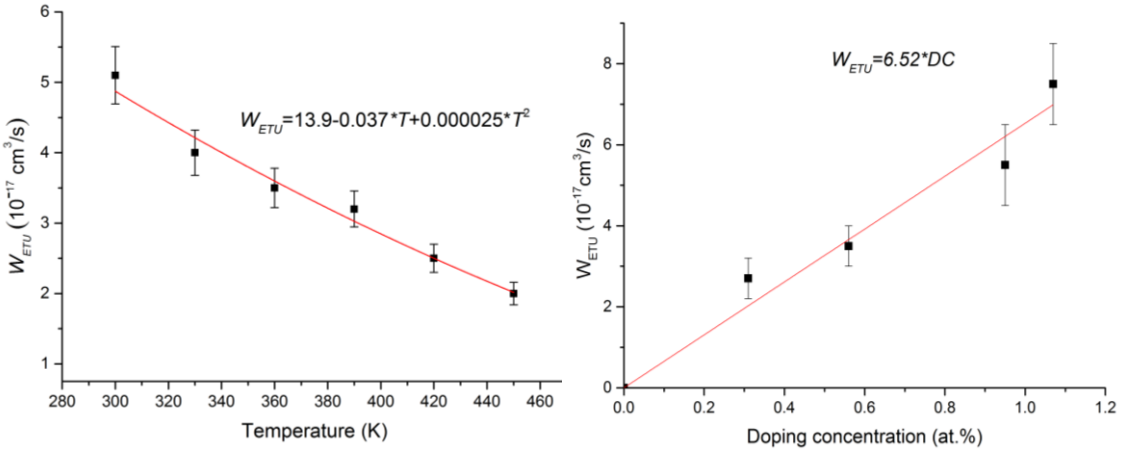

(a) (b)

Figure 4-13 (a) Temperature and (b) concentration dependence of the W_{ETU} coefficient for Nd:YAG

The two plots in Fig 4-13 show the ETU dependence on temperature for 1 at.% doped Nd:YAG and at RT the Nd^{3+} concentration dependence for doping levels ranging from 0.3 at.% to 1.1 at.% in YAG. The magnitude of the ETU coefficient varies according to the equation from RT up to the investigated temperature, 450 K.

$$W_{ETU} = 13.3 - 0.037T + 0.000024T^2 \qquad 4\text{-}2$$

Over the concentration range investigated, the ETU coefficient is found to follow a linear dependence on doping concentration (DC). The dependence equation was fixed to pass through the origin to allow for the probability of energy transfer processes tending to zero as the inter-ionic distance tends to infinity. The linear fit of the experimentally determined ETU coefficient is:

$$W_{ETU} = 6.52xDC(.at\%) \qquad 4\text{-}3$$

up to the investigated concentration of 1.07 at.%. Guy *et al* reported a quadratic relation of upconversion to varying doping concentration of Nd:YAG [7], whereas Lima et al using the Z-scan technique reported linear dependency of upconversion for Nd doped glasses [17]. We claim no phenomenological significance from our experimentally measured linear dependence but to within experimental uncertainty this is the simplest function capable of fitting our results.

ETU effect on CW laser performance

The dominant effect of ETU in a CW laser is an increase in pump-power threshold, as the excited-state density required in upper laser-level, must contend with the loss of ions not associated with stimulated emission. Bjurshagen and Koch [1] reported the effect of ETU for laser threshold and spatial distribution, which varies the population inversion density, and the amount of ETU will vary quite significantly for smaller mode waist ratio. The average population inversion is clamped at the threshold level and the effect of ETU can be measured on threshold power hence ETU loss is clamped for mode overlap of 1.2. Kim *et al* [5] provided an analytic expression for the laser threshold, P_{th} for end pumped CW lasers. The part outside the square bracket is a standard expression for laser threshold for quasi-four level laser, in presence of reabsorption. While the part in square bracket is a modification to account for the ETU effect.

$$P_{th} \approx \frac{h\nu_p \pi \omega_p^2}{2(f_1 + f_2)\sigma\tau\eta_q\eta_{LP}}(L_T + 2f_1\sigma\eta_{LP}N_t l_R)\left[1 + \frac{W_{ETU}\tau\alpha_p}{4(f_1 + f_2)\sigma\eta_{LP}}(L_T + 2\eta_{LP}f_1\sigma N_t l_R)\right] \qquad 4\text{-}4$$

In order to apply this equation to estimate the effect of ETU on laser threshold, we assumed followings:

a. Crystal length is three absorption lengths so near complete pump absorption occurs.
b. Pump focusing is arranged such that it's confocal parameter is equal to the crystal length
c. Pump diode is a typical 100 μm, 0.22 NA fibre-coupled and has 3.5 nm FWHM, a specification of Dilas fibre coupled diode [18]
d. Mode overlap ~1.2 [19], with a Gaussian laser mode and top-hat pump beam
e. Internal cavity loss is assumed 1.0 %

It should be noted that due to the fast multi-phonon non-radiative decay from the energy levels populated by ETU, to the $^4F_{3/2}$ and $^4I_{9/2}$ levels, additional pump-power required to reach laser threshold is deposited as heat in the gain medium, and, that occurs predominantly at the pump input face where the inversion density is greatest.

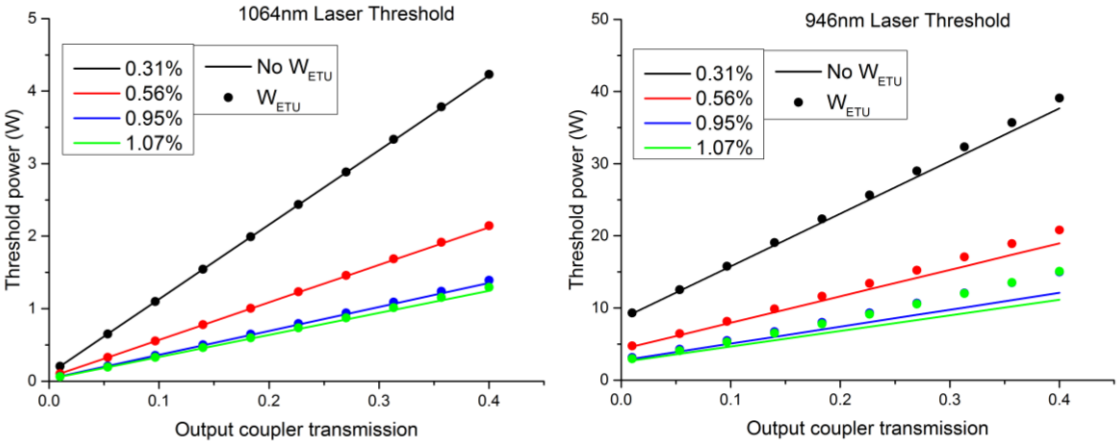

(a) (b)

Figure 4-14 The effect of ETU on laser threshold for (a) 1064nm and (b) 946nm Nd:YAG CW lasers. Simulation without considering W_{ETU} is drawn line and with considering W_{ETU} is spotted for 4 different doping concentration.

A theoretical study of the expected laser threshold was made for Nd:YAG, corresponding to different dopant concentrations and cavity output coupling. ETU shows no significant effect on the laser threshold for the 1064nm transition, primarily due to the relatively low population inversions required to reach the necessary gain levels. Calculated pump radii were set to 510 µm, 360 µm, 280 µm and 265 µm for 0.3, 0.6, 1.0 and 1.1 at.% doped crystals with lengths of 42.4 mm, 21.2 mm, 12.7 mm, and 11.6 mm, respectively. Pump absorption coefficients were calculated using the room temperature case of the Eq.2.15, with given absorption cross section studied in Chapter 3. However for 946 nm, where the emission cross section is nearly 7 times smaller than for 1064 nm, and also suffers weak reabsorption loss, has a noticeably higher laser threshold. Furthermore the effects of ETU becomes significant above an output coupler transmission of ~15 %, particularly for the higher doping concentrations, i.e. 0.95 at.% and 1.1 at.%. This implies that an additional heat load due to ETU at the input face is unavoidable for high dopant concentration and high output coupling.

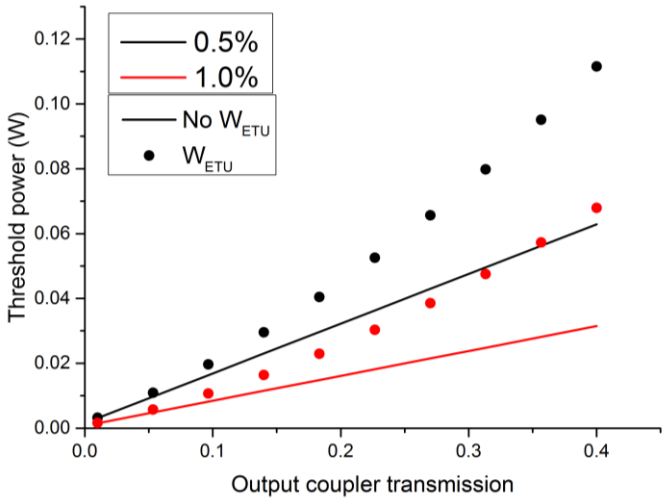

Figure 4-15 Effect of ETU on laser threshold for Nd:YVO4 1064 nm CW laser, Simulation without considering W_{ETU} is drawn line and with considering W_{ETU} is spotted.

A comparable analysis with Nd:YVO4, with its very strong absorption characteristics allowing short crystals with polarized pump beams. Consequently it was assumed that crystals of length 3.0 mm and 1.5 mm could be employed for 0.5 at.% and 1.0 at% doped crystals, respectively, implying 41 µm and 29 µm pump-beam radii for the pump beam parameters chosen. Figure 4-15 shows the high inversion density and high ETU coefficient of Nd:YVO4 leads to a large increase in the laser threshold for output coupler transmission in excess of 10 %.

ETU effect on pulsed laser performance

In contrast for pulsed systems (and high-gain small-signal amplifiers) we follow a different methodology. In this case, for simplicity, we assume a uniformly inverted gain medium, a good approximation of a well-designed flashlamp pumped system or diode-laser side-pumped system as is often favoured for high energy, low-repetition-rate Q-switched systems. To allow for a sensible comparison between different gain media we have plotted the effective lifetime vs gain per unit length and compared them on the same graph. Effective life times are calculated using an analytical solution to the Bernoulli equation, here we neglect the cross-relaxation component and assume that the lifetime of the $^4F_{3/2}$ level is the measured fluorescence lifetime of the crystal. Guyot *et al* [6] expressed the effective lifetime, τ_e depends on the product $N_1(0)W\tau$,

$$\frac{\tau_e}{\tau} = \ln\left[1 + \frac{(e\ -1)}{1 + N_1(0)W\tau}\right] \qquad 4\text{-}5$$

Figure 4-16 shows the gain vs inversion density for the tested crystals, for dominant 1 µm transition terminating in the $^4I_{11/2}$ level, and the weaker transition terminating in the $^4I_{9/2}$ ground

state. For the 1 μm case, Nd:YVO4 excels in achieving the highest gain per unit length. However, for the case of quasi-four-level transition reabsorption losses require a certain inversion-density to reach transparency. This coupled to the lower emission cross section for this transition results in ETU playing a significant role, as shown in Fig 4-17. The figure shows effective lifetime vs inversion density, derived from Eq.4-5. Nd:YLF, suffers the most the effect of ETU, where it's effective lifetime is almost halve by the time it reaches 2 $dBcm^{-1}$ gain. For the quasi-four-level transition of Nd:GdVO4, there is an advantage over Nd:YVO4, since the gain is generally higher, while still maintaining the lifetime. However vanadates still require higher inversion density compare to Nd:YAG, which is a significant drawback. Nd:YAG require the least inversion density to reach transparency and still maintain both its gain and fluorescence lifetime higher than other crystals.

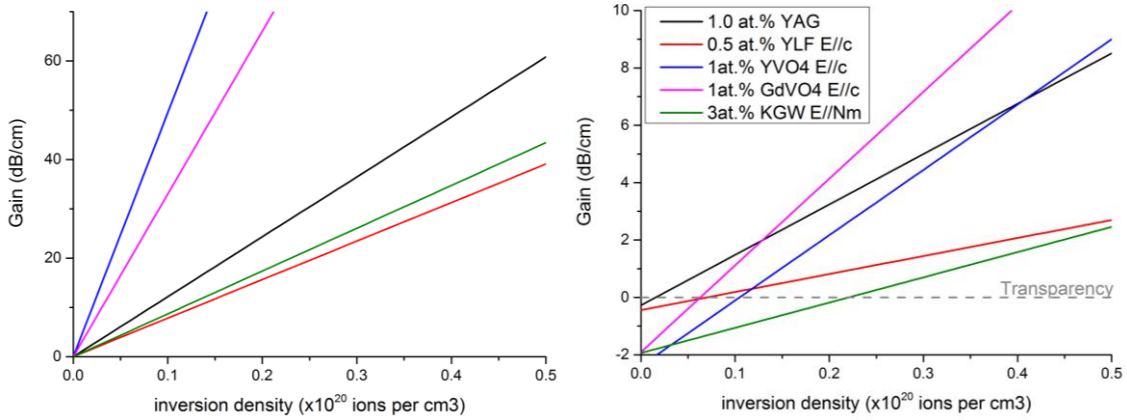

(a) (b)

Figure 4-16 Gain per unit length in function of Nd inversion density for different crystals for (a) $^4F_{3/2} \rightarrow {}^4I_{11/2}$ transition and (b) $^4F_{3/2} \rightarrow {}^4I_{9/2}$ transition

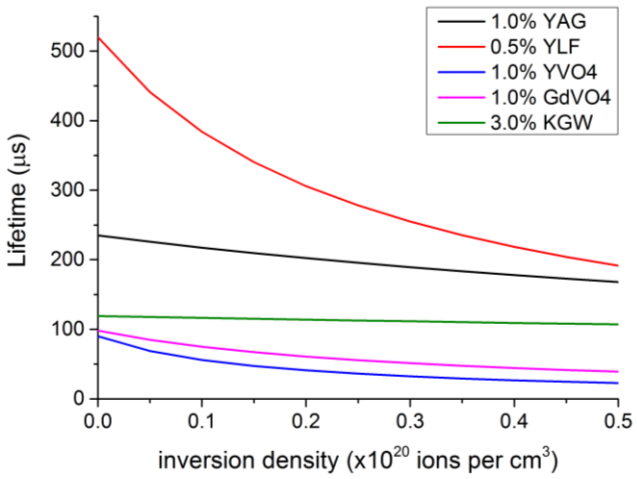

Figure 4-17 The effective lifetime for Nd-doped crystals as a function of their population inversion density, including the effects of ETU.

4.5 Summary

In this chapter we have reported a detailed study of measurement of the ETU coefficient of Nd:YAG along with several other Nd-doped crystals. In addition, the effects of dopant concentration and temperature dependence for Nd:YAG crystals were examined. It was shown that the Z-scan technique offers a simple and sensitive measurement of the ETU coefficient, simply by monitoring the transmission of a pump-beam at various irradiance levels, obtained via the varying incident beam size. Using a simple two level rate equation model to fit the experimental data, a good correlation was obtained, giving confidence in the derived ETU coefficients. Comparison of popular Nd-doped laser crystals placed the relative strength of the ETU coefficient into perspective, Fig 4-12, showing that Nd:YAG has a relatively good position in terms of this parameter.

A theoretical study of the effect of ETU on the lower-gain quasi-four-level transition of Nd:YAG, showed that it was significantly more detrimental than for the dominant 1-micron transition. The predicted laser threshold was analysed considering the effect of including the measured ETU coefficient in the CW regime. ETU had minimal effects for the dominant 4-level transitions, however, it was quite significant for quasi-four-level transitions and systems with high population inversion such as Q-switch operation or amplifier systems. With comparing the effect of ETU to Nd^{3+} doped crystals which has been investigated, Nd:YAG was the least susceptible to the impact of ETU for quasi-four-level transition lasing threshold and gain and fluorescence lifetime for the system with high population inversion and proves the superior characteristics.

References

1. S. Bjurshagen, and R. Koch, "Modeling of energy-transfer upconversion and thermal effects in end-pumped quasi-three-level lasers," Applied Optics 43, 4753-4767 (2004).

2. N. P. Barnes, B. M. Walsh, R. L. Hutcheson, and R. W. Equall, "Pulsed F-4(3/2) to I-4(9/2) operation of Nd lasers," Journal of the Optical Society of America B-Optical Physics 16, 2169-2177 (1999).

3. T. Riedener, P. Egger, J. Hulliger, and H. U. Gudel, "Upconversion mechanisms in Er3+-doped Ba2YCl7," Physical Reviews B 56, 1800-1808 (1997).

4. M. Malinowski, R. Piramidowicz, Z. Frukacz, G. Chadeyron, R. Mahiou, and M. F. Joubert, "Spectroscopy and upconversion processes in YAlO3+ : Ho3+ crystals," Optical Materials. 12, 409-423 (1999).

5. J. W. Kim, J. I. Mackenzie, and W. A. Clarkson, "Influence of energy-transfer-upconversion on threshold pump power in quasi-three-level solid-state lasers," Optics Express 17, 11935-11943 (2009).

6. Y. Guyot, H. Manaa, J. Y. Rivoire, R. Moncorge, N. Garnier, E. Descroix, M. Bon, and P. Laporte, "Excited-State-Absorption and Up-conversion Studies of Nd3+-Doped-Single Crystals Y3Al5O12, YLiF4, and LaMgAl11O19," Physical Reviews B 51, 784-799 (1995).

7. S. Guy, C. L. Bonner, D. P. Shepherd, D. C. Hanna, and A. C. Tropper, "High-inversion densities in Nd : YAG: Upconversion and bleaching," IEEE Journal of Quantum Electronics 34, 900-909 (1998).

8. Y. F. Chen, C. C. Liao, Y. P. Lan, and S. C. Wang, "Determination of the Auger upconversion rate in fiber-coupled diode end-pumped Nd : YAG and Nd : YVO4 crystals," Applied Physics B-Lasers and Optics 70, 487-490 (2000).

9. B. Ferrand, D. Pelenc, I. Chartier, and C. Wyon, "Growth by LPE of Nd:YAG Single-Crystal layers for Wave-guide Laser Applications," Journal of Crystal Growth 128, 966-969 (1993).

10. A. A. Kaminskii, Laser Crystals (Springer-Verlag, Berlin, Germany, 1990).

11. V. Lupei, and A. Lupei, "Emission dynamics of the F-4(3/2) level of Nd3+ in YAG at low pump intensities," Physical Reviews B 61, 8087-8098 (2000).

12. T. Y. Fan, G. J. Dixon, and R. L. Byer, "Efficient GaAlAs Diode-Laser-Pumped operation of Nd-YLF at 1047-nm withIntracavity Doubling to 523.6 nm," Optics Letters 11, 204-206 (1986).

13. W. Seelert, H. P. Kortz, and W. M. Yen, "Excited State Absorption and 4F3/2 Lifetime shortening in Diode Pumped Nd:YLF Q-switch lasers," in Advanced Solid Stated Lasers, Optical Society of America, Santa Fe, US, (1992).

14. R. Beach, P. Reichert, W. Benett, B. Freitas, S. Mitchell, A. Velsko, J. Davin, and R. Solarz, "Scalable diode-end-pumping technology applied to a 100-mJ Q-switched Nd3+:YLF laser oscillator," Optics Letters 18, 1326-1328 (1993).

15. C. Jacinto, D. N. Messias, A. A. Andrade, and T. Catunda, "Energy transfer upconversion determination by thermal-lens and Z-scan techniques in Nd3+-doped laser materials," Journal of the Optical Society of America B-Optical Physics 26, 1002-1007 (2009).

16. M. Pollnau, P. J. Hardman, M. A. Kern, W. A. Clarkson, and D. C. Hanna, "Upconversion-induced heat generation and thermal lensing in Nd : YLF and Nd : YAG," Physical Reviews B 58, 16076-16092 (1998).

17. W. J. Lima, V. M. Martins, A. F. G. Monte, D. N. Messias, N. O. Dantas, M. J. V. Bell, and T. Catunda, "Energy transfer upconversion on neodymium doped phosphate glasses investigated by Z-scan technique," Optical Materials 35, 1724-1727 (2013).

18. DILAS, http://www.dilas.com/products2016.

19. T. Taira, W. M. Tulloch, and R. L. Byer, "Modeling of quasi-three-level lasers and operation of cw Yb:YAG lasers," Applied Optics 36, 1867-1874 (1997).

Part II

Cryogenic Lasers

Chapter 5:

End-pumped cryogenic Nd doped lasers

5.1 Introduction

In this chapter we report the demonstration of end-pumped lasers with cryogenically-cooled neodymium-doped gain media, in particular two garnet crystals, Nd:YAG and Nd:GSAG. The transition of interest is that between the metastable $^4F_{3/2}$ and the ground-state $^4I_{9/2}$ energy levels, with the strongest emission lines being at 946 nm for Nd:YAG and 942 nm for Nd:GSAG. Under room temperature operation the performance of these quasi-four-level lasers is limited by their relatively low-gains and finite population in the terminal laser level, i.e. reabsorption losses, both of which get worse with increasing temperatures (as discussed in Chapter 3), in addition to the potential additional heat loading produced via Energy Transfer Upconversion (as discussed in Chapter 4). It is clear that the spectroscopic and thermo-optic advantages expected for cryogenic-cooling of the gain media should enable distinct improvements in laser performance for these systems.

Cryogenically-cooled Yb^{3+}-doped crystal-lasers have been developing rapidly over the past 15 years, with a 455 W-average-power end-pumped system reported by T.Y. Fan *et al* [1]. Yb doped gain media are essentially free of concentration quenching, excited-state absorption (ESA), and upconversion processes, since the Yb^{3+} 4f electronic shell has only one vacancy and therefore only two associated energy levels, namely $^2F_{5/2}$ and $^2F_{7/2}$. Consequently, it is particularly attractive in terms of energy scaling due to its longer energy storage lifetime than neodymium. However, the emission wavelength between the two energy-levels of Yb^{3+} is limited to the 1 micron region, for example the Yb:YAG laser normally operates with a wavelength of 1029 nm, for which with the terminal laser Stark-level positioned at 612 cm^{-1} and at RT contain 5.5 % of the total available ions . Under normal RT operation the Yb-laser efficiency is strongly dependent upon the unsaturable reabsorption losses and relative distribution of the pump and laser fields in the crystal [2, 3]. In contrast, when the Yb-doped crystal is cryogenically-cooled there is a trade-off between reducing the reabsorption loss and maintaining an efficient pump-absorption, despite narrowing spectral lines, versus the benefits of the improving thermo-optical properties with reducing temperatures to around 80 K [1, 4, 5].

The 946 nm transition of Nd:YAG, when directly pumped to the metastable level, e.g. at 869 nm, is a comparable energy configuration to Yb^{3+}, with only two manifolds coupling the pump and emission channels. Moreover, it has a QD of only 8%, comparing favourably with 9 % for 940 nm pumped Yb:YAG laser. In addition, the stronger ground state Stark splitting for Nd^{3+} with respect to Yb^{3+}, leads to nearly classical four-level characteristics with near zero reabsorption loss below ~120 K in a YAG host. As such, this sub-micron emission wavelength for the Nd-transition, under cryogenic conditions, has the potential to achieve high-efficiency and high-power performance.

In the following sections of this chapter we first present the two main diode-laser pump source configurations used for the following cryo-cooled laser operation. Then we report the first demonstration of a multi-watt diode-laser-end-pumped cryo-cooled Nd:YAG laser system, with the two different pump configurations. During the initial characterization the cryo-cooled 946 nm laser was operated in a Quasi CW (QCW) regime to avoid significant thermal loading of the crystal, so that we could concentrate on spectroscopic enhancements associated with cooling the crystal. 942 nm Nd:GSAG laser operation is also reported for the temperature range from RT to LNT. Cavity stability and thermal modelling is discussed for the respective lasers, before concluding the chapter.

5.2 Diode-laser pump configurations

Two diode-laser pump sources were exploited for the end-pumped laser systems, the first a commercial fibre-coupled diode-laser and the second in-house developed Volume Bragg Grating (VBG) locked single diode-bar array.

Fibre coupled diode-laser pump

The first pump system consists of a fibre-coupled diode laser (Jenoptik, JOLD-30-CPXF-1L) and two lenses to produce an image of the fibre core in the crystal. The fibre diameter of the pump diode module is 400 μm, with a numerical aperture (NA) of 0.22. Measurement of the beam quality for this source found the M^2 ~ 170. The diode laser was mounted on aluminium heat-sink to remove the heat and control the temperature. The peak lasing wavelength of the diode is around 808 nm at 47°C for a 4 % duty cycle with a period of 50 ms and when driven with 40 A of current the output power is 1 W. The diode driver was triggered by function generator for QCW operation with a 2 ms pulse duration, which is longer than fluorescence lifetime of Nd^{3+} to ensure that the system was in steady state. Using an afocal telescope arrangement with lenses of focal lengths of f_1 = 65 mm and f_2 = 100 mm, the smallest pump beam diameter in the crystal is 600 μm, corresponding to an average beam radius of ~390 μm throughout the crystal length, l. The

calculated averaged pump-beam is determined by a weighted Beer-Lambert law accounting for an inverse absorption coefficient much shorter than the crystal length [6].

VBG-locked diode-array-laser pump

A second pump source was constructed for in-band pumping, comprising a 870 nm bar-type diode laser from Jenoptik (JOLD-80-CPNN-1L). The diode has 19 emitters and was lensed in-house with Fast-Axis and Slow-Axis Collimators (FAC & SAC), with a maximum 70W output power available, using a 70 A driver (Lambda GEN20-76). The M^2 parameters for this source were measured to be 1.8 for the fast axis, and, 300 for slow axis. However after blocking the side residue beams and additional power loss from collimating lenses and VBG, 60 W of pump power was obtained.

In addition a VBG (Optigrate – model RBG-868.2-25) was mounted on a kinematic mount in close proximity to the SAC, to lock the diode-laser wavelength to the absorption peak, as illustrated in Fig 5-1. With the VBG locking, the absorption coefficient was improved to ~3 cm^{-1} for a 1 at.% Nd:YAG cooled to LNT, which is equivalent to the typical 808 nm diode-laser absorption coefficient at RT. Without the VBG, at the maximum drive-current the central pump-diode wavelength was 870.4 nm with a FWHM spectral width of 2.2 nm. As shown in the Chapter 3 the absorption efficiency changed with cooling the crystal to LNT, for the diode laser operating at 70 A and a 10 mm long 1 at.% Nd:YAG crystal the measured absorption efficiency dropped from 75 % to 43 %, for the raw spectra. However, with the VBG to lock the pump wavelength, resulting in a spectrum that was centred at 868.4 nm with a bandwidth of ~0.3 nm FWHM, the absorption increased to 90 % due to the 3-fold increase in the peak absorption coefficient. Even though the absorption peak of Nd:YAG at LNT is at 868.54 nm, a ~0.15 nm offset. Figure 5-1 shows the pump diode spectra when it operated at 70 A, emitting 70 W, the picture clearly shows the effect of using VBG.

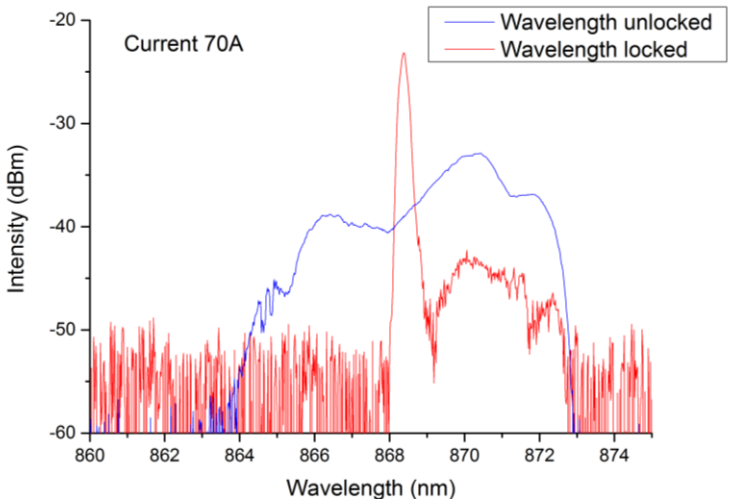

Figure 5-1 Diode Emission spectra with and without locked using VBG

The principle of diode laser emission stabilization requires an external device that feeds a narrow-band emission back into the optical cavity [7]. Recently this approach has been adapted the use of a photorefractive-glass, in which a periodic planes of refractive index steps are created within the volume of glass [8]. The periodic variation provides wavelength selective feedback, i.e. a Bragg reflector. Internal feedback devices, known as distributed Bragg reflector (DBR) or distributed feedback (DFB) can also be made as part of the diode itself via an etching process. Although, the VBG stabilization is known for better temperature stability compared with DFB/DBR structures. [9, 10]. Primarily because the VBG is an external device that is physically decoupled from the semiconductor diode. The external layout allows independent temperature control to tune the peak wavelength, while for internal devices the grating dimensions are strongly dependent on the diode power. This is because the bulk glass has a lower thermal expansion coefficient and the volume grating is less susceptible to thermal distortion of the medium. Figure 5-2(a) illustrates the change in λ_{PEAK} for the VBG-locked diode-laser depending on the pump power, going from 1 W to 70 W. It shows a peak shift of 0.11 nm (2 pm/W), due to the pump absorption in the uncooled glass. In the next plot, Fig 5-2(b), the peak shift was observed at a constant pump power of 70 W, while heating up the VBG with a temperature controlled resistive element attached to the mounting plate. For a 60 K temperature rise we observed a 180 pm increase in the λ_{PEAK} value, that is a ~3 pm/K temperature dependence. From the observed wavelength shift with the VBG with increasing pump power, the small absorption creates a thermal gradient and expansion of the grating period, we predict that the associated temperature rise was ~40 K at the maximum pump power. Due to the narrow band nature of the 868.54 nm absorption-peak for LNT-cooled-Nd:YAG, this slight shift in λ_{PEAK} can be significant and needs to be accounted when defining the specifications for the VBG.

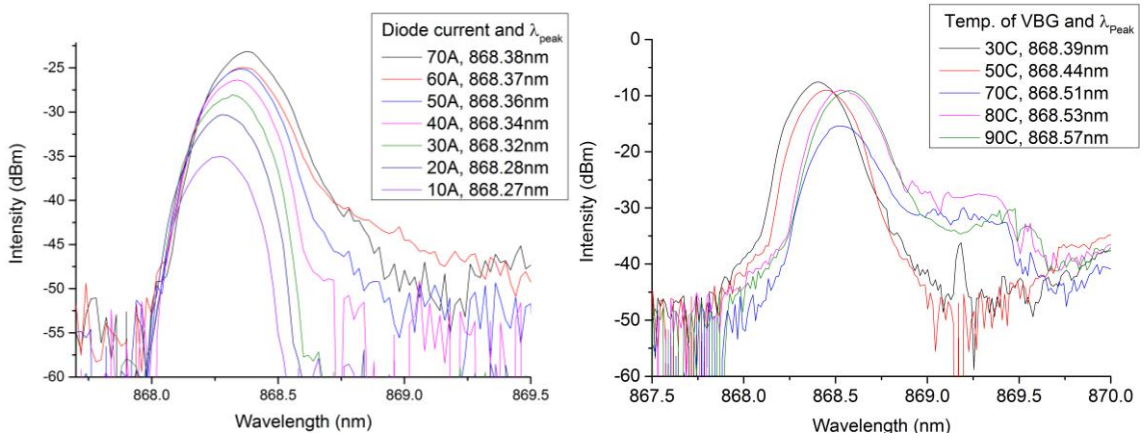

(a) (b)

Figure 5-2 Measurements of the diode-laser spectrum for changes in (a) diode current and (b) temperature of VBG

As peak wavelength is fixed by the internal grating of device, different VBGs were required to conduct the experiment in RT. This is particularly important as experiments were carried in both RT and LNT. Two different VBG oriented at absorption peak for RT and LNT was prepared. UV cured glue was used to fix the VBG on an aluminium mount. 365 nm LED light source was tested to minimize the UV exposure to the VBG device which is known as UV photo-sensitive glass. The UV exposure may shift the peak and/or broaden the locked wavelength because of the absorption rate changes [11]. With UV gun, the rate of change is increased to 2.6 pm/W which is 0.6 pm/W higher than using a 365 nm LED as a curing source. It is essential to decouple the locking device against thermal deposition from the diode laser that the device absorbs less and to improve temperature stability. Further VBG installation and experiment was conducted using a 365 nm LED light source to cure UV glue.

In order to focus the pump beam tightly into crystal, half of emitters were excluded using a sharp sided HR mirror set in front of diode. The passing light was passed through two cylindrical lens (f_x = 37.5 mm and f_x =300 mm), spaced by ~330 mm, expanded the beam. The collimated beam was then focused using a f = 100 mm (Ø 40) spherical lens. The final beam quality of the focused pump light was estimated to be M_x^2 ~ 150 by M_y^2 ~ 1.8, with the beam waist of w_x ~ 330 μm and w_y ~ 200 μm. A maximum power of 15 W was available, after a ½ waveplate and broadband cube polarizer were used as a variable attenuator, allowing the diode to be operated at it's highest power and longest peak wavelength when VBG locked.

5.3 Nd:YAG laser operation

Two separate end-pumped Nd:YAG laser configurations were investigated, 1) a Brewster-angled and 2) an AR-coated crystal (the latter actually designed for side-pumped operation). Neither were optimal for an end-pumping experiment, rather configuration 1) was a proof of principle experiement that highlighted the spectroscopic benefits of the cryo-cooled concept and provided the first multi-Watt 946 nm Nd:YAG laser demonstration. In contrast, configuration 2) was investigated to understand the benefits of in-band pumping, and also as a means of investigating unexpected losses associated with the side-pumping experiment that will be discussed in Chapter 6.

5.3.1 Brewster cut slab setup

The experimental set-up shown in Fig 5-3 used a 10 x 10 x 25 mm^3 (W x H x L), 1 at.% Nd:YAG crystal. By mounting the crystal on a copper cold-finger bolted to the bottom of the liquid-nitrogen dewar, isolated from the ambient room temperature by a evacuated housing, as detailed

in Chapter 3 for the subambient absorption measurements, it could be arranged to be at Brewster cut with a large clear aperture.

Figure 5-3 shows a schematic of the cavity and the first pumping configuration. The cavity was built with two plane mirrors and one curved mirror in a V-fold cavity. The crystal was located at the centre of the vacuum chamber, and when arranged at the Brewster facet had an effective length of 11.3 mm. The plane mirror, M_1, was a pump-in-coupling mirror, highly reflective at 946 nm and highly transmissive at 808 nm. The turning mirror, which was tilted by 25° in the plane of the Brewster face, had a radius of curvature (ROC) of 300 mm, and high reflectance (HR) coating for 946 nm. Mirror M_3 was a series of plane output-couplers at various reflectivities from 85 %R to 98.5 %R at 946 nm. The cavity optics (M_1~M_3) were coated to have a high transmittance(HT) at 1064 nm, to avoid gain competition and parasitic lasing with the dominant $^4F_{3/2} \rightarrow {}^4I_{11/2}$ transition. For the configuration trialled the cavity mode size was strongly dependent upon thermal lensing. To ensure that the effective thermal lens formed in crystal was, on average, weak, for the various operating temperatures we investigated, the pump was operated in a QCW mode, even though this effect would be dramatically weaker at the coldest temperatures [12]. There was an additional ~2 % loss associated with the cryostat windows and the Brewster cut gain medium, giving a total round trip cavity loss of ~4 %.

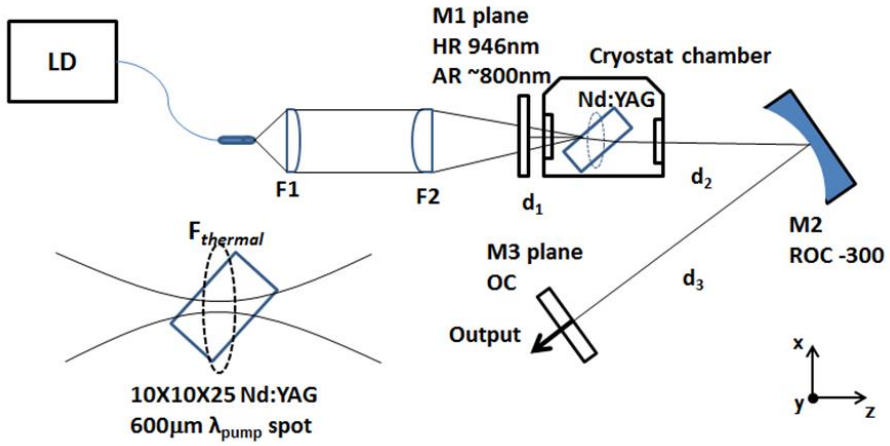

Figure 5-3 Schematic of the first Brewster's cut Nd:YAG laser setup

The total average power incident on the crystal was only 1 W, but the absorbed peak pump-power was 25 W, which enables us to simulate reabsorption loss and in some cases a significant thermal lens could form as if it were CW operation. Nonetheless the threshold pump-power was measured via a Si photodiode, and an optical spectrum analyzer was used to check the lasing spectrum to ensure operation at 946 nm. Output power was measured using a Gentec thermopile power meter (Gentec, UP19K).

5.3.2 AR coated slab setup

Figure 5-4 illustrates the second experimental setup, using an AR coated Nd:YAG ZIGZAG slab turned side-on to enable it to be configured for end-pumping. Although designed and produced for the side-pumped ZIGZAG configuration, to be discussed in Chapter 6, this configuration was built to test the laser crystal efficiency and to determine if there were losses associated with the AR coating when the crystal was cooled to LNT. A 1 at.% Nd^{3+} doped crystal it's flat and parallel faces were 4 x 10 x 5 mm^3 (H x W x L). Each "side-face" of the crystal had been AR coated to suppress parasitics and ASE for the high-gain 1 μm transition. A similar V-fold cavity, as per Fig 5-3, was formed using two plane mirrors and one curved mirror. However, in this setup the curved mirror used had an ROC of 150 mm, chosen to improve mode-matching with the second in-band pumping configuration used for this experiment. A protective mirror was inserted in the pump path to reflect any 1 μm parasitic laser beams impinging on the pump-diode, which could cause catastrophic damage.

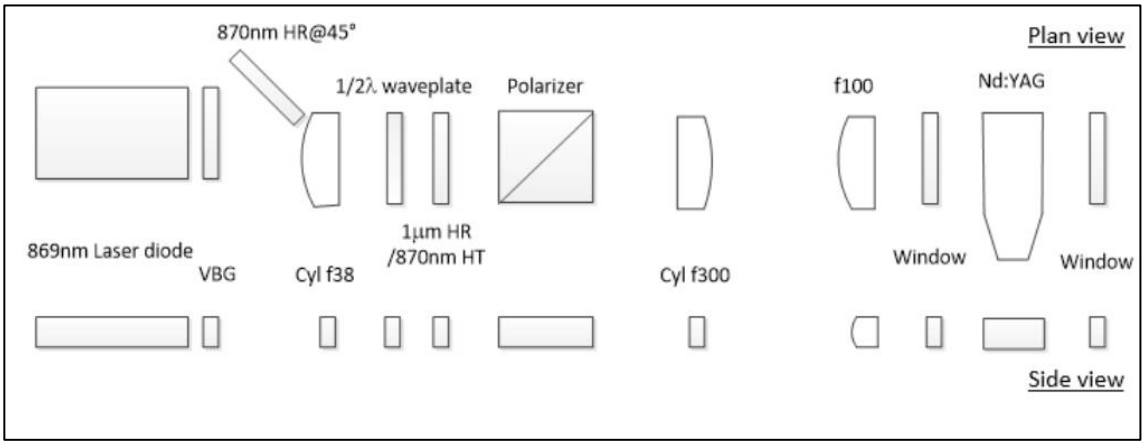

Figure 5-4 Schematic of pump system for AR coated Nd:YAG crystal, plan view and side view

5.3.3 Results

5.3.3.1 Brewster cut: QCW operation

In the configuration 1) shown in Fig 5-3, the 946 nm laser performance was investigated for various temperatures from RT down to LNT. Figure 5-5 clearly illustrates the significant spectroscopic advantages for this transition by going to cryogenic temperatures, independent of thermo-optical effects. At 20 Hz, with 2 ms pulses, the maximum available average (peak) pump power was 1 W (25 W). Despite the increase in peak absorption cross section at 808 nm the actual pump-absorption efficiency for the fibre-coupled diode laser reduced due to the narrowing line

width, going from 84 % at RT to 48 % at LNT as illustrate in Fig 5-5 for the incident 0.8 W (20 W) pump power.

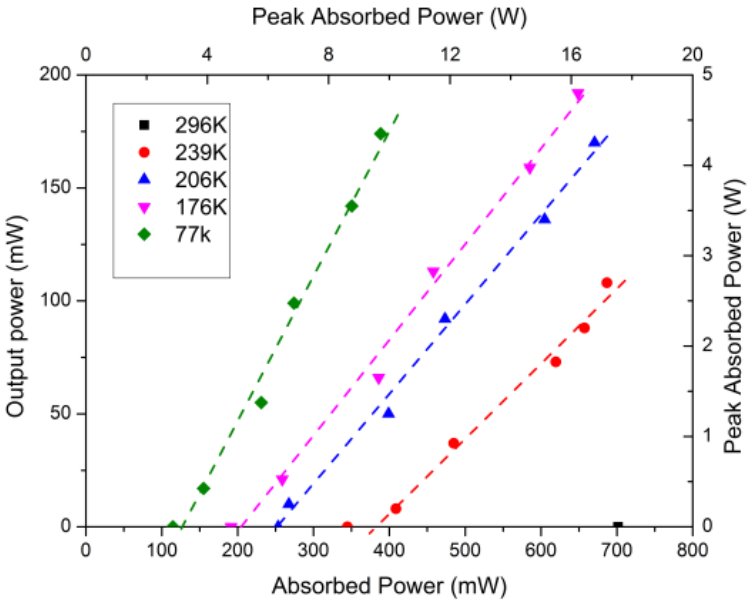

Figure 5-5 QCW laser operation of Nd:YAG 946 nm, for 77 K – 296 K

At RT laser threshold was reached at around the maximum available absorbed power, i.e. 700 mW, however at LNT it was only 114 mW leading to a slope efficiency of 63 %. Despite having the highest slope at LNT, the maximum QCW output power was obtained with a crystal temperature at 176 K, 190 mW (4.75 W peak) falling to 170 mW (4.25 W peak) at LNT, for the same incident pump power. Table 5.1 summarizes the laser performance achieved at different crystal temperatures with respect to absorbed pump power. Beam quality was monitored using the method described in section 2.5, and at the maximum power gave $M_x^2 \sim 1.15$, $M_y^2 \sim 1.25$, with $D4_\sigma$ beam widths, $w_x = 376$ μm and $w_y = 390$ μm, at the output coupler.

While the 946 nm transition at RT is quasi-four-level with a degeneracy factor, which was introduced in chapter 1, i.e. $\gamma = 1.012$ compared to $\gamma = 1$ for a true four level system and $\gamma = 2$ for a true three-level system [13], the relatively long crystal length employed here had a comparatively large reabsorption loss. Using the B notation of Risk [2], being the ratio of the reabsorption to fixed cavity losses, we see (Table 5-1) that it ranged from 1.3 at RT to essentially zero at LNT. An increasing slope efficiency for the QCW laser with decreasing crystal temperature is a result of a combination of a modest value for $S \sim 10$ (a normalized parameter proportional to the intra-cavity laser power [2]) at the maximum output power, and the gradually decreasing B value, as demonstrated by the dS/dF curves of reference [2]. The reducing threshold condition with lower temperatures is a combination of a diminishing Boltzmann occupation factor in Z5 with an increasing population in R1 and increasing emission cross section between these Stark levels.

Furthermore it is worth noting that despite the crystal length at LNT, $\gamma = 1 + 1.3 \times 10^{-7}$, which confirms that the laser is working as a four level system.

Table 5-1 QCW laser results of 946nm Brewster-angled Nd:YAG laser system

	QCW (2 ms pulse 4 % duty cycle)				
Cu mount temp (K)	77	176	206	239	296
P_{th} (mW)	114	191	253	344	700
η_s (%)	63	42	40.7	31.5	-
B [2]	$3x10^{-5}$	0.135	0.39	0.85	1.3
f_{Z5}	$1x10^{-7}$	$6x10^{-4}$	$1.5x10^{-3}$	$3x10^{-3}$	$7.4x10^{-3}$
f_{R1}	0.83	0.66	0.64	0.62	0.59
σ_e ($Z_5 \leftrightarrow R_1$) (pm^2)	10.9	9.7	9.3	8.7	6.6

5.3.3.2 Brewster cut: CW operation

With the laser crystal cooled to LNT, operation of Nd:YAG slab was investigated in CW mode. We observed a maximum output power of 3.8 W for 12.8 W of absorbed pump power (25 W from fibre facet) leading to a slope efficiency of 47 %, Fig 5-6. We expected thermo-optical advantages [5] and a cavity design should be stable with a thermally induced focal lens around 100 mm. However we observed strong modal instability whilst trying to measure M^2 in "real-time" setup, making it impossible to record the value. Using the approach of Hello *et al* [14], it is evident that the ~2 W thermal load at LNT can only produce a thermal lens focal length as short as 1 m, assuming the thermo-optic properties of 2 at.% Yb:YAG [15] (as this is the same host medium with a similar impurity level, size of Nd^{3+} is twice that of Yb^{3+}), but which can be >50 % stronger in the x with respect to y-axis, depending upon the thermal interface impedance (R_{th}). Moreover if R_{th} between heat source and LN was high (>100 Kcm^2W^{-1}) it is possible for the crystal temperature to rise by >50 K with a subsequent increase in the *B* factor and reduction in slope efficiency. However, this should not lead to the rapid modal switching we observed. One other source for cavity instability may have been the crystal mounting configuration along with the asymmetric

crystal shape and cooling path, exacerbated by the Brewster facets, introducing astigmatic aberrations and perturbations favouring higher order modes. The Cu block that has been mounted up the crystal was bolted to cold finger of LN dewar, that had no interface material between two Cu surfaces. Uneven thermal contact between the Cu-Cu components, and Cu to crystal, could lead to the temperature distribution, in the region of the slab varying and creating temperature beating effects with establishing effects for the cavity mode [16]. Further improvements in the crystal geometry and the thermal interface with the cryogen will significantly improve the power scaling potential of this transition.

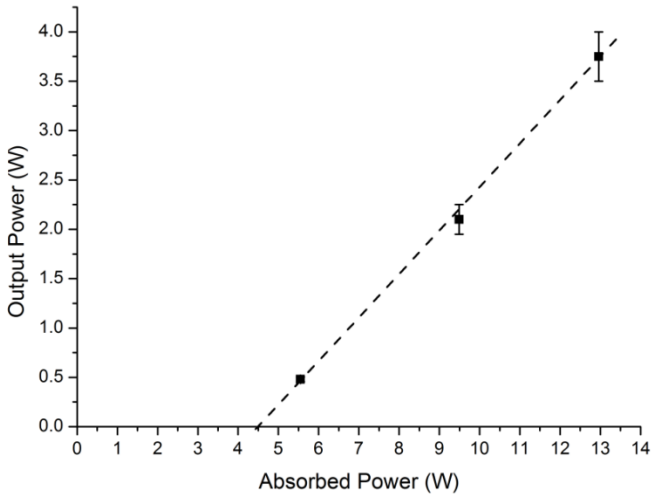

Figure 5-6 Brewster cut Nd:YAG CW operation at 77K

5.3.3.3 AR coated Slab CW operation

In the configuration 2) shown in Fig 5-4, CW 946 nm laser performance was investigated at LNT. In the first instance a simple two mirror cavity was tested, however, parasitic lasing at 1061 nm overpowered the 946 nm emission. Instead with a V-fold cavity ensuring good mode matching between pump field and laser mode, but also by introducing substantially more loss using a HR 946 nm/HT at 1 μm mirror. The pump absorption was measured to be 72 % of the incident pump power and with a 90 %R output-coupler mirror we obtained an output of 5.5 W for 13.6 W of absorbed pump light, corresponding to a 47 % slope efficiency as shown in Fig 5-7. The laser spectrum was measured using an OSA to ensure the laser operation was only at 946 nm. Both laser output power and pump power was measured using a Gentec water-cooled power meter (UP55M).

The lasing threshold was found to be around 1.7 W, and while the power and pointing stability was found to be good, the beam quality was not measured this time. Based on the laser threshold results, a Findlay-Clay calculation was made to determine the cavity losses, as shown in Fig 5-8,

which indicated that there were 5.5 % round-trip losses for this cavity. The loss from the two vacuum windows, were measured to be only 0.1 % per dielectric coating, therefore contributing about 1 % per round trip. The AR coating on the crystal was also originally shown to have very low loss at the laser wavelength, a further fraction of a percent round trip. Finally the total heat load at the lasing threshold was very low, with much less than 1 W was absorbed pump power, therefore it would appear unlikely that significant aberrations could have contributed to the overall losses. It was found later that there had been some damage on the crystal's surfaces, which may have come from contamination during the initial setup of the new cavities. Damage zones were found to be worse outside of the pumped area, but may have still interacted with the oscillating light. We will discuss further in the next chapter, but the true loss mechanism is currently unknown and the configuration needs further testing under the situation of high-vacuum and cryogenic operation.

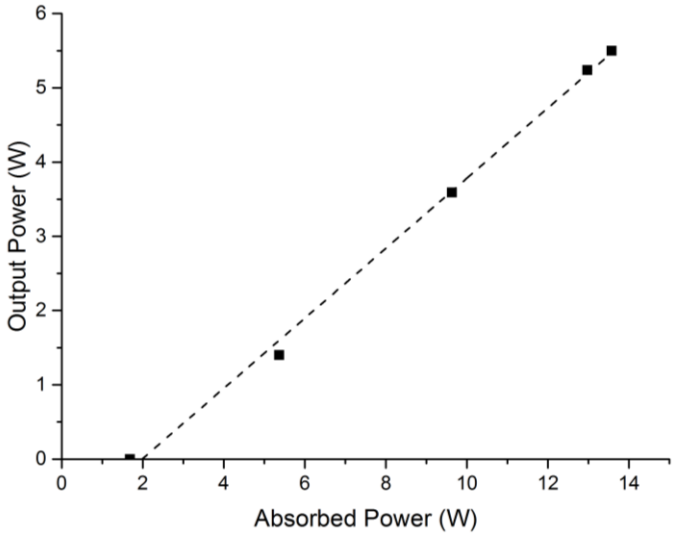

Figure 5-7 CW performance for the AR-coated Nd:YAG end-pump configuration

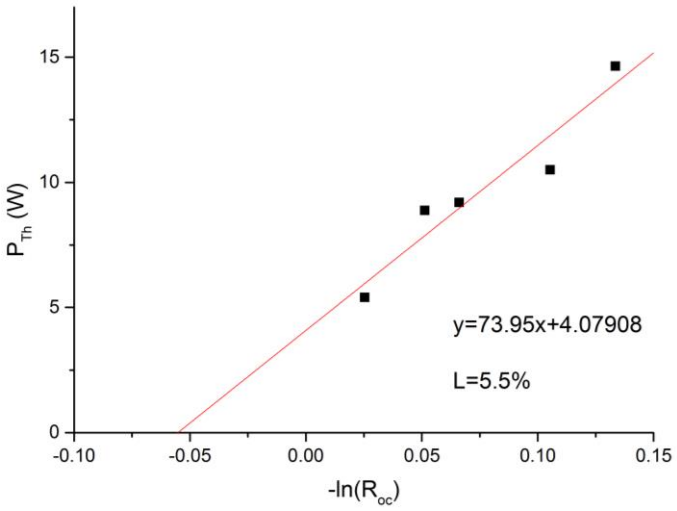

Figure 5-8 Findlay-clay loss measurement for the AR coated Nd:YAG crystal

946nm transition becomes four-level transition at 77 K as the reabsorption loss is 0. The ratio of gain coefficient of dominant energy transition, 1061 nm (g_{1061}) and 946 nm (g_{946}) is given by

$$\frac{g_{1061}}{g_{946}} \propto \frac{\sigma^{se}{}_{1061}}{\sigma^{se}{}_{946}} \qquad 5\text{-}6$$

Where $\sigma^{se}{}_{1061}$ and $\sigma^{se}{}_{946}$ are the effective emission cross section at the named wavelength. The measured spectroscopic data is listed in Chapter 3 and Appendix A, 78 pm^2 and 8.4 pm^2 respectively. The ratio of two gain is ~9.3. Since the signal gain paths overlapped completely the strong gain competition is inevitable. The threshold ratio can be compared with measured cavity loss, L which is 5.5 % for 946 nm cavity, Two reflective mirrors have high reflectivity for 946 nm and 5 % reflection for 1061 nm. OC was found 10 % for 946 nm and 30 % for 1061 nm. 1061 nm had extra losses due to the AR coating from two windows which will add ~0.5 % losses per round trip. The laser threshold in Eq.2-63 can be simplified as following;

$$P_{th}{}^{946} = A\frac{T_{3,946} + L_{946}}{\sigma_{se,946}} \qquad 5\text{-}7$$

$$P_{th}{}^{1061} = A\frac{\left(T_{1,1061} + T_{2,1061} + T_{3,1061}\right) + L_{1061}}{\sigma_{se,1061}} \qquad 5\text{-}8$$

Where $A =$ rest of P_{th} terms

Where $\sigma_{se,946}$ and $\sigma_{se,1061}$ are the effective emission cross sections for 946 nm and 1061 nm, respectively, and L_{946} is measured 5.5 % and L_{1061} is assumed to be 6 % as AR coatings for windows will add extra losses. $T_{x,xxx}$ are the transmittance of each cavity mirrors, T1, T2 and T3 as output coupler, respectively. The ratio of two transitions thresholds is ~ 1.8, as shown in Fig 5-9. The reflectivity of cavity mirrors was low enough to prevent feed back loop for the dominant 1061 nm transition. The cavity suppressed the dominant transition and no ASE was observed during the 946 nm oscillation. In our case, two mirror cavity failed to suppress 1061 nm and 946 nm was vanished.

Figure 5-9 shows that threshold power is very sensitive for 946 nm and 30 % lower when loss reached 1 %, which implies nominal AR coating reflectance. Gain compression in this case is expected to be higher as the ratio of two transition is near 2.5. Dominant 1 μm transition is less effected by losses from crystal coatings as cavity suppression is already very high. Hence if the crystal loss is increased over 15 % our 3-mirror cavity would not suppress 1061 nm oscillation.

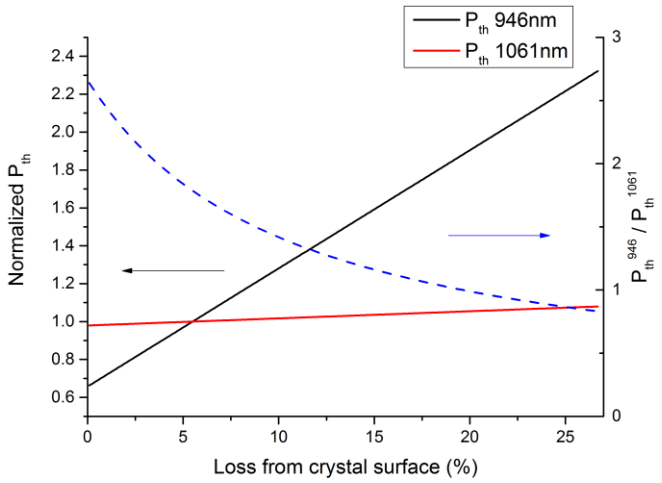

Figure 5-9 Comparison of normalized P_{th} depends upon crystal loss (%)

The overall performance of the AR coated end-pump system shows better result compare to Brewster-angled end-pump system. The AR coated system has lower lasing threshold and improved slope efficiency compare to Brewster cut slab, also observes improved mode stability. The slab was cu mounted on its two faces via thick indium foil (200 μm), That implies a proper thermal contact has removed dynamic thermal fluctuation However laser efficiency is still limited due to high losses implied during vacuum operation.

By introducing better thermal contact, applying thermal greases between Cu to Cu contact and uniform pressure between Cu to crystal via thicker indium the modal stability improved significantly. Laser efficiency is still limited despite the dramatic heat dissipation along the heat load.

5.4 Nd:GSAG QCW operation

For Nd:GSAG the strongest emission line wavelength for the $^4F_{3/2} \rightarrow {}^4I_{9/2}$ transition is at 942 nm, which was potentially a candidate for H_2O-vapour DIAL LIDAR [17, 18], and if frequency doubled is suitable for several applications in display, optical data storage, submarine communications and biomedical fluorescence spectroscopy [19, 20]. We report the realisation of a cryogenically-cooled Nd:GSAG laser system and discuss the problems encountered with this material and in its rod-geometry.

5.4.1 Experimental set-up

The experimental setup for Nd:GSAG is very similar to Fig 5-3, where the crystal rod used was doped with 1 at.% Nd^{3+}, had a 3mm diameter and was 7 mm long, with the two end faces AR

coated for the laser wavelength. The crystal was wrapped in indium foil and fixed to a Cu mount. The rod has notable differences with respect to the Nd:YAG experiment, as the heat dissipation and stress distribution for this crystal was radial.

The fibre coupled pump diode detailed in section 5.2 was configured to produce a 600μm diameter beam in the crystal. The average pump beam size along the crystal length was estimated to be 332 μm, assuming the smallest spot location at the mid-point of crystal. The diode spectra was measured then tuned for QCW operation (with the same conditions employed for the Nd:YAG laser, i.e. 2ms envelope, 4% duty cycle for 20Hz), heating the diode up to 47°C to tune the central wavelength to the absorption peak around 808nm.

Cavity is very similar to the schematic of Figure 5-3, however 2nd curved mirror was replaced to new R -200 mm curved mirror, all mirrors were coated for HR at 9xx nm and HT for 1 μm to suppress the higher gain for the latter. Several OC mirrors were tested, with their reflectivity ranging from 85 % to 98.5 % at 942 nm. The average power incident upon the crystal was only 1W, with a peak power of 25 W. Long pulses enabled us to simulate steady state conditions for the reabsorption loss and thermal lensing during a pulse, as it would be in CW operation. The crystal was tested from RT to LNT via temperature tuning of crystal. The fundamental cavity mode diameter in the Nd:GSAG crystal was calculated by the ABCD matrix method, with a beam waist of around 550 μm. Over the crystal length the average beam diameter is ~660 μm, which gives an overlap factor a = w_p/w_l ~ 1.21 [2]. The laser wavelength was confirmed using an OSA, showing that only 942 nm output was present. Output power was measured using a Gentec (UP19K), lasing threshold was observed using a large-area Si-photodiode.

5.4.2 Result and discussion

The output power was measured using various reflectivity output couplers: 87.3 %, 91.2 %, 93.7 % and 97.3 %. Table 5-2 summarizes the results of the laser performance for each at RT.

Table 5-2 RT QCW Nd:GSAG laser performance at 942 nm.

Roc (%)	P (mW)	P_{th} (mW)	M^2_x	M^2_y
97.3	210	243	1.15	1.21
93.7	205	340	1.08	1.18
91.2	137	540	1.09	1.26
85.5	63	690	1.15	1.24

Round trip cavity losses was estimated to be 2 %, major degradation was from poor coating quality on GSAG supplied with. The coating reflectance was tested prior laser built up using a 946 nm Nd:YAG guide laser which was built in-house for AR reflectance measurement. The beam reflectance from 1st coated surface was measured 0.4 % and 0.7 % for mixed reflected beam from 1st and 2nd surfaces. The reflected beam from the crystal surface was first observed by using CCD camera and the power was measured by using a quantum detector. Round trip loss from crystal coating loss is 1.4 %, other 0.6 % loss is caused from M_1 and M_2, scattering or absorption. The beam quality of both axes were near 1.2 at its maximum power.

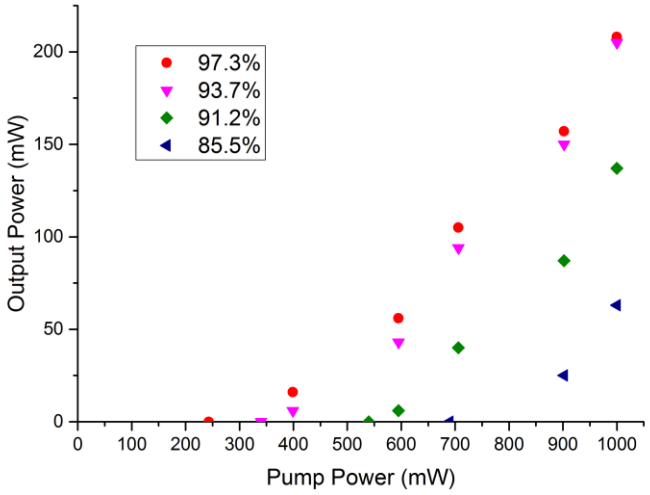

Figure 5-10 Nd:GSAG QCW performance at RT,for various OC reflectivity

The crystal was encapsulated by a high-vacuum chamber to isolate the crystal from the ambient environment when cooling to cryogenic temperatures. Each surface of the two chamber windows was designed to have a transmission of 99.7~99.9 %T, adding an extra 1.2 % loss in a cavity round trip was expected with the RT experiments. For the best performing configuration at RT, with the 97 %R OC, the output power dropped to 150 and 110 mW after adding the 1st and 2nd chamber windows, respectively. The actual added extra loss was estimated ~3.5 % in round trip instead of 1.2%. That corresponds poor optical coating quality for our windows, estimating around 99.5~99.6 %T per coating. The total loss adds up by 8 additional AR surfaces in round trip. In addition, 5 % of the pump beam was reflected by the 1st window, with corresponding reduction in absorbed power. Notwithstanding, upon cooling of the crystal the output power reached 190 mW when the crystal temperature reached 170 K, then started to decay back to 150 mW at 77 K, due to a reducing absorption efficiency. Figure 5-11 shows the change of both output power, which is shown on the left y-axis, and P_{out}/P_{abs}, shown on the right y-axis according to the temperature of the crystal. As shown Fig 5-11, output power was changing for all the temperature, the output power has increased as the temperature of crystal reached 220 K then started to decrease. The

absorption efficiency of the incident pump light was calculated according to the measured absorption cross section and measured pump spectra. The calculated absorption efficiency changed from 71 % at RT to 43 % at LNT. The optical to optical efficiency improved significantly at cryogenic temperature, despite the output power starting to decrease below 170 K.

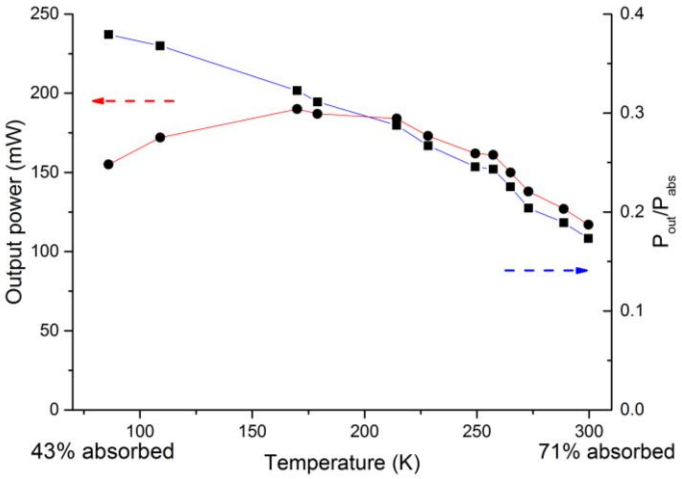

Figure 5-11 Nd:GSAG QCW output power and Pout/Pabs changes for 77K – 300K

Another important aspect for this setup was the mechanical stress induced by the different thermal contraction rates between the Cu-mount and the crystal. Depolarization loss (polarization extinction ratio) was measured using a linearly-polarized He-Ne probe laser beam passing through the crystal, and a cube polarizer as an analyzer after the crystal. Since the thermal expansion coefficient of Cu is 16.5 x $10^{-6}K^{-1}$ and Nd:GSAG, thought to be less than Nd:YAG (6.9 x $10^{-6}K^{-1}$ at RT), it is expected that the strain in the compressed crystal would result in birefringence. Even though the crystal was wrapped with indium-foil, the induced depolarization via mechanical stress is evident as shown in Fig 5-12. The polarization extinction ratio decreased by almost 10 times at LNT compared with RT.

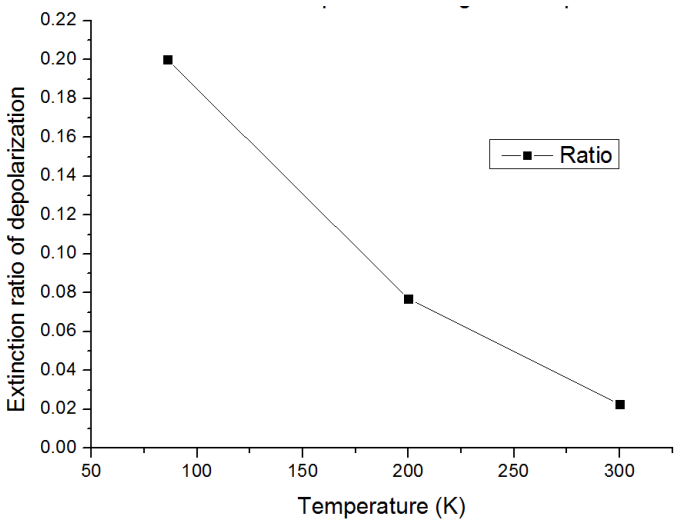

Figure 5-12 Measured depolorazation as a function of the Nd:GSAG rod temperature

The set-up was tested in CW mode operating at LNT, with a maximum output power measured to be ~3.5 W. However, the pump-in-coupling coating, the side absorbing pump light, of crystal was damaged shortly after reaching the maximum pump power available. A beam profile of a He-Ne probe laser showed the damaged spot when imaged on a CCD camera, Fig 5-13(a). Similarly, a microscope image of damaged area, Fig 5-13(b), clearly showed up areas of concern. The damage spots sizes were approximately 80 μm (X-axis) x 50 μm (Y-axis). The damage picture and symptom are a typical of dielectric coatings damage caused by over damage-threshold power levels [21]. Although, the peak intensity of both pump and laser light, was ~3.5 W kW/cm^2, lower than the specified damage threshold. The gap between the crystal and Cu is filled by thin indium foil (~50 μm thick) to improve the thermal contact and to provide a yielding interface. Nonetheless the dielectric coating on the crystal at cryogenic temperature degraded or showed signs of delamination, as observed previously [22]. This may cause the change of transmittance of coating and lower the damage threshold in the case of running at cryogenic temperatures [23].

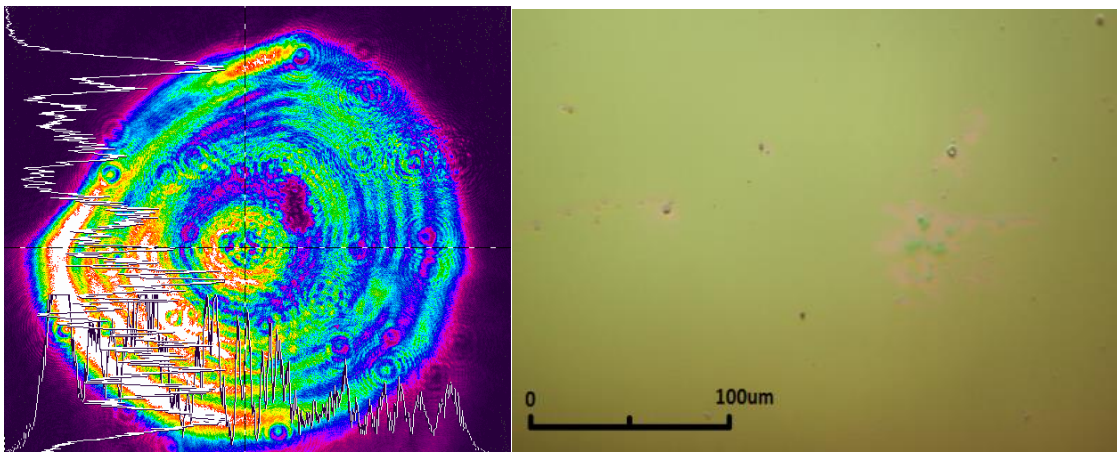

(a) (b)

Figure 5-13 Images of coating damage taken for (a) a beam profile of a passing He-Ne laser beam through the crystal and (b) a microscope.

5.4.3 Temperature profile gradient effects On thermal effects in solid state lasers: the case of Nd-doped materials

The discussion in Chapter 2, which discussed presented the dependence of that thermal lensing in the gain media, generally shows the increasing in the dioptric power for end-pumped systems. The thermal lens focal length changes via the improved thermal conductivity, *k* of gain media in cryogenic temperature. the temperature dependence of thermo-mechanical parameter of crystals are reported in number of journals [15, 24, 25], garnet crystal is shown in Fig 5-14, increased thermal conductivities and reduced thermal expansion and thermo-optic coefficients as temperature decreased.

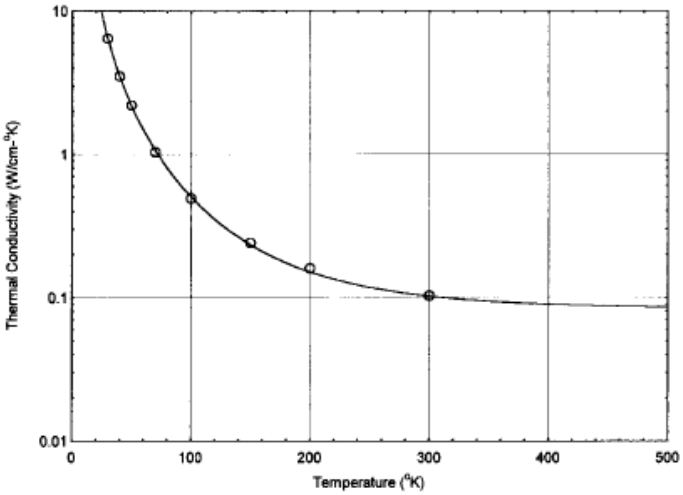

Figure 5-14 YAG thermal conductivity from 30K to 500K, data [25] and fit [26] as a function of temperature, image from [26]

The temperature profile of 1.0 at% doped Nd:YAG at LNT is plotted in Fig 5-15. The result is numerically iterated as discussed in Chapter2. We applied effective absorption coefficient fit which was obtained in Chapter 3 and applied a least-squares analytical fit, that generated by Brown [26]. The parameters used for the Nd:YAG laser experiment, were applied to the model, using identical pump power, pump beam, and a crystal geometry. We also used ideal pump source having a nominal fibre coupled diode spectral width and ideally overlapped with laser mode.

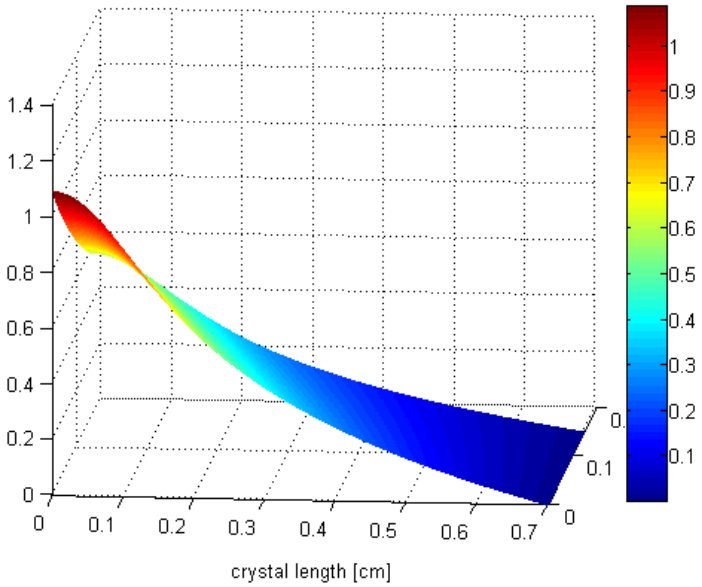

Figure 5-15 Temperature distribution along y-z plane for end-pumped Nd:YAG laser crystal rod, at 77K

The model defines based on the assumption that mechanical pressure has unchanged throughout the crystal rod. The model can be seen that cryogenic cooling leads to better heat dissipation along crystal, providing simultaneous radial heat dissipation. Our model accounts boundary temperature of crystal, that is not equal to cooling block due to improper contact or surface conductance, H . Measuring the actual H coefficient is very difficult, Carslaw and Jaeger [16] presented major heat transfer hold off is due to the thin oxide layer in between crystal and mount. Here we assumed 1 $Wcm^{-2}K^{-1}$ for the boundary temperature prediction. Chenais *et al* [27] derived the temperature of crystal rod edge with respect to pump light and crystal radius, and expressed in Eq.2-9 in section2.2. However current crystal mount is under high physical compression while cooling down, which has no reliance on the numerical model.

5.5 Summary

In this chapter we have undertaken a study of end-pumped cryogenically-cooled laser systems using Nd:YAG and Nd:GSAG gain media. Assessing the spectroscopic properties of the pump absorption band, in addition to the laser performance enhancement devoid of thermal effects, was achieved by operating the laser in a low duty-cycle QCW regime. We observed a better than 6-fold reduction in absorbed threshold power and a 2-fold increase in the maximum slope efficiency, to 63 % at LNT. The comparison of two different gain geometries suggests the heat distribution within gain facet and its path is a vital design factor.

The potential laser performance for 9xx nm Nd^{3+} transition is dramatically improved with respect to that obtainable at room temperature, where the laser would only just reach threshold, while for CW operation at LNT we obtained 3.8 W output power for 12.8 W of absorbed pump leading to a slope efficiency of 47 %.

AR coatings at cryogenic temperatures appear to be weaker, suggesting there is a high vacuum or cryogenic temperature related effect that degrades coating damage threshold. The thermal stress between two interfaces, coating degradation under intense cooling, and contamination under the high vacuum conditions, are the possible reasons for the lower observed damage threshold. Two coating damage events were observed for two different crystal designs and setups.

The mechanical stress induced by two materials, Cu and crystal added extra depolarization losses. In LNT our crystal has 10 folds increased compare to RT. A slab was bonded on one side has less depolarization losses when it reached LNT. However it failed to dissipate large amount of heat when it pumped CW, which implies dynamic changes of thermal and mechanical variations across the gain crystal. Both mechanical and thermo-optical stresses are far more complex than the

numerical model presented in Chapter 2. The various issues discussed in this chapter clearly highlights engineering requirements for pursuing the cryogenic laser operating in high vacuum chamber. In the following chapter we address new pumping geometry to avoid such a dynamic behaviour.

References

1. T. Y. Fan, D. J. Ripin, R. L. Aggarwal, J. R. Ochoa, B. Chann, M. Tilleman, and J. Spitzberg, "Cryogenic Yb3+-doped solid-state lasers," IEEE Journal of Selected Topics in Quantum Electronics 13, 448-459 (2007).

2. W. P. Risk, "Modeling of Longitudinally Pumped Solid-State Lasers Exhibiting Reabsorption Losses," Journal of the Optical Society of America B-Optical Physics 5, 1412-1423 (1988).

3. T. Y. Fan, and R. L. Byer, "Modeling and CW Operation of a Quasi-3-Level 946 nm Nd-YAG Laser," IEEE Journal of Quantum Electronics 23, 605-612 (1987).

4. D. C. Brown, "The promise of cryogenic solid-state lasers," IEEE Journal of Selected Topics in Quantum Electronics 11, 587-599 (2005).

5. D. C. Brown, S. Tornegard, J. Kolis, C. McMillen, C. Moore, L. Sanjeewa, and C. Hancock, "The Application of Cryogenic Laser Physics to the Development of High Average Power Ultra-Short Pulse Lasers," Applied Science-Basel 6 (2016).

6. S. Bjurshagen, and R. Koch, "Modeling of energy-transfer upconversion and thermal effects in end-pumped quasi-three-level lasers," Applied Optics 43, 4753-4767 (2004).

7. K. Petermann, *Laser diode modulation and noise*, Dordrecht, Kluwer Academic Pulishers (1988).

8. B.L. Volodin, S.V. Dolgy, E.D. Melnik, E. Downs, J. Shaw, and V. S. Ban, "Wavelength stabilization and spectrum narrowing of high-power multimode laser diodes and arrays by use of volume Bragg gratings," Optics Letters 29, 1891 (2004).

9. P. Leisher, K. Price, S. Karlsen, D. Balsley, D. Newman, R. Martinsen, and S. Patterson, "High-Performance Wavelength-Locked Diode Lasers," in High-Power Diode Laser Technology and Applications Vii, M. S. Zediker, ed. (SPIE International Society of Optical Engineering, Bellingham, 2009).

10. L. Yufeng, V. Negoita, T. Barnowski, S. Strohmaier, and G. Treusch, "Wavelength locking of high-power diode laser bars by volume Bragg gratings," 2012 IEEE Photonics Society Summer Topical Meeting Series, 29-30 (2012).

11. J. Levy, R. Feeler, and J. Junghans, "VBG Controlled Narrow Bandwidth Diode Laser Arrays," in High-Power Diode Laser Technology and Applications X, M. S. Zediker, ed. (SPIE International Society of Optical Engineering, Bellingham, 2012).

12. H. Glur, R. Lavi, and T. Graf, "Reduction of thermally induced lenses in Nd : YAG with low temperatures," IEEE Journal of Quantum Electronics 40, 499-504 (2004).

13. B. M. Walsh, "Review of Tm and Ho materials; spectroscopy and lasers," Laser Physics 19, 855-866 (2009).

14. P. Hello, E. Durand, P. K. Fritschel, and C. N. Man, "Thermal Effects in Nd-YAG Slabs 3D Modeling and Comparison with Experiments," Journal of Modern Optics 41, 1371-1390 (1994).

15. R. L. Aggarwal, D. J. Ripin, J. R. Ochoa, and T. Y. Fan, "Measurement of thermo-optic properties of Y3Al5O12, Lu3Al5O12, YAIO(3), LiYF4, LiLuF4, BaY2F8, KGd(WO4)(2), and KY(WO4)(2) laser crystals in the 80-300 K temperature range," Journal of Applied Physics 98 (2005).

16. H. S. Carslaw, and J. C. Jaeger, *Conduction of Heat in Solids,* Oxford University Press, (1986).

17. E. Browell, S. Ismail, and W. Grant, "Differentail absorption lidar (DIAL) measurements from air and space," Applied Physics B 67, 399-410 (1998).

18. V. Wulfmeyer, and J. Bosenberg, "Ground-based differential absorption lidar for water-vapor profiling: assessment of accuracy, resolution, and meteorological applications," Applied Optics 37, 3825 (1998).

19. R. Treichel, C. Czeranowsky, B. Ileri, K. Petermann, and G. Huber, "Mixed garnet laser crystals for water vapour DIAL transmitter," in Proceedings of the 5th International Conference on Space Optics, B. Warmbein, ed. (ESA Publications Division C/O Estec, 2200 Ag Noordwijk, 2004), pp. 639-642.

20. H. Rhee, T. Riesbeck, F. Kallmeyer, S. Strohmaier, H. J. Eichler, R. Trichel, and K. Petermann, "Frequency conversion concepts for the efficient generation of high power 935 - 942 nm laser radiation," in Photonics West (Peter E. Powers, San Jose, US, 2006), p. 610308.

21. W.Koechner, *Solid-state laser engineering*, 6th edition (Springer, 2005).

22. H. Wang, W. L. Zhang, and H. B. He, "Laser-induced damage behaviors of antireflective coatings at cryogenic condition," Applied Optics 51, 8687-8692 (2012).

23. K. Mikami, S. Motokoshi, T. Somekawa, T. Jitsuno, M. Fujita, and K. A. Tanaka, "Temperature dependence of laser-induced damage threshold of optical coatings at different pulse widths," Optics Express 21, 28719-28728 (2013).

24. P. H. Klein, and W. J. Croft, "Thermal Conductivity, Diffusivity, and Expansion of Y2O3, Y3 Al5O12, and LaF3 in the Range 77°–300°K," Journal of Applied Physics 38, 1603 (1967).

25. G. A. Slack, and D. W. Oliver, "Thermal Conductivity of Garnets and Phonon Scattering by rare-Earth Ions," Physical Review B-Solid State 4, 592 (1971).

26. D. C. Brown, "Ultrahigh-average-power diode-pumped Nd:YAG and Yb:YAG lasers," IEEE Journal of Quantum Electronics 33, 861-873 (1997).

27. S. Chenais, F. Druon, S. Forget, F. Balembois, and P. Georges, "On thermal effects in solid-state lasers: The case of ytterbium-doped materials," Progress in Quantum Electronics 30, 89-153 (2006).

Chapter 6:

Cryogenic side-pumped Zig-Zag laser

6.1 Introduction

The end-pumped cryogenic system described in previous chapter was power-limited via optical damage to the dielectric coatings and modal instability. This chapter presents a side-pumped zig-zag (ZZ) Nd:YAG slab design and its implementation in a cryogenically-cooled laser system. Section 6.2 introduces the ZZ slab design and discusses the theoretical modelling that describes the efficiency of the laser. The model accounts for the pump extraction efficiency for an internally reflected signal path in the gain media and also the temperature distribution along the pump face. A side-pumping configuration allows for a simple bar-type diode-laser pump arrangement using geometric optics in free space, and where the gain crystal can accommodate high pump-power providing a smooth absorbed-power distribution. Section 6.3 introduces the laser resonator design. Section 6.4 introduces the experimental setup employed for our ZZ slab, giving a discussion on the geometric optical pump systems to achieve efficient pump light delivery. In the following section, we report the performance of the prototype ZZ slab laser system, which was operated at room temperature emitting 1.064 μm, then tested with the ZZ slab cooled to cryogenic temperatures, for both the 1.061 μm and 0.946 μm transitions. Finally in Section 6.6 we conclude with a discussion on the issues encountered and further power scaling prospects.

6.2 ZigZag slab

6.2.1 ZZ slab introduction

Nowadays, selection of wide range of diode lasers is available which enable to pump the gain medium in one direction. The design of TEM00 mode laser became much simpler by using diode laser as a pump source as well. As discussed in previous chapter, conventional end-pumped system limits TEM00 mode due to thermo-optical distortion induced by heat deposited. Side-pumped slab crystal has capable to use its multiple facets for cooling, pumping and resonating. Slab designs also have advantage in power scaling over cylindrical rod. Two key advantages are high cooling surface-area to pump-volume ratio and its one-dimensional temperature gradient. These features have shown a better heat dissipation capability [1]. A number of slab geometry

and pump schemes have been suggested to various solid-state lasers [2-4]. The approached designs take advantage of efficient heat removal through the large cooling faces creating one-dimensional heat flow. Early works [5-9] introduced facial pumped, zigzag resonating geometry for using lamp as a pump source, demonstrating improvements in laser performance. For using a flashlamp as a pumping source approaching uniform distribution over facial area were held back its concept, this was because of its engineering difficulties and low efficiency which were typically 1% electrical to optical efficiency.

Soon after diode-lasers become practical to use, that brought up more efficient laser design and approaches for slab lasers and refined repeatedly as the technology has developed [10-12]. The side-pumped active medium offer rectangular diode-bar fit-in geometry which allows simple diode-coupling optics. Side-pumped, face-cooled ZZ slab is a well-known solution that drastically reduces the thermally induced birefringence and lensing [1]. Laser mode passing between internal faces by total internal reflection (TIR) under ZZ geometry. The laser mode correct the thermal distortion by averaging it on each TIRs. The geometry also increases the extraction of pump from the edge of pump facets where the pump density is highest. However the field of strong pump absorbing surface induced rather stronger lensing along in the transverse direction, also the power extraction is limited due to strong astigmatism developing along two cooling faces.

Richards *et al* [13] reported coplanar-pumped folded slab (CPFS) design that can extract out most of pump absorbed near pump facets. The pump field is collimated in the mode plane to maximize the overlap which improves the extraction efficiency. His design used pathing 11 TIRs along ZZ bounces and both entrance and exit faces are Brewster's angle cut. The dimension of the slab was chosen to match the size of pump field and laser mode providing length of Brewster face as a mode size. The mode travels the pump field twice on each single pass hence improves the effective gain volume four times against conventional rod.

6.2.2 Slab Design

The ZZ slab lasers have been revised in previous section 6.2.1. In this section we discuss the ZZ slab design that can fulfil the requirement for Q-F-L laser source operating in cryogenic temperature. Despite the ZZ geometry has been used to scale solid-state laser. It is difficult to use the ZZ slab for Q-F-L or three-level lasers, due to reabsorption of the stimulated emission and requirements for high pump brightness overlapping the cavity mode in the gain material. As discussed in Chapter 1, the reabsorption loss associated with the Q-F-L 946 nm transition of Nd:YAG, from the lower manifold becomes negligible below 120 K. Therefore, a cryogenically-cooled side-pumped Nd:YAG ZZ slab enables high pumping-powers in a modest volume of the

gain medium, which offers a significantly longer path through the excited region for the cavity mode, favouring the still relatively low-gain 946 nm transition. A one-dimensional heat flow through the large top and bottom surfaces also reduces the effects of thermal lensing and depolarization losses, which are a well-known limitation to power scaling [14].

The reflection of the signal beam off the polished side wall, exploiting total internal reflection (TIR), provides a good overlap of the resonating signal beam at an oblique angle to pump field. One significant drawback of many ZZ designs is the potential pump extraction efficiency; this is limited by overlap of the fundamental mode and sheet-like pump field at the side

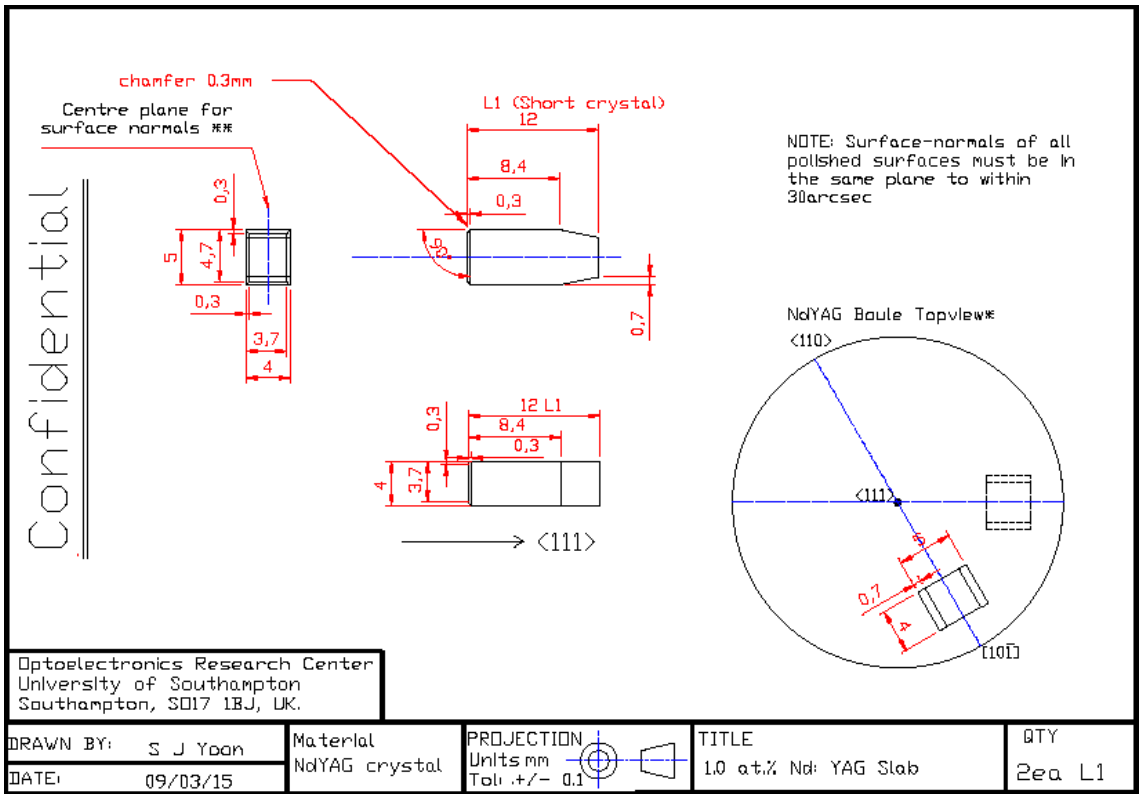

Figure 6-1 Schematic view of the ZZ slab design

Figure 6-1 shows the schematic top view of the ZZ slab. The approach of Richards was to “fold” a classic ZZ slab in half, to maximise the numbers of passes through a thin gain sheet produced with a proximity coupled FAC diode-laser, making for a compact and simple laser. Due to the critical angle in YAG being 33.4°, the bounce angles for the side and end walls where chosen to be 40° and 50° respectively, to ensure TIR at each interface. Two bounces from each side wall and a single bounce at the end wall provides 5 bounces in total in a single pass through the slab. The entrance and exit facets of the slab are cut at Brewster’s angle to provide a high degree of polarization selectivity per cavity round trip. We allowed 0.2 mm chamfer at the end wall edges to produce an aperture inside crystal, providing an element of cavity mode control for the right cavity conditions. The dimensions of the crystal were chosen to ensure a good pump absorption

for side-pumping and reasonable match the cavity mode size, filling the Brewster's cut facets, which enables a near circular output to be achieved for a $D_{4\sigma}$ ~900 μm beam size in the 4 mm thickness dimension of the slab and weak astigmatic thermal lensing. Finally following the formalism set out by Ostermeyer *et al*. the crystal cut axis was chosen to minimize the depolarization effects during pumping [15].

Table 6-1 Specifications selected for ordering the Nd:YAG ZZ slab

Material:	Laser grade Nd:YAG (i.e. must have minimal other impurities)
Nd concentration:	1.0 ± 0.1 at.%
Length:	11.98mm ±0.2 mm
Width:	5.0 ±0.1 mm
Thickness:	4.0 ±0.1 mm
Faces to be polished	**5 faces, two 8.39mm x 4.0mm faces** and **two 3.59mm x 4.0mm faces** and **5.0mm x 4.0mm face**
Clear aperture on polished faces	>95%; special attention should be taken with the 3.59mm x 4.0mm faces. >90% for two 8.39mm x 4.0mm faces and 5.0mm x 4.0mm face
Cut angle	11.2°± 0.1°
Polished faces surface finish (width x thickness):	10/5 scr/dig
Polished faces surface flatness:	λ/8 at 633 nm
Side faces parallelism:	<30 arc sec*
Coatings: two 8.39mm x 5.0mm faces only	AR (<0.5%R) 810±20nm for 0 to 25° AR (<0.5%R) 870±20nm for 0 to 25° AR (<0.5%R) 1060±20nm for 0°
Coatings damage threshold:	> 10J/cm^2 and 500MW/cm^2 10ns pulses
Surface finish for other 3 faces:	fine grind for the 11.98mm x 5.0 mm faces and for the 4.29 mm x 4.0mm face
Surface flatness (**width x length**):	<5 microns PV

The top and bottom faces of the ZZ slab were conduction cooled, with 200 μm thick indium foil (purity - 99.9 %) acting at the interface between crystal and the Cu mount. Both side facets were AR coated for wavelengths from 800 nm to 1.1 μm, firstly to reduce pump losses and second to prevent the strong 1 μm ASE leading to gain-depletion, or parasitic lasing paths along pump sides, reducing the performance for the 946 nm output. It should be noted that the AR coating does not affect the TIR condition of the cavity mode inside the ZZ slab. The second pumping configuration detailed in the previous Chapter comprised a 870 nm 70 W diode-bar, with it's wavelength locked using a VBG, matched for narrow absorption band of Z1→R2 transition. One benefit of the 870 nm pump wavelength is that it lowers the heat generation within crystal due to its lower quantum defect, compared to the conventional 808 nm pump wavelength. Due to the shift in the peak wavelength of the pump transition as a function of crystal temperature. Two VBGs with different central reflection wavelengths were used to attempt to maximize pump absorption at RT and LNT.

6.2.3 Pump Extraction Efficiency

The slab design, its width, height, and angle for TIR were chosen to maximize the overlap between pump and laser field. Primarily this was to ensure efficient optical to optical conversion between pump and laser signal and good energy storage that is easily extracted from the laser material. To determine the expected overlap efficiency we will start by assuming that the pump beam has a Gaussian distributed in the two axes defined by the junction of the diode-laser, which can be given as,

$$I(x,y,z) = \frac{2P_p}{\pi w_x w_y} e^{(-\alpha z)} e\left(-2\left(\frac{x^2}{w_x{}^2}\right)^{S1} - 2\left(\frac{y^2}{w_y{}^2}\right)^{S2}\right) \qquad 6\text{-}1$$

Where P_p is incident pump power and pumping region is given by w_x and w_y, α is absorption coefficient, z is pumping direction. $S1$ and $S2$ provides Gaussian profile information, 1 as normal Gaussian and 2 or 3 for super Gaussian. Assuming there is 60 W of pump light with a $D_{4\sigma}$x beam width of 7.8 mm and a $D_{4\sigma}$y beam height of 0.9 mm, the pump intensity distribution coupled into the slab is shown in Fig 6-2(a). In this example, 80 % of the pump is being absorbed over the width of the slab.

A normalized Gaussian cavity mode, which has a 400 μm beam radius just as it is about to enter the Brewster cut faces of the slab, for which the beam is nearly filling the entire aperture, is shown in Fig 6-2(b). Neglecting interference effects from stimulated light travelling in opposite directions, the normalized signal irradiance is doubled when two ZZ beams overlap, for which we

can observe 5 TIR nodes (dark regions Fig 6-2(b)) at the crystal's boundaries as predicted. However, there are two central areas where there is little overlap, in addition to the higher-inversion regions at the pump face where the propagating stimulated light has relatively low power, i.e. in the wings of the Gaussian. These areas between well saturated nodes will reduce the extraction efficiency and are potential seeding points for parasitic lasing paths.

Following the analytical steady-state population inversion detailed in Eq.2-22, for a given pump and signal irradiance, the simplified equation to derive the inversion population fraction is;

$$\frac{n_2(x,y,z)}{n_0} = \frac{\sigma_p I_p(x,y,z) / h\upsilon_p}{\sigma_p I_p(x,y,z) / h\upsilon_p + \sigma_s I_s(x,y,z) / h\upsilon_s + \tau_f} \qquad 6\text{-}2$$

here $I_p(x,y,z)$ and $I_s(x,y,z)$ are the spatially depended pump and signal intensities, σ_p and σ_s are the cross sections for pump and emission, $n_2(x,y,z)$ is spatially depended population excited out of total population, n_0 .

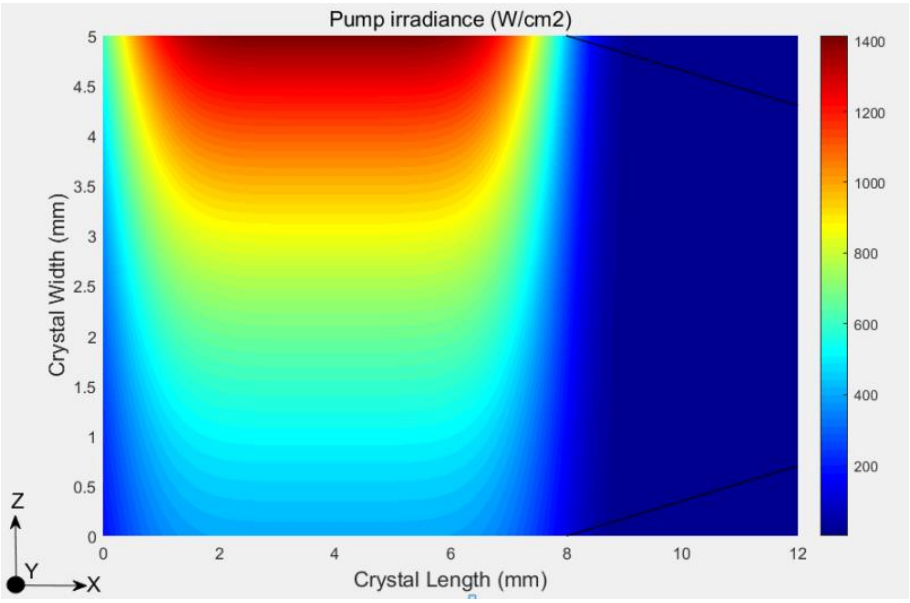

(a)

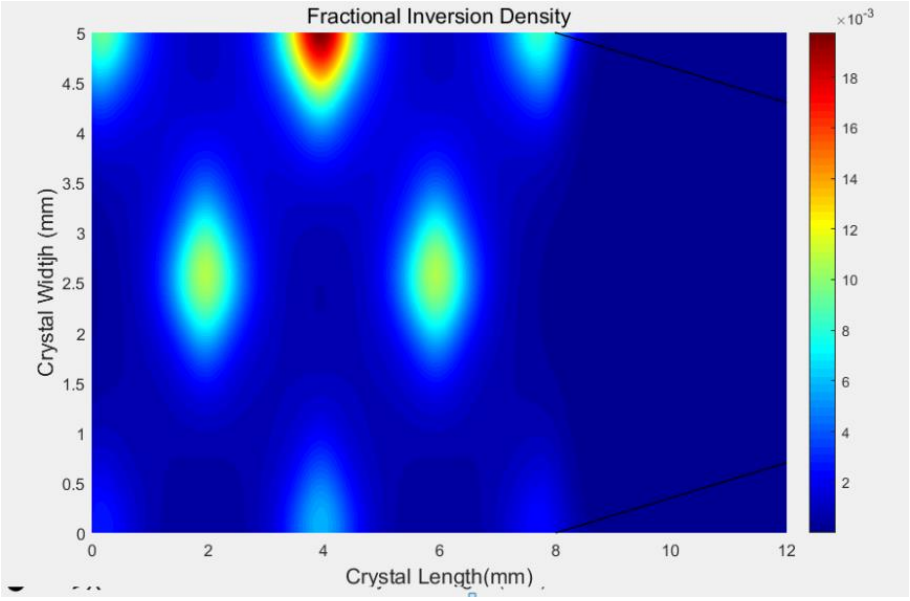

(b)

Figure 6-2 (a) Modelled pump irradiance for a side pumped slab, (b) fractional inversion density, n_2/n_0

The empty 'unabsorbed' anti-node locates between two nodes at Z = 5 mm, X = 4 mm, giving extinction ratio of ~20 times higher than that at the node. This suggests there could be a significant possibility of generation of higher-order cavity modes or parasitic-lasing in the area between the saturated nodes where there are overlapping beams. As such for cryogenic cooler Nd:YAG operating at 946 nm, there could be strong ASE at 1 μm, proving challenging to suppress depletion of the gain and lowering the extraction efficiency of the laser, where there is not sufficient saturation of this inversion in the wings of the fundamental cavity mode. These untapped regions stand out in fluorescence imaging of a ZZ slab, looking down at the top of a side pumped slab whilst capturing the 1 micron emission, as shown in Fig 6-3. In Fig 6-3(a) the measured fluorescence denoted population inversion defined by fluorescence of the pumped ZZ slab, before laser cavity was aligned. When the ZZ cavity was aligned, the captured fluorescence changes dramatically, Fig 6-3(b), showing clearly comparable images to that predicted in Fig 6-2(b), i.e. a qualitative measure of the fractional population inversion. Small gradient was observed on Fig 6-3(a), which seemed the camera was saturated or not sensitive enough for showing distribution as seen on Fig 6-2(a).

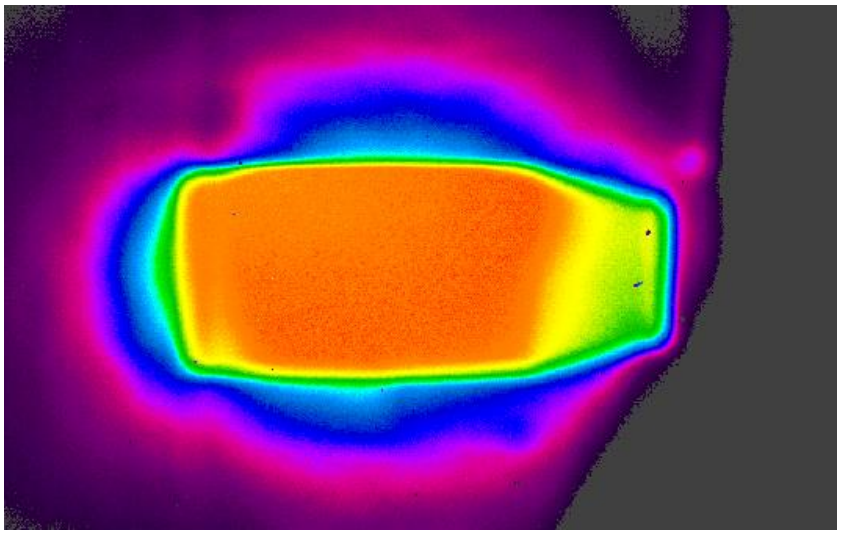

(a)

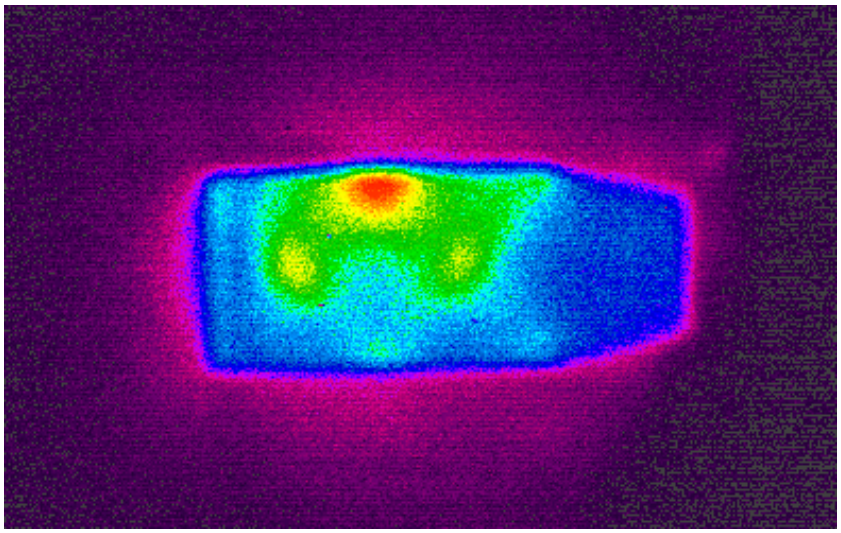

(b)

Figure 6-3 Measurement of 1 μm fluorescence from the top of a side-pumped ZZ slab, with the fluorescence captured (a) without and (b) with the laser cavity was aligned.

The actual measured dimensions of one of the slabs made for this work is shown in Fig 6-4. Small deviations from the target values, mostly within specified tolerances, led to a reduced aperture through the respective polished Brewster faces, themselves 0.1° out of from their ideal orientation. In effect the Brewster windows and rear face of slab (with respect to the input/output faces) act as apertures within the cavity, in the x-axis, and as such their relative positions with respect to the optic axis is critical for achieving low loss. For optimal conditions the beam path will be that which is passing through these apertures with the least loss, in the case of the actual slab received, the signal path was asymmetric in the plane, leaving unoccupied area on shorter side (8.4 mm) compared with the larger side (8.7 mm). The position of the antinodes are not mirrored in the actual fluorescence about the centre of the slab. It was observed that the output power was 15 % lower when aligning the cavity to have antinodes at mirrored positions

along the longer faces. Therefore the optimised signal path for the studied slab had to be asymmetric to fulfil minimise losses through the internal apertures, i.e. the Brewster face and chamfers on the rear face. Further cavity alignment was made while measuring residue signal beams, as such it was found that there were extra losses at the Brewster windows associated with the cavity modes' slight deviation from Brewster's cut incidence and therefore a non-zero reflectance for the p-polarization state.

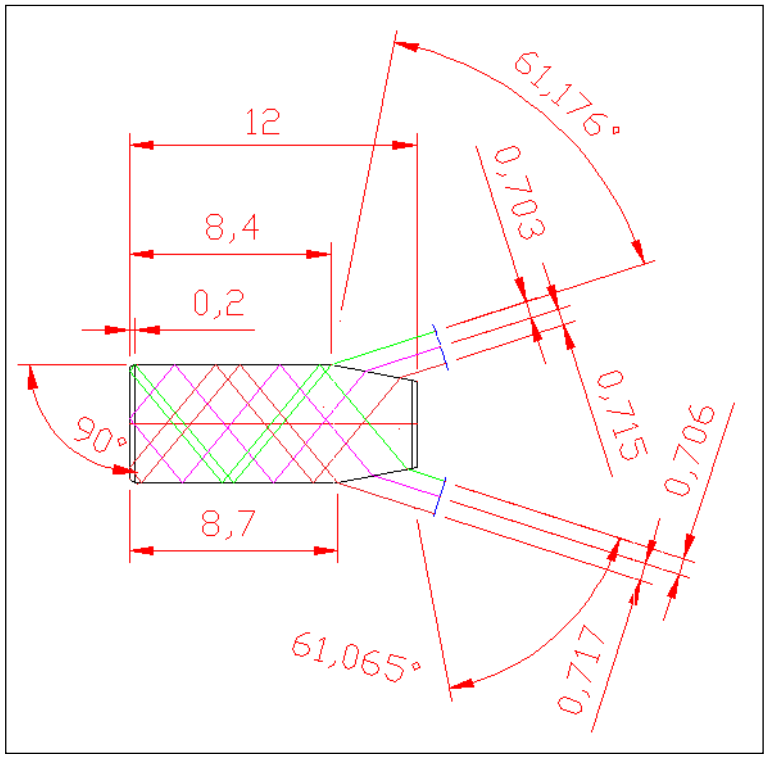

Figure 6-4 The measured dimension of ZZ slab crystal

6.2.4 Temperature distribution

Side pumping of slabs can allow one directional heat flow towards the cooling surfaces, with the thermal distribution dependent on the materials thermal conductivity and boundary conditions, i.e. thermal resistance of the contact with the cold finger. Eggleston *et al* [1] reported the thermal distribution within slabs, and Hello *et al* [16] reported both analytic and numerical solutions to the heat transport equation dependence on the choice of the boundary conditions, i.e. face, side, or top-bottom cooling. The gain medium for a cryogenically-cooled system is usually configured to be in vacuum to avoid condensation and convective heating, as such we can assume zero thermal radiation from the open-sides of our slab and that all heat is transferred through facets in contact with the metal fixtures. The heat flux under temperature time dependence, is given by Eq.2-2.

$$\nabla^2 T(x,y,z) = -\frac{Q}{k_c(T)} \qquad 6\text{-}3$$

Two graphs in Figure 6-5 plot the 2D temperature profiles in the width by height directions for the ZZ slab detailed above, at 300 K and 77 K. The model assumes 60 W of pump-power and the second pump configuration detailed in section 5.2, i.e. the VBG-locked pump at 869.4 nm, with a beam radius in the height axis of 450 μm and absorption rate determined by rate equations, using the spectroscopic data of Chapter 3, therefore simulating the setup that will be discussed later as used in the laser experiments. The model only has defined uniform heat distribution along the side pumped facets, however the model shows good comparison of heat dissipation for two temperature regime.

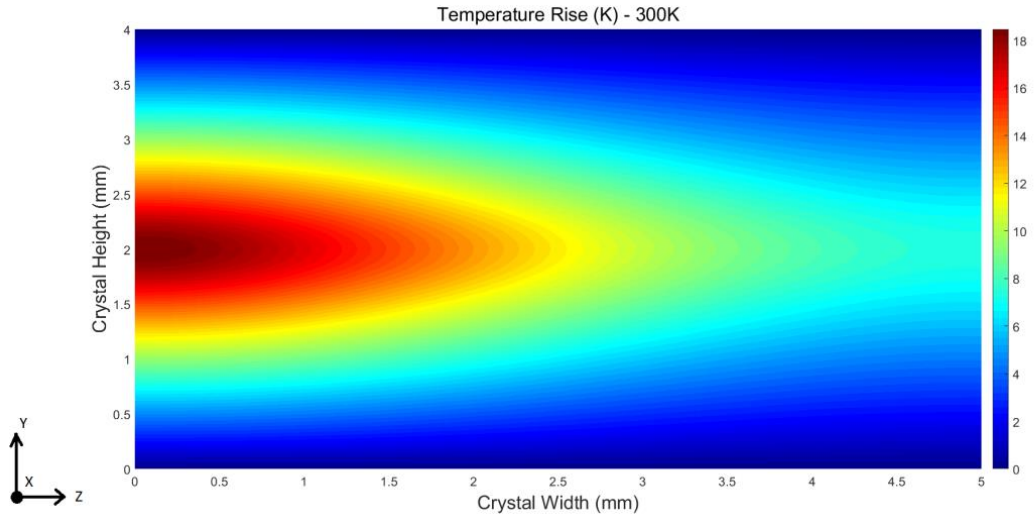

(a)

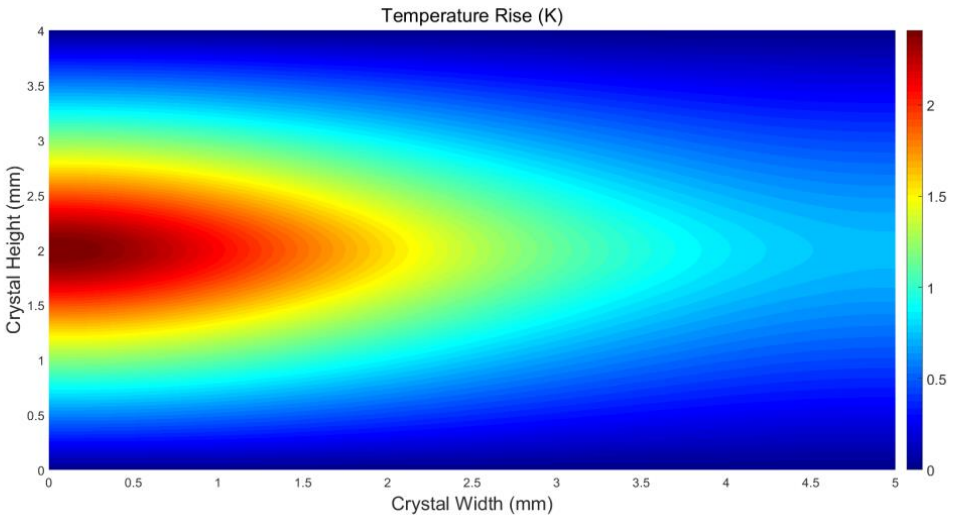

(b)

Figure 6-5 Temperature profile of side-pumped slab estimated at (a)300K and (b) 77K

The thermal distribution is compared for the two temperatures of interest, assume same irradiance pump field is provided. The absorption coefficient was defined prior to fit in two

temperatures for using wavelength locked pump diode. The absorption coefficient is ~30 % higher when crystal is at LNT. The results show the peak temperature rise is almost 19 K at RT, but only 2.5 K at LNT, clearly demonstrating favourable properties in the cryogenic regime, as the thermal gradients define the physical distortion and thermo-optical properties of the material. In both cases a stronger thermal lens is formed in the Y-axis of the slab, with the oblique angle of incidence of the optical axis for the cavity mode plus the TIR from the side faces averaging out thermo-optic effects in the other two axes. Therefore there is a stronger cylindrical lens in the y-axis compared to the orthogonal axis with respect to y- and the optic-axis of the propagating beam. Several techniques can be introduced to avoid this, i.e. cavity design to accommodate the thermal lens effect [17-19]. Another route for managing the thermal lensing available to the ZZ slab design, is to extend the side length of the slab, i.e. number of nodes, therefore providing the potential to maintain the pump power density with more pump light along the increased side-wall dimension. Mudge *et al* [20] have tested 9 nodes on one side, in a double-side pumped CPFS with over 34 mm sides (total length was 36.8 mm) producing 18.5 W single mode and 32 W multimode 1 μm emission for 100 W of pump power.

We designed CPFS to satisfy cavity perspective following Richards has reported [13]. The slab has 5 TIR bounces, 4 at side faces and a single bounce at the end face, each has angle of incidence of 40° and 50°, respectively. The length of slab is 12 mm, providing total 32 mm long ZZ paths along crystal. The width is 5 mm, which is 2 absorption length with using wavelength locked in-band pump diode, later practical absorption was increased to 90 % during experiment. Both side faces were AR coated to prevent 1 μm ASE and to optimize pump transitions. Mode size is physically limited by the end-face chamfer (for horizontal axis of mode) and the pump volume (for vertical axis of mode), respectively. Later this chapter we discuss the cavity design and associated laser experiment.

6.2.5 ZZ slab – conclusion

This section reviewed a number of design considerations for using the ZZ slab, including tolerance and thermal management issues. While the ZZ slab clearly offers advantageous thermo-optical properties that can overcome some of the issues of end-pumped systems in terms of simplicity of the pumping configuration and advantages in both mechanical stress and thermal gradients within crystal, there is still an open question whether the efficiency can be improved to make the approach interesting for power-scaling.

6.3 Cavity modelling

In this section we present two cavity, linear cavity and Z-cavity that has been used for CPFS laser operation as shown in Fig 6-6. Linear cavity is first introduced in room temperature 1064 nm emission. The cavity length was very short to oscillate laser in stability region when crystal is pumped from side facets. Z-cavity introduced a stable cavity design that can produce a diffraction-limited laser mode with near-symmetrical beam parameters at the output coupling mirror. The optimum cavity-mode radius at the slab entrance, to extract the pump field efficiently but not being clamped at Brewster faces or rear-face chamfers, should be <500 μm ($1/e^2$) as the X-axis effective width of the Brewster faces is ~1.5 mm in the ideal case and less when real tolerances are accounted. Similarly, for the Y-axis the optimum is ~450 μm, corresponding to the pump beam's height. The folded single-pass path length in the crystal is 32 mm long and the pump field is located at the middle of the crystal.

Figure 6-6(b) shows a Z-cavity design consisting of 4 mirrors and a crystal. The model accounts thermal lens on Y-axis as shown in Fig 6-8. The distance between the crystal to the flat HR-end-mirror (M_1) is 50 mm (D_1), and two tilted curved mirrors R_2=500 mm (M_2) and R_3=200 mm (M_3) form a telescope, positioned 250 mm (D_2) and 425 mm (D_2+D_3) from the crystal, respectively. The position (D_4) and output coupler reflectance were varied, and the tilt of the turning mirrors was set to 20° to minimize astigmatism. A plot, Fig 6-7, from the model shows the beam radii for the two orthogonal axes within the cavity. The radii between end mirror and first curved mirror matched the designated fundamental mode.

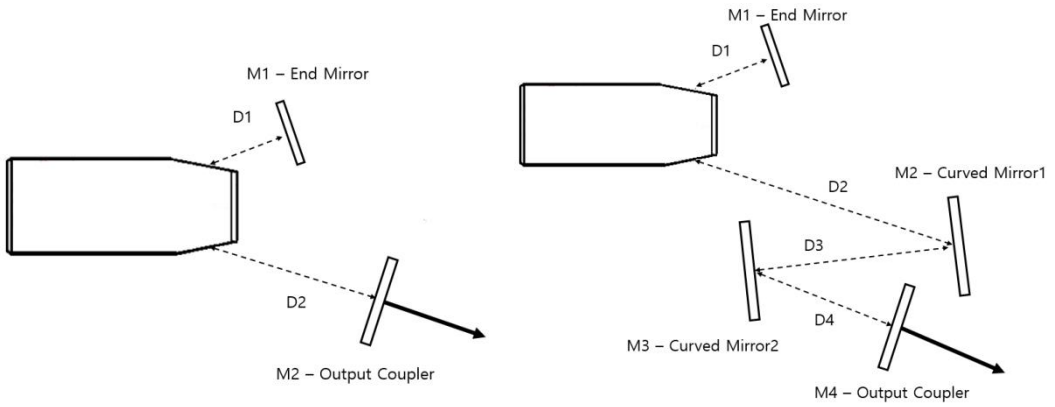

(a) (b)

Figure 6-6 Schematic diagram of the investigated, (a) linear cavity, and (b) Z-cavity.

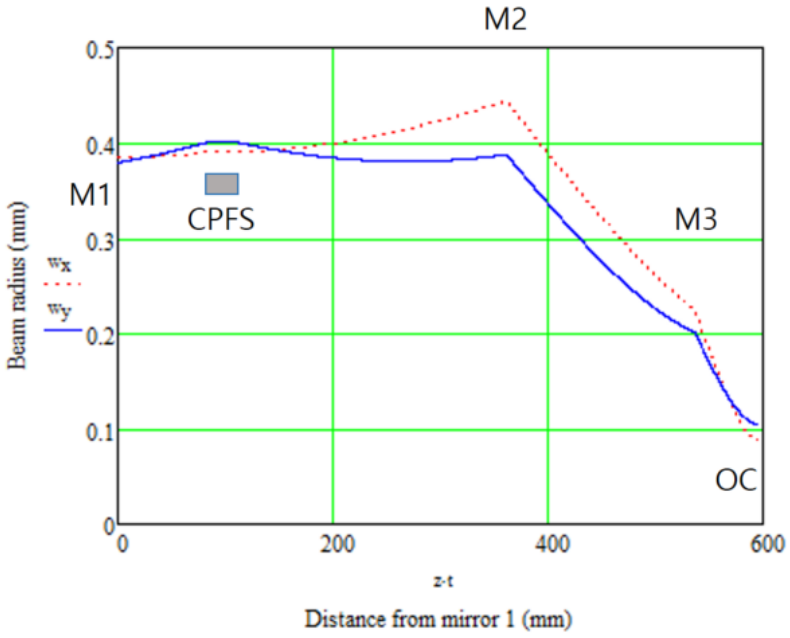

Figure 6-7 Tracking the internal beam waist along Z-cavity

The resonator was designed so that it could compensate for a thermal lens in the Y-axis, upto 2500 mm to a flat plane. Figure 6-8 plotted the effect of thermal lens in using plane mirror OC (Fig 6-7) and effect of beam radii change over thermal lens changes within ZZ slab. In room temperature the core is ~20 K higher than that at the boundary of slab, which will form strong thermal lens in cavity as described in section 6.5.2. However the thermal gradient is negligible or very low when crystal is at LNT. A Z-cavity with Plane-mirror OC was tested in RT before testing at LNT. Figure 6-9 plot the change of beam waist at crystal by moving D_4, distance between M_3 and OC. As D_4 gets closer to M_3, the beam waist increases where it gets filtered by intra-cavity aperture (4.6 mm).

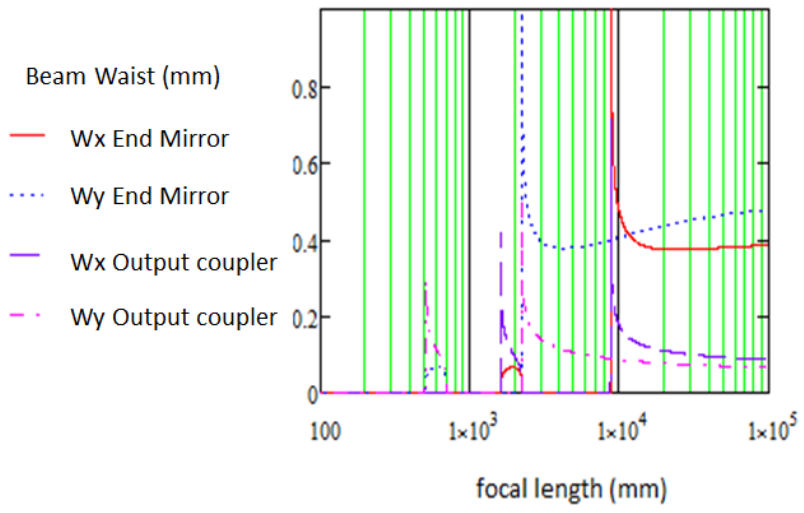

Figure 6-8 Tracking the change of beam waist on End mirror and plane OC for changing thermal lens

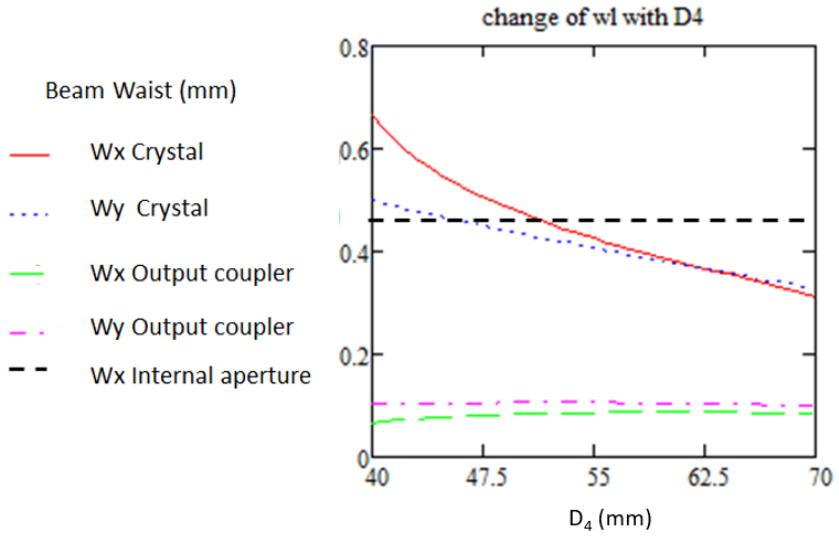

Figure 6-9 Tracking the change of beam waist at crystal for changing D_4

6.4 Experimental setups

A series of experiments were conducted using the ZZ slab that have been discussed in the previous section. Using the second pump source detailed in Section 5.2, i.e. the VBG-locked diode-bar laser, the pumping lay-out is very similar to that explained in Chapter 5. However, the full diode-bar width was used as the output was designed to match the side width of the ZZ slab using a final f = 300 mm spherical focussing lens, Fig 6-11. As such the pump beam was focused in the crystal to an area of 7.8 mm X 900 μm. To maintain a constant wavelength by operating the diode-laser at one current and fixed to the optimum temperature, a variable attenuator was built through the combination of a ½ waveplate and a polarizer, which enabled the incident power to be varied. For protection of the diode-laser a 1μm wavelength blocking filter was installed between the diode-bar and focusing lens. Access windows for the vacuum chamber were AR coated, as were the side faces of crystal, each measured to be on the order of 0.1 % reflectance at the pump wavelength.

First experiment which was conducted in RT has set a ZZ slab sandwitched between water cooled Cu mount. Simple linear cavity was first tested for dominant 1064 nm at RT then Z-Resonator was tested. 946nm transition was later tested at cryogenic condition using Z-cavity. Single node was tested in cryogenic operation to improve the extraction efficiency.

Crystal is 4 mm high and Indium foils are 200 μm thick. The mounting depth was ~4.1 mm high. The CPFS slab was affixed to the cryo dewar cold finger as shown in Fig 6-10. The mount was designed to minimize the mechanical stress along crystal. The spacing between Cu body to its lid was 4.1 mm, with two Indium foils accounting 400 μm, 4 mm high crystal has 0.6 mm space in RT

accounting for Cu constraint while it reaches LNT. Constant pressure was applied using a torque-controlled wrench setting the 35 cN/m applied to both two bolts onto Cu lid. Polarized He-Ne was measured with crystal before clamping the bolts, this was to measure the depolarization loss due to mechanical stress. Mechanical stress will introduce birefringence since the crystal is isotropic, which presents as a loss for a polarized cavity mode. In setting up our slab, a HeNe laser beam was used as a probe passing through the slab while the transmitted power was monitored, until a preset torque was applied to the clamping mount. The measured value was kept constant for cooling the crystal down to LNT.

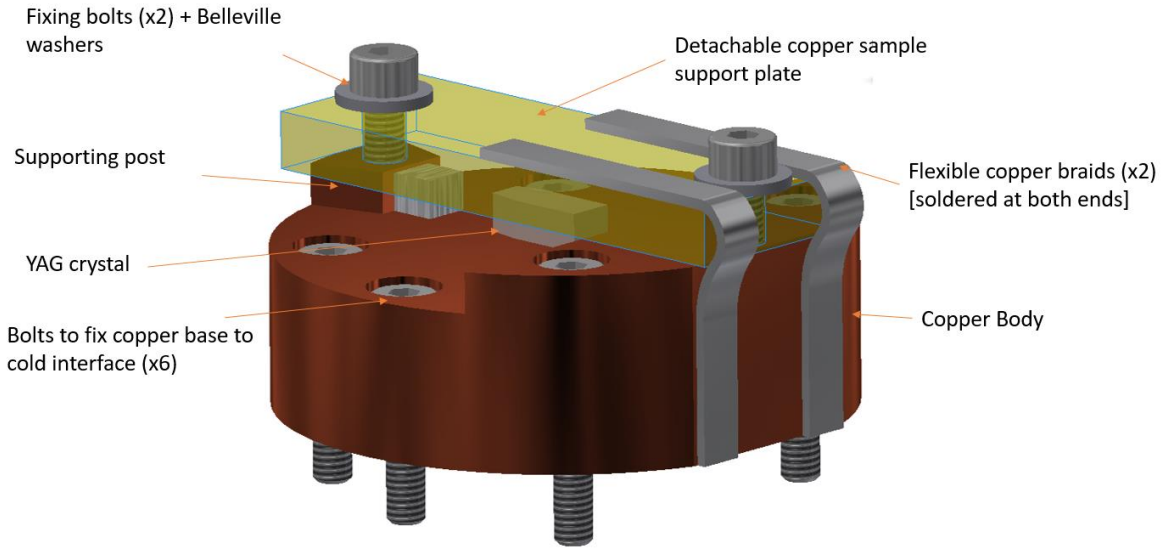

Figure 6-10 Mechanical overview of Cu body and top lid. The 'body' was attached to Cu finger

The setup was later changed by replacing the focussing lens with a f_y = 100 mm cylindrical lens to focus the pump beam to a width of 3.5 mm, Fig 6-12. This was to test the extraction efficiency by concentrating the pump light where the signal path nodes were at the side faces and therefore avoid pumping into the anti-nodes.

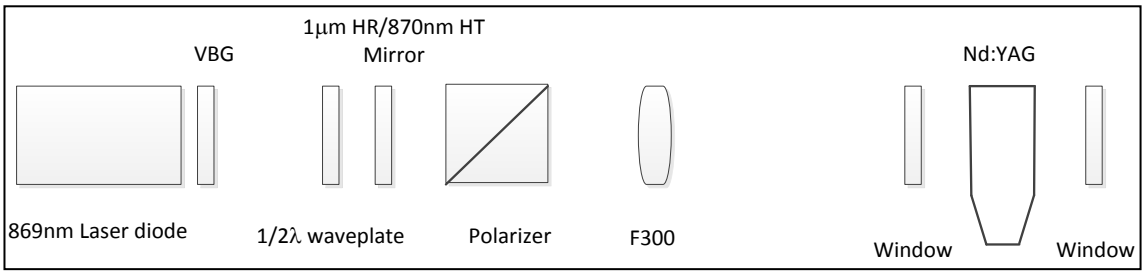

Figure 6-11 Schematic of pump system set-up for pumping two nodes, Plan view

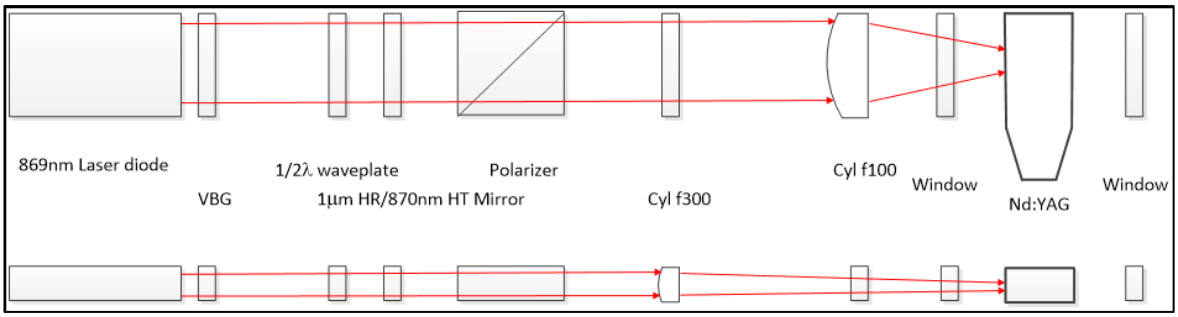

Figure 6-12 New pump optic configuration and beam path for single node pump, Plan view (top) and side view (bottom)

A 1064 nm linearly polarised probe laser was built prior to operating the ZZ slab laser, to test the transmittance through the ZZ slab along it's optical path as per a single pass through the cavity, i.e. via the two Brewster's cut faces and 5 internal bounces, (four of which were TIR from an AR coated side face, as previously discussed). A transmittance of ~99.9 % was measured with this probe laser, with a minor reflection observed from the first Brewster window, thought to be a result of residual s-polarization in the probe beam.

Efficient laser operation with the ZZ slab is highly dependent on the cavity alignment with respect to the pump field. To achieve a near-loss-free round-trip, the cavity mode has to be precisely positioned with respect to the intra-cavity apertures of the ZZ slab faces and in the plane of the pump. It is important to establish two conditions; an optimal beam size passing through the crystal and optimal angle of incident at the Brewster faces. Employing the Z-cavity with two tilted curved mirrors provides enough flexibility to enable these conditions.

6.5 Results

6.5.1 Room temperature performance: 1µm transition

Linear and Z-cavities

To test the performance of the ZZ slab, two resonators, a linear cavity and a Z-cavity as shown in Fig 6-6, were first trialled at RT for the standard 1064 nm lasing transition. As such it was not necessary to include the vacuum housing and its windows around the crystal. The linear cavity used a 500 mm ROC concave mirror and a flat output coupler (87 %R), spaced 6 mm and 10 mm from the crystal, respectively. For this arrangement the cold-cavity mode size (radius) in the crystal is 200 µm. Figure 6-13(a) shows the linear cavity output power when it was QCW pumped (2 % duty cycle).

For the Z-cavity a flat mirror was used as an end-mirror positioned 80 mm away from crystal, with a concave 500 mm ROC mirror, then another 200 mm ROC mirror, and finally a plane output coupler, each at spaced by a distance of 250 mm, 175 mm and 60 mm, respectively. As seen from Fig 6-7, in this arrangement the cold-cavity mode size in the crystal is approximately 0.4 mm. Figure 6-13 (b) is a plot of the QCW laser output for the Z-cavity cavity using the 81 %R output coupler. The laser experiment at RT was conducted without window port which requires for using vacuum chamber. The windows were AR coated and only used when crystal was cooled to LNT.

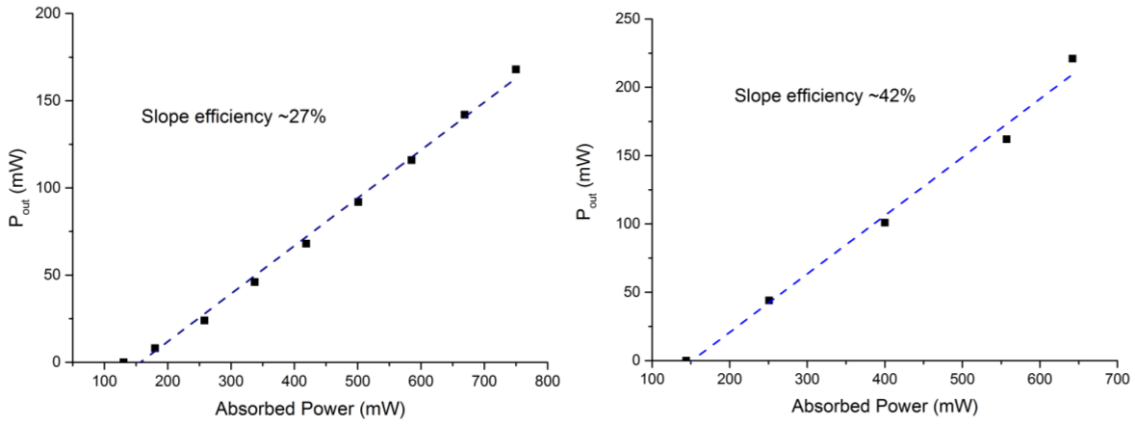

(a) (b)

Figure 6-13 QCW 1064 nm laser performance for the (a) linear cavity and, (b) Z-cavity, at 300 K

There was improved slope efficiency for the Z-cavity with respect to the linear cavity, due to the larger beam size in the crystal, and therefore it is expected that it can extract more of the pump power with lower losses compared to the potential higher-order-modes. Threshold was lower for the linear cavity, due to the lower output coupling and the smaller beam size in the crystal. For both cases the resonator stays stable for the available pump power, as the thermal load was deliberately kept small by operating at a low duty cycle.

At RT the linear cavity, detailed above, was then tested in a CW pumping regime. Testing various output couplers, the maximum power was reached for 81%R. It can be clearly seen that the output power started to roll over when the absorbed power reached ~30 W, as shown in Fig 6-14.

Indirectly measuring the near field image at the OC, via a 2X magnification telescope using 250 mm and 500 mm spherical lenses, and M^2 through the combination of the near and far field beam profiles, as described in the section 2.5, enabled the characterisation of the thermal lens induced under CW pumping. M^2 and the beam waist size at the plane output coupler, were measured with respect to absorbed pump power as shown in Fig 6-15(a). As expected, the thermal load in the crystal induces a worsening beam quality in the Y-axis, while in the X-axis it is

a weaker effect, typical for a side-pumped ZZ slab configuration. Taking the measured beam quality and W_{nf}, a 2 times magnified image of the spot size at the OC, the embedded diffraction-limited beam size at the output coupler, W_o, is calculated by the imaging relations of the intermediate telescope between the laser and M^2 measurement setup. It is noted that the fundamental cavity mode is relatively stable for both axes, although there is still a monotonic decrease in beam size with increasing power and induced effective-thermal-lens strength in the respective axes. Exploiting the cavity modelling and measured beam quality and waist size at the OC, an estimation of the thermal-lens dioptric power as a function of the absorbed pump power is calculated, shown in Fig 6-15(b). The Y-axis curve is linear until 25 W, after which there is a sudden change above a thermal lens power of 5 m^{-1}, with an associated change in the beam quality in the Y-axis. The X-axis was stayed less effected via pump power, but it became highly multi-moded as w_l/w_p is ~ 0.44.

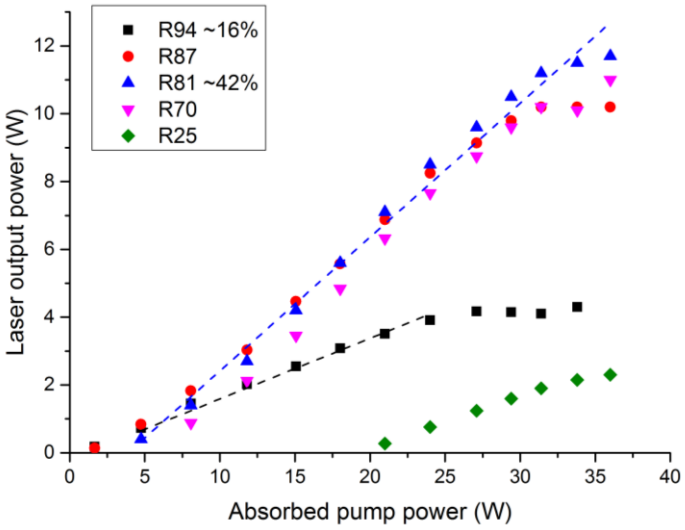

Figure 6-14 CW laser performance with various output coupler

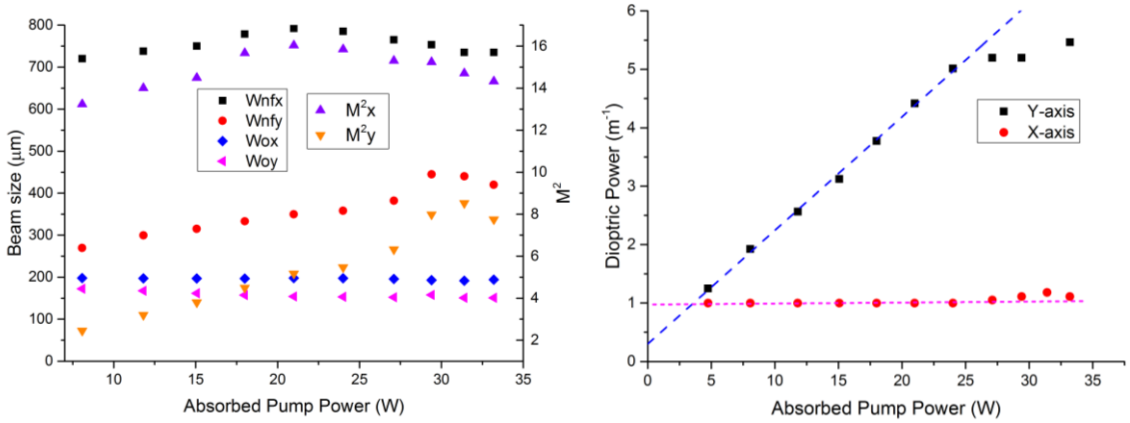

(a) (b)

Figure 6-15 (a)Measure of beam waist at output coupler and beam quality for pump light and (b) estimated dioptric power for pump absorbed

A Findlay-Clay analysis [21] for the linear cavity configuration was undertaken in order to determine the intra-cavity losses, shown in Fig 6-16. Since this simple cavity comprising of one HR end mirror, various reflectivity of output couplers, the residual round-trip loss of 1.1 % is expected to be predominantly associated with loss associated with the ZZ slab. There are few associated losses caused from, as depicted in Fig 6-4, asymmetric Brewster cut forced optic axis go slightly off the optimum to get through ZZ slab without physical distortion or aberration induced through the internal aperture, where chamfer has involved in. This is the case when the beam size of probe laser is well collimated and show marginal losses.

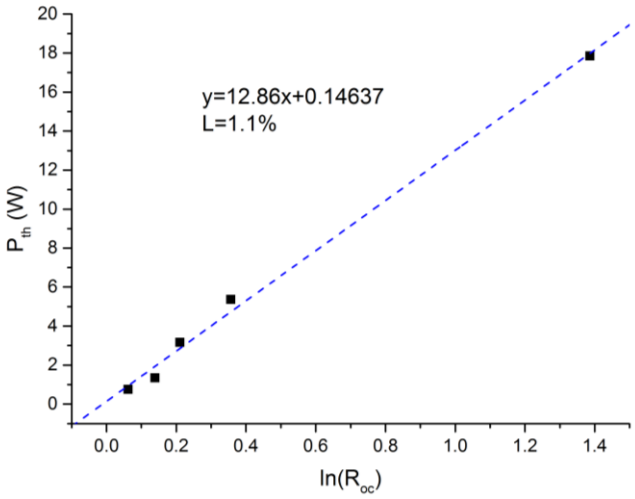

Figure 6-16 Findlay-Clay analysis for CW RT linear cavity

To characterise the Z-cavity in the QCW pumping regime, the same near-field and M^2 measurement method was used, for which we obtained the results shown in Fig 6-17(a). M^2_y for the Z-cavity is relatively constant at around 1.4, while the OC was moved 40-70 mm away from mirror M_3. In contrast, for the X- axis, the beam quality was strongly dependent upon the position of the OC. As the OC moves closer to mirror M_3, M^2_x is ~ 1.4, and well overlapped with M^2_y for distances shorter than 47 mm (D_4). However, the beam quality increased gradually as D_4 was pushed to 70 mm, where it almost reached a value of 5. It is to be noted that $W_{nf}x$ increased almost 2-fold at this distance as well. This is because the signal mode passing through the Brewster faces became smaller (450 μm at 50 mm (D_4) → 320 μm at 70 mm (D_4)) as shown in Figure 6-9, reducing the losses for the higher modes allowing them to oscillate. It is to be noted that embedded Gaussian $W_{nf}y$ increased almost 2-fold at this distance as D_4 increase from 40 to 70mm. This is because mode resonate in y-axis is well matched to pump field, i.e. optimizing w_l/w_p. For W_ox, the embedded Gaussian beam radius got increased when D_4 is reduced due to over filling the Brewster face. When D_4 moved beyond 55 mm, both radii are reduced as embedded Gaussian mode reduced. In which case, the X-axis allows higher mode to oscillate via Brewster face. On the other hand, output power is increased as D_4 moved away from M_3 due to

higher order modes filling in horizontal pump field, also P_{th} lowered via smaller mode size. The position of D_4 is designed to fill in the pump field in Y-axis for optimizing the overlap with pump field and also to match the intra-slab aperture for its X-axis. The approach shows that for D_4 in the range of 50-55 mm there is a good optimum in the overlap providing good beam quality, in the current case for when the thermal load is negligible. Figure 6-17(b) plots the change in maximum power and threshold with respect to change of D_4. Thresholds are observed to increase as signal mode gets bigger in the gain media when D_4 gets closer to M_3, while the output power starts to drop below D_4 = 55 mm.

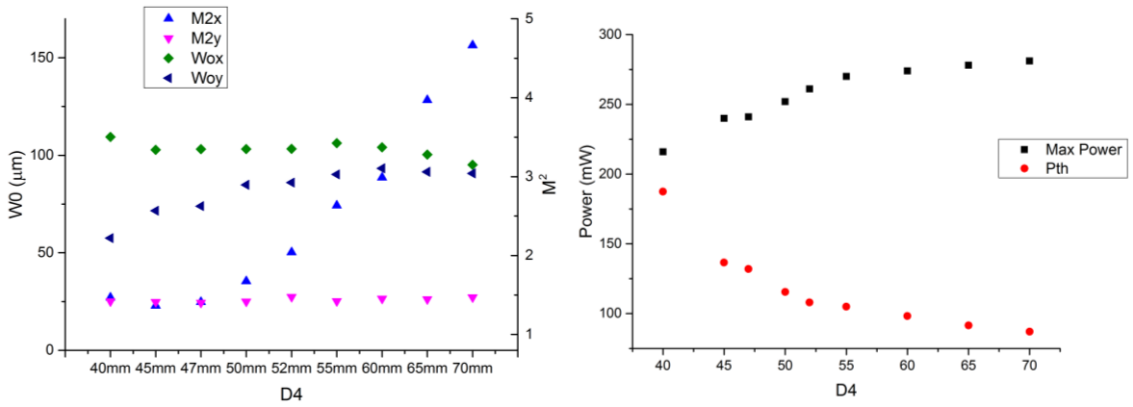

(a) (b)

Figure 6-17 (a) Measured beam waist dimensions for the major/minor axes at the output coupler (M_4), and associated beam quality, as a function of D_4, and; (b) the change in maximum output and threshold powers as a function of D_4.

6.5.2 Cryogenically-cooled Nd:YAG: 1µm performance

Z-cavity two-nodes pumping

An initial pump configuration was setup to pump the ZZ slab with a beam area of 7.8 mm X 900 µm as described in section 6.2.2, and illustrated in Fig 6-2 and Fig 6-3. The configuration of the cryogenic UHP vacuum setup is described in Chapter 3 and 5, within which the ZZ slab was affixed to the cryo-dewar cold finger, as depicted in fig 6-10. Two AR coated Suprasil 300* [22] windows provide optical access to the crystal in the vacuum chamber, the coating optimized to be <0.1 % R at 946nm, however, at 1.06 µm the theoretical AR coating reflectance (loss) was about 0.4~0.5 %R per surface, i.e. for 8 passes per cavity round-trip a total loss of 3.2~4.0 %. The laser performance for the Z-cavity is shown in Fig 6-18, for several output couplers. Another potential loss mechanism for Nd:YAG, an isotropic gain media, is a stress induced depolarization and associated losses at the Brewster faces of the ZZ slab, as discussed in

**SUPRASIL300 is a synthetic fused quartz graded with low OH contents. <1dB/km for 946nm and 1064nm*

the previous chapter. Induced birefringence for a polarised HeNe probe laser was measured while cooling the crystal at rate of ~1 K/min (i.e. it took 220 minutes to reach LNT from RT), and found to be negligible for the passive crystal.

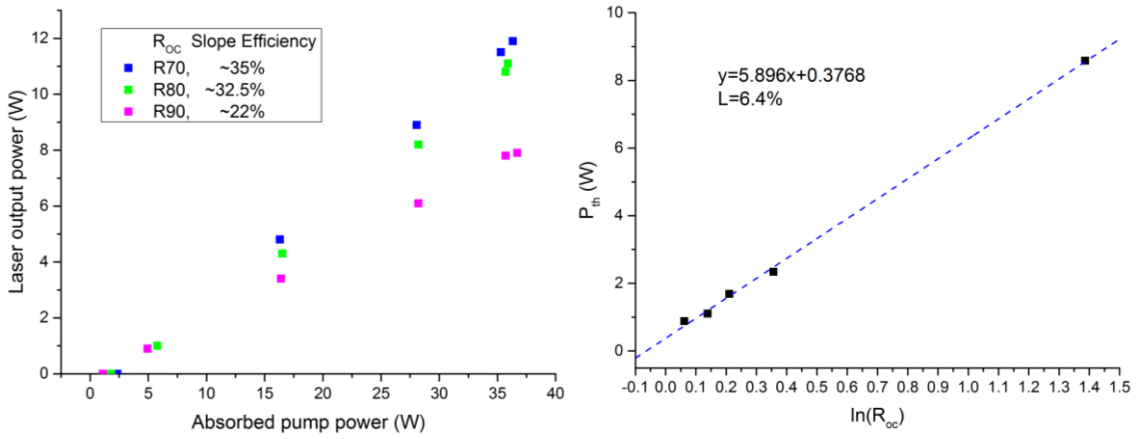

(a) (b)

Figure 6-18 Measurement of the LNT (a) 1061 nm laser performance for various OC mirrors, and (b) the round trip cavity loss using Findlay-clay analysis

In this configuration, the dominant emission is switched to 1061 nm instead of 1064 nm due to change of gain at LNT. Figure 6-18 illustrates the strong gain at 1061 nm has lowered the threshold compare to RT peak pump power. The peak laser threshold at RT with given cavity was 7.5 W (OC 70%R), which is 5 W higher than operating in cryogenic temperature. However the loss measured is 6.4 %, as plotted in Fig 6-18(b). The output power obtained with 3 different OC reflectance is plotted in Fig 6-18(a). The maximum delivered output power is 11.9 W (OC 70 %R) when 36 W is absorbed. The slope efficiency only has improved 7 % compare to QCW Z-cavity in RT and recorded lowered efficiency compare to linear cavity in RT. We found the position of anti-nodes were not in the middle of pump field (4 mm on Y-axis), as depicted in fig 6-2 and that leaves larger unextracted pump field in gain medium. This is due to asymmetric crystal cut as shown in Fig 6-4. The optimal mode path is limited via Brewster faces, that are asymmetric, internal 'aperture' and pump extraction. We have observed the position of anti-node has shifted 0.3 mm. The measurement was conducted using a camera that has installed behind ZZ slab, using a filter that can reflect unabsorbed pump light (870 nm HR). The output power was dropped more than 15 % when the alignment was made to set the anti-node position at the centre.

Z-cavity one node pumping

In an attempt to improve the overlap of the pump with the TIR node of the cavity mode, we replaced the 300 mm spherical lens, shown in Fig 6-11, with two cylindrical lenses, a schematic of the new configuration is shown in Fig 6-12. The pump beam size in the Y-axis was unchanged

because the spherical lens was replaced by an f_y = 300 mm cylindrical lens, however in the x-axis the beam width was reduced to 2.5 mm in the ZZ slab using a f_x = 100 mm cylindrical lens. Such a beam width was chosen for shrinking the overlap between a single TIR node and pump field in Y-axis. In addition, the f_x lens was mounted on a goniometer so that the pump field in crystal could be rotated slightly to optimize the overlap of the line-focus to the plane of the bouncing laser signal.

At the time that this laser experiment was conducted, i.e. replacing the 300 mm spherical lens, using two cylindrical lenses to fill in one node, the 2-node Z-cavity laser had dropped in slope efficiency to 30 %. We will discuss what had caused the loss in laser performance in the later discussion section. Nonetheless, pumping the single TIR node with the two cylindrical lenses, improved the output power slope efficiency to 35 %. Fig 6-19 also illustrates the further improvement achieved by using a goniometer to align the pump field to the plane of the bouncing cavity mode, with the efficiency increasing further from 35 % to 42 %. In total a 40 % improvement for pumping the two TIR Nodes (without the optimisation of the line focus to the cavity mode).

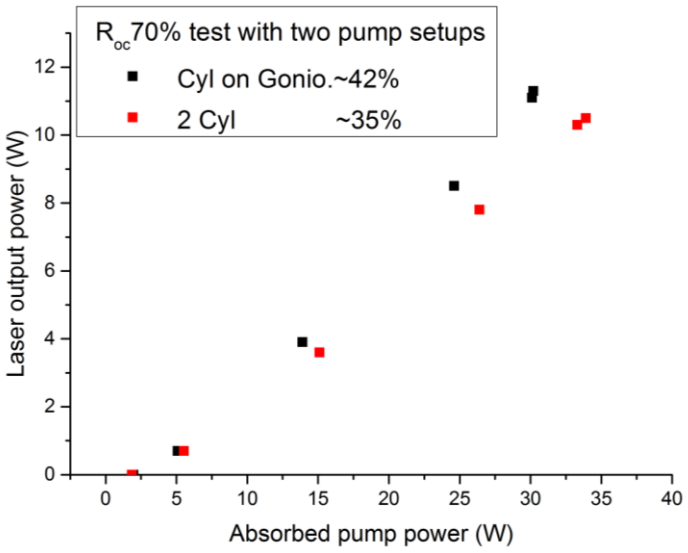

Figure 6-19 Laser performance with a 70 %R OC, and testing single TIR node pumping and goniometer line focussing alignment set-up

6.5.3 Cryogenic 946 nm operation

Two-node and one node pumping

In this final results section we report the operation of the cryogenically cooled Nd:YAG ZZ slab laser operating on the 946nm transition. Starting with the same Z-cavity design detailed in the previous section, the 1 μm mirrors were replaced with specialised dichroic HR mirrors in order to

resonate the desired 946 nm, while suppressing the high-gain emission at 1 μm. The chamber windows were the same Suprasil 300 AR coated for 946 nm.

Two pump configurations, described in the previous 1μm experimental section were trialled here with 946nm laser. Figure 6-20(a) shows the performance for the 946 nm laser with a 2 node pumping arrangement, before the goniometer was employed, and using various output coupler mirrors. Operation solely at 946 nm was confirmed via an OSA, however, in the case of cavity misalignment the output could suddenly switch to a highly multimode 1μm laser. This implies that the cavity suppression at 1 μm was marginal, which was determined to be due to a peak of ~20% in the reflectance spectrum of the turning mirrors at 1061 nm. Fortunately, with further tilting of the turning mirrors to ~20°, the 1061 nm reflectance could be tuned to a thorough of ~10 % for each turning mirrors. Therefore, the slightly larger fold-angle enhanced the loss at the dominant transition, but also improved the correction of the astigmatism coming from the Brewster cut slab. In the first configuration a maximum output power of 4.0 W was achieved with a slope efficiency of 22 %, using a 90 %R output coupler.

A better result was obtained using a single node pump configuration (Fig 6-12), with the final cylindrical lens mounted on a goniometer for optimising the pump plane with the cavity optic axis. As shown in Fig 6-20(b), using the optimum OC from the previous experiment, the slope efficiency improved to 30 % and a maximum power of 6.3 W was obtained. This was still significantly lower than expected however, and it was realised that the losses in the cavity were not as low as anticipated.

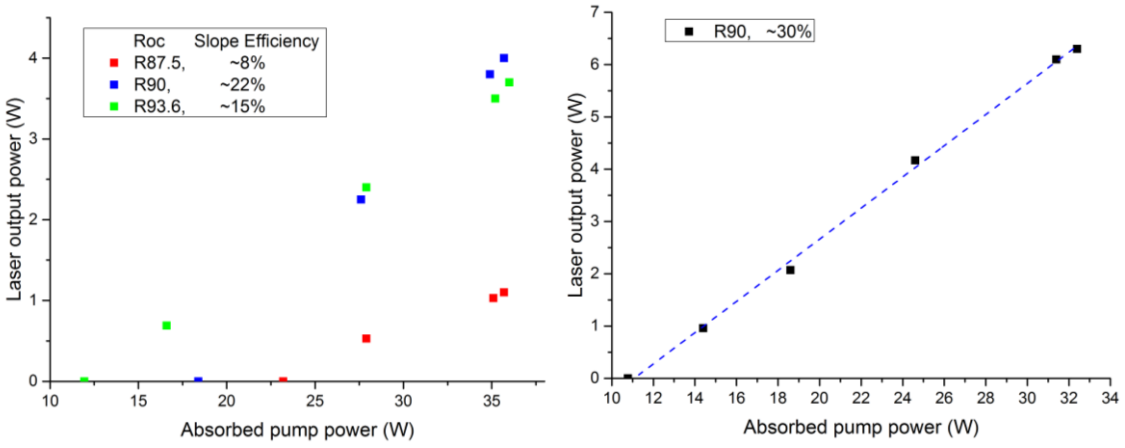

(a) (b)

Figure 6-20 Measure of cryogenic 946 nm laser performance for (a) two nodes pump and (b) single node pump, pump field levelled using goniometer

The cavity loss was re-measured via the Findlay-Clay method again, and it was discovered that the 0.67 % loss of the first configuration had increased to 3.5 % during the respective experiments. It was also found that there was significant 1 μm emission from side facet of CPFS, that may have also been extracting some of the available gain. To investigate the source of the additional losses, the vacuum chamber was re-opened and it was revealed that the AR coatings were damaged on the sides of the crystal. Two types of damage were identified, residue spots and coating deformation, assumed to be either contamination of the faces that when exposed to the high field intensities at the TIR nodes lead to damage sites.

A new second crystal was the installed and tested in the limited time available for being able to do experimental work. Both side-pumped and end pump configurations were investigated. Again the 2nd ZZ slab also experienced power degradation when operated under cryogenic conditions. This was later found to be optical damage and contamination of the side surfaces. Further experimental work was not possible with both crystals damaged, and the resolution of this issue is to be a topic of future work in the group.

The damage threshold of dielectric coatings is usually an order of magnitude lower compared to the crystal substrate [23]. Coating laser induced damage threshold values are usually measured and specified in a clean and controlled environment, which unfortunately appears to have been compromised in the vacuum chamber around the two ZZ slabs tested. Upon inspection of the damaged surfaces with a white light interferometer (Model: ZeScope by Zemtrics), it was identified that the AR coating damage/defects were of different forms, as shown in Fig 6-21 and Fig 6-22, for the 1st and 2nd crystals, respectively. The figures shows particles deposited in the lower left corner in Fig 6-21, while the other shows the morphology of a damaged region on the surface of the 2nd crystal. There is a chance that the damages were caused by chamber contamination, either from vacuum grease (used between the cold finger and the upper mount of the crystal mounting block) creeping to the clean surfaces. Or it may also be due to the fallout from burning a hole in the superinsulation (a multi-laminate of nylon and aluminium foil) lining inside the vacuum head, possibly occurring with the 1 μm cryogenic experiments and stray reflections from the Brewster faces during alignment. Similarly, it may have been a result of depolarisation of the laser beam passing through the slab, associated with thermally induced stresses in the crystal, and where the s-polarisation is then rejected by each Brewster face to be reflected off towards the wall where the burn was observed

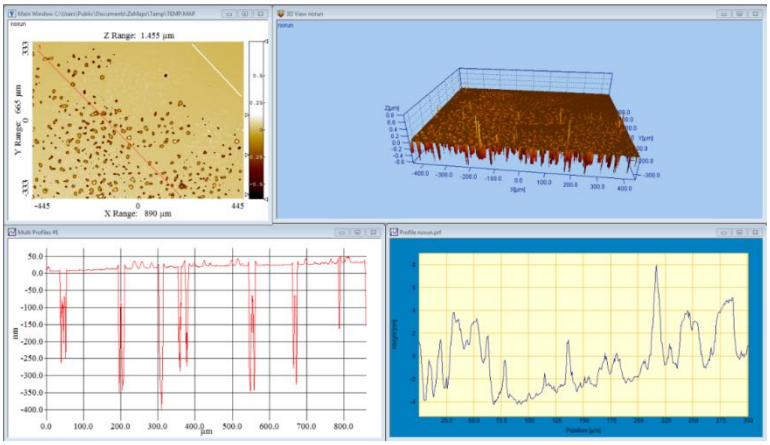

Figure 6-21 Damaged surface of 1st crystal taken by ZeScope

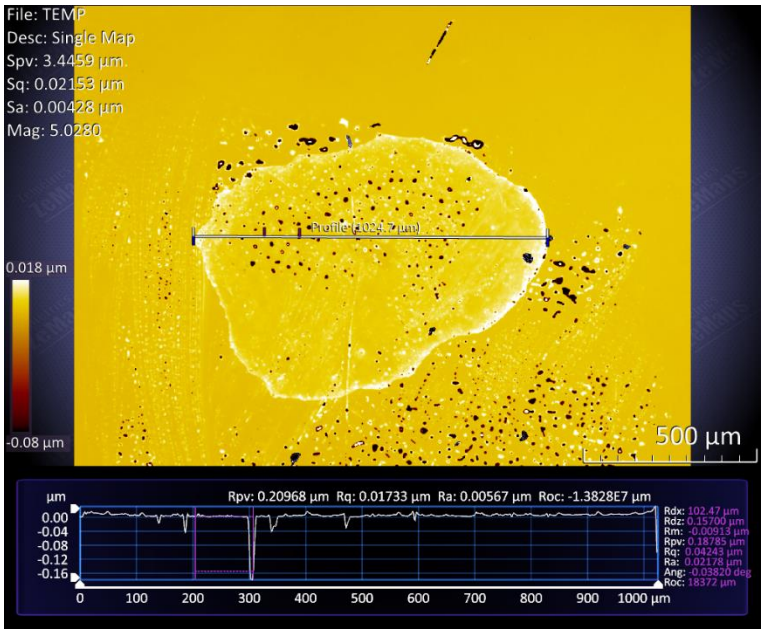

Figure 6-22 Damaged surface of 2nd crystal taken by ZeScope

6.5.4 Discussion and future work

In summary, although the output power of the 946 nm cryogenic ZZ slab laser was limited to 6.3 W, there is clearly room for improvement through ensuring that the crystal is not contaminated or damaged. New investigations will have to be undertaken to identify the root cause of the AR coating damage, whether it is a) associated with it being in high-vacuum and defects forming through leaching out of oxygen from the film; b) contamination from some organic source from within the vacuum head; c) stress induced in the films associated with the differential thermal expansion of the crystal and dielectric film; or, d) a mechanism as yet to be determined.

Thermo-mechanically induced depolarisation loss is unchanged while the slab was cooled to LNT as described in section 6.4. However due to large deviation between Cu and YAG crystal at LNT

and high Cu constraint, while it got cold forced cold pressure welded (CPW) the YAG onto Cu via indium foil. Mechanical stress depends on the temperature of material and the heat deposited. Future experimental exercises would require measuring the depolarization losses with emission polarization. The Polarization extinction ratio (PER) can be measured with output power, as only 30 % s-pol is reflected from Brewster faces pump light.

6.6 Summary

In this chapter we presented the design and implementation of a side-pumped ZZ slab laser using an in-band wavelength-locked diode-laser pump source. Starting at RT with a linear cavity configuration we were able to determine the thermal lensing behaviour of the slab under CW pumping and 1064 nm operation, leading to a maximum dioptric power of 5 m^{-1} in the Y-axis, and 1 m^{-1} in the X-axis. In QCW operation at 1 μm and RT, the efficiency of the slab laser was studied in the absence of thermal loading, where it was determined that special care for the crystal tolerances would be paramount for future designs, and optimisation of the line focus to the lowest loss optical axis of the ZZ slab produced the best performance. Using a Z-cavity to ensure the best extraction efficiency, 1 μm laser operation was tested at LNT, which was then followed by 946 nm operation. A maximum output power of 11 W for 42 % optical-optical efficiency was achieved at 1061 nm under cryogenic operation, despite non-optimal intra-cavity windows and a ~6.5% round trip loss. Unfortunately the performance of the cryogenically cooled 946 nm Nd:YAG laser, delivered only 6.3 W for a ~20 % optical to optical efficiency, which was limited by damage constraints on the ZZ slab. Optical coating damage thresholds and coating characteristics under cryogenic operation still need to be verified. The AR coatings require optimization for both cryogenic temperature and high vacuum environment. With optimised system configurations operation of the 946 nm transition at cryogenic temperatures, where it is has an essentially 4-level energetic process and comparable quantum defect to Yb:YAG, we are confident that further power scaling will be possible.

References

1. J. M. Eggleston, T. J. Kane, K. Kuhn, J. Unternahrer, and R. L. Byer, "The Slab Geometry Laser .1. Theory," IEEE Journal of Quantum Electronics 20, 289-301 (1984).

2. T.S. Rutherford, W.M. Tulloch, E.K. Gustafson, and R. L. Byer, "Edge-pumped quasi-three-level slab lasers: Design and power scaling," IEEE Journal of Quantum Electronics 36, 205-219 (2000).

3. J. L. Blows, J.M. Dawes, and J. A. Piper, "A simple, thermally-stabilized, diode ene-pumped, planar Nd:YAG laser," Optics Communications 162, 247-250 (1999).

4. K.M. Du, N.L. Wu, J.D. Xu, J. Giesekus, P. Loosen, and P. R, "Partially end-pumped Nd:YAG slab laser with a hybrid resonator," Optics Letters 23, 370-372 (1998).

5. G.J. Hulme, and W.B. Jones, "Total internal reflection face pumped laser," SPIE Proceeding 0069, Optical Design Problems in laser Systems 69, 38-45 (1975).

6. J. P. Chernoch, "High power Nd:YAG mini-FPL," Final Rep. AFAL TR-75-93 (1975).

7. T. Henningsen, "Evaluation of CaLaSOAP:Nd for use in a one joule, 30Hz laser designator," Res.Rep.72-1C1-LAMAT-R1 (1972).

8. W.B. Jones, L.M. Goldman, J.P. Chernoch, and W. S. Martin, "the mini-FPL - A face pumped laser: Concept and implementation," IEEE Journal of Quantum Electronics 8, 534 (1972).

9. J.P. Chernoch, W.S. Martin, and A. J.C, "performance characteristics of a face pumped, face cooled laser, the mini-FPL," Tech. Reps. AFAL-TR-71-3 (1971).

10. R. Beach, P. Reichert, W. Benett, B. Freitas, S. Mitchell, A. Velsko, J. Davin, and R. Solarz, "Scalable diode-end-pumping technology applied to a 100-mJ Q-switched Nd3+:YLF laser oscillator," Optics Letters 18, 1326-1328 (1993).

11. W. Seelert, H. P. Kortz, and W. M. Yen, "Excited State Absorption and 4F3/2 Lifetime shortening in Diode Pumped Nd:YLF Q-switch lasers," in Advanced Solid Stated Lasers, Optical Society of America, Santa Fe, US, (1992).

12. T. Y. Fan, G. J. Dixon, and R. L. Byer, "Efficient GaAlAs Diode-Laser-Pumped operation of Nd-YLF at 1047-nm with Intracavity Doubling to 523.6 nm," Optics Letters 11, 204-206 (1986).

13. J. Richards, and A. McInnes, "Versatile, Efficient, Diode-pumped Minature Slab Laser," Optics Letters 20, 371-373 (1995).

14. W.Koechner, *Solid-state laser engineering*, 6th edition (Springer, 2005).

15. M. Ostermeyer, D. Mudge, P. J. Veitch, and J. Munch, "Thermally induced birefringence in Nd:YAG slab lasers," Applied Optics 45, 5368-5376 (2006).

16. P. Hello, E. Durand, P. K. Fritschel, and C. N. Man, "Thermal Effects in Nd-YAG Slabs 3D Modeling and Comparison with Experiments," Journal of Modern Optics 41, 1371-1390 (1994).

17. V. Magni, "Resonators for Solid-state Lasers with Large-Volume Fundamental Mode and High Alignment Stability," Applied Optics 25, 107-117 (1986).

18. V. Magni, G. Valentini, and S. D. Silvestri, "Recent Developments in Laser Resonator Design," Optical and Quantum Electronics 23, 1105-1134 (1991).

19. A. E. Siegman, *Lasers*, University Science Books, (1986).

20. D. Mudge, M. Ostermeyer, P. J. Veitch, J. Munch, B. Middlemiss, D. J. Ottaway, and M. W. Hamilton, "Power scalable TEMOO CWNd : YAG laser with thermal lens compensation," IEEE Journal of Selected Optics in Quantum Electronics 6, 643-649 (2000).

21. D. Findlay, and R. A. Clay, "The measurement of internal losses in 4-level lasers," Physics Letters 20, 277-278 (1966).

22. "Heraeus, Suprasil 300," https://www.heraeus.com.

23. W. Koechner, *Solid state laser engineering,* 6th edition (Springer, New York, 2006).

Chapter 7:

Conclusions and future prospects

7.1 Summary of thesis

This thesis has reported research work towards cryogenic lasers in pursuit of power scaling Nd doped quasi-four-level transition and characterising its spectroscopic properties. First two introductory chapters have discussed context and motivation of the project and theoretical foundations. In *Part I: Spectroscopy of Nd Doped Crystals*, we reported absorption and emission cross section changes with respect to temperature of crystal. The measurement for various Nd doped crystals were taken experimentally. Upconversion parameters were also measured applying a Z-scan technique. *Part II: Cryogenic Lasers*, we introduced both end-pump and side-pump configuration to establish efficient $^4F_{3/2} \rightarrow {}^4I_{9/2}$ laser transition using a cryogenic cooling technique. This chapter summarise the key results and progresses of this thesis.

First part of this thesis reported the measure of spectroscopy of Nd^{3+} ion doped crystals at wide range of temperatures. In Chapter3, Nd doped YAG, GSAG, YLF and KGW were measured for its absorption and emission spectroscopy. The collected data mapped the absorption rate changes for given diode laser spectra and change of gain with respect to temperature. The peak absorption of 808 nm at LNT increased almost 3 fold compare to RT but total absorption was decreased as absorption bandwidth got shortened by 30 %. The 870 nm absorption band, which pumps the ions in ground state ($^4I_{9/2}$) directly to metastable ($^4F_{3/2}$), is capable for approaching low QD. The reduction of QD is attractive for reducing the heat dissipation during energy conversion process in lasers. The absorption bandwidth is narrow that requires tightening the pump bandwidth. The gain for Q-F-L transition also increased 2-folds when Nd:YAG crystal reached 77 K. Numerical approximations were presented by using a simple polynomial fit for the wavelength of interest. The fitted numerical value is applicable for wide range of temperature with high accuracy. Drastic spectroscopic changes showed a strong reabsorption of fluorescence for the transition from ground manifold to metastable manifold through the significantly increased peak. The zero-ground absorption increased severely hence reabsorb the fluorescence, thus reciprocity method was utilized for this transition instead of F-L method. However higher order transitions among ground manifold matched well as well as beyond cryogenic temperatures.

In Chapter 4 a Z-scan technique was introduced. It was to determine ETU parameter for Nd doped crystals. ETU of Nd^{3+} ion doped YAG crystal was tested for its temperature dependence and also by its dopant concentration dependencies. We observed that the ETU coefficient is dependent to the doping concentration and temperature of crystal. The dependencies are reported by a function of dopant concentration, 6.5 X $10^{-19}cm^3/s/at.\%$ and with function of temperature, 0.4 $\%K^{-1}$. The ETU parameter of other Nd doped crystals such as KGdW, YLF, YVO4, and GdVO4 were also tested applying a same technique. Laser performance was modelled where the ETU has been included as an adding non-radiative decay for excited ions in metastable level. The simulation showed that ETU has minimal effect when resonator operates in CW, generating for the dominant 4-level transition. However ETU becomes significant for Q-F-L transition and for the systems that requires high population inversion as it's proportional to the population in metastable. YAG crystal confirmed its prevalence in the solid-state laser operation in both CW and highly inverted media such as high gain amplifier or Q-switched lasers.

Second part of this thesis we reported an investigation of cryogenic laser operation. Both end-pump and side-pump configuration approach was tested with crystals cooled to cryogenic temperature. Cryogenic Q-F-L laser capitalized lower lasing threshold and better slope efficiency. Moreover we discussed the spectroscopic considerations for the absorption band enhancement and higher gain of Q-F-L transition and the devoid of thermal effects within crystal.

We investigated an end-pumped laser system which used Nd:YAG Brewster face as assessing laser signal. With 946 nm oscillate with 4 % duty cycle QCW, laser demonstrated 60 % slope efficiency and 50 % optical to optical efficiency with respect to the 808 nm absorbed pump. The beam quality factor, M^2 was near or less than 1.25 in both X and Y axis. The maximum CW power measured from this cryogenic end-pump system was limited at 3.8 W. The maximum power was limited by modal instability at higher pump power. Both crystal end was AR coated to minimize the cavity loss and to optimize pump light. Optical damages on its AR coatings were found during the experiment, and also had experienced depolarization loss raised 10-folds due to mechanical constrained during cooling progress. The slab was pumped by wavelength-locked 869 nm diode bar, aimed to minimize QD nearly 8 %. Output power was limited by pump power establishing 5.5 W CW output power with 50 % slope efficiency for this geometry. We demonstrated a cavity gain comparison between the dominant four-Level-transition to weaker Q-F-L-transition, the estimation is to compare the necessary resonator gain suppression at LNT. By introducing V-cavity and Z-cavity and with superior mirror coatings the Q-F-L has achieved lower laser threshold.

Associated heat load for end-pump & side-pump systems were simulated. The model used temperature dependent thermo-mechanical parameters and spectroscopy parameters because of

its temperature dependences at cryogenic temperature. The thermally induced lens changes the cavity parameter, hence alters cavity stability and mode size in the gain media. The dioptric power was traced for Zigzag laser in RT according to the pump power absorption. The real-time beam quality measurement was demonstrated, it observed the change of beam waist and beam quality in real time of which accounted modal changes within crystal.

Chapter 6 presented a series of laser experiment using a ZZ side-pump Nd:YAG crystal. The demonstration was conducted for both cryogenic and RT operations. The test was performed for dominant 1 μm transition and 946 nm transition. The 1 μm laser performance was restricted due to additional loss from windows. The optical system for pump diode was configured to fill in a single node and two nodes within side-pump facets. With two-node pumping configuration, there was an wasted area where pump was inefficiently extract out. The single-node pump configuration induced improvement of the extraction efficiency. With a single–node, well matched pump and signal mode have improved the laser performance, resulting a higher output power and better slope efficiency. No parasitic lasing was observed during laser operation but later presented when resonator was misaligned. The parasitic was spotted via the area where optical damages presented on AR coatings. The coating damages have decreased the gain suppression under highly excited gain. This is due to increase of 1 μm gain being allowed in Fabry - Perot resonator. VBG was added in our Nd:YAG laser system in order to lock the pump diode spectra and to maximize the total absorption when crystal is cold. The total absorption of conventional diode, which has ~3 nm FWHM, was only 45 % at LNT due to narrow absorption band of Z1 → R2 transition (868 nm). The VBG demonstrated 90 % of absorption by locking the pump spectra at 868.4nm with FWHM of 0.3 nm. The total absorption has increased to 90 % by heating the device to 70°C in order to shift the locking wavelength at 868.51 nm. The heat absorbed in VBG changes refractive index of device and hence changes the grating period. The quantum defect by using this pump spectra has dropped significantly for emitting Q-F-L transition. However, its matching sensitivity would become an issue when high pump power is launched, increasing thermal load to both VBG and laser crystal hence shift the spectral peak of both pump light and crystal absorption. Further power scaling was limited by the dielectric coating damages and the optical contamination within cryogenic vacuum system. We found optical damage for both rod and slab crystal. Two different damage types were discussed, a catastrophic damage and field of pit holes and redepositions around pump field. LIDT (laser induced damage threshold) of coating became lower at cryogenic temperature. This is due to change of thermo-mechanical stress between dielectric film and the crystal substrate. The stress between different thermal expansion during cooling and laser operating has lower film strength [1]. The stress can be reduced by choosing a coating material that matches thermal properties to the substrate or use a

single layer coating as Mikami has referred in [2]. With cryostat operated in high vacuum condition, the loss kept increasing and got worse over time of laser operation. Further investigations of the contamination and damages are being conducted by colleague.

In conclusion, overall presented work summarizes the current progress towards cryogenic high power quasi-four-level laser. The reported spectroscopy data proved the benefits of cryogenic operation and are very useful resources toward laser design. Despite the power scaling limitations due to round-trip losses caused by optical damages and contaminations, we have gained a better understanding of the cryogenic system and ultra-high-vacuum environment. Once the artifect is known and removed from cryogenic system we predict that it should be possible to improve the system efficiency and reach further power scaling.

7.2 Future works

7.2.1 Further Power scaling of quasi-four-level transition

We have discussed power scaling strategy of Q-F-L cryogenic laser in this thesis. Although both end-pump and side-pump configurations have been demonstrated, further power scaling requires better understanding of vacuum operation and thermo-characteristics of gain crystal when it reached cryogenic temperature. For the laser operation, the first step is to find new AR coatings that can provide high LIDT in LNT. AR coating on either configuration, where pump light or laser signal passes, is mandatory to accommodate high efficiency for this non-dominant gain. ZZ slab approach has presented relatively lower pump extraction efficiency. It is expected that side pump configuration experiences lower efficiency. However using the Brewster face as signal assess plane, it does not require AR coating for laser signal hence LIDT has minimal effect. Hence we recommend Brewster plane for further power scaling. Upon successful demonstration of single node pump, the extended version of ZZ slab should allow the multi nodes pump such as 4 nodes or 8 nodes per side.

ETU parameter of 1 at.% Nd:YAG was reported for temperature range of 300 K - 450 K. The result showed the parameter is proportional to temperature and have detrimental effect depend on pump ‘purity’. Upon successful demonstration of VBG, it should follow the effect of ETU against highly effective absorbance. We also discussed the effect of ETU towards laser performance of low gain CW lasers or systems requiring high population inversion. As we have not measured the ETU at cryogenic temperature ETU parameters were not included in actual laser model. Further ETU measurements via Z-scan for cryogenic temperature should give insight into transitions between energy levels at cryogenic temperature and provide more descriptive laser design. There

are plans for future experiment using automated Z-scan setups, leading time efficient data collection and minimize a man-make error.

In-band pump system, such as 869 nm of Nd:YAG absorption transition, allows smaller QD. Q-F-L transition pumped by 869 nm has less than 10 % of QD which is well equivalent to Yb^{3+} doped gain media. VBG was obtained as an external device to lock the pump wavelength. Due to narrow absorption band, shifting of 0.1 nm pump peak spectra dropped absorption by 10 % for Nd:YAG crystal. Other Nd^{3+} doped crystals have similar behaviour as the band is very narrow and closely depend on temperature. The VBG's central peak should be carefully chosen prior to choose a laser crystal. The device also requires sensible peak wavelength tuning via temperature control for best absorption match. This is adequate method of tuning 0.1nm peak since VBG makers usually provide manufacturing tolerance [3].

End pumping configuration establishes highly efficient, low lasing threshold compare to side-pumping system. We suggest using a lower doping concentrated crystal as low as 0.3 at.% for end-pump configuration. Lower dopant promises lower thermal load at the pump facet hence weaker thermal lens is induced to the cavity, and upconversion transition has less effect to the system if there is any. End-pumping configuration also incorporated well for Q-switch operation near perfect beam quality. Q-switching of Q-F-L in RT is inefficient due to reabsorption losses however the population of lower energy level is near zero in LNT leaves negligible reabsorption losses. The cavity dumping is suggested for the Q-switch operation of cryogenic system. Cavity dumping uses optical modulating switch, such as Pockel's cell (Electo-optic modulator) and extract out intense short pulse from resonator. It is suitable for wide range of repetition rate, from 1 Hz to 600 kHz regime [4]. The pulse duration is stable for this operation since the energy stored in crystal only circulates the resonator when modulator couples the cavity. The modulator quickly decouple the resonator hence the light that being circulated in resonator extracts out within a round-trip. The pulse duration is therefore stable as long as keeping the same coupling time, where modulation is allowed. Further investigation is expected measuring the thermos-optical parameters such as thermal conductivity. The thermo-optical parameters are known as impurity dependent and usually more conductive for lower concentration [5]. Using a lower dopant concentrated crystal builds a better heat dissipative media however it would give a more accurate information by measure and compare the thermo-optical parameters.

7.2.2 DUV cryogenic lasers

The most effective $^4F_{3/2} \rightarrow {}^4I_{9/2}$ transition of Nd:YAG is 946 nm in both cryogenic or room temperature. We can achieve DUV (deep ultra violet) via the harmonic generation of 946 nm,

along with 266 nm quadrupling the fundamental wavelength, 1064 nm of Nd:YAG. Laser spectra under 266 nm was usually considered as field of Excimer laser. Excimer has been widely used in many field of applications, in industry and medical use. However it requires regular gas replacement, which assessing fluorine and chlorine, and periodic gas chamber refurbishment [6]. The vast approach in quasi-four-level transitions opens up new spectral window around ~900 nm and the ones below 266 nm. The raise of emission peaks at 885 nm and 892 nm in LNT allows not only a 236 nm (quadruple of 946 nm) but also 222 nm (quadruple of 885 nm or 892 nm) and are capable of replacing some existing excimer laser spectra such as KrF, 248 nm or KrCl, 222 nm. At the time of writing, we have been able to extend the study of cryogenic laser by our colleagues. The successor of the project will probably follow up the demonstration of DUV generation.

In the long term, the approach of cryogenic laser finds a variety of novel applications. The power scaling of novel wavelength where the gain was previously inaccessible or inefficient in room temperature, is available.

References

1. H. Wang, W. L. Zhang, and H. B. He, "Laser-induced damage behaviors of antireflective coatings at cryogenic condition," Applied Optics 51, 8687-8692 (2012).

2. K. Mikami, S. Motokoshi, T. Somekawa, T. Jitsuno, M. Fujita, and K. A. Tanaka, "Temperature dependence of laser-induced damage threshold of optical coatings at different pulse widths," Optics Express 21, 28719-28728 (2013).

3. Optigrate, http://www.optigrate.com/BragGrate_Mirror.html2016.

4. Gooch&Housego, LightGate Series, http://www.goochandhousego.com/product-categories/pockels-cells/

5. R. L. Aggarwal, D. J. Ripin, J. R. Ochoa, and T. Y. Fan, "Measurement of thermo-optic properties of Y3Al5O12, Lu3Al5O12, YAlO(3), LiYF4, LiLuF4, BaY2F8, KGd(WO4)(2), and KY(WO4)(2) laser crystals in the 80-300 K temperature range," Journal of Applied Physics 98 (2005).

6. D. Basting, and G. Marowsky, *Excimer Laser Technology,* Springer Science & Business Media, (2005).

Appendix A

Absorption and emission spectroscopy of laser crystals at various temperature

This appendix provides series of spectroscopic data associated with each crystal and the respective temperatures. The following figures show the absorption and emission cross section of chosen crystals. The crystal and dopants are listed as follow:

Nd:YAG 1at.%

Nd:GSAG 1at.%

Nd:YLF 0.5at.% (c-cut)

Nd:KGW 3at.% for E//Nm and E//Np (Ng cut) and 4at.% for E//Ng (Nm cut)

Nd:YVO4 0.5at.% (c-cut)

Nd:GdVO4 0.5at.% (c-cut)

A.1 Absorption cross section of Nd:YAG

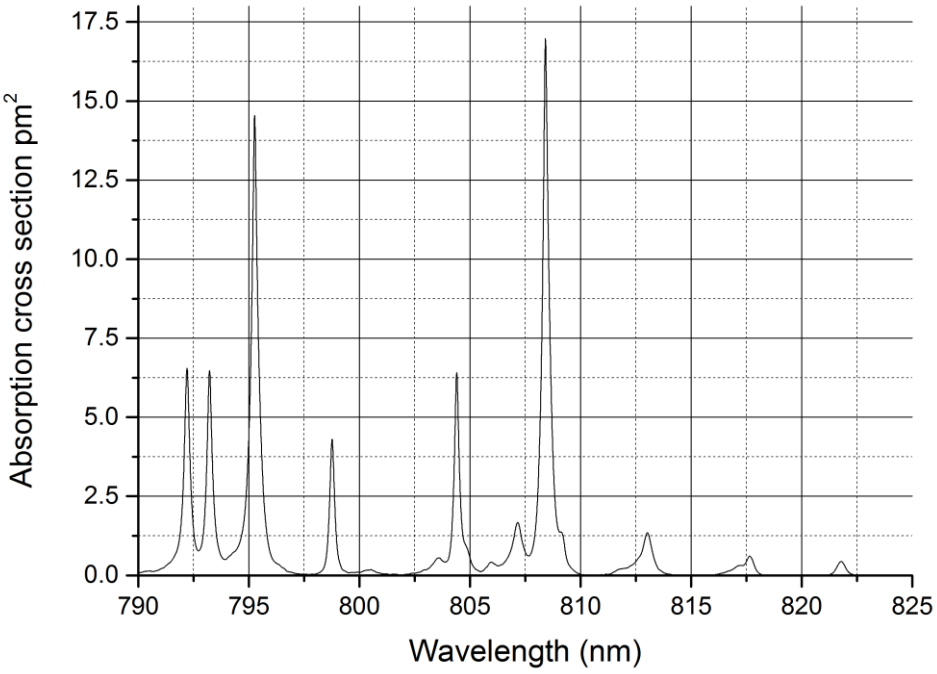

Figure A-1 Absorption cross section of Nd:YAG at 77K

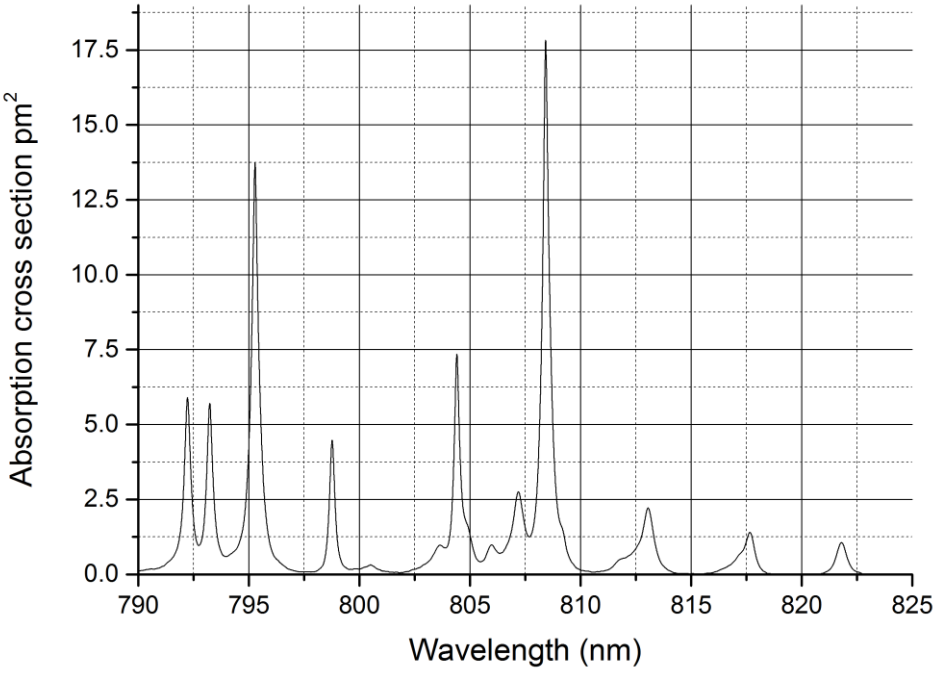

Figure A-2 Absorption cross section of Nd:YAG at 109K

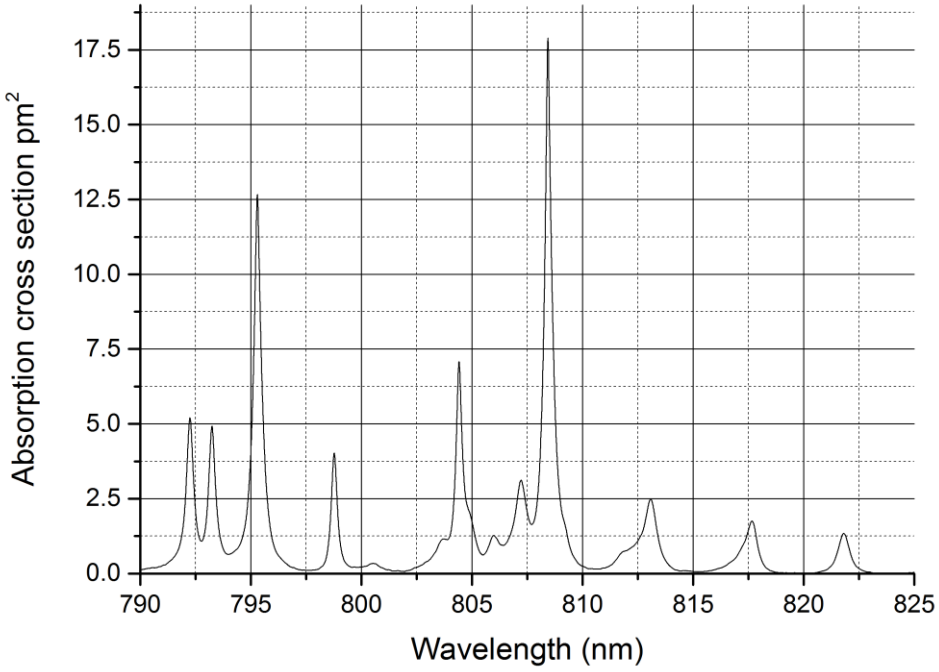

Figure A-3 Absorption cross section of Nd:YAG at 129K

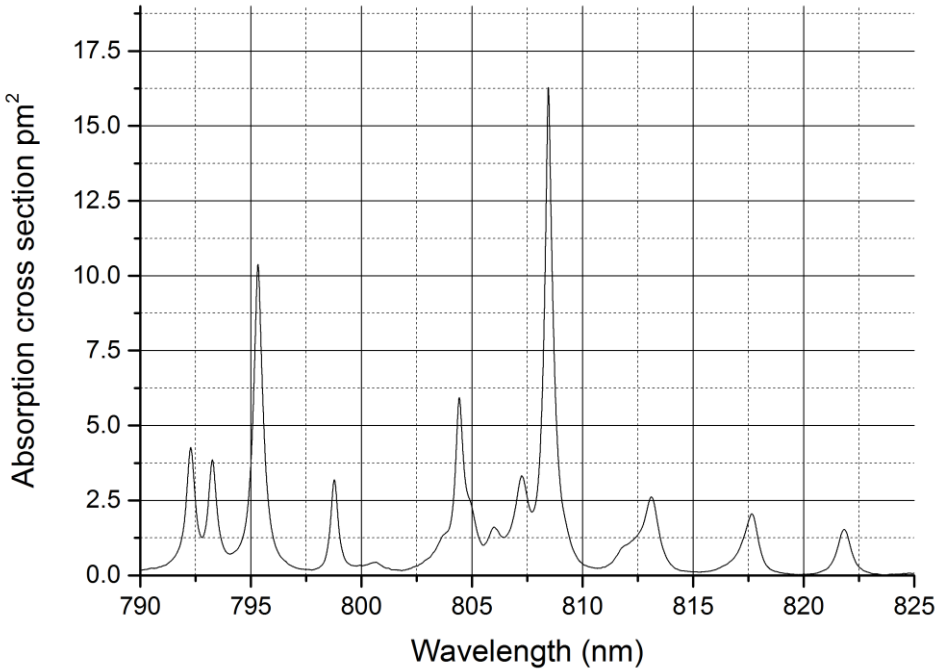

Figure A-4 Absorption cross section of Nd:YAG at 157K

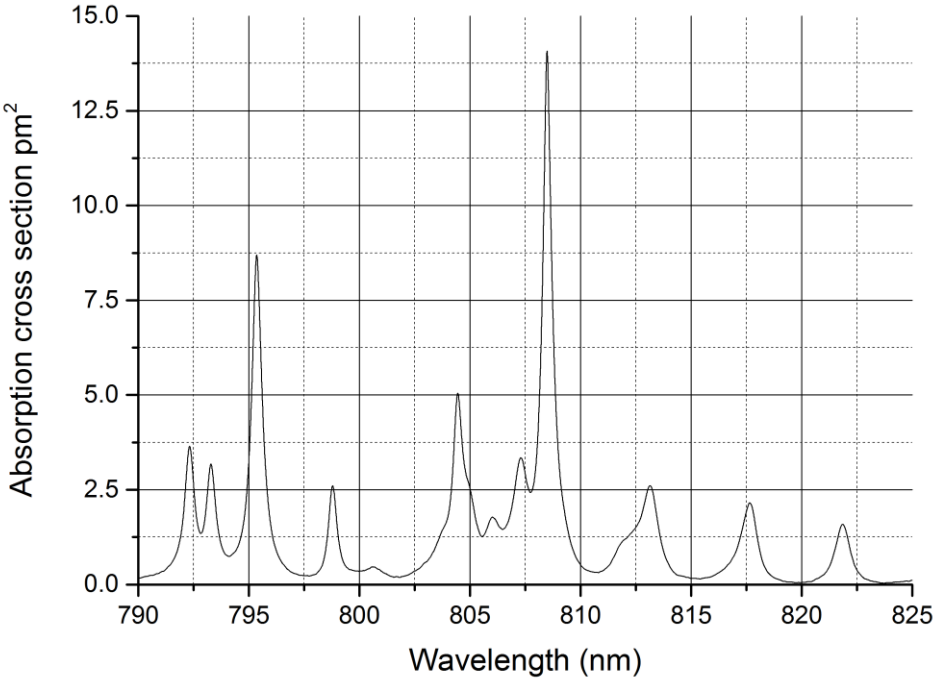

1

Figure A-5 Absorption cross section of Nd:YAG at 186K

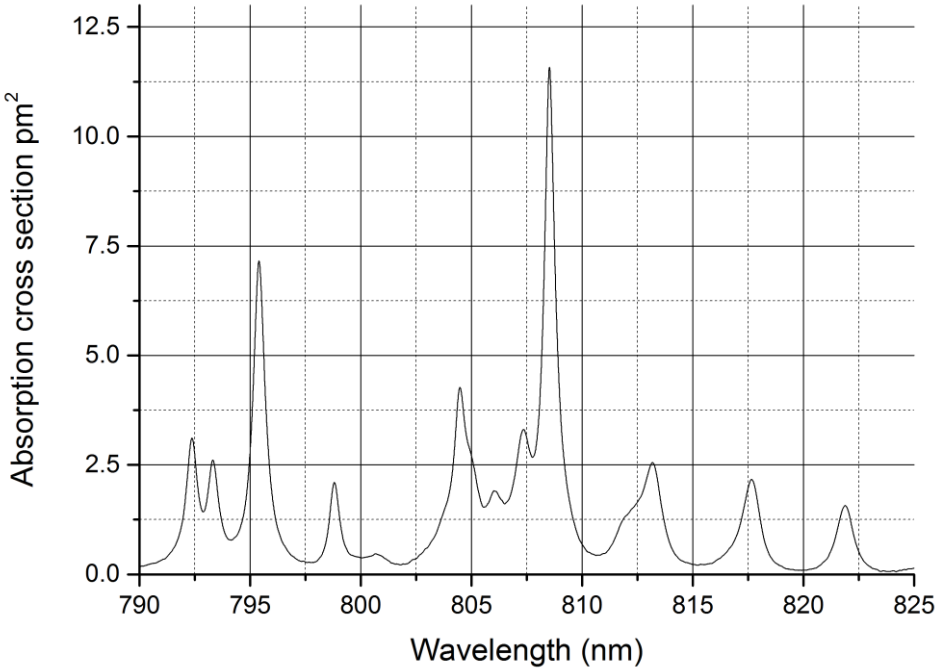

Figure A-6 Absorption cross section of Nd:YAG at 211K

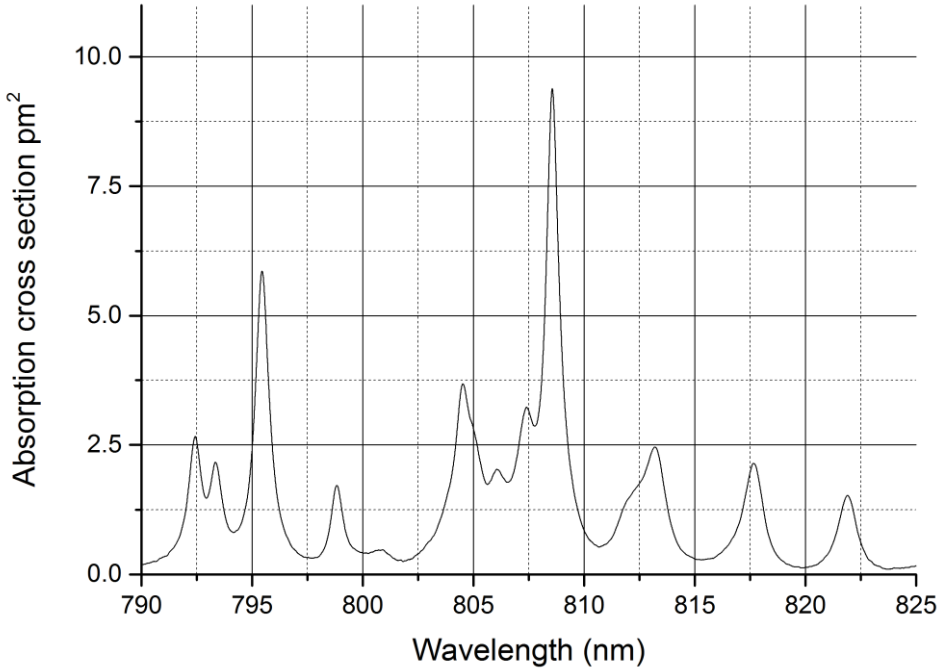

Figure A-7 Absorption cross section of Nd:YAG at 244K

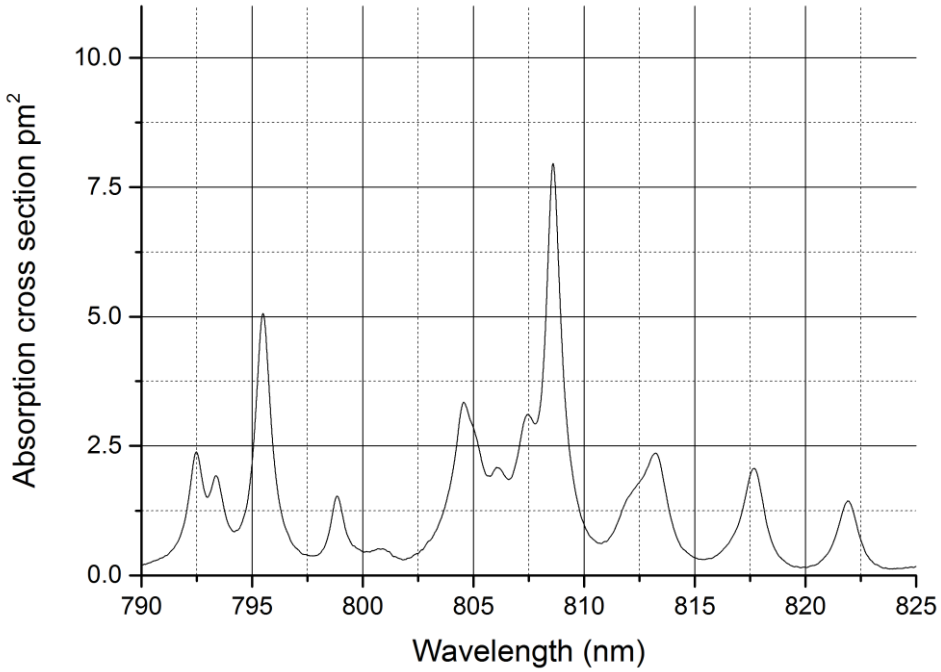

Figure A-7 Absorption cross section of Nd:YAG at 273K

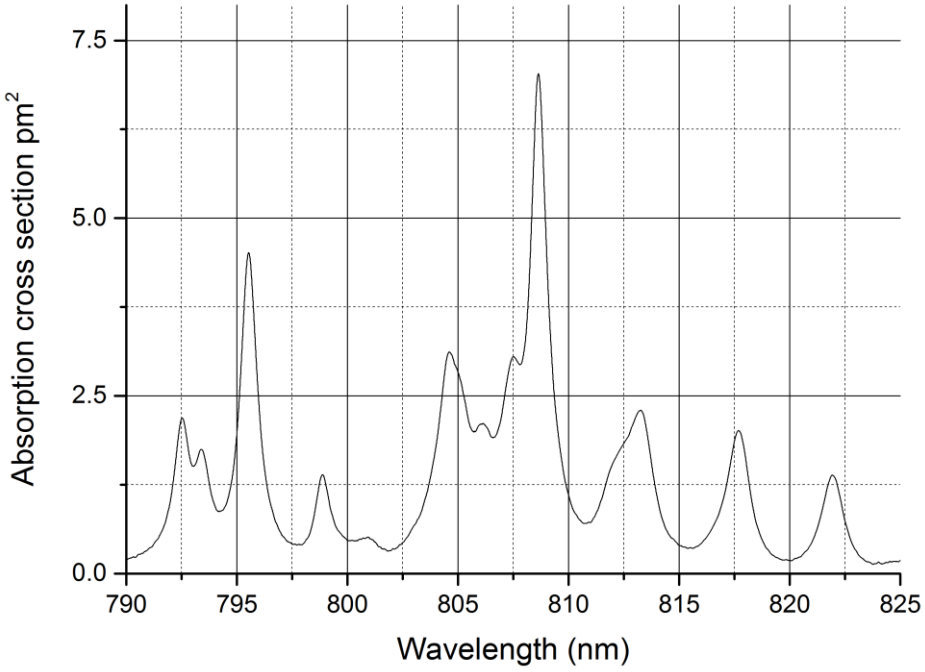

Figure A-8 Absorption cross section of Nd:YAG at 296K

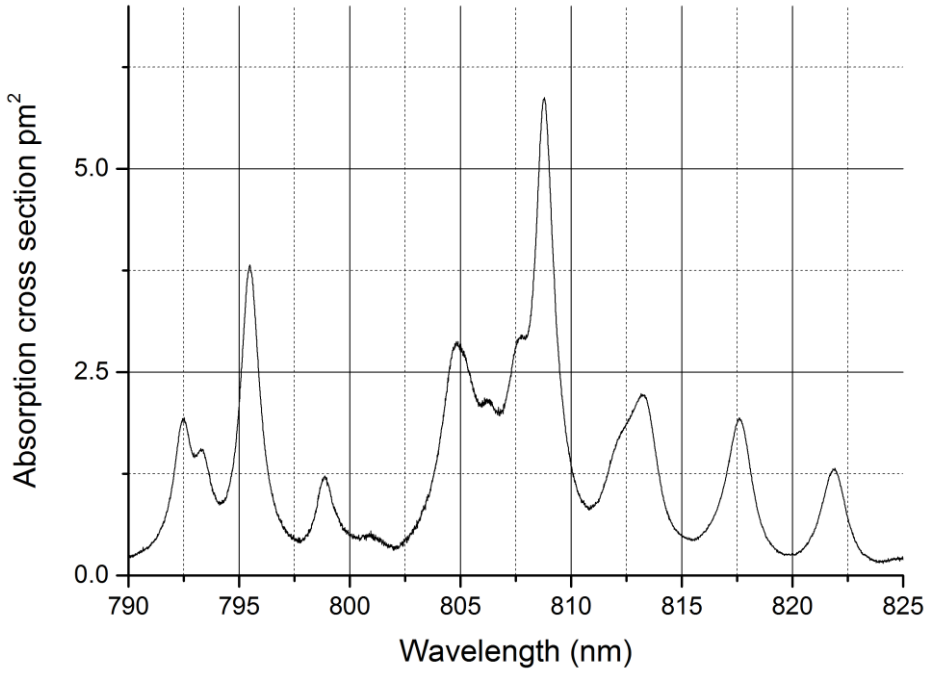

Figure A-9 Absorption cross section of Nd:YAG at 330K

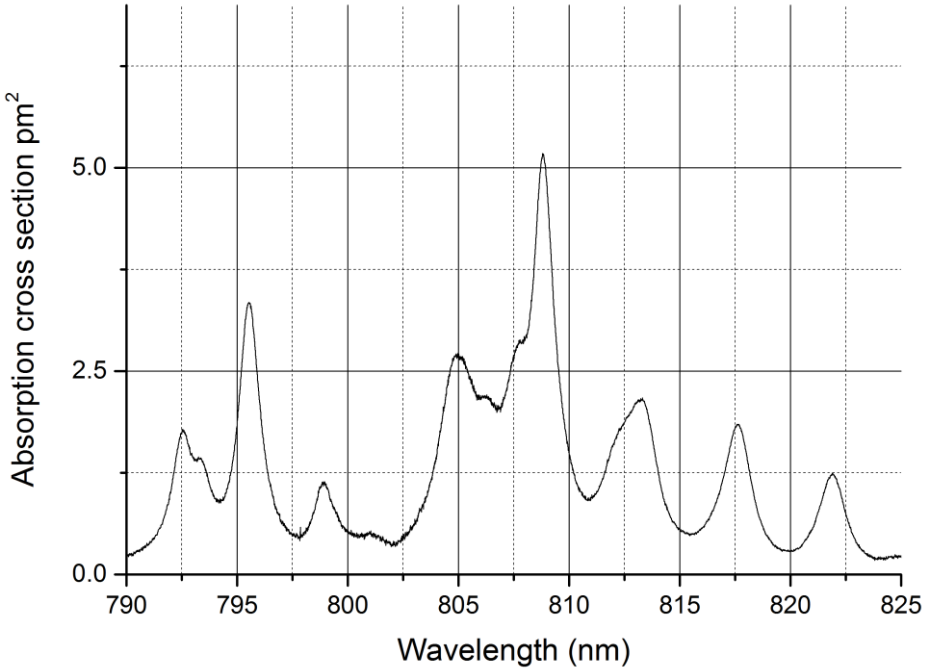

Figure A-10 Absorption cross section of Nd:YAG at 360K

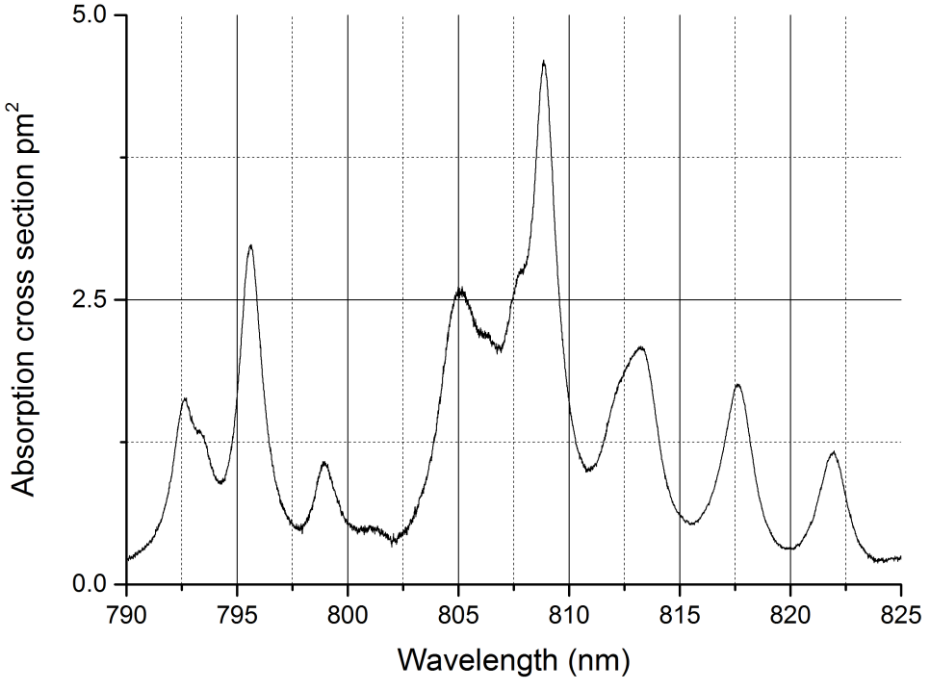

Figure A-11 Absorption cross section of Nd:YAG at 390K

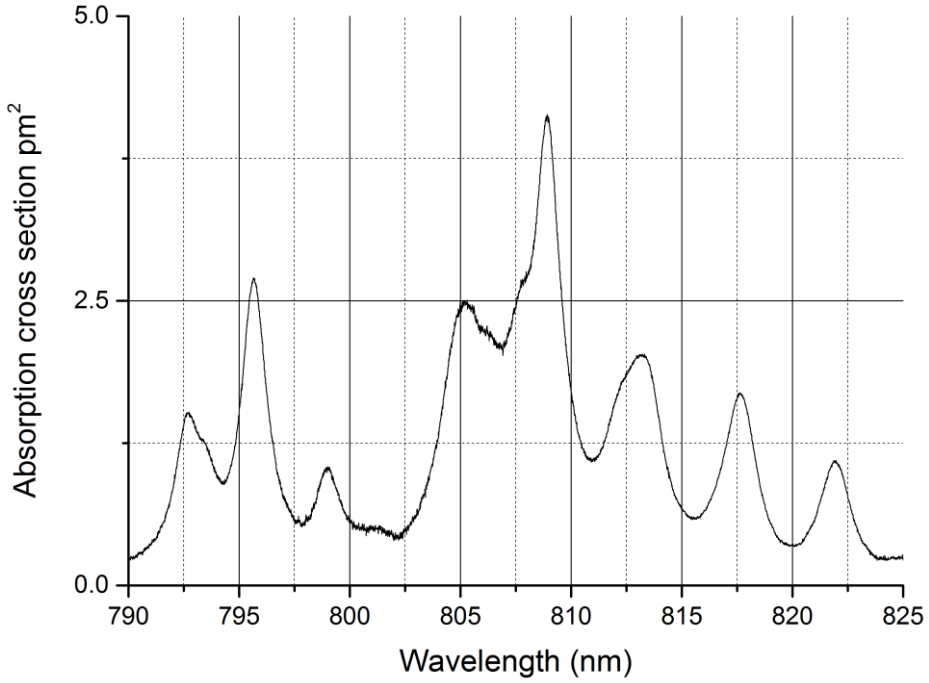

Figure A-12 Absorption cross section of Nd:YAG at 420K

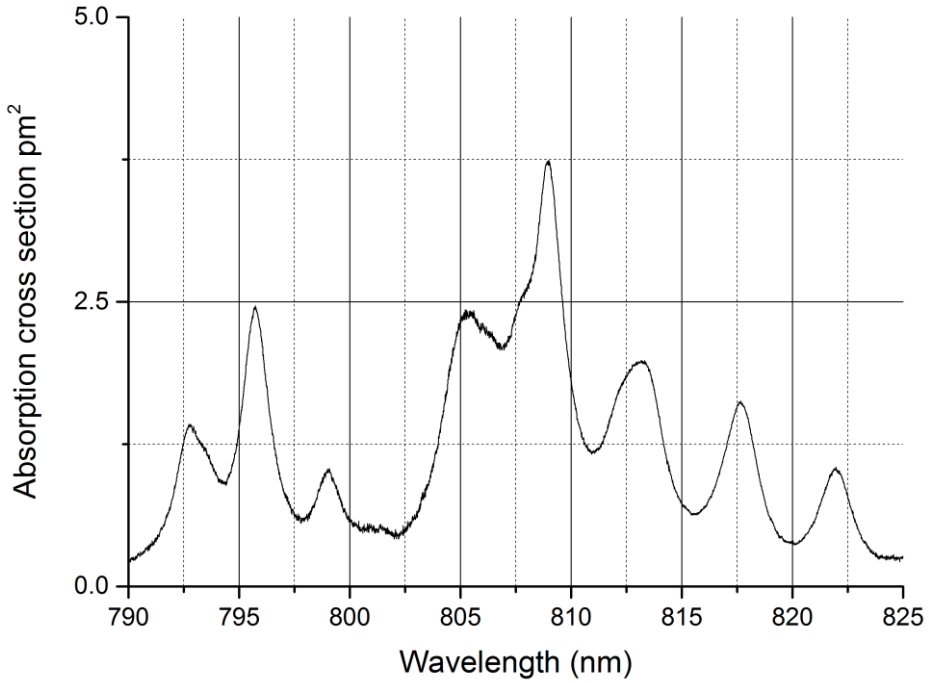

Figure A-13 Absorption cross section of Nd:YAG at 450K

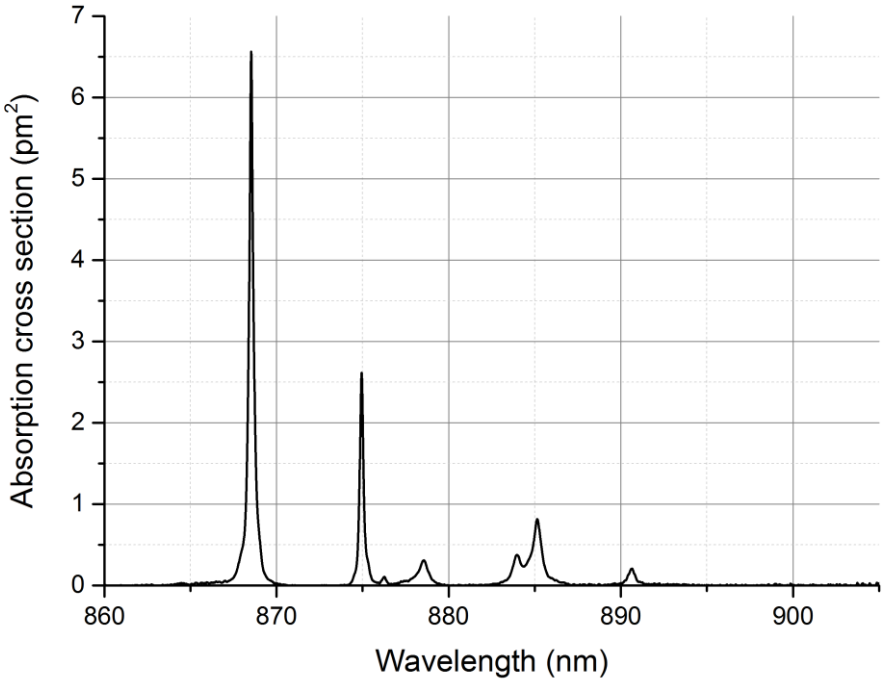

Figure A-14 Absorption cross section of Nd:YAG, 860-905nm, at 77K

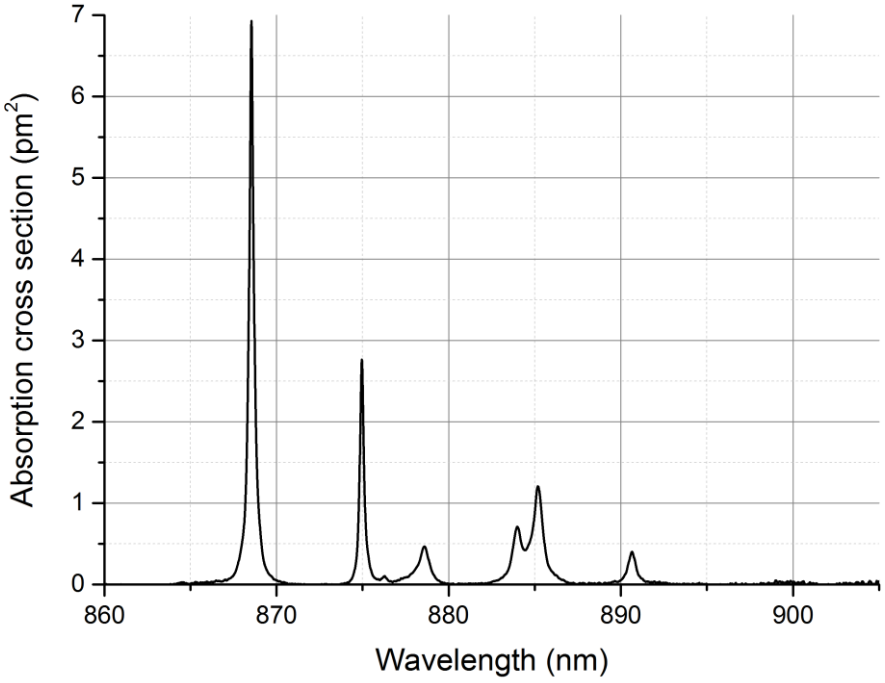

Figure A-15 Absorption cross section of Nd:YAG, 860-905nm, at 100K

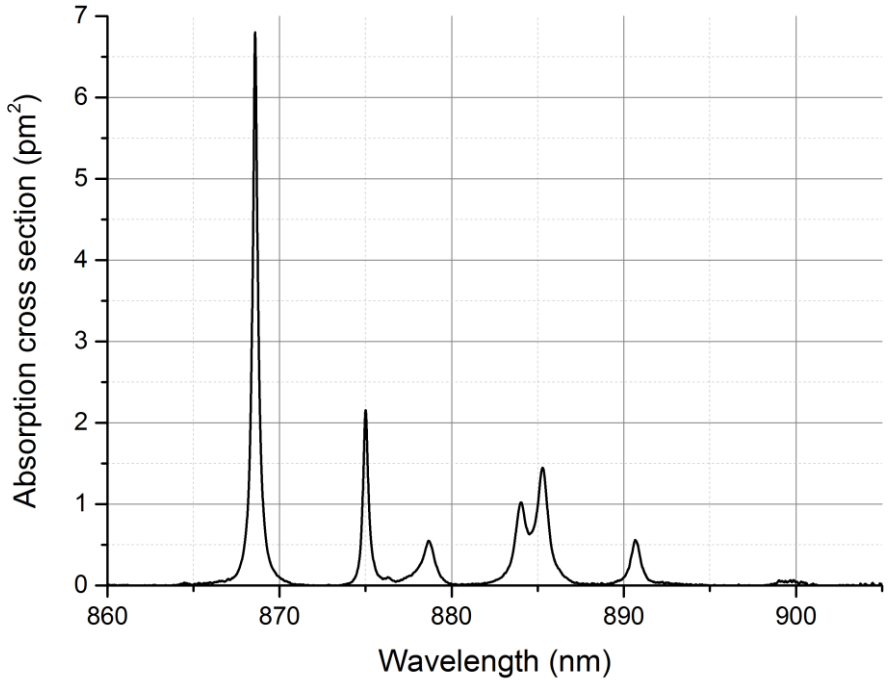

Figure A-16 Absorption cross section of Nd:YAG, 860-905nm, at 137K

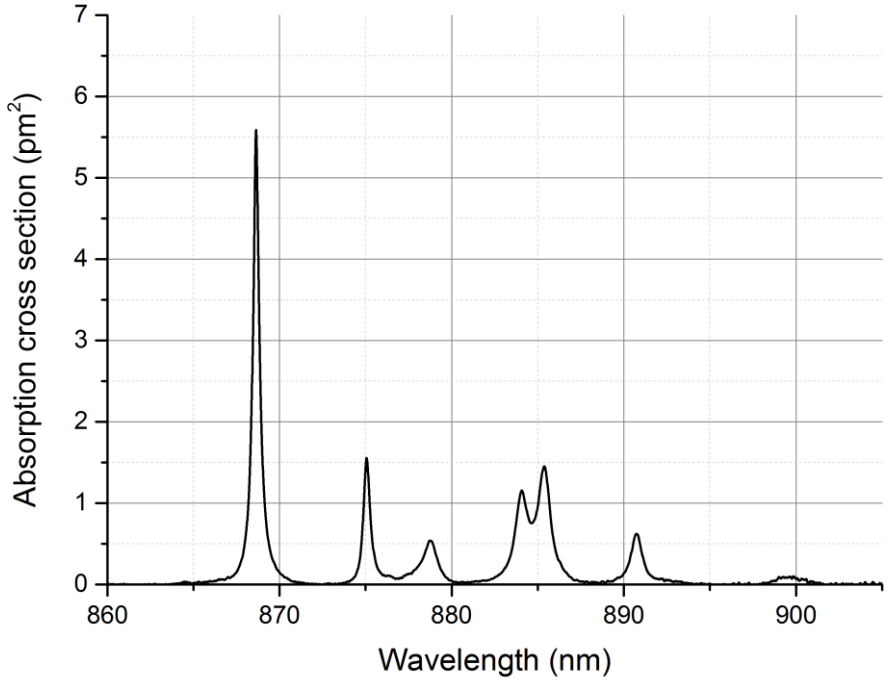

Figure A-17 Absorption cross section of Nd:YAG, 860-905nm, at 175K

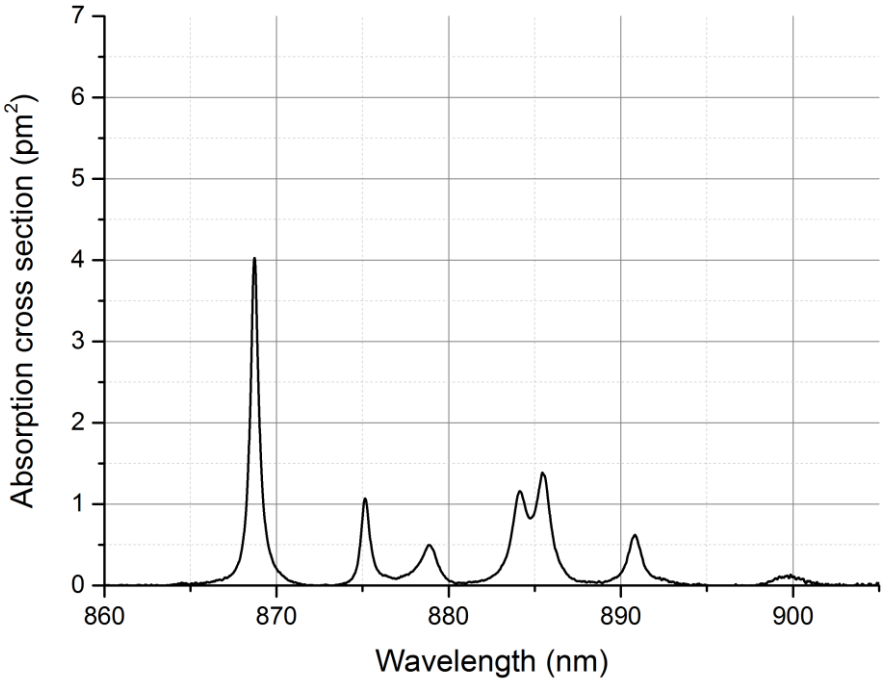

Figure A-18 Absorption cross section of Nd:YAG, 860-905nm, at 214K

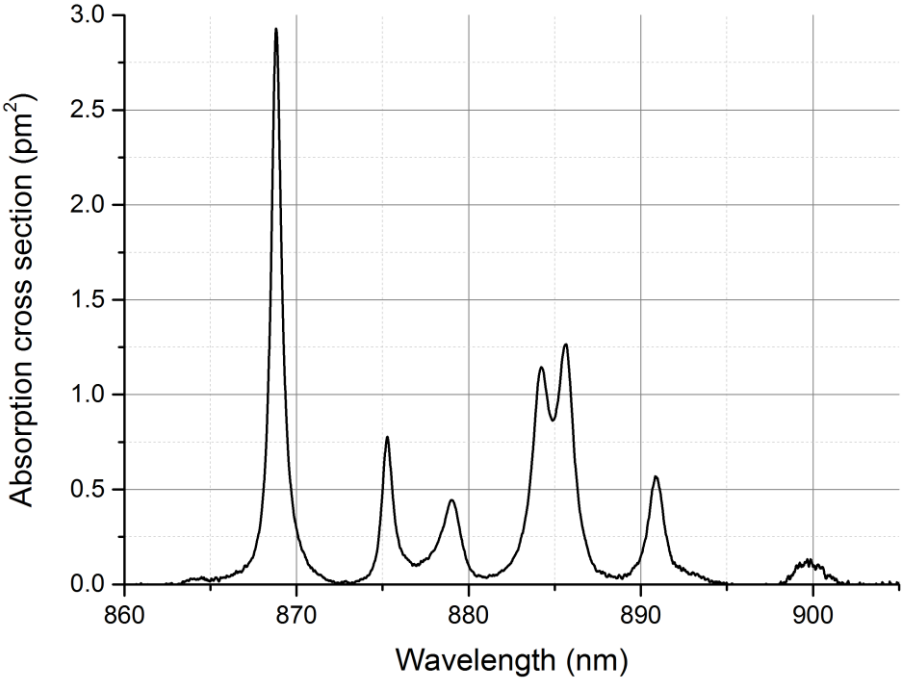

Figure A-19 Absorption cross section of Nd:YAG, 860-905nm, at 262K

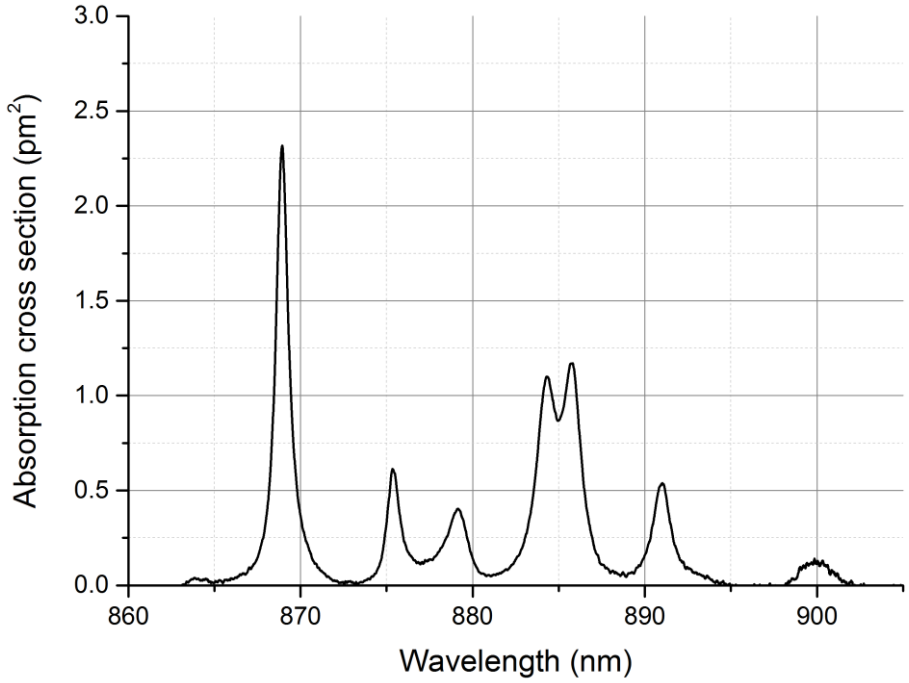

Figure A-20 Absorption cross section of Nd:YAG, 860-905nm, at 296K

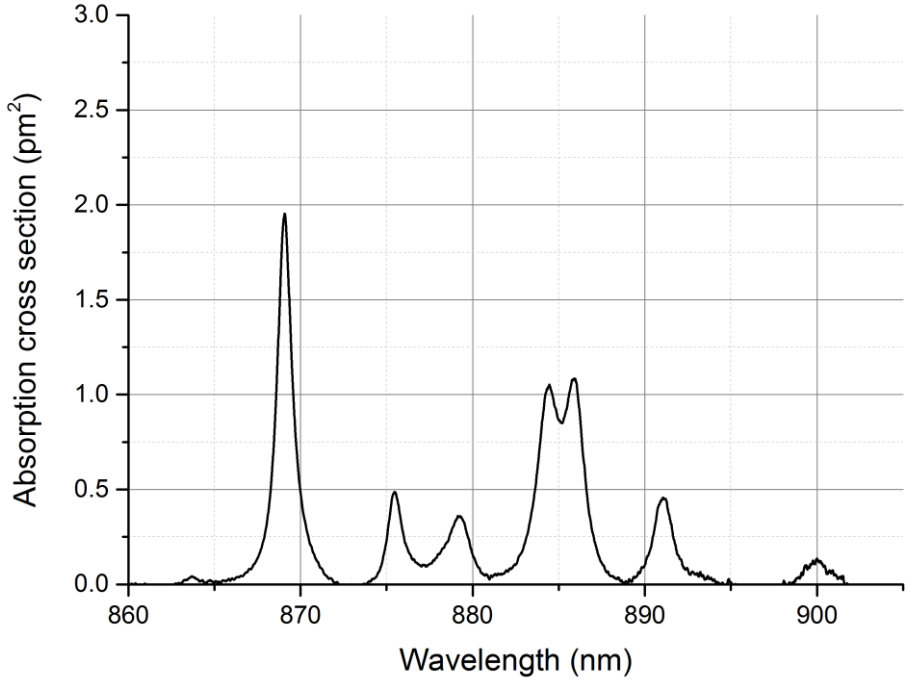

Figure A-21 Absorption cross section of Nd:YAG, 860-905nm, at 330K

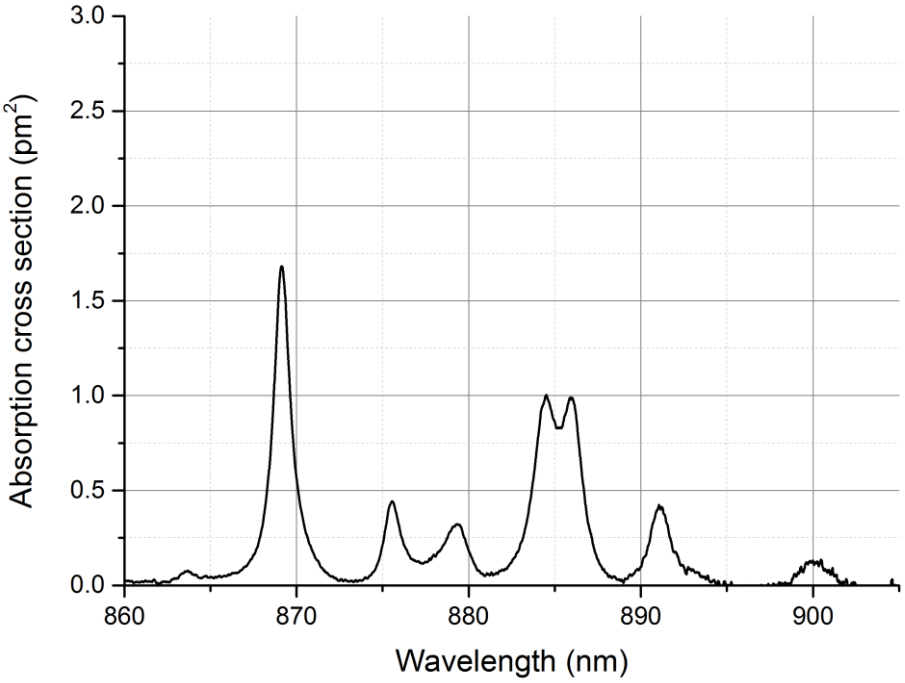

Figure A-22 Absorption cross section of Nd:YAG, 860-905nm, at 360K

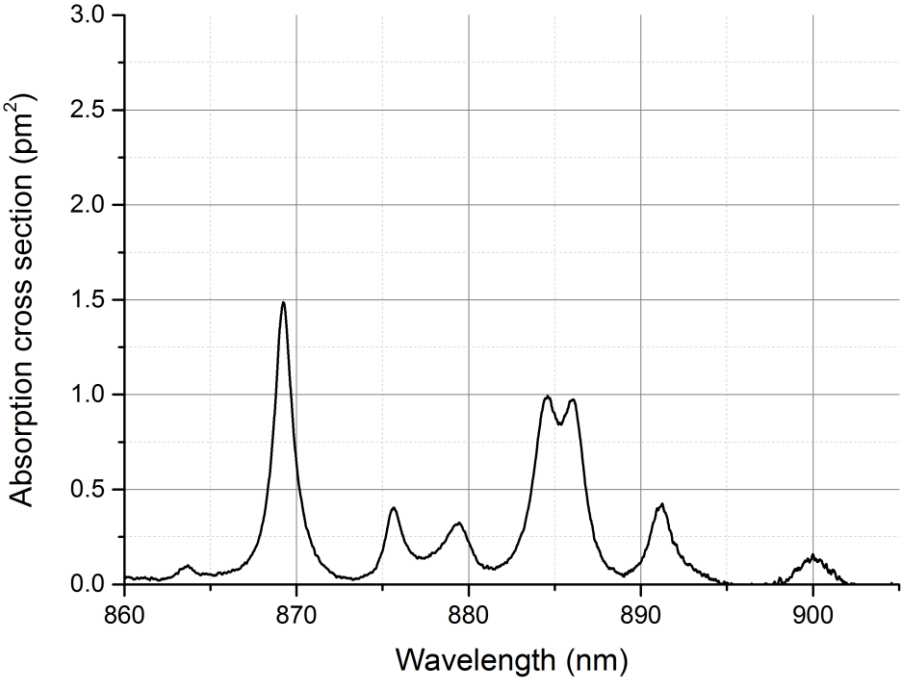

Figure A-23 Absorption cross section of Nd:YAG, 860-905nm, at 390K

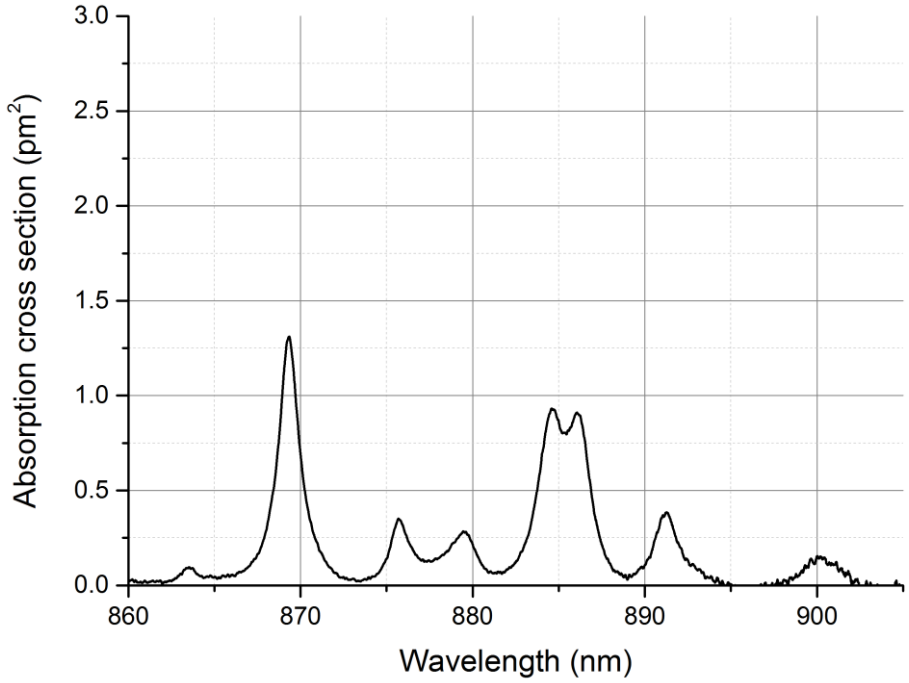

Figure A-24 Absorption cross section of Nd:YAG, 860-905nm, at 420K

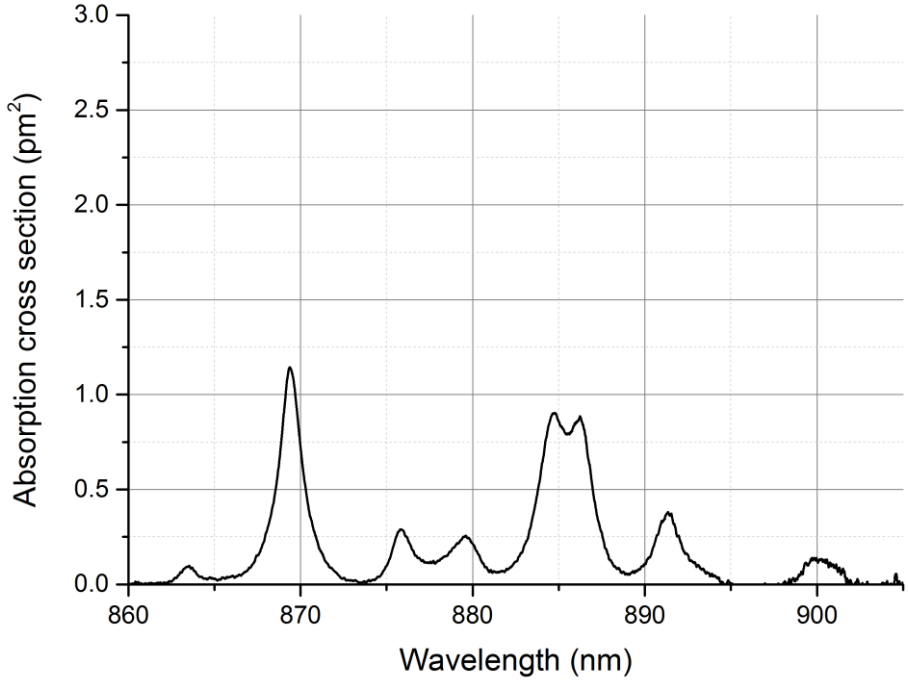

Figure A-25 Absorption cross section of Nd:YAG, 860-905nm, at 450K

A.2 Absortpion cross section of Nd:GSAG

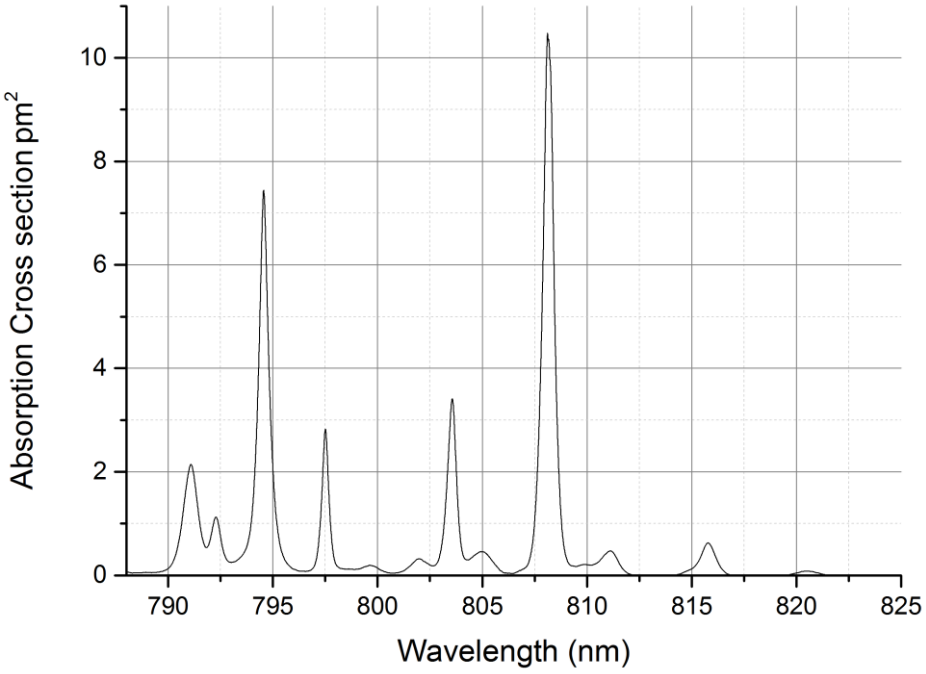

Figure A-26 Absorption cross section of Nd:GSAG at 77K

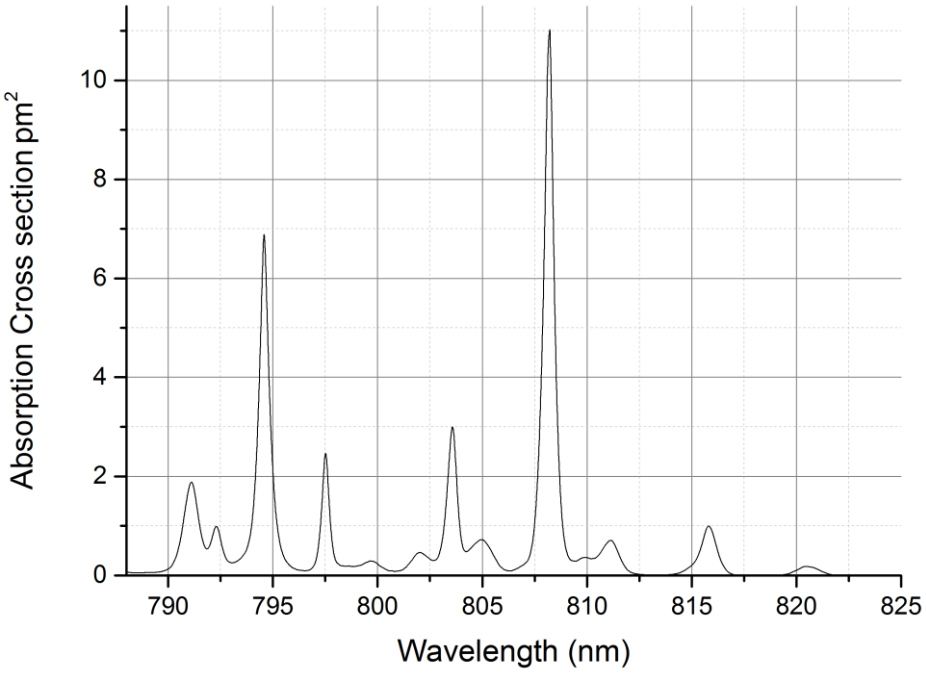

Figure A-27 Absorption cross section of Nd:GSAG at 98K

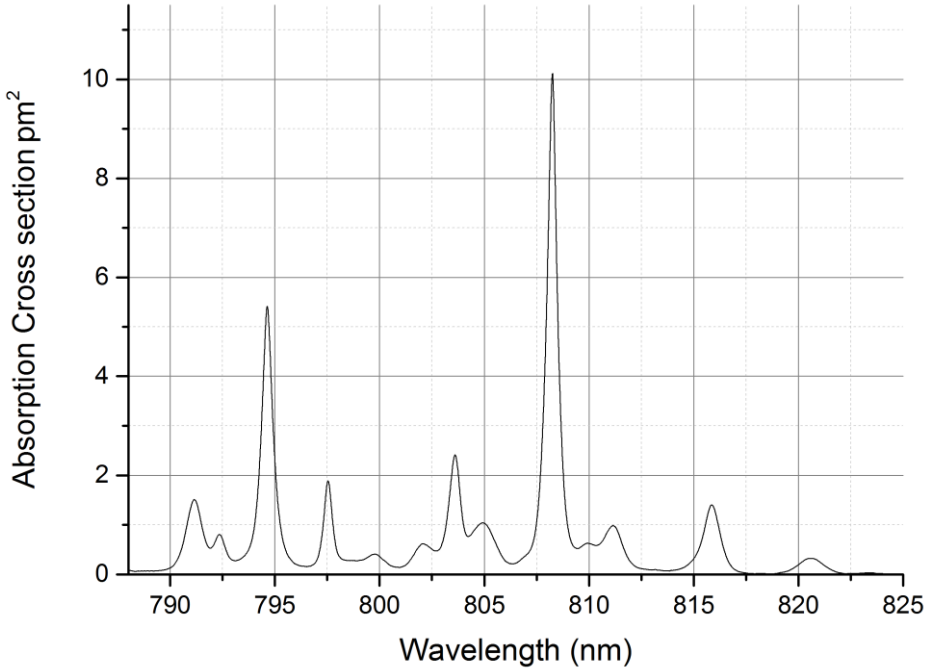

Figure A-28 Absorption cross section of Nd:GSAG at 137K

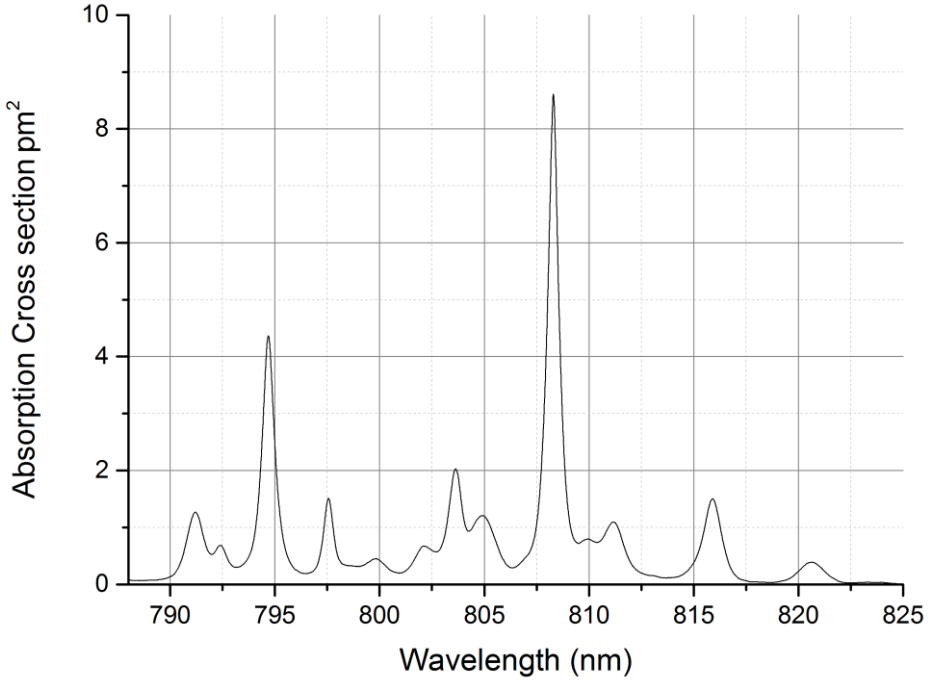

Figure A-29 Absorption cross section of Nd:GSAG at 173K

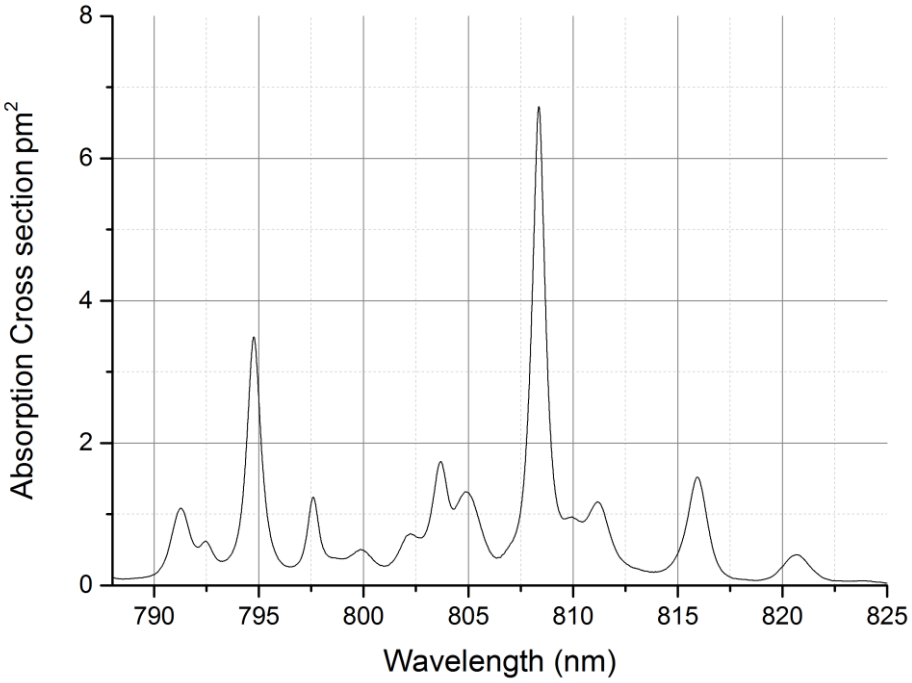

Figure A-30 Absorption cross section of Nd:GSAG at 210K

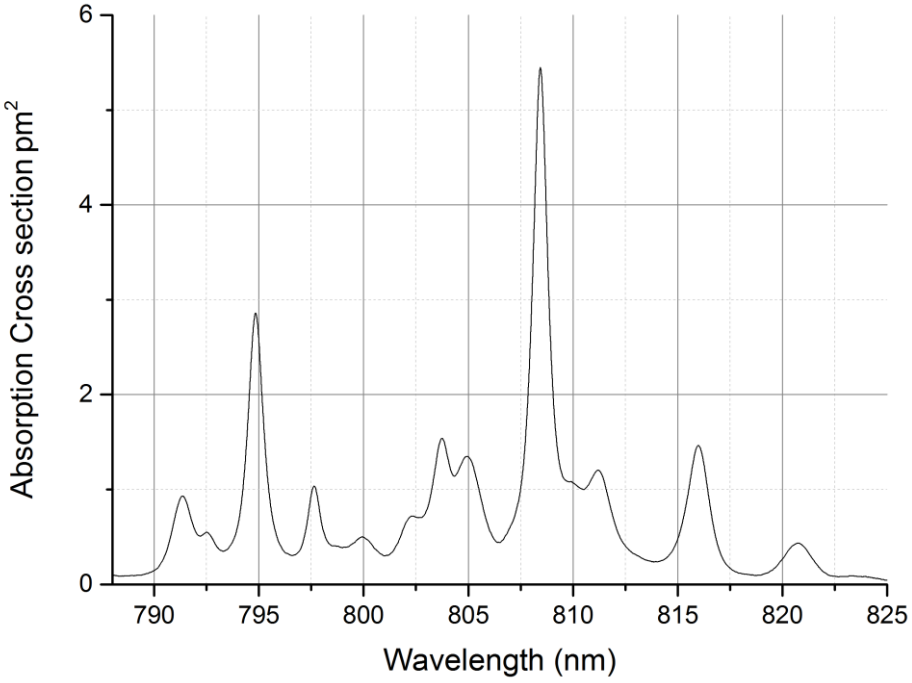

Figure A-31 Absorption cross section of Nd:GSAG at 246K

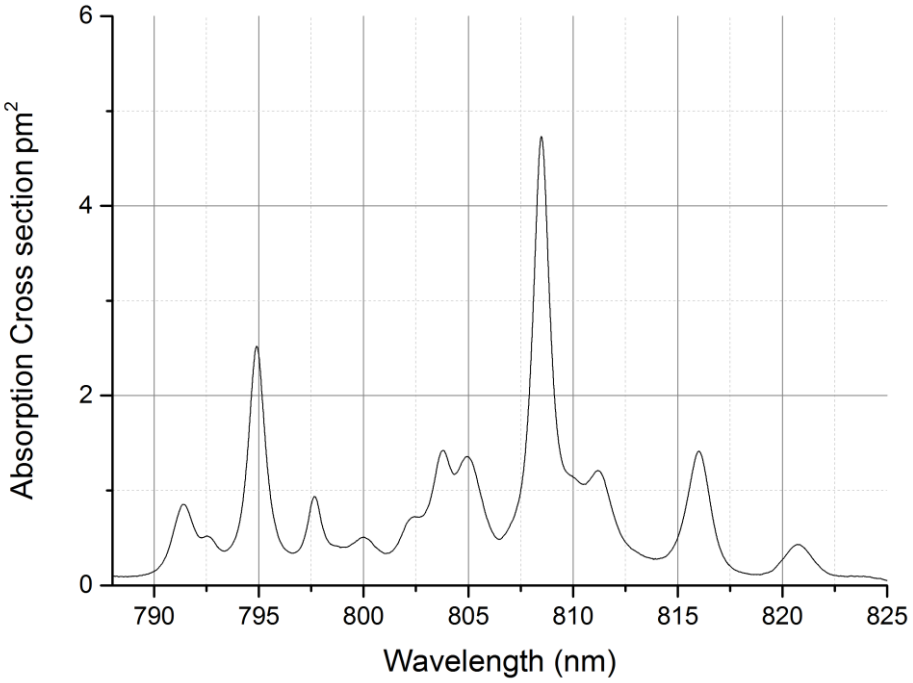

Figure A-32 Absorption cross section of Nd:GSAG at 273K

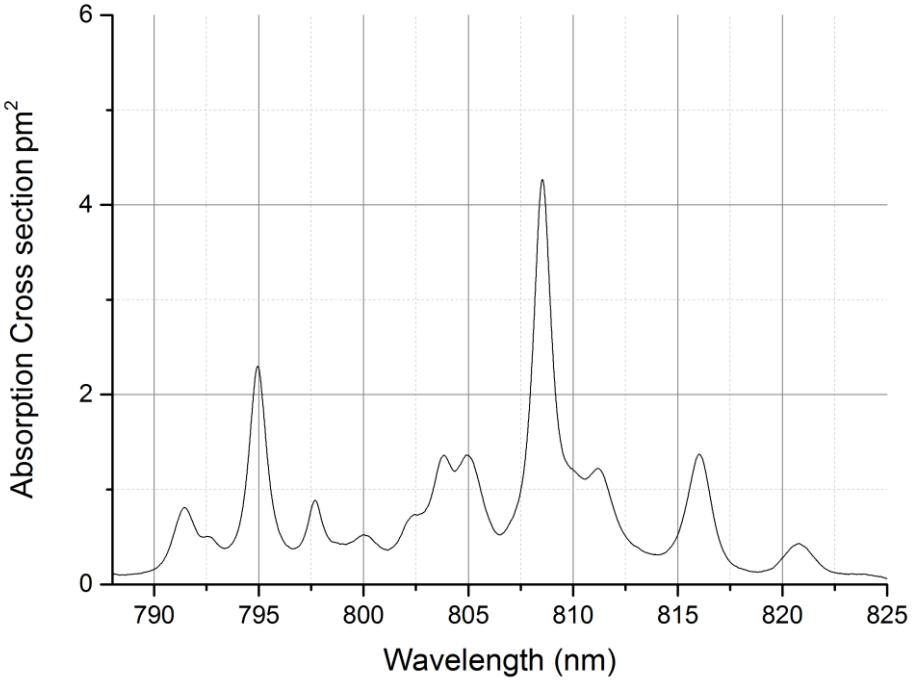

Figure A-33 Absorption cross section of Nd:GSAG at 293K

A.3 Absorption cross section of Vanadates

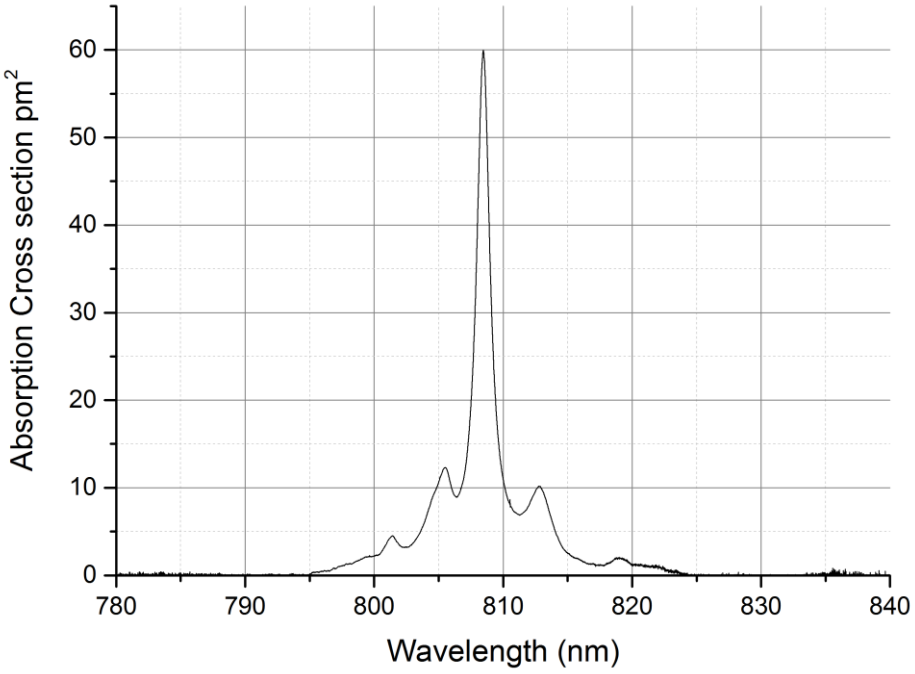

Figure A-34 Absorption cross section of Nd:YVO4, E//c at 300K

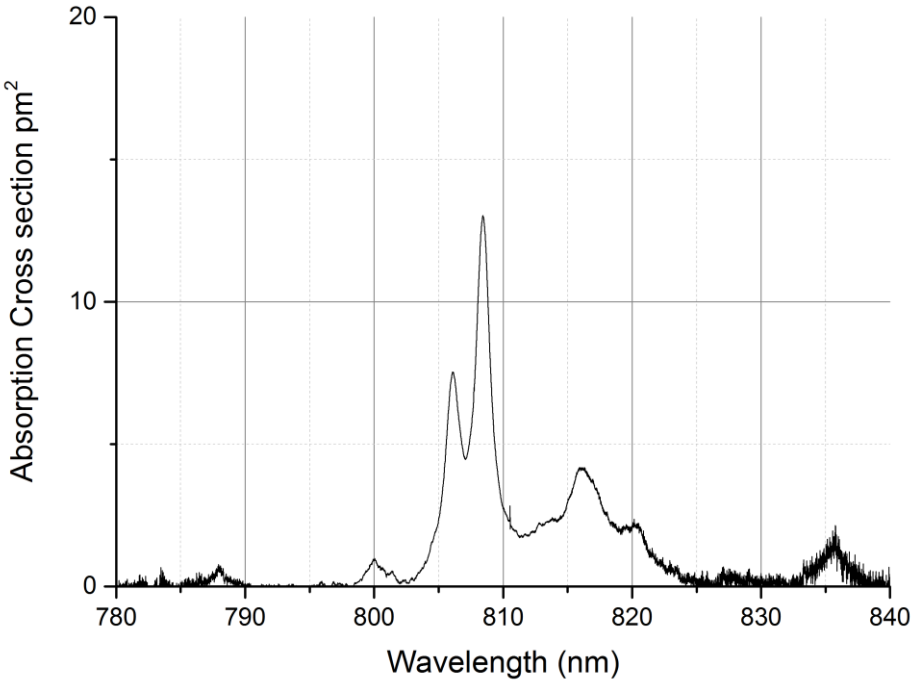

Figure A-35 Absorption cross section of Nd:YVO4, E//a at 300K

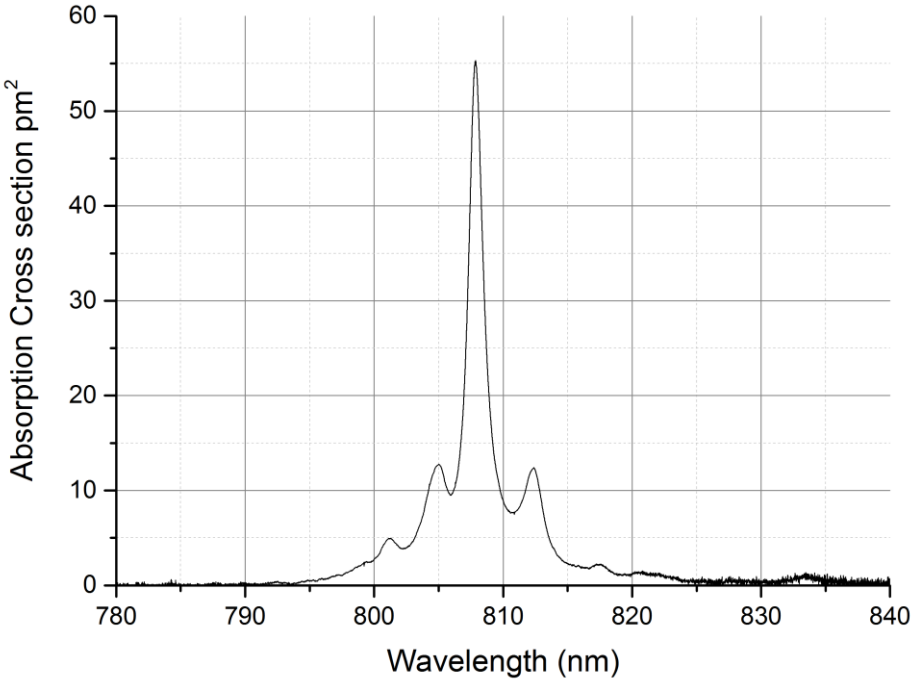

Figure A-36 Absorption cross section of Nd:GdVO4, E//a at 300K

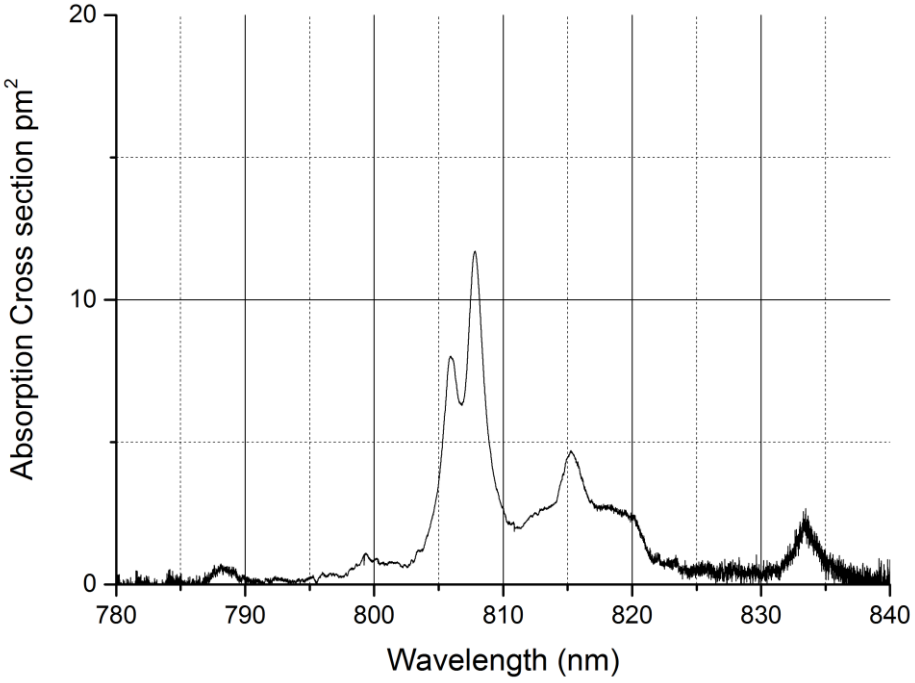

Figure A-37 Absorption cross section of Nd:GdVO4, E//a at 300K

A.4 Absorption cross section of Nd:YLF

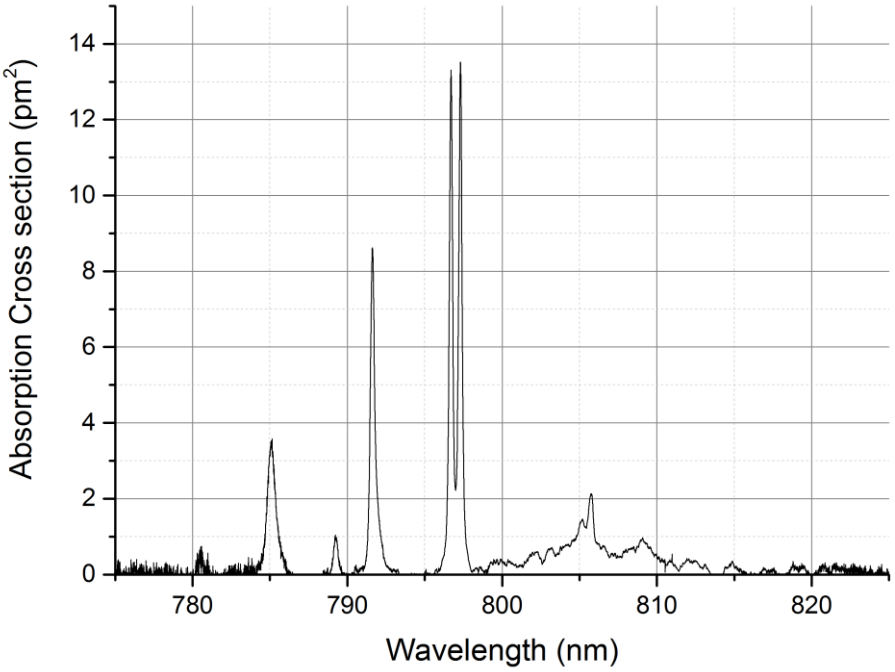

Figure A-38 Absorption cross section of Nd:YLF, E//a at 77K

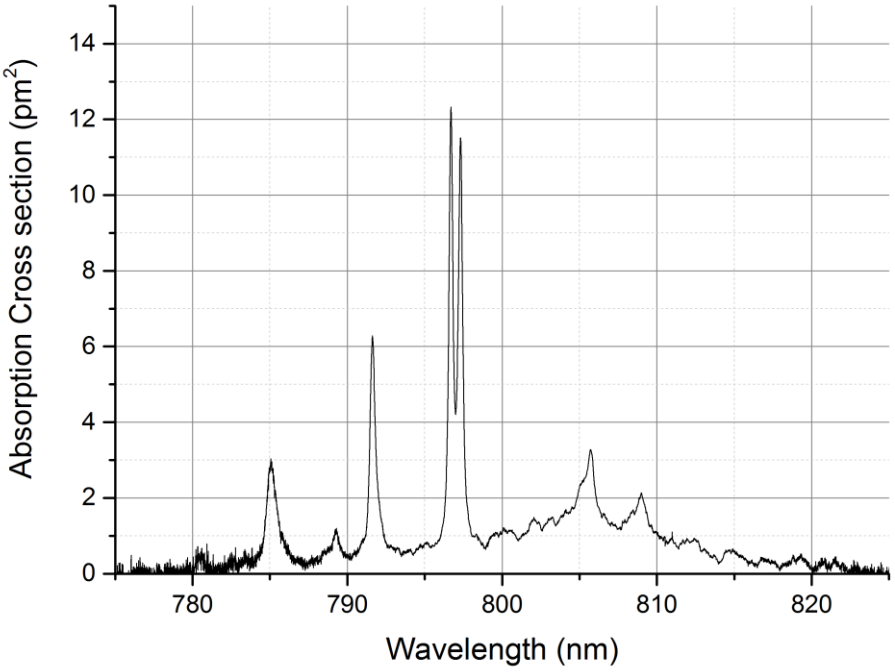

Figure A-39 Absorption cross section of Nd:YLF, E//a at 109K

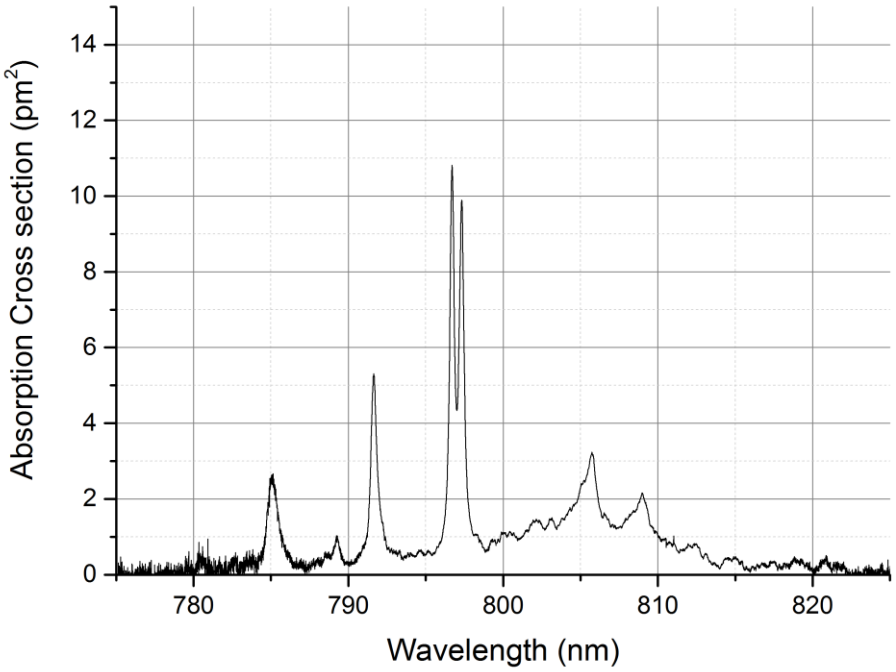

Figure A-40 Absorption cross section of Nd:YLF, E//a at 129K

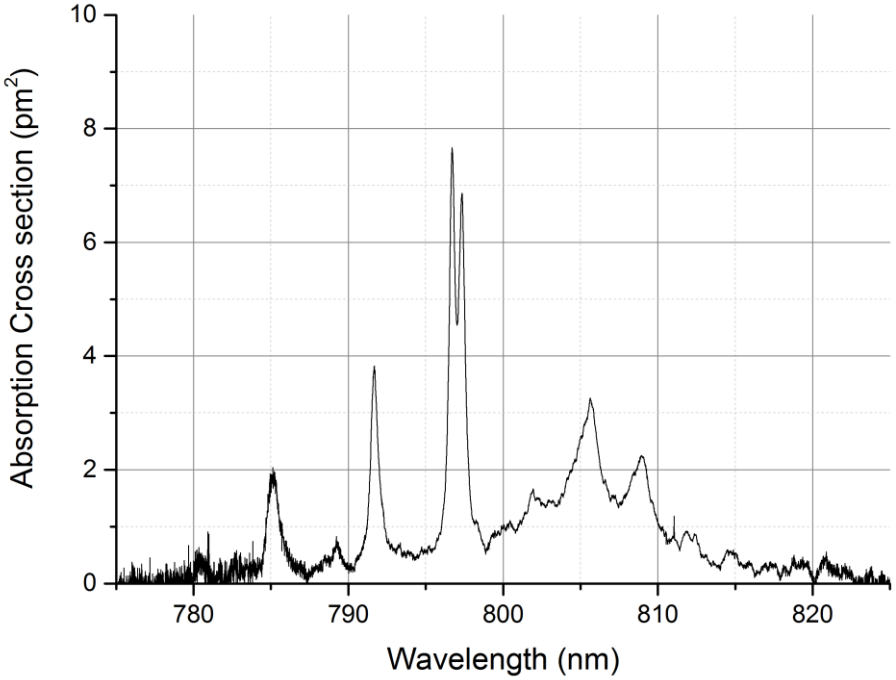

Figure A-41 Absorption cross section of Nd:YLF, E//a at 157K

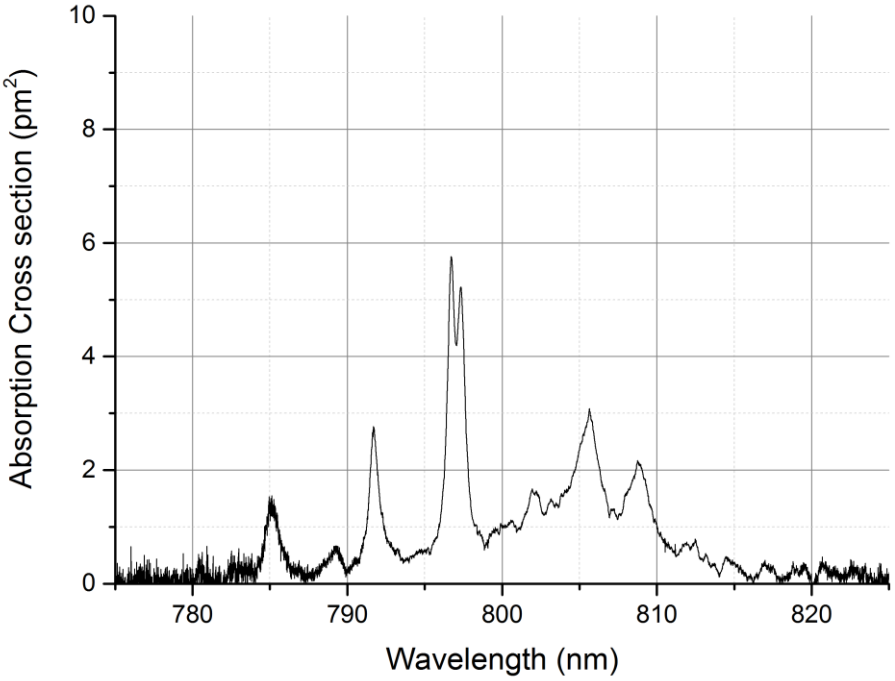

Figure A-42 Absorption cross section of Nd:YLF, E//a at 186K

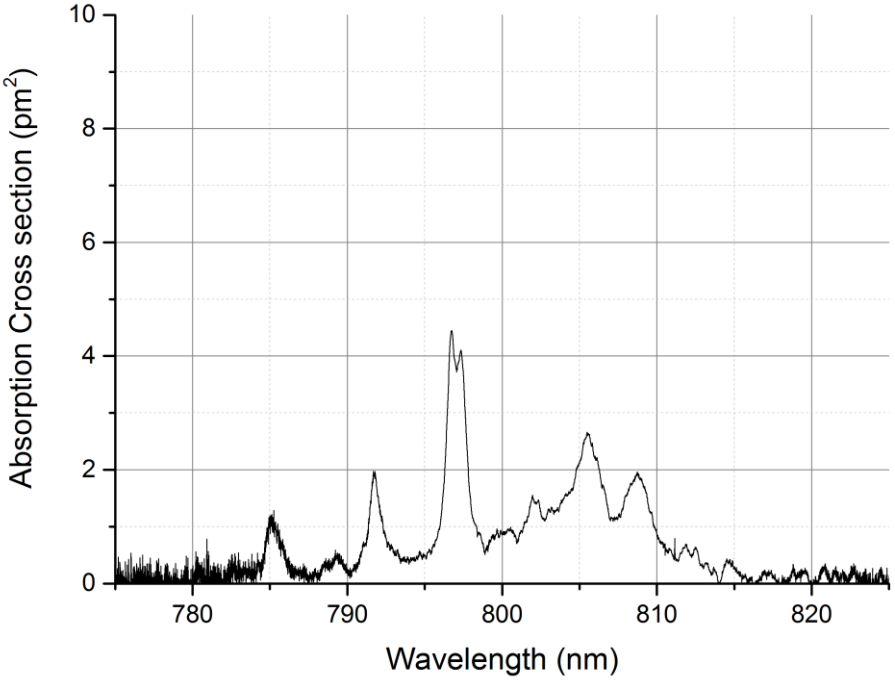

Figure A-43 Absorption cross section of Nd:YLF, E//a at 211K

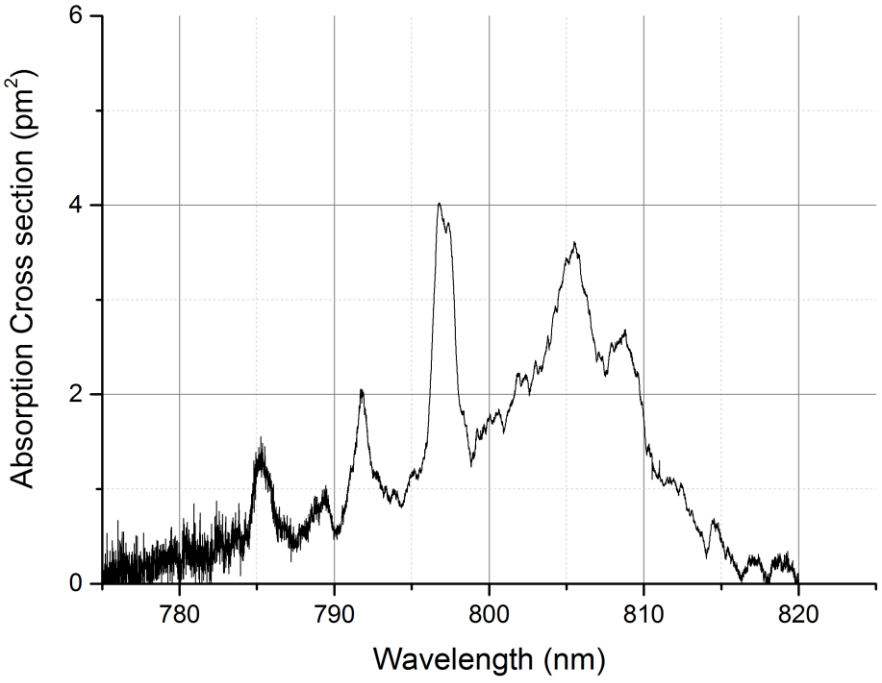

Figure A-44 Absorption cross section of Nd:YLF, E//a at 244K

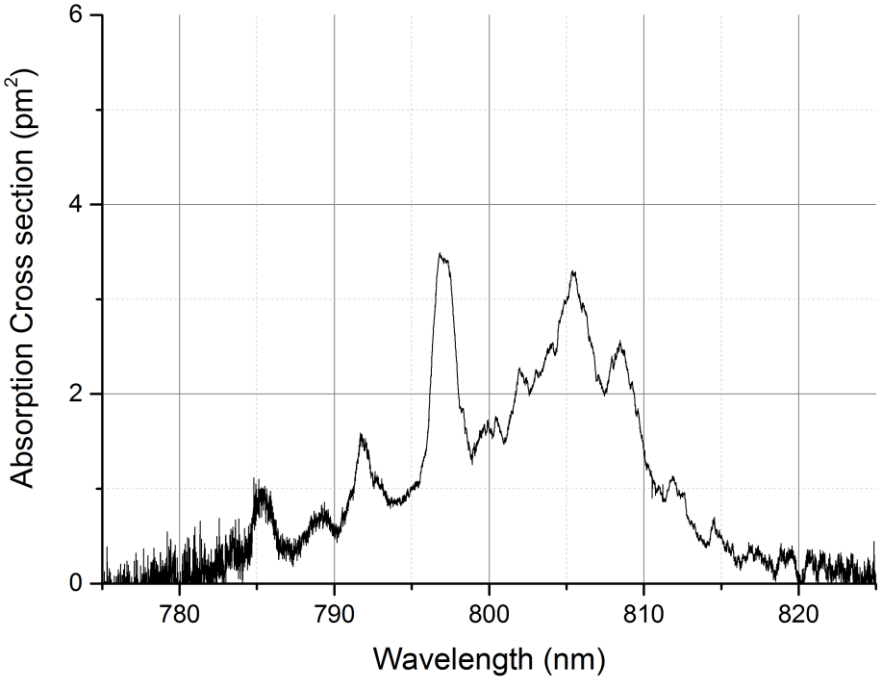

Figure A-45 Absorption cross section of Nd:YLF, E//a at 273K

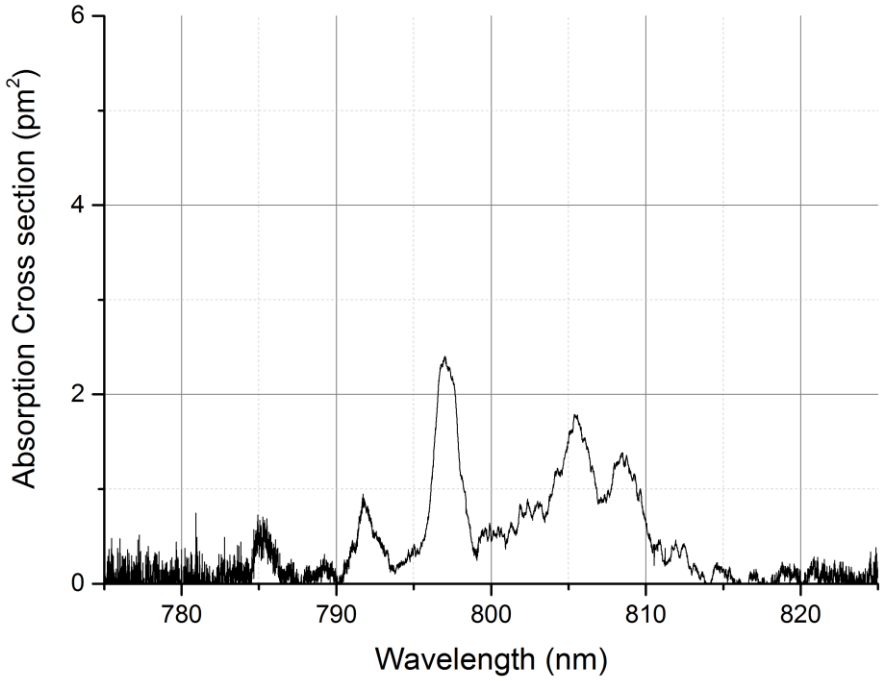

Figure A-46 Absorption cross section of Nd:YLF, E//a at 300K

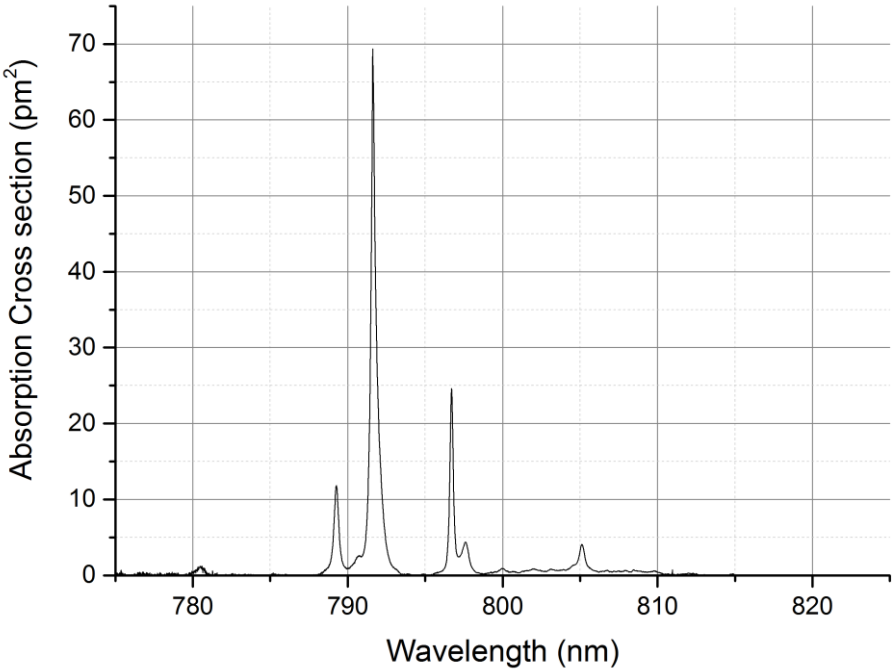

Figure A-47 Absorption cross section of Nd:YLF, E//c at 77K

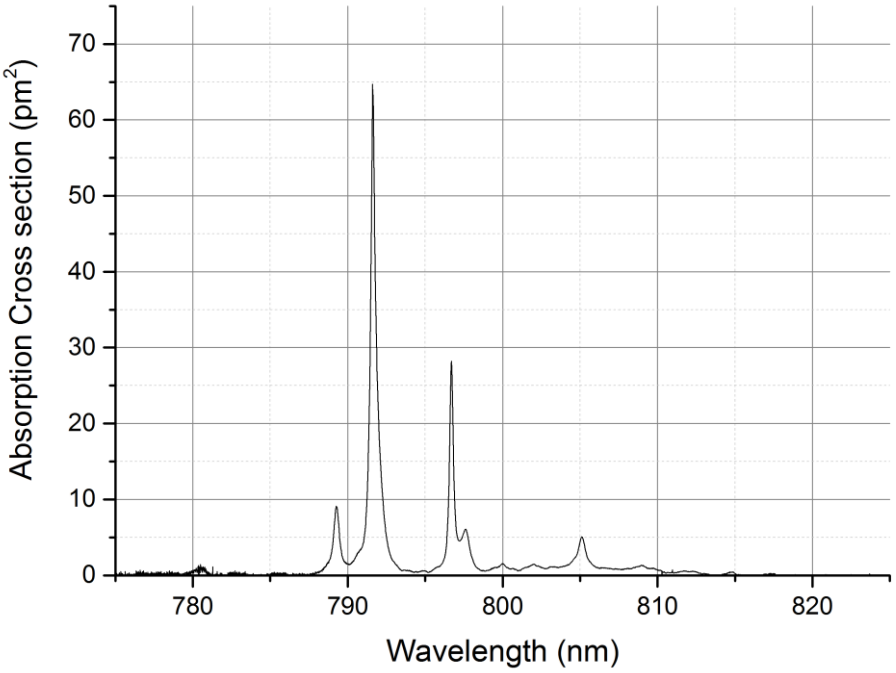

Figure A-48 Absorption cross section of Nd:YLF, E//c at 109K

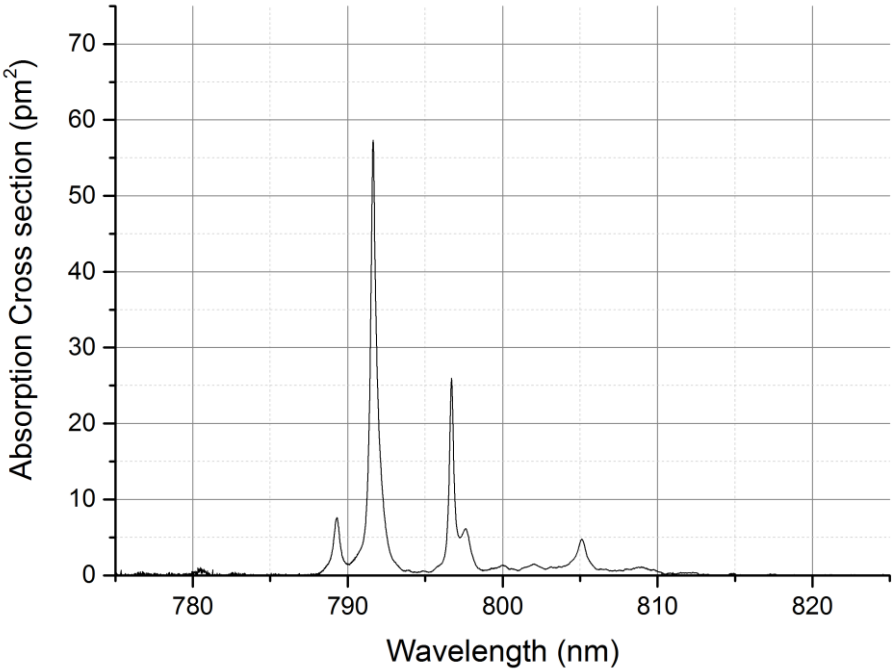

Figure A-49 Absorption cross section of Nd:YLF, E//c at 129K

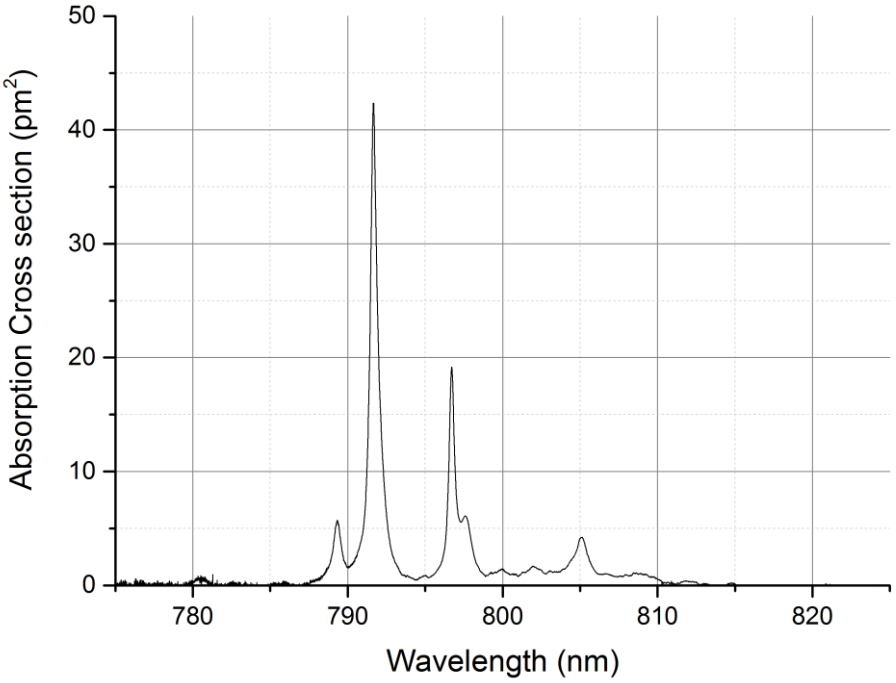

Figure A-50 Absorption cross section of Nd:YLF, E//c at 157K

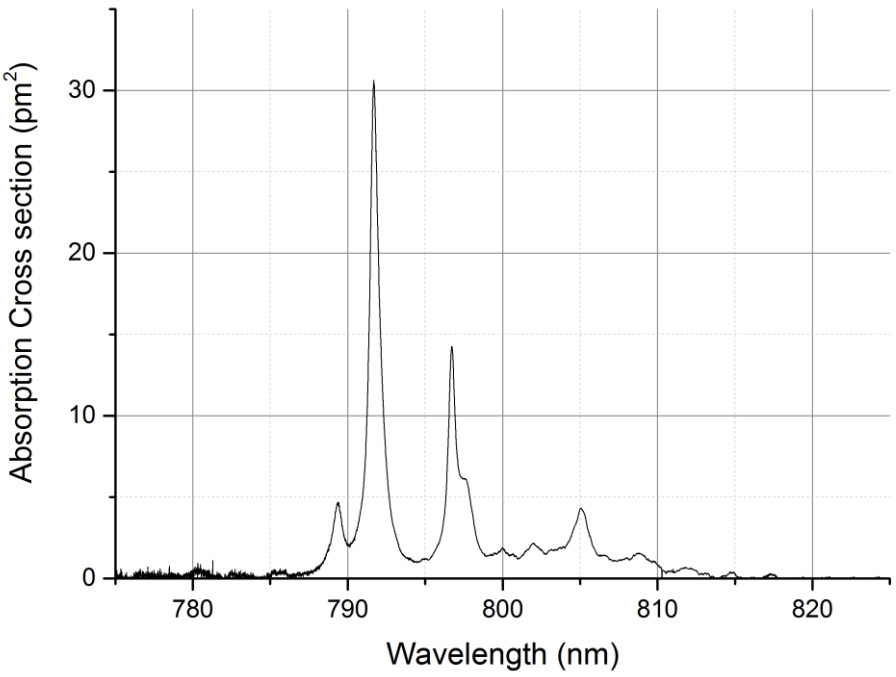

Figure A-51 Absorption cross section of Nd:YLF, E//c at 186K

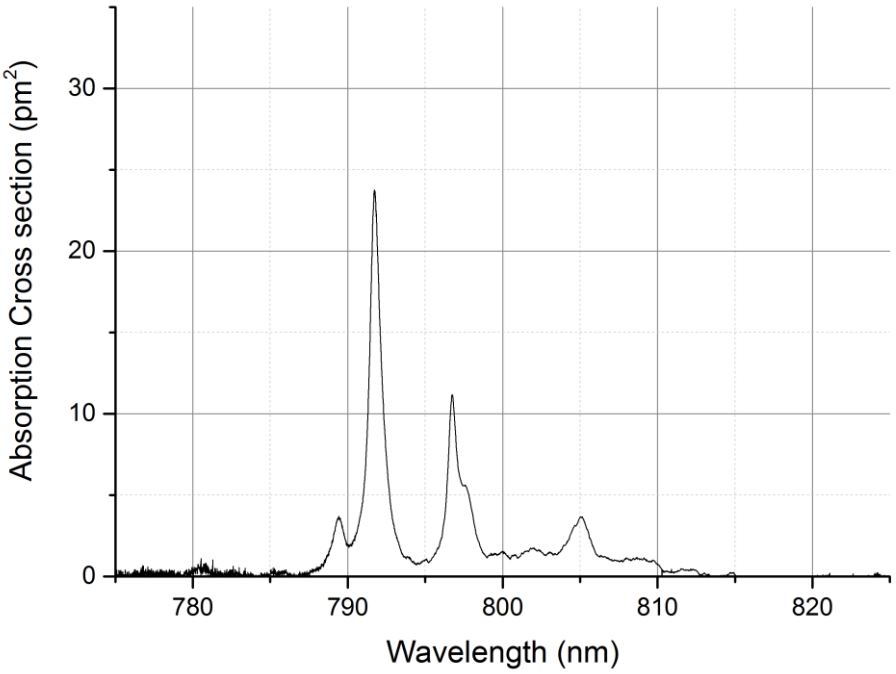

Figure A-52 Absorption cross section of Nd:YLF, E//c at 211K

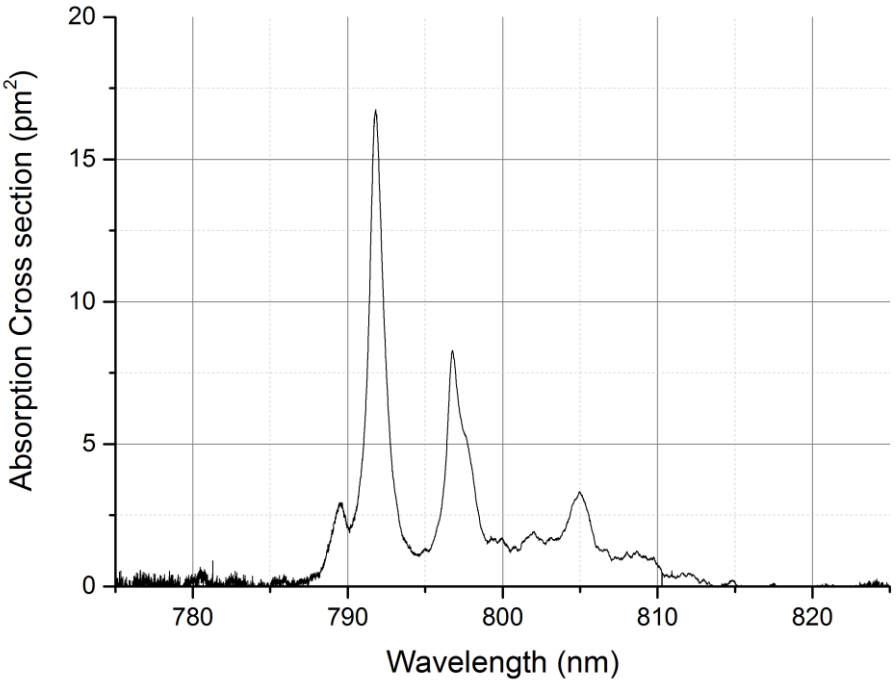

Figure A-53 Absorption cross section of Nd:YLF, E//c at 244K

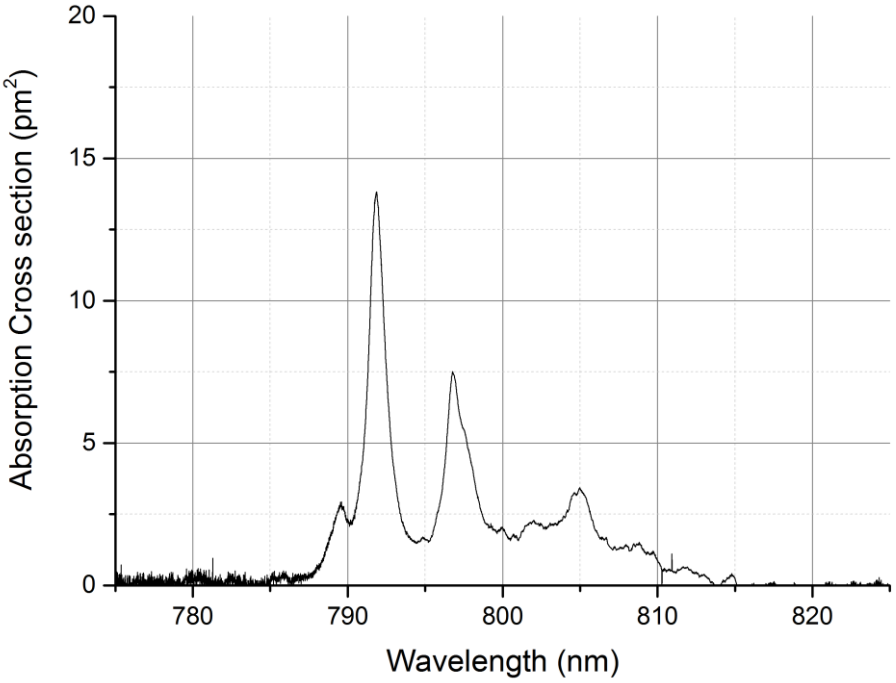

Figure A-54 Absorption cross section of Nd:YLF, E//c at 273K

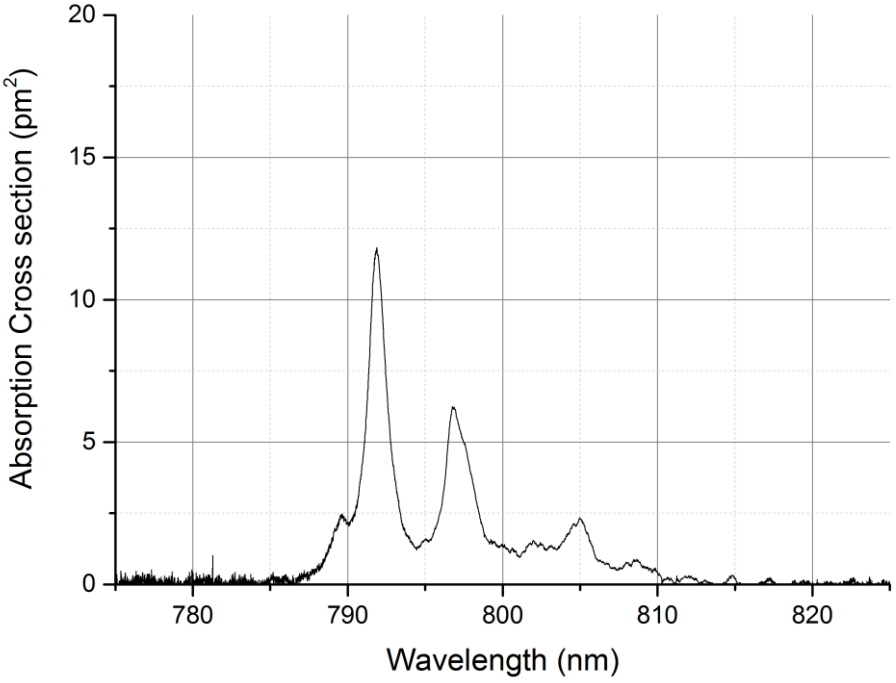

Figure A-55 Absorption cross section of Nd:YLF, E//c at 296K

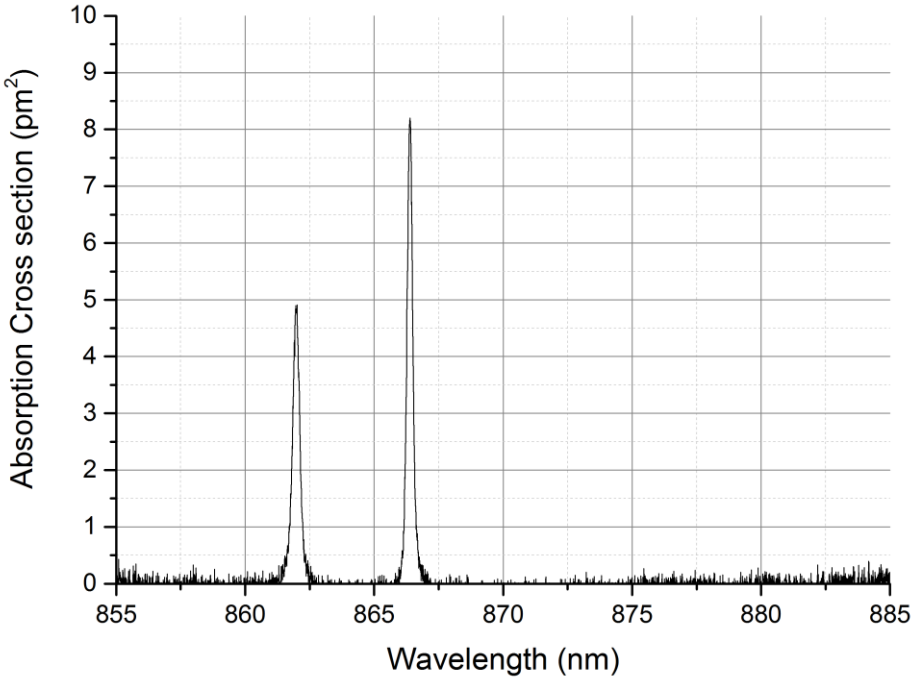

Figure A-56 Absorption cross section of Nd:YLF, E//a, 855-885nm at 77K

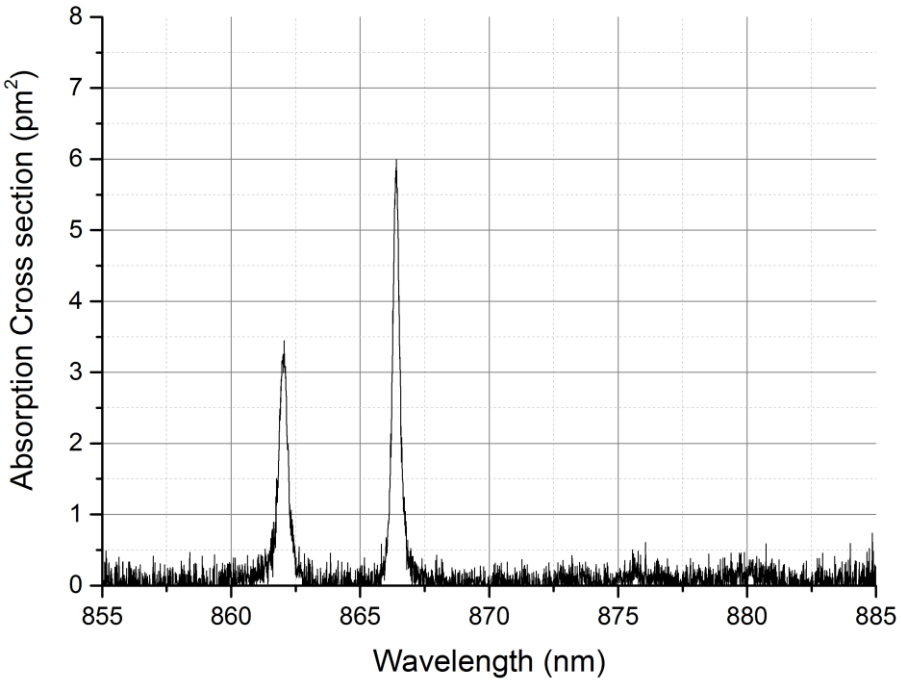

Figure A-57 Absorption cross section of Nd:YLF, E//a, 855-885nm at 100K

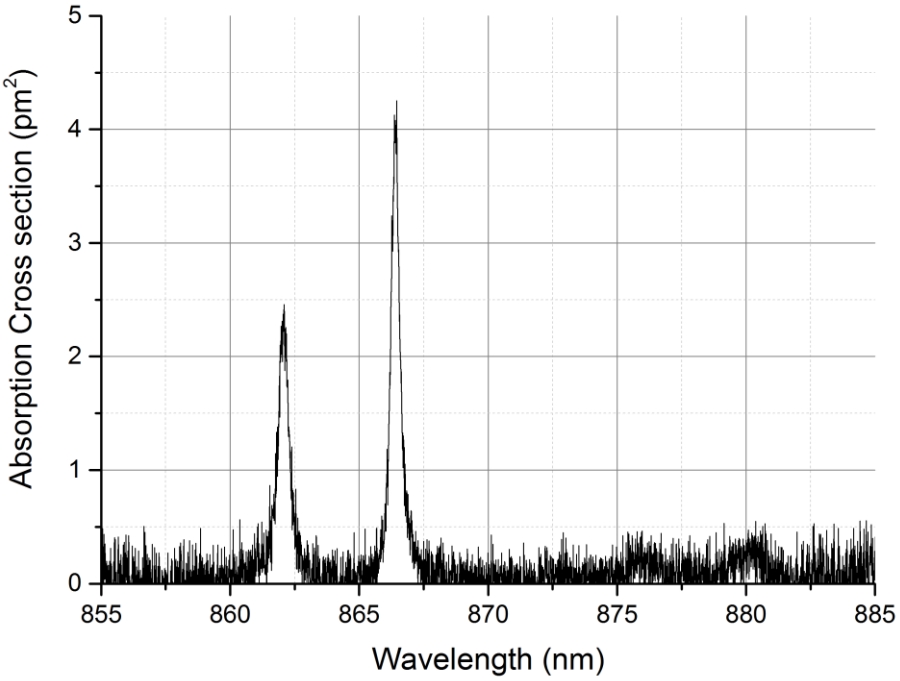

Figure A-58 Absorption cross section of Nd:YLF, E//a, 855-885nm at 125K

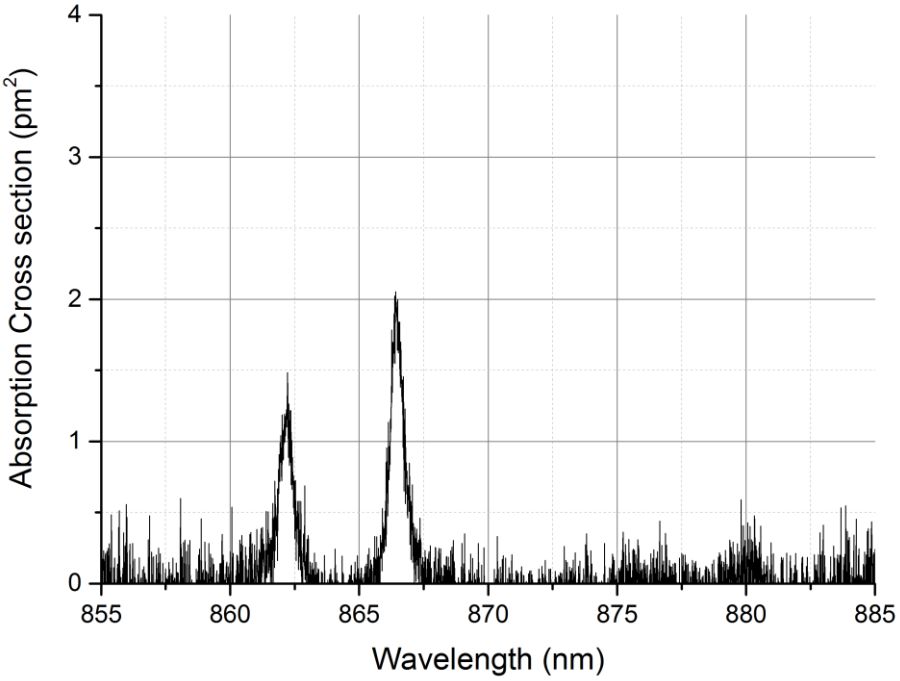

Figure A-59 Absorption cross section of Nd:YLF, E//a, 855-885nm at 180K

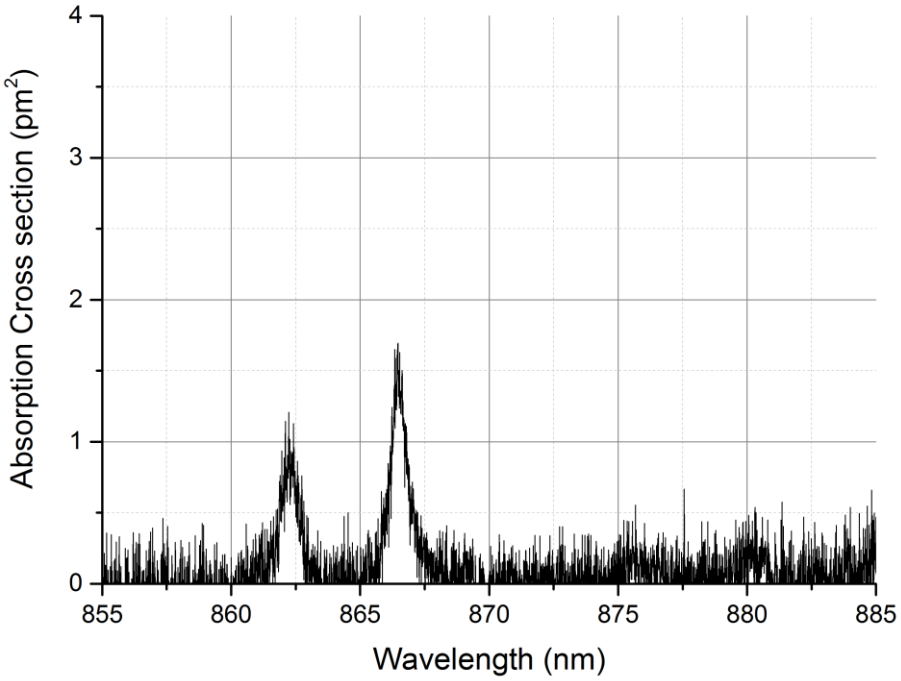

Figure A-60 Absorption cross section of Nd:YLF, E//a, 855-885nm at 208K

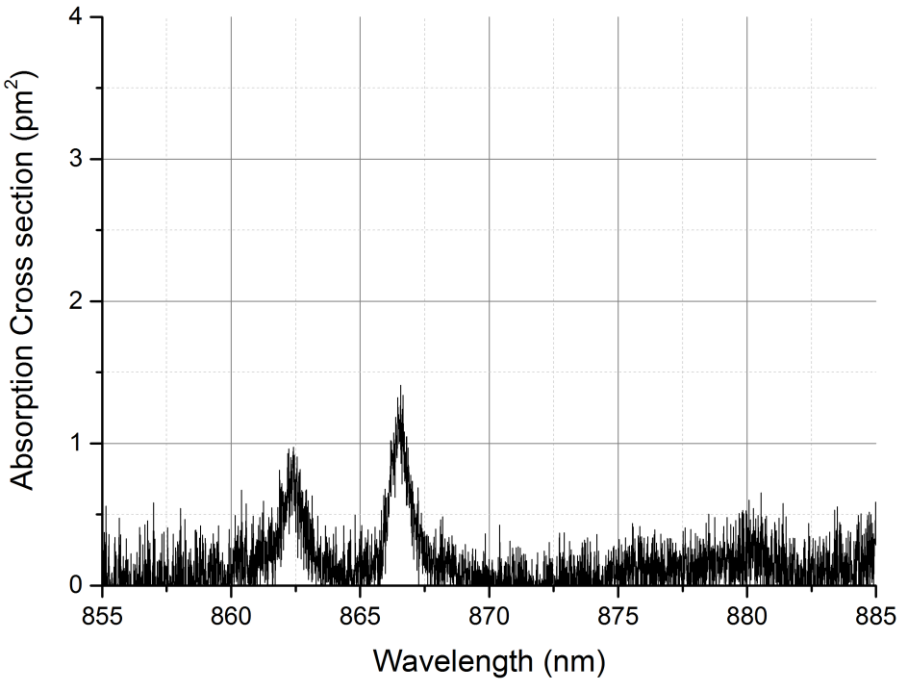

Figure A-61 Absorption cross section of Nd:YLF, E//a, 855-885nm at 242K

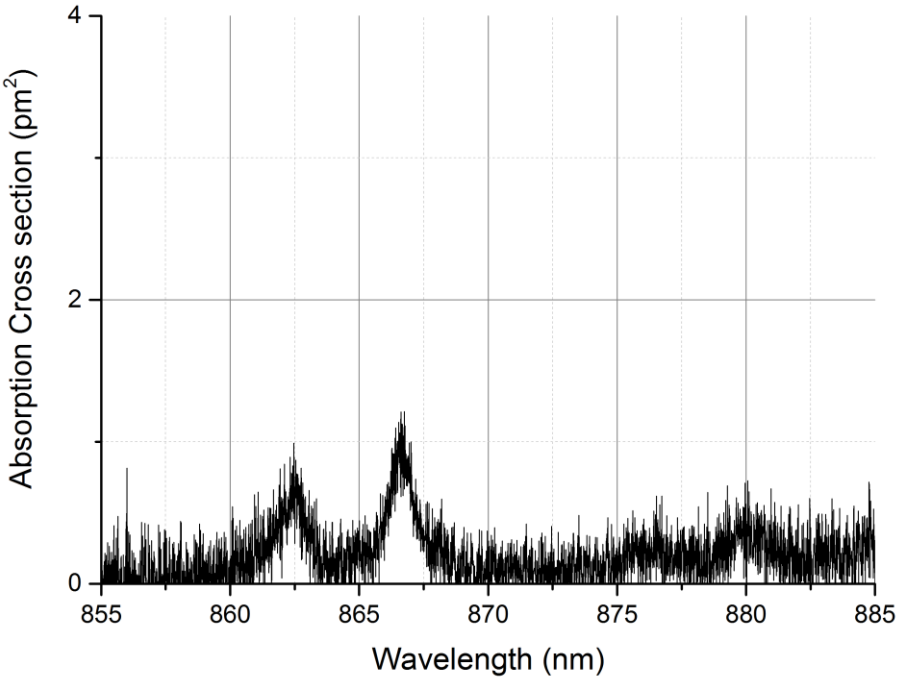

Figure A-62 Absorption cross section of Nd:YLF, E//a, 855-885nm at 273K

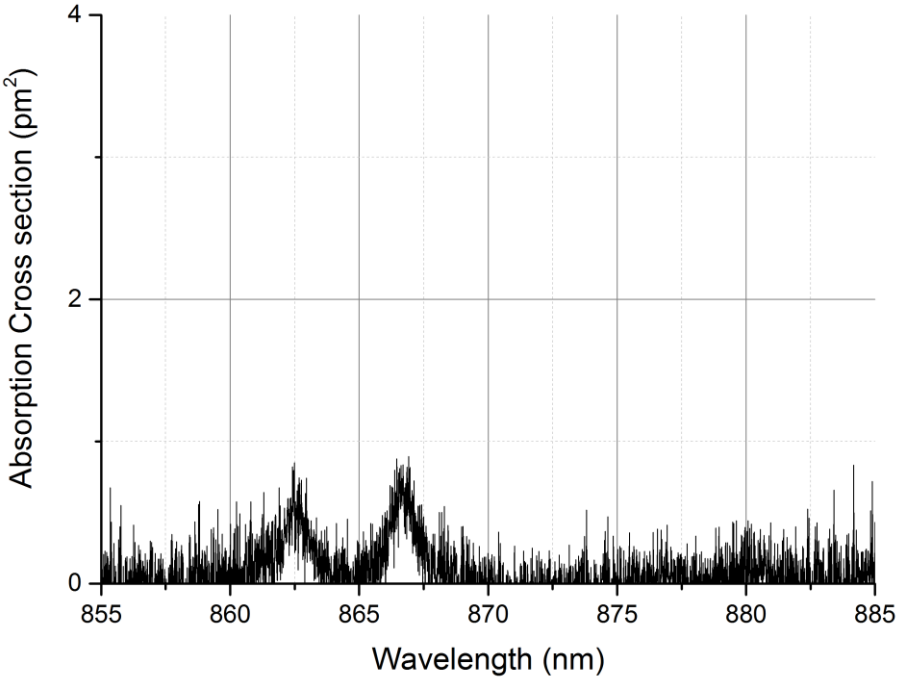

Figure A-63 Absorption cross section of Nd:YLF, E//a, 855-885nm at 296K

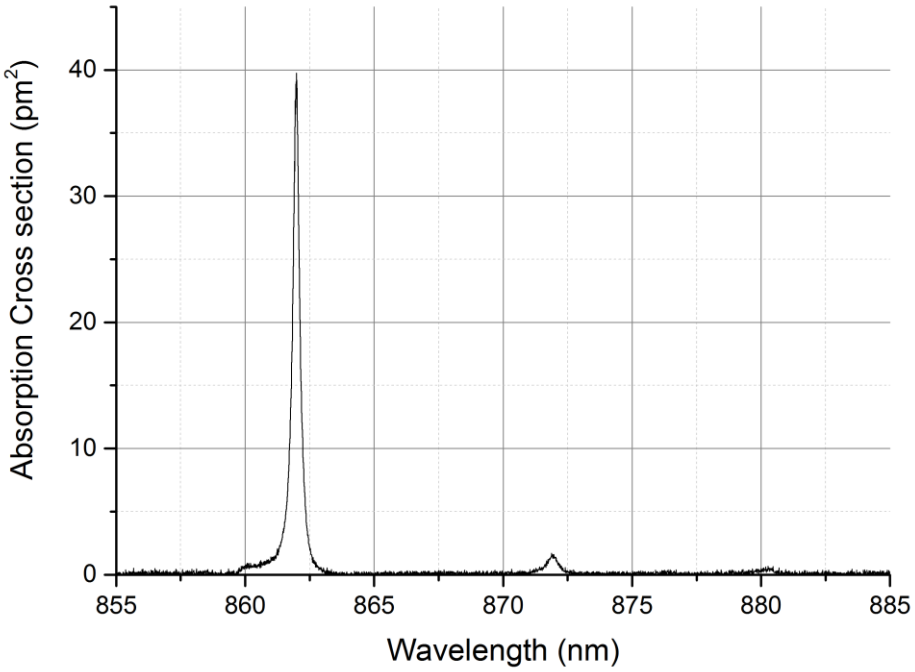

Figure A-64 Absorption cross section of Nd:YLF, E//c, 855-885nm at 77K

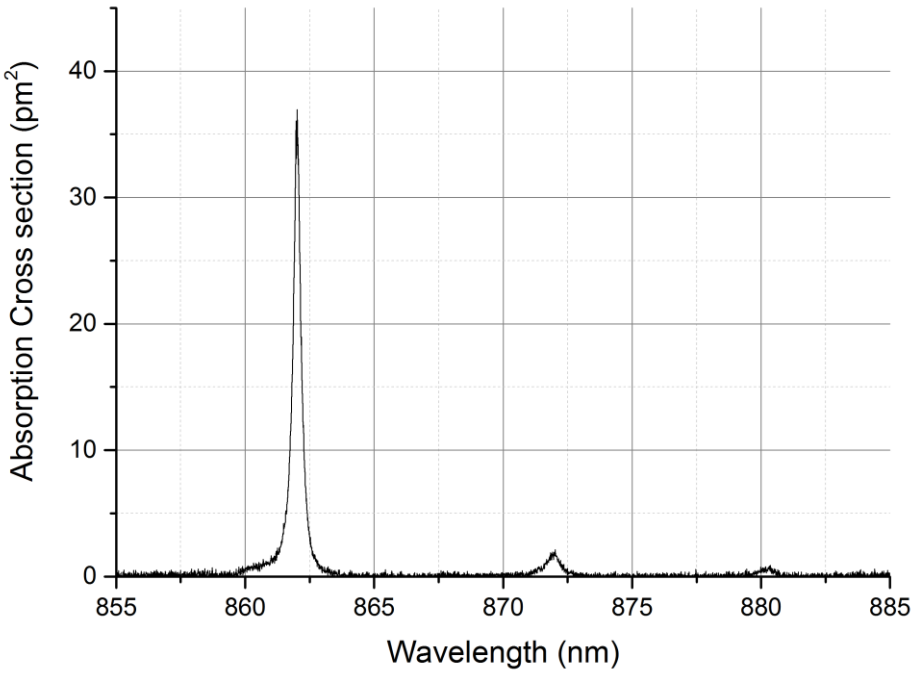

Figure A-65 Absorption cross section of Nd:YLF, E//c, 855-885nm at 100K

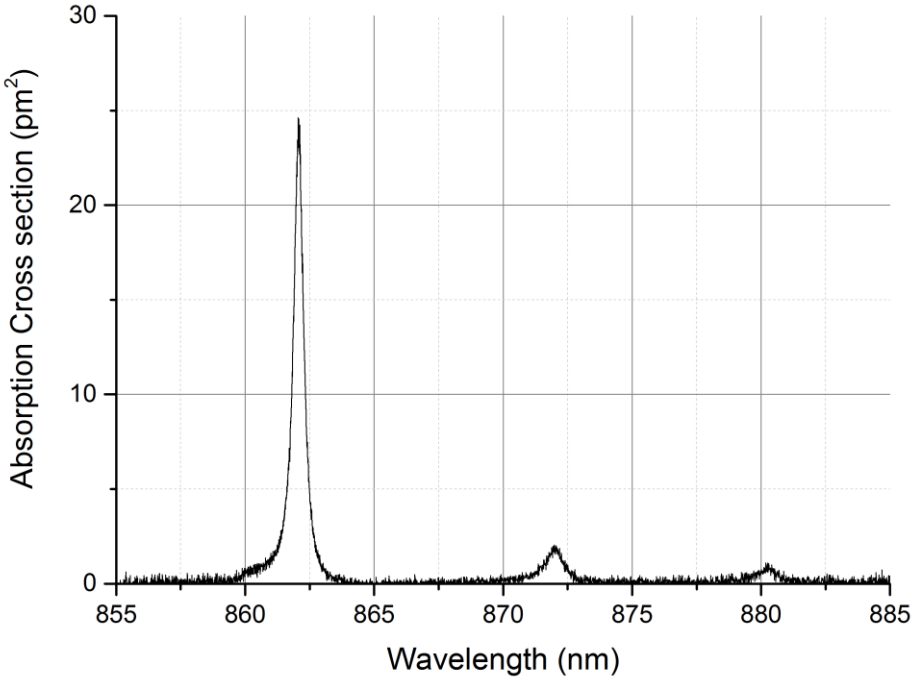

Figure A-66 Absorption cross section of Nd:YLF, E//c, 855-885nm at 125K

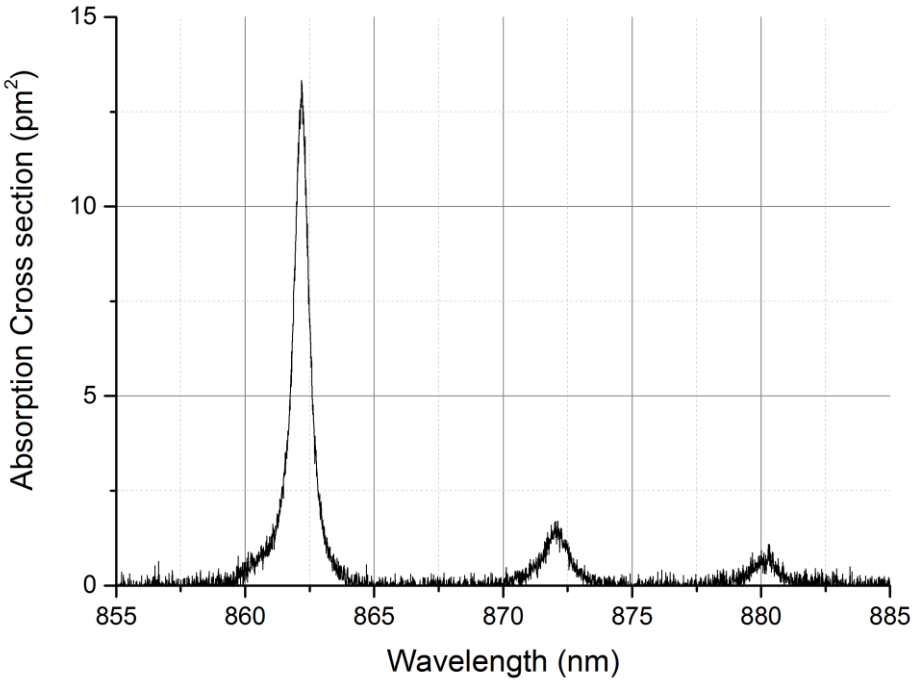

Figure A-67 Absorption cross section of Nd:YLF, E//c, 855-885nm at 180K

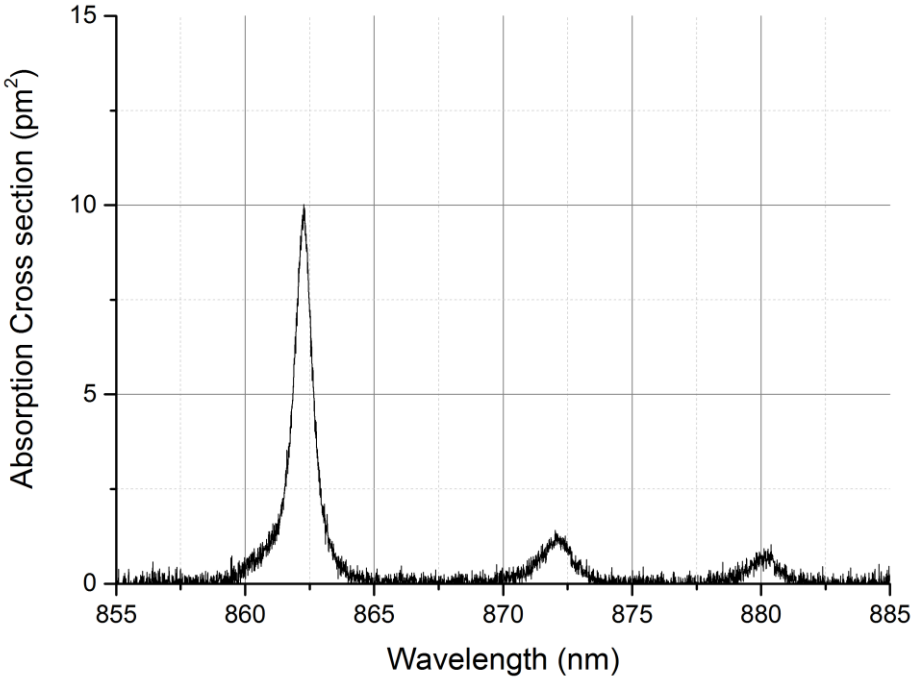

Figure A-68 Absorption cross section of Nd:YLF, E//c, 855-885nm at208K

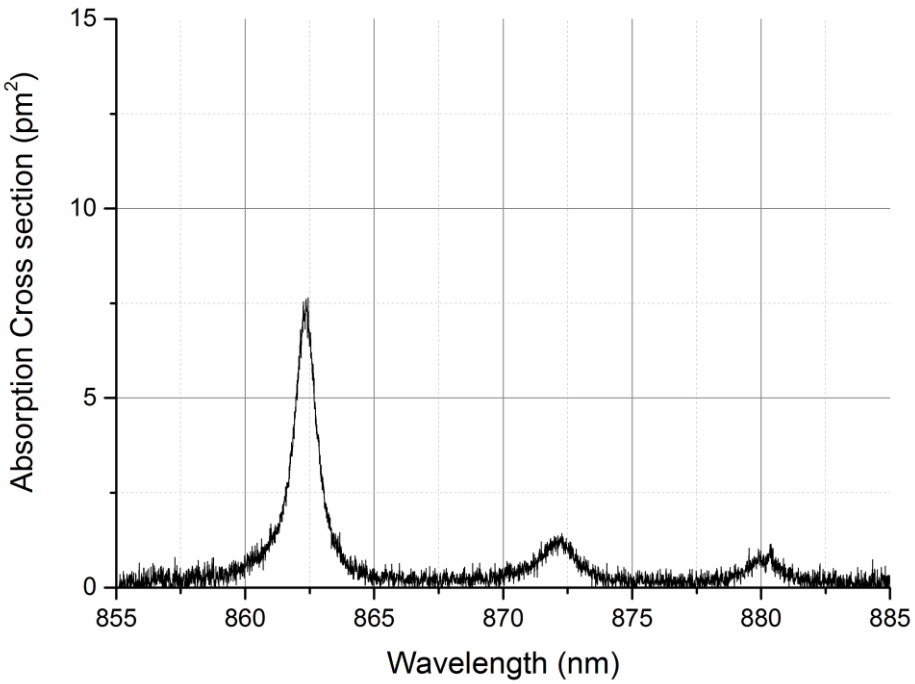

Figure A-69 Absorption cross section of Nd:YLF, E//c, 855-885nm at 242K

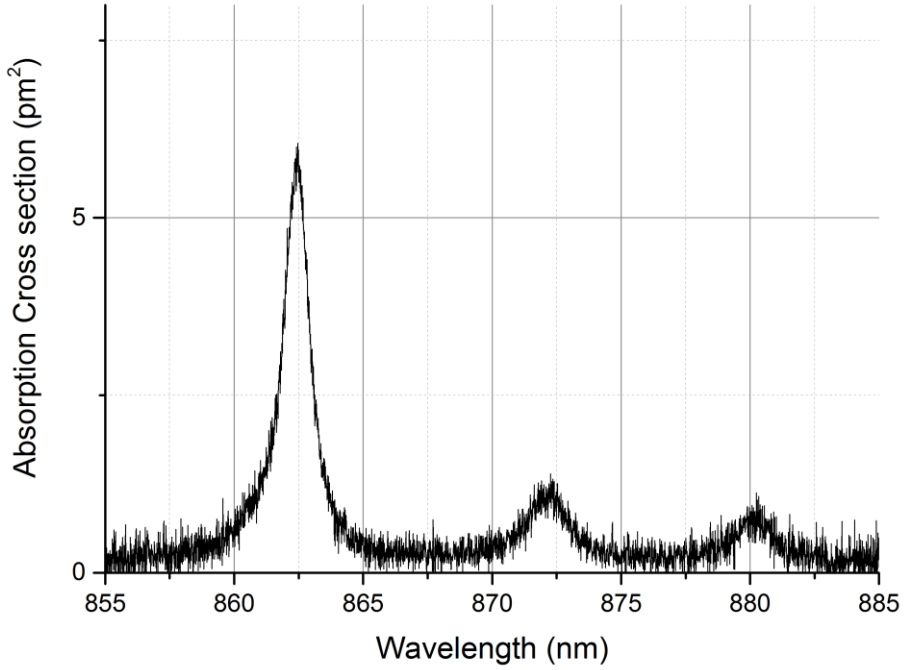

Figure A-70 Absorption cross section of Nd:YLF, E//c, 855-885nm at 273K

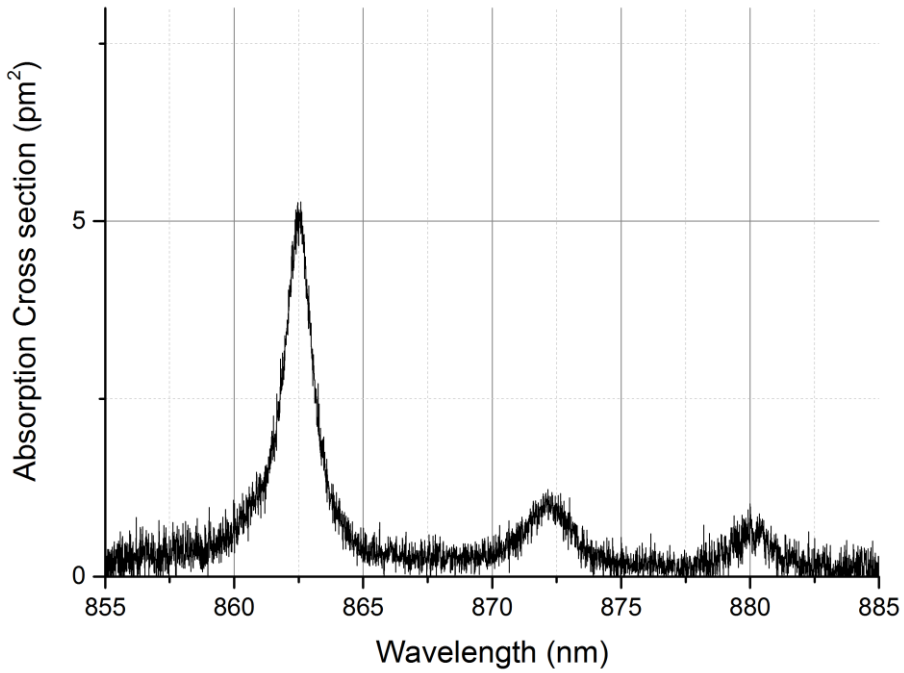

Figure A-71 Absorption cross section of Nd:YLF, E//c, 855-885nm at 296K

A.5 Absorpstion cross section of Nd:KGW

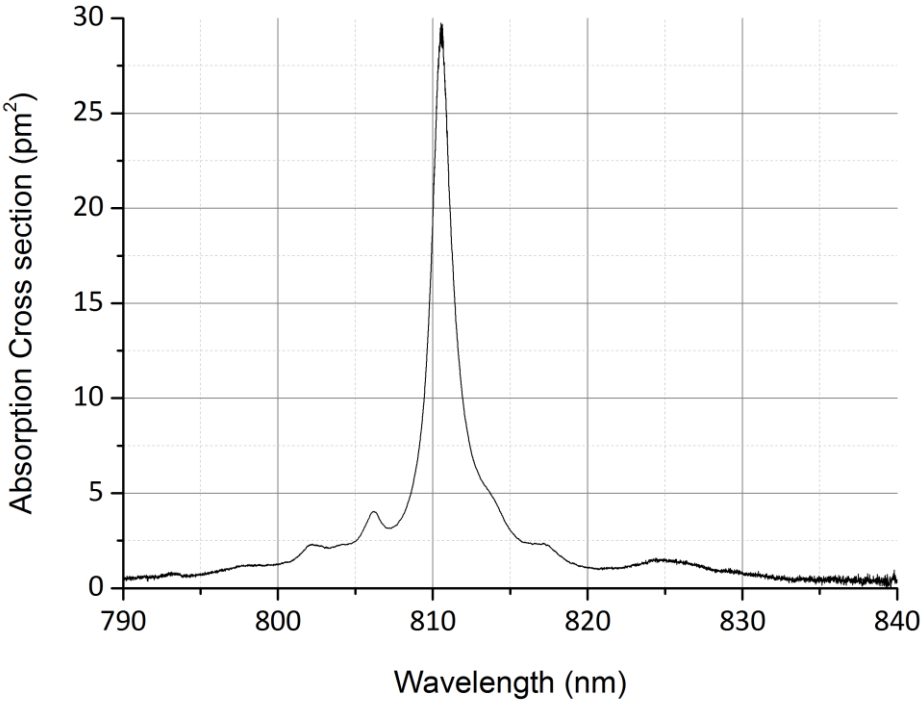

Figure A-72 Absorption cross section of Nd:KGW, E//Nm at 300K

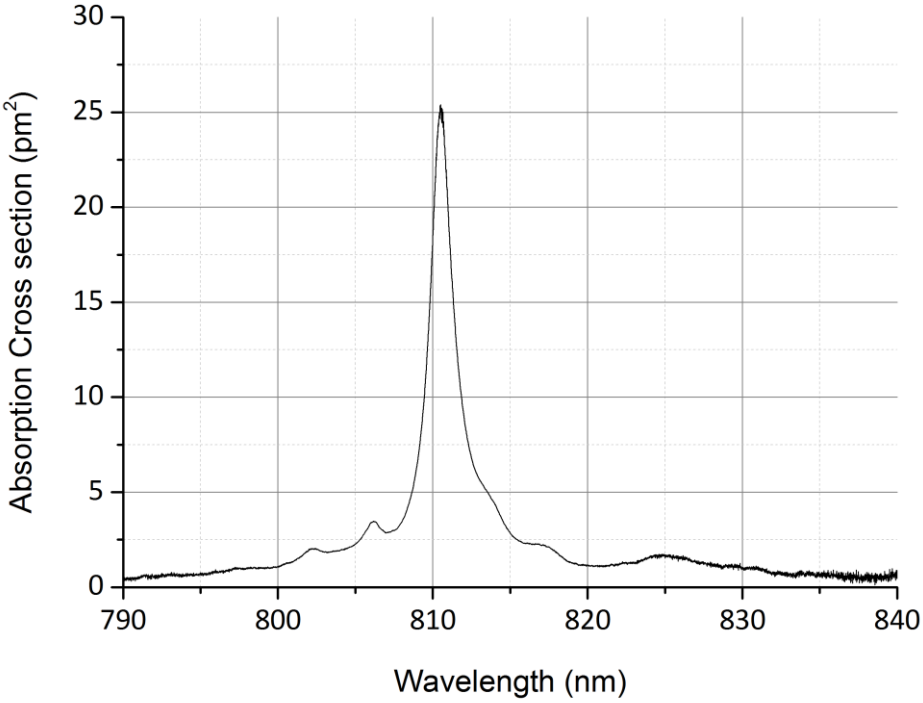

Figure A-73 Absorption cross section of Nd:KGW, E//Nm at 330K

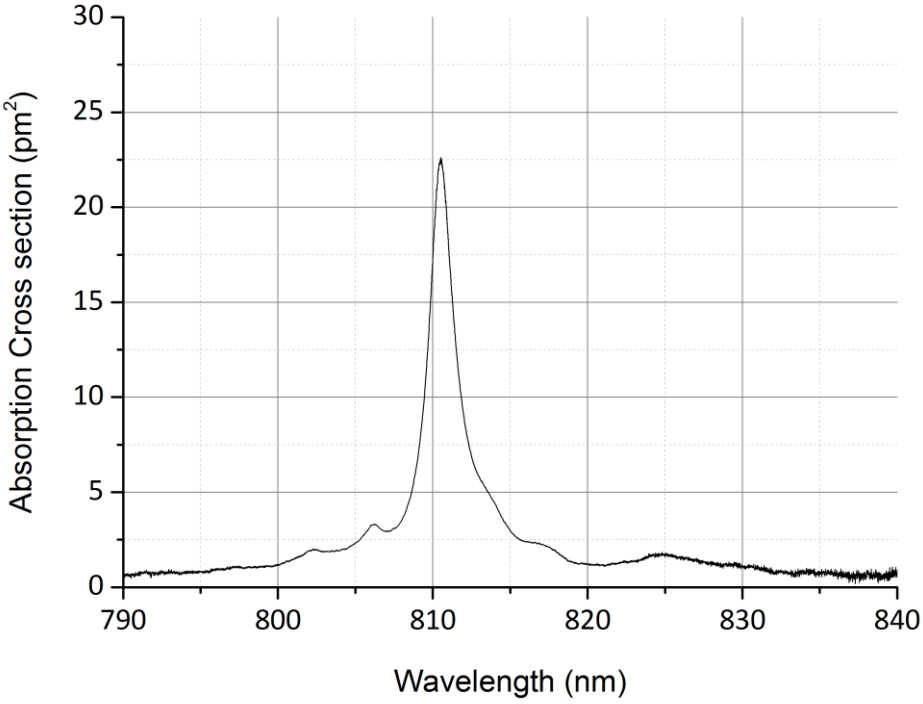

Figure A-74 Absorption cross section of Nd:KGW, E//Nm at 360K

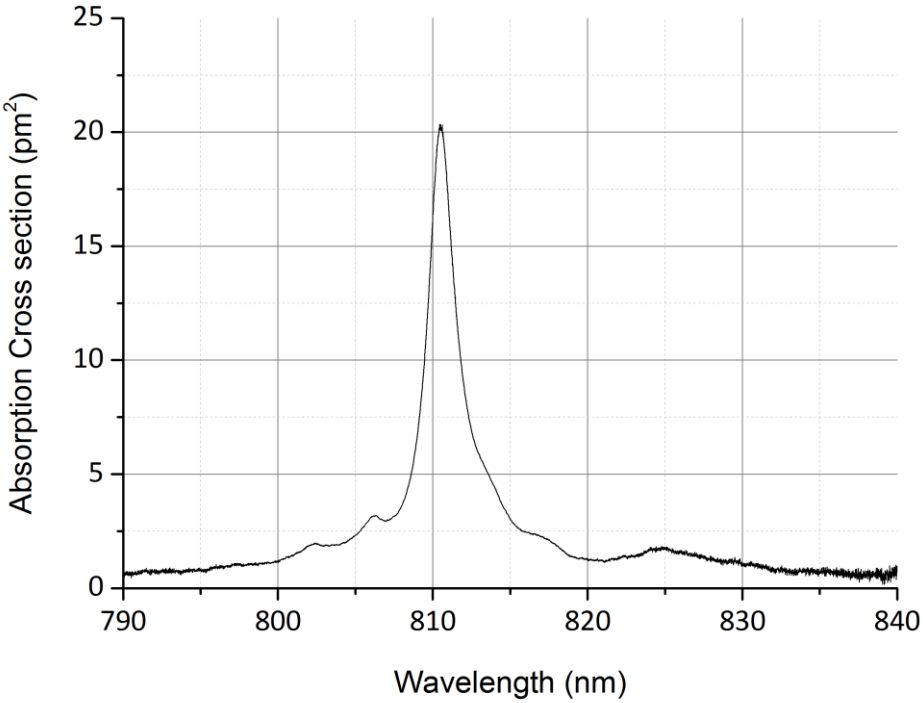

Figure A-75 Absorption cross section of Nd:KGW, E//Nm at 390K

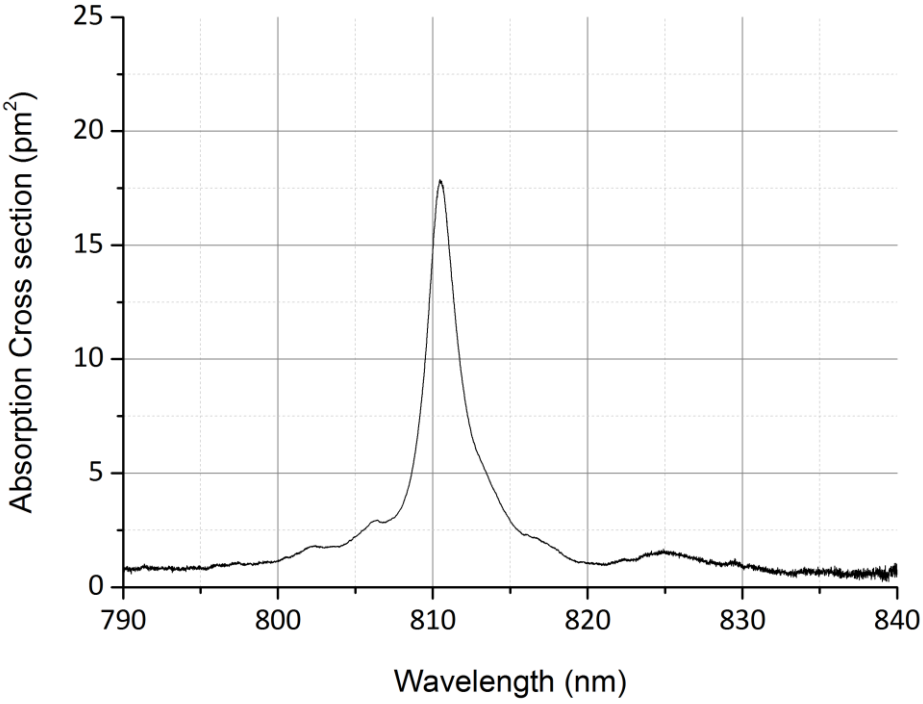

Figure A-76 Absorption cross section of Nd:KGW, E//Nm at 420K

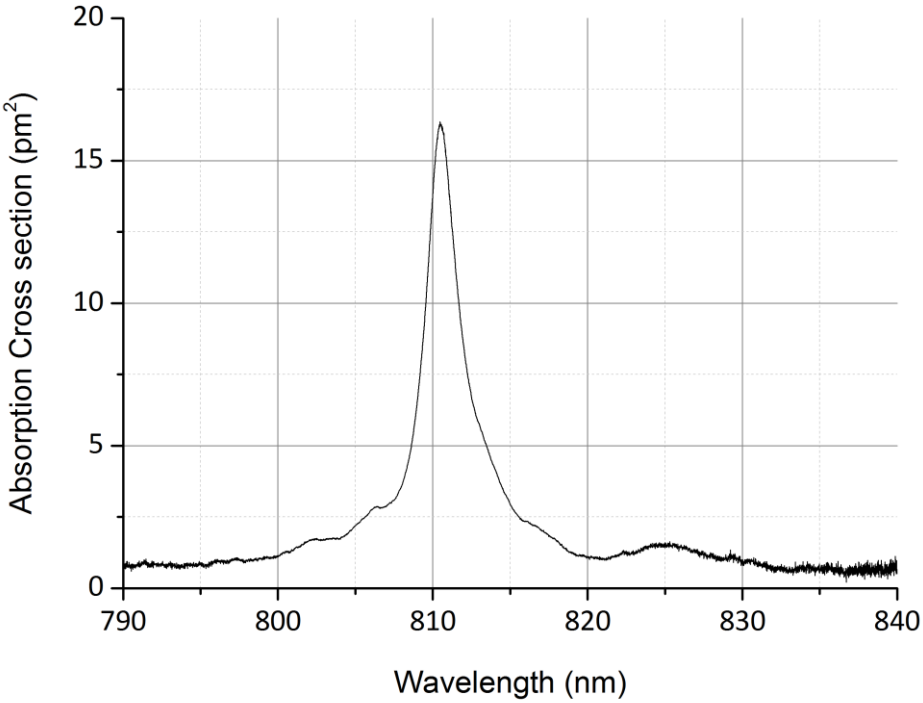

Figure A-77 Absorption cross section of Nd:KGW, E//Nm at 450K

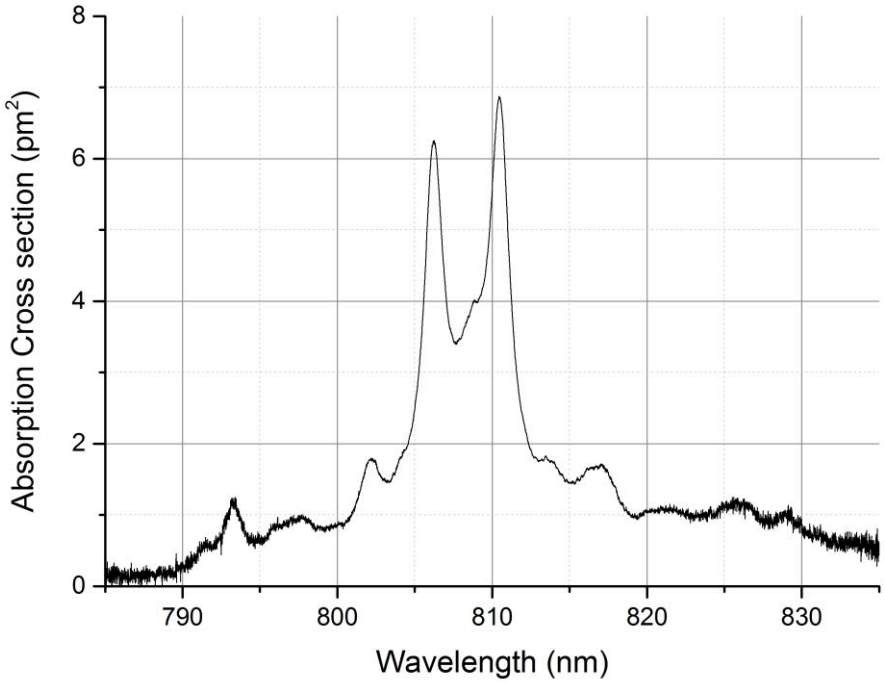

Figure A-78 Absorption cross section of Nd:KGW, E//Np at 300K

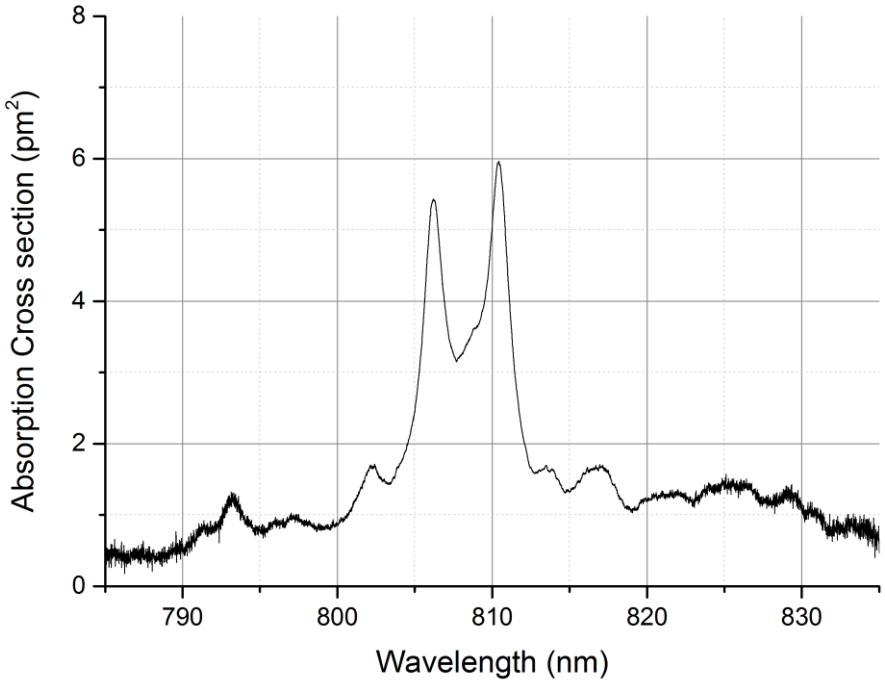

Figure A-79 Absorption cross section of Nd:KGW, E//Np at 330K

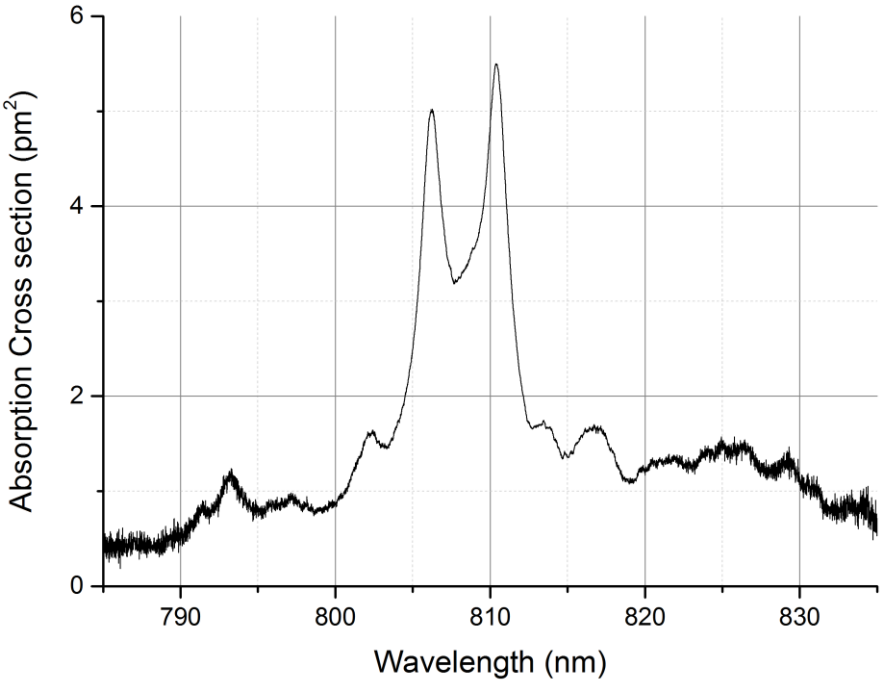

Figure A-80 Absorption cross section of Nd:KGW, E//Np at 360K

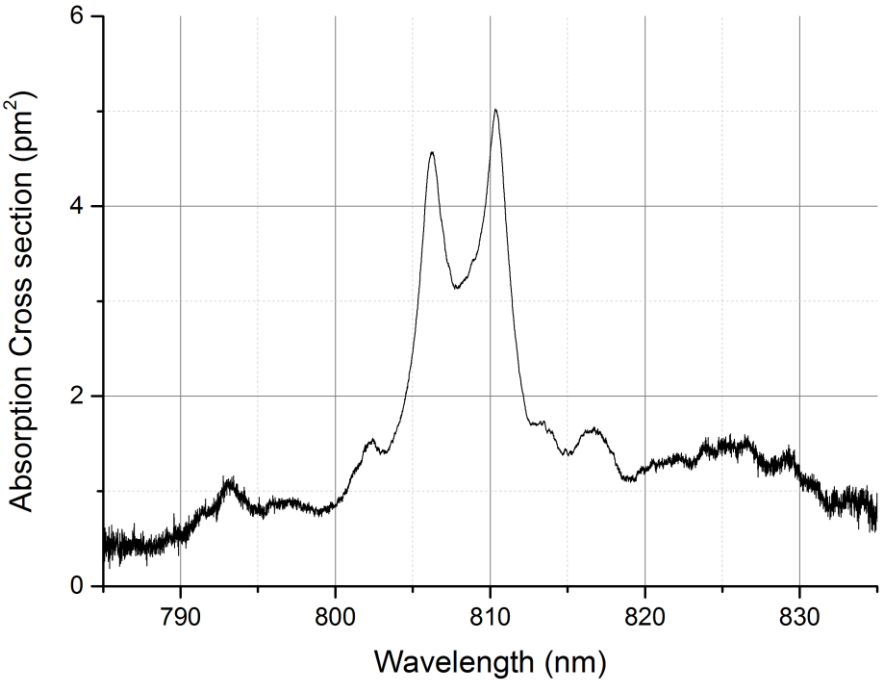

Figure A-81 Absorption cross section of Nd:KGW, E//Np at 390K

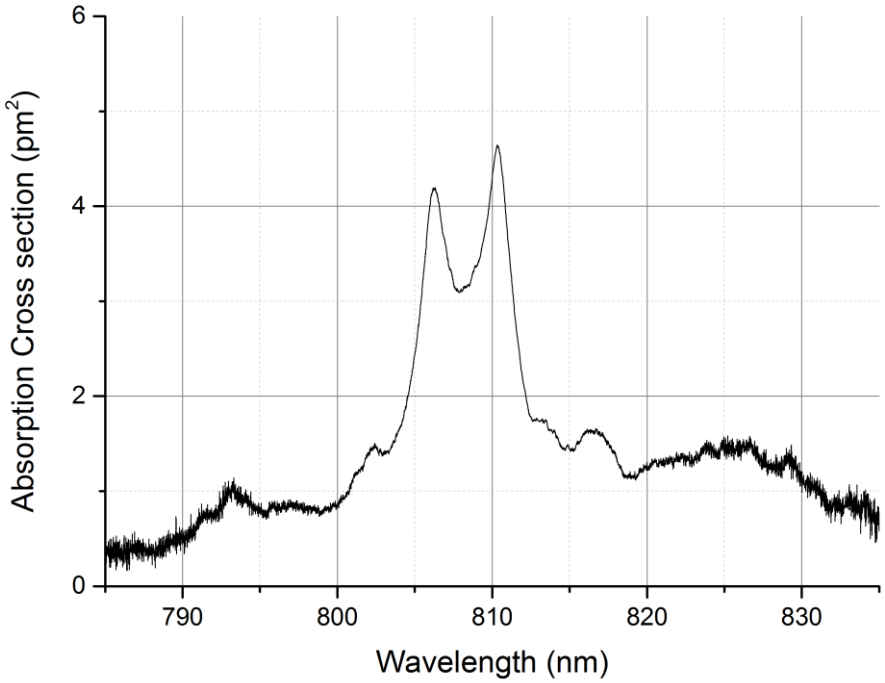

Figure A-82 Absorption cross section of Nd:KGW, E//Np at 420K

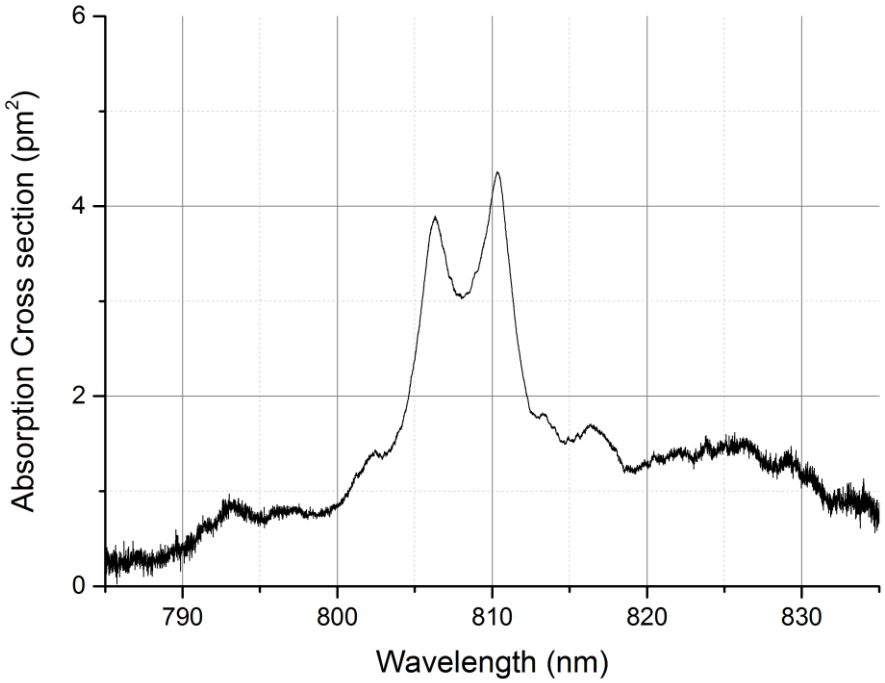

Figure A-83 Absorption cross section of Nd:KGW, E//Np at 450K

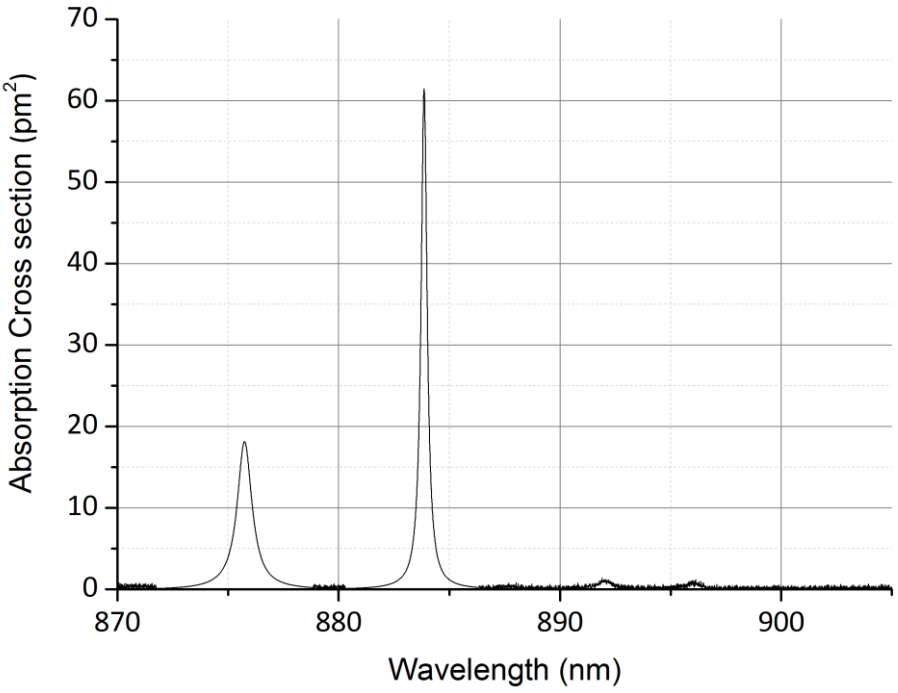

Figure A-84 Absorption cross section of Nd:KGW, E//Nm, 870-905nm at 77K

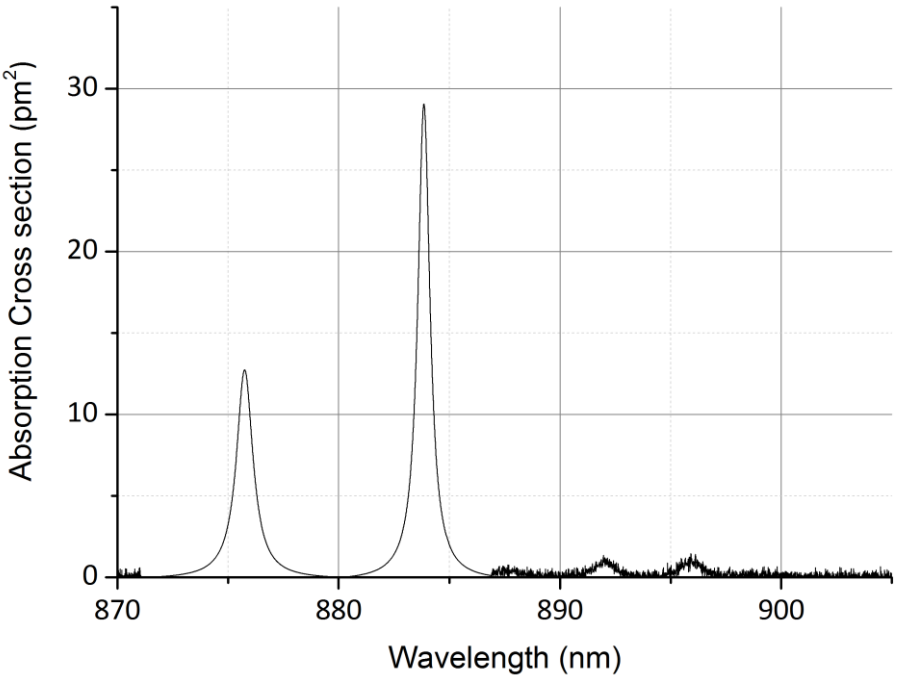

Figure A-85 Absorption cross section of Nd:KGW, E//Nm, 870-905nm at 125K

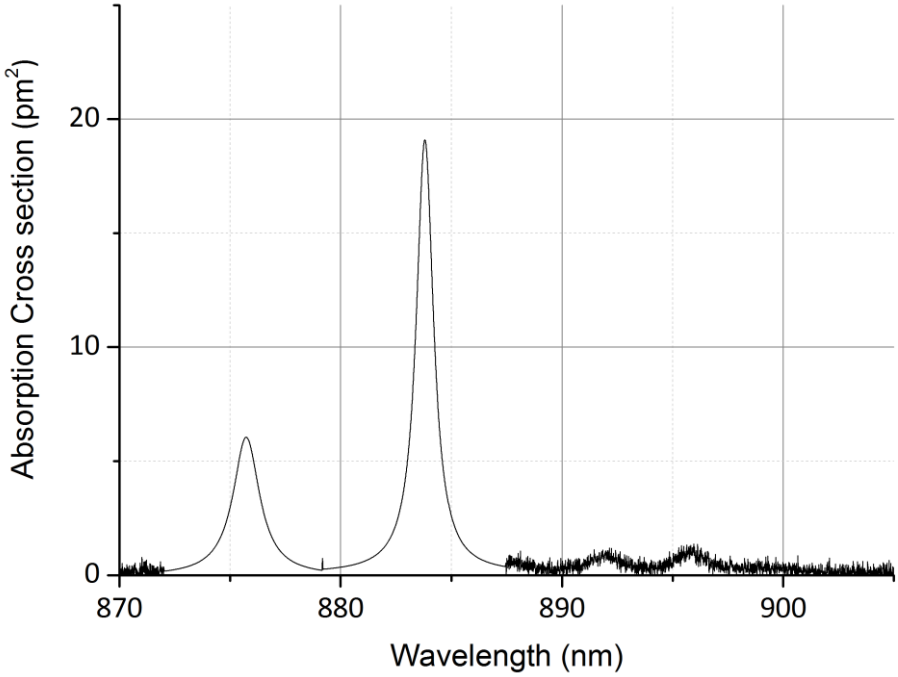

Figure A-86 Absorption cross section of Nd:KGW, E//Nm, 870-905nm at 195K

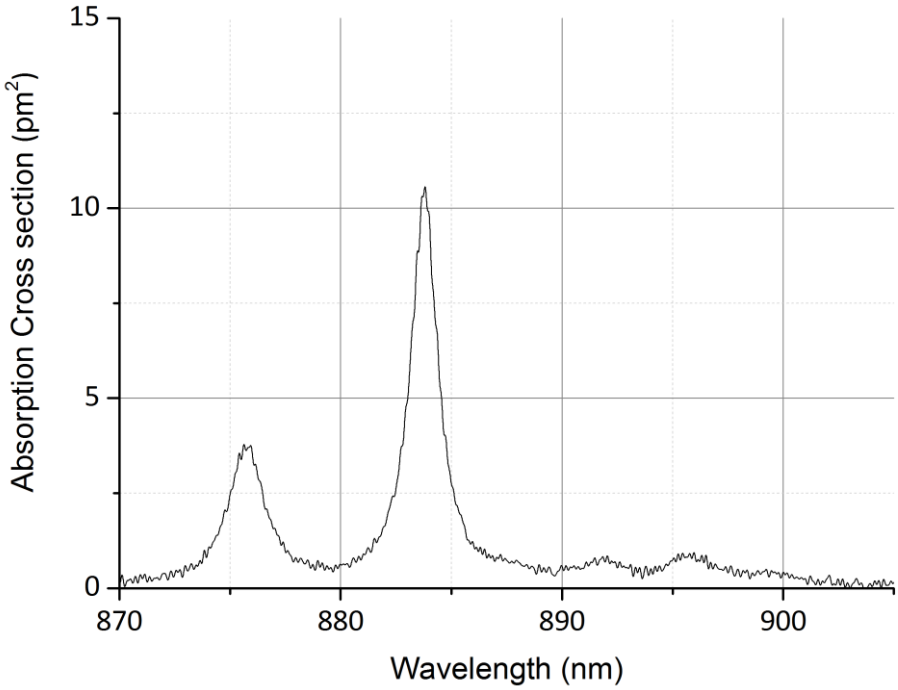

Figure A-87 Absorption cross section of Nd:KGW, E//Nm, 870-905nm at 273K

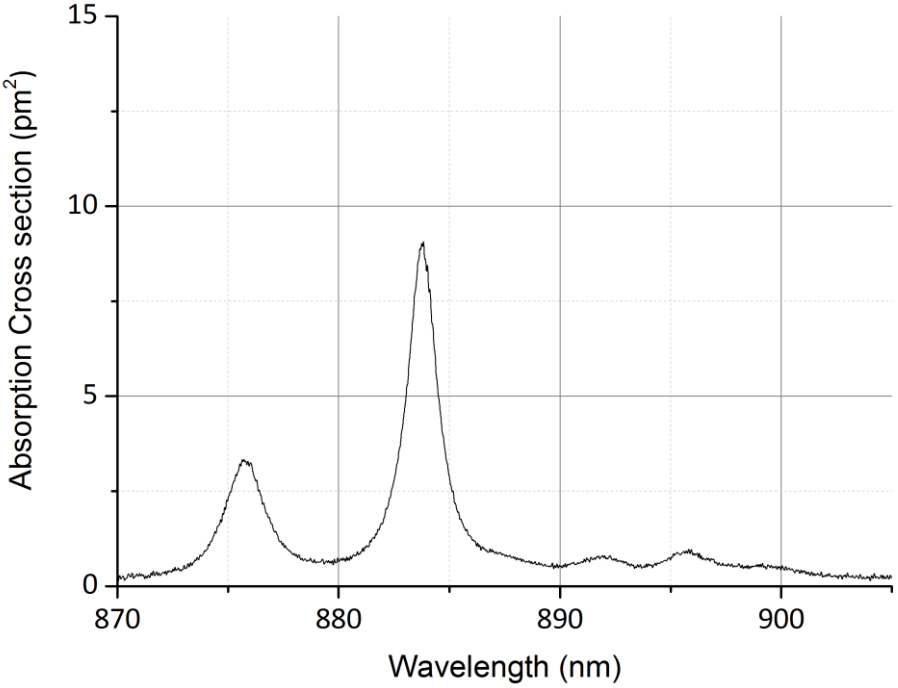

Figure A-88 Absorption cross section of Nd:KGW, E//Nm, 870-905nm at 300K

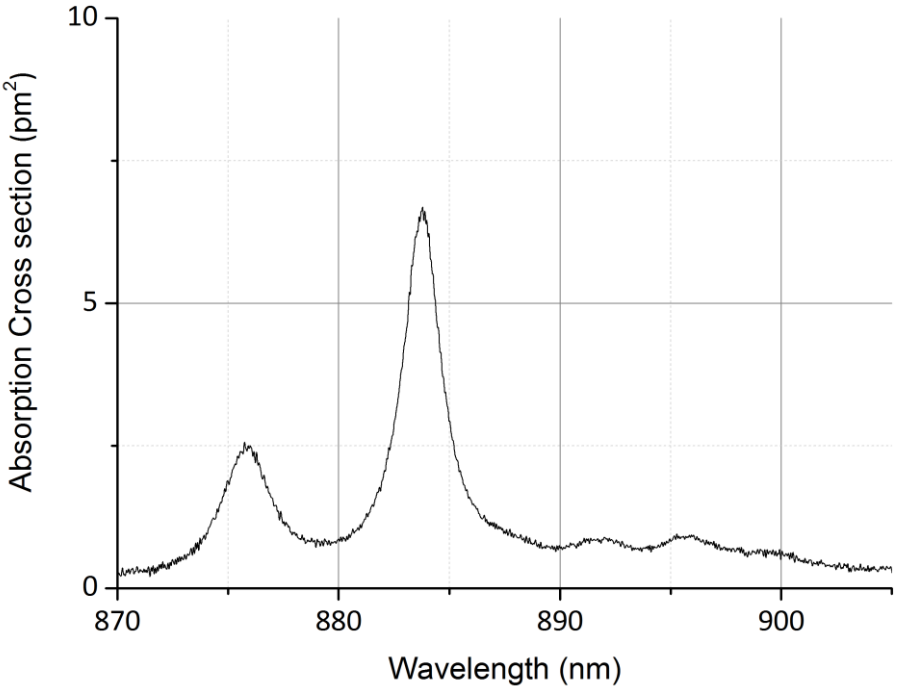

Figure A-89 Absorption cross section of Nd:KGW, E//Nm, 870-905nm at 360K

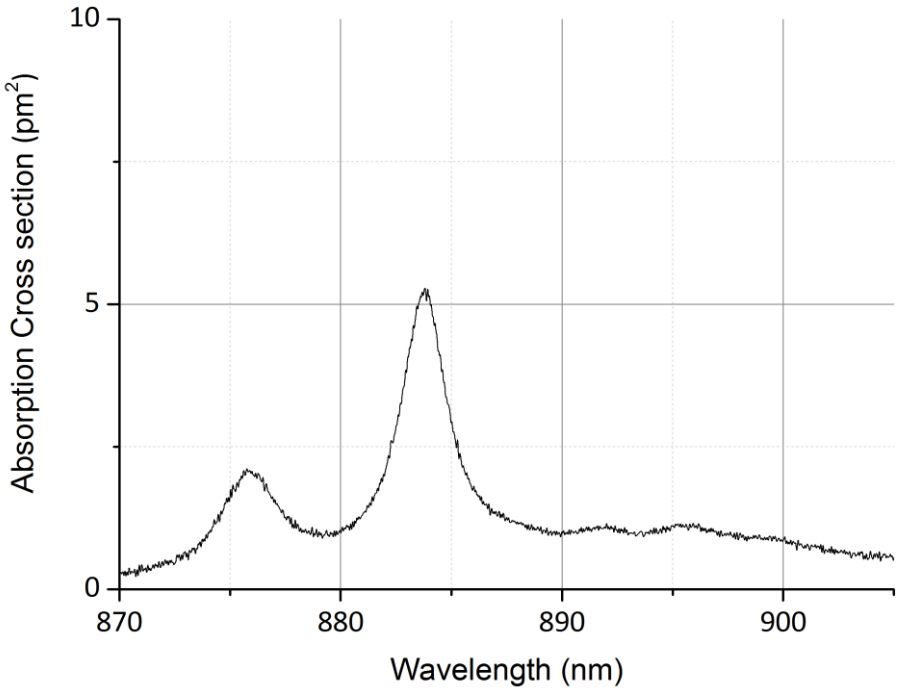

Figure A-90 Absorption cross section of Nd:KGW, E//Nm, 870-905nm at 420K

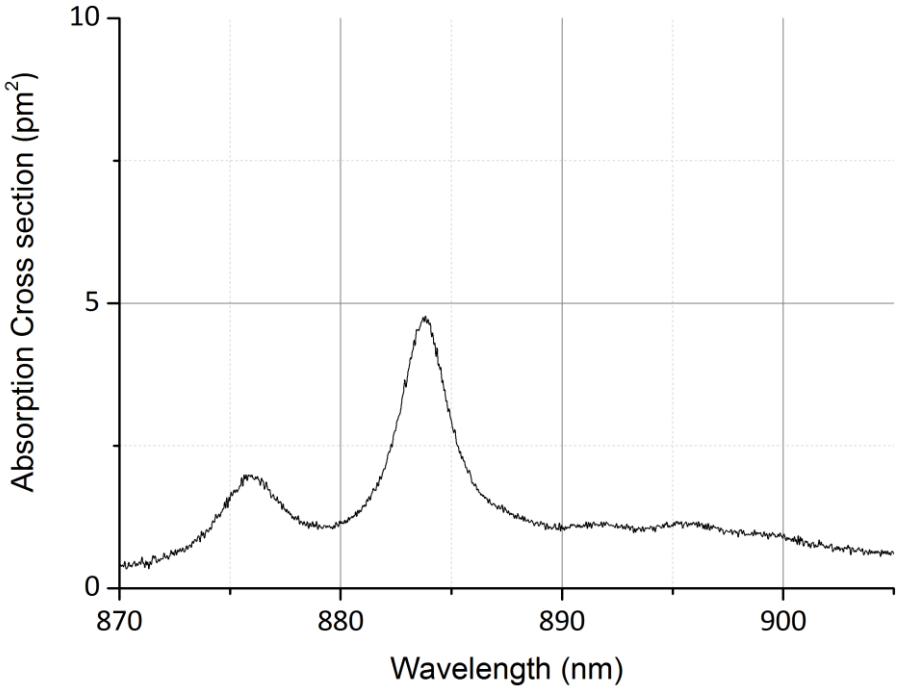

Figure A-91 Absorption cross section of Nd:KGW, E//Nm, 870-905nm at 450K

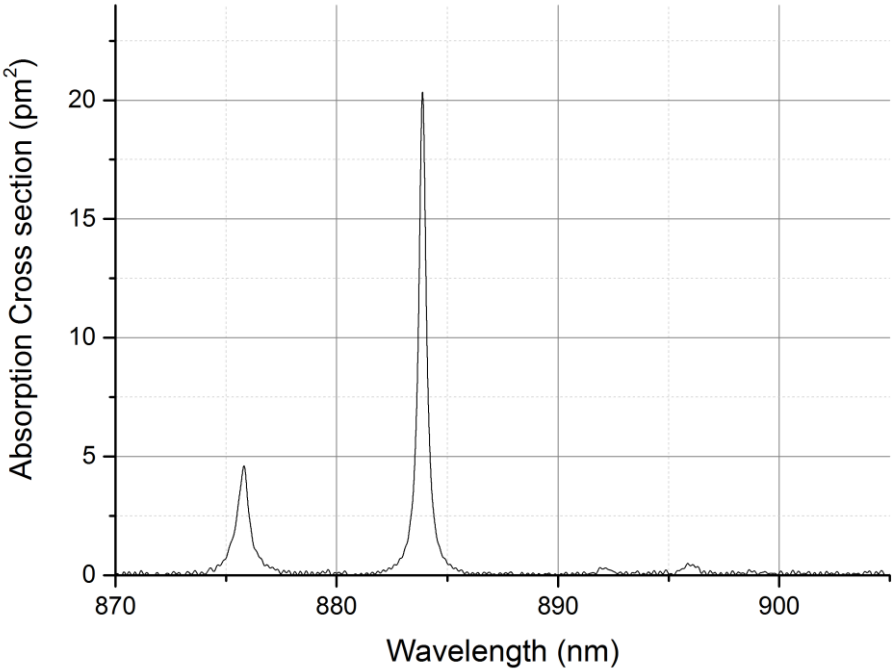

Figure A-92 Absorption cross section of Nd:KGW, E//Np, 870-905nm at 77K

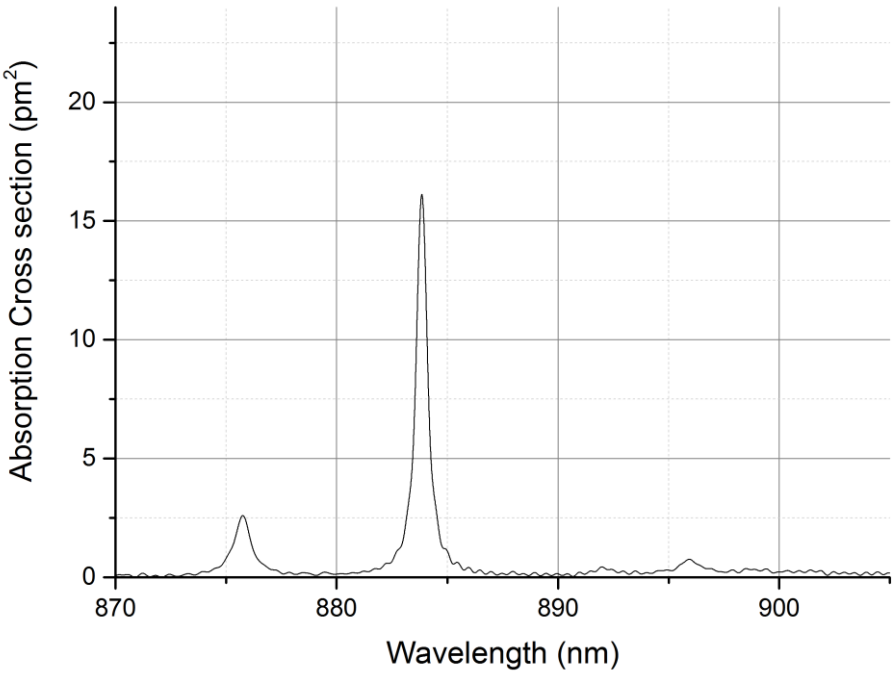

Figure A-93 Absorption cross section of Nd:KGW, E//Np, 870-905nm at 125K

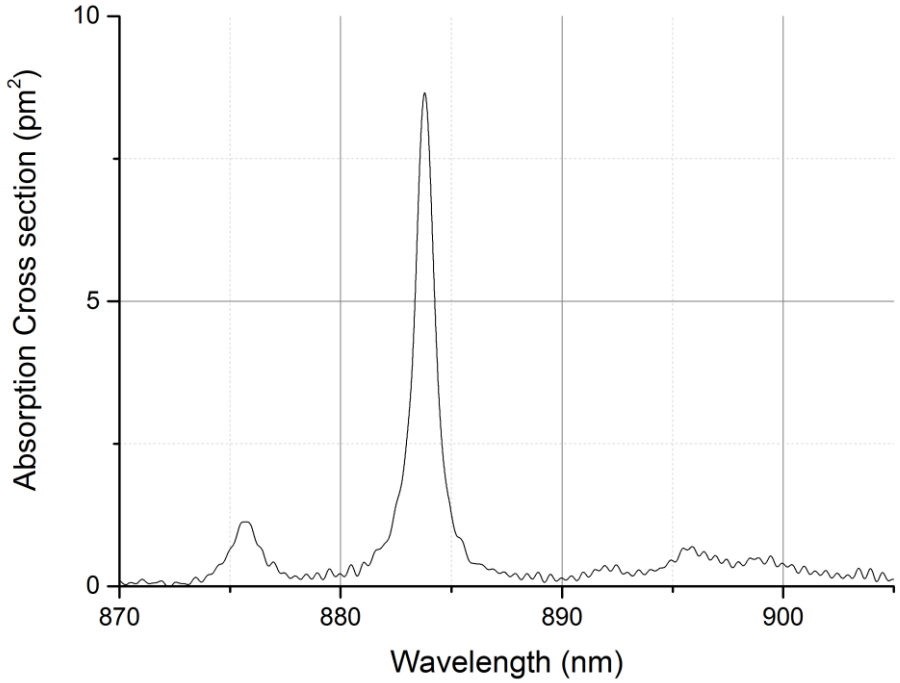

Figure A-94 Absorption cross section of Nd:KGW, E//Np, 870-905nm at 200K

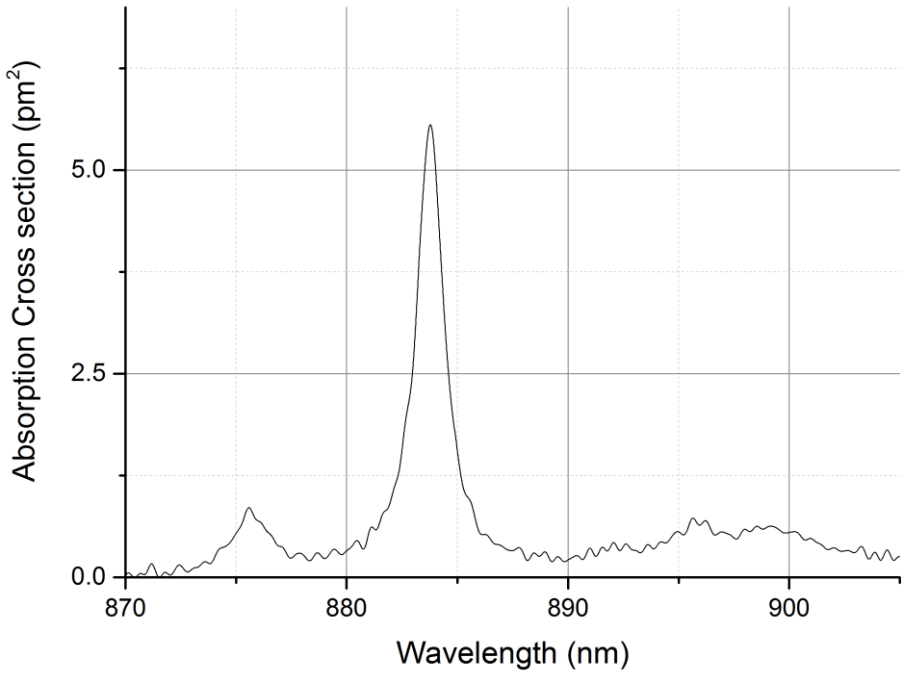

Figure A-95 Absorption cross section of Nd:KGW, E//Np, 870-905nm at 273K

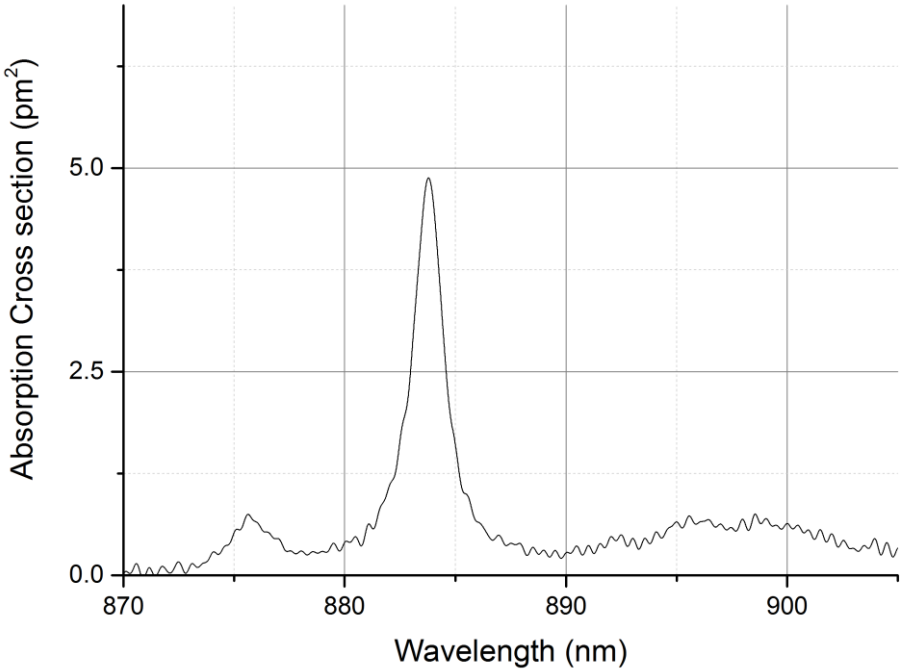

Figure A-96 Absorption cross section of Nd:KGW, E//Np, 870-905nm at 300K

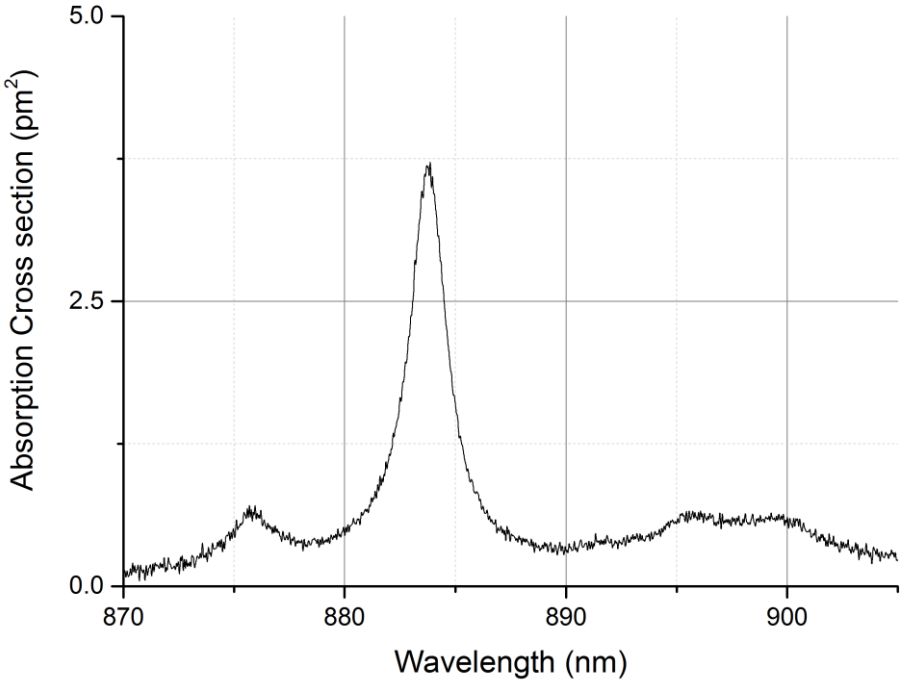

Figure A-97 Absorption cross section of Nd:KGW, E//Np, 870-905nm at 360K

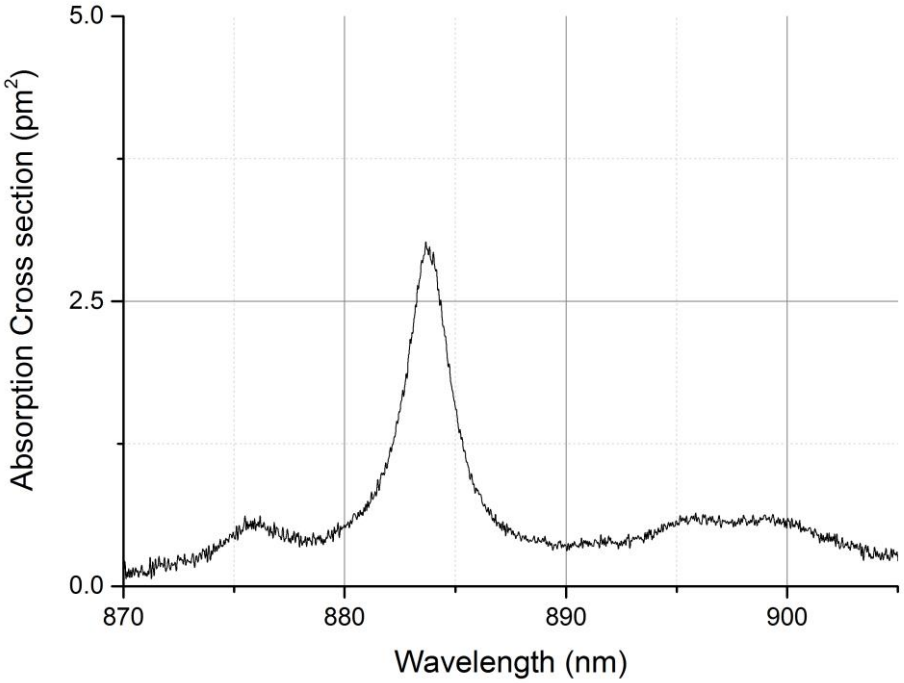

Figure A-98 Absorption cross section of Nd:KGW, E//Np, 870-905nm at 420K

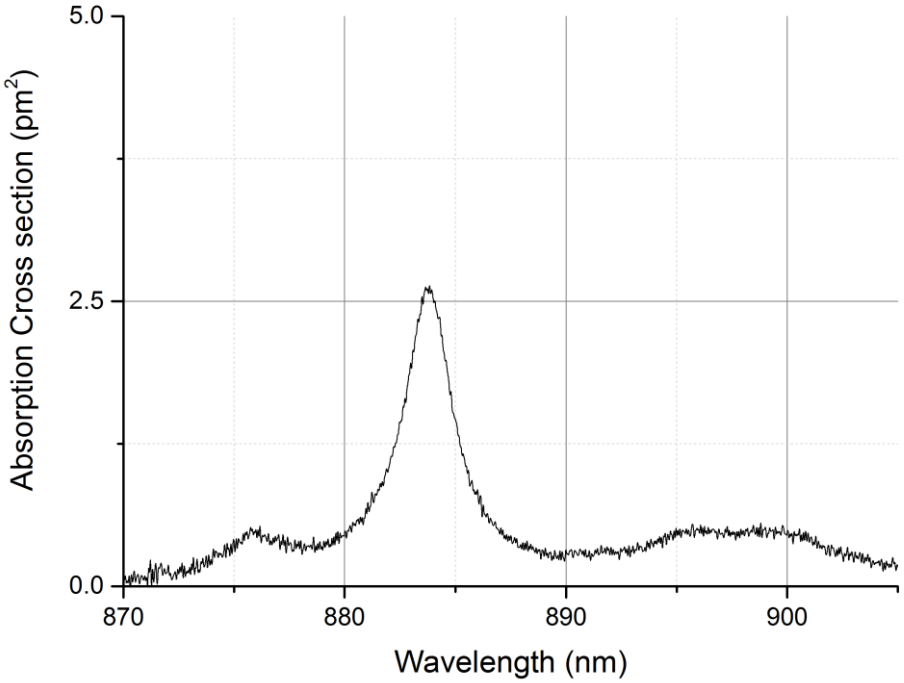

Figure A-99 Absorption cross section of Nd:KGW, E//Np, 870-905nm at 450K

A.6 Emission cross section of Nd:YAG

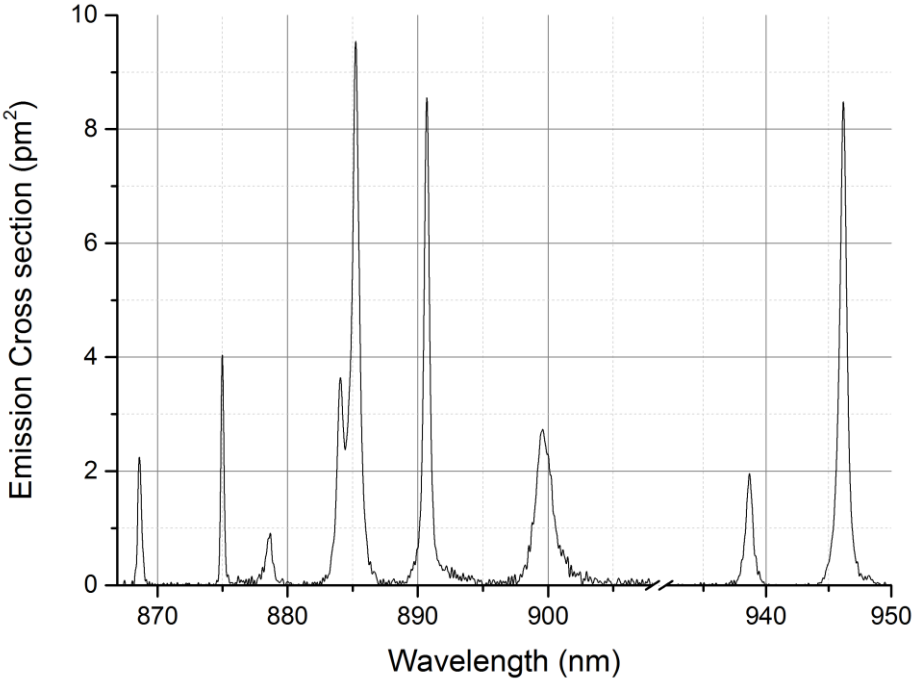

Figure A-100 Emission cross section of Nd:YAG $^4I_{9/2}$ at 77K

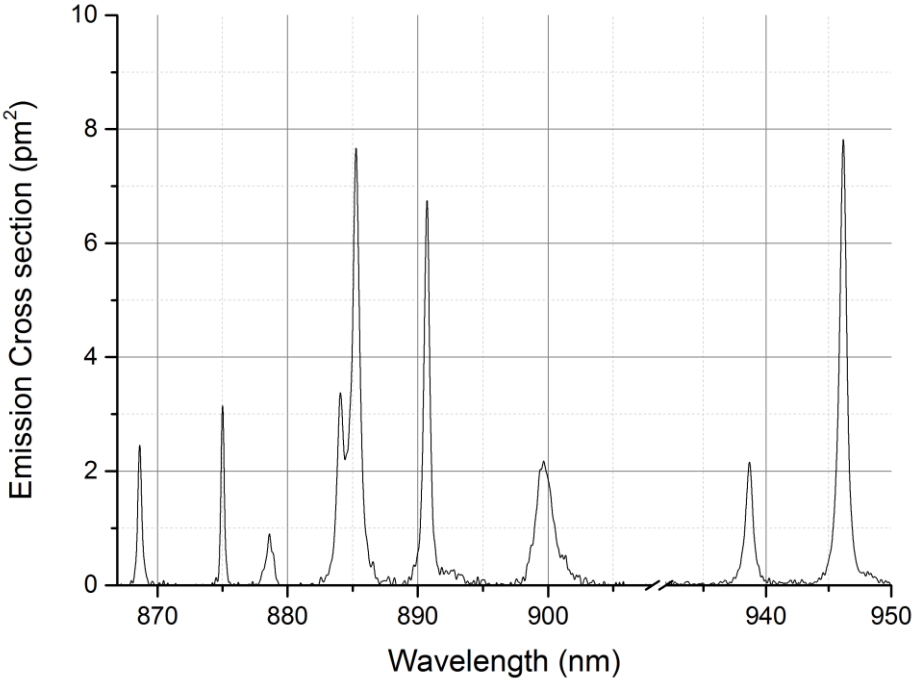

Figure A-101 Emission cross section of Nd:YAG $^4I_{9/2}$ at 100K

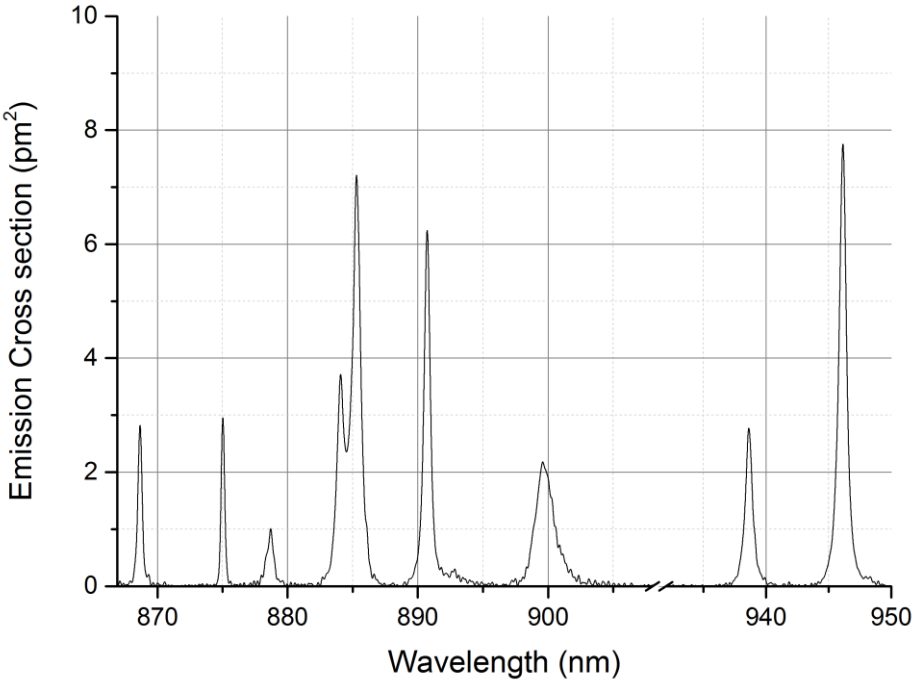

Figure A-102 Emission cross section of Nd:YAG $^4I_{9/2}$ at 125K

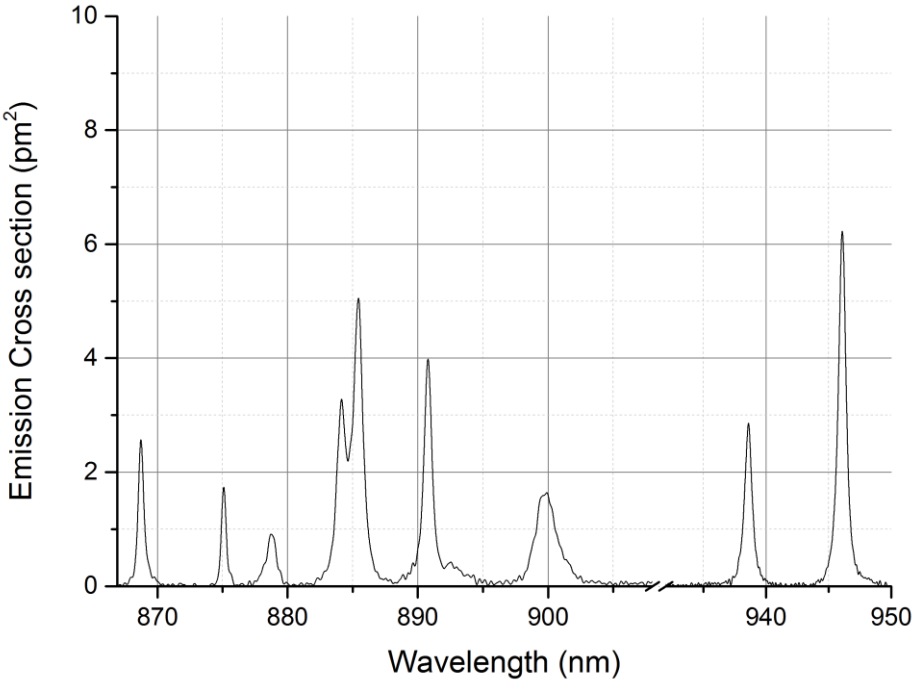

Figure A-103 Emission cross section of Nd:YAG $^4I_{9/2}$ at 165K

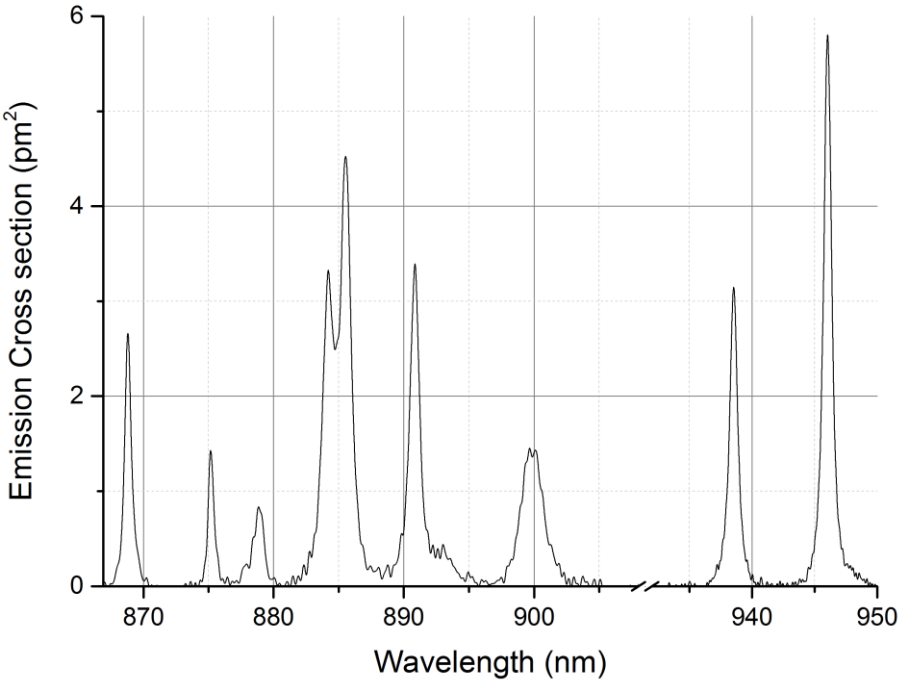

Figure A-104 Emission cross section of Nd:YAG $^4I_{9/2}$ at 200K

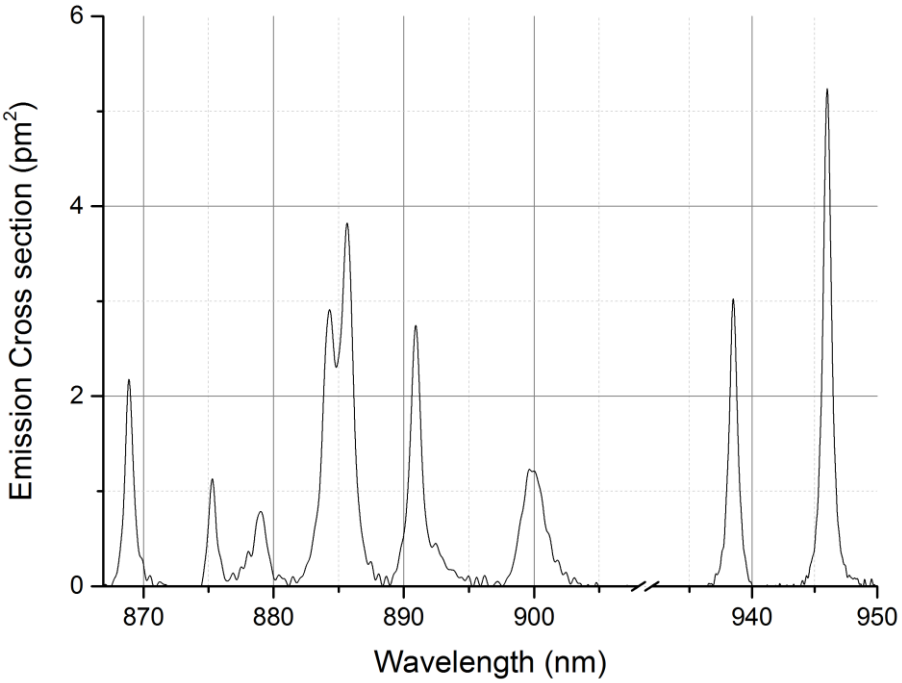

Figure A-105 Emission cross section of Nd:YAG $^4I_{9/2}$ at 240K

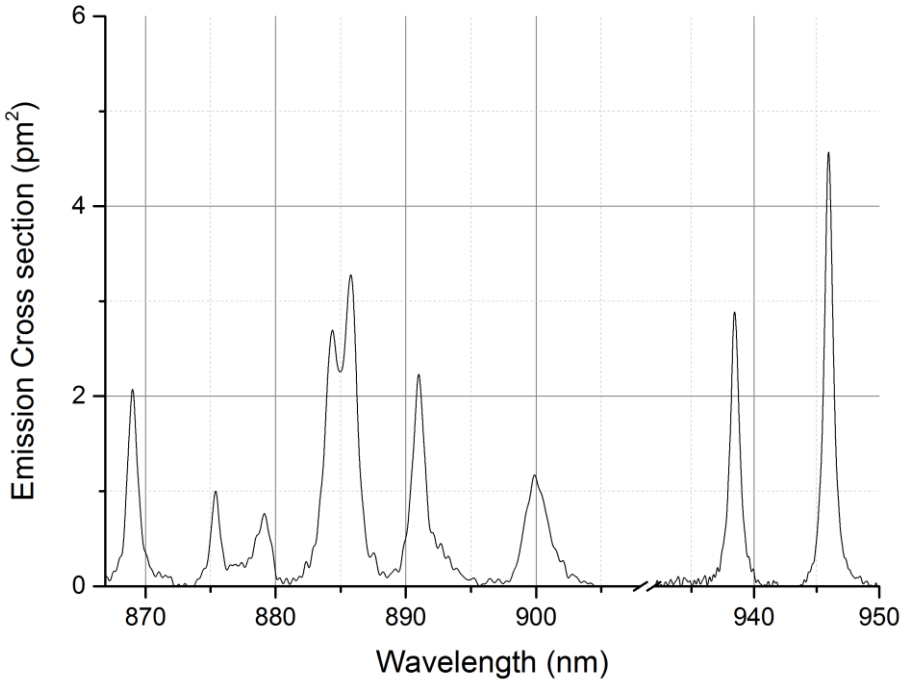

Figure A-106 Emission cross section of Nd:YAG $^4I_{9/2}$ at 273K

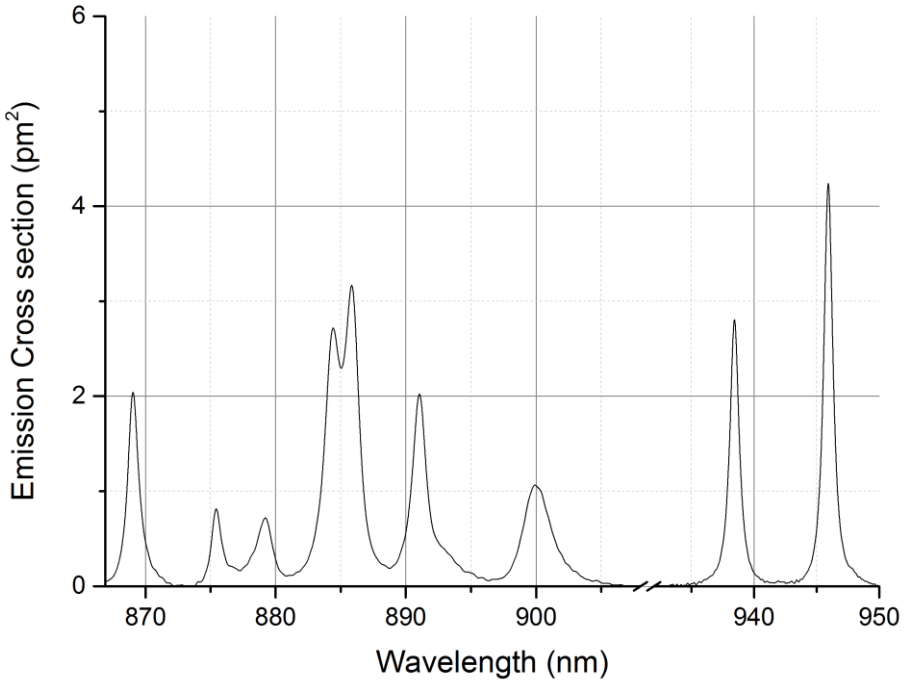

Figure A-107 Emission cross section of Nd:YAG $^4I_{9/2}$ at 300K

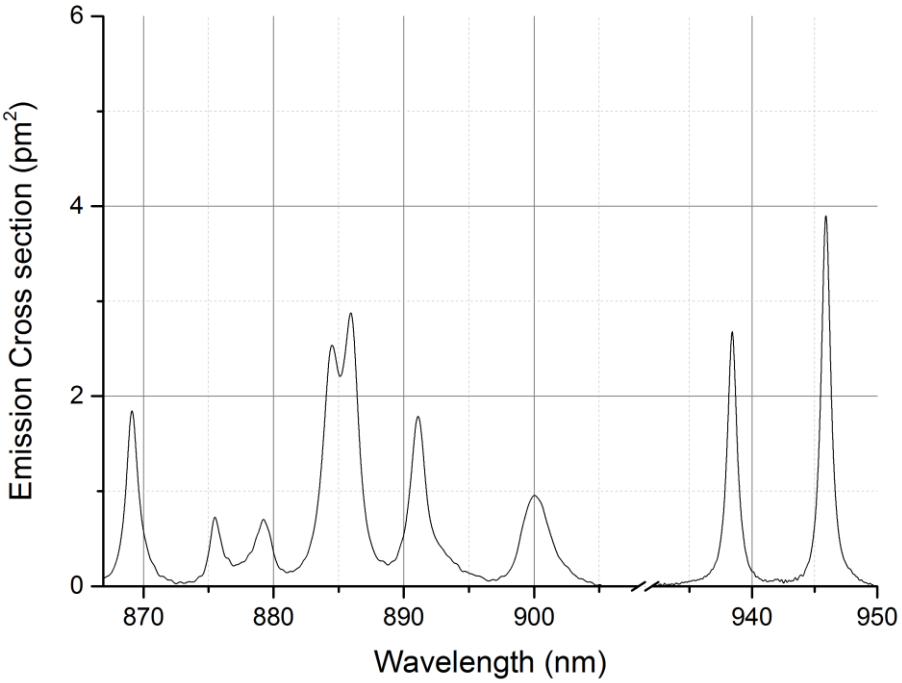

Figure A-108 Emission cross section of Nd:YAG $^4I_{9/2}$ at 330K

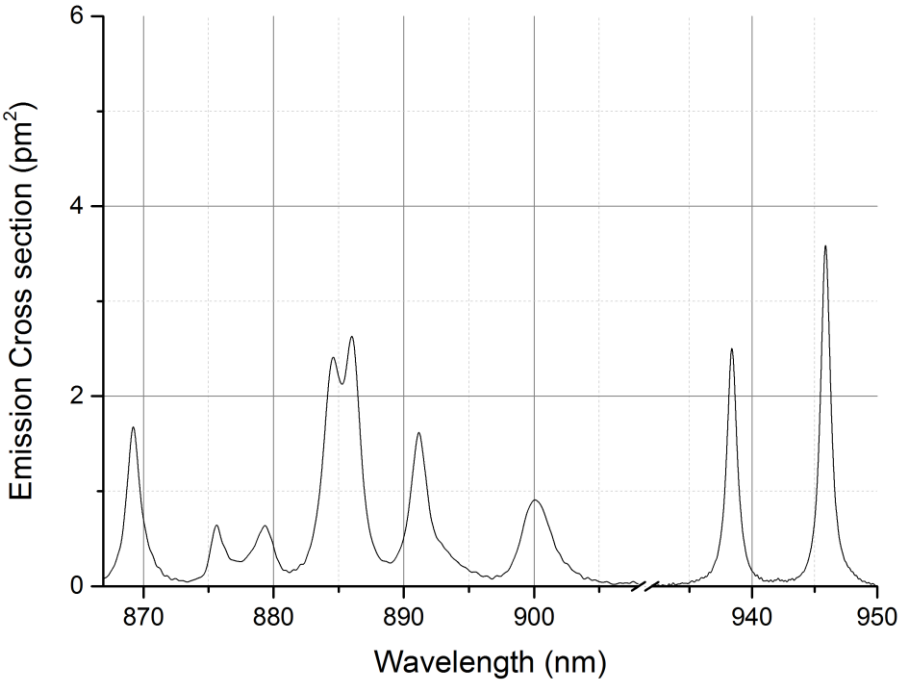

Figure A-109 Emission cross section of Nd:YAG $^4I_{9/2}$ at 360K

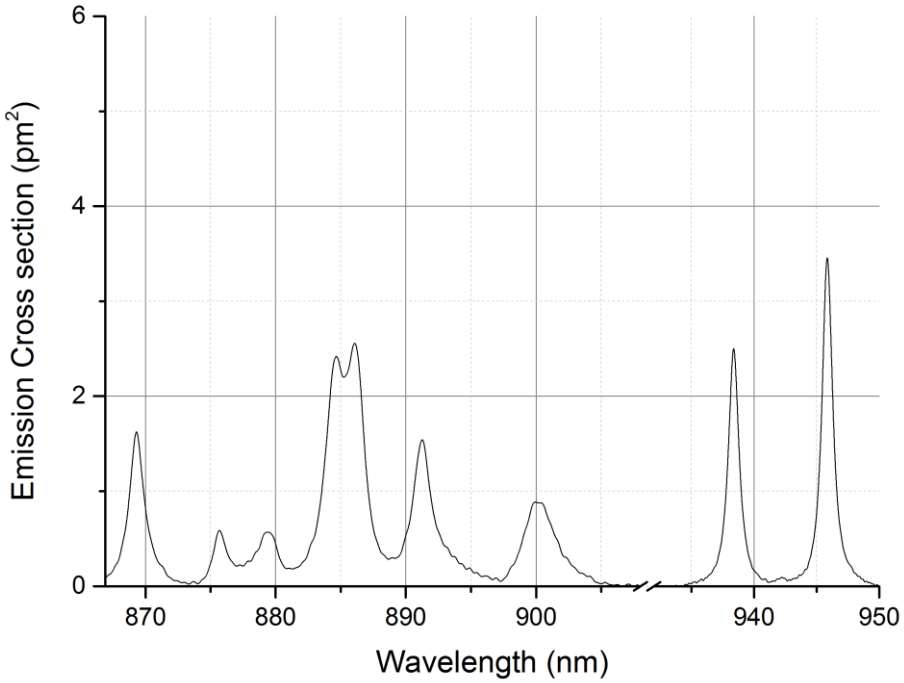

Figure A-110 Emission cross section of Nd:YAG $^4I_{9/2}$ at 390K

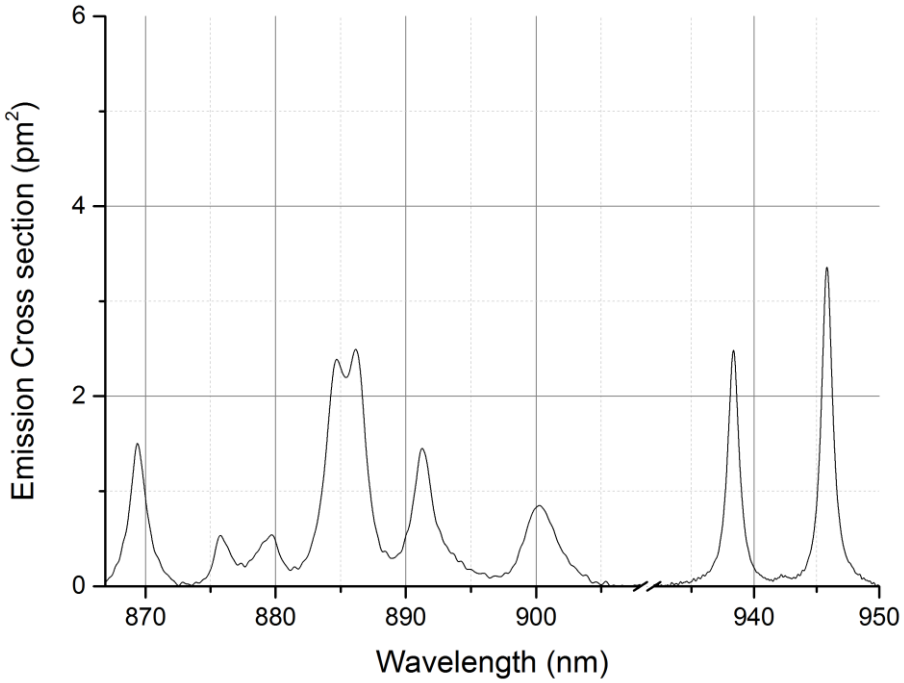

Figure A-111 Emission cross section of Nd:YAG $^4I_{9/2}$ at 420K

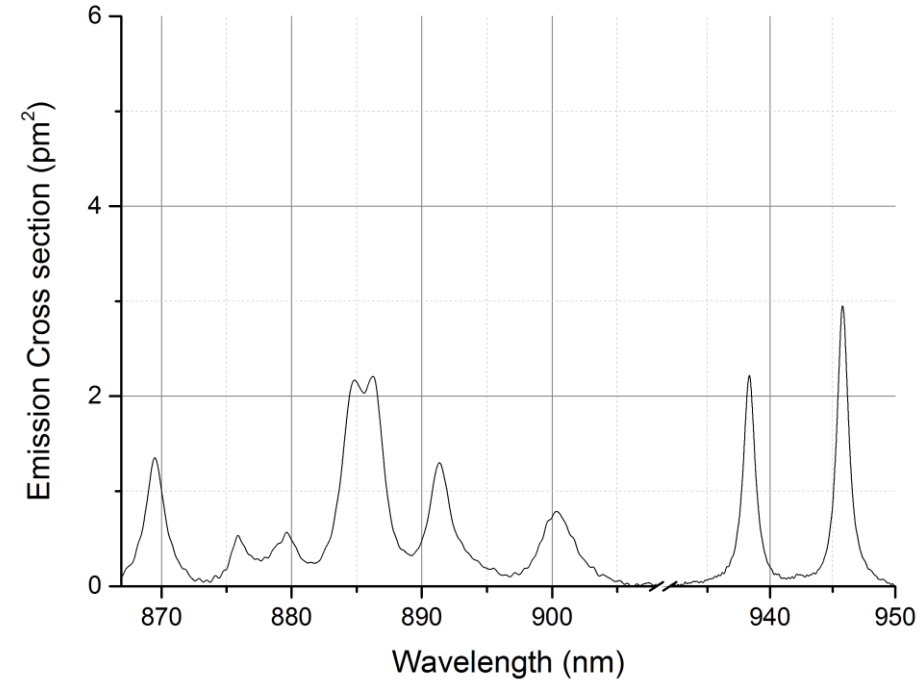

Figure A-112 Emission cross section of Nd:YAG $^4I_{9/2}$ at 450K

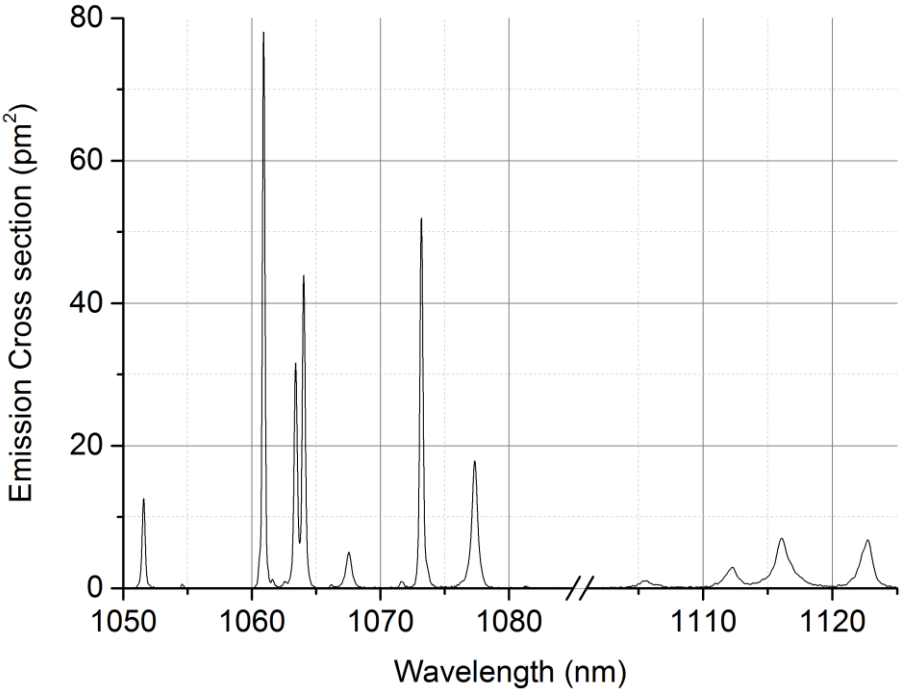

Figure A-113 Emission cross section of Nd:YAG $^4I_{11/2}$ at 77K

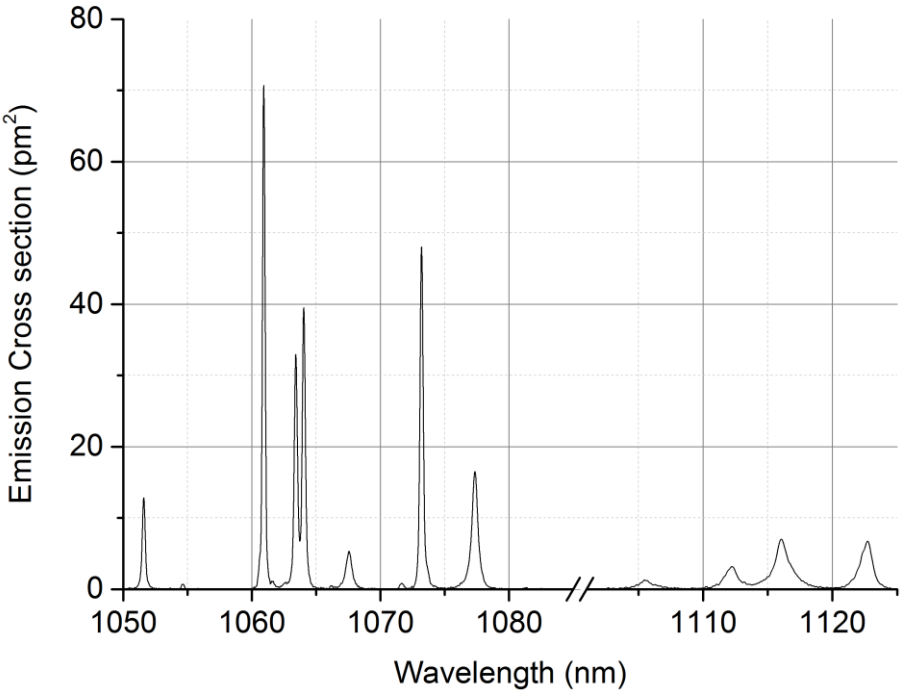

Figure A-114 Emission cross section of Nd:YAG $^4I_{11/2}$ at 100K

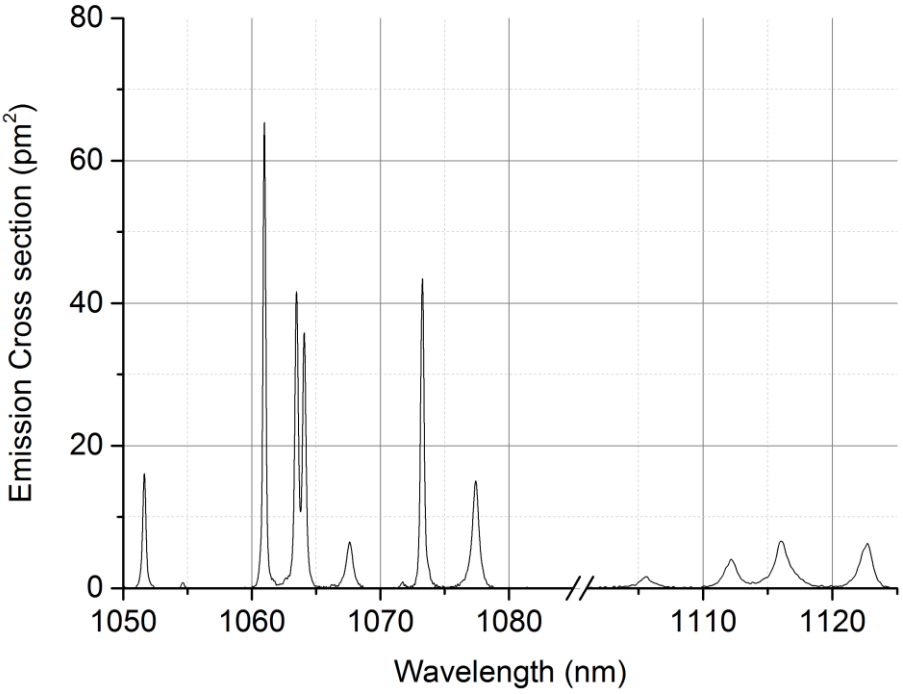

Figure A-115 Emission cross section of Nd:YAG $^4I_{11/2}$ at 125K

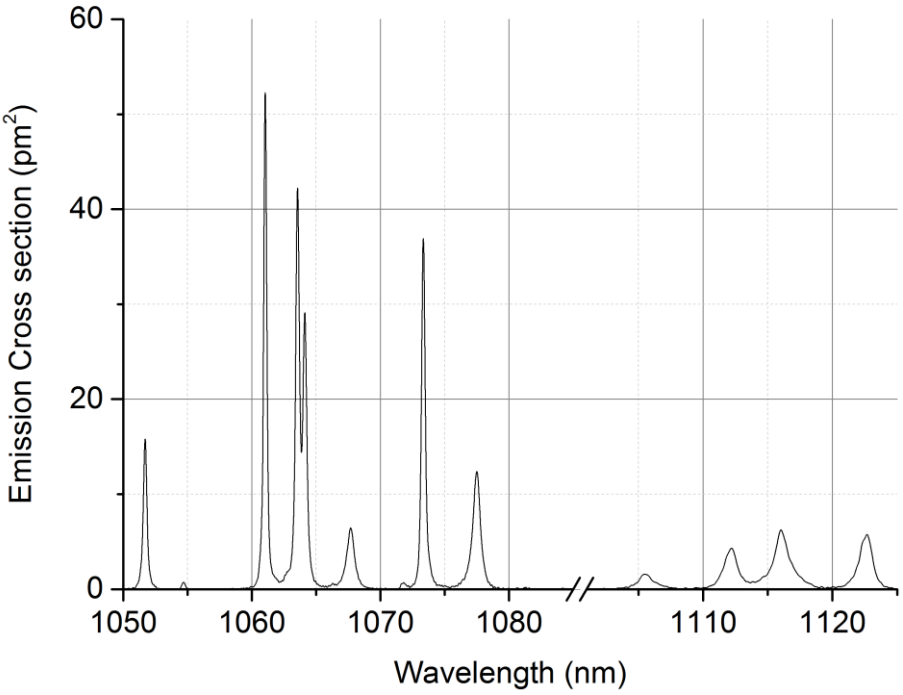

Figure A-116 Emission cross section of Nd:YAG $^4I_{11/2}$ at 165K

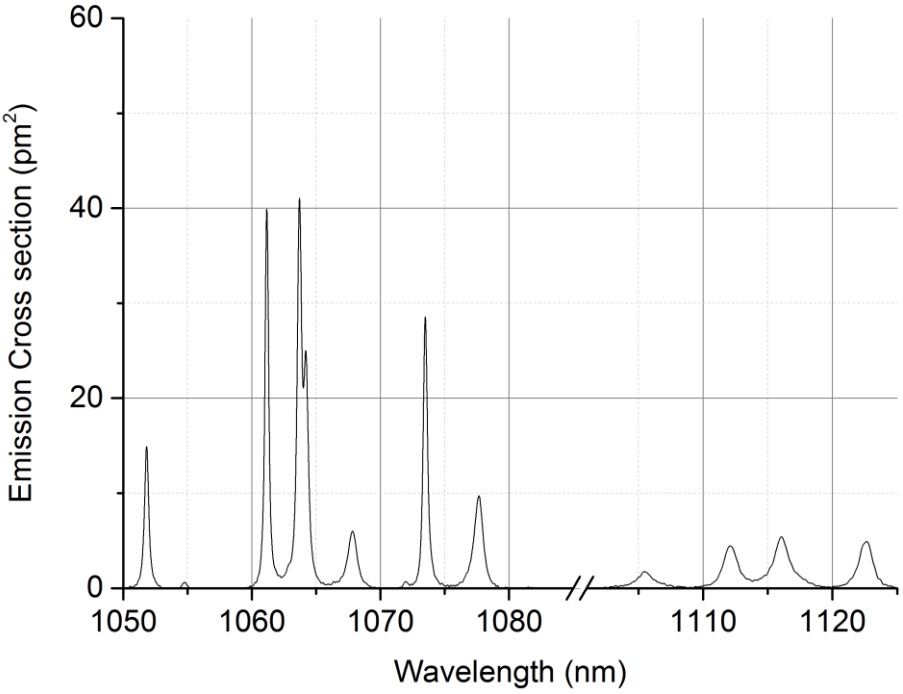

Figure A-117 Emission cross section of Nd:YAG $^4I_{11/2}$ at 200K

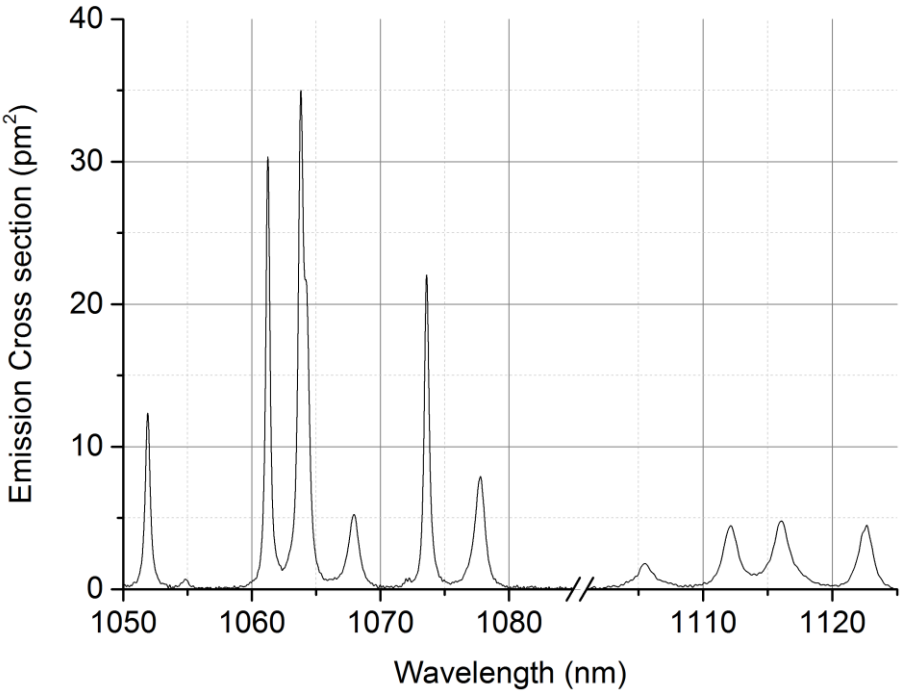

Figure A-118 Emission cross section of Nd:YAG $^4I_{11/2}$ at 240K

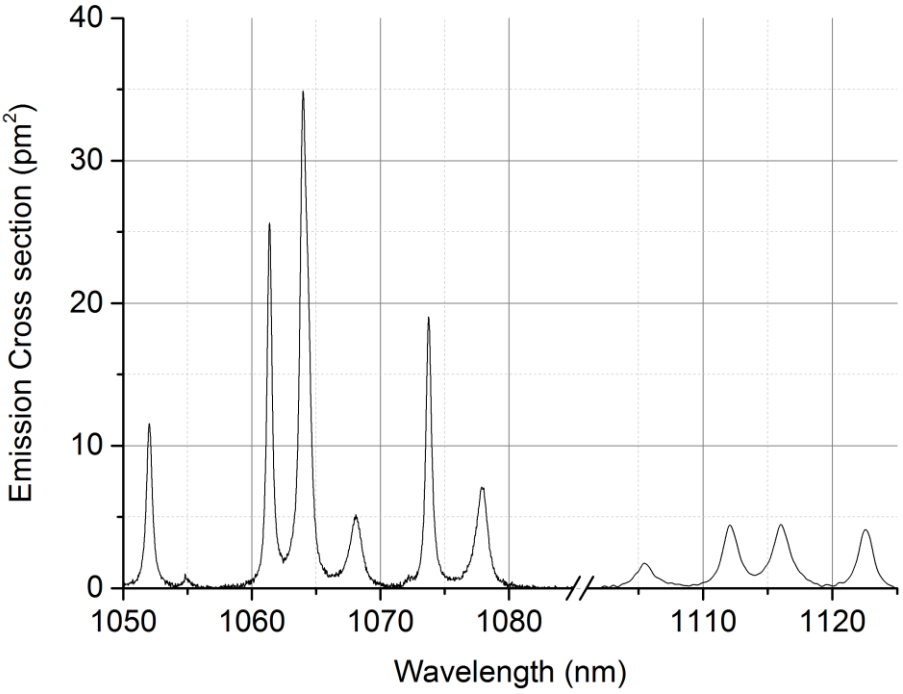

Figure A-119 Emission cross section of Nd:YAG $^4I_{11/2}$ at 273K

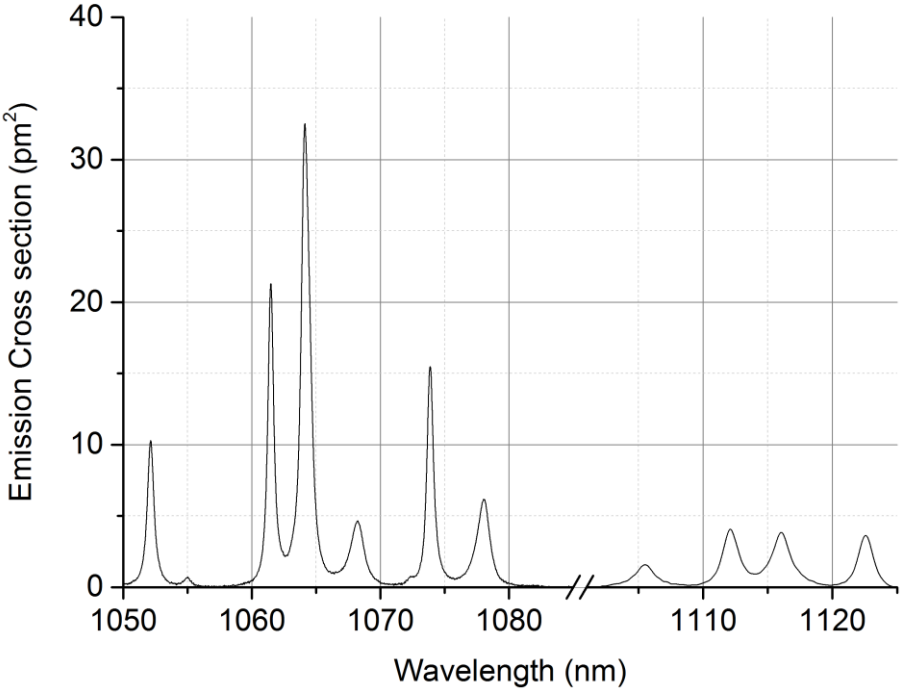

Figure A-120 Emission cross section of Nd:YAG $^4I_{11/2}$ at 300K

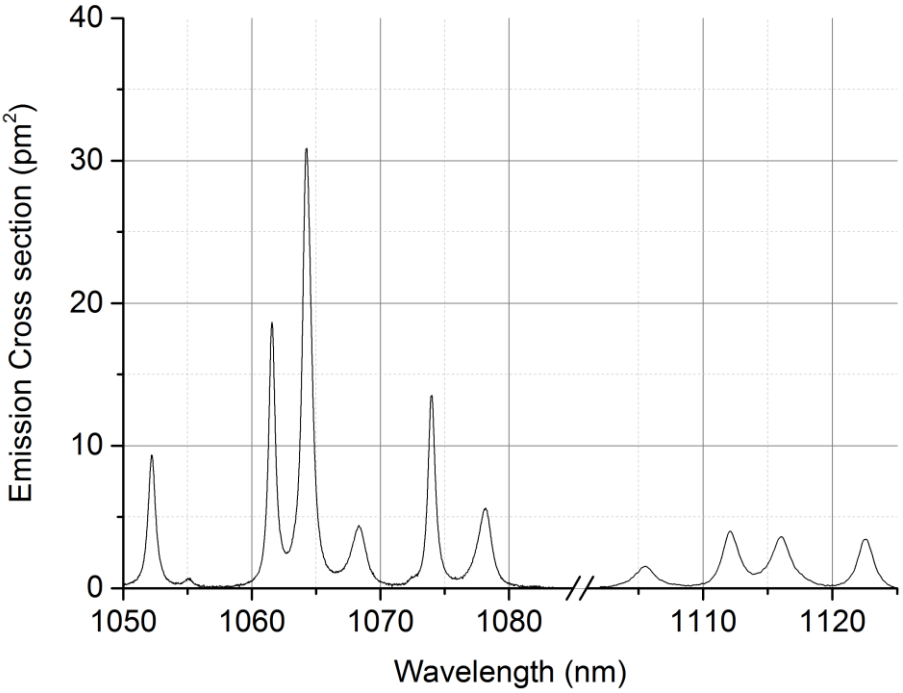

Figure A-121 Emission cross section of Nd:YAG $^4I_{11/2}$ at 330K

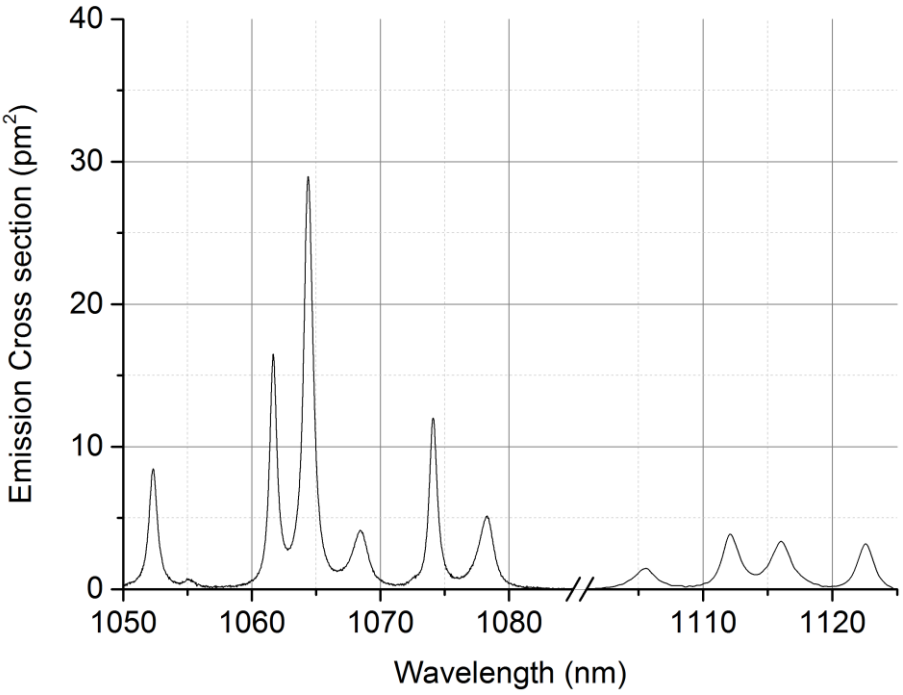

Figure A-122 Emission cross section of Nd:YAG $^4I_{11/2}$ at 360K

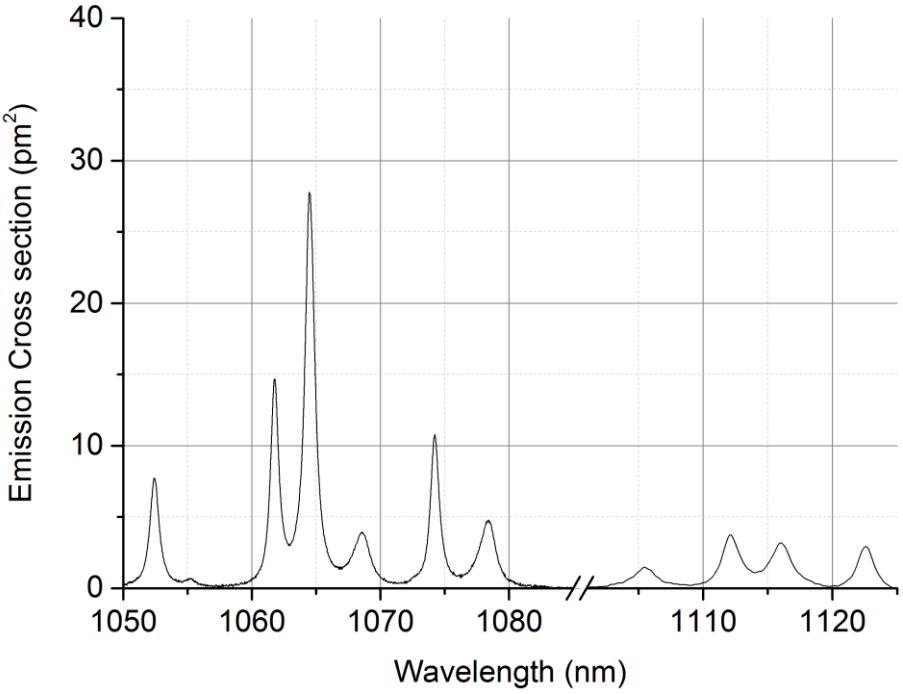

Figure A-123 Emission cross section of Nd:YAG $^4I_{11/2}$ at 390K

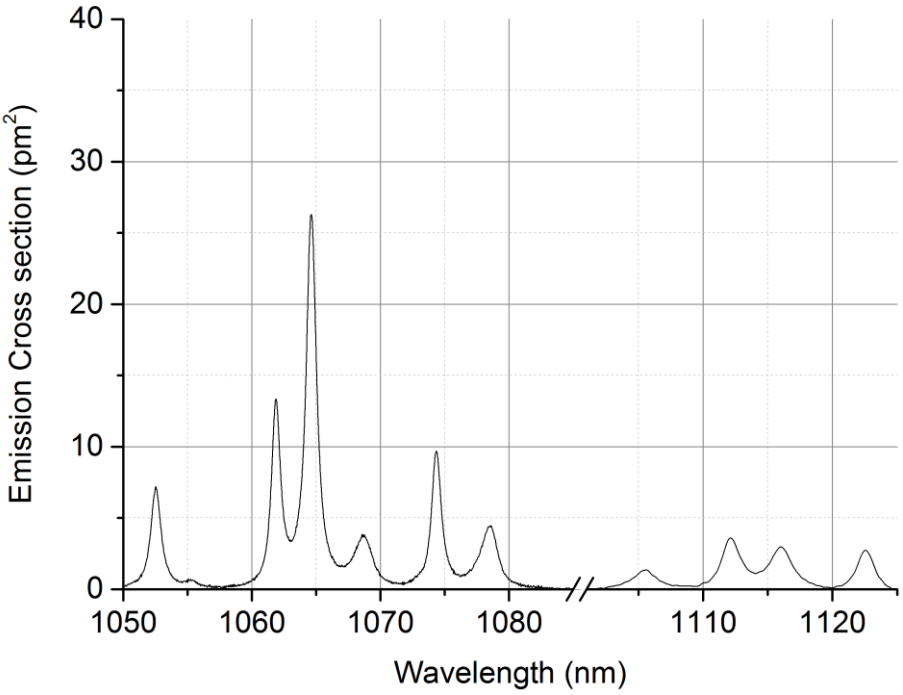

Figure A-124 Emission cross section of Nd:YAG $^4I_{11/2}$ at 420K

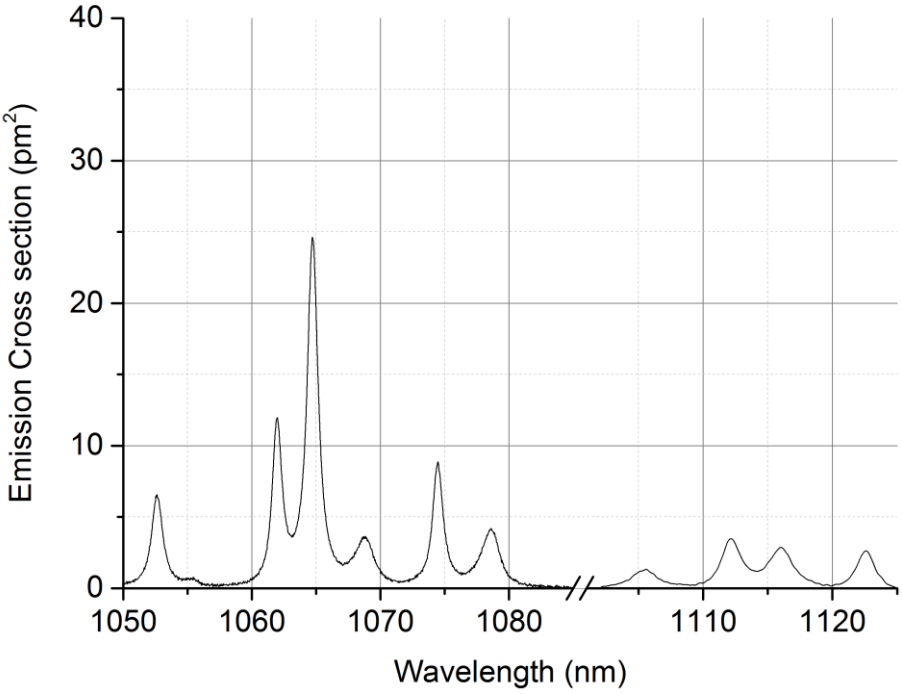

Figure A-125 Emission cross section of Nd:YAG $^4I_{11/2}$ at 450K

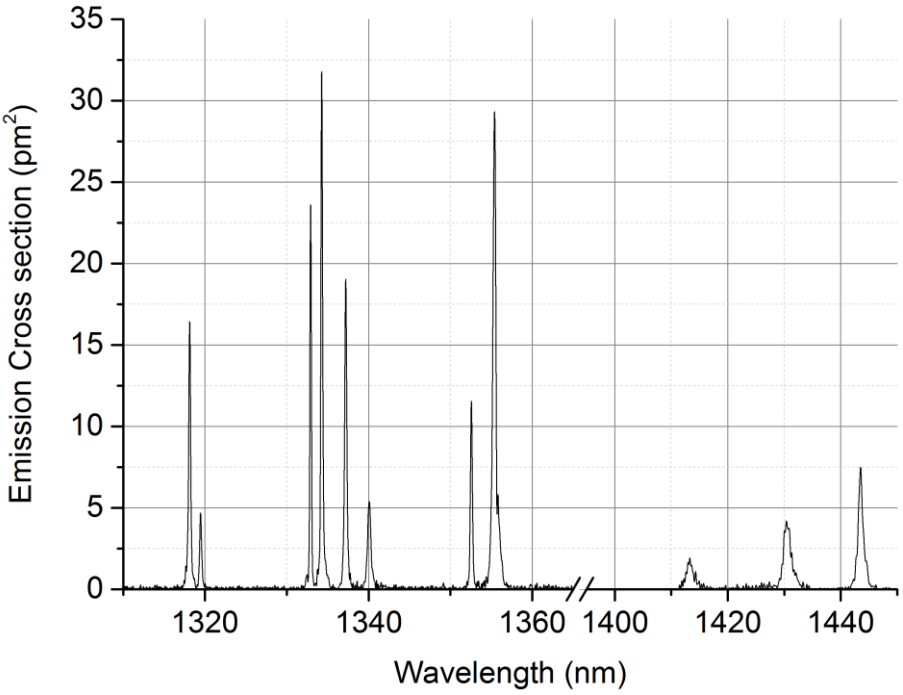

Figure A-126 Emission cross section of Nd:YAG $^4I_{13/2}$ at 77K

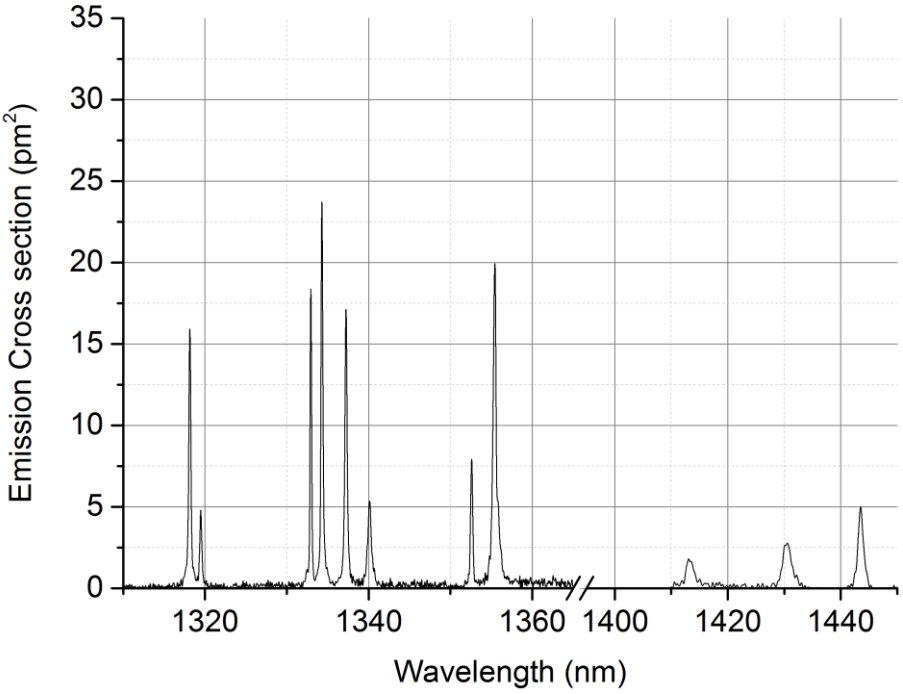

Figure A-127 Emission cross section of Nd:YAG $^4I_{13/2}$ at 100K

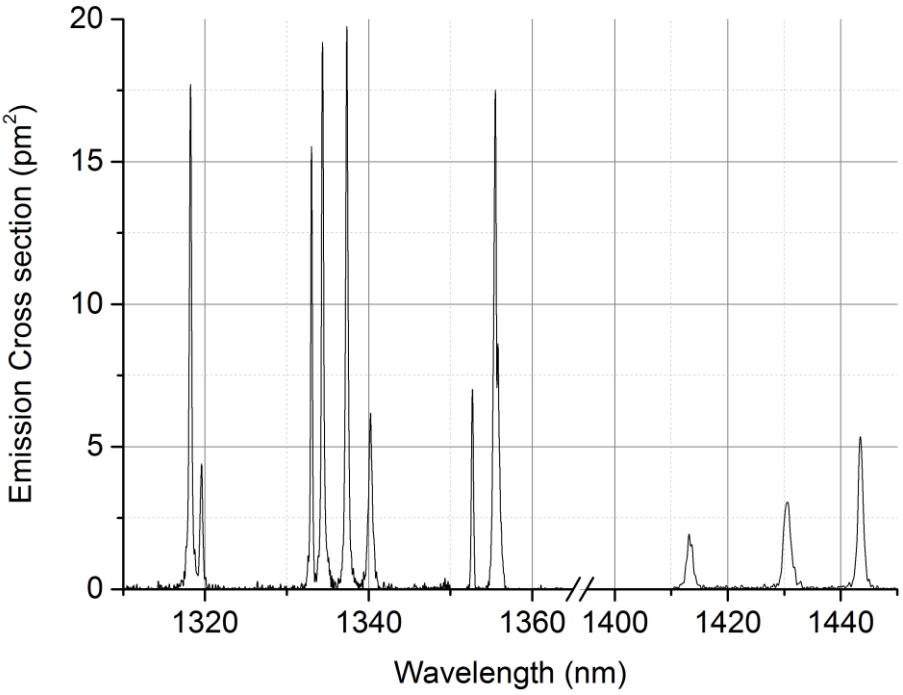

Figure A-128 Emission cross section of Nd:YAG $^4I_{13/2}$ at 125K

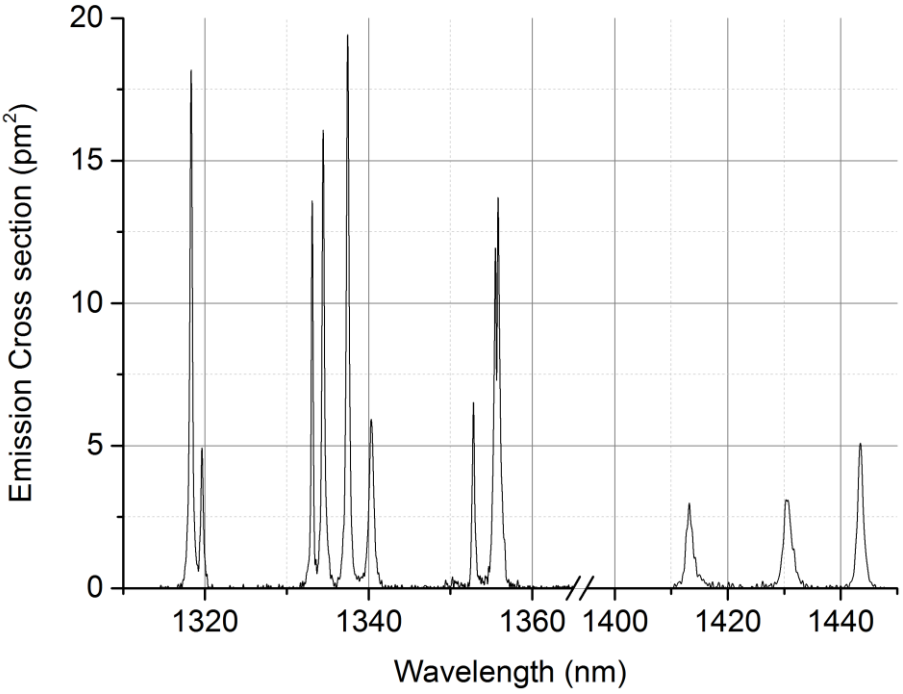

Figure A-129 Emission cross section of Nd:YAG $^4I_{13/2}$ at 165K

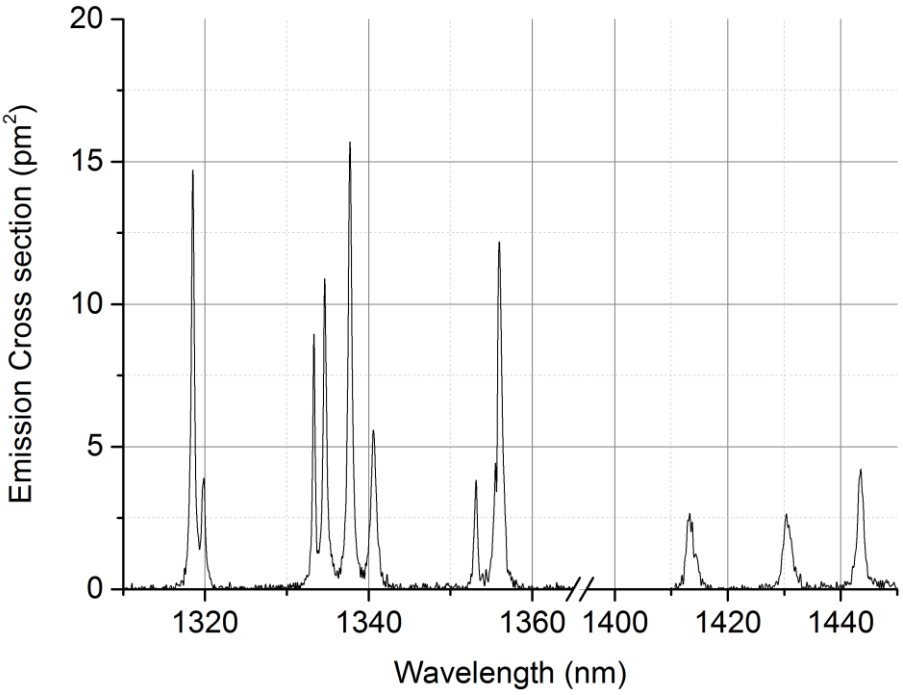

Figure A-130 Emission cross section of Nd:YAG $^4I_{13/2}$ at 200K

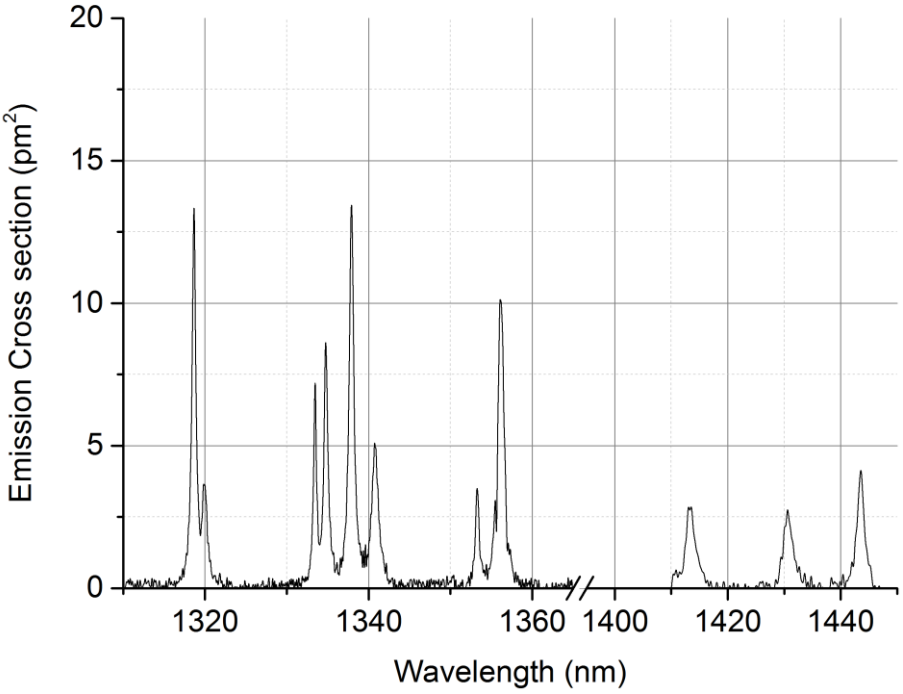

Figure A-131 Emission cross section of Nd:YAG $^4I_{13/2}$ at 240K

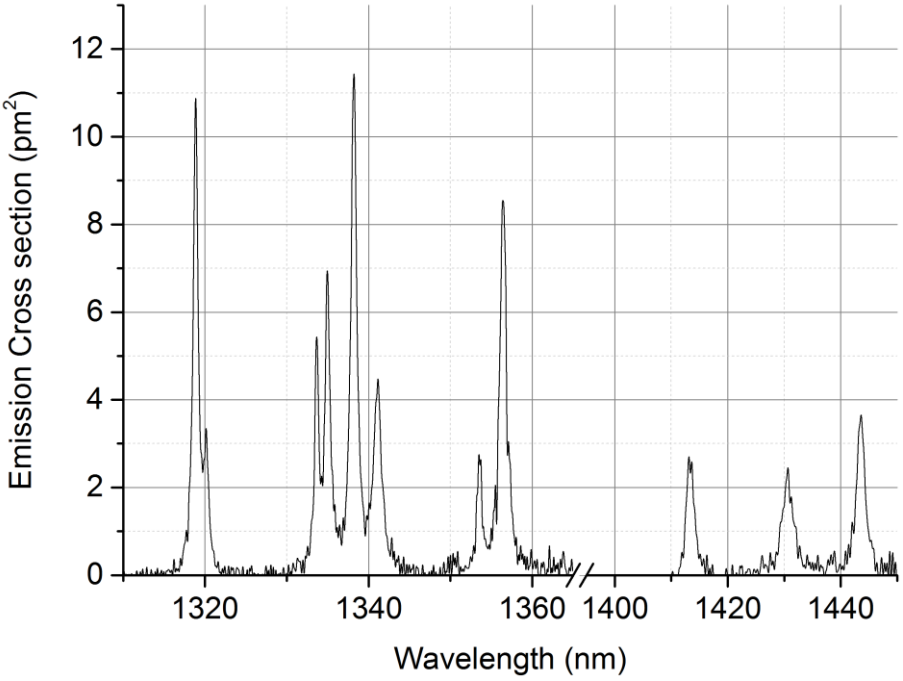

Figure A-132 Emission cross section of Nd:YAG $^4I_{13/2}$ at 273K

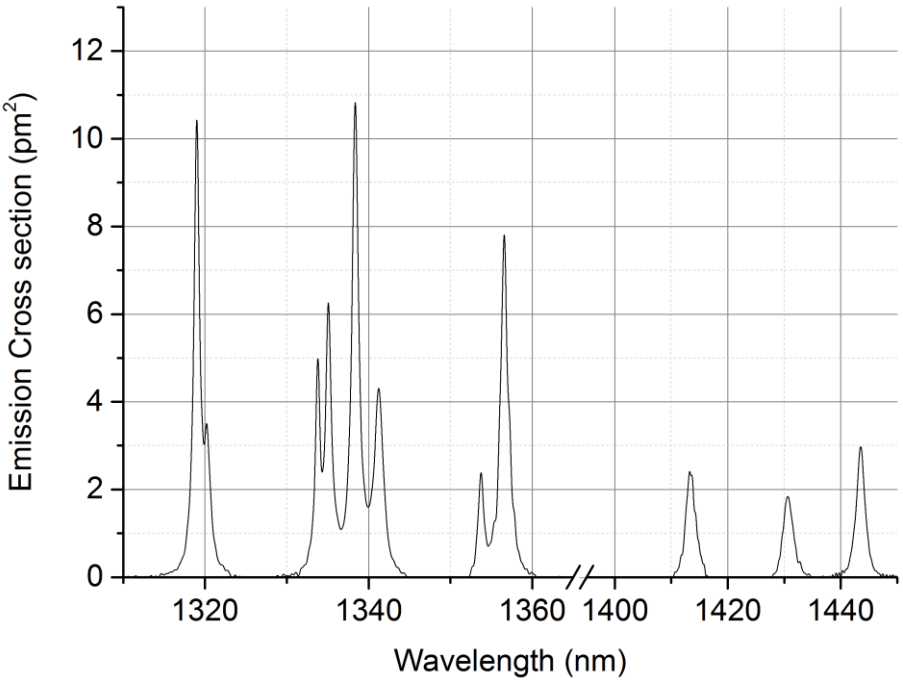

Figure A-133 Emission cross section of Nd:YAG $^4I_{13/2}$ at 300K

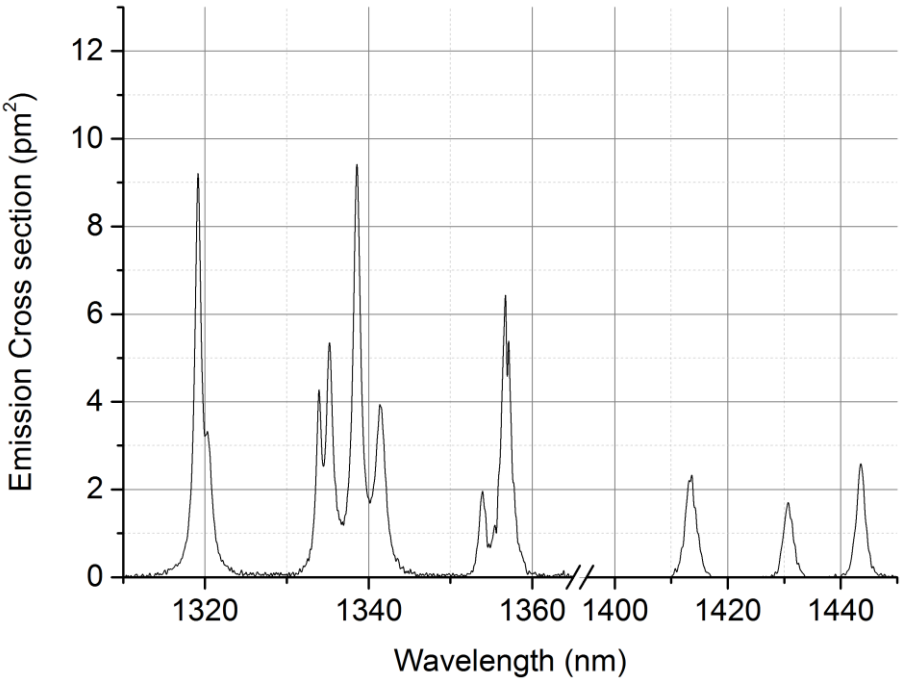

Figure A-134 Emission cross section of Nd:YAG $^4I_{13/2}$ at 330K

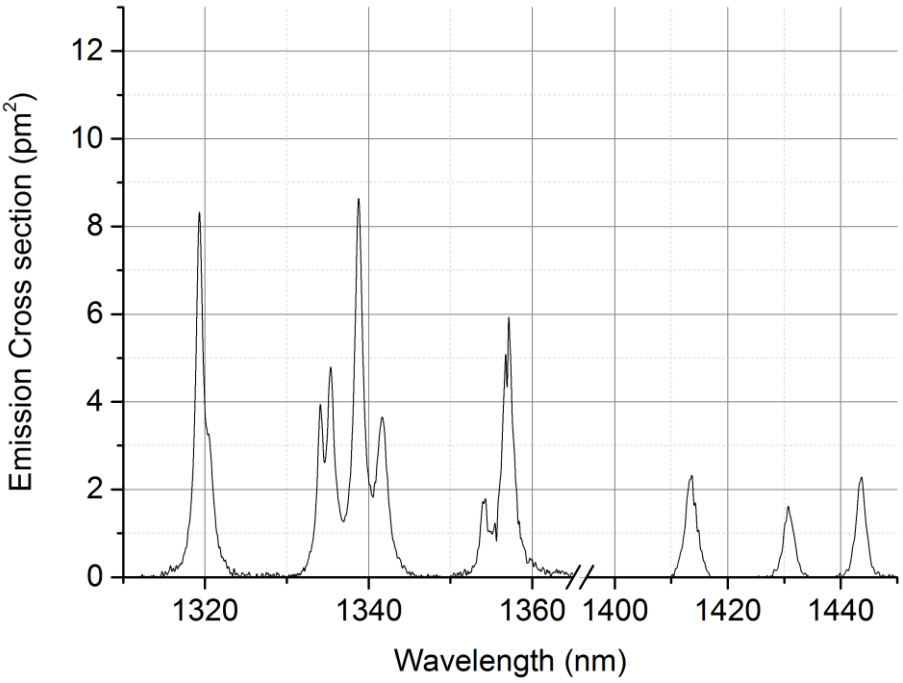

Figure A-135 Emission cross section of Nd:YAG $^4I_{13/2}$ at 360K

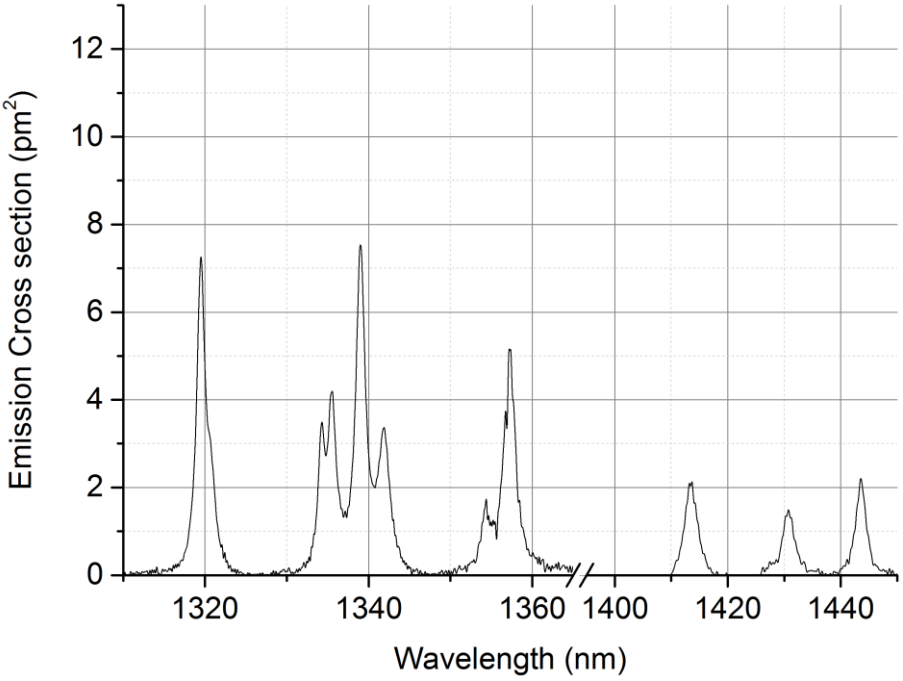

Figure A-136 Emission cross section of Nd:YAG $^4I_{13/2}$ at 390K

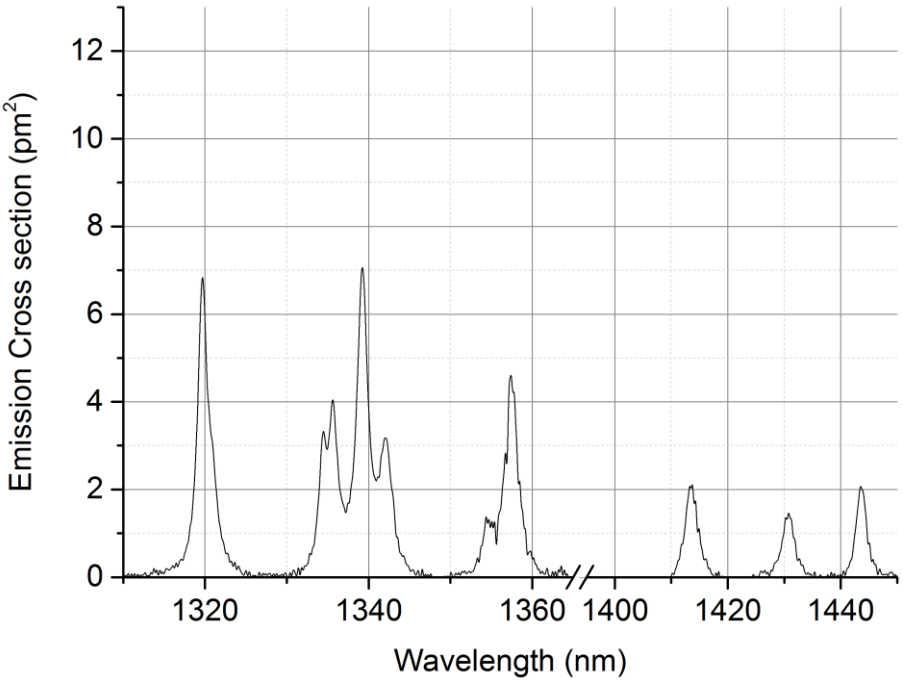

Figure A-137 Emission cross section of Nd:YAG $^4I_{13/2}$ at 420K

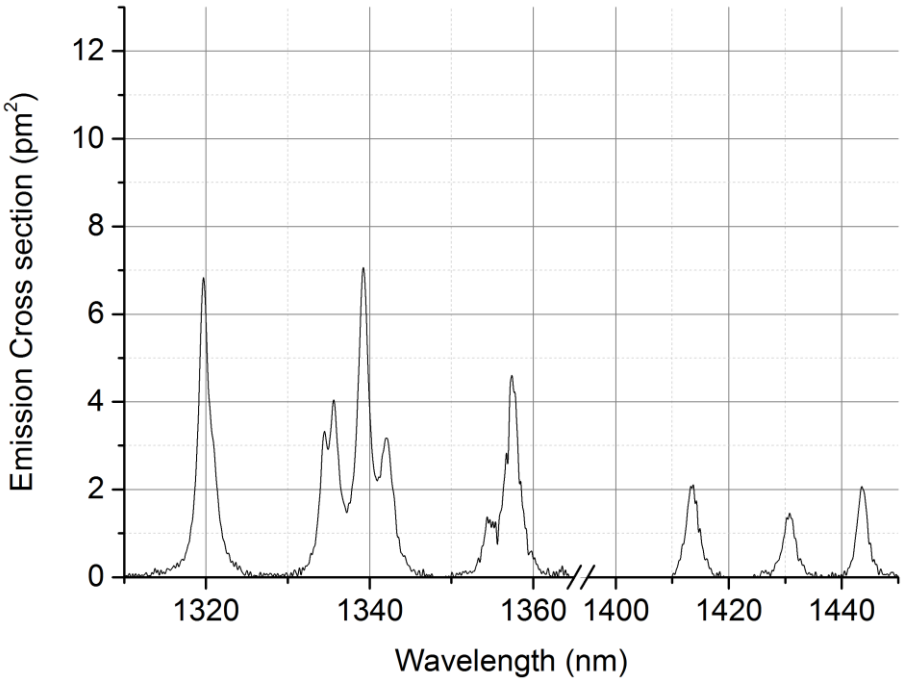

Figure A-138 Emission cross section of Nd:YAG $^4I_{13/2}$ at 450K

Table A-1 The change of λ_{PEAK}, λ_{FWHM} and σ_{SE} for laser transitions, for 200K - 300K, Nd:YAG

	300K			273K			240K			200K		
Transition	λ_{PEAK}	λ_{HWHM}	σ_{SE}	λ_{PEAK}	λ_{HWHM}	σ_{SE}	λ_{PEAK}	λ_{HWHM}	σ_{SE}	λ_{PEAK}	λ_{HWHM}	σ_{SE}
R1-Z4	900.09	2.08	0.98829	900.03	2.1	1.22	899.93	2.05	1.39	899.85	2.02	1.63
R2-Z5	938.45	0.828	2.67	938.45	0.804	2.88	938.5	0.752	3.02	938.54	0.7209	3.14
R1-Z5	945.92	0.841	3.93	945.95	0.795	4.56	946	0.756	5.23	946.04	0.715	5.802
R2-Y1	1052.11	0.571	10.1	1052.03	0.509	11.76	1051.91	0.42	12.67	1051.82	0.35	15.44
R2-Y2	1055.01	0.61	0.56	1054.92	0.518	0.65	1054.84	0.55	0.65	1054.78	0.244	0.65
R1-Y1	1061.47	0.5099	20.81	1061.38	0.457	25.23	1061.25	0.3739	29.82	1061.17	0.339	39.74
R1-Y2	1064.08	0.589	26.87	1063.97	0.5199	30.51	1063.82	0.434	32.56	1063.71	0.374	39.49
R2-Y3	1064.44	0.612	11.27	1064.37	0.559	13.87	1064.28	0.468	15.66	1064.22	3.95	20.8
R2-Y4	1068.17	1.19	4.46	1068.08	1.09	4.97	1067.92	0.94	5.29	1067.83	0.804	6.21
R1-Y3	1073.88	0.5517	15.79	1073.77	0.484	19.3	1073.61	0.404	22.67	1073.5	0.34	29.61
R1-Y4	1077.98	1.17	6.29	1077.89	0.986	7.19	1077.73	0.846	8.049	1077.63	0.727	10
R2-Y5	1105.51	1.78	1.67	1105.53	1.56	1.68	1105.55	1.56	1.67	1105.54	1.51	1.68
R2-Y6	1112.12	1.33	4.15	1112.1	1.31	4.36	1112.12	1.25	4.38	1112.12	1.12	4.53
R1-Y5	1116.07	1.71	3.81	1116.06	1.56	4.32	1116.06	1.56	4.63	1116.08	1.39	5.27
R1-Y6	1122.58	1.45	4.03	1122.57	1.39	4.48	1122.56	1.36	4.82	1122.57	1.24	5.38

Table A-2 The change of λ_{PEAK}, λ_{FWHM} and σ_{SE} for laser transitions, for 77K - 165K, Nd:YAG

	165K			125K			105K			77K		
Transition	λ_{PEAK}	λ_{HWHM}	σ_{SE}	λ_{PEAK}	λ_{HWHM}	σ_{SE}	λ_{PEAK}	λ_{HWHM}	σ_{SE}	λ_{PEAK}	λ_{HWHM}	σ_{SE}
R1-Z4	899.89	1.85	1.63	899.58	1.54	2.21	899.57	1.47	2.1	899.58	1.38	2.75
R2-Z5	938.6	0.677	2.92	938.64	0.63	2.87	938.64	0.64	2.67	938.68	0.6088	2.0286
R1-Z5	946.09	0.676	6.48	946.15	0.649	7.81	946.15	0.648	7.24	946.18	0.649	8.52
R2-Y1	1051.7	0.286	16.58	1051.64	0.253	16.97	1051.6	0.233	13.59	1051.59	0.226	13.37
R2-Y2	1054.7	0.215	0.78	1054.64	0.196	0.85	1054.64	0.212	0.756	1054.6	1.48	0.606
R1-Y1	1061.05	0.2788	52.04	1060.98	0.252	64.4	1060.93	0.237	70.64	1060.92	0.234	78.096
R1-Y2	1063.56	0.302	42.06	1063.48	0.266	42.26	1063.43	0.237	33.599	1063.41	0.2476	32.89
R2-Y3	1064.13	0.3099	27.49	1064.09	0.261	35.75	1064.05	0.23148	40.79	1064.05	0.2344	46.31
R2-Y4	1067.69	0.673	6.64	1067.61	0.588	6.74	1067.56	0.51	5.47	1067.55	0.467	5.17
R1-Y3	1073.35	0.288	38.85	1073.27	0.264	46.181	1073.21	0.255	51.48	1073.2	0.236	55.36
R1-Y4	1077.48	0.606	12.75	1077.4	0.533	15.42	1077.34	0.527	17.22	1077.33	0.461	18.41
R2-Y5	1105.58	1.29	1.6	1105.58	1.15	1.48	1105.59	1.42	1.17	1105.6	1.48	0.976
R2-Y6	1112.14	1.03	4.31	1112.15	1.01	3.92	1112.17	1.01	3.05	1112.19	1	2.749
R1-Y5	1116.08	1.31	6.02	1116.09	1.28	6.44	116.1	1.29	6.73	1116.13	1.31	6.69
R1-Y6	1122.58	1.17	6.21	1122.6	1.17	6.68	1122.63	0.98	6.85	1122.64	0.99	6.84

A.7 Emission cross section of Nd:GSAG

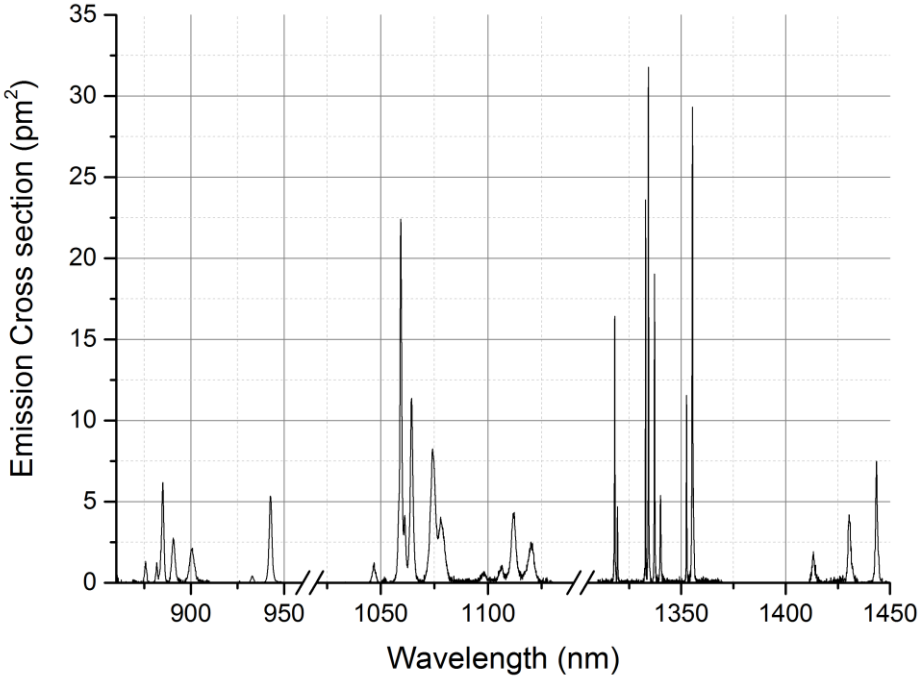

Figure A-139 Emission cross section of Nd:GSAG at 77K

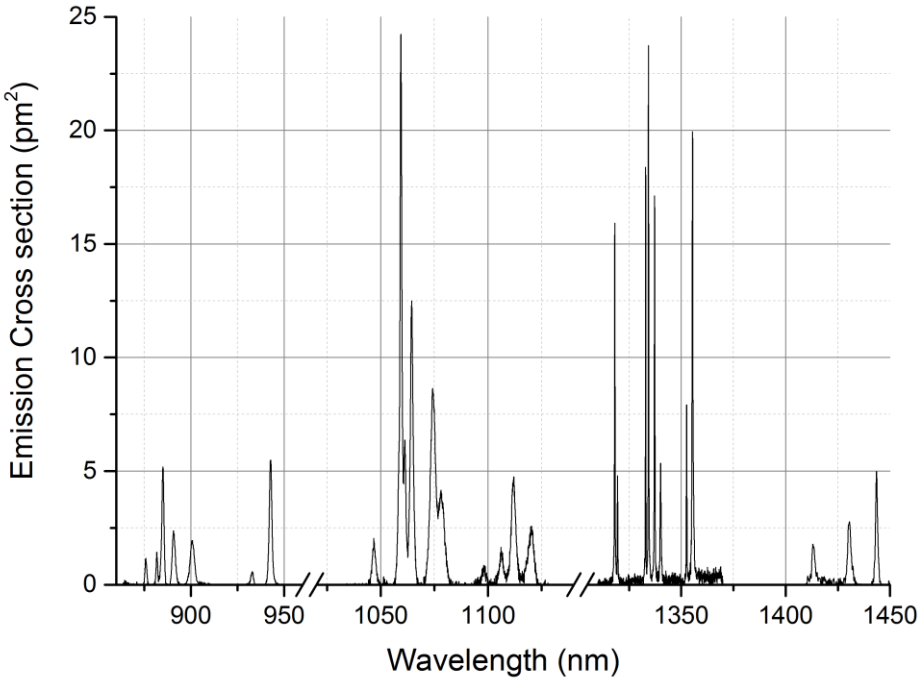

Figure A-140 Emission cross section of Nd:GSAG at 105K

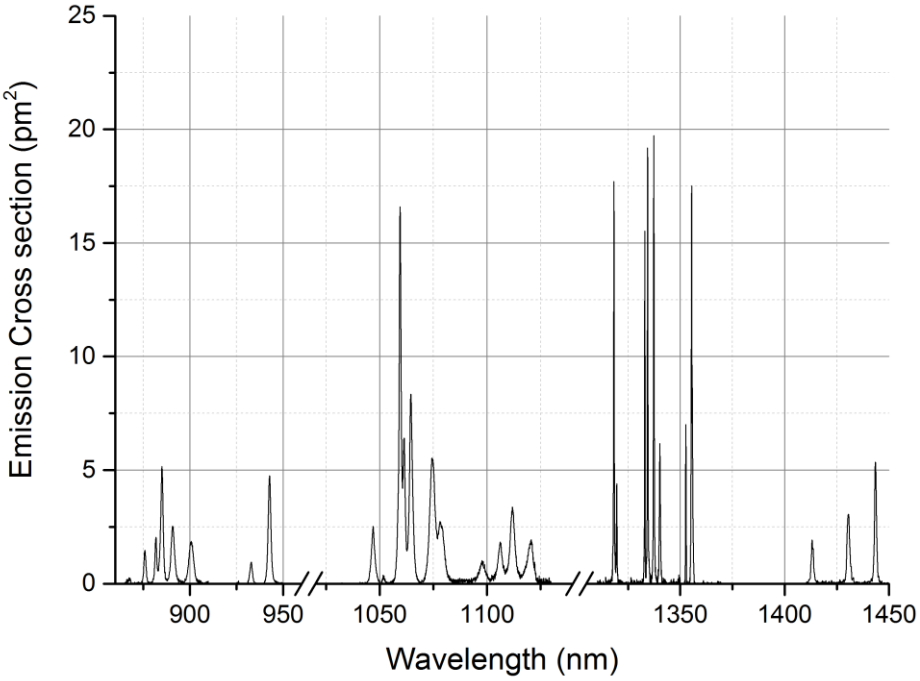

Figure A-141 Emission cross section of Nd:GSAG at 130K

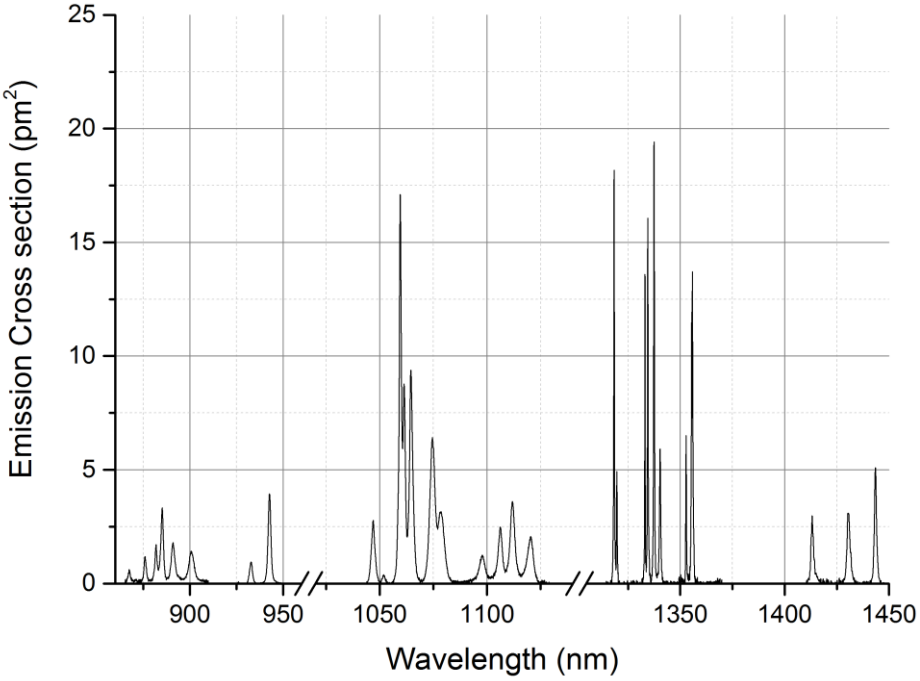

Figure A-142 Emission cross section of Nd:GSAG at 165K

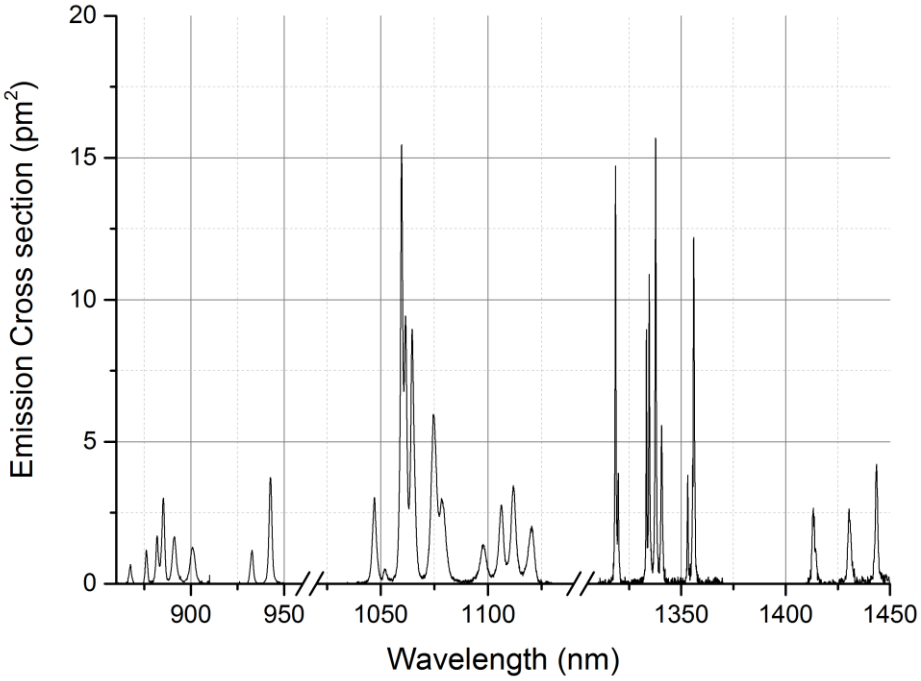

Figure A-143 Emission cross section of Nd:GSAG at 203K

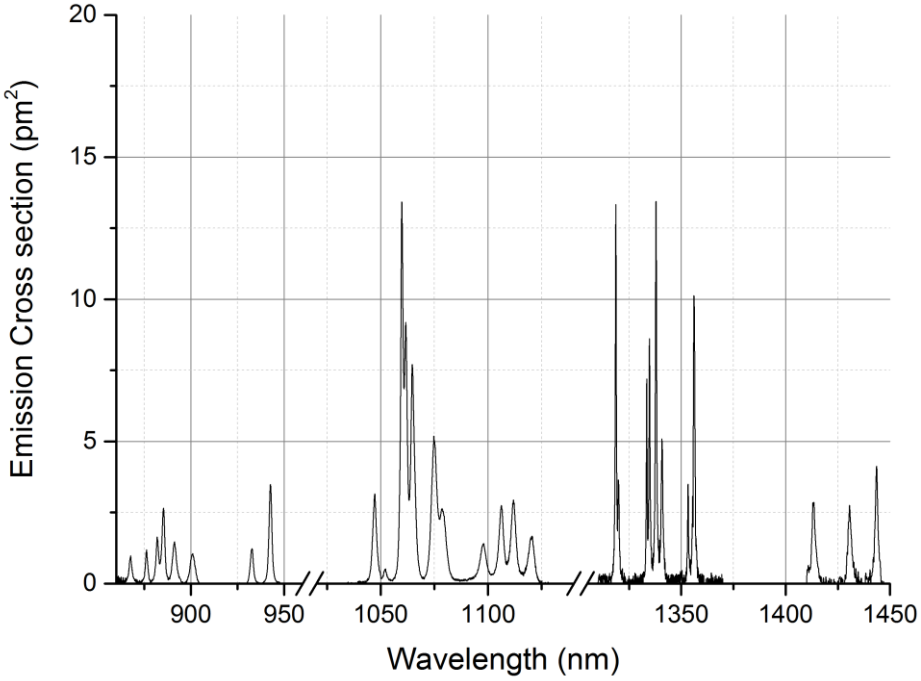

Figure A-144 Emission cross section of Nd:GSAG at 238K

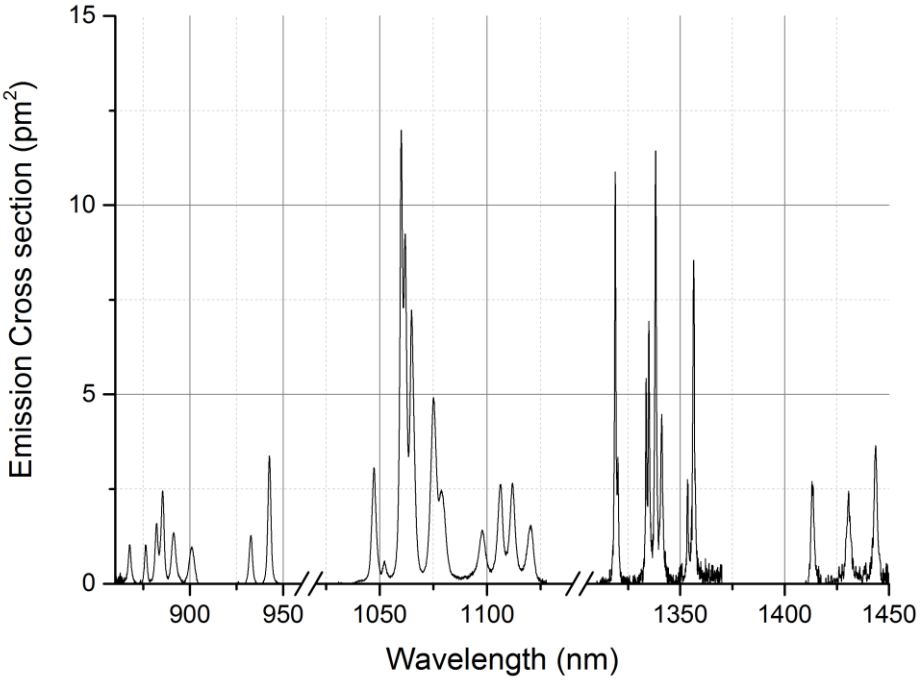

Figure A-145 Emission cross section of Nd:GSAG at 273K

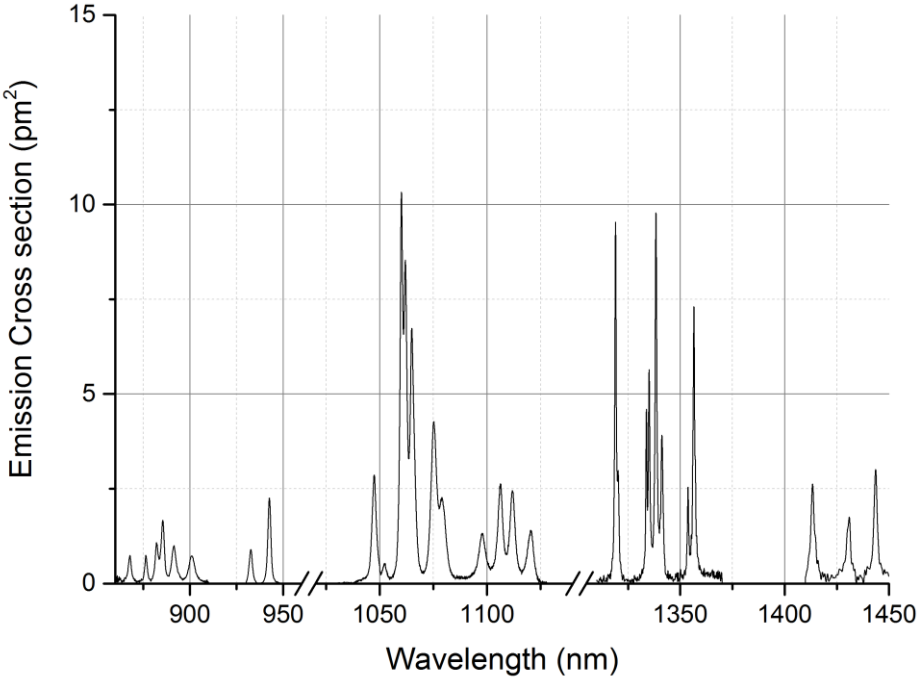

Figure A-146 Emission cross section of Nd:GSAG at 300K

A.8 Emission cross section of Nd:YLF

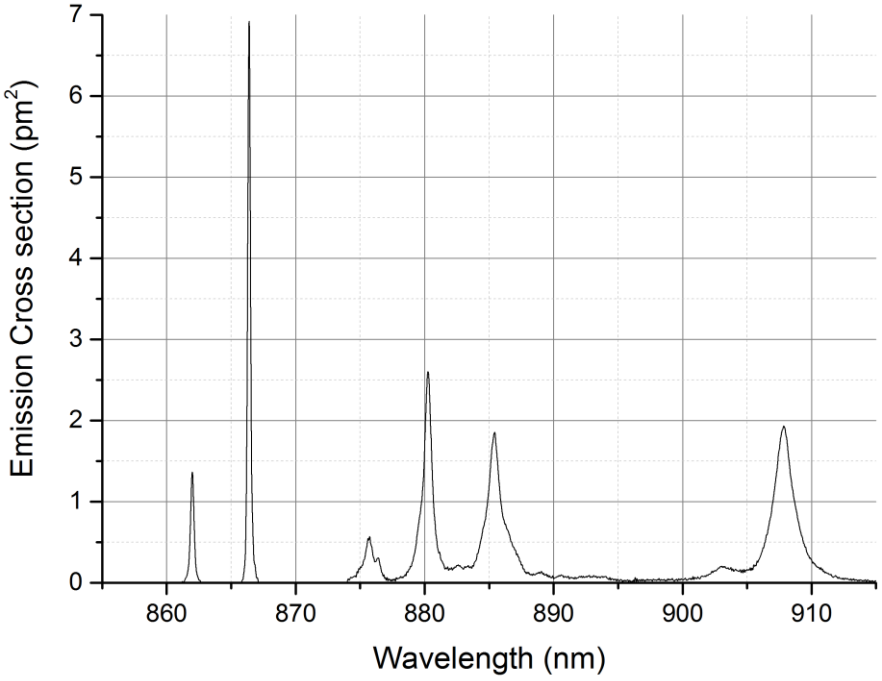

Figure A-147 Emission cross section of Nd:YLF $^4I_{9/2}$, E//a at 77K

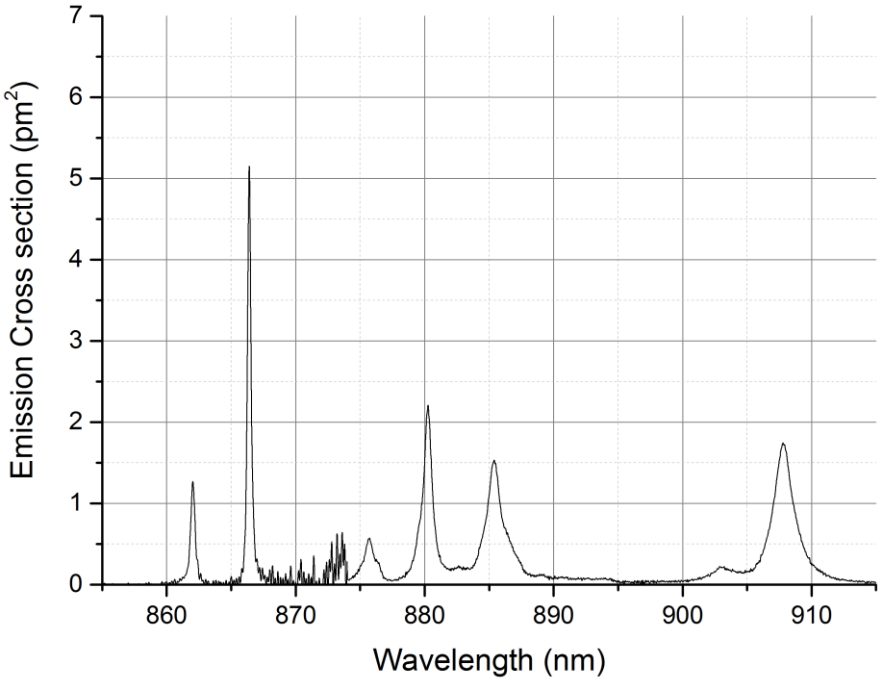

Figure A-148 Emission cross section of Nd:YLF $^4I_{9/2}$, E//a at 100K

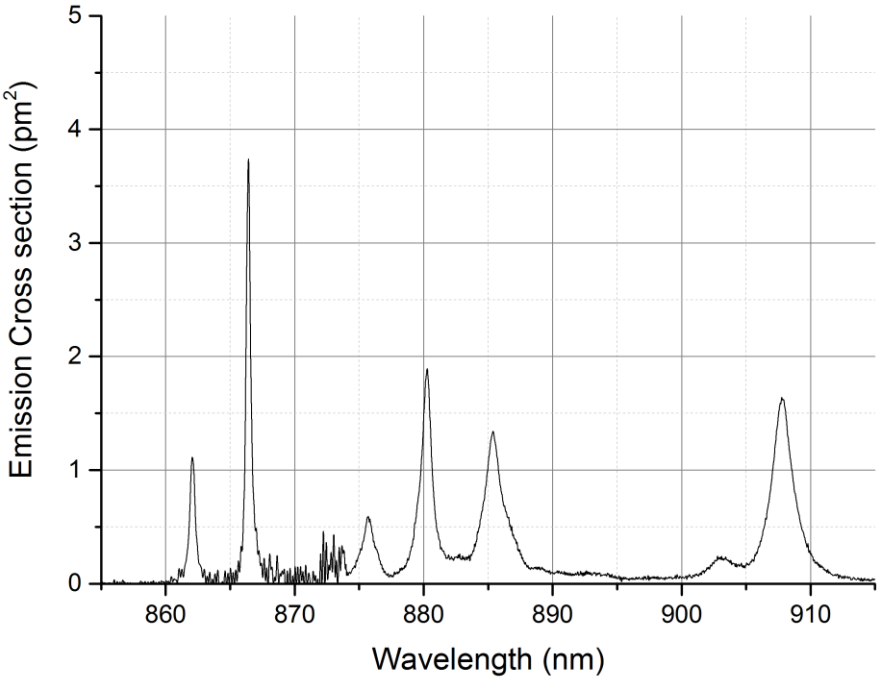

Figure A-149 Emission cross section of Nd:YLF $^4I_{9/2}$, E//a at 120K

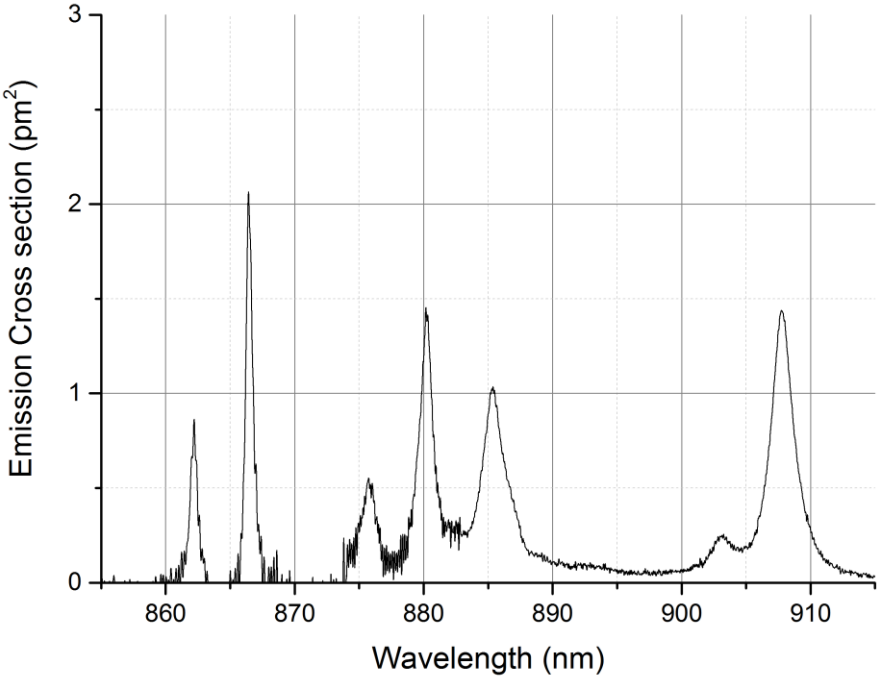

Figure A-150 Emission cross section of Nd:YLF $^4I_{9/2}$, E//a at 165K

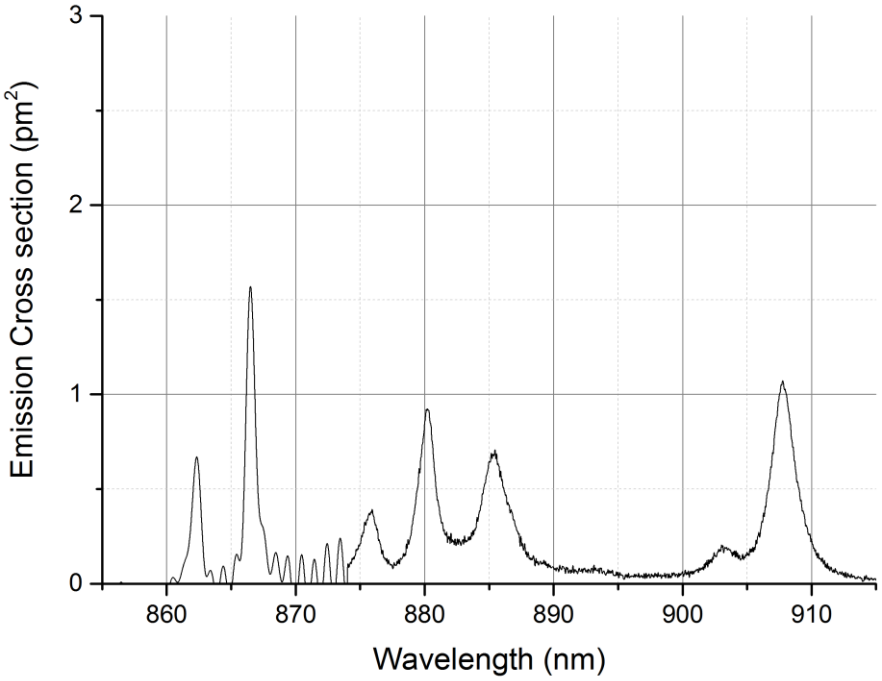

Figure A-151 Emission cross section of Nd:YLF $^4I_{9/2}$, E//a at 195K

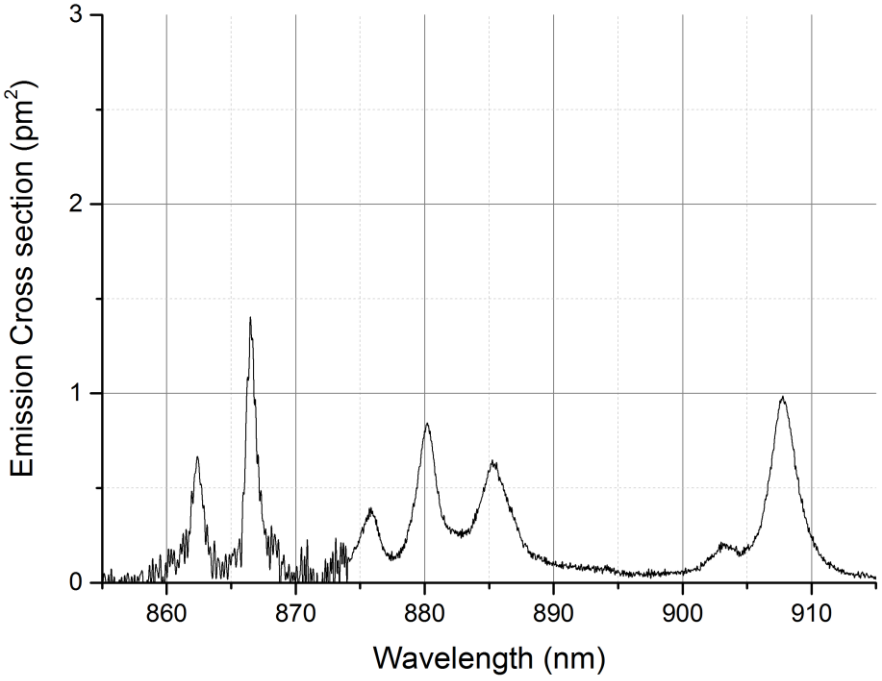

Figure A-152 Emission cross section of Nd:YLF $^4I_{9/2}$, E//a at 235K

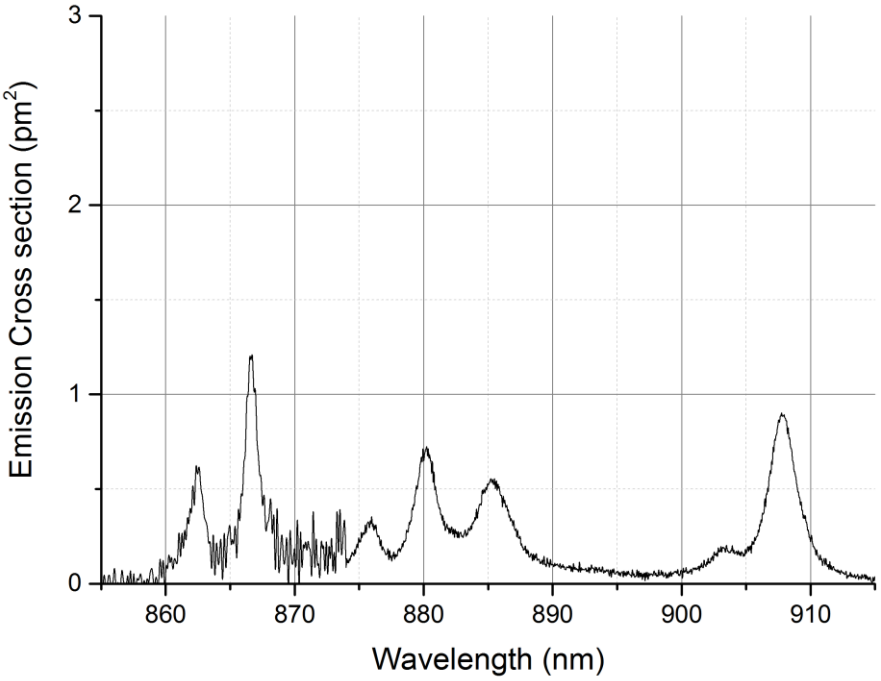

Figure A-153 Emission cross section of Nd:YLF $^4I_{9/2}$, E//a at 273K

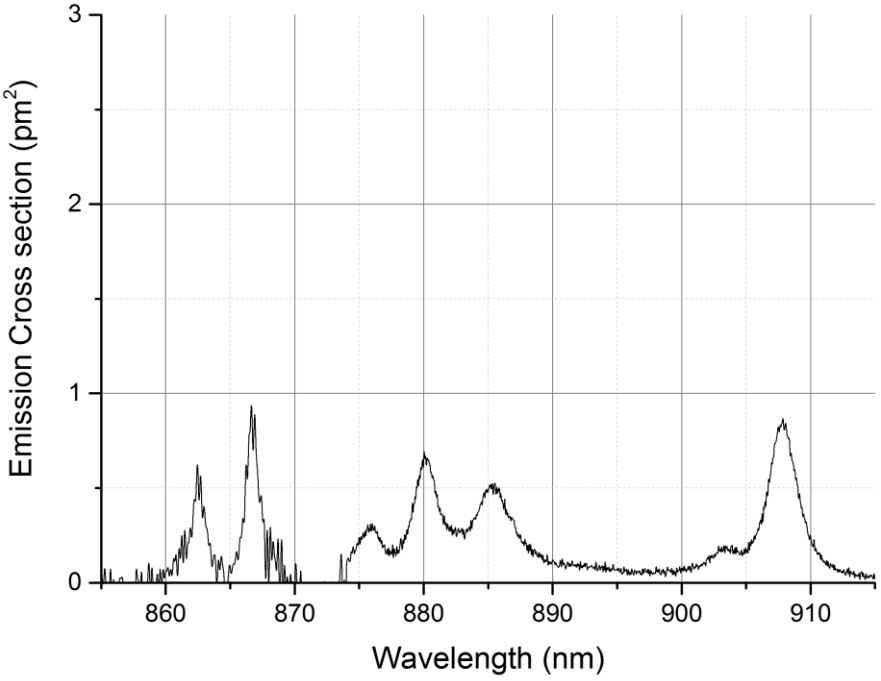

Figure A-154 Emission cross section of Nd:YLF $^4I_{9/2}$, E//a at 300K

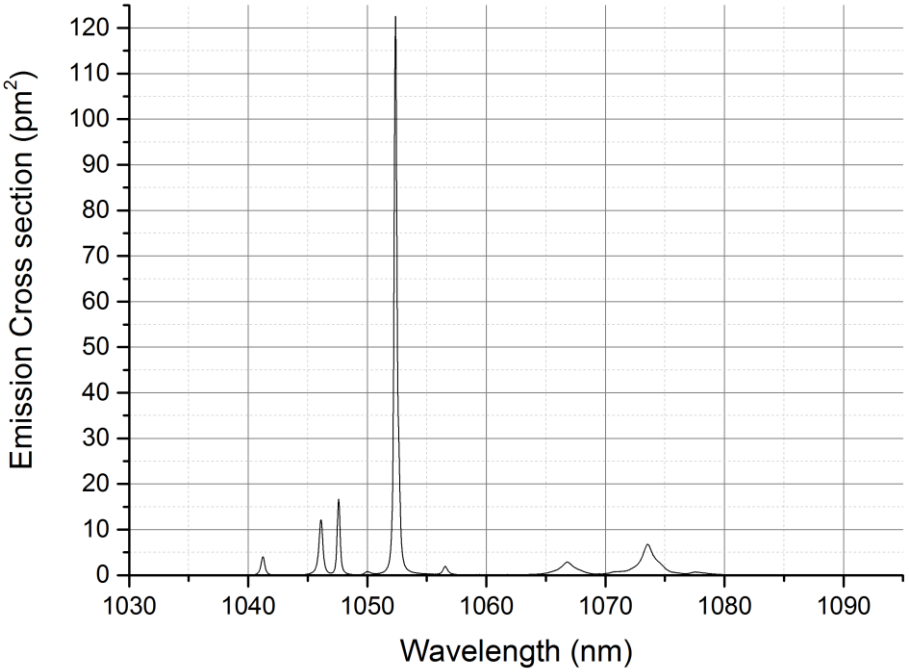

Figure A-155 Emission cross section of Nd:YLF $^4I_{11/2}$, E//a at 77K

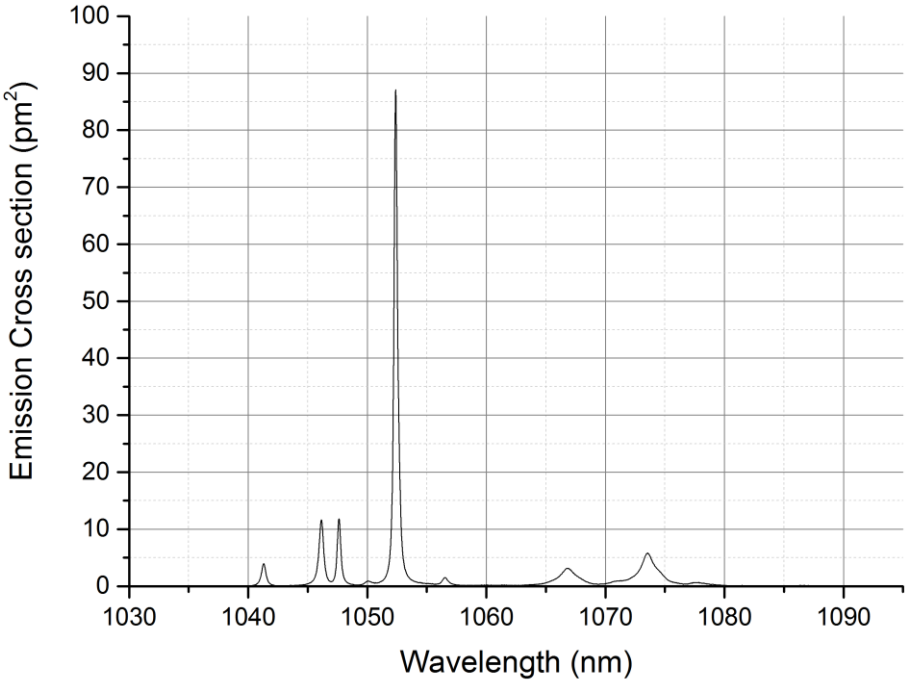

Figure A-156 Emission cross section of Nd:YLF $^4I_{11/2}$, E//a at 100K

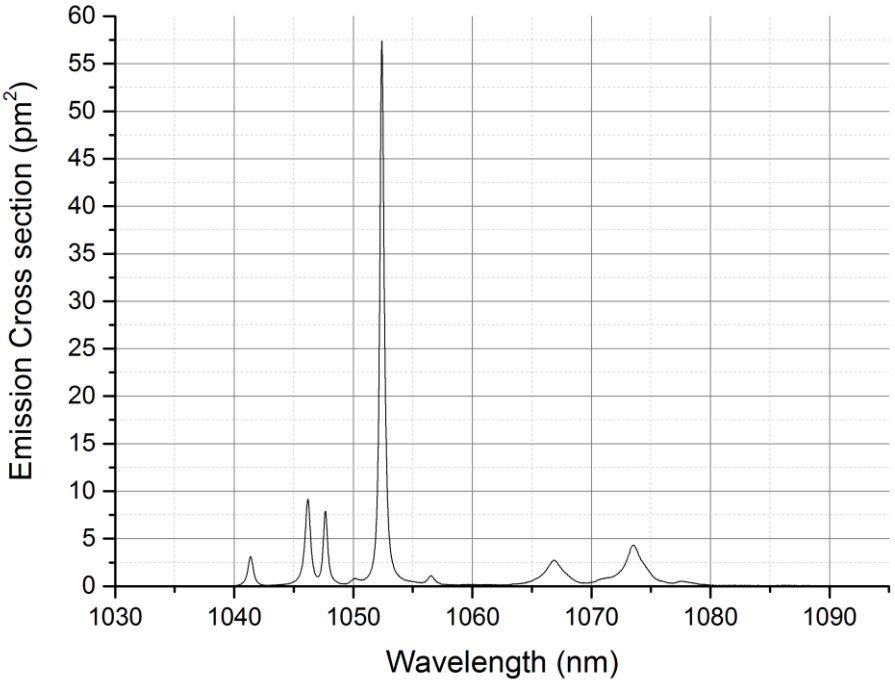

Figure A-157 Emission cross section of Nd:YLF $^4I_{11/2}$, E//a at 120K

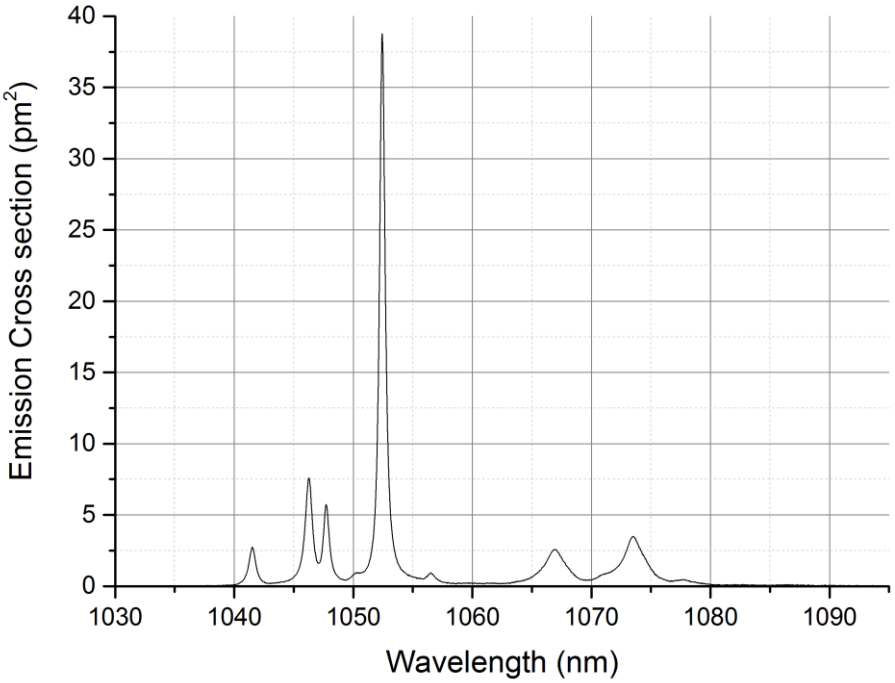

Figure A-158 Emission cross section of Nd:YLF $^4I_{11/2}$, E//a at 165K

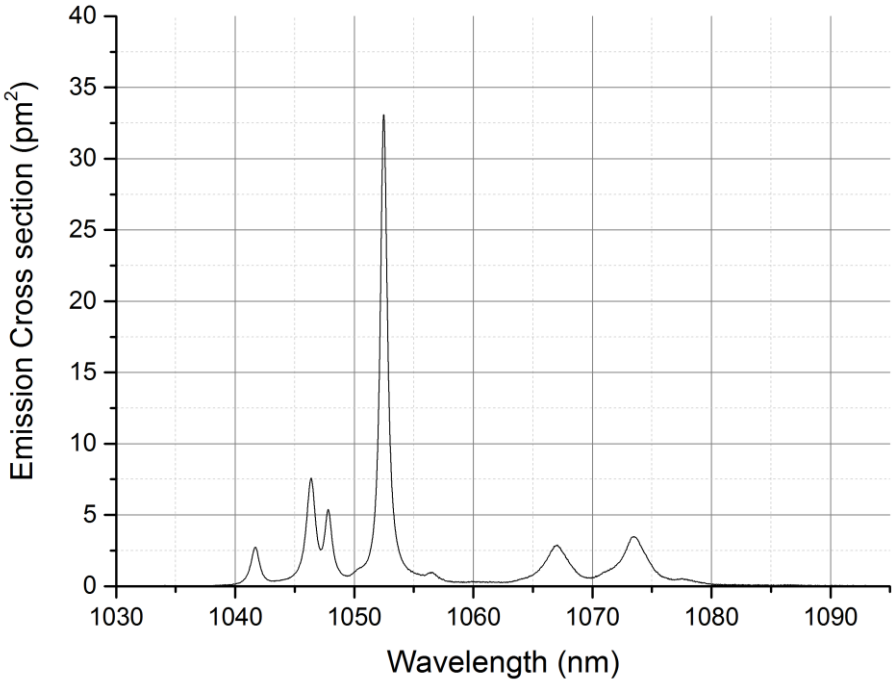

Figure A-159 Emission cross section of Nd:YLF $^4I_{11/2}$, E//a at 195K

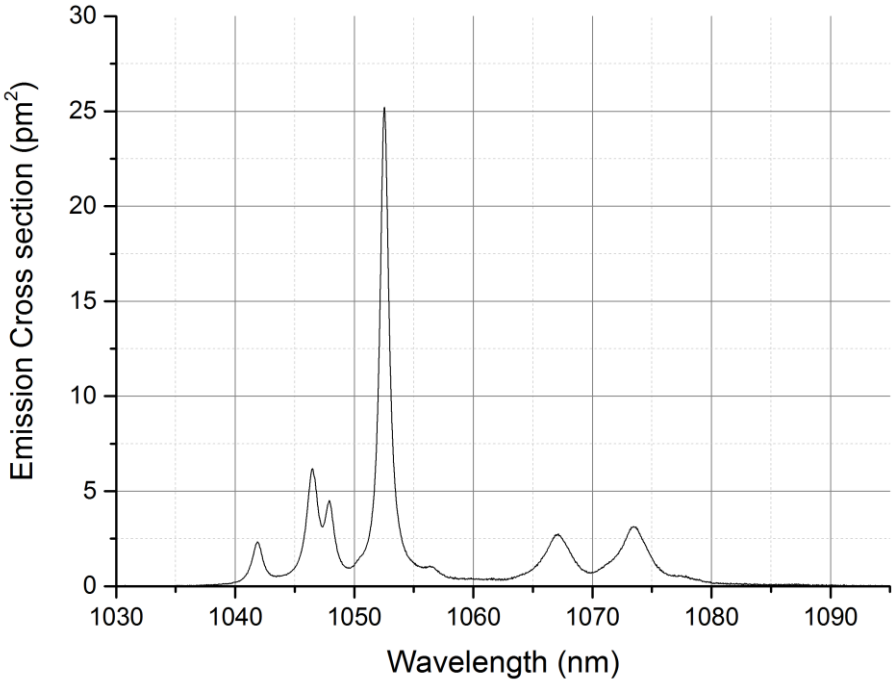

Figure A-160 Emission cross section of Nd:YLF $^4I_{11/2}$, E//a at 235K

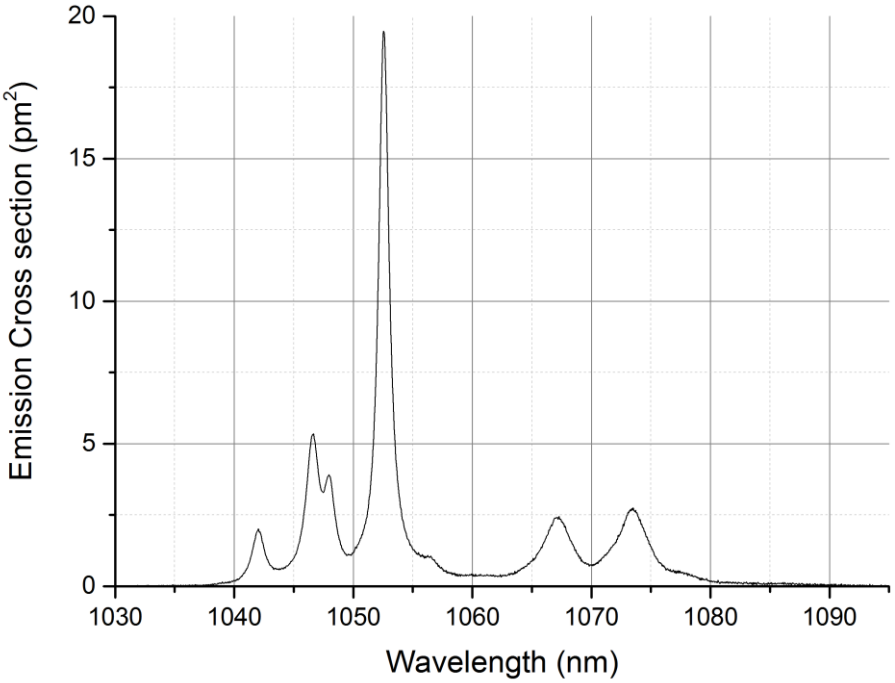

Figure A-161 Emission cross section of Nd:YLF $^4I_{11/2}$, E//a at 273K

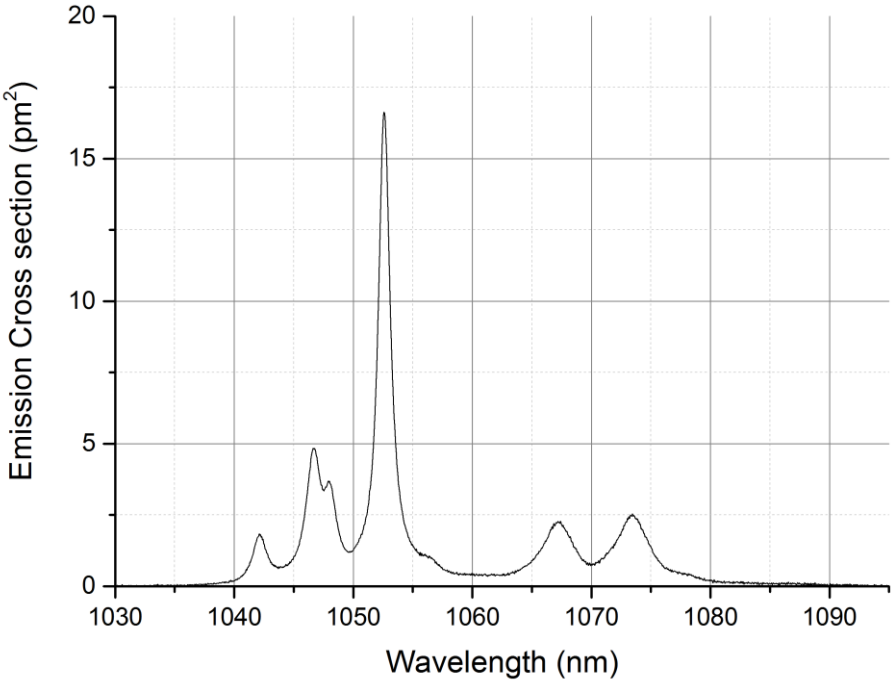

Figure A-162 Emission cross section of Nd:YLF $^4I_{11/2}$, E//a at 300K

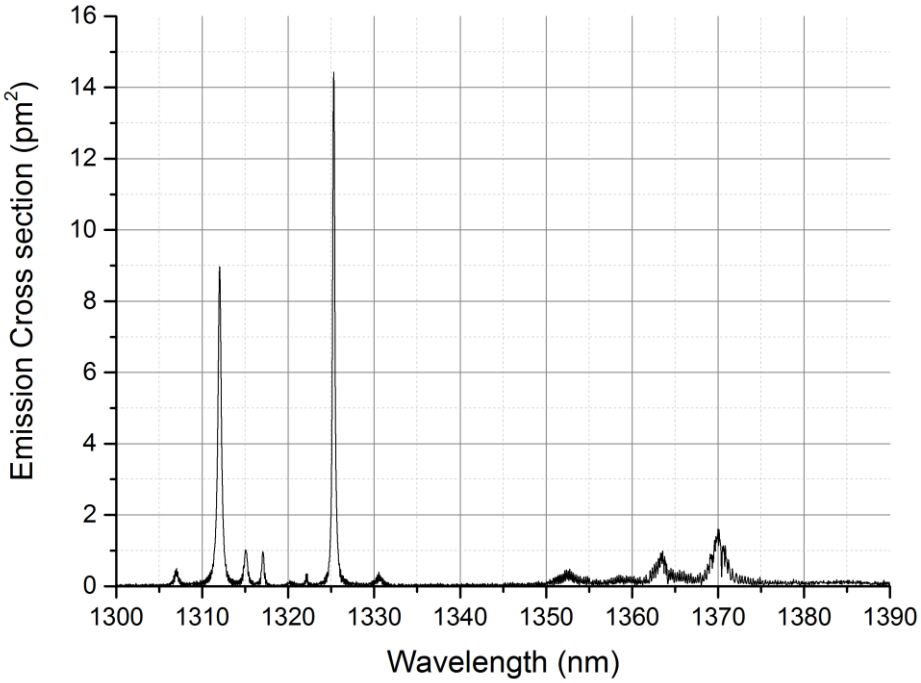

Figure A-163 Emission cross section of Nd:YLF $^4I_{13/2}$, E//a at 77K

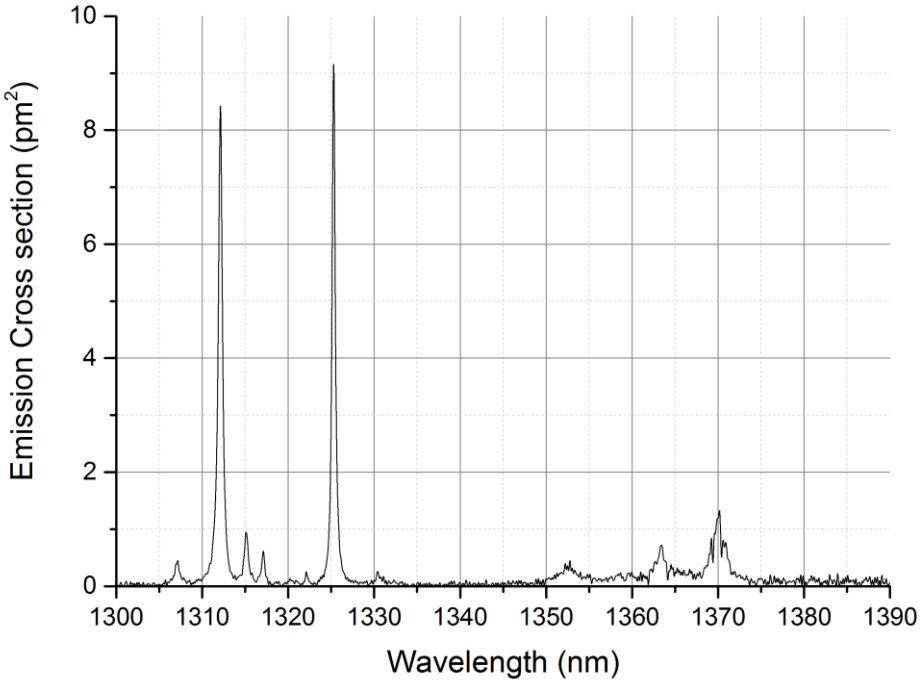

Figure A-164 Emission cross section of Nd:YLF $^4I_{13/2}$, E//a at 100K

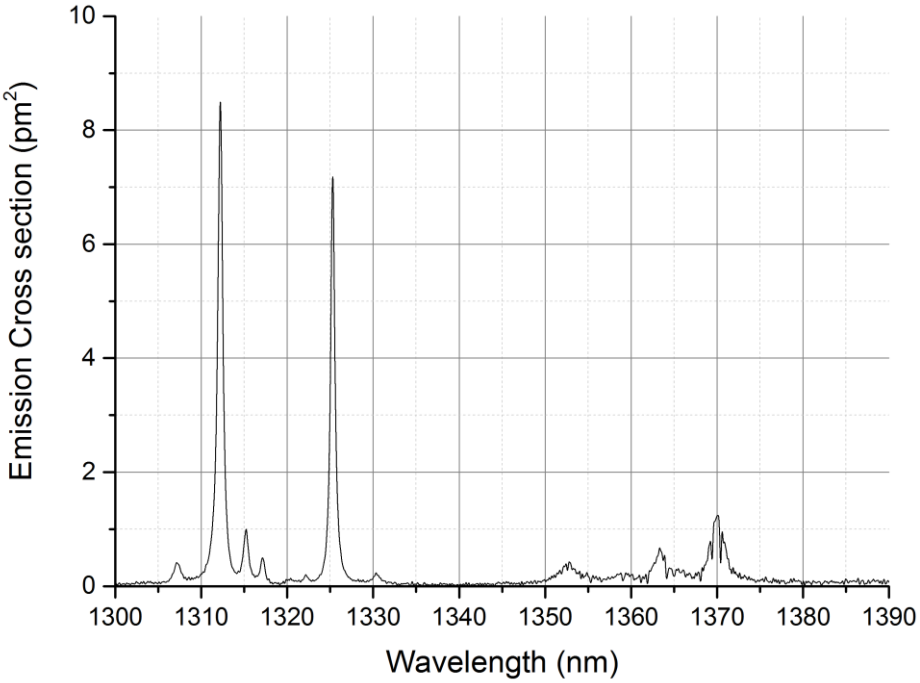

Figure A-165 Emission cross section of Nd:YLF $^4I_{13/2}$, E//a at 120K

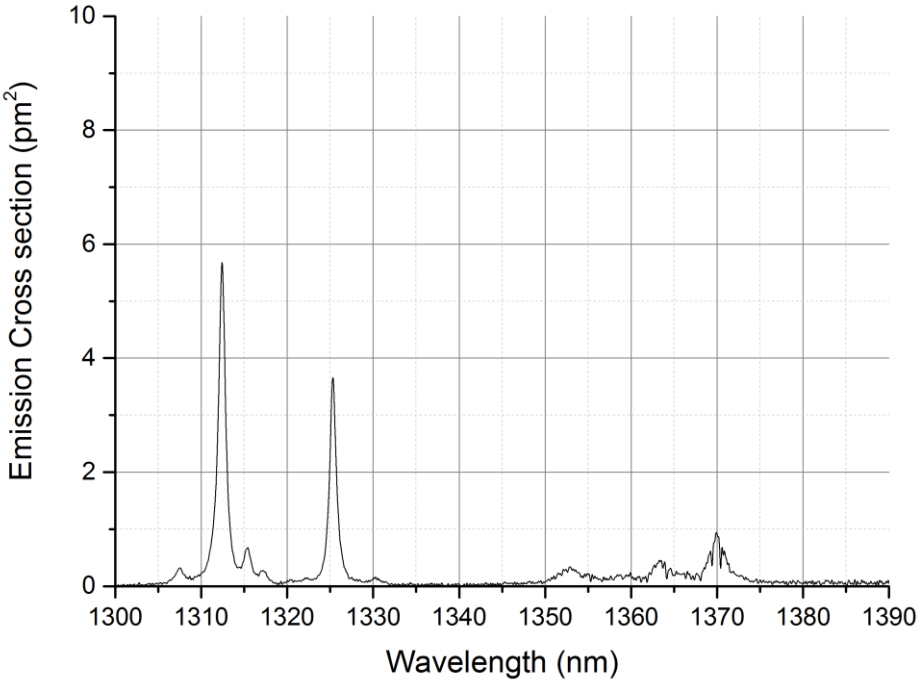

Figure A-166 Emission cross section of Nd:YLF $^4I_{13/2}$, E//a at 160K

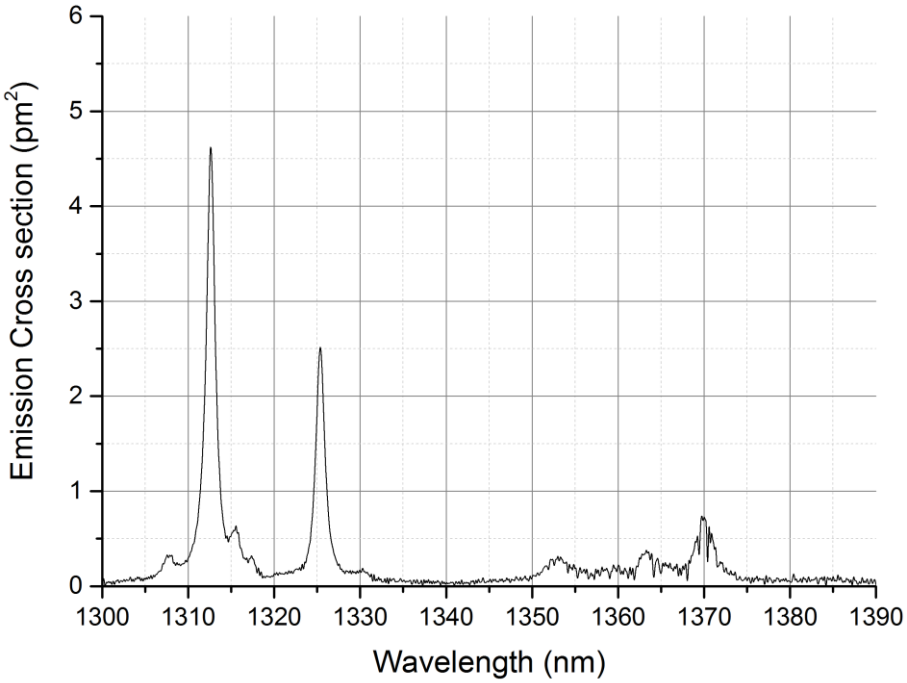

Figure A-167 Emission cross section of Nd:YLF $^4I_{13/2}$, E//a at 195K

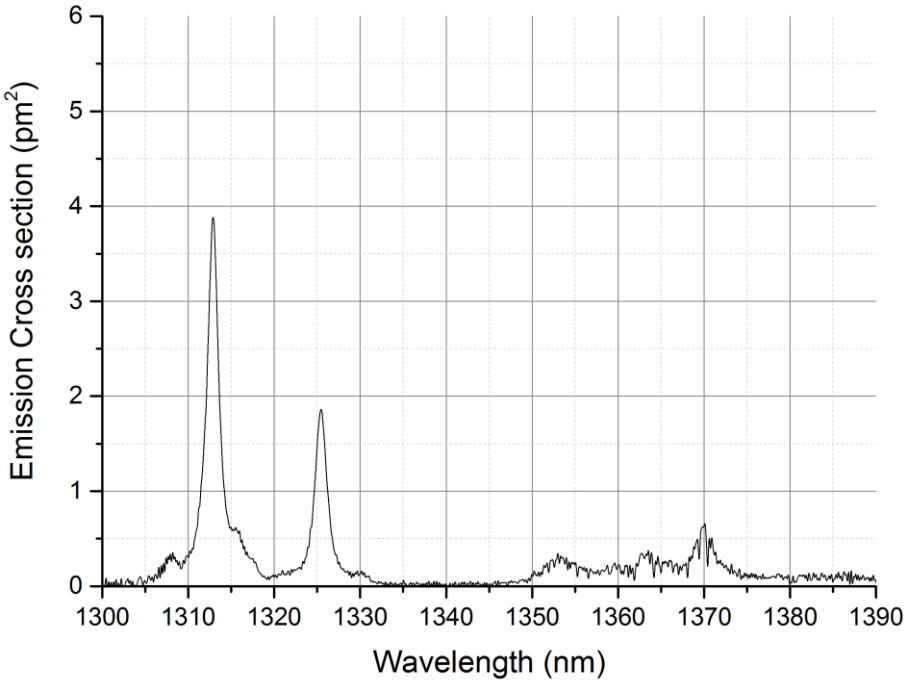

Figure A-168 Emission cross section of Nd:YLF $^4I_{13/2}$, E//a at 235K

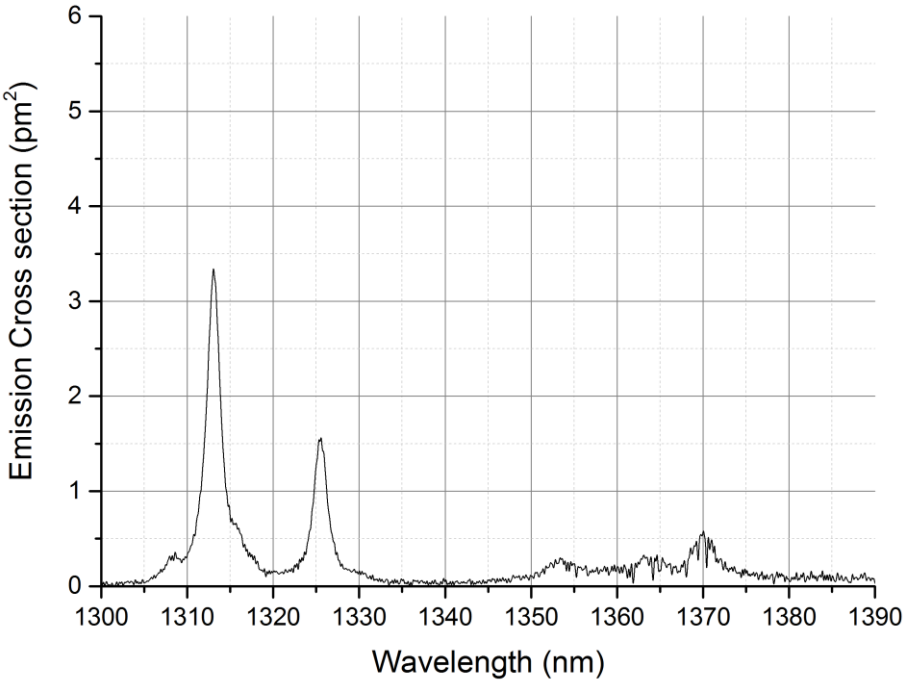

Figure A-169 Emission cross section of Nd:YLF $^4I_{13/2}$, E//a at 273K

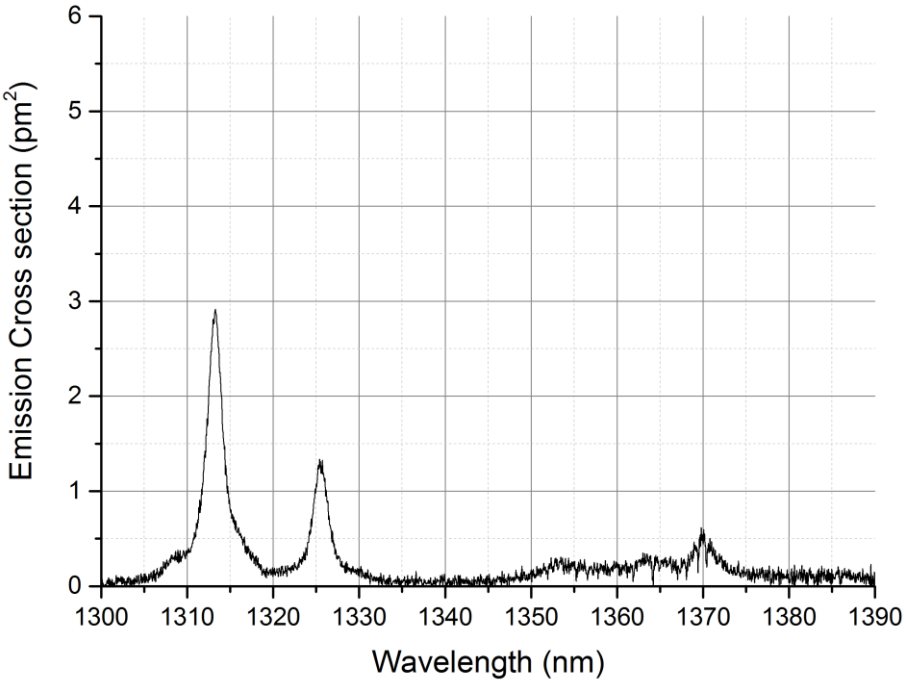

Figure A-170 Emission cross section of Nd:YLF $^4I_{13/2}$, E//a at 300K

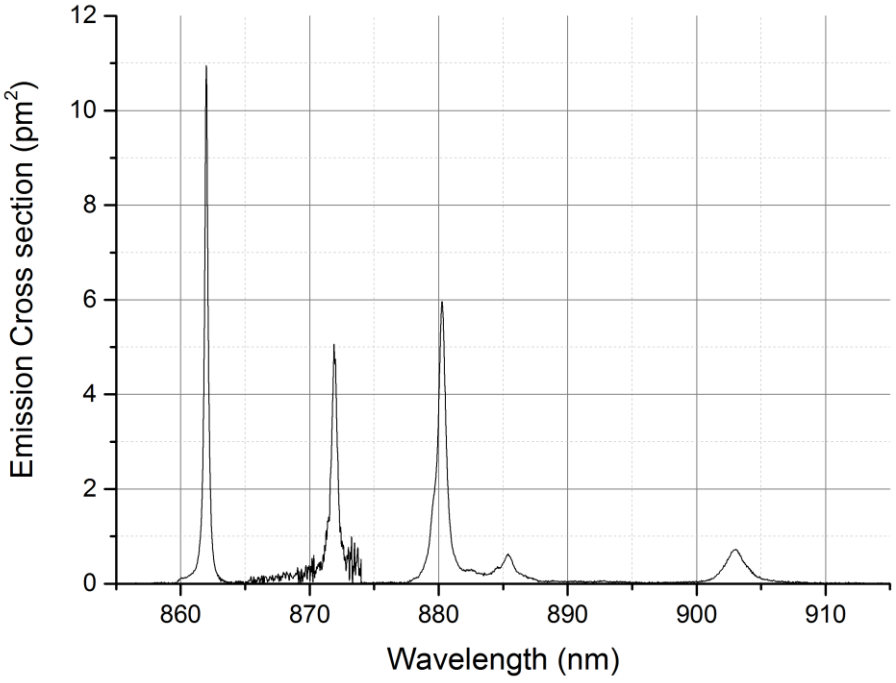

Figure A-171 Emission cross section of Nd:YLF $^4I_{9/2}$, E//c at 77K

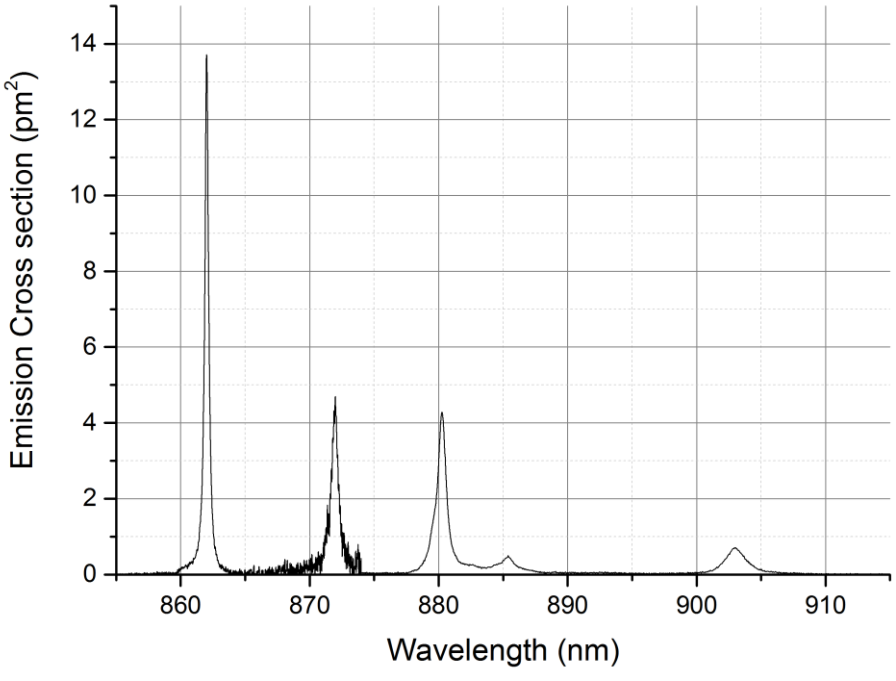

Figure A-172 Emission cross section of Nd:YLF $^4I_{9/2}$, E//c at 100K

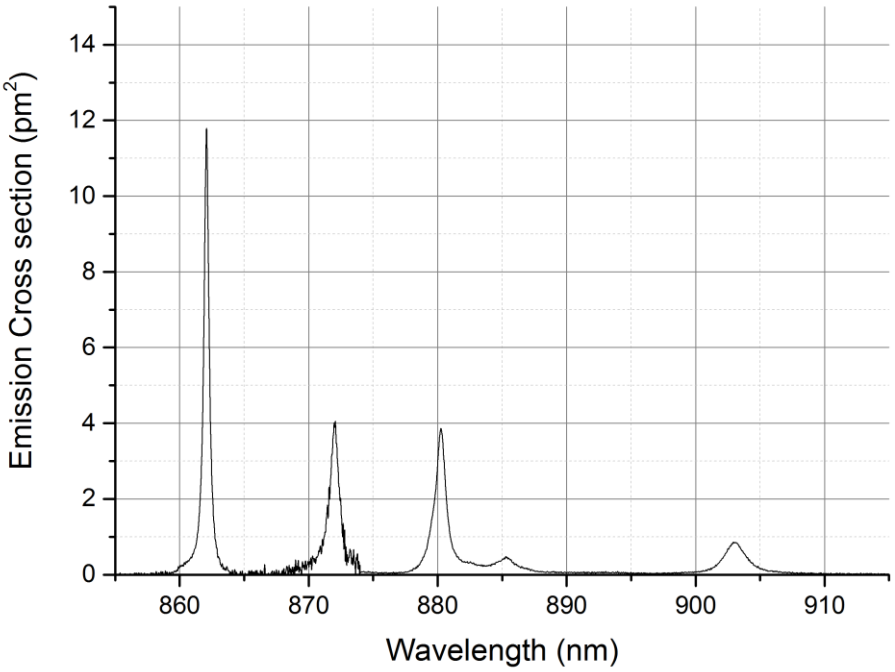

Figure A-173 Emission cross section of Nd:YLF $^4I_{9/2}$, E//c at 125K

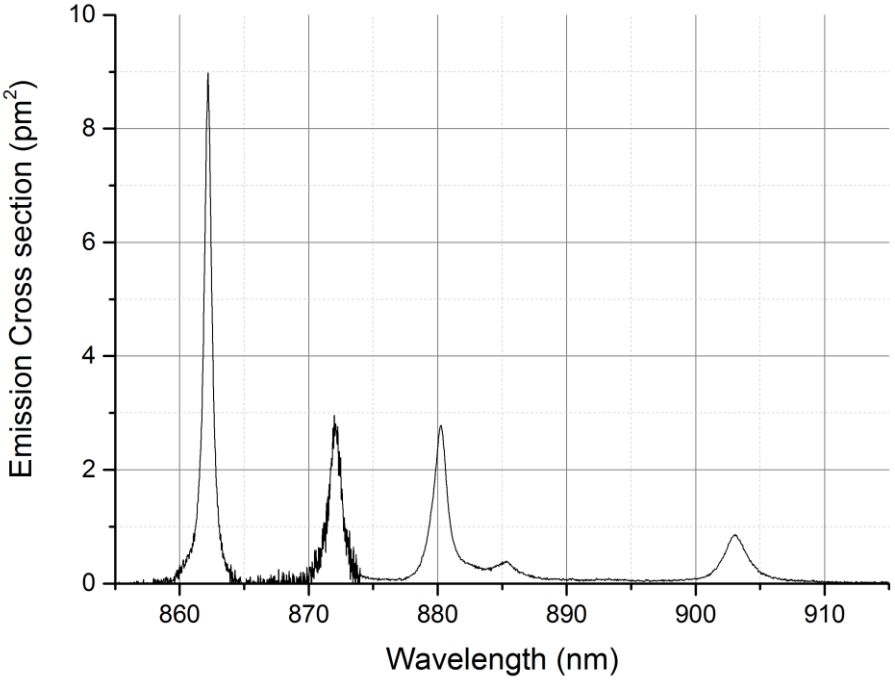

Figure A-174 Emission cross section of Nd:YLF $^4I_{9/2}$, E//c at 165K

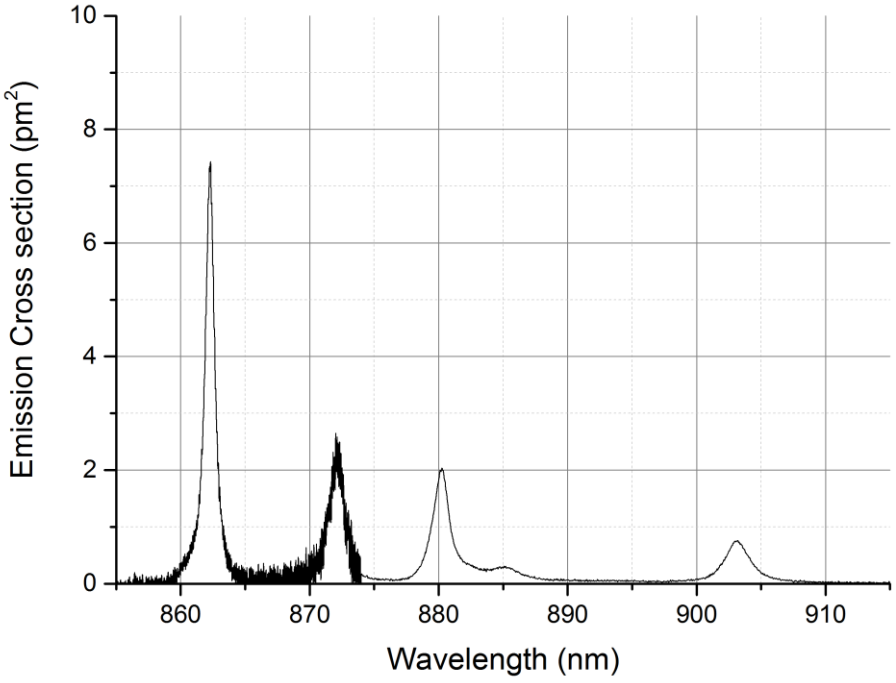

Figure A-175 Emission cross section of Nd:YLF $^4I_{9/2}$, E//c at 195K

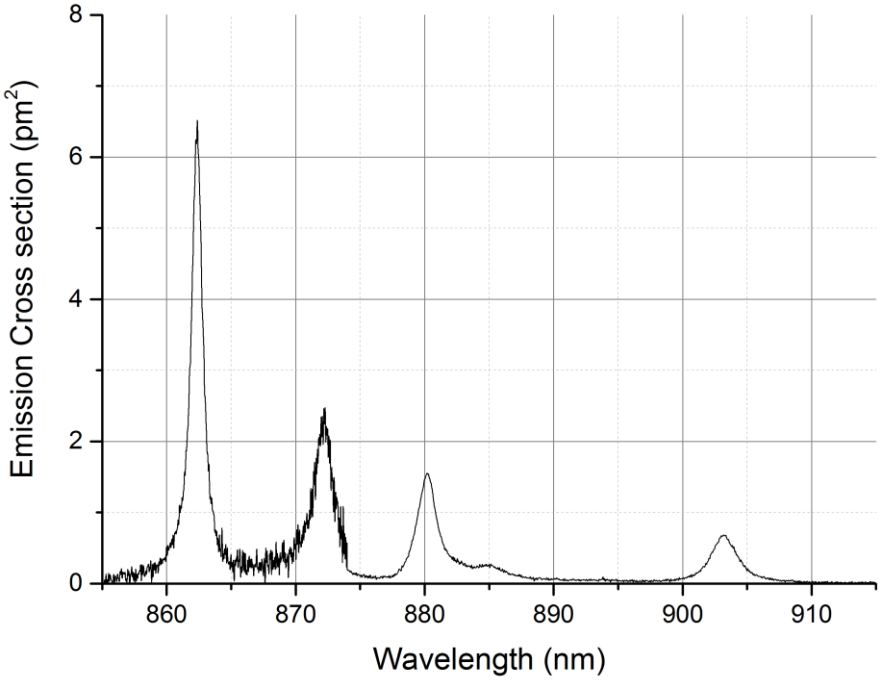

Figure A-176 Emission cross section of Nd:YLF $^4I_{9/2}$, E//c at 235K

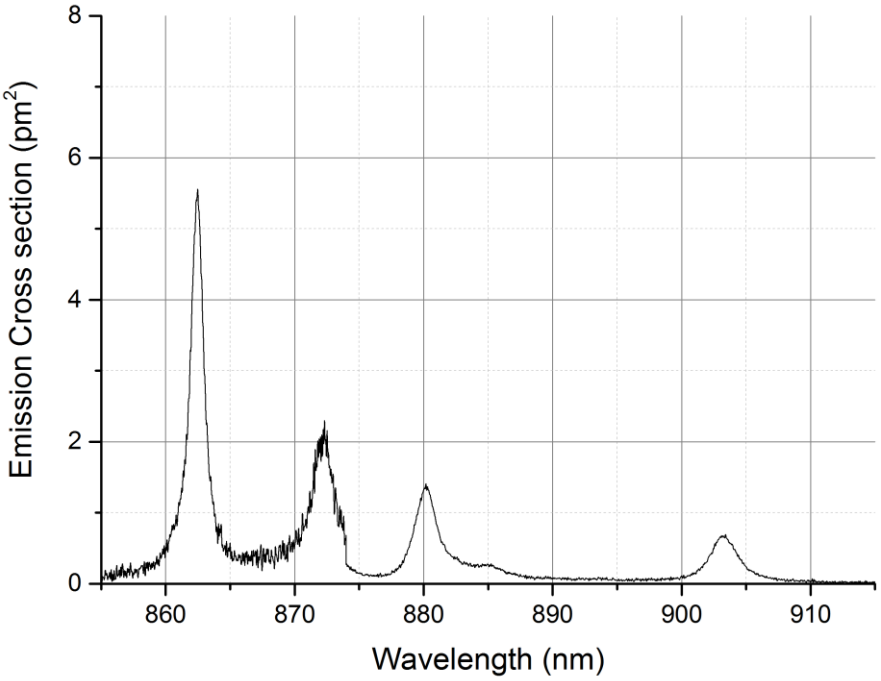

Figure A-177 Emission cross section of Nd:YLF $^4I_{9/2}$, E//c at 273K

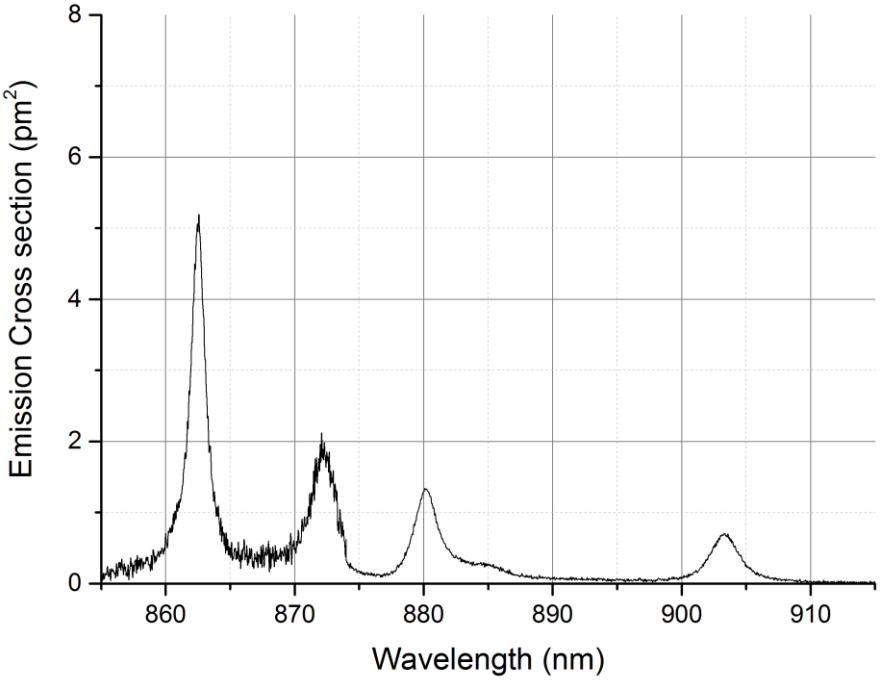

Figure A-178 Emission cross section of Nd:YLF $^4I_{9/2}$, E//c at 300K

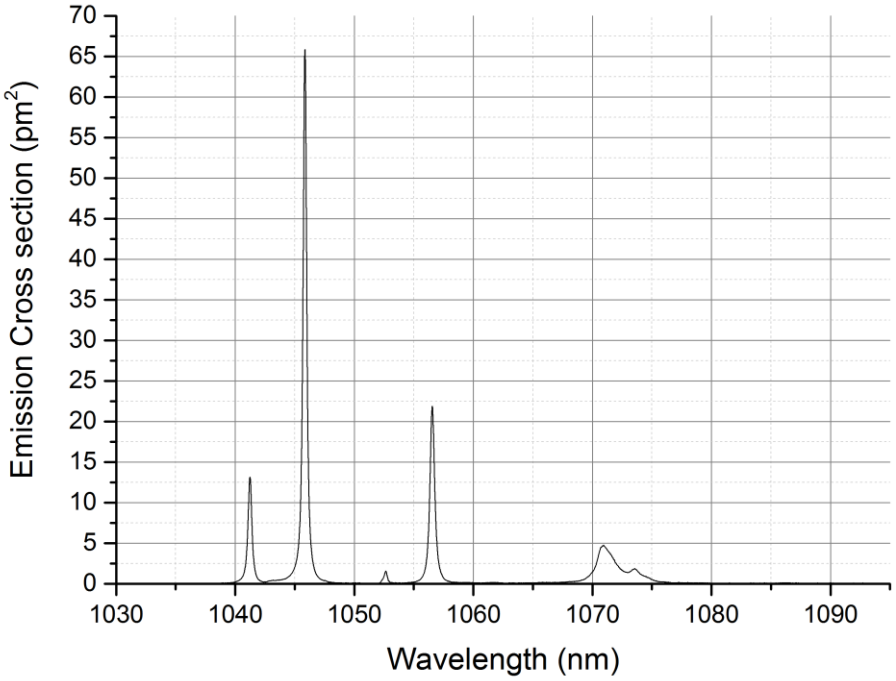

Figure A-179 Emission cross section of Nd:YLF $^4I_{11/2}$, E//c at 77K

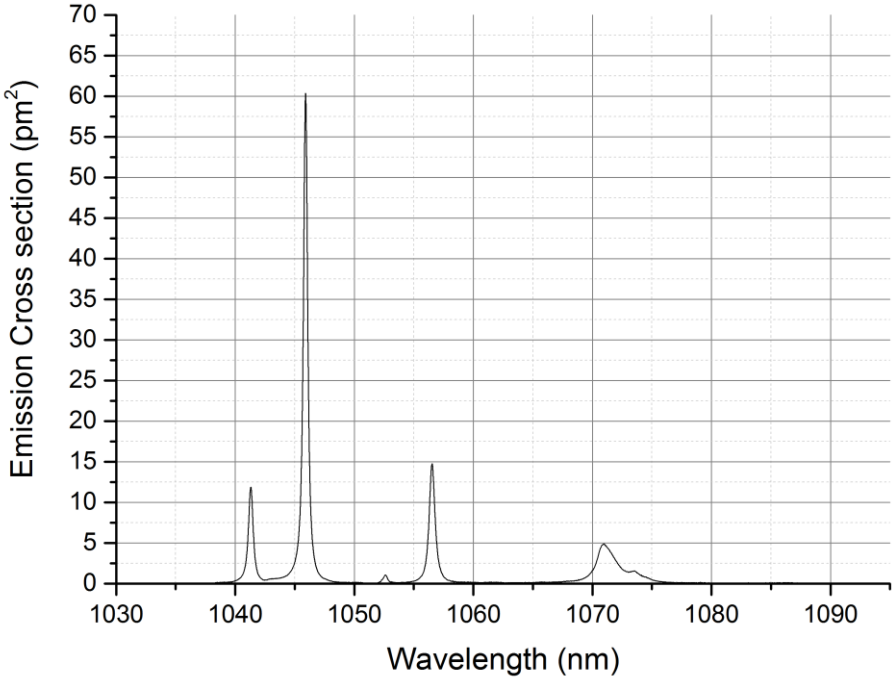

Figure A-180 Emission cross section of Nd:YLF $^4I_{11/2}$, E//c at 100K

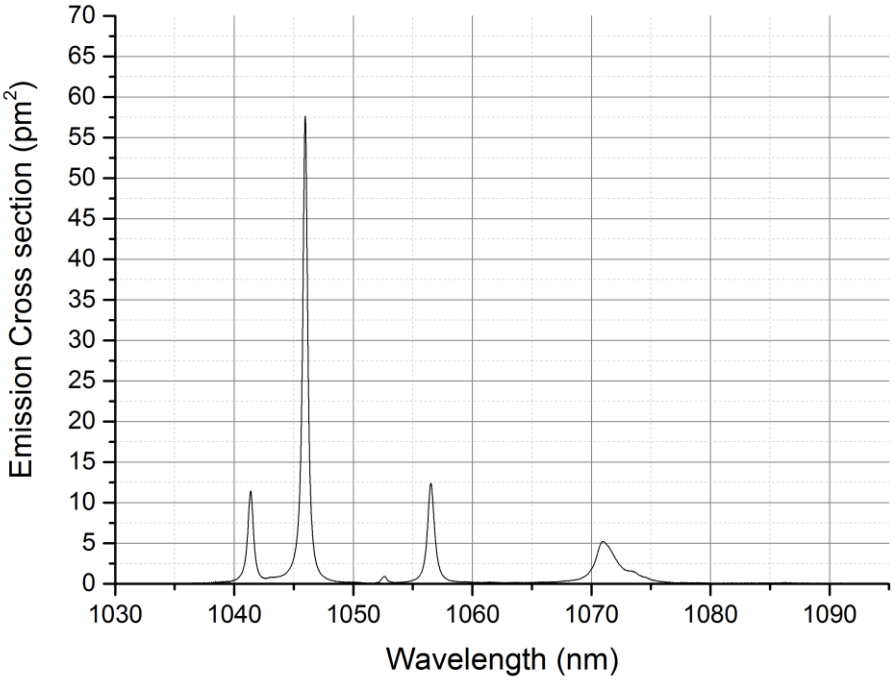

Figure A-181 Emission cross section of Nd:YLF $^4I_{11/2}$, E//c at 125K

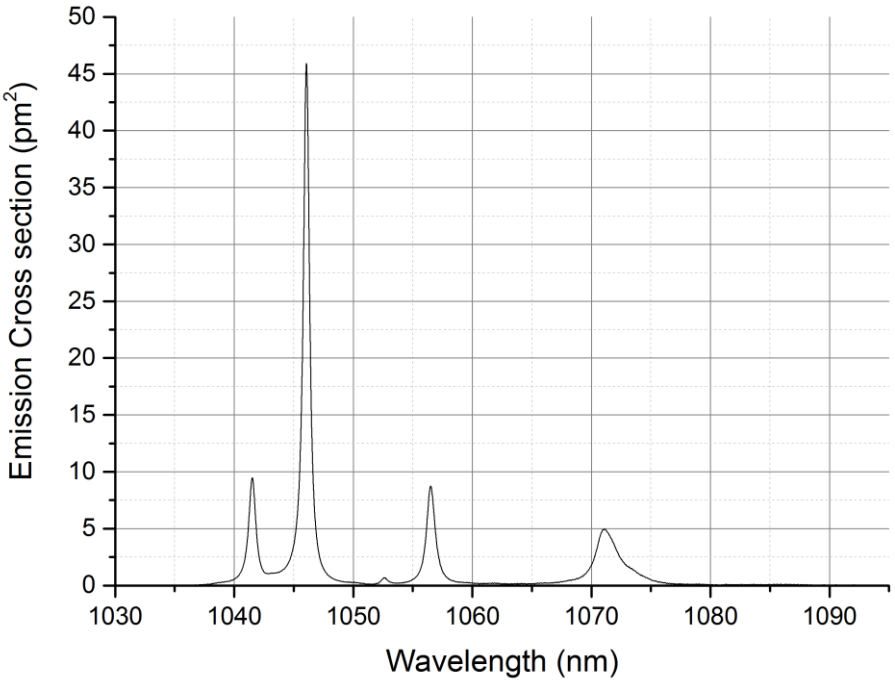

Figure A-182 Emission cross section of Nd:YLF $^4I_{11/2}$, E//c at 165K

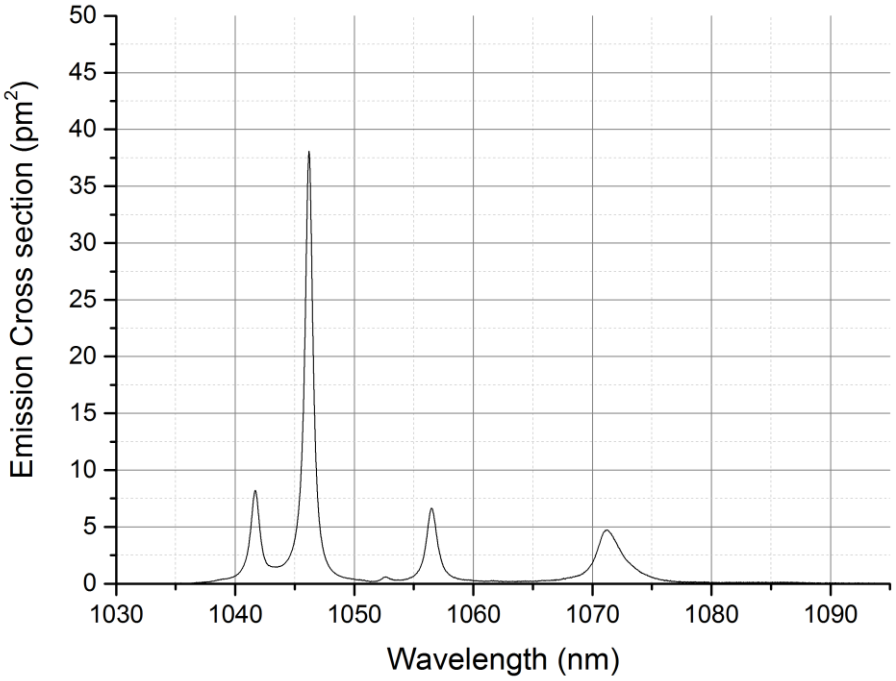

Figure A-183 Emission cross section of Nd:YLF $^4I_{11/2}$, E//c at 195K

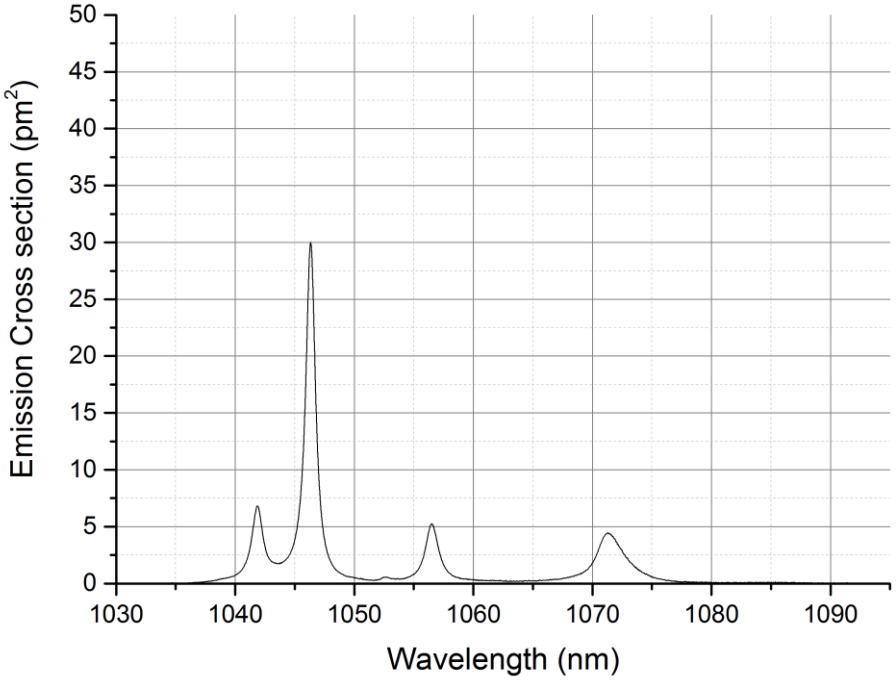

Figure A-184 Emission cross section of Nd:YLF $^4I_{11/2}$, E//c at 235K

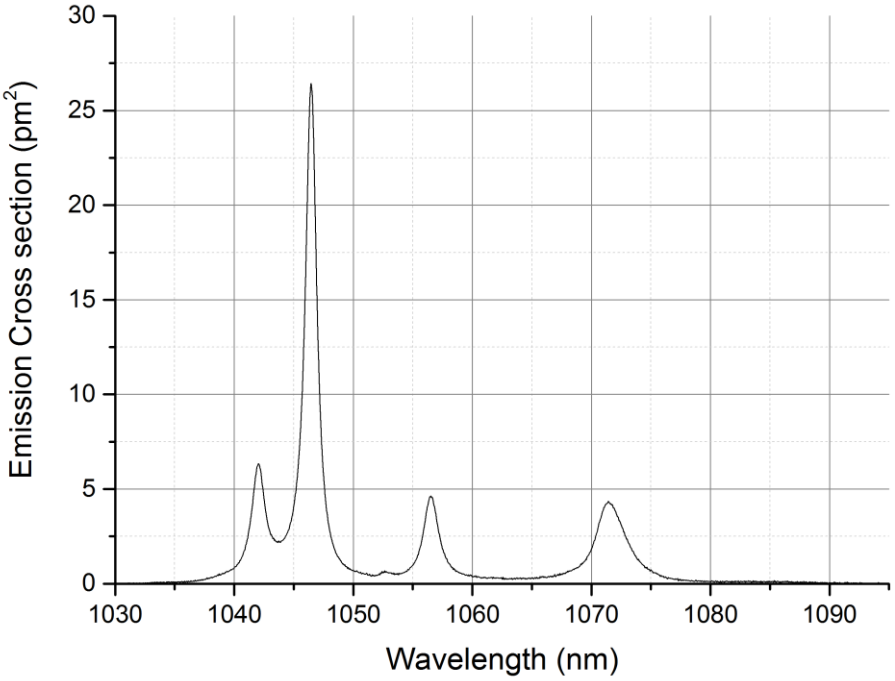

Figure A-185 Emission cross section of Nd:YLF $^4I_{11/2}$, E//c at 273K

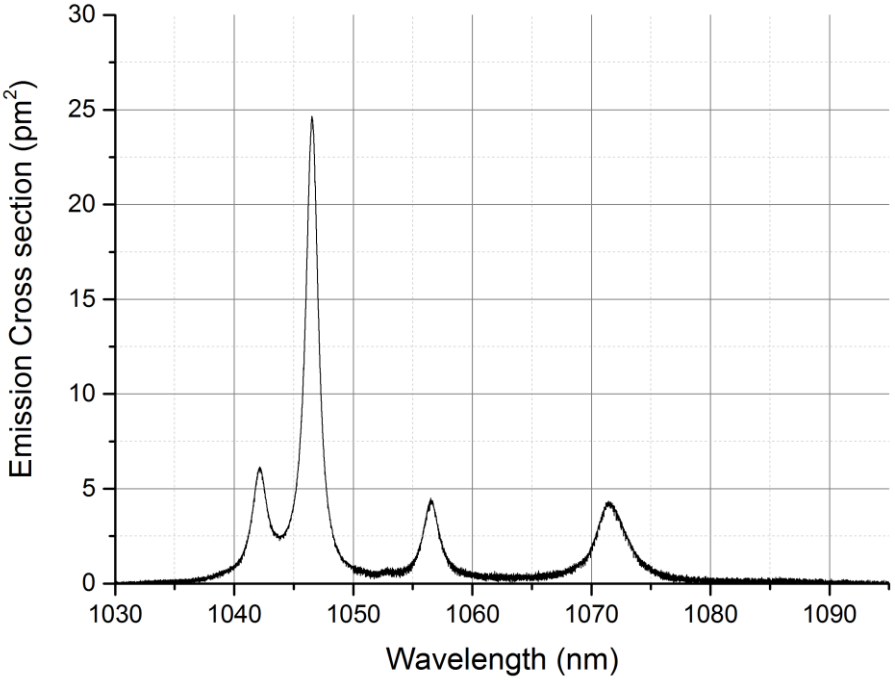

Figure A-186 Emission cross section of Nd:YLF $^4I_{11/2}$, E//c at 300K

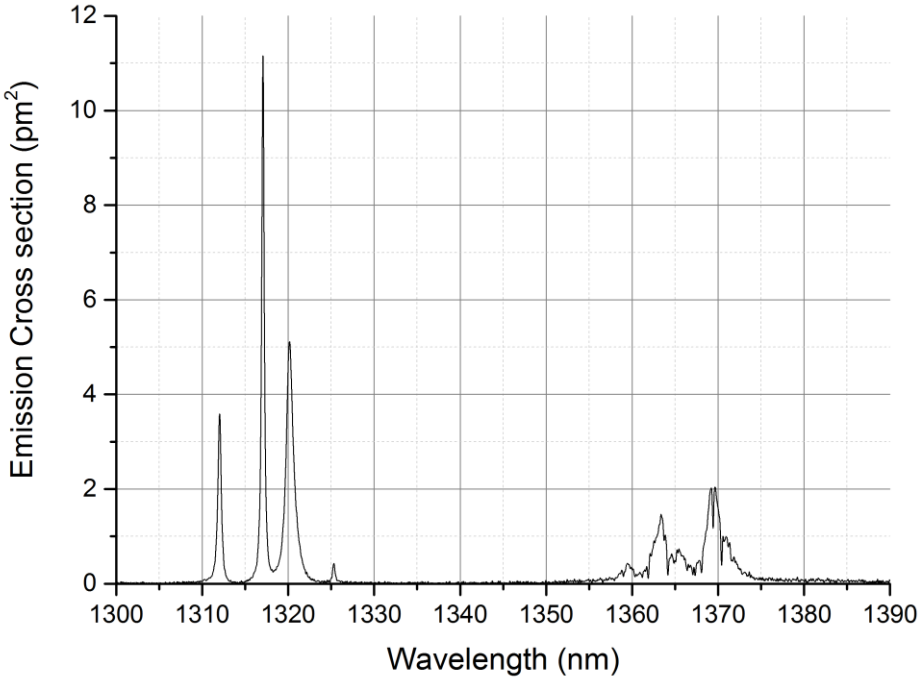

Figure A-187 Emission cross section of Nd:YLF $^4I_{13/2}$, E//c at 77K

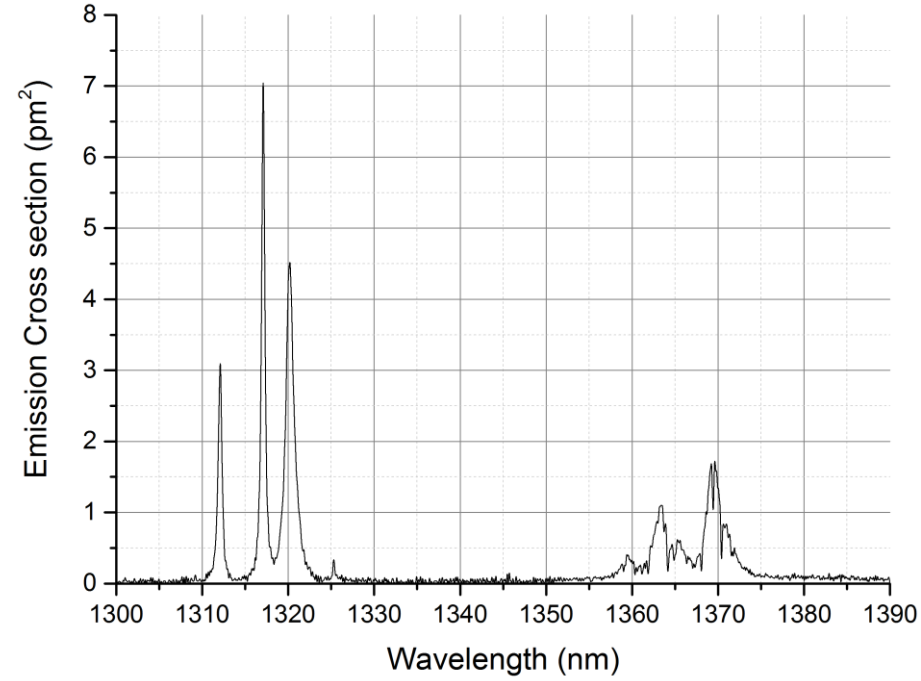

Figure A-188 Emission cross section of Nd:YLF $^4I_{13/2}$, E//c at 100K

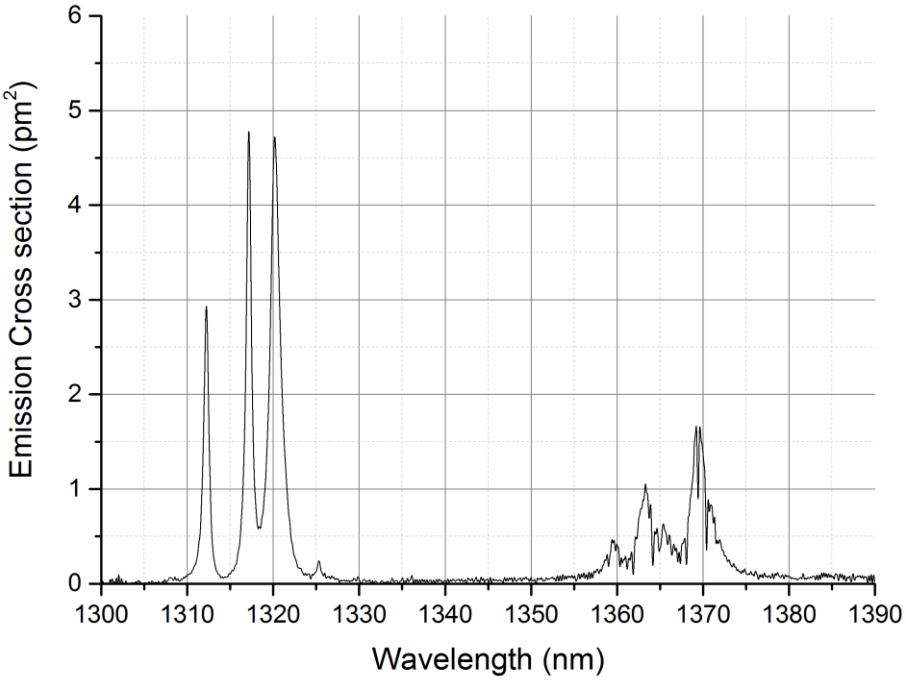

Figure A-189 Emission cross section of Nd:YLF $^4I_{13/2}$, E//c at 120K

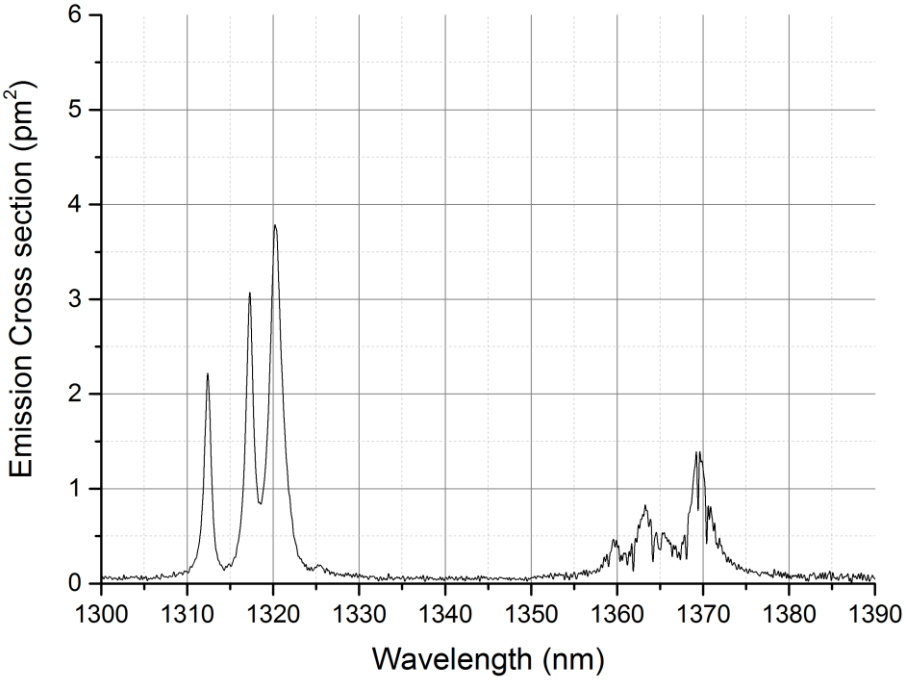

Figure A-190 Emission cross section of Nd:YLF $^4I_{13/2}$, E//c at 165K

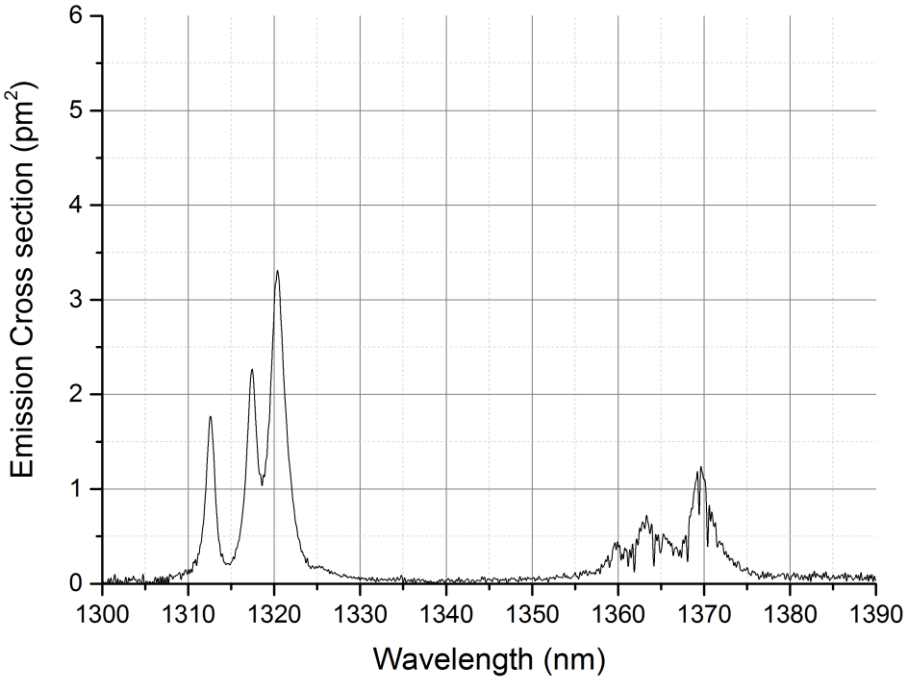

Figure A-191 Emission cross section of Nd:YLF $^4I_{13/2}$, E//c at 195K

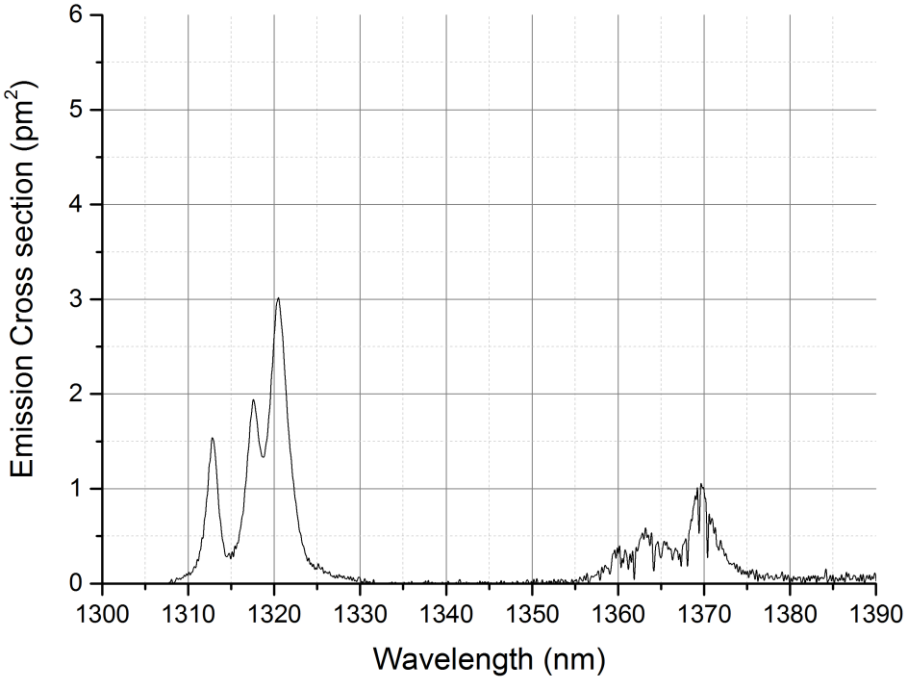

Figure A-192 Emission cross section of Nd:YLF $^4I_{13/2}$, E//c at 235K

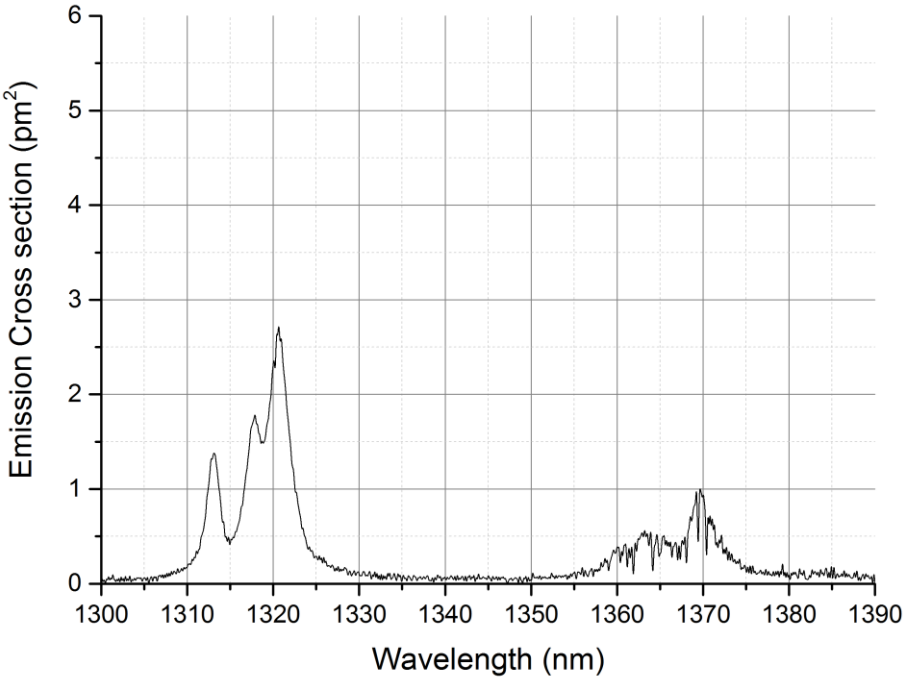

Figure A-193 Emission cross section of Nd:YLF $^4I_{13/2}$, E//c at 273K

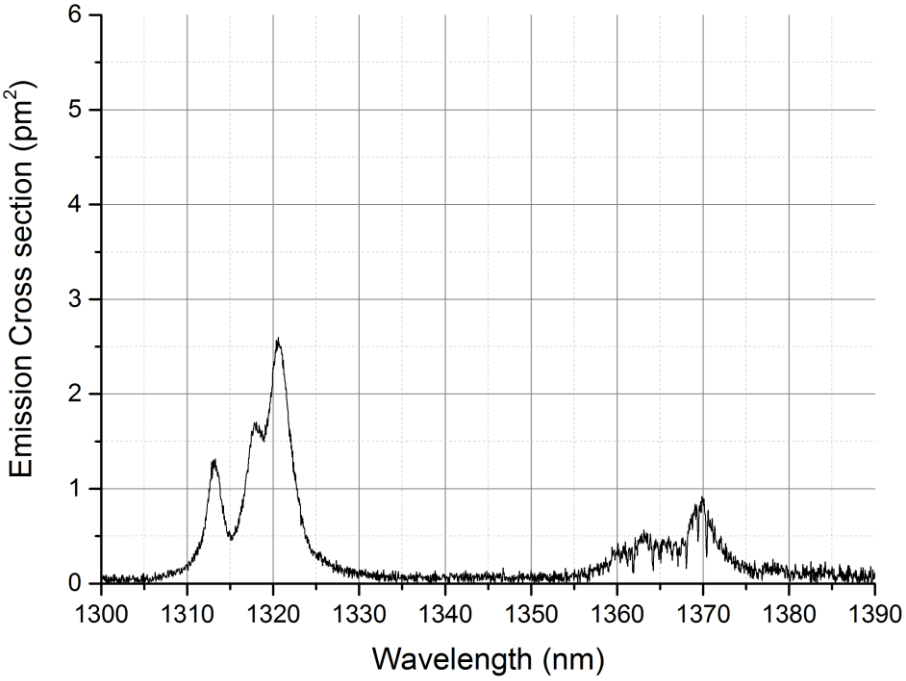

Figure A-194 Emission cross section of Nd:YLF $^4I_{13/2}$, E//c at 300K

A.9 Emission cross section of Nd:KGW

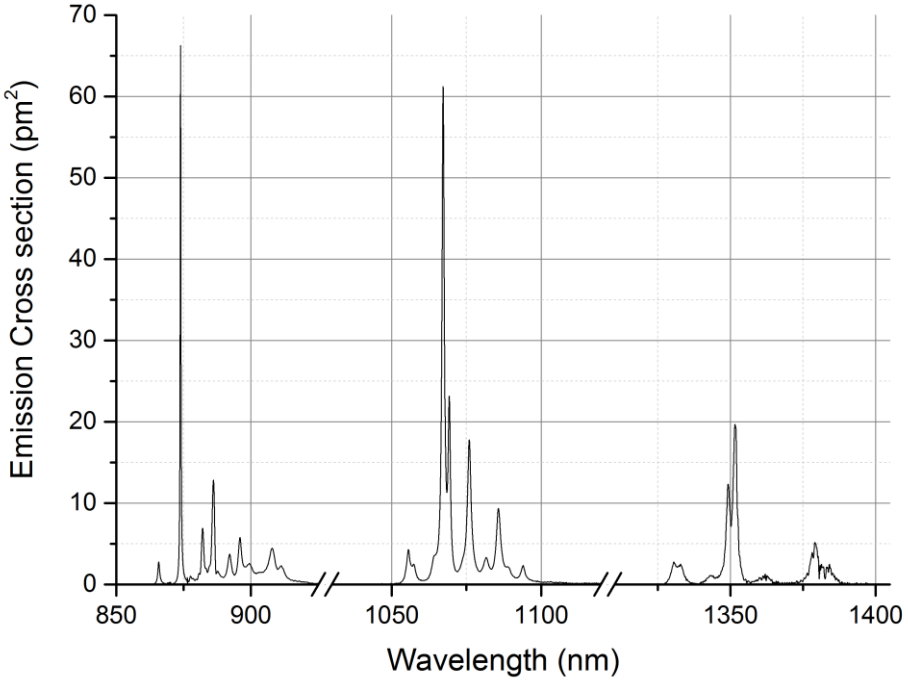

Figure A-195 Emission cross section of Nd:KGW, E//Nm at 77K

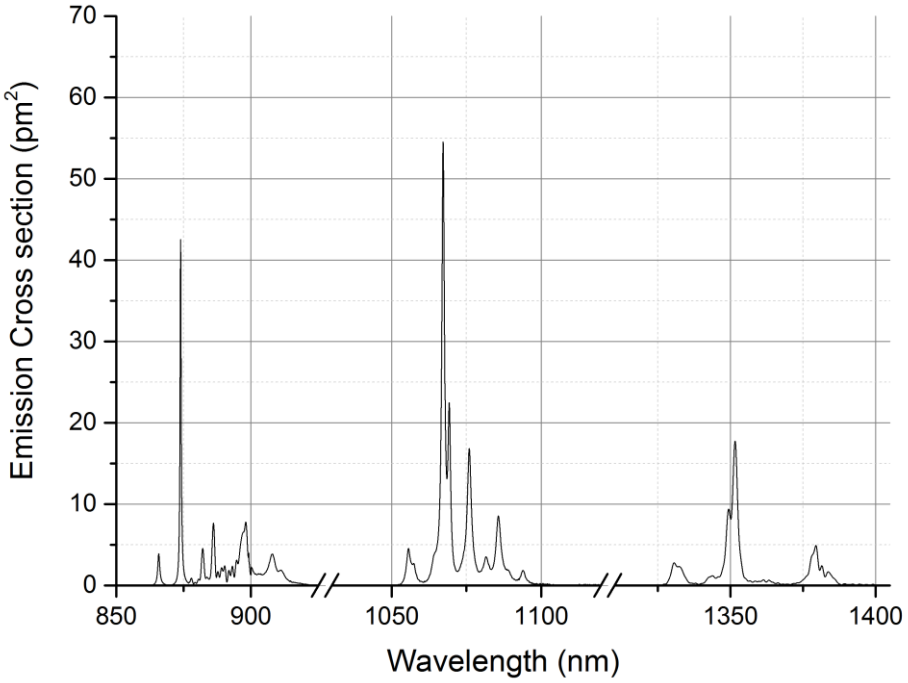

Figure A-196 Emission cross section of Nd:KGW, E//Nm at 95K

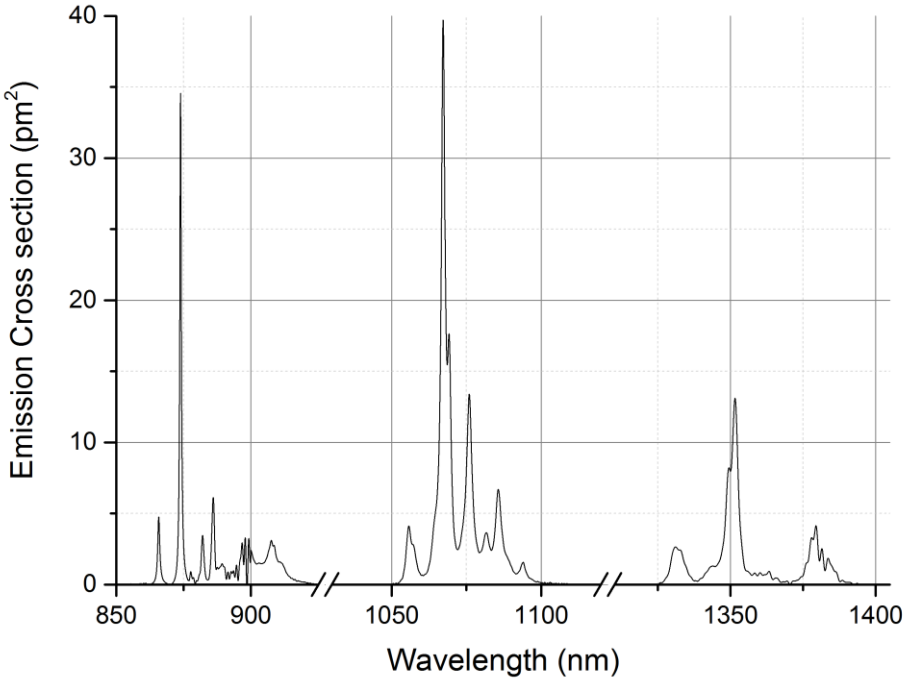

Figure A-197 Emission cross section of Nd:KGW, E//Nm at 123K

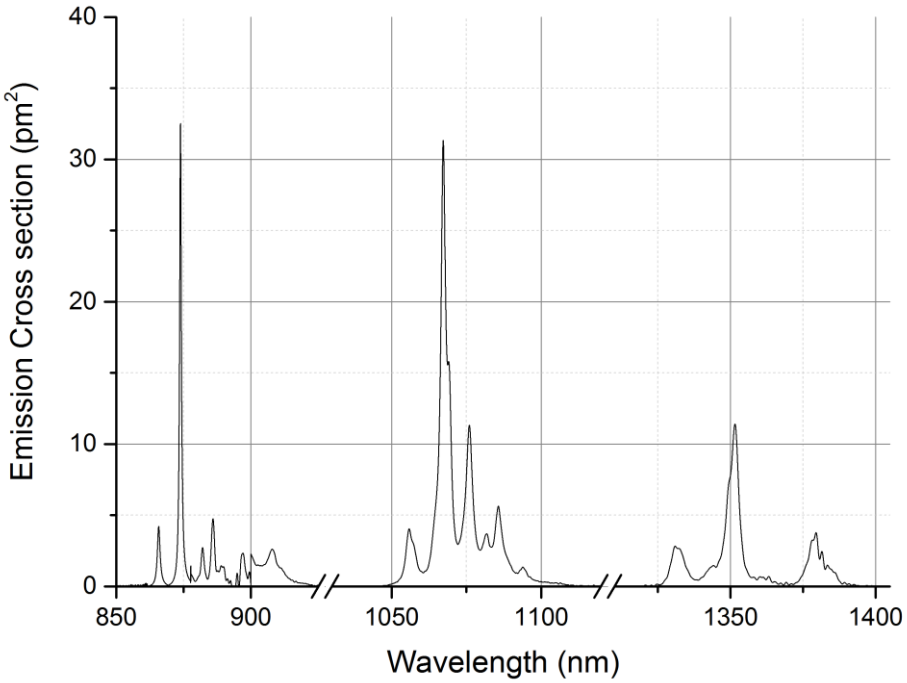

Figure A-198 Emission cross section of Nd:KGW, E//Nm at 162K

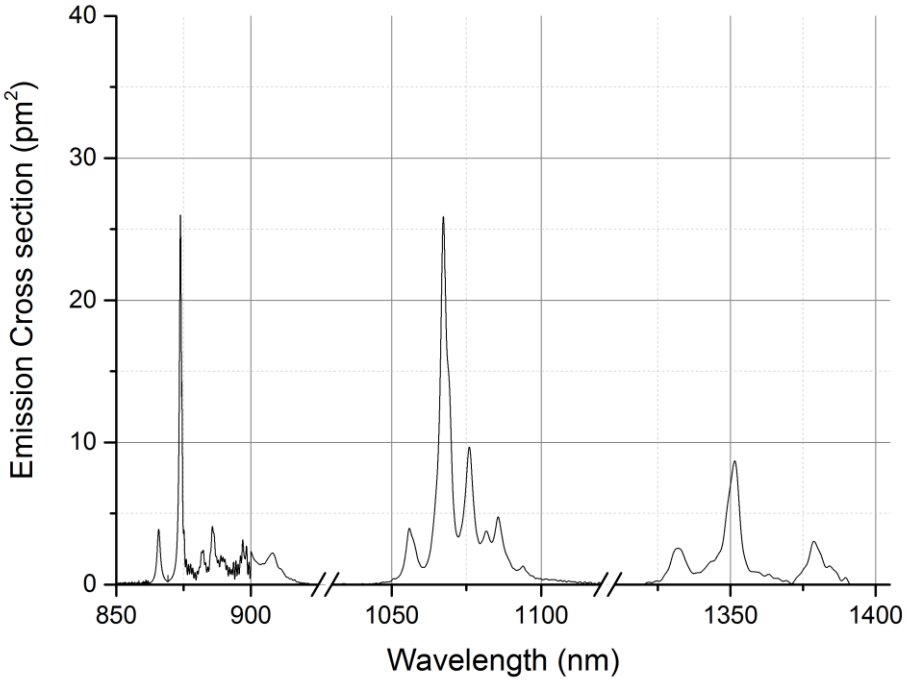

Figure A-199 Emission cross section of Nd:KGW, E//Nm at 195K

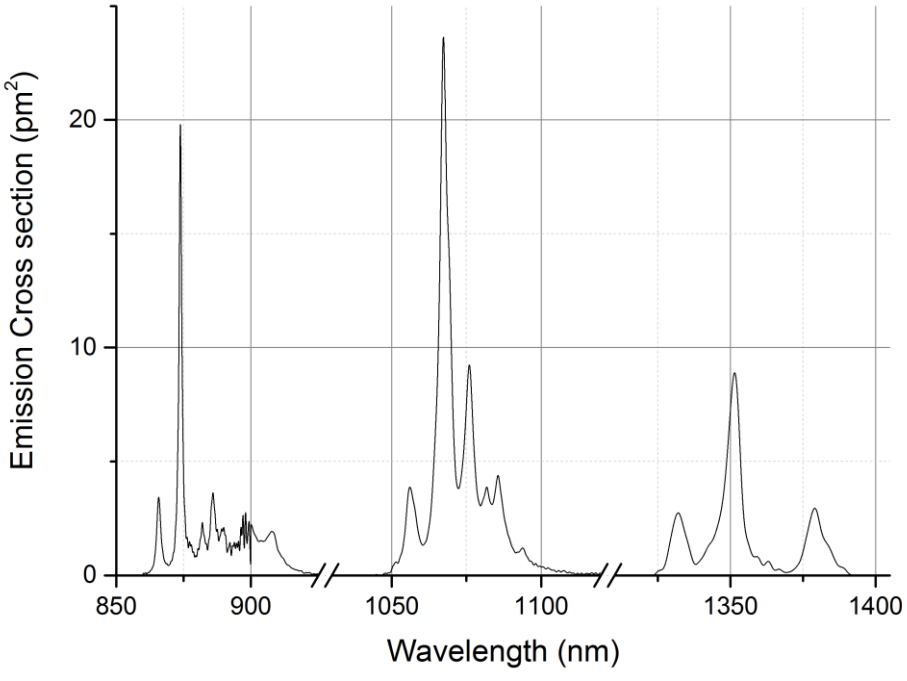

Figure A-200 Emission cross section of Nd:KGW, E//Nm at 235K

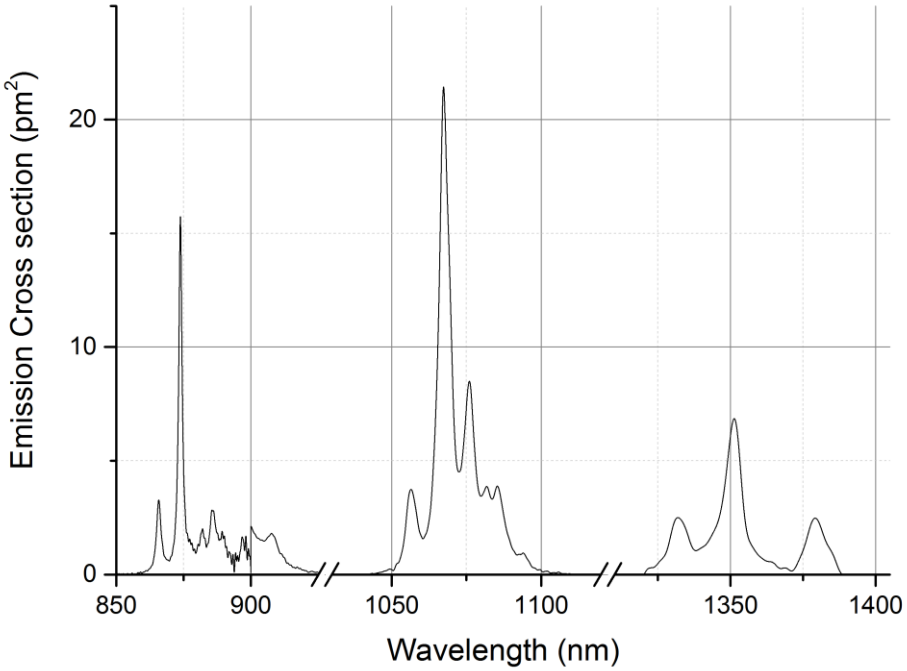

Figure A-201 Emission cross section of Nd:KGW, E//Nm at 270K

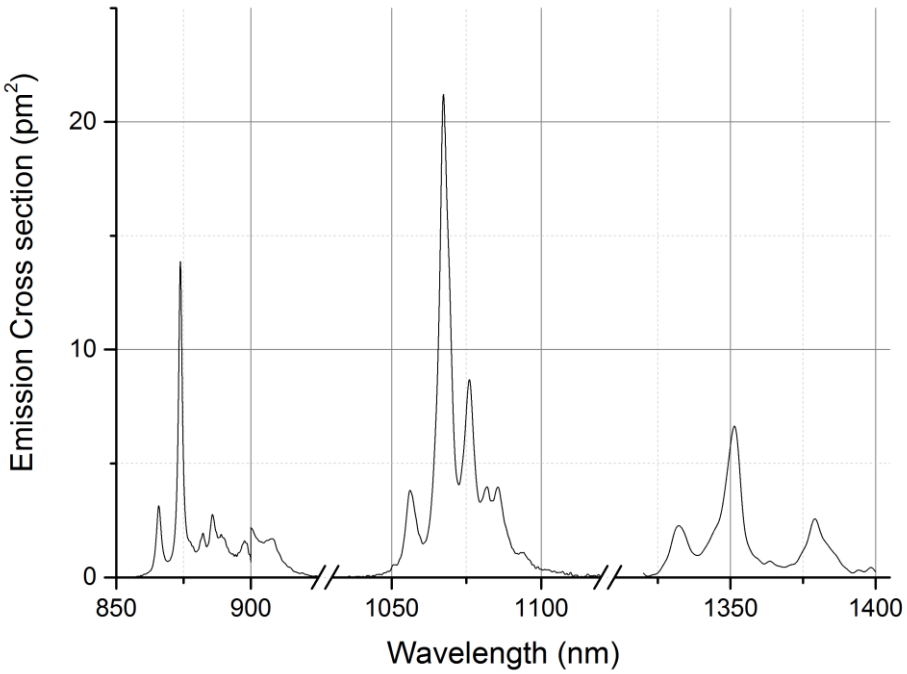

Figure A-202 Emission cross section of Nd:KGW, E//Nm at 300K

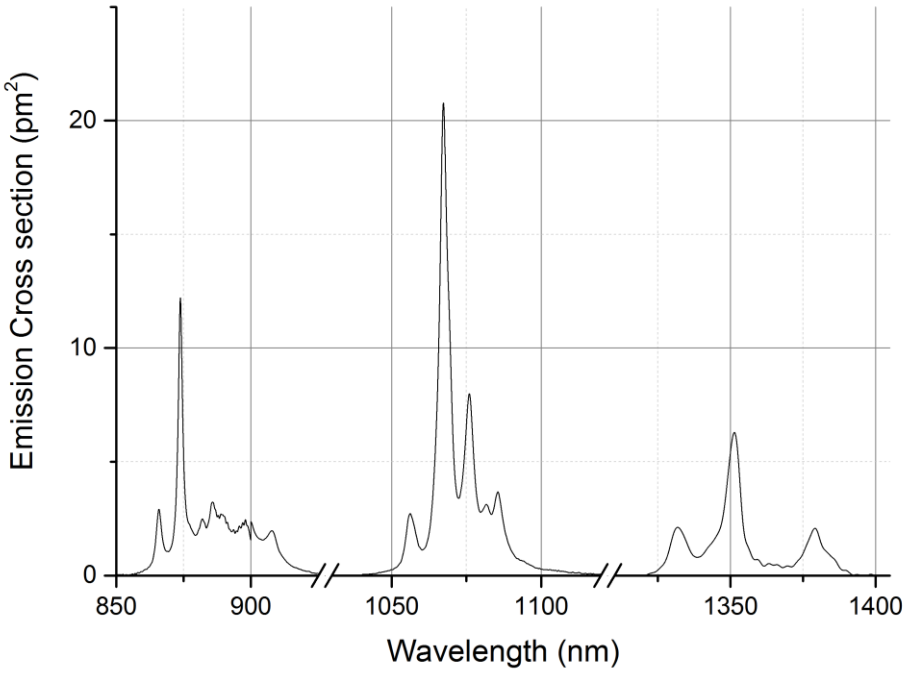

Figure A-203 Emission cross section of Nd:KGW, E//Nm at 330K

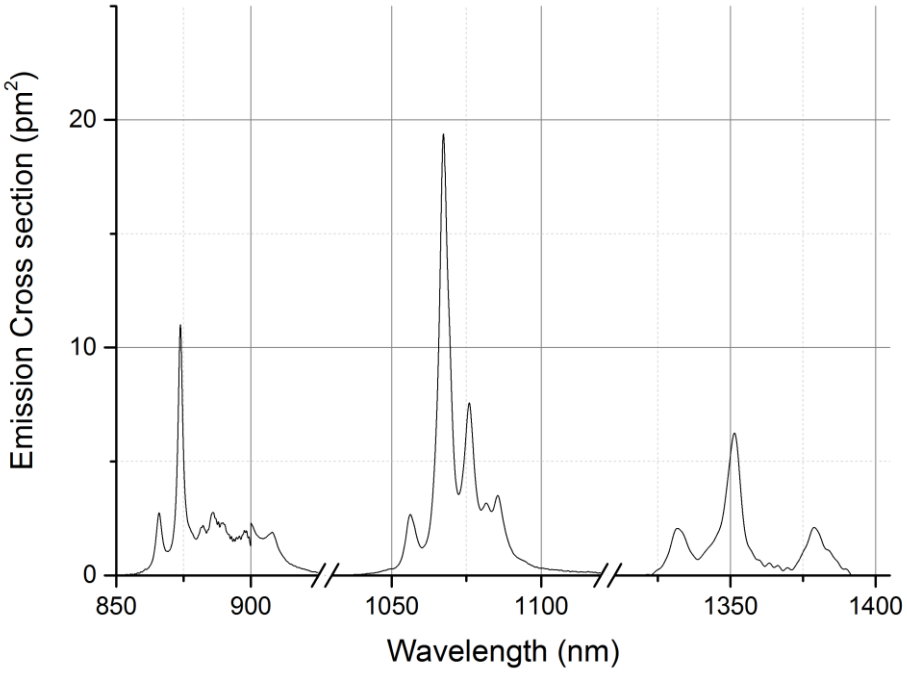

Figure A-204 Emission cross section of Nd:KGW, E//Nm at 360K

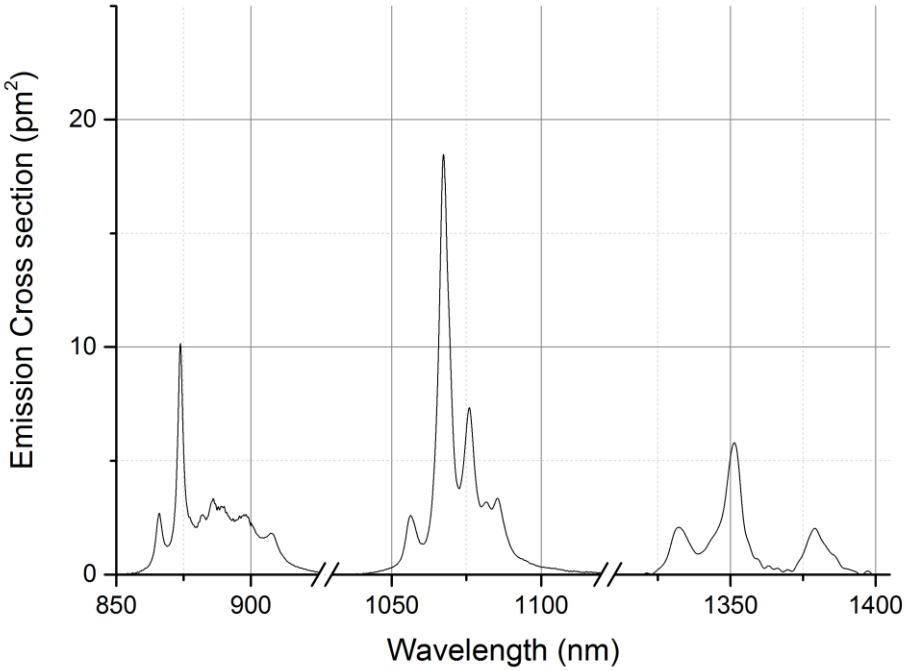

Figure A-205 Emission cross section of Nd:KGW, E//Nm at 390K

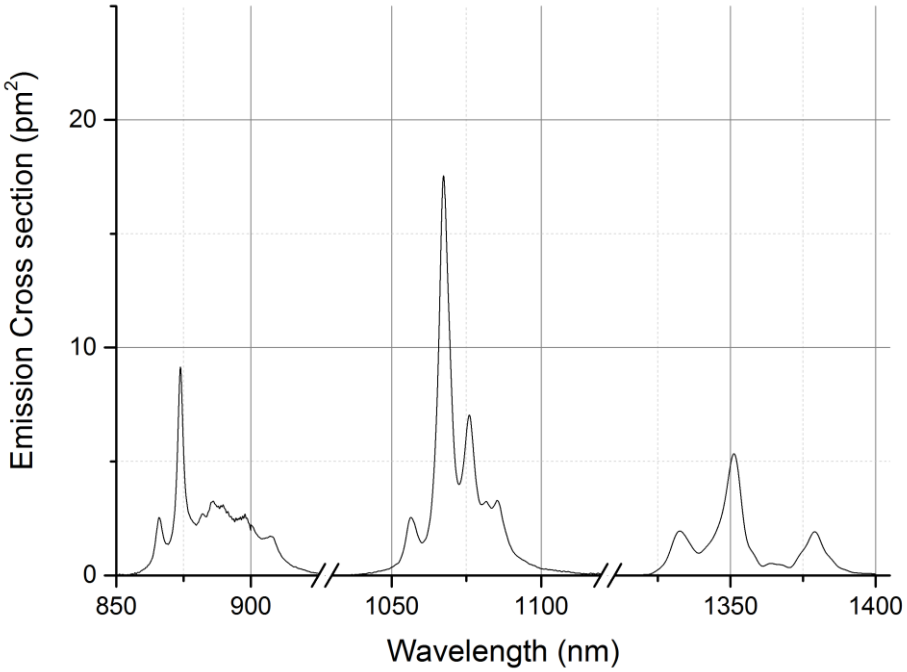

Figure A-206 Emission cross section of Nd:KGW, E//Nm at 420K

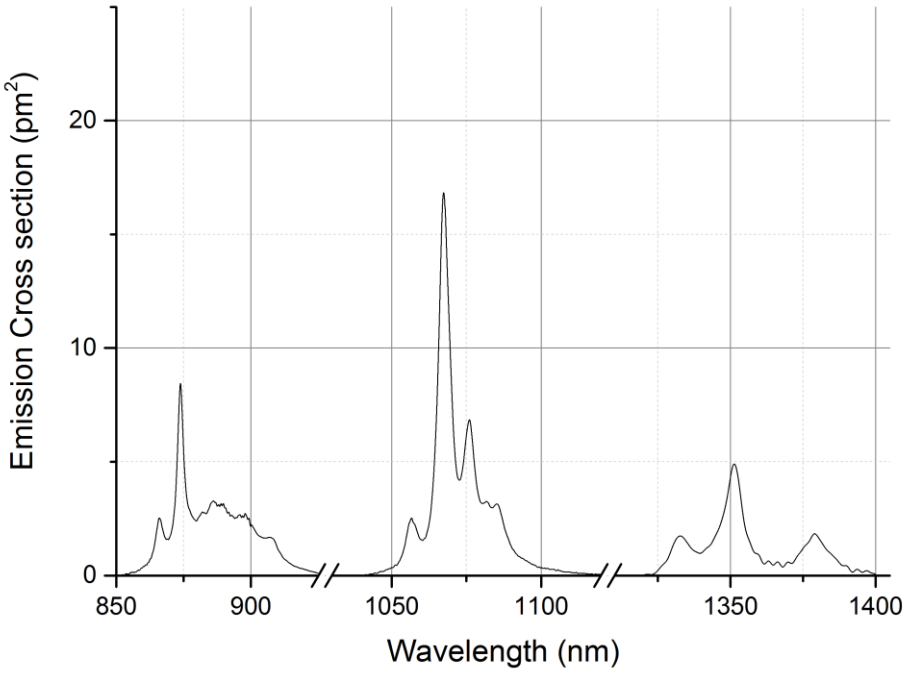

Figure A-207 Emission cross section of Nd:KGW, E//Nm at 450K

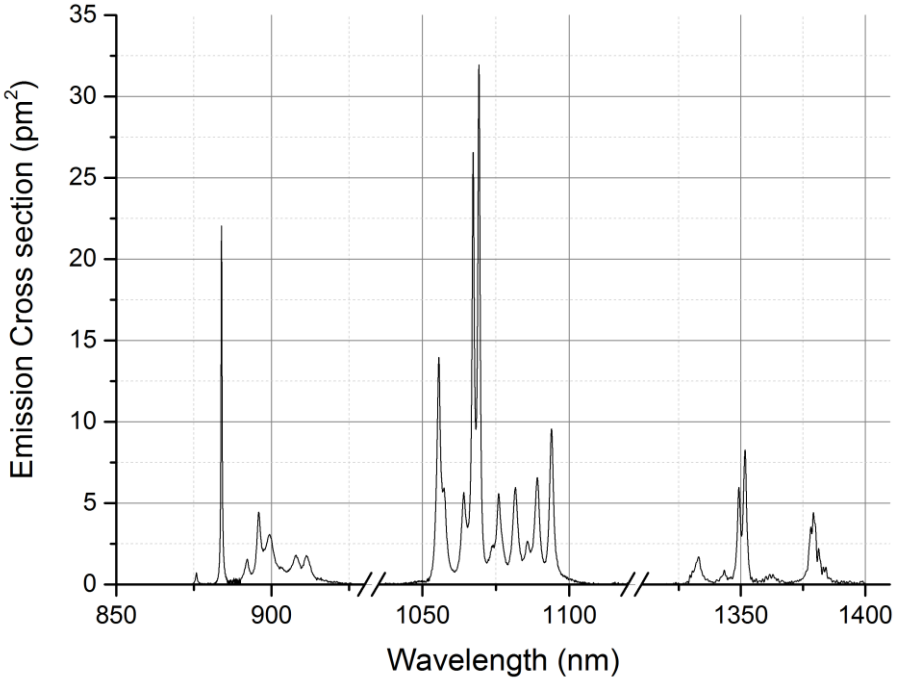

Figure A-208 Emission cross section of Nd:KGW, E//Np at 77K

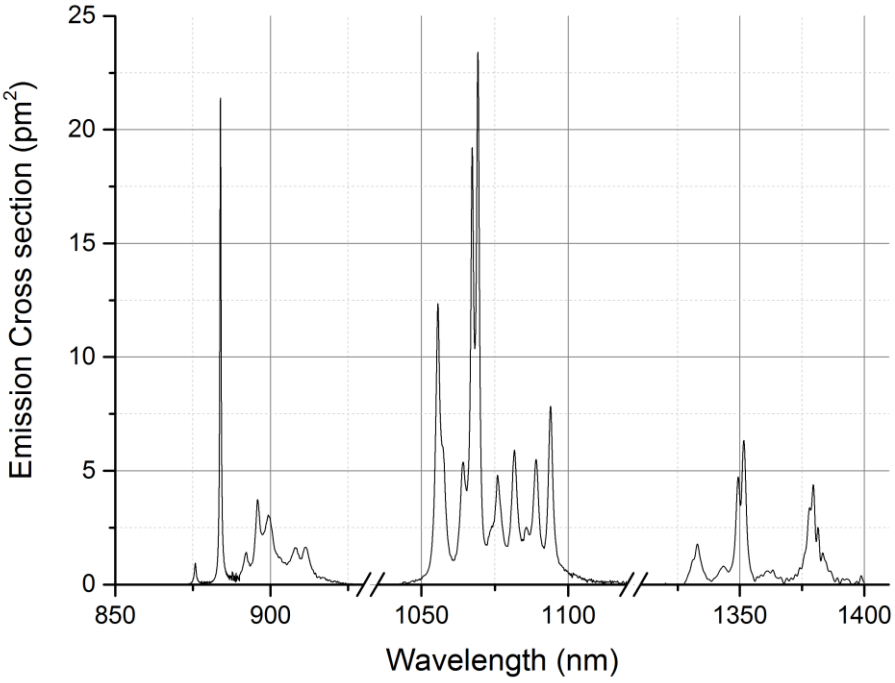

Figure A-209 Emission cross section of Nd:KGW, E//Np at 95K

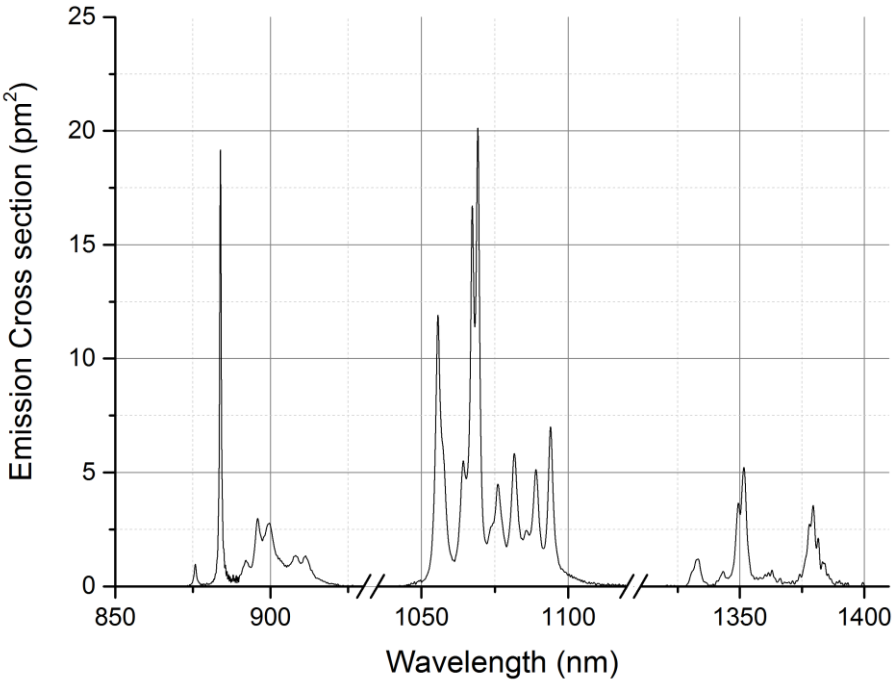

Figure A-210 Emission cross section of Nd:KGW, E//Np at 123K

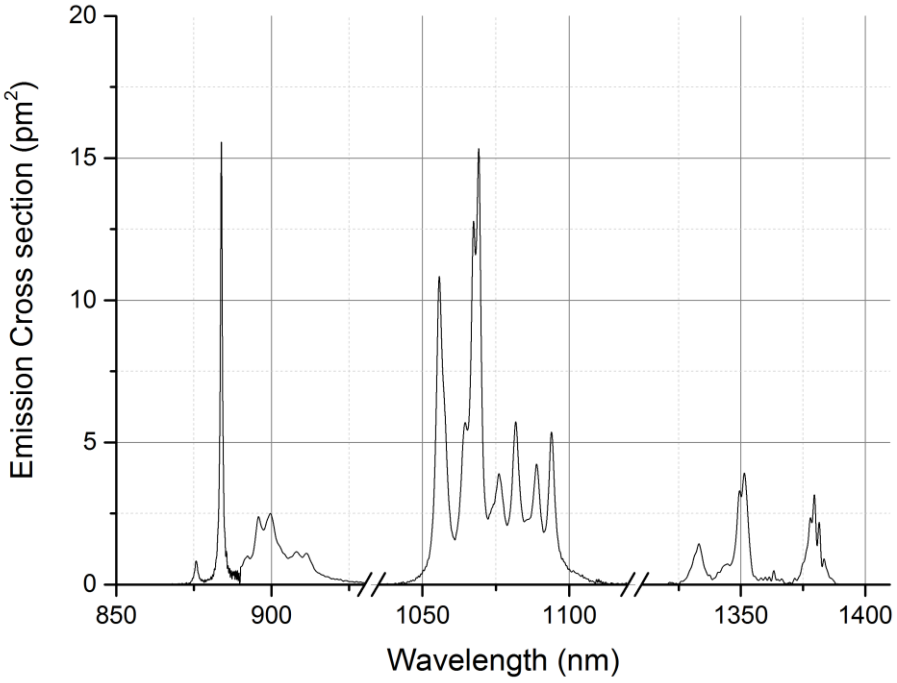

Figure A-211 Emission cross section of Nd:KGW, E//Np at 162K

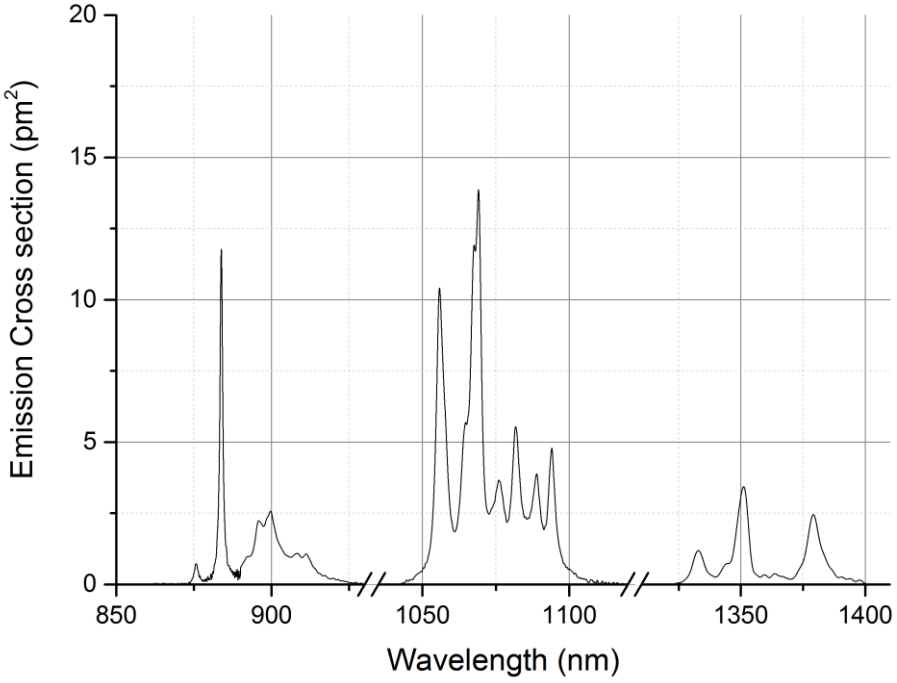

Figure A-212 Emission cross section of Nd:KGW, E//Np at 195K

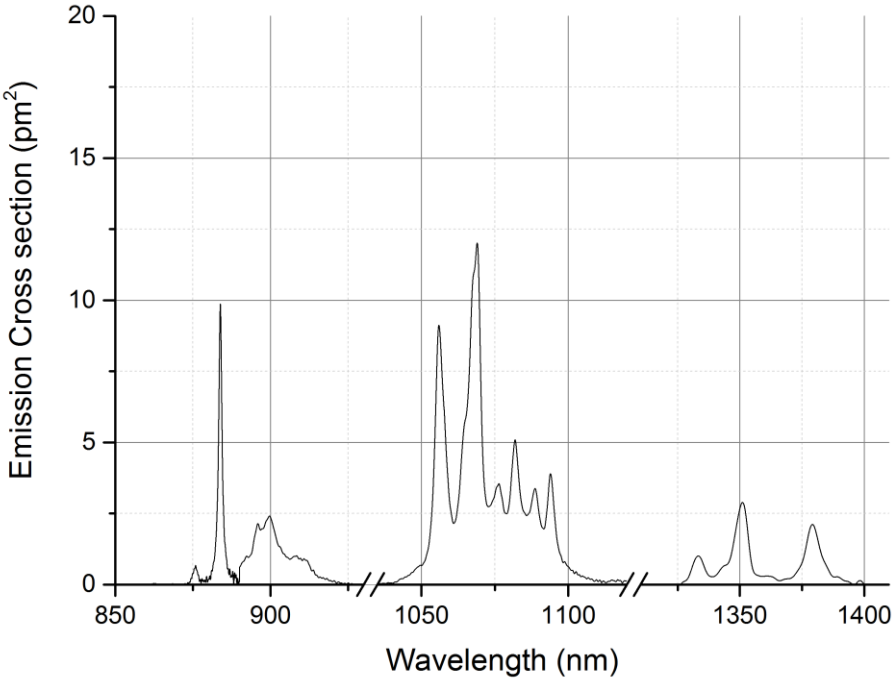

Figure A-213 Emission cross section of Nd:KGW, E//Np at 235K

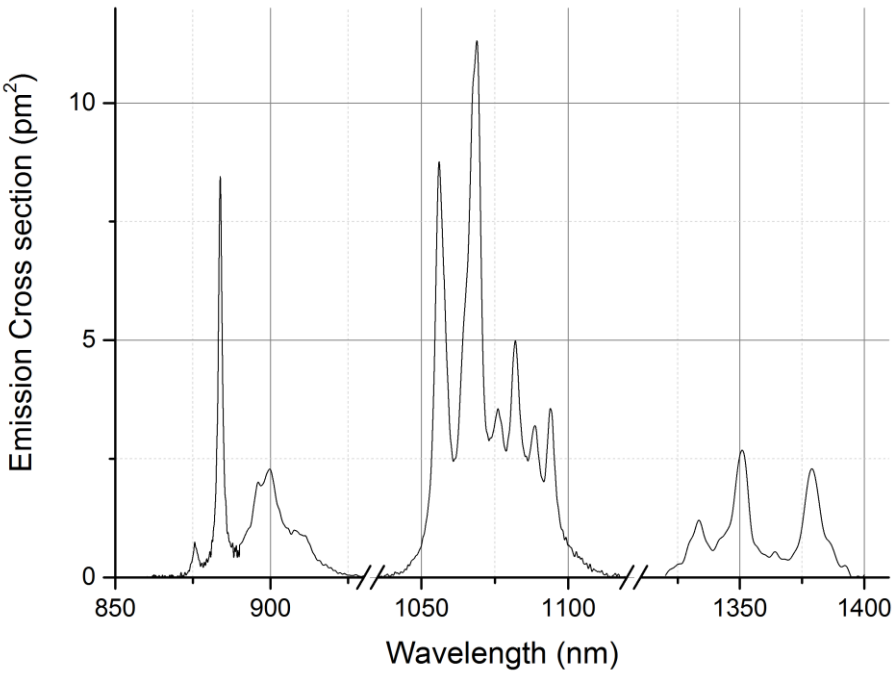

Figure A-214 Emission cross section of Nd:KGW, E//Np at 273K

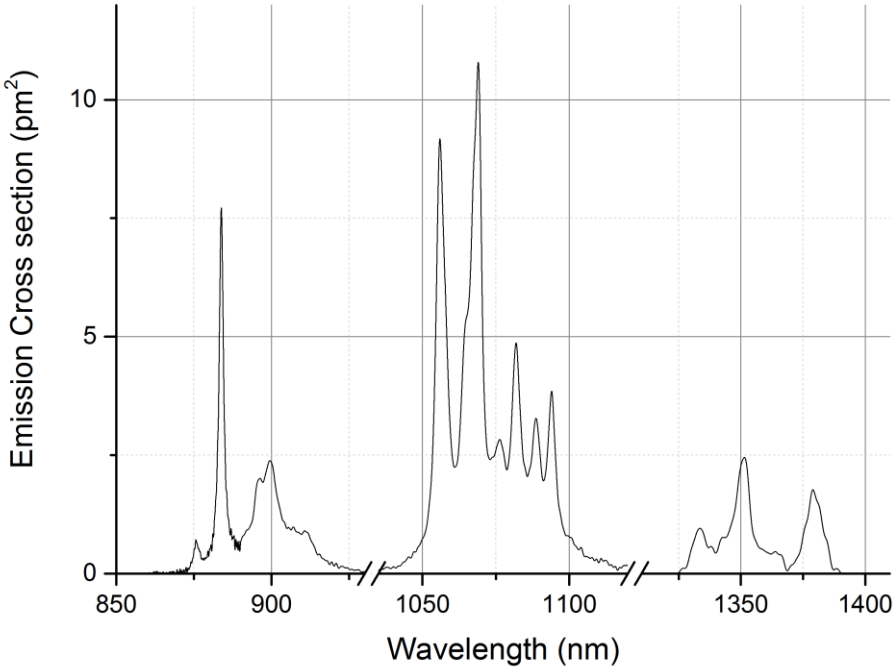

Figure A-215 Emission cross section of Nd:KGW, E//Np at 300K

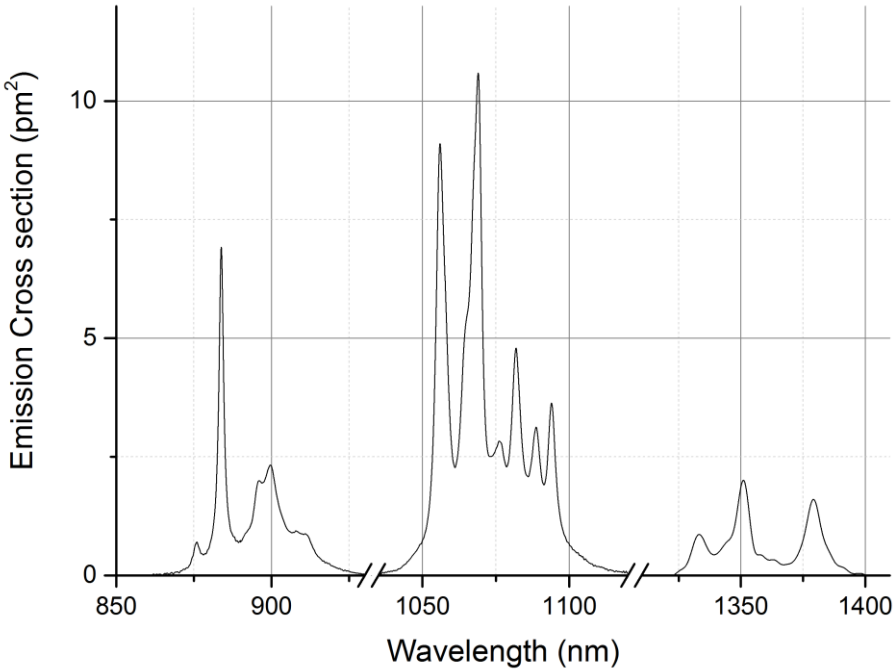

Figure A-216 Emission cross section of Nd:KGW, E//Np at 330K

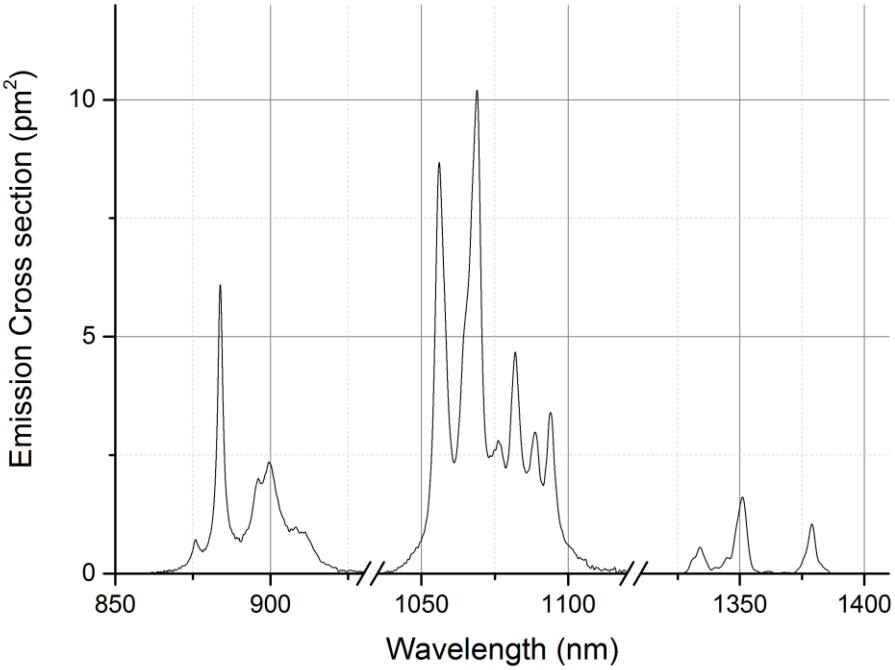

Figure A-217 Emission cross section of Nd:KGW, E//Np at 360K

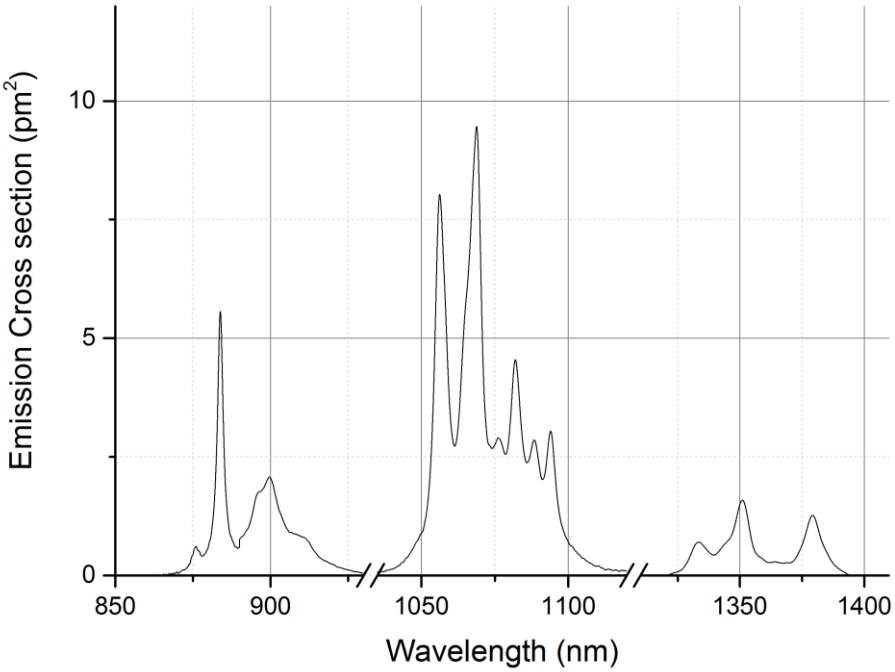

Figure A-218 Emission cross section of Nd:KGW, E//Np at 390K

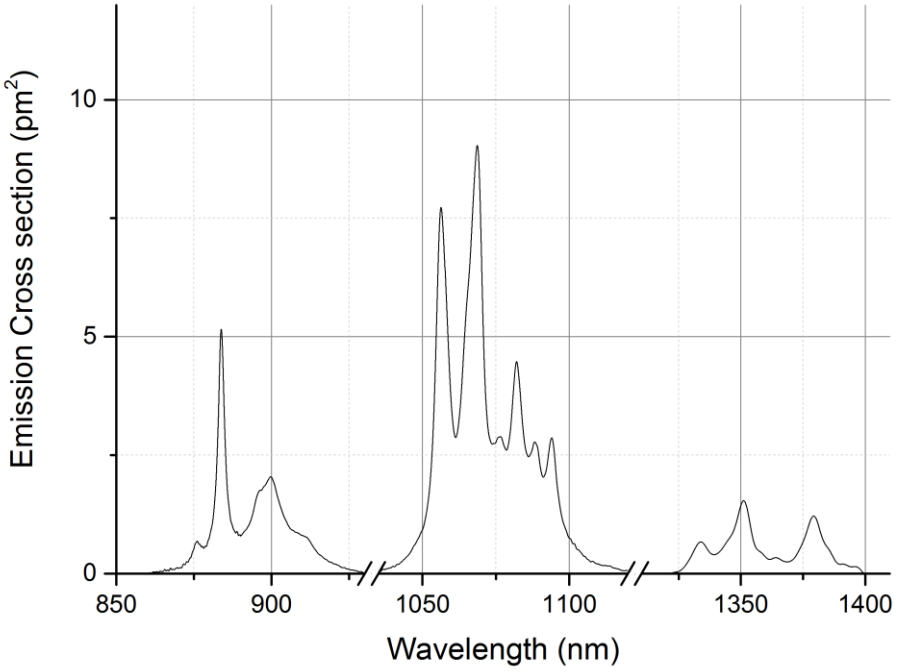

Figure A-219 Emission cross section of Nd:KGW, E//Np at 420K

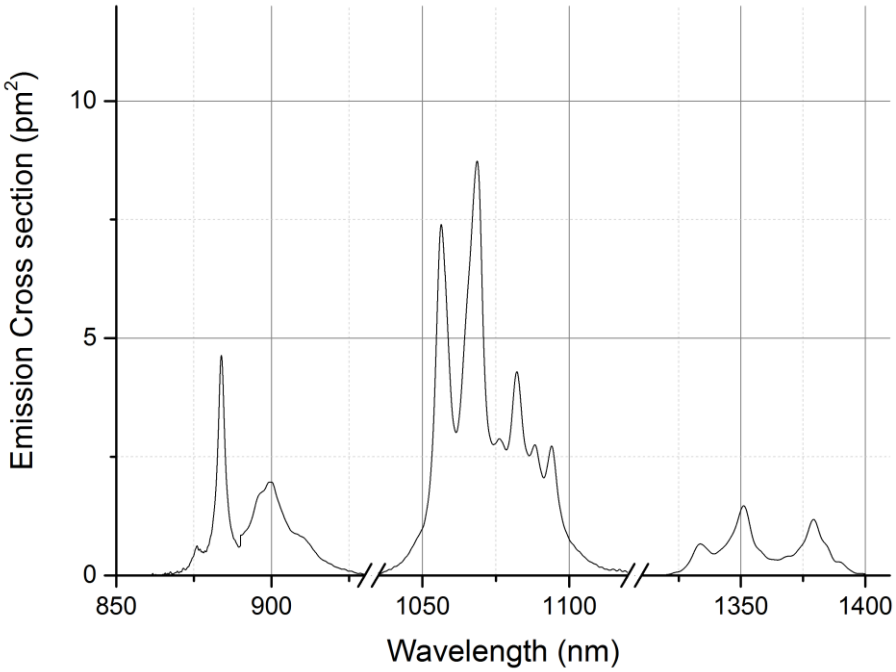

Figure A-220 Emission cross section of Nd:KGW, E//Np at 450K

List of Publications

Peer-reviewed Journals

1 P.Loiko, S.J.Yoon, J.M.Serres, X.Mateos, S.Beecher, R.B.Birch, V.G.Savitski, A.J.Kemp, K.Yumashev, U.Griebner, V.Petrov, M.Aguiló, F.Diaz, J.I.Mackenzie, “Temperature-dependent spectroscopy and microchip laser operation of Nd:KGd(WO4)2,” Optical Materials 58, 365 (2016)

2 S.J.Yoon, R.P.Yan, S.J.Beecher, J.I.Mackenzie, “Concentration dependence of energy transfer upconversion in Nd:YAG,” Optical Materials Express 5 (5), 926-931 (2015).

3 R.P.Yan, S.J.Yoon, S.J.Beecher, J.I.Mackenzie, “Measuring the elevated temperature dependence of upconversion in Nd:YAG,” IEEE Journal of Selected Topics in Quantum Electronics 21 (1) (2015)

4 S.J.Yoon, J.I.Mackenzie, “Cryogenically cooled 946nm Nd:YAG laser,” Optics Express 22 (7), 8069-8075 (2014)

Conference Publications

1 S.J.Yoon, S.J.Beecher, J.I.Mackenzie, “Temperature dependent Nd:KGW spectroscopy study,” CLEO/Europe - EQEC Munich 21-25 Jun 2015

2 S.J.Yoon, R.P.Yan, S.J.Beecher, J.I.Mackenzie, “Energy transfer upconversion measurements for popular neodymium-doped crystals,” SPIE Photonics West '15 San Francisco 7-12 Feb 2015

3 S.J.Yoon, R.P.Yan, S.J.Beecher, J.I.Mackenzie, “Concentration dependence of energy transfer upconversion in Nd:YAG” Advanced Solid State Lasers (ASSL) Shanghai 17-21 Nov 2014

4 S.J.Yoon, J.I.Mackenzie, ”Implications of the temperature dependence of Nd:YAG spectroscopic values for low temperature laser operation at 946nm,” SPIE Photonics Europe '14 Brussels 14-17 Apr 2014 9135-2

5 R.P.Yan, S.J.Yoon, S.J.Beecher, J.I.Mackenzie, “Measurement of energy transfer upconversion in Nd:YAG via the z-scan technique,” SPIE Conference 9135, Laser Sources and Applications II 2014

6 S.J. Yoon, J.I. Mackenzie, “Cryogenically cooled 946nm Nd:YAG laser,” Advanced Solid State Lasers (ASSL) Paris France 27 Oct-1 Nov 2013